

*NASA Conference Publication 3020—Vol. I  
Part 1*

# **Transonic Symposium: Theory, Application, and Experiment**

Jerome T. Foughner, Jr., *Compiler*  
*Langley Research Center*  
*Hampton, Virginia*

Proceedings of a symposium sponsored by the  
National Aeronautics and Space Administration,  
Washington, D.C., and held at  
NASA Langley Research Center  
Hampton, Virginia  
April 19–21, 1988

**ORIGINAL CONTAINS  
COLOR ILLUSTRATIONS**



National Aeronautics  
and Space Administration

**Scientific and Technical  
Information Division**

**1989**

## PREFACE

The last major Transonic Symposium was held at NASA Ames Research Center in February 1981. Since then, significant advances have been made in computer hardware, theoretical and computational methods, applications, experimental facilities, and testing techniques. Although much research remains to be done, these advances now provide us with capabilities in the transonic regime which we hardly envisioned 7 years ago. In order to assess the state of the art in transonic flow disciplines and to glimpse at future directions, the NASA Langley Research Center held a Transonic Symposium on April 19-21, 1988. Emphasis was placed on steady, three-dimensional external, transonic flow and its simulation, both numerically and experimentally.

Papers were presented by researchers from NASA, industry, and universities. The symposium included technical sessions on wind tunnel and flight experiments; computational fluid dynamics applications (industry overviews and configuration analysis design); inviscid methods and grid generation; viscous methods and boundary-layer stability; and wind tunnel techniques and wall interference.

The proceedings are published in two volumes as follows because of the range of classifications:

Volume I, Unclassified (Parts 1 and 2)  
Volume II, Unclassified, FEDD Restricted

A list of attendees is included in this document.

General Chairman:	P. J. Bobbitt
Organizing Committee:	M. D. Salas
	L. E. Putnam
	J. T. Foughner
Technical Committee Chairman:	
Theory and Computational	J. L. Thomas
Applications	E. G. Waggoner
Experiments	L. W. McKinney

**PRECEDING PAGE BLANK NOT FILMED**



## CONTENTS

PREFACE .....	iii
ATTENDEES .....	ix

### Volume I - Part 1

#### SESSION 1: WIND TUNNEL AND FLIGHT EXPERIMENTS

Chairman: P. J. Bobbitt

AIRFRAME/PROPULSION INTEGRATION CHARACTERISTICS AT TRANSONIC SPEEDS .....	1
William P. Henderson and Bobby L. Berrier	
FLIGHT RESEARCH AND TESTING .....	33
Terrill W. Putnam and Theodore G. Ayers	
SHOCK-BOUNDARY-LAYER INTERACTION IN FLIGHT .....	61
Arild Bertelrud	

#### SESSION 2: CFD APPLICATIONS, INDUSTRY OVERVIEWS

Chairman: E. G. Waggoner

TRANSONIC CFD APPLICATIONS AT BOEING .....	79
E. N. Tinoco	
THE APPLICATION OF CFD FOR MILITARY AIRCRAFT DESIGN AT TRANSONIC SPEEDS .....	109
C. W. Smith, W. W. Braymen, I. C. Bhateley, and W. K. Londenber	
APPLIED TRANSONICS AT GRUMMAN .....	133
W. H. Davis	
TRANSONICS AND FIGHTER AIRCRAFT: CHALLENGES AND OPPORTUNITIES FOR CFD .....	153
Luis R. Miranda	
COMPUTATION OF AIRCRAFT COMPONENT FLOW FIELDS AT TRANSONIC MACH NUMBERS USING A THREE-DIMENSIONAL NAVIER-STOKES ALGORITHM .....	175
George D. Shrewsbury, Joseph Vadyak, David M. Schuster, and Marilyn J. Smith	
TRANSONIC AERODYNAMIC DESIGN EXPERIENCE .....	195
E. Bonner	

#### SESSION 3: INVISCID METHODS AND GRID GENERATION

Chairman: J. L. Thomas

EULER SOLVERS FOR TRANSONIC APPLICATIONS .....	217
Bram van Leer	

**PRECEDING PAGE BLANK NOT FILMED**

AN EMBEDDED MESH PROCEDURE FOR LEADING-EDGE VORTEX FLOWS .....	231
Kenneth G. Powell and Earl M. Murman	
ASYMPTOTIC METHODS FOR INTERNAL TRANSONIC FLOWS .....	261
T. C. Adamson, Jr., and A. F. Messiter	
WAVE DRAG DUE TO LIFT FOR TRANSONIC AIRPLANES .....	293
Julian D. Cole and Norman D. Malmuth	
VECTOR POTENTIAL METHODS .....	309
M. Hafez	
DEVELOPMENTS AND TRENDS IN THREE-DIMENSIONAL MESH GENERATION .....	341
Timothy J. Baker	
GENERATION OF UNSTRUCTURED GRIDS AND EULER SOLUTIONS FOR COMPLEX GEOMETRIES ...	377
Rainald Löhner, Paresh Parikh, and Manuel D. Salas	

#### Volume I - Part 2\*

#### SESSION 4: CFD APPLICATIONS, CONFIGURATION ANALYSIS AND DESIGN Chairman: L. E. Putnam

TRANSONIC PROPULSION SYSTEM INTEGRATION ANALYSIS AT MCDONNELL AIRCRAFT COMPANY .....	409
Raymond R. Cosner	
AERODYNAMIC ANALYSIS OF THREE ADVANCED CONFIGURATIONS USING THE TRANAIR FULL-POTENTIAL CODE .....	437
M. D. Madson, R. L. Carmichael, and J. P. Mendoza	
METHOD TO PREDICT EXTERNAL STORE CARRIAGE LOADS AT TRANSONIC SPEEDS .....	453
Bruce S. Rosen	
STEADY AND UNSTEADY TRANSONIC SMALL DISTURBANCE ANALYSIS OF REALISTIC AIRCRAFT CONFIGURATIONS .....	467
John T. Batina, David A. Seidel, Robert M. Bennett, Herbert J. Cunningham, and Samuel R. Bland	
INVERSE WING DESIGN IN TRANSONIC FLOW INCLUDING VISCOUS INTERACTION .....	497
Leland A. Carlson, Robert R. Ratcliff, and Thomas A. Gally	
EULER/NAVIER-STOKES CALCULATIONS OF TRANSONIC FLOW PAST FIXED- AND ROTARY-WING AIRCRAFT CONFIGURATIONS .....	521
J. E. Deese and R. K. Agarwal	

#### SESSION 5: VISCOUS METHODS AND BOUNDARY-LAYER STABILITY Chairman: M. D. Salas

NAVIER-STOKES AND VISCOUS-INVISCID INTERACTION .....	547
Joseph L. Steger and William R. Van Dalsem	

---

\*Part 2 is presented under separate cover.

3-D EULER AND NAVIER-STOKES CALCULATIONS FOR AIRCRAFT COMPONENTS .....	571
Veer N. Vatsa, Bruce W. Wedan, and Eli Turkel	
TURBULENCE AND MODELING IN TRANSONIC FLOW .....	581
Morris W. Rubesin and John R. Viegas	
TURBULENT EDDY VISCOSITY MODELING IN TRANSONIC SHOCK/BOUNDARY-LAYER INTERACTIONS .....	611
G. R. Inger	
STABILITY OF COMPRESSIBLE BOUNDARY LAYERS .....	629
Ali H. Nayfeh	
SECONDARY THREE-DIMENSIONAL INSTABILITY IN COMPRESSIBLE BOUNDARY LAYERS .....	691
Nabil M. El-Hady	

SESSION 6: WIND TUNNEL TECHNIQUES AND WALL INTERFERENCE  
Chairman: L. W. McKinney

TEST TECHNIQUES - A SURVEY PAPER ON CRYOGENIC TUNNELS, ADAPTIVE WALL TEST SECTIONS, AND MAGNETIC SUSPENSION AND BALANCE SYSTEMS .....	705
Robert A. Kilgore, David A. Dress, Stephen W. D. Wolf, and Colin P. Britcher	
AN LDA INVESTIGATION OF THREE-DIMENSIONAL NORMAL SHOCK WAVE BOUNDARY- LAYER INTERACTIONS .....	741
R. M. Chriss, W. R. Hingst, A. J. Strazisar, and T. G. Keith, Jr.	
INSTRUMENTATION ADVANCES FOR TRANSONIC TESTING .....	765
Percy J. Bobbitt	
WALL INTERFERENCE ASSESSMENT AND CORRECTIONS .....	817
P. A. Newman, W. B. Kemp, Jr., and J. A. Garriz	
TWO-MEASURED VARIABLE METHOD FOR WALL INTERFERENCE ASSESSMENT/CORRECTION .....	853
C. F. Lo and W. L. Sickles	
COMPARISON OF AIRFOIL RESULTS FROM AN ADAPTIVE WALL TEST SECTION AND A POROUS WALL TEST SECTION .....	867
Raymond E. Mineck	
CAPABILITIES OF WIND TUNNELS WITH TWO ADAPTIVE WALLS TO MINIMIZE BOUNDARY INTERFERENCE IN 3-D MODEL TESTING .....	891
Rainer Rebstock and Edwin E. Lee, Jr.	

Volume II\*

NATIONAL TRANSONIC FACILITY STATUS L. W. McKinney, W. E. Bruce, Jr., and B. B. Gloss.....	1
----------------------------------------------------------------------------------------------	---

---

\*Volume II is presented under separate cover.

REYNOLDS NUMBER EFFECTS ON THE TRANSONIC AERODYNAMICS OF A SLENDER WIND-BODY CONFIGURATION.....	41
James M. Luckring, Charles H. Fox, Jr., and Jeffrey S. Cundiff	
LAMINAR-FLOW FLIGHT EXPERIMENTS.....	59
R. D. Wagner, D. V. Maddalon, D. W. Bartlett, F. S. Collier, Jr., and A. L. Braslow	
LAMINAR-FLOW WIND TUNNEL EXPERIMENTS.....	105
William D. Harvey, Charles D. Harris, William G. Sewall, and John P. Stack	
COMPUTATIONAL SUPPORT OF THE X-29A ADVANCED TECHNOLOGY DEMONSTRATOR FLIGHT EXPERIMENT.....	147
E. G. Waggoner and B. L. Bates	
RESULTS OF CORRELATIONS FOR TRANSITION LOCATION ON A CLEAN-UP GLOVE INSTALLED ON AN F14 AIRCRAFT AND DESIGN STUDIES FOR A LAMINAR GLOVE THE FOP X-29 AIRCRAFT ACCOUNTING FOR SPANWISE PRESSURE GRADIENT.....	167
S. H. Goradia	

ATTENDEES  
NASA LANGLEY

ABEYOUNIS, W. K.  
Mail Stop 280

ABDOL-HAMID, K  
Analytical Services & Materials  
Mail Stop 280

ADCOCK, J.  
Mail Stop 267

AL-SAAD, J.  
N. C. State University  
Mail Stop 267

ALLISON, D. O.  
Mail Stop 294

ANDERSON, C.  
Mail Stop 159

ATKINS, H.  
Mail Stop 159

BANGERT, L.  
Mail Stop 280

BARE, E. A.  
Mail Stop 280

BARNWELL, R.  
Mail Stop 105A

BARTLETT, D.  
Mail Stop 261

BATES, B. L.  
Vigyan Research Associates, Inc.  
Mail Stop 294

BATINA, J. T.  
Mail Stop 173

BENNETT, B. B.  
Mail Stop 280

BERRIER, B. L.  
Mail Stop 280

BERTELUD, A.  
High Technology Corporation  
Mail Stop 163

BIEDRON, R. T.  
Mail Stop 128

BLAND, S. R.  
Mail Stop 173

BOBBITT, P. J.  
Mail Stop 285

BOYDEN, R.  
Mail Stop 267

BOYLES, G.  
Mail Stop 267

BRASLOW, A.  
Analytical Services & Materials  
Mail Stop 261

BROOKS, C. W., Jr.  
Mail Stop 359

BRUCE, W. E.  
Mail Stop 267

CAMPBELL, D.  
Mail Stop 294

CANNIZZARO, F. E.  
Old Dominion University  
Mail Stop 159

CARLSON, J. R.  
Mail Stop 280

CARPENTER, M. H.  
Mail Stop 156

CARRAWAY, D. L.  
Mail Stop 238

CARSON, G. T., Jr.  
Mail Stop 280

CHU, Julio  
Mail Stop 267

CLUKEY, P.  
Mail Stop 359

CLUKEY, S.  
Mail Stop 359

COMPTON, W. B.,  
Mail Stop 280

COVELL, P.  
Mail Stop 413

CUNDIFF, J. S.  
Mail Stop 294

DAGENHART, J. R.  
Mail Stop 339

DAVIS, R. E.  
Mail Stop 474

DESMARAIS, R.  
Planning Research Corporation  
Mail Stop 246

DODBELE, S.  
Vigyan Research Associates, Inc.  
Mail Stop 247

DRESS, D. A.  
Mail Stop 267

EL-HADY, N. M.  
Old Dominion University  
Mail Stop 359

EVANGELISTA, R.  
Analytical Services & Materials  
Mail Stop 359

FAULKNER, J.  
Mail Stop 390

FERRIS, J.  
Mail Stop 294

FLECHNER, S.  
Mail Stop 267

FOSS, W.  
Mail Stop 431

FOSTER, J.  
Mail Stop 294

FOUGHNER, J. T., Jr.  
Mail Stop 285

FOX, C. H., Jr.  
Mail Stop 295

FULLER, D.  
Mail Stop 267

GAINER, T.  
Mail Stop 359

GARRIZ, J.  
Vigyan Research Associates , Inc.  
Mail Stop 159

GATLIN, G. H.  
Mail Stop 286

GHAFFARI, F.  
Vigyan Research Associates, Inc.  
Mail Stop 294

GLOSS, B. B.  
Mail Stop 267

GORADIA, S. H.  
Vigyan Research Associates, Inc.  
Mail Stop 359

GREEN, L. L.  
Mail Stop 159

GUMBERT, C. R.  
Mail Stop 159

HALL, R. M.  
Mail Stop 294

HALLISSY, J. B.  
Mail Stop 294

HARRIS, C. D.  
Mail Stop 359

HARRIS, R. V., Jr.  
Mail Stop 116

HARVEY, W. D.  
Mail Stop 359

HEMSCH, M. J.  
Planning Research Corporation  
Mail Stop 294

HENDERSON, W. P.  
Mail Stop 280

HODGE, S.  
Mail Stop 159

JONES, G.  
Mail Stop 359

KALBURGI, V.  
Analytical Services & Materials  
Mail Stop 359

KAMEMOTO, D.  
Mail Stop 359

KEMP, W. B.  
LRC  
Mail Stop 267

KURUVILLA, G.  
Vigyan Research Associates, Inc.  
Mail Stop 159

LEE, E.  
Mail Stop 173

IGOE, W.  
Mail Stop 267

INGRALDI, A.  
Mail Stop 280

JACOBS, P.  
Mail Stop 294

JENKINS, R. V.  
Mail Stop 359

JOHNSON, C. B.  
Mail Stop 359

JOHNSON, T.  
Planning Research Corporation  
Mail Stop 294

JOHNSON, W. G., Jr.  
Mail Stop 267

LADSON, C. L.  
Mail Stop 285

LAMAR, J.  
Mail Stop 294

LEAVITT, L.  
Mail Stop 280

LUCKRING, J. M.  
Mail Stop 294

MADDALON, D.  
Mail Stop 261

MANGALAM, S.  
Analytical Services & Materials  
Mail Stop 915

MANN, M.  
Mail Stop 411

MAVRIPLIS, D.  
ICASE  
Mail Stop 132C

MCKINNEY, L. W.  
Mail Stop 285

MCGHEE, R.  
Mail Stop 339

MEHROTRA, S. C.  
Vigyan Research Associates, Inc.  
Mail Stop 912

MELSON, D.  
Mail Stop 159

MERCER, C.  
Mail Stop 280

MINECK, R.  
Mail Stop 294

MOLLOY, J. K.  
Mail Stop 116

MORGAN, H. L.  
Mail Stop 359

MURTHY, A.  
Vigyan Research Associates, Inc.  
Mail Stop 287

NAIK, D.  
Vigyan Research Associates, Inc.  
Mail Stop 280

NEELY, R. W.  
Mail Stop 173

NEWMAN, P. A.  
Mail Stop 159

PARIKH, P.  
Vigyan Research Associates, Inc.  
Mail Stop 159

PASCHAL, K.  
Mail Stop 359

PATTERSON, J. C., Jr.  
Mail Stop 246A

PENDERGRAFT, O. C.  
Mail Stop 280

PETERSON, J. B.  
Mail Stop 267

PFENNINGER, W.  
Analytical Services & Materials  
Mail Stop 261

PHILLIPS, P.  
Mail Stop 294

POPERNACK, T. G., Jr.  
Mail Stop 267

PUTNAM, L. E.  
Mail Stop 294

RADESPIEL, R.  
Mail Stop 287

RE, R.  
Mail Stop 280

REBSTOCK, R.  
National Research Council  
Mail Stop 287

ROSE, L. J.  
Mail Stop 139A

RUMSEY, C  
Mail Stop 128

SALAS, M. D.  
Mail Stop 159

SCHOONOVER, E.  
Mail Stop 294

SEIDEL, D. A.  
Mail Stop 173

SEKAR, B.  
Vigyan Research Associates, Inc.  
Mail Stop 156

SEWALL, W. G.  
Mail Stop 339

SMITH, L. A  
Mail Stop 294

SOMERS, D. M.  
Mail Stop 294

SOUTH, J. C.  
Mail Stop 128

STACK, J. P.  
Mail Stop 359

STAINBACK, P. C.  
Mail Stop 359

STRGANAC, T.  
Mail Stop 431

SWANSON, R. C.  
Mail Stop 159

SWITZER, G.  
Analytical Services & Materials  
Mail Stop 156

TAYLOR, J.  
Mail Stop 280

THAMES, F.  
Mail Stop 159

THIBODEAUX, J. J.  
Mail Stop 267

THOMAS, J. L.  
Mail Stop 128

TURKEL, E.  
ICASE  
Mail Stop 132C



VATSA, V. N.  
Mail Stop 159

VEMURU, C. S.  
Mail Stop 159

VENKATAKRISHNAN, V.  
Analytical Services & Materials  
Mail Stop 159

VIJGEN, P.  
High Technology Corporation  
Mail Stop 247

VRETAKIS, N. G.  
AFSCLO  
Mail Stop 221

WAGGONER, E. G.  
Mail Stop 294

WAGNER, R. D.  
Mail Stop 261

WAHLS, R. A.  
N. C. State University  
Mail Stop 156

WALKER, B.  
Mail Stop 359

WARREN, G. P.  
Mail Stop 128

WATSON, R.  
Mail Stop 163

WHITCOMB, R. T.  
Mail Stop 188E

WHITESIDES, J.  
George Washington University  
Mail Stop 269

WIESEMAN, C. D.  
Mail Stop 243

WILLIAMS, M. S.  
Mail Stop 267

WOLF, S.  
Vigyan Research Associates, Inc.  
Mail Stop 287

WOODSON, S.  
Mail Stop 294

WORNOM, S. F.  
Mail Stop 159

YAROS, S. F.  
Mail Stop 280

YATES, C.  
Mail Stop 246

ATTENDEES  
NON-LANGLEY

ADAMSON, Thomas C., Jr.  
The University of Michigan

AGARWAL, Ramesh K.  
McDonnell Douglas Research Labs.

AYERS, Theodore G.  
NASA Ames Research Center

BAKER, T. J.  
Princeton University

BENGELINK, Ronald L.  
Boeing Commercial Airplane Company

BHARADVAJ, Bala K., Dr.  
Douglas Aircraft Company

BONNER, Ellwood  
Rockwell International Corporation

BRAYMEN, William  
General Dynamics

CARLSON, Leland A.  
Texas A&M University

CHAN, Y. Y.  
National Aeronautical Establishment

CHEN, Lee T.  
McDonnell Douglas Corporation

CHRISS, Randall  
NASA Lewis Research Center

COLE, Julian D.  
Rensselaer Polytechnic

COLEHOUR, Jeffery L.  
Boeing Commercial Airplane Company

CONNELL, Stuart  
General Electric

COSNER, Ray R.  
McDonnell Douglas

DA COSTA, A. L.  
Boeing Advanced Systems

DANG, Thong  
Douglas Aircraft Company

DAVIS, Warren H., Jr.  
Grumman Corporation

DEESE, E. Jerry  
McDonnell Douglas Research Labs.

DIRLIK, Steven P.  
David Taylor Research Center

DOUGHERTY, F. Carroll  
University of Colorado

DRIVER, Cornelius  
Eagle Engineering, Incorporated

DUQUE, Earl P. N.  
NASA Ames Research Center

GEORGE, Mike  
Northrop Corporation

GOLDHAMMER, Mark I.  
Boeing

GORDNIER, Raymond E.  
University of Cincinnati

GREGOREK, Gerald M.  
Ohio State University

GROSSMAN, B.  
Virginia Polytechnic Institute  
and State University

GRUBER, Glenn J.  
Pratt & Whitney

HAFAZ, D. D.  
University of California-Davis

HASSAN, H. A.  
North Carolina State University

IDE, Hiroshi  
Rockwell International

INGER, George R.  
Iowa State University

ISHIMITSU, K. K.  
Boeing Advanced Systems

JAMESON, Antony  
Princeton University

KHOSLA, Prem K.  
University of Cincinnati

LAN, C. Edward  
University of Kansas

LEVINE, Mark  
Rockwell International

LO, Ching F.  
Calspan Corporation

LOFTIN, Laurence K., Jr.  
Self Employed

LORD, Wesley  
Pratt & Whitney

LYNCH, Frank T.  
Douglas Aircraft Company

MACWILKINSON, Derek G.  
McDonnell Douglas

MADSON, Mike  
NASA Ames Research Center

MAGUIRE, William B.  
David Taylor Research Center

MALMUTH, Norman D., Dr.  
Rockwell International Science Center

MASIELLO, Matthew  
Grumman Aerospace Corporation

MAYER, David  
Boeing Military Airplane Company

MIDDLETON, Wilbur D.  
Boeing Company

MIRANDA, L. R.  
Lockheed-California Company

MUELLER, Thomas J., Dr.  
University of Notre Dame

NACHMAN, Arje  
U. S. Air Force

NAYFEH, Ali H.  
Virginia Polytechnic Institute  
and State University

NIETUBILZ, Charles J.  
Ballistic Research Laboratory

POWELL, Ken  
University of Michigan

PUTNAM, Terry  
NASA Dryden Flight Research Facility

RATCLIFF, Robert  
Texas A&M University

ROSEN, Bruce S.  
Grumman Corporation

RUBESIN, M. W.  
NASA Ames Research Center

RUBIN, Stanley G.  
University of Cincinnati

SCHLEINIGER, Gilberto  
University of Delaware

SHREWSBURY, G. D.  
Lockheed-Georgia Company

SMITH, Charles  
General Dynamics

SMITH, Norbert F.  
McDonnell Douglas

SNYDER, James  
Wright Patterson Air Force Base

SORRELLS, Russell B.  
U. S. Air Force

STEGE, J. L.  
NASA Ames Research Center

TINOCO, E. N.  
Boeing Commercial Airplane Company

TSENG, Wei W.  
Naval Air Development Center

VAN LEER, Bram  
University of Michigan

VERHOFF, August Dr.  
McDonnell Aircraft Company

VOLPE, Giuseepe  
Grumman Aerospace Corporation

WEBBER, Geoff W.  
Lockheed Aeronautical Systems Company

WIGTON, Larry  
Boeing Aerospace Corporation

WILCOX, Peter  
Douglas Aircraft Company

WYCKOFF, John C.  
AMETEK

ZICKUHR, Tom  
Beech Aircraft Corporation

## AIRFRAME/PROPULSION INTEGRATION CHARACTERISTICS AT TRANSONIC SPEEDS

William P. Henderson and Bobby L. Berrier  
NASA Langley Research Center  
Hampton, Virginia

### ABSTRACT

The aerodynamic characteristics for both single and twin-engine high-performance aircraft are significantly affected by shock induced flow interactions as well as other local flow interference effects which usually occur at transonic speeds. These adverse interactions can not only cause high drag, but also cause unusual aerodynamic loadings and/or severe stability and control problems. Many new programs are under way to not only develop methods for reducing the adverse effects, but also to develop an understanding of the basic flow conditions which are the primary contributors. It is anticipated that these new programs will result in technologies which can reduce the aircraft cruise drag through improved integration as well as increase aircraft maneuverability through the application of thrust vectoring. This paper will attempt to identify some of the primary integration problems for twin-engine aircraft at transonic speeds, and demonstrate several methods for reducing or eliminating the undesirable characteristics, while enhancing configuration effectiveness.

### NOMENCLATURE

$C_D$	Total afterbody drag coefficient
$C_{Dtail}$	Drag coefficient of the tail surfaces (tail drag + interference)
$C_{D_n}$	Nozzle drag coefficient
$\Delta C_D$	Incremental drag coefficient
$C_m$	Pitching moment coefficient
$C_n$	Yawing moment coefficient
$C_p$	Pressure coefficient
$F/F_i$	Ratio of thrust to ideal thrust
$F_r/F_i$	Ratio of resultant (gross) thrust to ideal thrust
$H_T$	Horizontal tail
$l$	Length of model

M	Mach number
NPR	Nozzle pressure ratio
q	Dynamic pressure
VT	Vertical tail
X	Distance from nose of model to pressure orifice
$\alpha$	Angle of attack
$\beta$	Nozzle boattail angle
$\beta_{side}/\beta_{flap}$	Ratio of boattail angle of sidewalls to boattail angle of nozzle upper and lower flaps
$\delta_y$	Flow turning angle
$\delta_{y,i}$	Ideal flow turning angle
$\delta_{v,p}$	Deflection of the nozzle upper and lower flaps
$\phi$	Roll angle location of pressure measuring devices
$\theta$	Nozzle cant angle

#### Abbreviations:

AFT	Rear location
Axi	Axisymmetric
Fwd	Forward location
L.E.	Leading edge
Mid	Middle location
Non axi	Nonaxisymmetric
SMTD	STOL and Maneuver Technology Demonstrator

## INTRODUCTION

The mission requirements for the next generation fighter aircraft may dictate a highly versatile vehicle capable of operating over a wide range of flight conditions. This aircraft will most likely be designed for high maneuverability and agility, operate in a highly hostile environment, and possess STOL landing characteristics to operate from bomb damaged airfields (reference 1). Many design guidelines tend to be contradictory for the

subsonic and supersonic speed regimes and aircraft performance can be compromised by small changes in these design considerations.

The attainment of high performance is highly dependent upon the minimization of interference resulting from the integration of the propulsion exhaust system into the airframe, one of the most critical design features of an aircraft (reference 2). An indication of the relative importance of this area is illustrated in figure 1 where the percent of total aircraft drag attributed to the aircraft afterbody is presented for four twin-engine fighter aircraft. Representative aircraft from an "ideal" research configuration tested in 1961 to the F-18 aircraft tested in 1978 are shown. The afterbodies of these models comprised from 20 to 35 percent of the total model length, but produced 38 to 50 percent of the total aircraft drag. Up to half of the afterbody drag results from adverse interference in the afterbody region and pressure drag on the afterbody (see reference 3-6).

At the same time the designer is striving for a low drag configuration, he is also required to improve the maneuvering capability of the aircraft. This usually requires high thrust to weight and lift drag ratio, high usable lift coefficient, and adequate stability and control characteristics over a very wide operating envelope.

In responding to the need to reduce nozzle/afterbody drag and enhance vehicle maneuverability, the Propulsion Aerodynamics Branch at the Langley Research Center has conducted a number of responsive experimental and theoretical research programs. In these programs, items such as empennage location and nozzle boattail geometry have been investigated. Increasing maneuverability, particularly at post stall conditions where conventional controls are ineffective, requires the utilization of alternative control devices. One of the most effective, particularly at high angles of attack, relies on vectoring of the engine thrust. As indicated, the empennage is a source of high interference drag. Therefore, reducing the size of the empennage or eliminating it altogether would increase aircraft performance, but could cause serious problems for aircraft stability and control. Thrust vectoring can be a means to provide the necessary control power, or at least augment it. This means that effective thrust vectoring must be provided across the aircraft speed regime. Various concepts have been studied (see references 7 and 8) at transonic speeds and typical results will be discussed herein.

## **WIND TUNNEL**

All of the experimental investigations discussed herein were conducted in the Langley 16-Foot Transonic Tunnel. This tunnel is a continuous flow, single-return, atmospheric wind tunnel with a slotted octagonal throat and test section, and continuous air exchange. The tunnel has a variable speed range from  $M = 0.20$  to  $M = 1.30$ . Additional information regarding tunnel description and calibration is presented in reference 9.

## DISCUSSION

### Nozzle/Afterbody Integration

In an analysis of this type, where the integration characteristics of twin-engine high-performance aircraft are being studied, it is important to develop an understanding of the contribution of the various nozzle/afterbody components to the total aircraft drag. The model used in conducting this analysis is presented in figure 2.

The centerbody fuselage of this model was essentially rectangular in cross section having a constant width and height of 10.0 in. and 5.0 in. respectively. The four corners were rounded by a radius of 1.0 in. Maximum cross-sectional area of the centerbody (fuselage) was 49.14 in<sup>2</sup>. The support system forebody was typical of a powered model in that the inlets were faired over. The "wings" of the support system were mounted above the model centerline in a "high wing" position which is typical of many current fighter designs. The support system "wing" had a 45° leading edge sweep, a taper ratio of 0.5, an aspect ratio of 2.4, and a cranked trailing edge. The airfoil was symmetrical and the thickness ratios near the wing fuselage junction were realistic (approximately  $t/c = 0.067$ ). From BL 11.00 to the support booms, however, "wing" thickness ratio increased from  $t/c = 0.077$  to  $t/c = 0.10$  to provide structural support for the model and to permit transfer of compressed air from the booms to the model propulsion system.

The twin-engine aft-end was attached to the support system wing/centerbody by mounting on a six-component strain gage balance. The combined forces and moments for the afterbody shell, empennage surfaces, and outer nozzles were measured by the balance and are termed total aft-end forces in this paper. Clearance was provided between the metric and nonmetric portions of the model. The afterbody lines were chosen to be typical of current close-spaced twin-engine fighter designs, to fair the afterbody smoothly from the constant cross section of the centerbody down to the nozzles, and to house the afterbody balance, propulsion simulation system, and related instrumentation. Nozzle geometry simulated a convergent-divergent nozzle design with fully variable throat area and expansion ratio.

The contribution of the various nozzle/afterbody components to the total afterbody drag is presented in figures 3 to 5. This drag breakdown (taken from data in reference 10) is for the twin-engine configuration with dry power axisymmetric nozzles at a scheduled nozzle pressure ratio (NPR). Scheduled nozzle pressure ratio for the various test mach numbers is as follows:

M	NPR
0.60	3.5
.80	4.5
.90	5.0
.95	5.3
1.15	6.7
1.20	7.0



The circular symbols in figure 3 represent the drag data for the complete afterbody configuration and the square symbols for the nozzle/afterbody configuration without horizontal or vertical tails. An estimate shown by the dashed line was made of the drag increment attributed by the horizontal and vertical tails. This increment represents the skin friction and form drag at subsonic speeds and the skin friction and wave drag at supersonic speeds. The difference in drag between the dashed line and the total drag can be attributed to an adverse interference effect. This adverse drag increment is small at  $M = 0.60$  but increases dramatically as the Mach number approaches 0.95. From this curve it is obvious that the horizontal and vertical tails and their associated adverse interference effects are the major contributors to the nozzle/afterbody drag. This is better illustrated in figure 4 where the drag contribution of the tail surfaces (tail drag + interference effects) is presented as a function of the total afterbody drag for several configurations. As shown in this figure, the horizontal and vertical tails contribute as much as 60 to 70 percent of the nozzle/afterbody drag, and as shown in figure 3 at transonic speeds, about half of this drag can result from adverse interference effects.

Exploring the drag contribution of the various model components in a little more detail can be accomplished with the aid of figure 5. The square symbols in this figure, nozzle/afterbody drag (horizontal and vertical tails off) are the same as the data shown on figure 3. The diamond symbols represent the data for the nozzle alone. These data include the pressure drag obtained by integrating the nozzle static pressures and an estimated skin friction drag. An estimate was made of the friction drag of the afterbody, and this is shown added to the nozzle drag as the solid line. The remaining drag is attributed to the pressure drag on the afterbody which is seen to be about 20 drag counts at subsonic speeds and about 60 drag counts at supersonic speeds. Possibly, with some careful contouring and the elimination of the gutters between the engine, this drag increment can be reduced. From these data it would appear that the two major areas for increasing the performance (decreasing the drag) of a typical afterbody configuration are in the elimination of the interference drag associated with the horizontal and vertical tails and reducing the pressure drag associated with the afterbody.

#### Nonaxisymmetric Nozzles

For a number of years, the Langley Research Center has recognized that there are a number of advantages to the application of nonaxisymmetric nozzles in place of the current axisymmetric nozzles. Some of these benefits are indicated in reference 11. One of these benefits is the possible reduction in nozzle/afterbody drag due to a better integration of the afterbody. A number of configurations have been studied; one of these mounted in the 16-Foot Transonic Tunnel is shown in figure 6. The wings and forebody are the same as those of the previous model with the axisymmetric nozzle. Only the aft portion of the model (aft of the metric break) has been changed. The metric portion of the model consisted of the internal propulsion system, afterbody, tails, and nozzles. The afterbody lines (boattail) were chosen to provide a length of constant cross-section aft of the nonmetric centerbody, and to enclose the force balance and jet simulation system, while fairing smoothly downstream into the closely spaced nozzles. The afterbody shell and tail surfaces were attached to an afterbody force balance which was attached to the main force balance. The main force balance in turn was grounded to the

nonmetric wing-centerbody section. The nozzles were attached directly to the main force balance through the propulsion system piping.

The nonaxisymmetric (two-dimensional convergent-divergent) nozzle used in this investigation simulated a dry-power or cruise operating nozzle with a design NPR of about 3.5. The nozzle throat area ( $17.48 \text{ cm}^2$ ) and expansion ratio (1.15) were sized to be consistent with advanced mixed flow turbofan cycles. The ratio of total throat area to maximum body cross-sectional area was 0.11, and the nozzle throat aspect ratio was 3.45.

The experimental drag characteristics for this configuration (taken from reference 12) are shown compared to the configuration with axisymmetric nozzles in figures 7 and 8. In figure 7, the drag characteristics for the complete afterbody (tails on) configurations are presented. The drag characteristics for the configurations without the horizontal and vertical tails are presented in figure 8. At the lower test Mach numbers, the configuration (tails-on) with the nonaxisymmetric nozzles has the lowest drag. As the Mach number is increased, this trend changes and the drag for the configuration with the axisymmetric nozzles is significantly lower. For the tails off configurations, the configuration with the nonaxisymmetric nozzles has the lowest drag at mach numbers up to 0.90. This would seem to indicate that the nonaxisymmetric nozzle concept may be more sensitive to adverse tail interference effects than the axisymmetric nozzles at the Mach numbers where these effects are generally very high. At supersonic speeds, nozzle drag is significantly higher for the nonaxisymmetric nozzle, which means that some changes in the nozzle geometry and area distribution may have to be made in order to reduce drag.

#### Nozzle Boattail Drag Effects

A number of studies on methods of reducing the drag on nonaxisymmetric nozzles have been conducted. One such study, aimed at determining the effects of nozzle boattail geometry on the nozzle drag, is illustrated by several typical models which are shown in figures 9 and 10. The only difference between these two models is in the nozzle geometry; a  $7.5^\circ$  boattail nozzle is shown in figure 9 and a  $12.5^\circ$  boattail nozzle is shown in figure 10. The nozzle drag characteristics (taken from reference 13) presented as a function of boattail angle is shown in figure 11. The nozzle boattail angle for the model previously shown in figure 6 was about  $17^\circ$ . Based on these data, some significant drag reductions could be obtained with a small reduction in boattail angle. This of course would have to be traded against a potential weight increase usually associated with reducing boattail angle.

Most of the nonaxisymmetric nozzle designs that have been previously studied have taken almost all of the nozzle boattail on the top and bottom surfaces of the nozzle, leaving the sidewalls nearly flat. During earlier tests, where surface pressures were measured on the external surfaces of the nozzle, some significant difference in pressure distributions was noted. Pressure distributions on the upper and lower nozzle surfaces were much lower than pressure distributions on the nozzle sidewalls. It was felt that this difference would cause some cross flow around the nozzle creating a potential drag problem. As a result, a study was devised with the General Dynamics Corporation to measure the nozzle/afterbody drag for a configuration in which

the nozzle upper and lower surface boattail angles are traded against the sidewall boattail angle. The sketch of the model used in this study (taken from reference 14) is shown in figure 12, and the nozzle/afterbody drag coefficient variation as a function of the ratio  $\beta_{side}/\beta_{flap}$  for Mach numbers of 0.90 and 1.20 is presented in figure 13. The boattail angles for the nozzle upper and lower flaps and the sidewalls that correspond to the ratios presented in figures 12 and 13 are as follows:

$\beta_{side}/\beta_{flap}$	$\beta_{flap}, \text{deg}$	$\beta_{side}, \text{deg}$
0.50	15.0	7.5
1.00	13.5	13.5
1.77	11.0	19.5

The results of this study indicate that minimum nozzle/afterbody drag occurs when the boattail angles on all of the surfaces are approximately the same. It should also be noted that for  $\beta_{side}/\beta_{flap} = 1.0$ , the boattail angles are  $13.5^\circ$  which, according to figure 11, may be near the most optimum boattail angle for nonaxisymmetric nozzles at  $M = 0.90$ . The drag coefficient increases more rapidly as the ratio  $\beta_{side}/\beta_{flap}$  decreases below 1.0 than when it increases above 1.0. This occurs because as  $\beta_{side}/\beta_{flap}$  decreases, the upper and lower flap boattail angle increases while the sidewall boattail angles decreases. Since the upper and lower flap are considerably larger than the sidewall flaps, any adverse drag effects on the upper and lower flaps would be more significant than any potential decreases on the small sidewall flaps.

#### Effect of Empennage Location

While there are some significant benefits that can be realized with changes in the geometry of the nozzle/afterbody, the largest drag penalty at transonic speeds according to figure 3 was attributed to the horizontal and vertical tails. Several studies have been conducted to determine the effects of horizontal and vertical tail locations on the nozzle/afterbody drag. The results of these studies are summarized in figures 14, 15, and 16 and were taken from reference 10 for the configuration with axisymmetric nozzles and from reference 12 for the configurations with nonaxisymmetric nozzles (see figure 6). The afterbody had provisions for mounting both the vertical and horizontal tails in three axial locations as illustrated in figure 14. Note that the leading edge of the root chords for both horizontal and vertical tails could be placed at the same fuselage axial station. These locations will be termed fwd, mid, and aft respectively.

The effects of horizontal and vertical tail location on the nozzle drag are shown in figure 15 for dry power nozzles at  $\alpha = 0^\circ$  and Mach numbers of 0.90 and 1.20. The open symbols are for the configuration with axisymmetric nozzles and the solid symbols are for the configuration with nonaxisymmetric nozzles. Moving either the horizontal or vertical tails from the aft position (location closest to the nozzle) to the mid position results in a significant reduction in the nozzle drag. Further movement of the tails away from the nozzles had only a minor effect on the nozzle drag. However, when you look at the total aftend drag, the results are not so clear. In figure 16, the total

nozzle/afterbody drag is presented as a function of horizontal and vertical tail location. While a slight drag reduction trend can be deduced as the tails are moved away from the nozzles, there are still some configurations that show opposite effects. This would seem to indicate that as the tails are moved away from the nozzles on these twin-engine configurations, the adverse tail interference effects on nozzles are transferred to the afterbody. Thus, it would appear that there may be only two ways that can be utilized to eliminate this large adverse interference effect. One is to simply eliminate the horizontal and vertical tails and utilize some other method of achieving the necessary control power. The other is to develop an adequate computational method which can be utilized to carefully contour the nozzle/afterbody thereby eliminating the adverse interference effects.

### Computational Methods

Several computational methods are being developed that can be utilized in solving this complex nozzle/afterbody/empennage integration problem. One of these is a full-potential finite-volume transonic code called FLO-30V (reference 15), which is used to calculate the pressure distributions over the nozzle/afterbody including the effects of the empennage. In this code an integral boundary-layer calculation is performed in strip fashion. The resulting effective body and tail geometries are used as input to the code. This developmental code utilizes the method of Caughey and Jameson which is based upon the full potential equation and a mesh generation technique which wraps a C-type grid around the body and tails. Further discussion of the methods used in these calculations and of the comparisons of calculations with experimental data can be found in reference 16.

This code was applied to the sting-strut supported single-engine model which is presented in figure 17. This type of support system places the model centerline on the centerline of the wind tunnel and minimizes support interference on the afterbody and nozzle. The overall model arrangement, representing a typical single-engine fighter aft end, is composed of four major parts located as shown in the following table:

Part	x,in.	x/l
Forebody	0-40.89	0-0.57
Afterbody	40.89-64.89	0.57-0.91
Nozzle	64.89-71.70	0.91-1.00
Tail surfaces	Variable	Variable

The forebody consists of an ogive nose 24 inches in length with an initial angle of  $14^\circ$  and a constant-radius cylinder thereafter. The afterbody was designed to simulate closure ahead of the nozzle typical of a single-engine fighter configuration. The afterbody had provisions for mounting the vertical and horizontal tails at two different axial locations (forward and aft). The tail surfaces were tested in three empennage arrangements: aft, staggered, and forward. The nozzle used for this investigation simulated a variable geometry (fixed in dry power mode for this test), convergent-divergent, axisymmetric nozzle typical of those currently in use on modern

fighter aircraft. A complete description of the model is given in reference 16.

An assessment of the effectiveness of the FLO30V code at predicting the nozzle/afterbody/empennage pressures can be made with the aid of the comparisons presented in figures 18 and 19. A comparison of the theoretical calculations with experimental data for two rows of pressure orifices on the staggered empennage arrangement, one near the vertical tail at a roll angle of  $18^\circ$  and the other near the horizontal tail at a roll angle of  $72^\circ$ , is presented in figure 18 for a Mach number of 0.60 and for a Mach number of 0.90 in figure 19. The staggered tail arrangement was chosen for these comparisons because the data indicated that for the single-engine configuration, the empennage interference effects were lowest for this tail arrangement. The calculated results show reasonably good agreement with the experimental data at the lowest test Mach number ( $M = 0.60$ ). At the higher subsonic test Mach numbers ( $M = 0.90$ ), the discrepancy between the experiment and theory becomes more significant. The major reason for the discrepancy could probably be attributed to the approximations made to model the vertical tail and the lack of a model of the wake of the vertical tail. The FLO-30V calculations do account for viscous effects, but the boundary layers on the body and tail were computed separately as two-dimensional elements, so that the influence of the empennage is not included in the afterbody boundary-layer calculations. As a result, the FLO-30V calculation shows some influence of the empennage on nozzle/afterbody pressures, but does not predict the severity of the interference effects.

### Thrust Vectoring

As indicated previously, one of the most efficient ways of reducing the adverse interference drag caused by the horizontal and vertical tails is to simply remove them from the configuration. This could be accomplished if some other method were found to provide the necessary control power for the configuration. One of the obvious solutions would be to rely on thrust vectoring to fill this void. Thrust vectoring has been studied for some time and has been found to provide a number of potential enhancements to aircraft performance and effectiveness. Many of these are indicated in the following:

#### Increased Capabilities

- STOL
- Expanded envelope

#### Improved Performance

- Control Augmentation
  - Post stall operation
  - Higher instantaneous turn rates
  - Fuselage aiming
  - Direct force control
- Lower Drag
  - Reduced trim drag
  - Reduced control surface drag

- Lower Weight
  - Elimination of control surfaces
- Less Design Constraints
  - Supersonic wing design
  - Low  $q$  control surface sizing

### Improved Survivability

Methods of providing pitch vectoring have been under study for some time, (see reference 8). These studies have shown that many nozzles can be designed to provide high levels of pitch vectoring without a significant adverse impact on aircraft thrust performance. The challenge now becomes one of providing, in addition to the pitch vectoring, a high level of yaw vectoring. A number of configurational concepts have been studied. Some of these, shown in figure 20, were based on configurations studied in references 17 and 18.

The upstream yaw vectoring concept was achieved by modifying one of the nozzle sidewalls with a rectangular port located upstream of the nozzle throat. The port was sized to have an area equal to 30 percent of the unvectored dry power nozzle throat area. The port operates by deflecting two flaps. The forward flap was a simple flap hinged at the nozzle sidewall and extended into the external flow. The aft flap was also hinged at the nozzle sidewall, but it deflected both into the external flow as well as into the internal flow (about 45 percent of the internal nozzle width). These flaps were deflected at an angle of about  $70^\circ$  to the axial thrust direction.

The downstream (of throat) yaw vectoring concept (sidewall flaps) is based on modifying either the left or right sidewall or both sidewalls with a hinged flap extending downstream of the nozzle throat. The sidewall flaps hinged directly at the nozzle throat. Consequently, for a positive yaw vector angle (produces positive side force), the left sidewall flap extends out from the internal nozzle flow (expansion turn), while the right sidewall flap extended into the flow (compression turn). This type of concept does have some limitations in that there could be some interference between surfaces when simultaneous pitch and yaw vectoring are required.

The third concept consisted of externally mounted vanes, one on each side of the nozzle. The vanes hinged at the nozzle exit are deflected such that one vane extends into the jet exhaust flow whereas the other extends away from the jet exhaust flow. The height of the vanes was determined by the location of the nozzle when pitch vectoring is included. For a  $\pm 15^\circ$  nozzle pitch vector angle, the lower (or upper) trailing edge of the nozzle coincides with the lower (or upper) edge of the vane.

The static yaw vectoring results for these three concepts are presented in figure 21. On the left side of the figure, the measured yaw vector angle determined from static tests in the Langley Static Test Stand is presented. On the right side is the ratio of the measured yaw vector angle to the expected yaw vector angle (determined geometrically from the known deflection angles of the surfaces involved).

The results indicate that the rectangular port concept produced a high yaw vector (turning) angle, about the magnitude anticipated (based on  $\delta_y/\delta_{y,i} = 1.0$ ). This level of vectoring would be expected since the exhaust flow upstream of the nozzle throat is subsonic and past experience has shown that subsonic flow can be turned with only very small losses. The data for the sidewall flaps show significant variation in yaw vector angle with nozzle pressure ratio. At the lower NPR's the flow is probably separated off of the deflected flap on the expansion side (flap deflected away from the jet exhaust). As the nozzle pressure ratio increases, the flow tends to expand around the flap and the vector angle increases. The full potential of the yaw vector angle is probably not reached simply because the entire jet exhaust is not affected by the small sidewall flaps. The post-exit vanes produce the smallest level of yaw vectoring of any of the vectoring concepts studied at these static conditions. For this concept, the flow over the vane that was deflected away from the jet exhaust was totally separated. Therefore, it was totally ineffective at producing any contribution to yaw vectoring at all nozzle pressure ratios. In this case only the vane extending into the flow produced any yaw vectoring and it had to turn a supersonic exhaust stream which from past experience is very inefficient.

The external flow effects on the yaw vectoring produced by these three concepts are shown in figures 22 through 24. In these figures, the yawing moment multiplied by free-stream dynamic pressure is presented as a function of Mach number. It should be noted that for presentation purposes, the sign on yawing moment was changed from negative values (which would result from the positive flap deflections shown in figure 20) to positive values (which would result from negative flap deflections). On each of these figures, three pieces of data are presented. The circular symbols are the yawing moment based on the direct thrust contribution. These data were obtained from the yawing moment measured at static (wind-off) conditions multiplied by the ratio of the free stream static to the free stream dynamic pressure. The shaded area is the aerodynamic contribution of the vectoring device to the yawing moment measured by conducting the experimental test at jet-off conditions with external flow. The square symbols are the measured yawing moment at jet on conditions with external flow. The arrows shown in figures 22 to 24 indicate an induced external flow contribution to yawing moment caused by any interaction of the external flow with the jet-on vectored exhaust plume and any surrounding model surfaces. For the three cases presented in figures 22 through 24, the jet nozzle pressure ratio is 3.0. The yawing moment as a function of Mach number is presented for the upstream port in figure 22, for the sidewall flaps in figure 23, and for the post exit vanes in figure 24. For the upstream rectangular port configuration, the small flaps protruding from the side of the nozzles results in a small positive increment (aero. flap effect) in yawing moment which increases as the Mach number increases. The induced external flow contribution at jet on conditions, illustrated by the arrows, indicate that the external flow has an adverse contribution to the yawing moment. It is thought that this adverse effect could either be caused by the external flow altering the angle of the jet plume as it emanates from the side of the nozzle or by creating large negative pressures on the sidewall behind the jet plume. For the sidewall flap configuration (see figure 23), both the flaps themselves and the induced external flow contributions produced a positive increment in yawing moment. The increments are relatively small, which is expected since the flaps are small, and the deflection angle is only

20°. The largest external flow effects show up on the post-exit vane configuration (see figure 24). As shown, increasing Mach number causes large increases in the yawing moment obtained. The major portion of this increase is the result of a jet off aerodynamic effect on the vanes themselves. This is to be expected since the vanes are fairly large and protrude into the airflow, acting essentially like a vertical tail.

A summary of the thrust characteristics of these three yaw vector concepts at static conditions is presented in figure 25. On the left side of the figure, the ratio  $F/F_i$  which is the measured thrust along the body axis divided by the ideal thrust is presented. For thrust vectored configurations (symbols), reductions in this ratio from 1.0 are caused by the four following mechanisms: 1) skin friction, internal flow separation and exhaust flow divergence losses, 2) under- and over-expansion losses, 3) turning of the gross thrust vector away from the axial direction and 4) additional skin friction and pressure losses caused by the deployed thrust vectoring hardware and the actual turning process itself. The unvectored baseline configuration (dashed line) is affected by the first two mechanisms only. On the right side of the figure, resultant thrust ratio  $F_r/F_i$  is presented as a function of nozzle pressure ratio. This parameter eliminates the losses due to turning the gross thrust vector away from the axial direction (mechanism 3.) Thus, any differences between  $F_r/F_i$  for the baseline configuration and  $F_r/F_i$  for the vectored configurations are caused by additional losses due to the thrust vector hardware and the turning process itself (mechanism 4). Resultant thrust ratios for the sidewall flap configuration are very close to those of the baseline configuration. This result indicates that little or no additional losses occur due to turning the exhaust flow for this yaw vector concept. Similar results to these have been measured for pitch vector concepts which use upper and lower flaps to obtain a pitch vectoring capability. The post-exit vane configuration had 4 to 6 percent lower resultant thrust ratio than the baseline configuration. Lower performance for this configuration probably results from supersonic exhaust flow separation (on the vane deflected away from the exhaust) and additional skin friction drag on the vanes. The results for the upstream rectangular port configuration show extremely large resultant thrust ratio losses. This loss is not surprising since about 30 percent of the flow did not pass through the main nozzle throat and thus was not efficiently expanded by the nozzle divergent flaps. In addition, this concept probably also has additional separation losses from the backside of the aft flap which extends into the internal exhaust stream.

One disadvantage of the multiplane vectoring concepts is that they require additional mechanism (flap surface or other geometry) to achieve both pitch and yaw thrust vectoring. This is undesirable because of the added weight and complexity. One method of reducing some of this complexity is to utilize twin canted nozzles (see reference 7). This concept is shown in figure 26 and a close-up of the nozzles in is shown in figure 27. Canting of the nozzles is generally accomplished by rotating each of the nozzles about their respective thrust axis. With the nozzles canted, pitching moment is obtained by symmetric nozzle pitch vectoring whereas yawing moment is produced from asymmetric nozzle pitch vectoring. The advantage of this concept is that a pitch vectoring nonaxisymmetric nozzle can be utilized without having to modify the nozzle to accommodate additional mechanisms to obtain yaw vectoring capability.



The variation of pitching and yawing moment coefficients with angle-of-attack are shown in figure 28 at  $M = 0.20$  and  $NPR = 3.2$ . These results show that the increment in either  $C_m$  or  $C_n$  due to varying the nozzle flap deflection angle is constant over the angle-of-attack range tested. Pure pitching moment (no yaw) was obtained by a  $+20^\circ$  deflection of the flaps on both nozzles (square symbols on left side of figure 28). Pure yawing moment (no pitch) was obtained by a  $+20^\circ$  deflection of the right hand nozzle flaps and a  $-20^\circ$  deflection of the left hand nozzle flaps (square symbols on right side of figure 28). Although not shown here, there was no effect of sideslip on  $C_n$  over the angle-of-attack range tested. Also shown in figure 28 are the effects of a simultaneous pitch/yaw combination obtained by deflecting the left nozzle  $0^\circ$  and the right nozzle  $20^\circ$ . This is equivalent to  $10^\circ$  of pitch thrust vectoring to obtain pitching moment or  $\pm 10^\circ$  of differential pitch thrust vectoring to obtain yawing moment. For example, the pitching moment coefficient level shown for  $\delta_{v,p} = 0^\circ/20^\circ$  was essentially equal to that measured for  $\delta_{v,p} = 10^\circ$  (not shown). This result again illustrates that there is generally no coupling of the longitudinal and lateral control moments when using powered controls.

The effect of canting the nozzles on the nozzle/afterbody drag is presented in figure 29. Shown in this figure is an increment in drag coefficient which is defined as the difference in drag for the configuration with a nozzle cant angle of  $30^\circ$  and the same configuration with a cant angle of zero, plotted as a function of Mach number. As shown in figure 29, there is a drag reduction associated with canting the nozzles which at transonic speeds becomes very significant. It is felt that the primary cause for the drag reduction is that the gully between the engines has been nearly eliminated on the lower surface of the afterbody and opened up on the upper surface (see figure 27). There may be some difference in cross-sectional area, but this information has not been developed.

An example of a potential integration of the canted nozzle into the F-15 STOL and maneuver aircraft is shown in figures 30 and 31. For this integration concept, not only the pitch and yaw vectoring advantages are obtained, but the installation of a thrust reverser can be more efficient. For example, on the aircraft under surface, the reverser exhaust is deflected outwards possibly reducing the inlet hot gas reingestion problem and on the upper surface, the reverser exhaust is deflected away from the vertical tails possibly easing some adverse interference problems.

## CONCLUSIONS

A significant research program is ongoing in Langley's Propulsion Aerodynamics Branch on integrating the propulsion system into high performance aircraft concepts. This program has included nozzle design, nozzle/afterbody integration, empennage integration, and multiplane vectoring studies. The results of some of those studies presented in this paper are as follows:

1. A significant portion of the afterbody drag is due to the horizontal and vertical tails.

2. Nonaxisymmetric nozzles are competitive with axisymmetric nozzles.
3. Computational methods can provide necessary guidance in propulsion integration.
4. Thrust vectoring concepts are effective in providing combined pitch and yawing moments.

#### REFERENCES

1. Fletcher, J.; and Burns, B.R.A.: "Supersonic Combat Aircraft Design," AIAA Paper No. 79-0699, March 1979.
2. Nichols, Mark R., "Aerodynamics of Airframe-Engine Integration of Supersonic Aircraft," TN D-3390, 1966, NASA.
3. Corson, Blake W., Jr.; and Runckel, Jack F.: "Exploratory Studies of Aircraft Afterbody and Exhaust-Nozzle Interaction," TM X-1925, 1969, NASA.
4. Runckel, Jack F.: "Interference Between Exhaust System and Afterbody of Twin-Engine Fuselage Configurations," TN D-7525, 1974, NASA.
5. Glasgow, E. R.; and Santman, D. M.: "Aft-End Design Criteria and Performance Prediction Methods Applicable to Air Superiority Fighters Having Twin Buried Engines and Dual Nozzles," AIAA Paper No. 72-1111, Nov.-Dec. 1972.
6. Glasgow, E. R.: "Integrated Airframe-Nozzle Performance for Designing Twin-Engine Fighters," AIAA Paper No. 73-1303, November 1973.
7. Capone, Francis J.; and Mason, Mary L.: Multiaxis Aircraft Control Power from Thrust Vectoring at High Angles of Attack. NASA Technical Memorandum 87741, June 1986.
8. Berrier, Bobby L.; and Re, Richard J.: A Review of Thrust-Vectoring Schemes for Fighter Applications. AIAA Paper No. 78-1023, July 1978.
9. Corson, Blake W.; and Runckel, Jack F., Jr.: Calibration of the Langley 16-Foot Transonic Tunnel with Test Suction Air Removal. NASA TR R-423, 1974.
10. Leavitt, Laurence D.: Effect of Empennage Location on Twin-Engine Afterbody/Nozzle Aerodynamic Characteristics at Mach Numbers From 0.6 to 1.2. NASA Technical Report 2116, May 1983.
11. Capone, F. J.: The Nonaxisymmetric Nozzle - It is for Real. AIAA Paper 79-1810, August 1979.
12. Capone, Francis J. and Carson, George T.: Effects of Empennage Surface Location on Aerodynamics of a Twin Engine Afterbody Model with Nonaxisymmetric nozzles. NASA Technical Paper 2392. February 1985.

13. Pendergraft, Odis C. Jr.; Burley, James R.; and Bare, E. Ann: Parametric Study of Afterbody/Nozzle Drag on Twin Two-Dimensional Convergent-Divergent Nozzles at Mach Numbers from 0.60 to 1.20. NASA Technical Paper 2640, October 1986.
14. Bangert, Linda S., Leavitt, Laurence D., and Reubush, David E.: Effects of Afterbody Boattail Design and Empennage Arrangement on Aeropropulsive Characteristics of a Twin-Engine Fighter Model at Transonic Speeds. NASA Technical Paper 2704, June 1987.
15. Putnam, Lawrence E.; and Bissinger, N. C.: Results of AGARD Assessment of Prediction Capabilities for Nozzle Afterbody Flows. AIAA - 85-1464, July 1985.
16. Henderson, William P.; and Burley, James R. II: Effect of Empennage Arrangement on Single-Engine Nozzle/Afterbody Static Pressures at Transonic Speeds. NASA Technical Paper 2753, November 1987.
17. Berrier, Bobby L.; and Mason, Mary L.: A Static Investigation of Yaw Vectoring Concepts on Two-Dimensional Convergent-Divergent nozzles. AIAA Paper 83-1288, June 1983.
18. Berrier, B. L.; and Mason, M. L.: Static Investigation of Post-Exit Vanes for Multiaxis Thrust Vectoring. AIAA Paper 87-1834, June 1987.

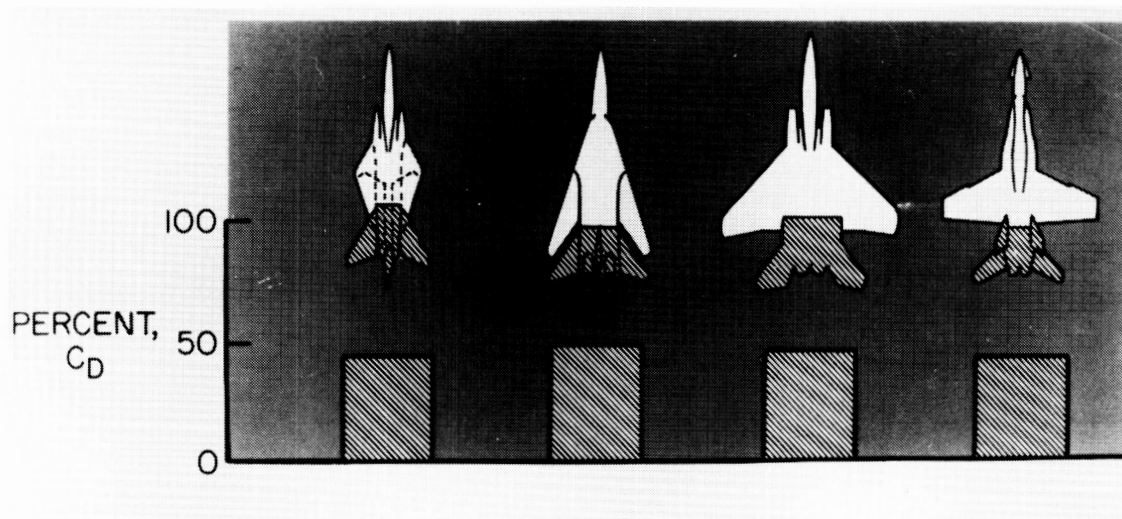


Figure 1. Nozzle/afterbody/empennage drag for high-performance aircraft.

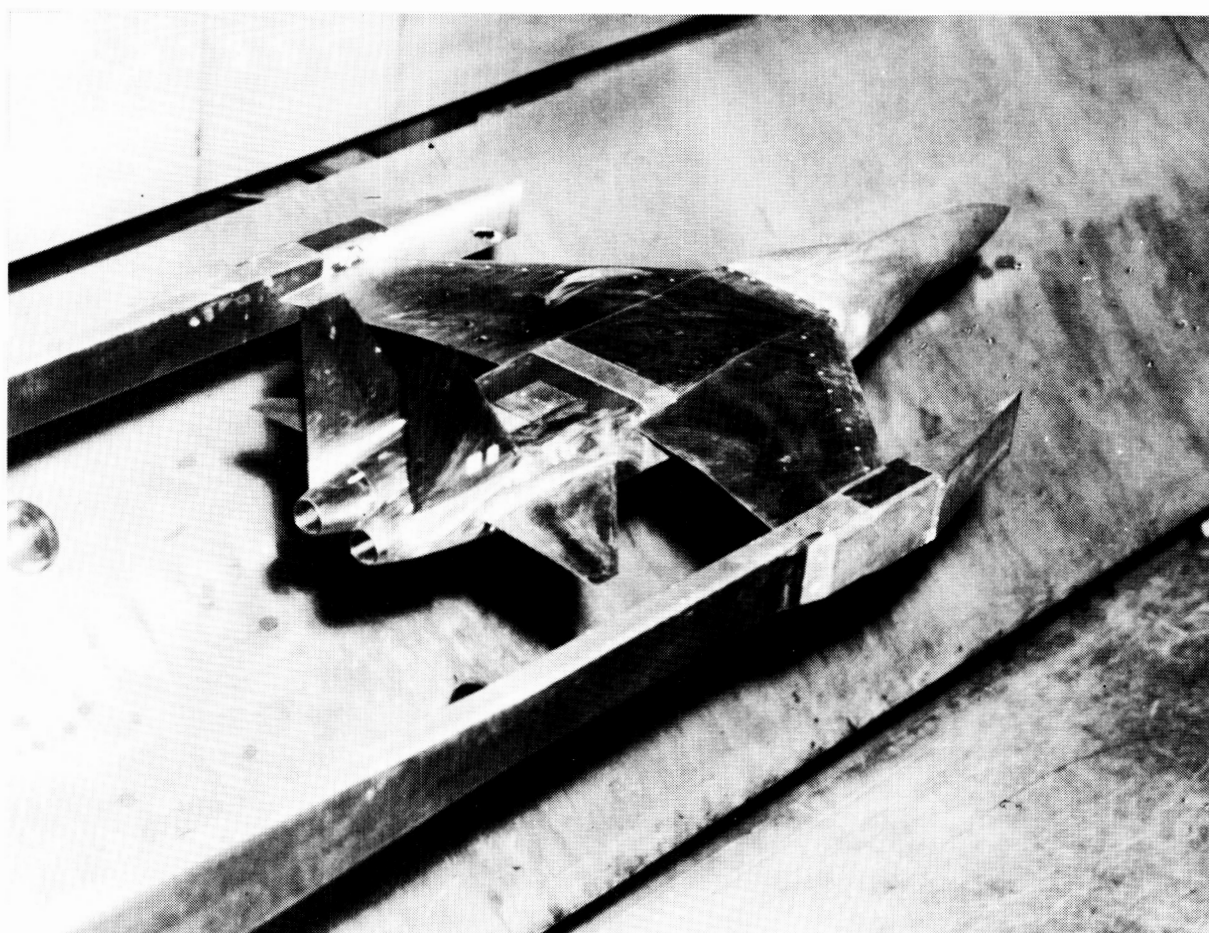


Figure 2. Model with twin axisymmetric nozzles.

$\alpha = 0^\circ$ , scheduled NPR  
axisymmetric dry power nozzles

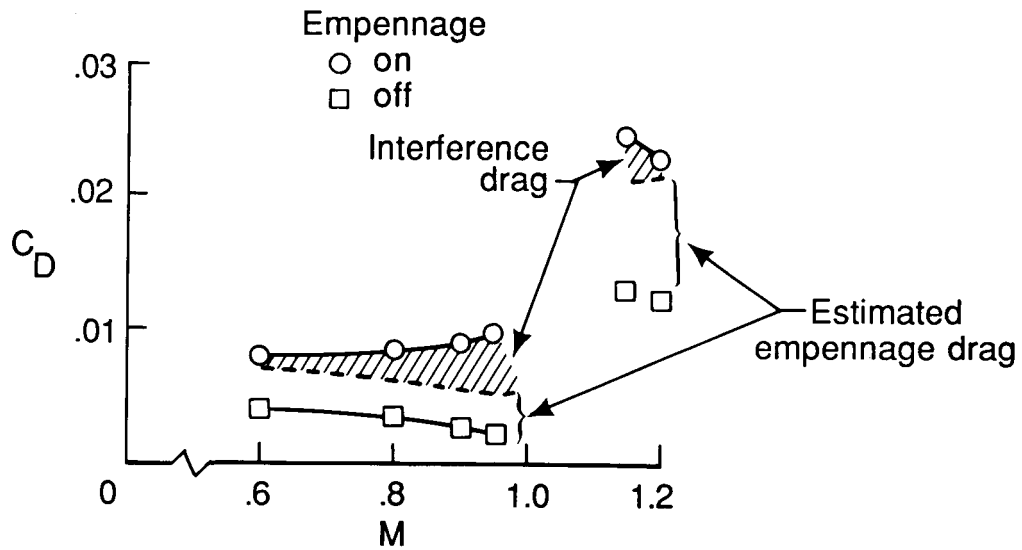


Figure 3. Nozzle/afterbody/empennage drag breakdown.

Axisymmetric dry power nozzle, aft horizontal tails,  $\alpha=0^\circ$

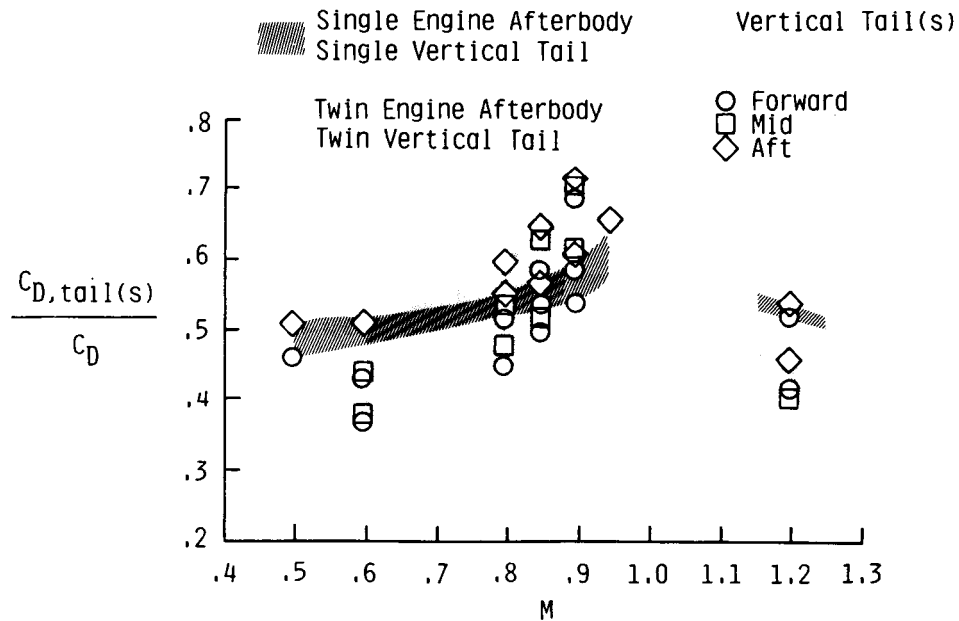


Figure 4. Ratio of tail drag to afterbody drag.

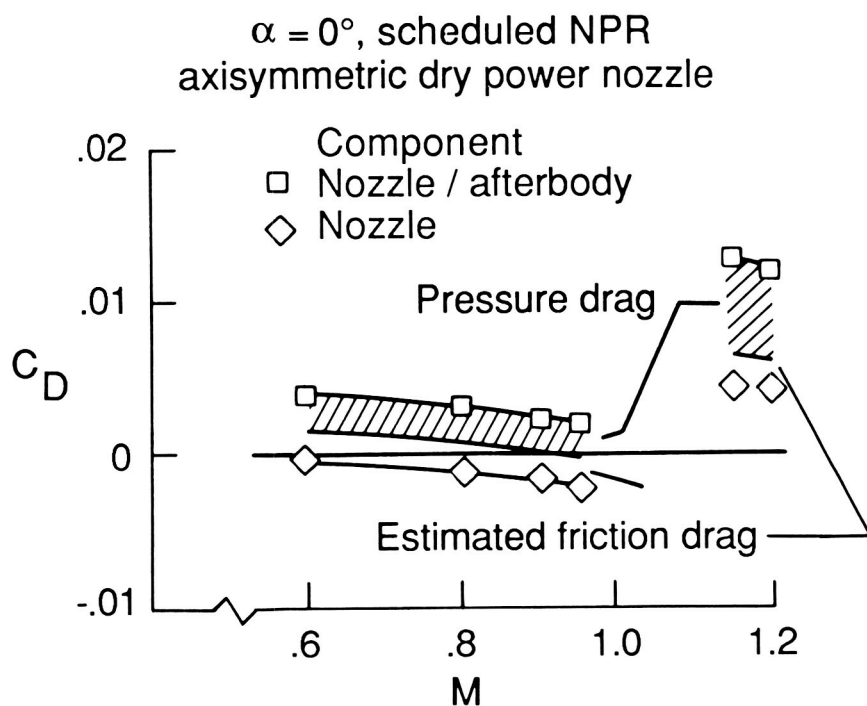


Figure 5. Nozzle/afterbody drag breakdown.

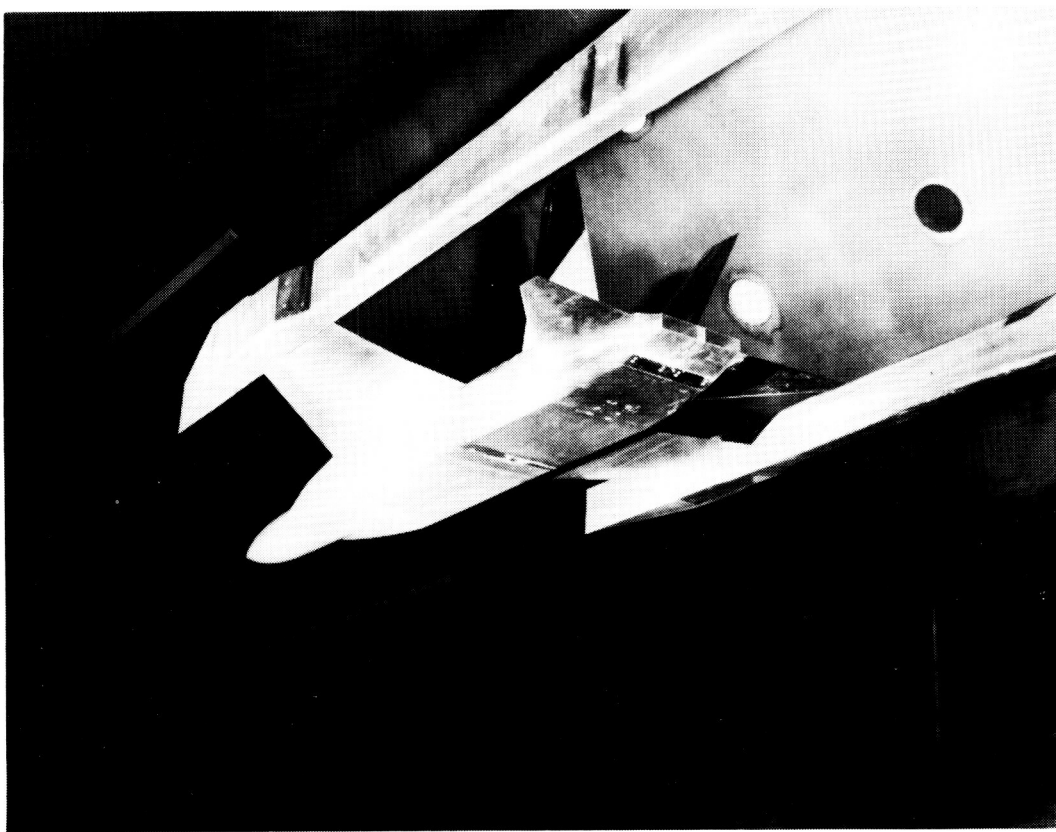


Figure 6. Model with twin nonaxisymmetric nozzles.

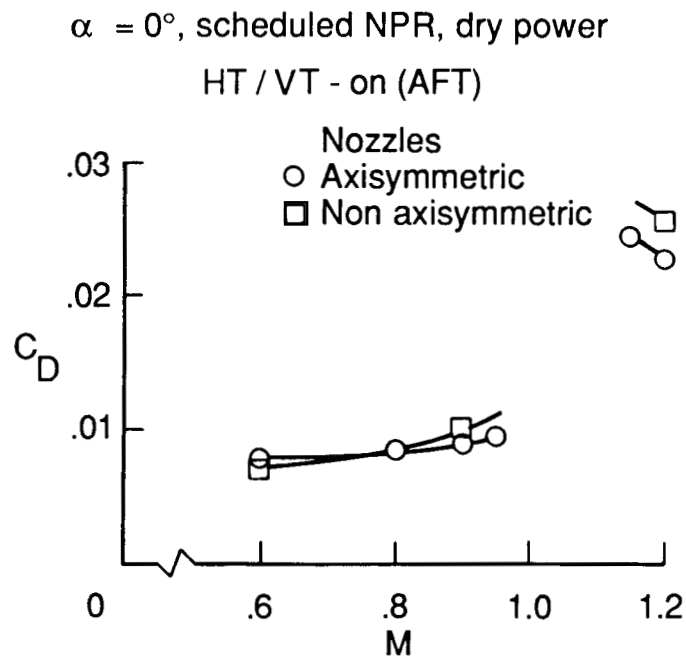


Figure 7. Drag comparison for model with empennage and various nozzle types.

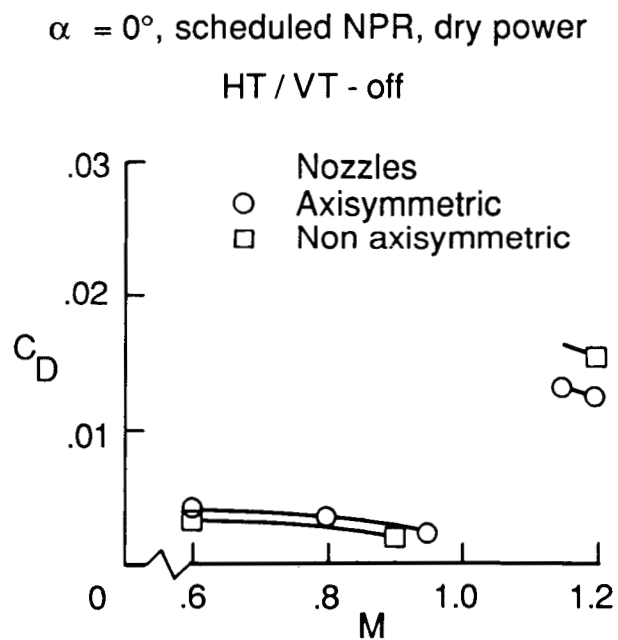


Figure 8. Drag comparison for model without empennage and various nozzle types.

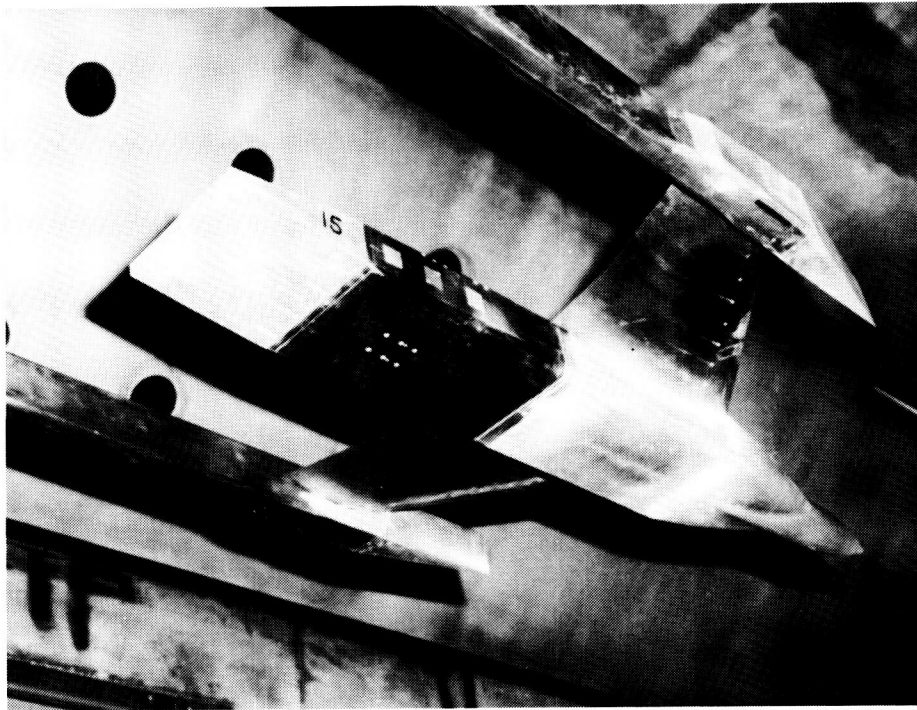


Figure 9. Model with 7.5° boattail nonaxisymmetric nozzles.

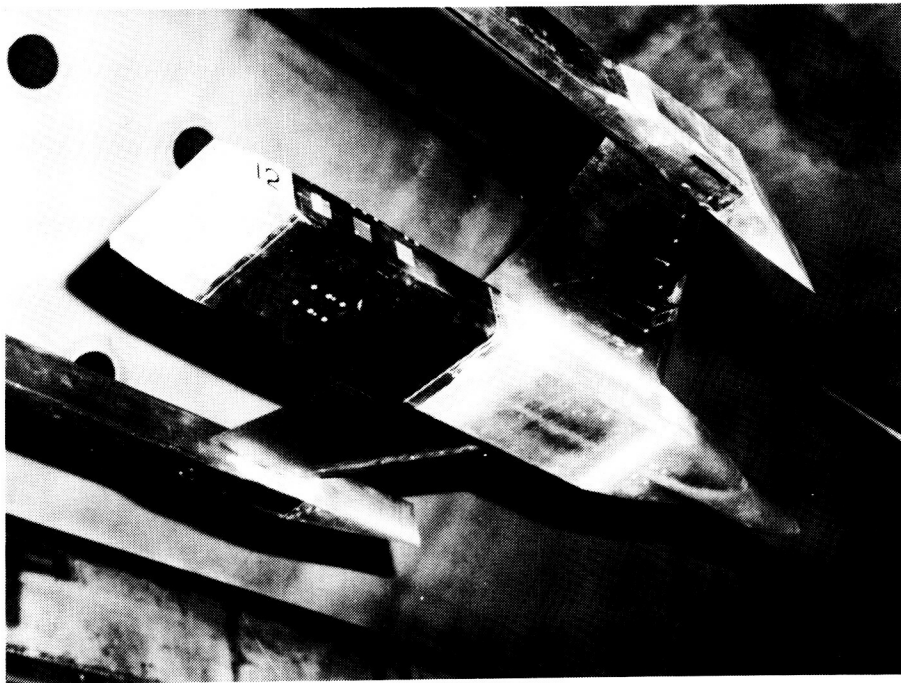


Figure 10. Model with 12.5° boattail nonaxisymmetric nozzles.



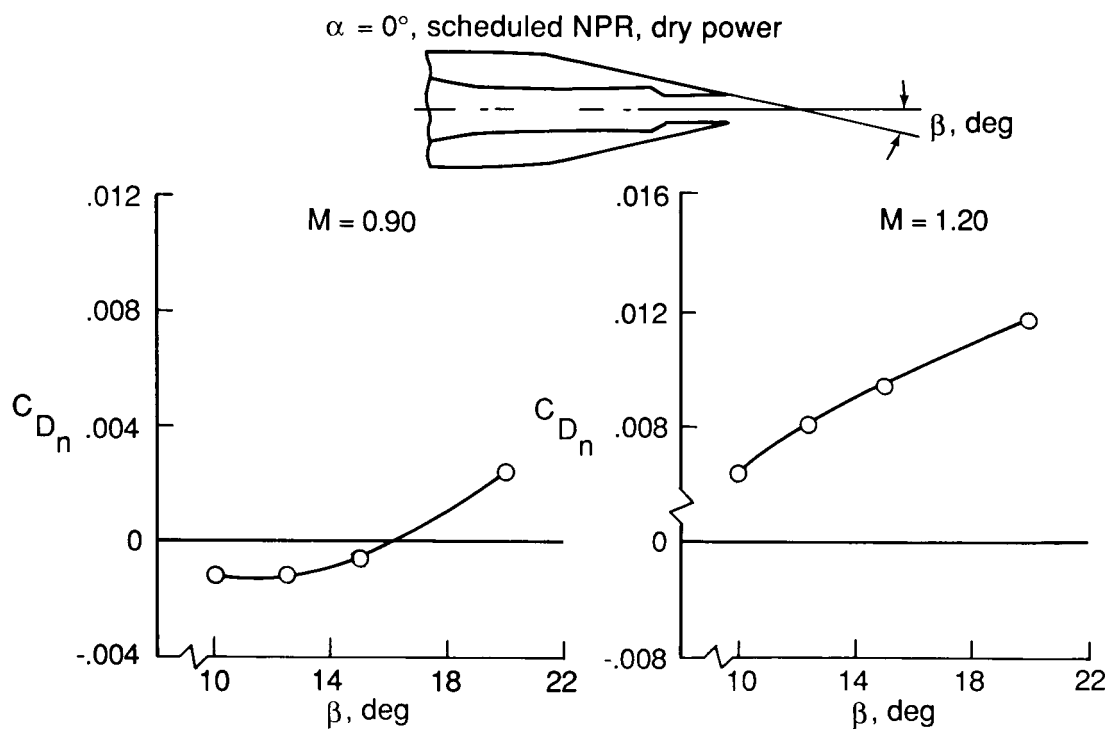


Figure 11. Effect of nozzle boattail angle on nozzle drag.

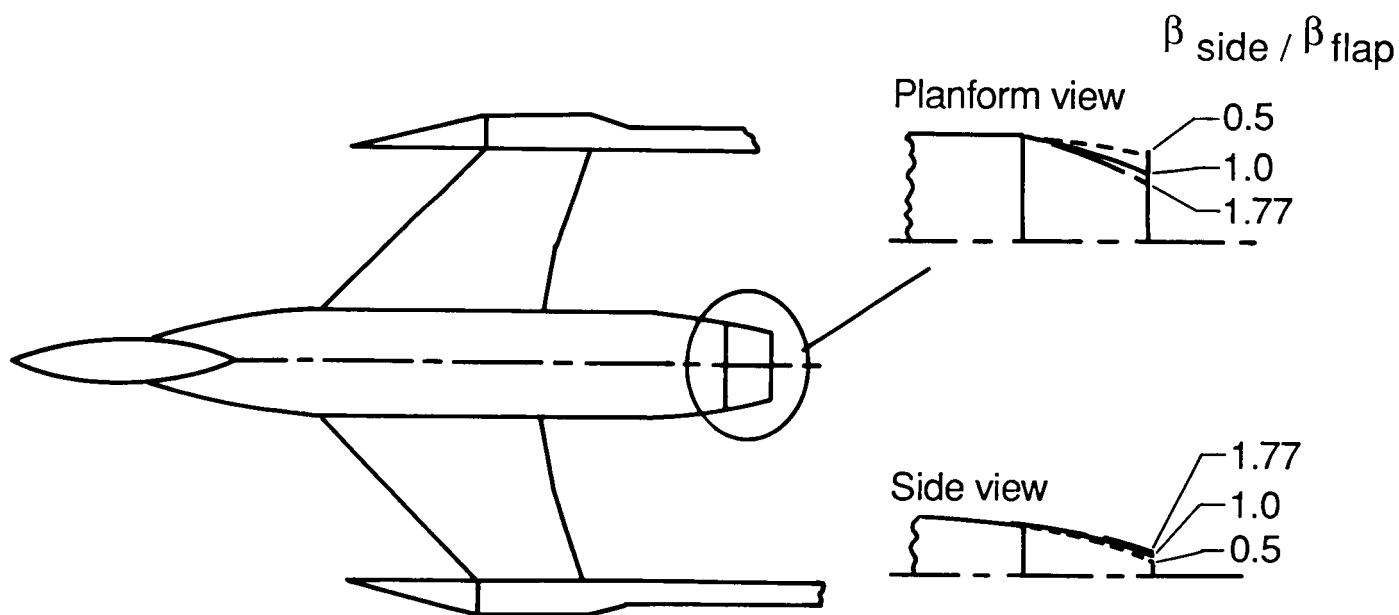


Figure 12. Model showing nozzle boattail angle trade study.

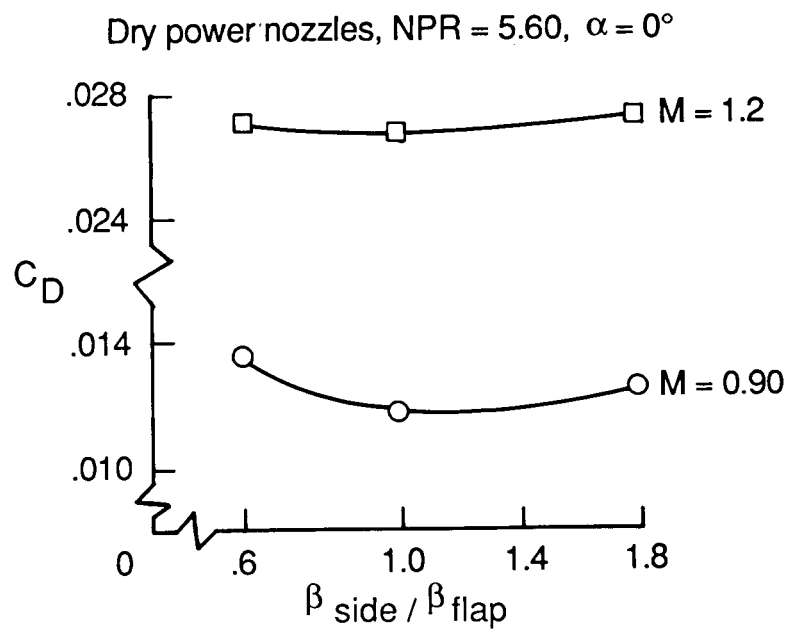


Figure 13. Effect of nozzle sidewall vs. upper/lower flap boattail angle.

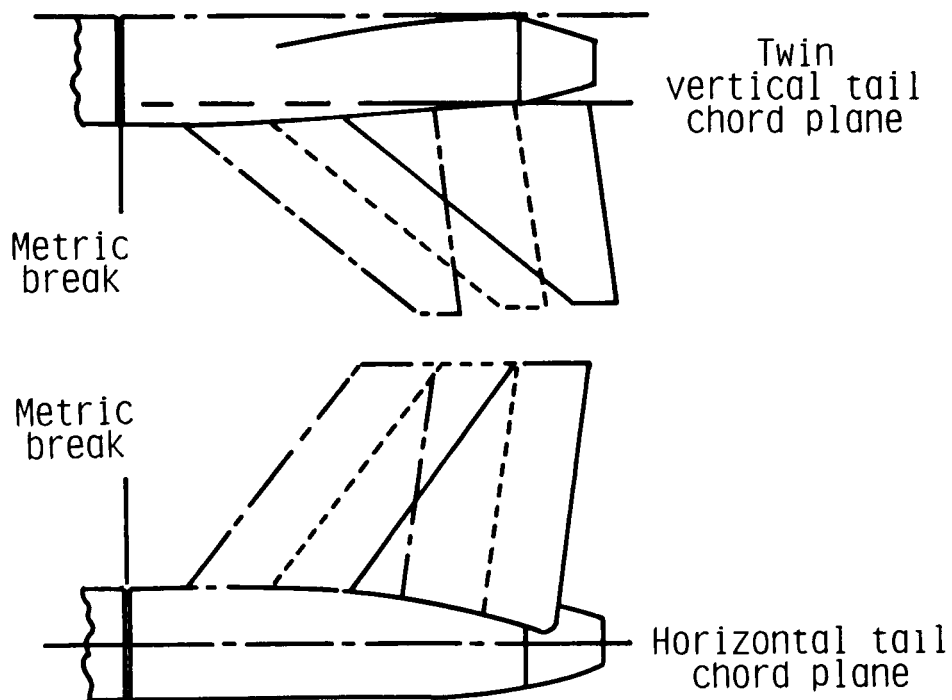


Figure 14. Empennage locations on fuselage.

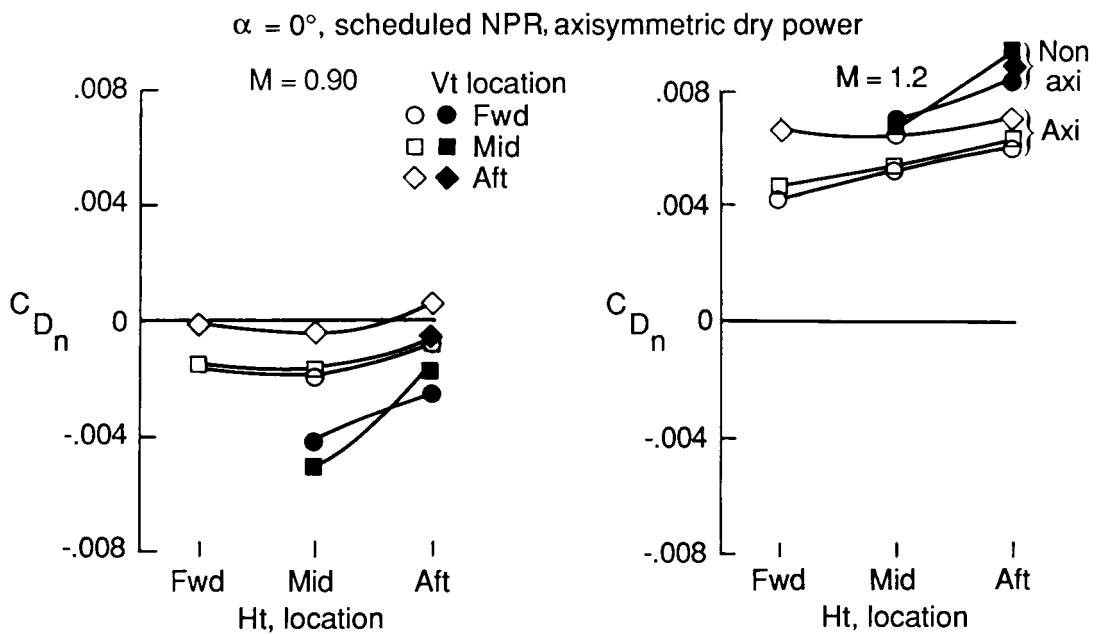


Figure 15. Effect of horizontal and vertical tails on nozzle drag.

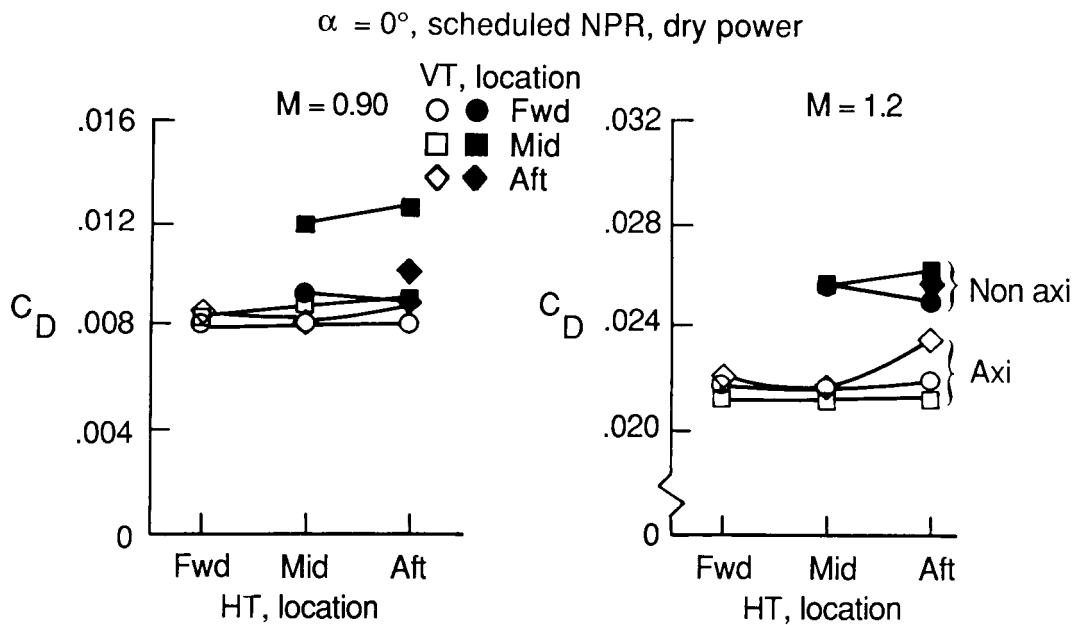


Figure 16. Effect of horizontal and vertical tails on total nozzle/afterbody drag.

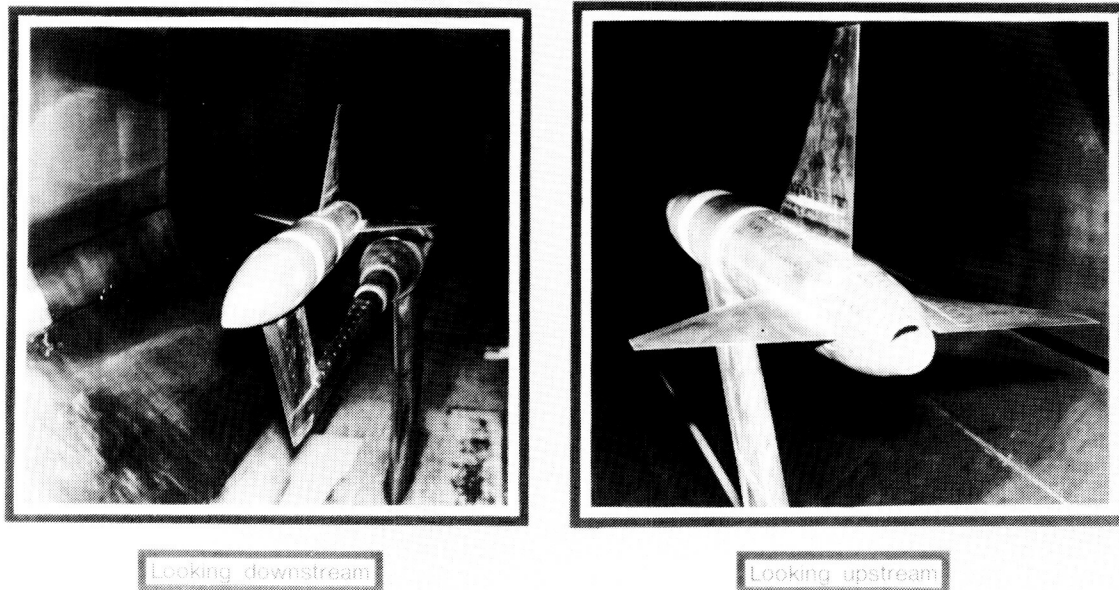


Figure 17. Model installed in the 16-Foot Transonic Tunnel.

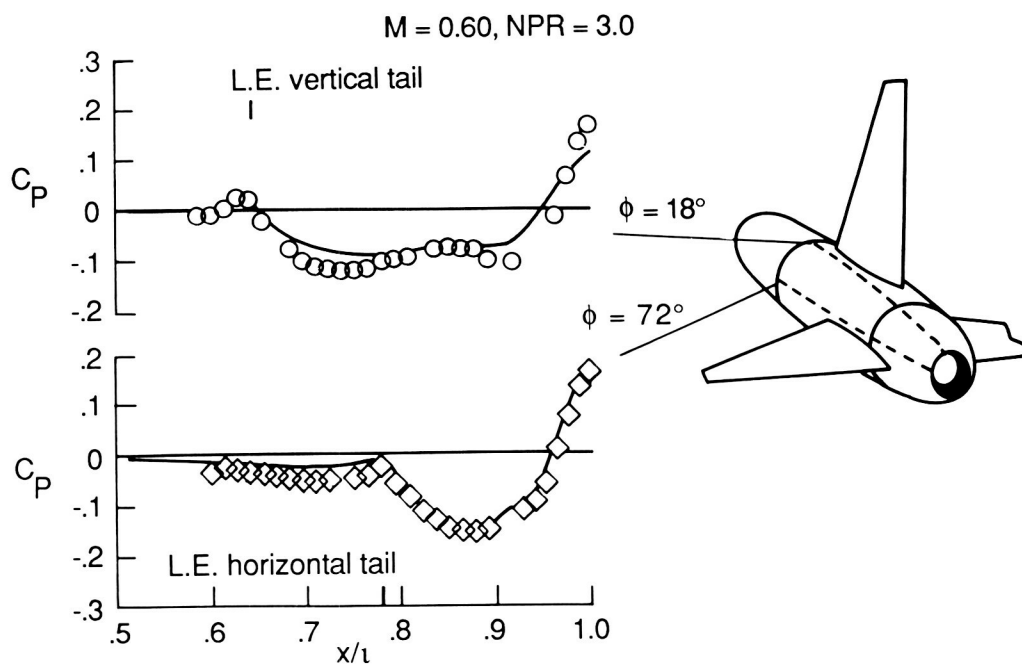
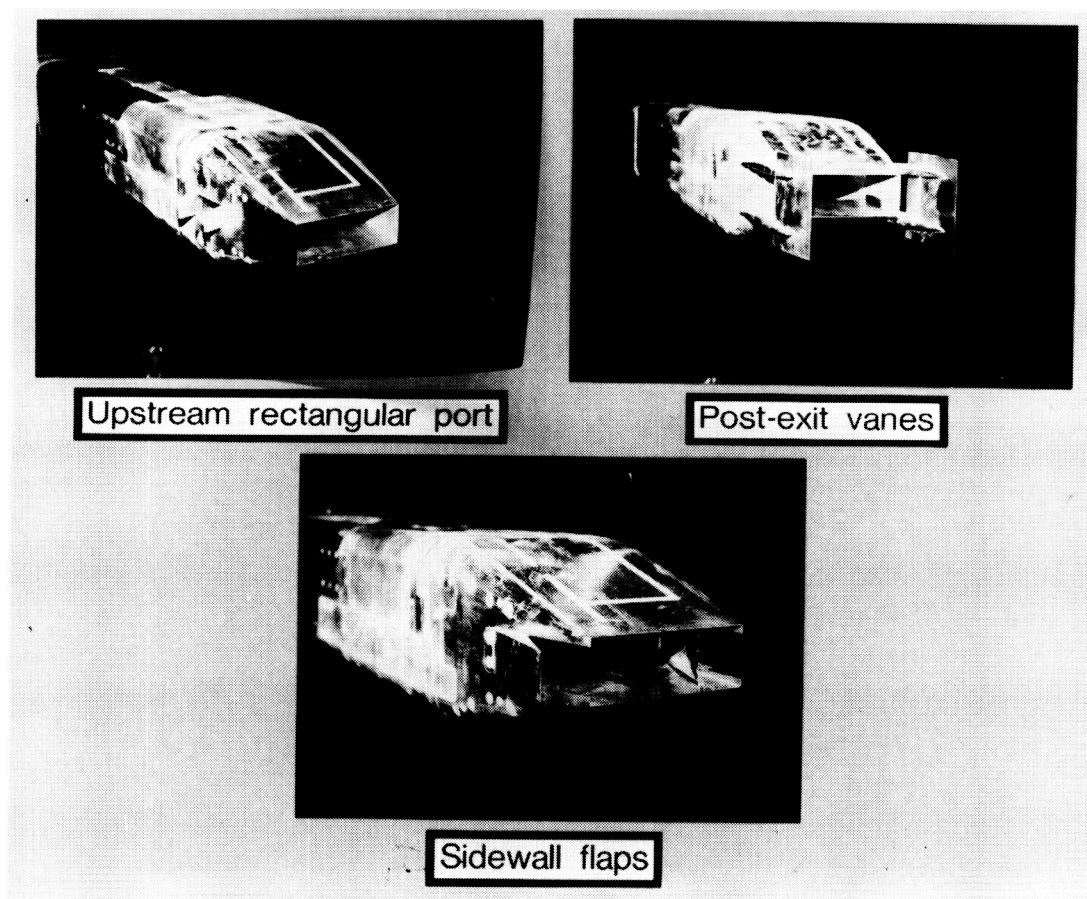
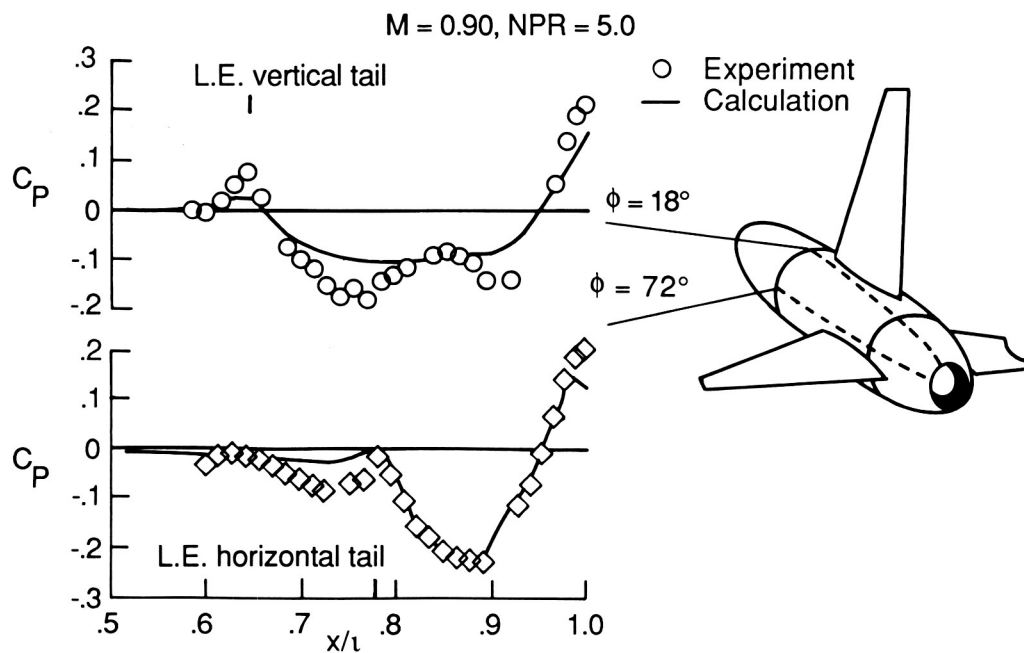


Figure 18. Comparison of experimental and theoretical pressure coefficients at  $M = 0.60$ .



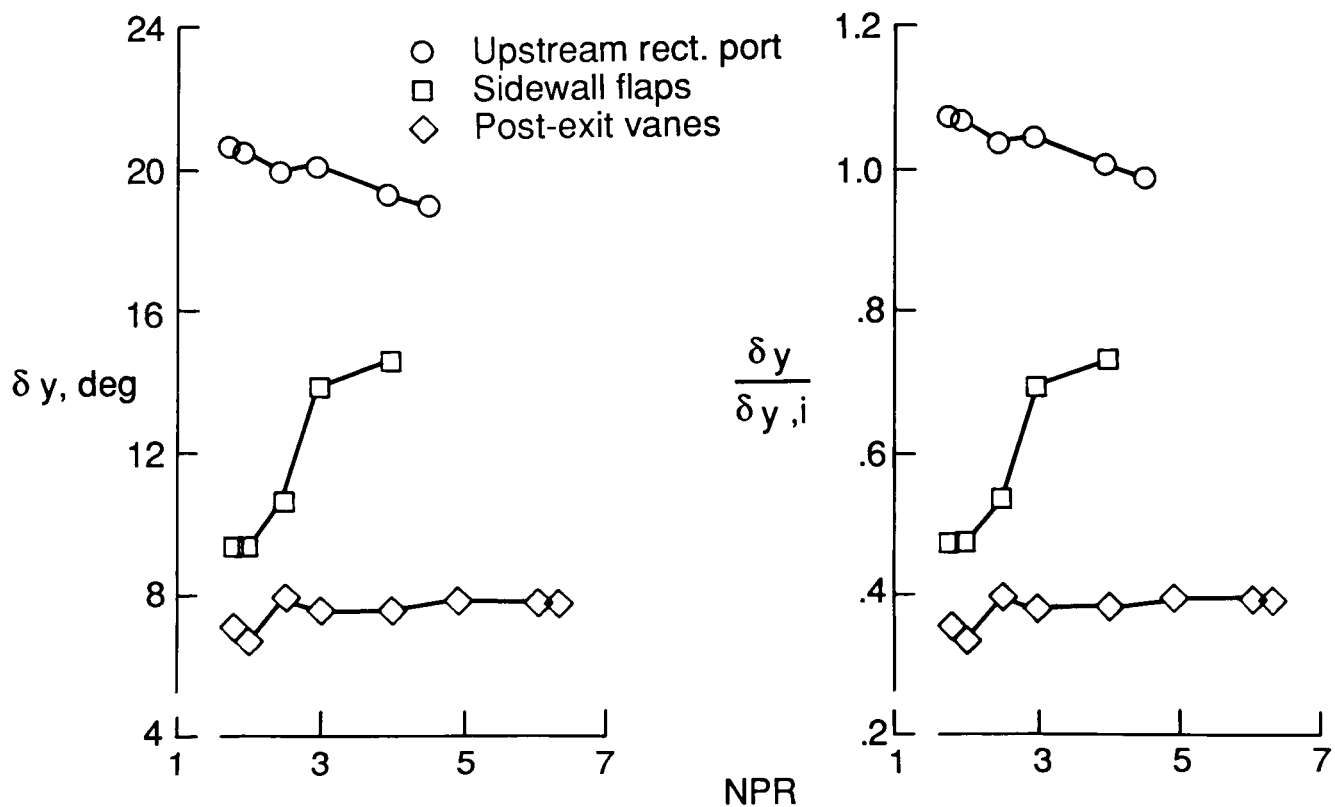


Figure 21. Flow turning performance of yaw vector concepts at  $M = 0.0$ .

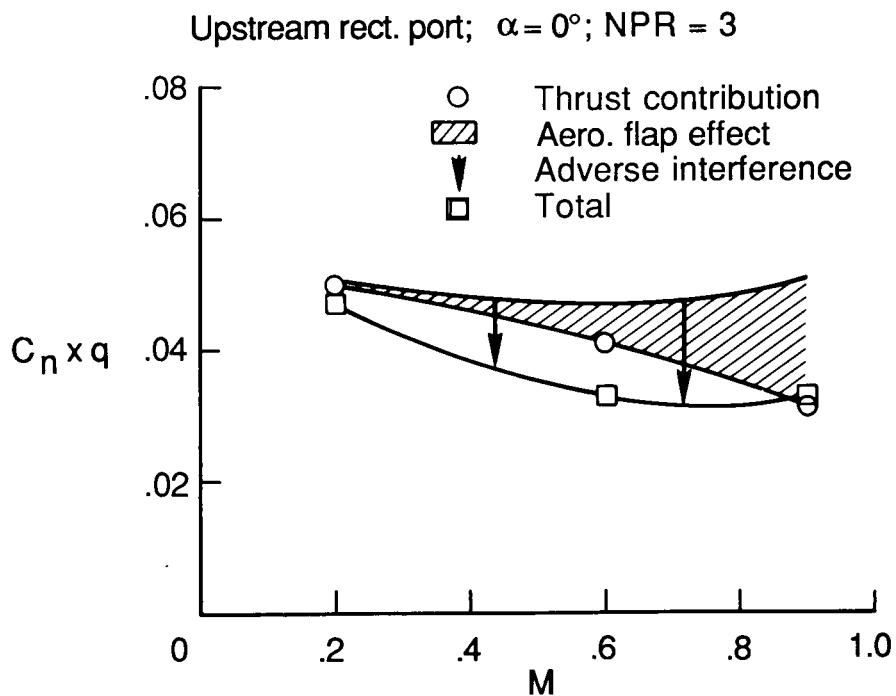


Figure 22. External flow effects on vectored thrust yawing moment for upstream rectangular port model.

Sidewall flaps;  $\alpha = 0^\circ$ ; NPR = 3

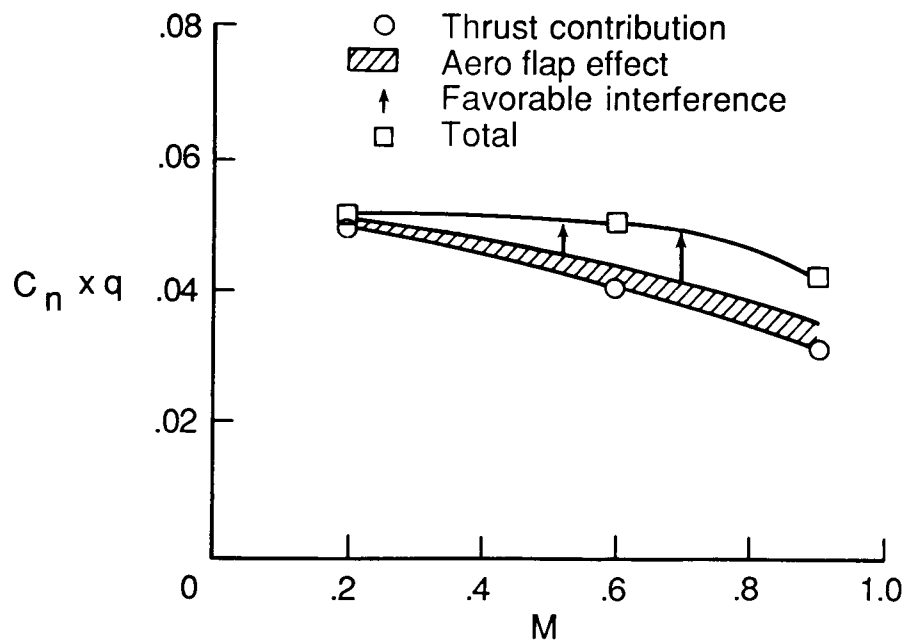


Figure 23. External flow effects on vectored thrust yawing moment for model with sidewall flaps.

Post-exit flaps;  $\alpha = 0^\circ$ ; NPR = 3

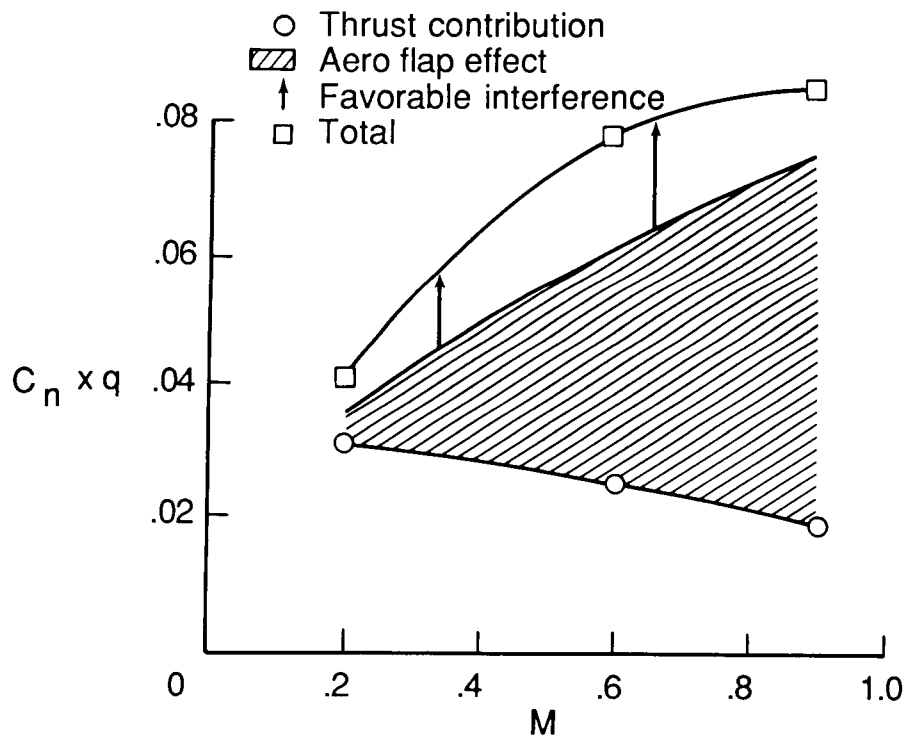


Figure 24. External flow effects on vectored thrust yawing moment for model with post-exit flaps.

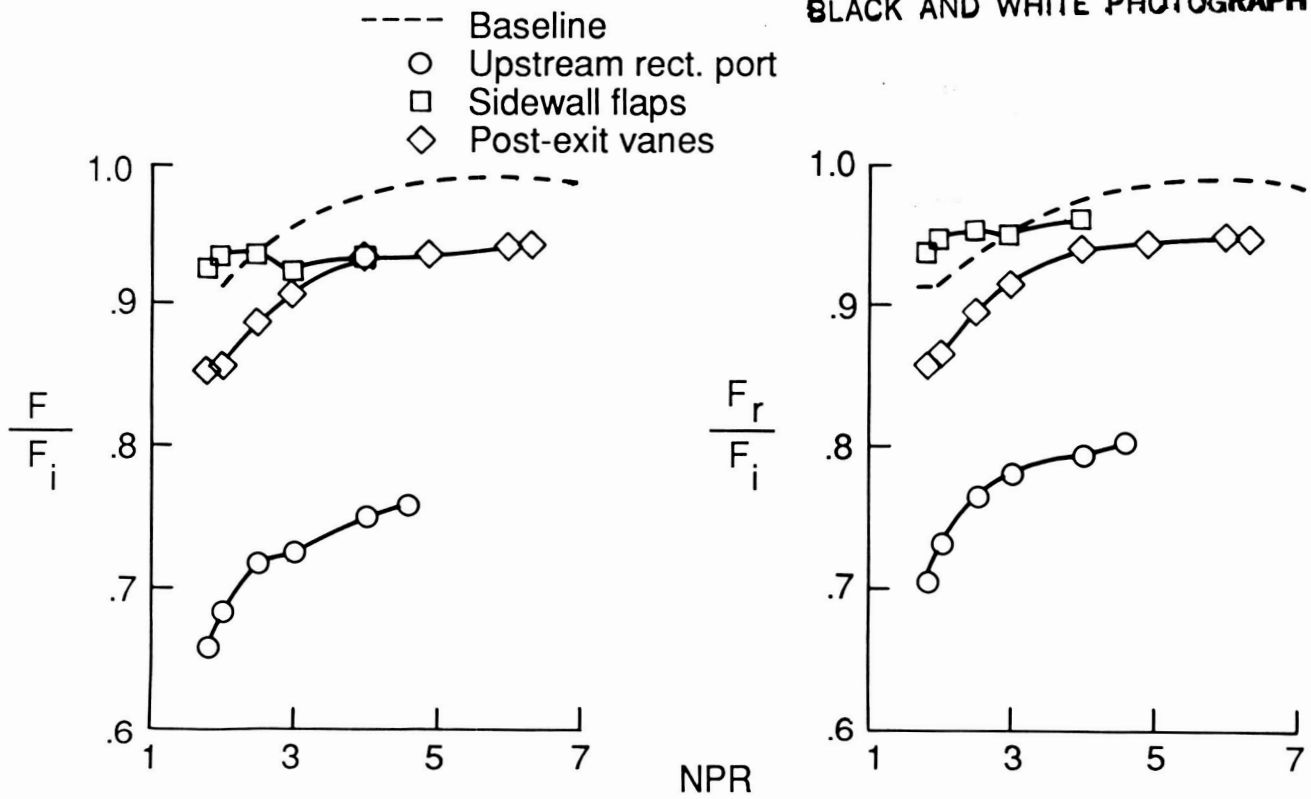


Figure 25. Thrust performance of yaw vector concepts at  $M = 0.0$ .

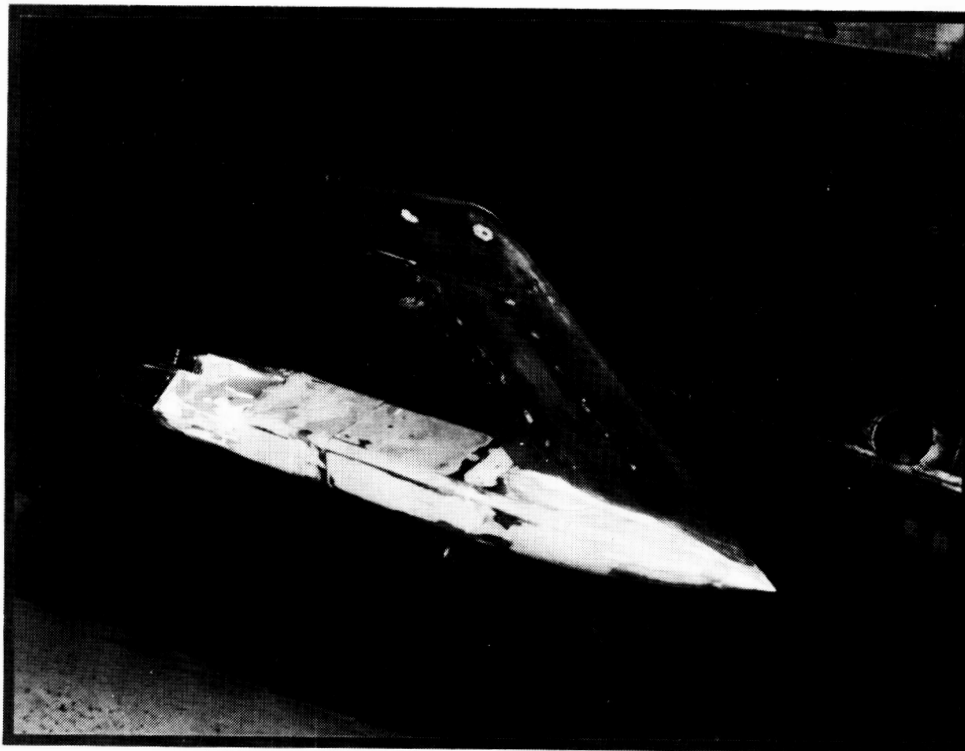


Figure 26. Model with canted nozzles in the 16-Foot Transonic Tunnel.



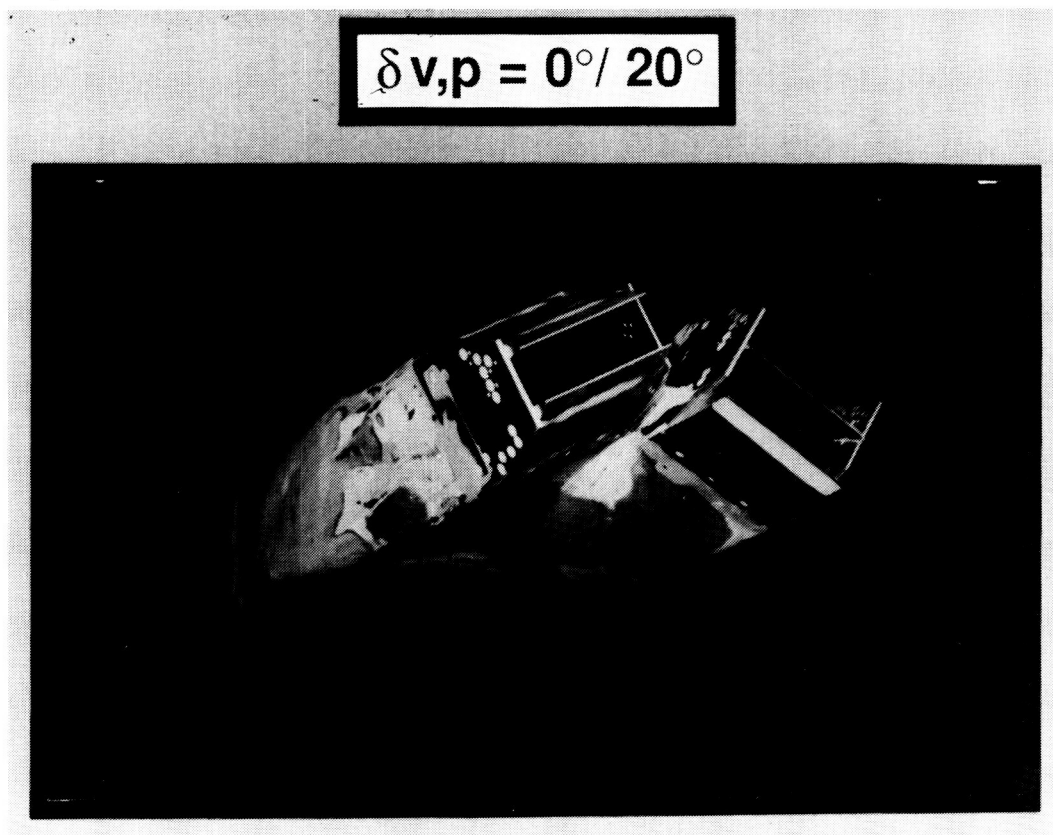


Figure 27. Model with nozzles canted  $30^\circ$ .

Dry power,  $\theta = 30$ ,  $M = 0.20$ ,  $NPR = 3.2$

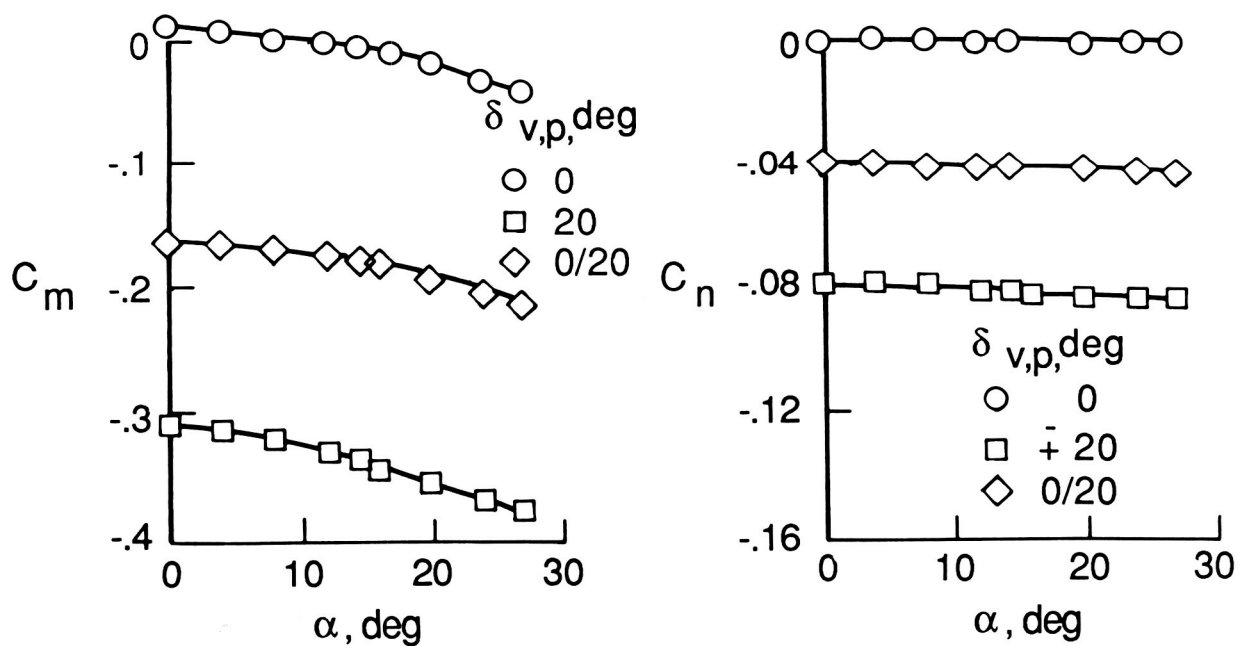


Figure 28. Effect of nozzle flap deflection on pitching and yawing moments.

$$\Delta C_D = \text{Nozzles canted } 30^\circ - \text{Nozzles canted } 0^\circ$$

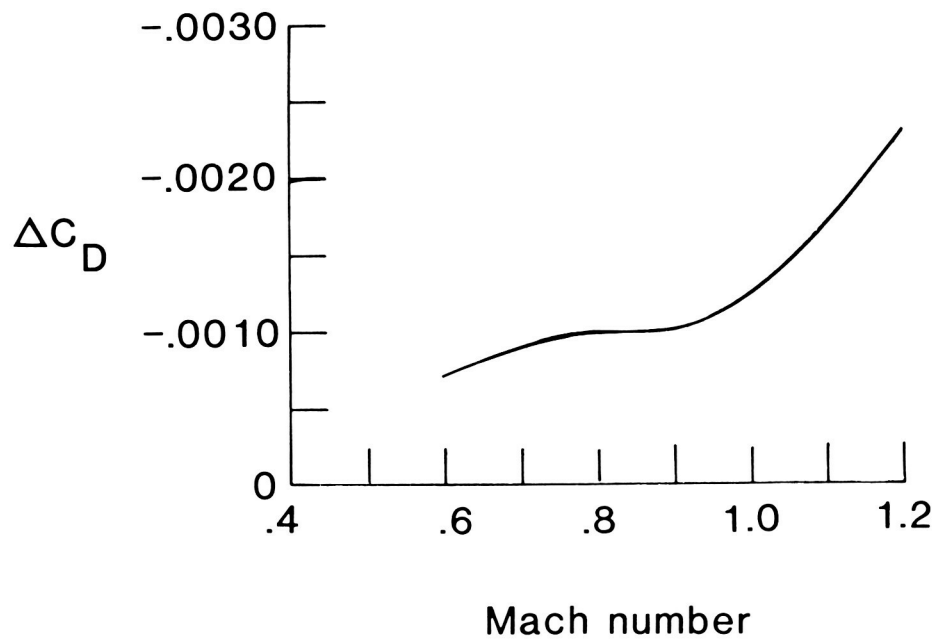


Figure 29. Drag reduction due to canted nozzles.

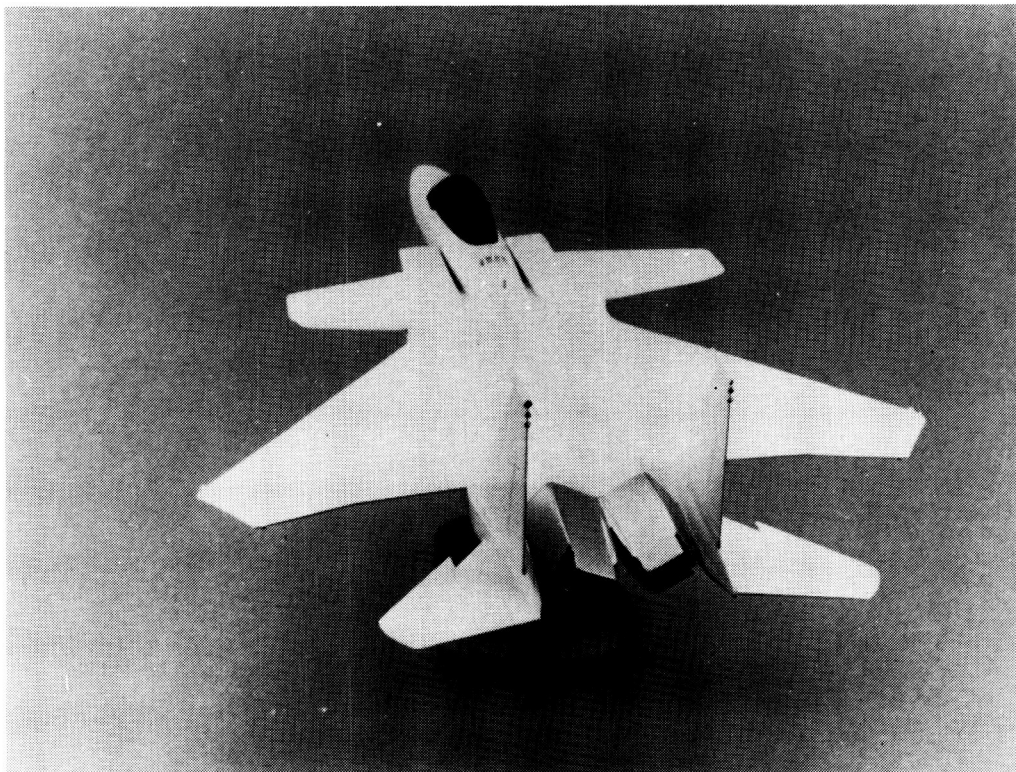


Figure 30. Top view of the F-15 SMTD with canted nozzles.

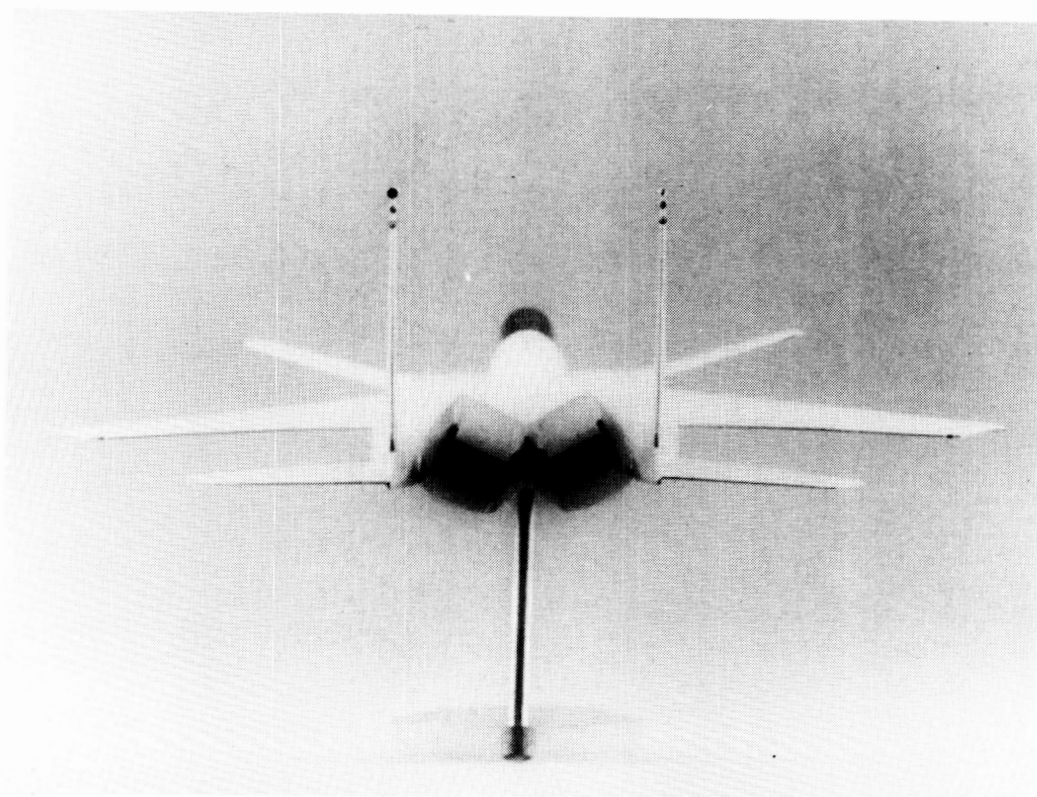


Figure 31. Rear view of the F-15 SMTD with canted nozzles.

ORIGINAL PAGE  
BLACK AND WHITE PHOTOGRAPH

**FLIGHT RESEARCH AND TESTING**

Terrill W. Putnam and Theodore G. Ayers  
Dryden Flight Research Facility  
Edwards, CA

**INTRODUCTION**

Flight research and flight testing form a critical link in the aeronautics research and development chain. Brilliant concepts, elegant theories, and even sophisticated ground tests of flight vehicles are not sufficient to prove beyond a reasonable doubt that an unproven aeronautical concept will actually work and perform as predicted. Flight research and testing provide the ultimate proof that an idea or concept performs as expected. Ever since the Wright brothers, flight research and testing have been the crucible in which aeronautical concepts have advanced and been proved to the point that engineers and companies have been willing to stake their future to design and produce new aircraft. That is still true today as shown by the development of the experimental X-30 aerospace plane which will be used to validate advanced concepts by testing them in an experimental aircraft prior to committing to the production of a military or commercial vehicle.

As modern aircraft have become more sophisticated and complex, flight research has become increasingly important as a way to validate both overall aeronautical concepts and individual technology experiments. This has required that new approaches to flight research be developed that range from experimental construction techniques, advanced instrumentation and computer controlled maneuvers to new real-time and postflight analysis and display techniques. The development of high speed, large capacity computers has paved the way for the emergence of computational fluid dynamics (CFD) as a tool for the aircraft conceptual design process. For these CFD tools to be useful it is critical that the fluid dynamic models be validated in a realistic environment. This has also pushed the development of new wind tunnels and associated test techniques, but the final validation still requires the design of carefully formulated flight research programs and experiments to provide the kind of comprehensive data that is required for code validation. There is still much flight research to be done to develop and provide the data that adequately describe a maneuvering airplane in a dynamic, nonstandard atmosphere for validation of both CFD and ground test techniques.

The Dryden Flight Research Facility of NASA Ames Research Center (Ames-Dryden) continues to be involved in a number of flight research programs that

require understanding and characterization of the total airplane in all the aeronautical disciplines, for example the X-29. Other programs, such as the F-14 variable sweep transition flight experiment, have focused on a single concept or discipline. Ames-Dryden also continues to conduct flight and ground-based experiments to improve and expand the ability to test and evaluate advanced aeronautical concepts. A review of significant aeronautical flight research programs and experiments is presented here to illustrate both the progress being made and the challenges to come.

## FLIGHT RESEARCH

Historically, flight research has played a pivotal role in the advancement of aeronautical science and technology. Indeed, it was the flight research with gliders (Fig. 1) that led the Wright brothers to the discovery that the camber of 1 to 12 recommended by Otto Lilienthal was not as good as the camber of 1 to 22 that the Wrights used in one of their designs. The Wrights also discovered in flight that the center of pressure on a cambered surface moved aft as angle of attack is reduced at low angles of attack, which is opposite to the center of pressure movement on a plane surface. This led, of course, to the construction of their wind tunnel so they could acquire data that allowed them to design the first successful self-powered airplane.

One of the first projects completed by the executive committee of the National Advisory Committee for Aeronautics (NACA) in 1915 was a facilities survey of industry, government, and universities. Out of that work, it was concluded that NACA would require both a laboratory and a flight test facility. This led to the establishment of the Langley Memorial Aeronautical Laboratory in 1920. The two pronged approach to aeronautical problems at Langley—model tests and full scale flight tests—established the interdependence of these two test disciplines. Emphasis on this dual approach has been strong ever since and is today a cornerstone of the NASA aeronautics program.

The loss of a Lockheed P-38 Lightning and the pilot during a dive test early in World War II focused the need for a more complete understanding of the essential characteristics of transonic flight. Because of an inability of current wind tunnels to operate and produce reliable data in the transonic speed range, Robert Gilruth, a NACA engineer devised a method of conducting transonic research. He had observed that significant supersonic flow existed on the top of a North American P-51 wing during dives, even though the aircraft speed was only approximately Mach 0.75. As the first application of the wing-flow technique, a small airfoil model was mounted perpendicular to the P-51 wing upper surface (Fig. 2). Subsequently, many other airfoils were tested, and this technique provided the most systematic and continuous plots of transonic data

assembled by NACA at that time. This approach was used to experimentally confirm that thin wings were best for supersonic flight. The wing-flow technique was also the first experimental validation of R.T. Jones' theory which predicted that in transonic and supersonic flight the drag of a wing would be significantly reduced if it were swept.

The research airplane was conceived by John Stack of Langley in 1933 when he designed an airplane which he used to assess the performance that was theoretically achievable. In 1940 he began to have active discussions with NACA management and the military on the need for a research airplane that would provide the data necessary to understand the compressibility problems that the military airplanes were experiencing in high-speed dives. The golden era for experimental research airplanes began in 1944 when the Army Air Force undertook the development of an experimental rocket-powered aircraft, the Bell XS-1, which was designed to penetrate the "sonic barrier" (Fig. 3). At about the same time the Navy contracted with Douglas for the development of the turbojet-powered Douglas Model 558 high-speed test airplane designed to gather research data in the critical transonic speed range. These were followed by the X-2, X-3, X-4, X-5, and the XF-92A. The Bell XS-1 met its objective of achieving supersonic flight on October 14, 1947 with Captain Chuck Yeager at the controls in the skies over the California desert. The X-2 also was dedicated to solving the problems of supersonic flight, while the other aircraft were designed to investigate advantages of and problems with new configurations. The Douglas X-3 had a low-aspect-ratio thin wing; the Douglas D-558-2 had swept wings; the Northrop X-4 was semitailless; the Bell X-5 had variable sweep wings; and the Convair XF-92A was designed with a delta wing.

By 1954 it became apparent that the problems and challenges of hypersonic flight could best be addressed through the development and flight test of a manned Mach 7 research aircraft. The Air Force, Navy, and NACA signed a Memorandum of Understanding establishing a Research Airplane Committee to provide the technical direction necessary to develop and test the X-15 airplane (Fig. 4). The program was designed to assess the problems and develop solutions associated with hypersonic flight such as structural design, aerodynamic heating and heat transfer, energy management and the transition from the reaction controls used in space to the aerodynamic controls used in the atmosphere. The X-15 was the most successful research airplane program ever undertaken as shown by the 199 flights accomplished in just over nine years. Until the first orbital flight of the space shuttle Columbia in 1981, the X-15 held the altitude and speed records for winged aircraft, with flights as high as 67 miles and a maximum speed of Mach 6.7. The knowledge and experience gained in the X-15 program led directly to the systems and techniques used in the space shuttle.

As NASA moved into the space age in the early 1960s, it became apparent that lifting re-entry spacecraft would be much more useful than ballistic capsule craft in that they could maneuver in the atmosphere and land horizontally on the earth at a predetermined location. A series of lifting body concepts were developed at NASA Langley, NASA Ames, and under contract to the Air Force that culminated in the development and flight test of several designs (Fig. 5). The vehicles were designed to use rocket propulsion to boost them to the Mach 3 speed regime, at which time the rockets would be turned off and they would glide back to an unpowered landing at Edwards. All the craft had a very low lift-to-drag ratio and therefore descended very rapidly. The need to know and monitor the kinetic and potential energy state of these vehicles in real time in order that decisions on landing locations could be made in case of emergency, further developed and refined the energy management concepts that were initially started for the X-15 program. The primary research objectives for these vehicles centered around the flying qualities issues associated with essentially wingless craft in the critical landing phase and in the transonic speed range where vehicle characteristics are typically less well-defined in ground tests. The successful completion of this program with the successful runway landing series of the Martin X-24B (Fig. 6) provided the confidence that the space shuttle could indeed re-enter from space unpowered and land precisely at a predetermined location by carefully managing the total vehicle energy. The ability to land unpowered was critical to the success of the shuttle program since a large weight penalty would be incurred at launch if air-breathing engines were required to land the vehicle.

Even with this extensive base of data and knowledge of the flying qualities of lifting bodies, the need for flight test and research was amply demonstrated during the shuttle approach and landing tests (ALT) program (Fig. 7) when pilot-induced oscillation (PIO) tendencies were exhibited by the shuttle on its first concrete runway landing. Researchers at NASA Ames-Dryden then accepted the challenge to develop modifications to the shuttle control system that would suppress any PIO tendencies during the critical approach and landing phase of flight. A PIO suppressor was developed using the Dryden shuttle simulation, and it was then verified in flight using the F-8 Digital Fly-By-Wire aircraft (to be described later). Because of the potential problems associated with pilot-induced oscillations and the convincing demonstration of a reasonable and cost-effective solution, the PIO suppressor was incorporated into the shuttle flight control system prior to the first orbital flight and subsequent landing.

The late 1960s and early 1970s brought a resurgence of interest in the problems associated with supersonic flight, principally those impeding the development of an efficient, economically viable and environmentally

compatible supersonic transport. A flight research program was initiated using the North American XB-70 aircraft (Fig. 8) to acquire supersonic cruise data. This aircraft was used in an extensive program to acquire data to assist in the development and validation of computer codes to predict the sonic boom overpressure signature characteristics of large, high-flying supersonic aircraft. In addition, studies of flying qualities were conducted at both supersonic speeds and during landing approach, as well as experiments to characterize boundary-layer noise and the aeroelastic response of large aircraft to gusts. This program provided valuable insight into and developed solutions to some of the problems associated with high-altitude, high-speed cruise flight.

The Lockheed YF-12A and YF-12C aircraft (Fig. 9) were loaned to NASA to conduct research in propulsion, structures, and flight dynamics at supersonic cruise flight conditions. One particularly difficult problem was to assess the relative contributions of aerodynamic and thermal loads imposed on the aircraft structure at Mach 3 cruise conditions. Extensive data acquired in flight from a heavily instrumented YF-12A, in conjunction with data acquired from heating a complete airplane in the Ames-Dryden Flight Loads Research Facility, allowed the aerodynamic and thermal load contributions to be separated. The YF-12C was instrumented for propulsion system measurements and the program yielded such surprising results as the fact that the inlet bypass system provided more yaw power at cruise than the aircraft rudders and that the mixed compression inlets were producing more than 1/2 the total propulsive thrust at Mach 3.2. Flight dynamics problems encountered in the XB-70 program also resurfaced. Flying through local pressure and temperature variations at high speed cause variations in speed (because Mach number is a function of pressure and temperature) with subsequent changes imposed on the aircraft attitude by the autopilot, which resulted in altitude variations of several thousand feet. This problem was successfully overcome by integrating the control of the propulsion and flight control systems. An unexpected benefit of this control integration was an aircraft range increase of 7 percent. This technology was incorporated in the operational SR-71 fleet several years ago as a result of the NASA flight research program.

Flight research and test have long been the preferred way to prove new aerodynamic concepts or configurations. Concepts that improve vehicle performance in the transonic speed range have routinely been validated in flight because of the difficulty in making accurate and precise measurements in wind tunnels at transonic speeds. One of the proof-of-concept programs that was very successful was the application of Dr. Richard Whitcomb's supercritical wing concept to a Vought F-8A aircraft (Fig. 10). This aircraft was chosen because the wing could be easily removed and replaced with a new design, the landing gear retracted into the fuselage, not the wing, and because the F-8 had



supersonic speed capability. The concept did indeed improve the transonic efficiency of the F-8 by as much as 15 percent and was widely accepted, as shown by the numerous commercial and military aircraft produced with supercritical airfoils. This program was a model for cooperation between the wind tunnel and flight research community, and indeed provided very good correlation between the wind tunnel and flight results.

As new aircraft were designed to achieve higher and higher levels of performance, it became increasingly difficult to design hydromechanical flight control systems that were lightweight, survivable, and had adequate levels of redundancy to assure that the aircraft would not be lost due to control system malfunctions. Electronic controls and especially digital electronic controls seemed to be the cure for many of these problems. In the early 1970s, Ames-Dryden embarked on a flight research program using a modified Vought F-8C (Fig. 11) to identify problems associated with digital flight controls and to assess the postulated benefits. When the aircraft first flew in 1972, it marked the first time a manned aircraft had flown with a digital flight control system with no mechanical backup. The program progressed in two phases, with the first one using modified Apollo computers to control flight, while the second phase involved the development and flight test of a new triplex computer system. This program was a technology pacesetter, as shown by the wide-spread application of the technology to aircraft designed and produced subsequently. Another very important contribution from this program was the development of the processes and procedures necessary to verify and validate software and hardware for flight-critical systems. These approaches have been imitated and expanded upon by all the organizations that have successfully produced and flown digital flight control systems in manned airplanes.

One of the keys to obtaining significantly improved performance for subsonic transport aircraft is to reduce the drag by maintaining laminar flow over large portions of the wing and fuselage. Recent tests with a Grumman F-14 aircraft (Fig. 12) as a test bed have indicated that laminar flow is achievable naturally at transonic speeds on swept wings at representative sweep angles. Gloves of foam and fiberglass were fabricated and attached to the production F-14 wing with the section designed to provide a favorable pressure gradient over much of the wing chord. This was another example of the requirement and viability of conducting basic research on boundary-layer transition in flight. Only in flight is the researcher able to evaluate boundary-layer transition under realistic noise and natural turbulence levels at the design conditions. The flight environment also allows the experiment to be evaluated at off-design yet realistic flight conditions. Innovative instrumentation developments and low-cost glove fabrication techniques have been applied to acquire boundary-layer-transition data in flight and in the real atmosphere that is definitive and of

laboratory quality. This flight experiment has provided critical data that prove the feasibility of constructing a swept-wing transport that can achieve considerable amounts of natural laminar flow with the attendant drag reductions and fuel economy, and it has provided the benchmark data from the flight environment for the validation of airfoil design and boundary-layer stability codes.

Another way which laminar flow can be achieved is by properly tailoring the pressure distribution and removing a small portion of the boundary layer near the airplane skin by sucking through slotted or porous skin. The NASA JetStar airplane (Fig. 13) was used to demonstrate the effectiveness and reliability of laminar-flow control under representative flight conditions by simultaneously testing alternative leading-edge flow control concepts on each wing. A spanwise section of the JetStar wing leading edge was modified to include laminar-flow control, insect protection, and deicing capability. One leading-edge test article used a slotted skin, while the other test article used a porous skin. Both test articles were tested under rigorously controlled research flight conditions, and the airplane was operated at a number of commercial airports throughout the United States in representative airline operational environments, including winter and summer weather conditions. This program has demonstrated the effectiveness and reliability of leading-edge laminar flow control in a realistic environment for two different concepts (slots and porous skins) and has shown that while laminar flow is greatly reduced in clouds and ice particles, it immediately returns upon exiting the clouds.

As previously noted in the discussion on the YF-12 program, the integration of the propulsion and flight control system can provide significant improvements in airplane performance with minimum weight or cost penalties. An integrated flight and propulsion control system has been developed and flight-demonstrated on a McDonnell F-15 aircraft (Fig. 14). The program was entitled highly integrated electronic control (HIDEC) and several different control modes were investigated. One mode, the advanced engine control system (ADECS), modulated the engine stall margin as a function of flight condition and engine state. It also anticipated dynamic maneuvers by using pilot stick inputs which were then traded off for increased thrust. Engine thrust was increased as much as 11 percent at subsonic flight conditions, resulting in significantly improved aircraft performance. Rate of climb was increased approximately 14 percent and constant-altitude acceleration at maximum power was increased by 24 percent. Other control modes have been implemented which greatly improve engine life by reducing engine temperatures while maintaining thrust, or reducing fuel usage while maintaining constant thrust. Integrated controls research in flight has been very effective since the behavior of the integrated control system in a dynamic environment is critical to its usefulness, and it has accelerated the acceptance and application of the technology previously noted

with respect to the operational SR-71 aircraft. The USAF has also incorporated the ADECS technology into their improved-performance F110 and F100 engines that power the advanced F-15 and F-16 aircraft.

The new aerodynamic concepts that are developed analytically and in ground facilities continue to require validation in the dynamic environment of flight, as shown by the advanced fighter technology integration (AFTI)/F-111 mission adaptive wing program (Fig. 15). The performance benefits of a smooth variable-camber wing have been validated, and an advanced digital control system that optimizes aircraft performance throughout the flight envelope is being evaluated. Automatic performance-seeking control modes attempt to maximize the relevant performance parameter through an on-line control approach that couples the flight control and wing camber control systems to produce either an optimum cruise configuration or an optimum maneuvering configuration, while at the same time compensating for random gust inputs to the airplane. Results to date indicate that range improvements of 25 percent and increased sustained maneuver capability of 20 percent are achievable.

The Grumman X-29 airplane (Fig. 16), the first new experimental airplane in more than twelve years, has been exploring the performance and configuration advantages of the forward-swept-wing concept. At the same time, several other emerging technologies that were incorporated into the airplane have been tested and evaluated. These include relaxed static stability (-35 percent); three-surface longitudinal control; thin, supercritical, aeroelastically tailored composite wing; close-coupled wing and canard; and digital flight control system. The successful integration of these technologies and the performance benefits accruing from them have been demonstrated and are in the process of being correlated with predictions and wind tunnel test results. The X-29 program has required the development and application of new instrumentation and real-time analysis techniques in order to safely and efficiently expand the flight envelope. A new optical deflection measurement system was developed to accurately measure the wing deflection in flight for correlation with ground test results and to characterize the shape for aerodynamic correlations. New methods for extracting aerodynamic derivatives from highly unstable aircraft were developed, based on parameter estimation techniques. Ground-based methods for predicting the divergence of forward-swept wings had to be adapted for use in flight to assure the safe expansion of the flight envelope. Other real-time analyses have been developed and will be discussed later in this paper.

The NASA high-angle-of-attack program has recently focused on the F-18 configuration as representative of designs that can achieve high-angle-of-attack flight. The program consists of coordinated computational fluid dynamic

analysis, simulation, wind tunnel testing, and flight research. Ames-Dryden has responsibility for conducting the flight research using a specially instrumented McDonnell F-18 aircraft (Fig. 17). The F-18 airplane features a long strake or leading-edge extension (LEX) from the nose to the wing leading edge. These LEXs generate strong streamwise vortices at angle of attack, caused by the separated flow emanating from the sharp edges, which then roll up into a pair of vortices. This vortical action can have favorable effects by generating additional lift at moderate angles of attack, supplementing the lift of the wing. They can have unfavorable effects if the vortices burst near vertical tails or stabilizers and cause buffet on the structure. The initial flight research has been directed at characterizing the aerodynamic flows associated with the forebody and LEXs, both on the surface and off the surface of the airplane.

A smoke generator system has been installed in the airplane so that smoke can be injected into the vortex core at the apex of the LEX in order to make the vortex visible. These vortices have been photographed (Fig. 18) on the F-18 high-angle-of-attack research vehicle (HARV) using a remotely operated camera installed in the wingtip. The vortex burst is evident in the figure and is characterized by a rapid expansion of the core, coupled with a rapid deceleration of the axial velocity. The impingement of these vortices on tail surfaces has significant impact on the structural fatigue life of the tail structure, and methods for minimizing interaction of these vortices with the tails are being investigated.

At high angles of attack vortices are also generated on the upper surface of the forebody of the F-18. Previous studies have shown the existence of two primary and two secondary vortices. These vortices can be either symmetrical with respect to the nose or asymmetrical depending upon the angle of attack and nose apex angle. A system to visualize the surface flow of these forebody vortices has been installed on the F-18 HARV. Propylene glycol monomethyl ether (PGME), a liquid, is mixed with dye and emitted out of surface orifices on the nose cone and forebody while flying. When the pilot has stabilized the airplane, the fluid is released and the airplane flight conditions are held constant for approximately one minute while the dye dries. The resulting dye patterns are then photographed on the ground after the flight. Presented in Fig. 19 are the results of one test at an angle of attack of  $30^\circ$ , angle of sideslip  $2^\circ$ , and chord Reynolds number of  $8.9 \times 10^6$ . Where the streamlines flow together, a separation line has formed that indicates where the surface flow separates from the surface to form streamwise vortices. Secondary vortices of opposite rotation are induced by the primary vortices and the separation lines for both primary and secondary vortices are visible in the figure. When these vortices are symmetrical, the side forces on the forebody are small, but at higher angles of attack these vortices can become asymmetrical and produce significant side forces. At approximately  $40^\circ$  angle of attack the directional

stability of the F-18 diminishes to near zero, and the airplane goes into a mild wing rock with the angle of sideslip varying from  $+14$  to  $-7^\circ$ . This is believed to be caused by the oscillatory nature of the asymmetric nose vortex shedding.

The F-18 HARV has produced some very dramatic results for correlation with wind tunnel and computational efforts and many challenges remain to provide the high-quality, detailed data necessary for a thorough understanding of the complex nonlinear flow phenomena that characterizes high-angle-of-attack flight.

The development and application of new instrumentation, test, and analysis techniques is the lifeblood of any experimentally oriented organization, and flight research is no exception. The key to this activity is a core of experienced and innovative flight researchers working together with instrumentation development engineers and technicians. Several new approaches have already been highlighted in this paper, such as using liquid crystals to detect transition, smoke generators for vortex visualization, and the optical deflection measurement system; however, much remains to be done. New methods for the analysis of flight data are also required to enhance flight safety and improve productivity. Two recent advances in this area include the ability to conduct flight control system dynamic stability analyses in real time and the ability to measure, compute, and display in real time the aircraft aeroperformance.

The design criteria for the statically highly unstable (up to -35 percent at certain flight conditions) forward-swept-wing configuration of the X-29 aircraft included minimum levels of gain and phase margins in the digital flight control system. These margins are normally obtained from the open-loop frequency response of systems with feedback control in an extensive postflight data reduction and analysis process. Using the old methods of envelope expansion, only one new flight condition or control system configuration could be flown each flight because a stability analysis had to be performed before proceeding to the next condition and was therefore quite time-consuming. Recent improvements in the computational capabilities of the Western Aeronautical Test Range have allowed a significant amount of flight data to be analyzed on line. Consequently, a capability to perform a frequency domain analysis of the combined airframe/flight control system using fast Fourier transform (FFT) techniques has been developed. At the same time the ability to compare the response of the airplane with that of the simulator—again while the airplane is in flight—in both the frequency and time domains was implemented.

Figure 20 depicts schematically how the open-loop frequency response is obtained from pilot-generated frequency sweeps, on line, without altering the control system structure. An actual mission control center display is in the

lower right-hand corner, and an experienced flight control engineer can "read" the gain and phase margins directly from the plot; of course those margins are also displayed in digital format. The predicted response of the airplane control system combination is generated from a linearized aircraft simulation for the exact input provided by the pilot and is immediately overlaid on the plot so that near-real-time comparisons between predicted and actual response can be accomplished. The linear equations of motion are also utilized to produce time-history comparison plots in real time showing the differences between the airplane and the linearized version of the simulator (Fig. 21).

A very important side benefit has accrued from the development of this capability. The inherently hazardous initial envelope clearance can proceed faster and at lower risk because the necessary information is presented to the flight test team in near-real time. Since envelope clearance was possible at several test points on the same flight, it has been estimated that the use of this on-line capability resulted in a 30-percent reduction in time required to clear the X-29 flight envelope. Furthermore, the on-line analysis eliminated the post-flight data reduction requirement for stability margins.

A new real-time aeroperformance analysis technique has been developed as part of the X-29 flight research program. This ability to compute and graphically display real-time aeroperformance flight results includes the calculation of the flight-derived drag polar, lift curve, and aircraft specific excess power. A key element of this new method was the concurrent development of a real-time in-flight net thrust algorithm in conjunction with Computing Devices Company of Ottawa, Canada.

The performance flight research phase of the X-29 program required the rapid acquisition and evaluation of flight data to model the aircraft lift and drag characteristics. A limited number of flights were available to completely define the aerodynamics and determine the performance potential of the forward-swept wing and its related technologies, such as the close-coupled wing/canard configuration and the wing automatic camber control mode. Dynamic flight maneuver techniques, coupled with body-mounted accelerometer measurement methods, were used to quickly define the drag polar shape and minimum drag level. Maneuver dynamic effects, instrumentation system capability, maneuver flight techniques, attainment of target flight conditions, and other factors affected the quantity—and more importantly—the quality of the flight data obtained. The real-time aeroperformance analysis capability allowed for quick, accurate, postmaneuver evaluation of maneuver technique and data quality, increasing the productivity of the flight program. Shown in Fig. 22 is a schematic of drag polar creation by a series of aircraft maneuvers. Starting from 1-g stabilized flight, a pushover-pullup maneuver was performed that

reduced both the lift and the drag. This was immediately followed by a windup turn that steadily increased both lift and drag. The technique also gave an immediate postflight measure of performance for comparison with predictions or other analyses. Accuracy of the drag polars was estimated to be better than  $\pm 2.5$  percent over the entire engine power range, based on the extensive test cell calibrations of the flight engine conducted at Lewis Research Center.

The gross thrust and inlet air flow momentum, or ram drag, were computed in real time at up to 12.5 times/sec. The gross thrust algorithm calculates thrust based on a one-dimensional isentropic flow analysis in the engine afterburner section and the exhaust nozzle. The algorithm requires gas pressure measurements from three afterburner locations and includes the turbine exhaust total pressure, the afterburner entrance and exit static pressure, as well as the free-stream static pressure. Because no additional instrumentation was required to compute ram drag, the real-time value of net thrust was computed from gross thrust minus ram drag. The resulting net thrust was corrected for the inlet spillage and nozzle propulsive drag components in real time from table look-up estimates to yield the net available propulsive force required to compute in-flight aircraft drag. A real-time graphics display was also developed to display drag polars, lift curves, and specific excess power as a function of Mach number. An example of a drag polar that was computed and displayed in real time is shown in Fig. 23.

An accurate aeropropulsion analysis technique has been developed that significantly improves the productivity of the flight research team, and because it all but eliminates the requirement for extensive postflight data reduction and analysis, the transfer of flight results to the user should be increased dramatically.

## FUTURE DIRECTIONS

The need for and payoff of flight research continues to be required for the advancement of aeronautical technologies. Many opportunities are looming on the horizon and promise significant breakthroughs in performance and the economics of flight. The resurgence of interest in high-speed transports (Fig. 24) has caused the identification of several technology development areas that need or would greatly benefit from flight validation. Chief among these is the development and demonstration of viable supersonic laminar-flow concepts. Conceptual experiments have been defined for test on a General Dynamics F-16XL (Fig. 25), and planning for a coordinated ground and flight research program is under way. To understand and assess the effects of aerodynamic heating on laminar flow, experiments using a YF-12 aircraft as a testbed airplane are in the preliminary discussion phase. Similarly, flight demonstration of

advanced propulsion concepts such as the supersonic throughflow fan and air turboramjets will require flight validation in order to reduce the risk sufficiently for commercial development.

To establish the viability of a short takeoff, vertical landing (STOVL) fighter aircraft (Fig. 26) with an acceptable weight penalty will likely require the development of an experimental or technology demonstrator aircraft. Significant advances in propulsion system and integrated control system capability are required, and validation of these advances will be required in the real and dynamic flight environment before the risk is acceptable. Strategists in the government are predicting that the military is going to need aircraft that possess supersonic dash performance, all-weather operational ability, high air-to-air agility, and short takeoff and vertical landing capability. The key to the integration and maturing of these capabilities will be the development and flight test of an aircraft.

One of the biggest challenges facing the aerospace community, if not the biggest, is the development and flight test of the X-30 hypersonic research airplane (Fig. 27). This program focuses technology development on the X-30 vehicle, which is to be used to demonstrate the successful merging of aeronautical and space technologies across the speed range from takeoff to orbit velocities. There are enormous challenges in developing airbreathing propulsion systems that will provide the necessary thrust at all required speeds and altitudes. New structural materials are essential for both the engine and airframe to maintain their structural strength in extremely adverse environments. Integration of the propulsion control, flight control, and thermal management systems is crucial to the operational success of this vehicle. The flight research community is faced with the development of new instrumentation, air data systems, real-time analysis techniques, ground structural test, simulation and integrated test capability, and other capabilities in order to safely and efficiently conduct the X-30 flight research program. Flight research has been and will continue to be the critical link in the development, acceptance, and application of advanced aeronautical concepts.



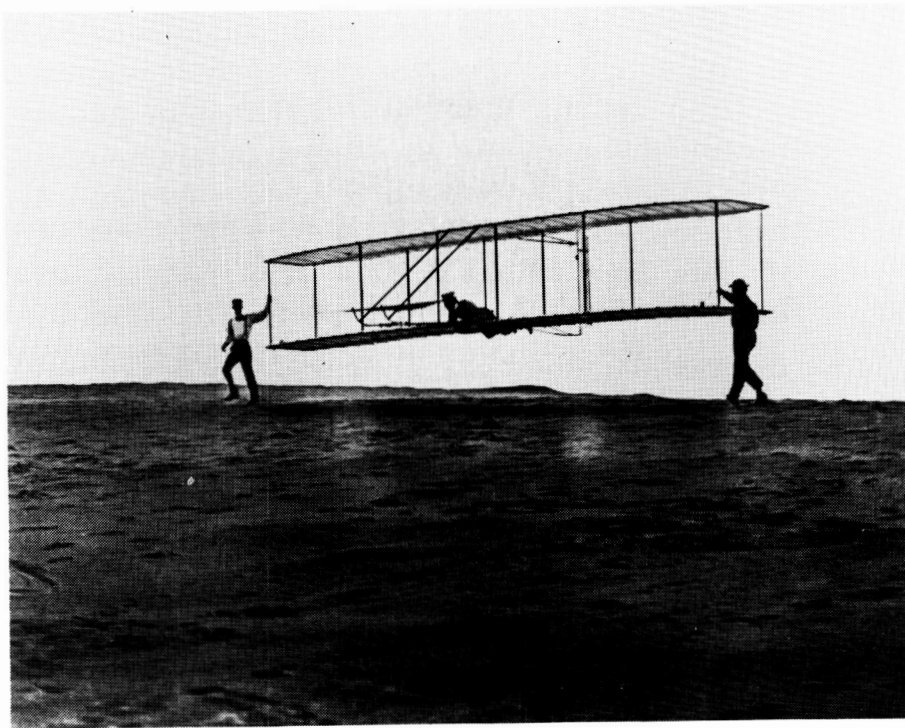


Fig. 1 Wright brothers glider.



Fig. 2 P-51 wing with model.

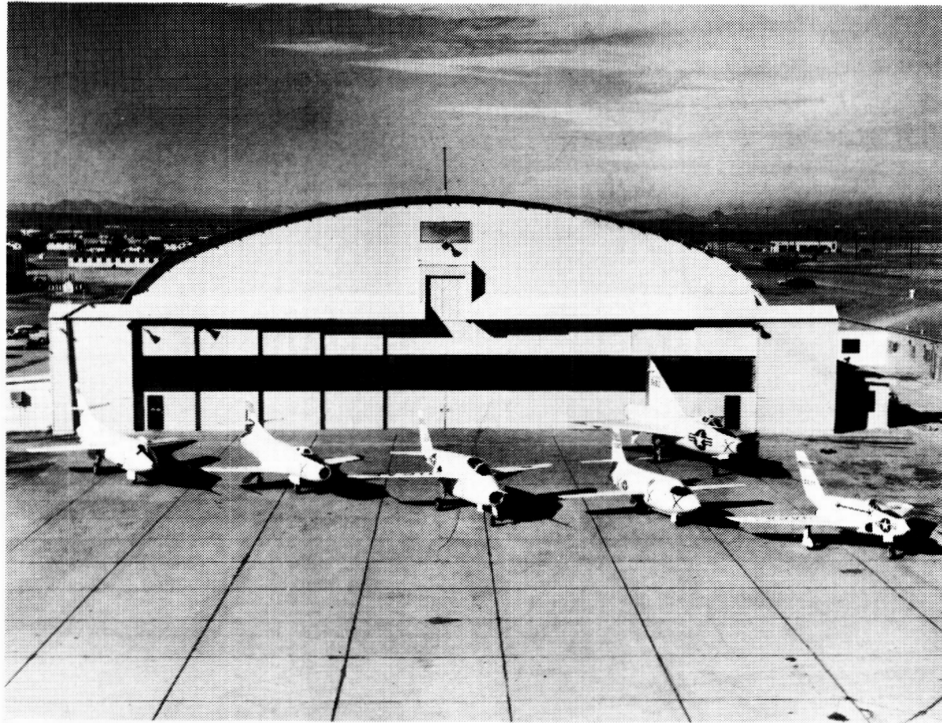


Fig. 3 X airplanes.



Fig. 4 X-15.

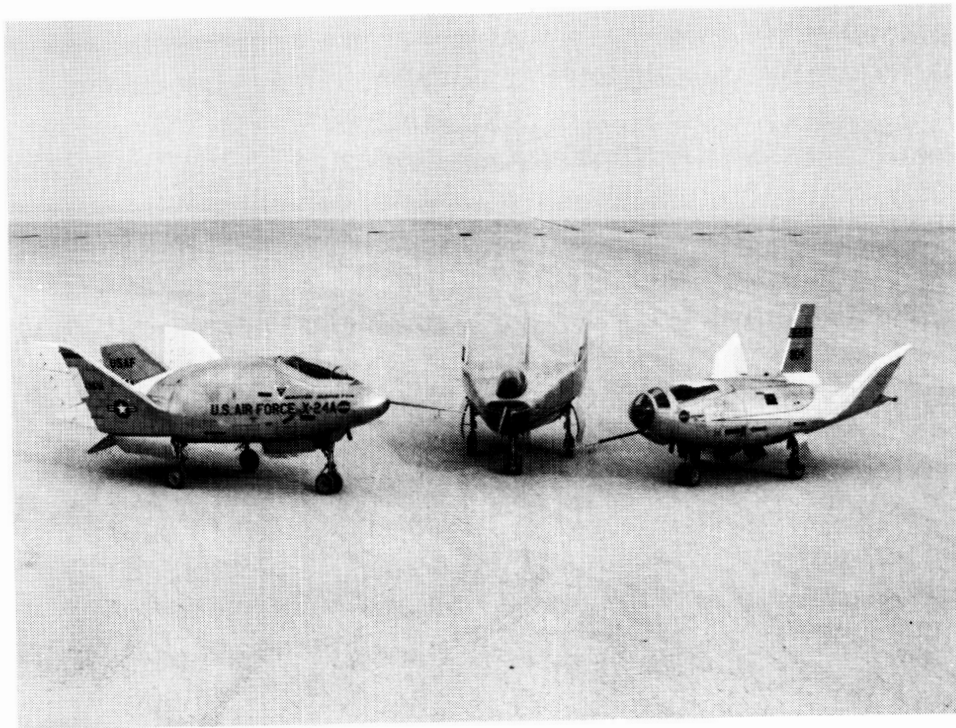


Fig. 5 M-2, HL-10, and X-24A.

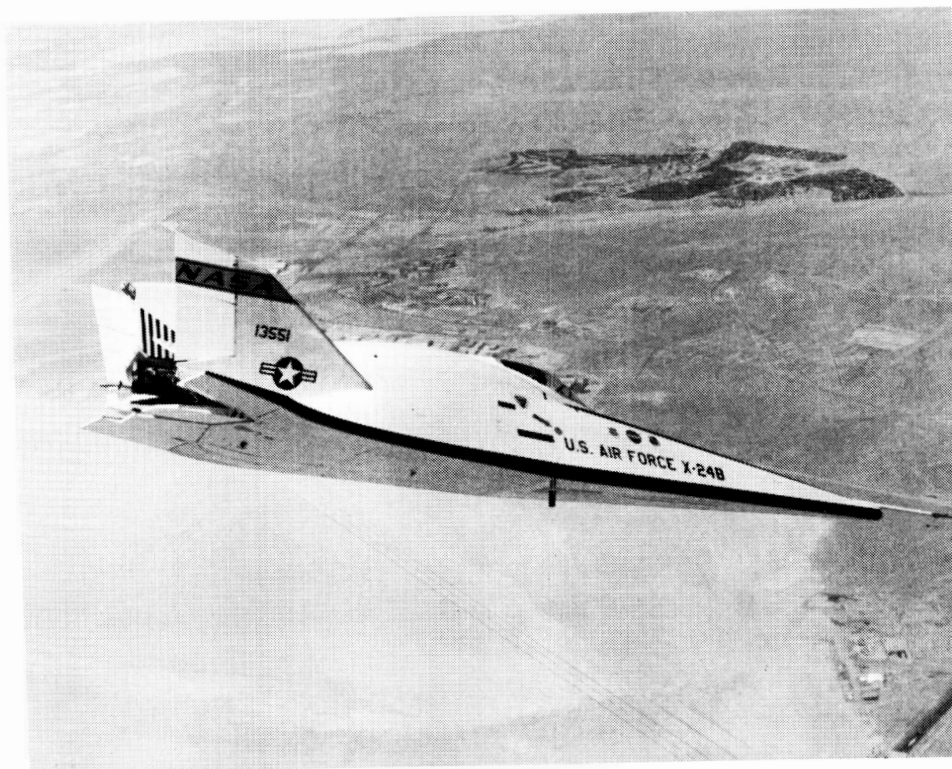


Fig. 6 X-24B.



Fig. 7 747 with shuttle.

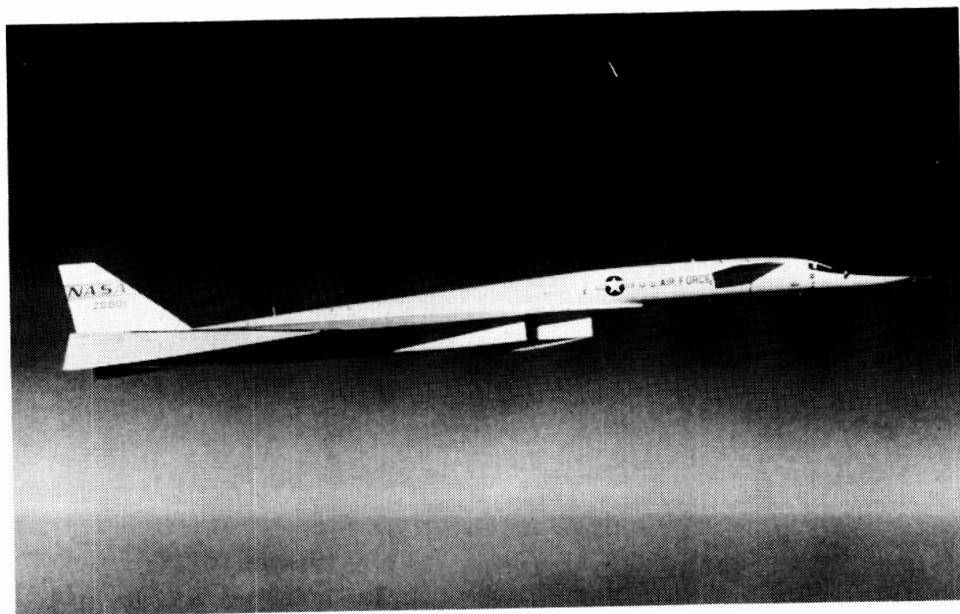


Fig. 8 XB-70.

ORIGINAL PAGE  
BLACK AND WHITE PHOTOGRAPH



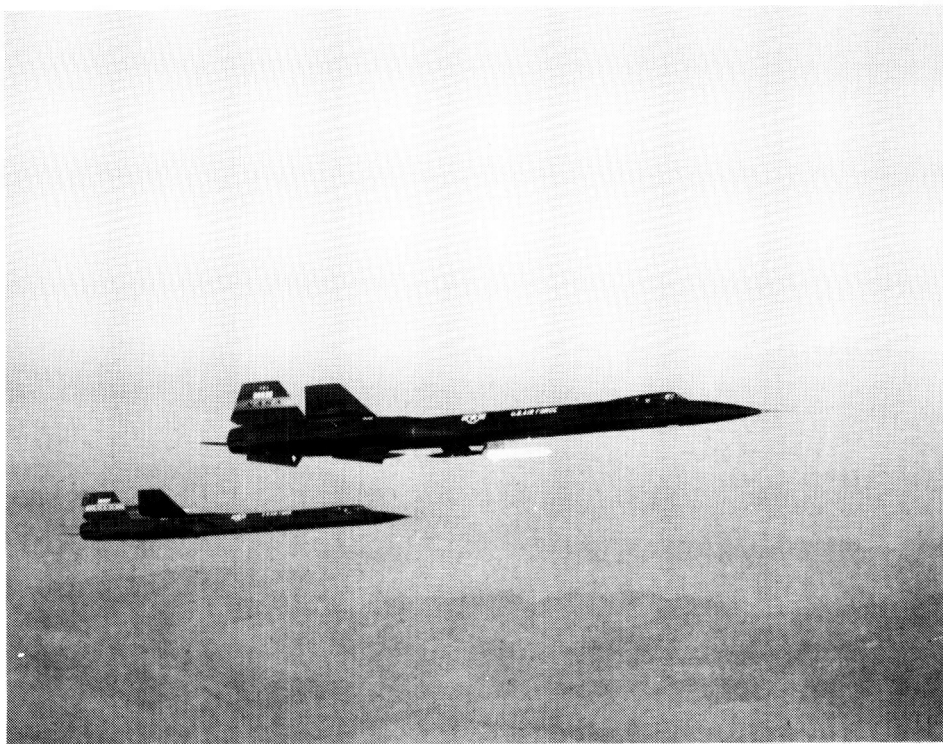


Fig. 9 YF-12 aircraft.



Fig. 10 F-8 Supercritical wing.



Fig. 11 F-8 digital fly-by-wire.

## Flow Visualization Results

$\Lambda = 20^\circ$ ,  $\Lambda_{\text{equiv}} = 15^\circ$ ,  $\beta = -5^\circ$ ,  $M = 0.7$ ,  $H_p = 20,000$  ft  
 $\alpha = 0.7^\circ$

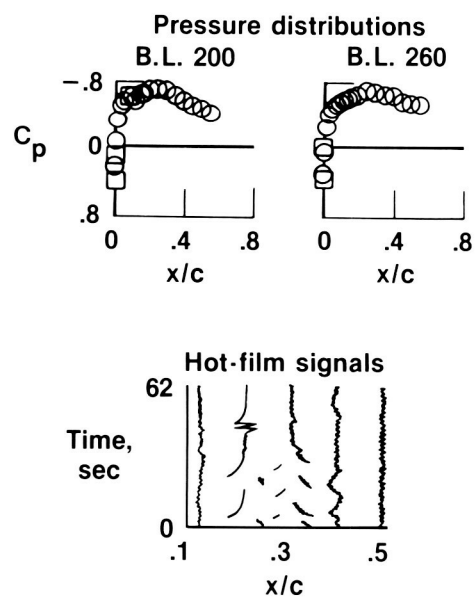


Fig. 12 F-14 flow visualization with liquid crystals.



Fig. 13 JetStar.



Fig. 14 HIDECA airplane.





Fig. 15 Advanced fighter technology integration (AFTI)/F-111.



Fig. 16 X-29.





Fig. 17 F-18 at high alpha.

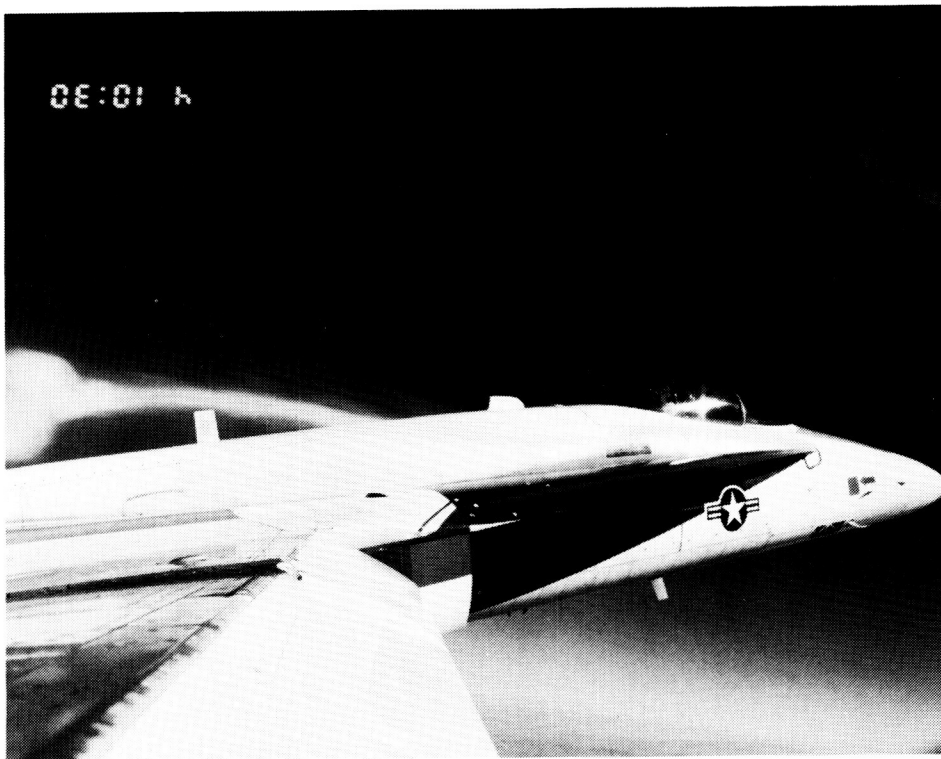


Fig. 18 F-18 vortex.

# F-18 HARV

## Surface Flow Visualization

ORIGINAL PAGE  
BLACK AND WHITE PHOTOGRAPH

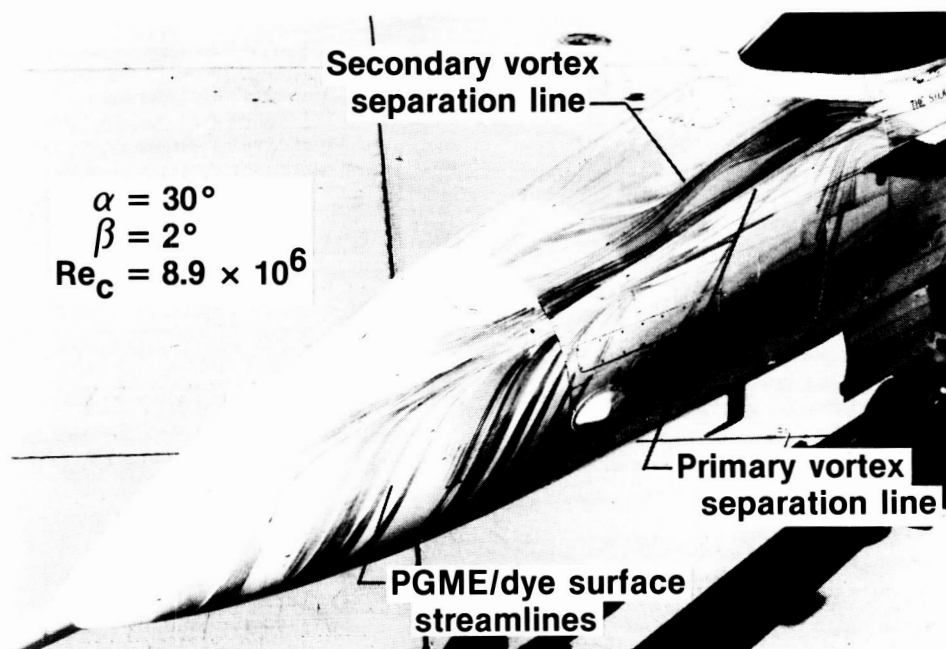


Fig. 19 PGME patterns on F-18.

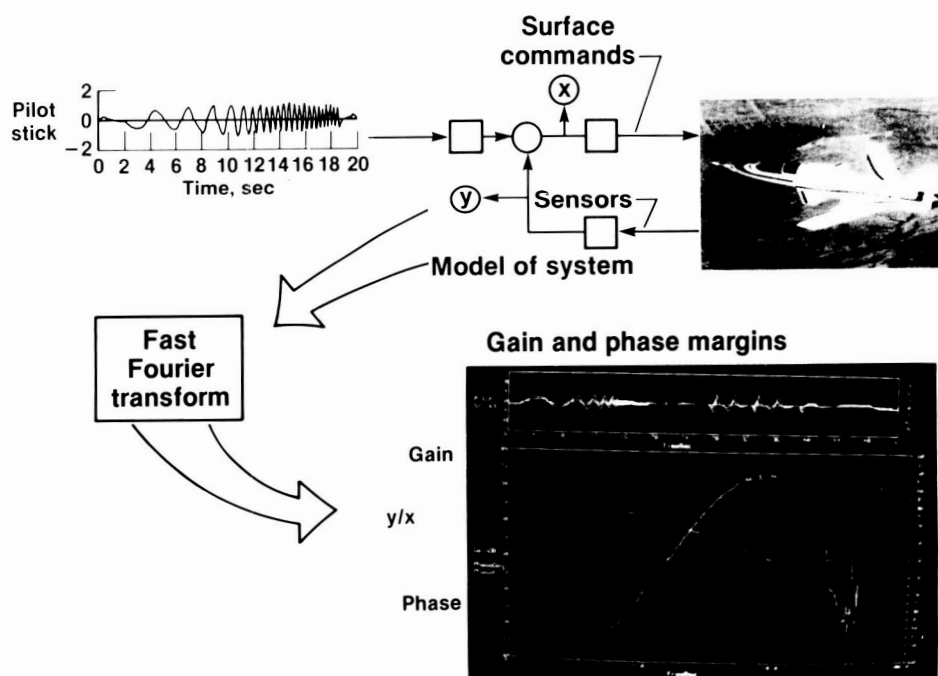


Fig. 20 Flight-determined frequency response for unstable airframes.

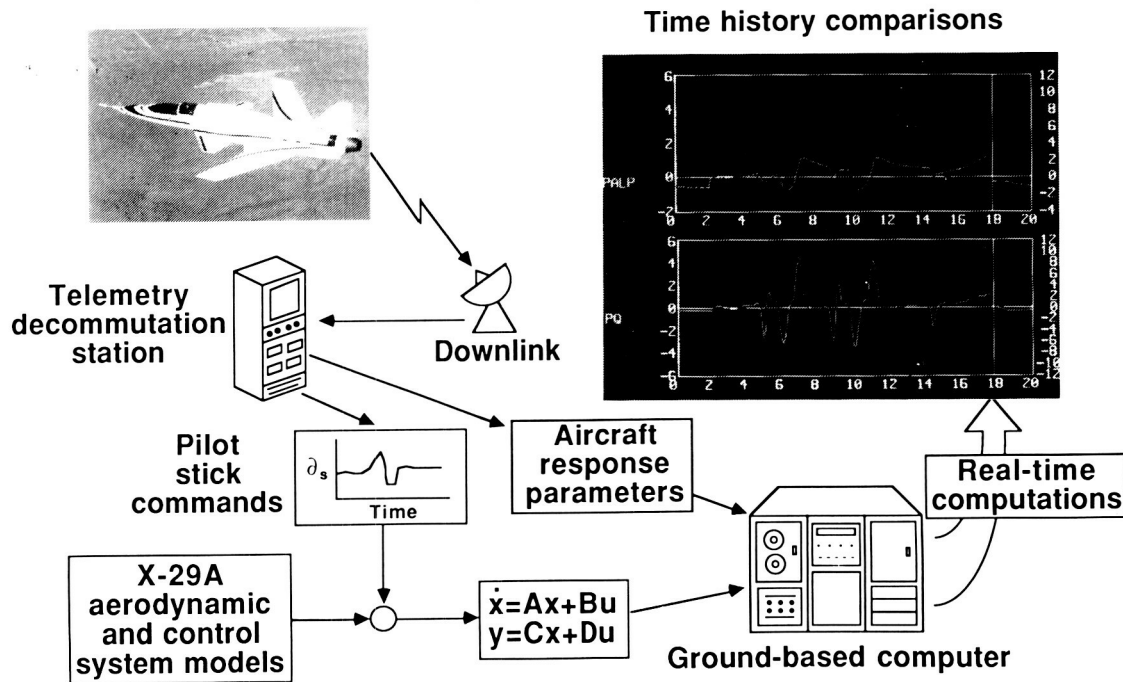
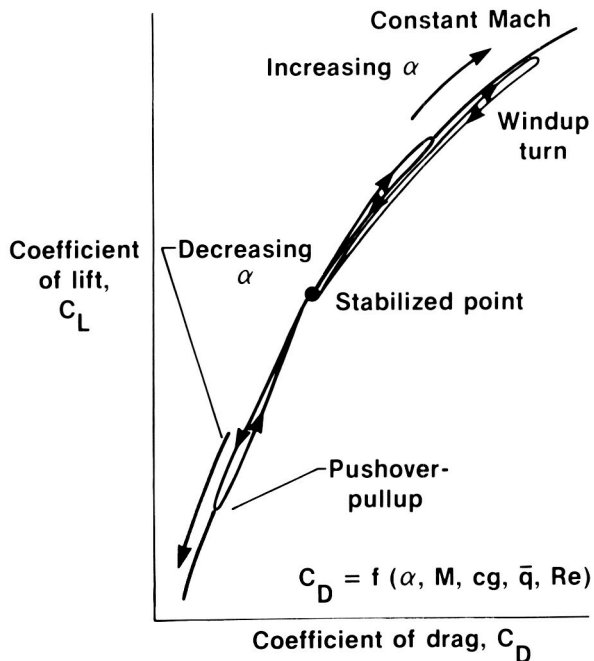


Fig. 21 Real-time comparison of linear simulation to flight.

## Flight Test Approach



- Maneuvers flown to obtain polar shapes
  - Dynamic maneuvers
  - Maneuvers sweep alpha range
- Maneuvers
  - Pushover-pullup
    - 0- to 2-g maneuver
    - Covers lower to medium alpha range
  - Constant thrust windup turn
    - 1 g to target  $N_z$
    - Covers medium to high alpha range

Fig. 22 Flight test maneuvers for drag polar creation.

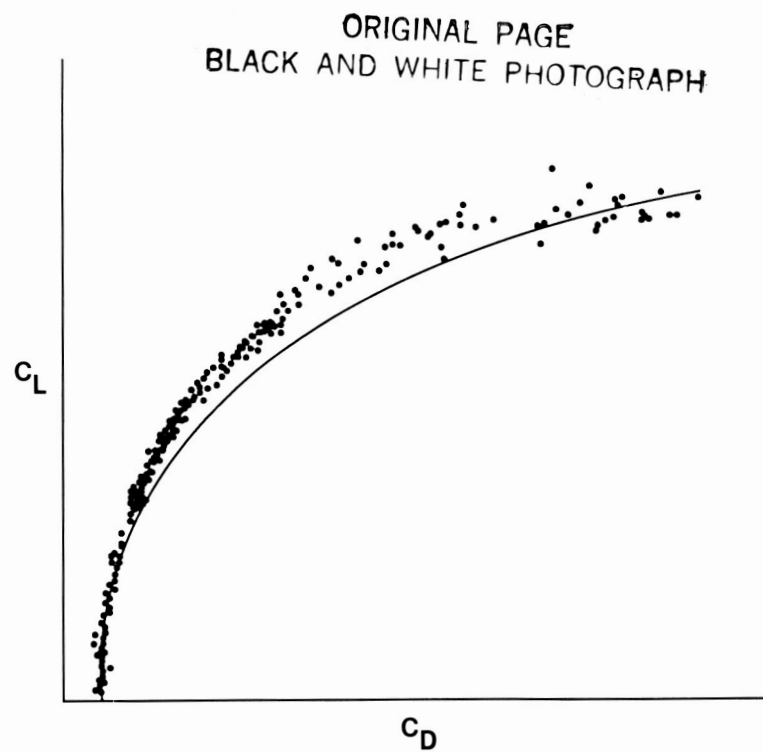


Fig. 23 Sample real-time drag polar.

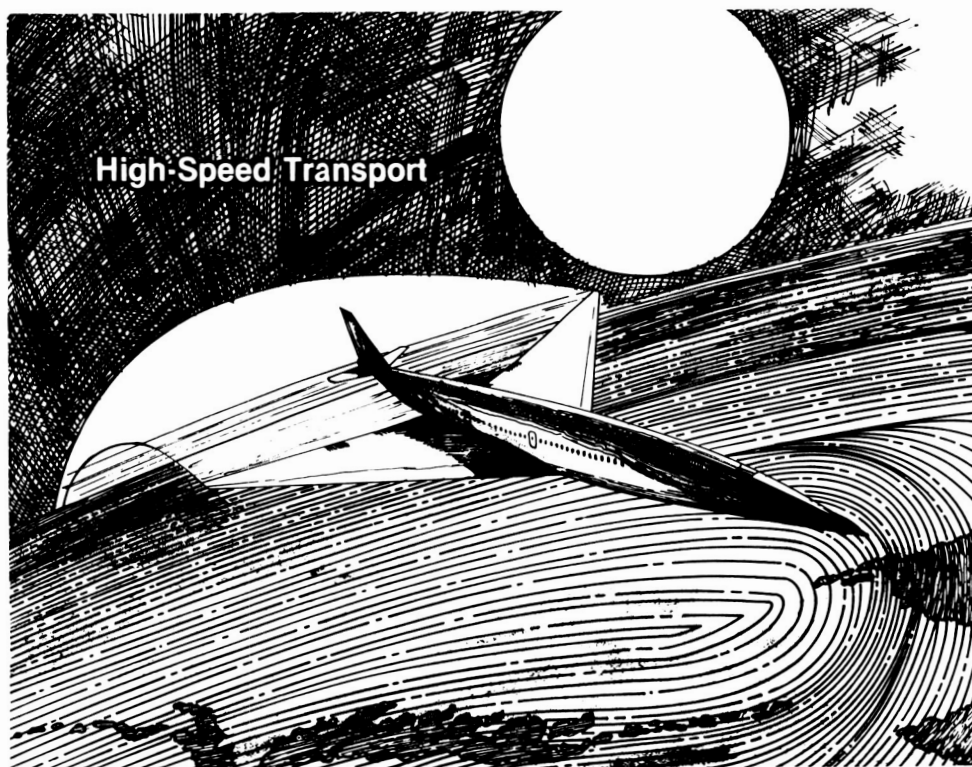


Fig. 24 Drawing of high-speed transport.



Fig. 25 F-16XL.



Fig. 26 Conceptual STOVL fighter.

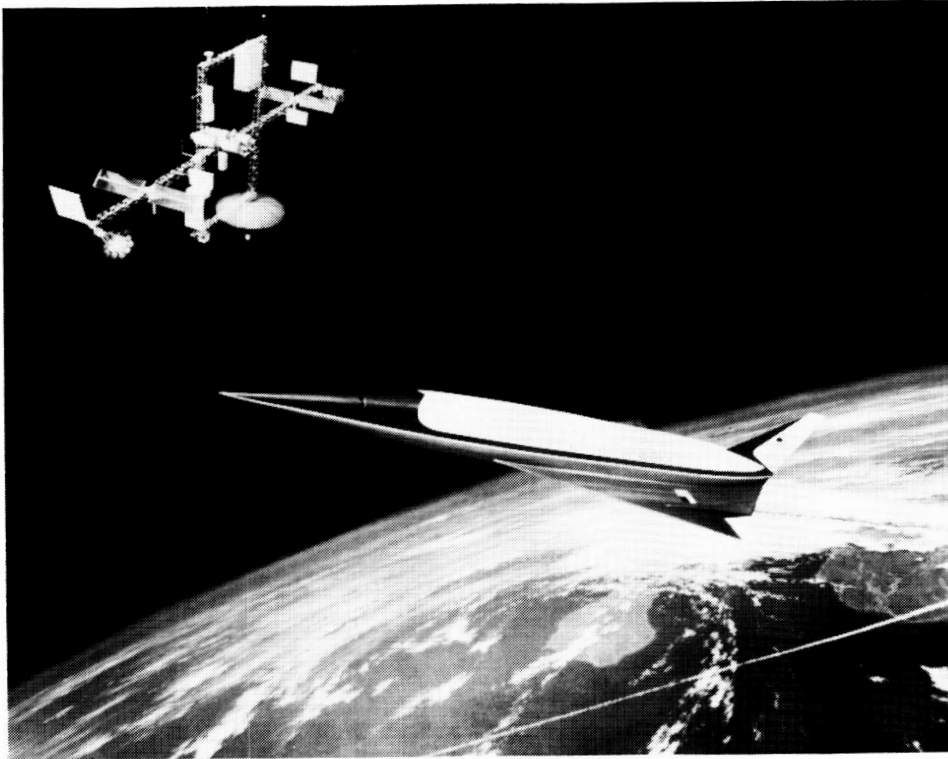


Fig. 27 National Aero-Space Plane (NASP).

# SHOCK-BOUNDARY-LAYER INTERACTION IN FLIGHT

Arild Bertelrud  
High Technology Corporation  
Hampton, Virginia

## SUMMARY

A brief survey is given on the study of transonic shock - boundary-layer effects in flight. Then the possibility of alleviating the adverse shock effects through passive shock control is discussed. A Swedish flight experiment on a swept wing attack aircraft is used to demonstrate how it is possible to reduce the extent of separated flow and increase the drag-rise Mach number significantly using a moderate amount of perforation of the surface.

## BACKGROUND

The problem of shock-induced separation and associated buffeting became an important problem in aircraft development in the 1940s and the 1950s. Initially a large part of the investigations performed concerned flight tests, as it was a problem very much concerned with the direct flight application. Also, as long as the phenomenon was relatively unknown, it was not clear how much information the wind tunnel tests were able to give. Often observations in flight were verified in wind tunnels, and gradually it was possible to develop empirical relationships of use in the aircraft design.

Some of these early observations were of use much later. Notably, the aileron buzz phenomenon on the Lockheed F-80A airplane (Gadberg and Ziff, ref.1) was successfully computed by Steger and Bailey (ref.2) and Levy and Bailey (ref.3) with an unsteady, thin-layer Navier-Stokes code thirty years later.

For further information the reader is referred to Spreiter (ref.4) who has given an extensive historical survey concerning the early flight experiments and how they were correlated with theory and wind tunnel tests. Pearcey and Holder (ref.5) give an account of various investigations performed up to the mid-50s, including a variety of shock-modifying schemes.

Another period of intense effort also in flight testing was the discrepancy between tunnel predictions and flight reality experienced for the Lockheed C-141, where shock location in the wind tunnel case was 20% chord in front of the flight data (ref.6). A series of wind tunnel and flight experiments (ref.7) eventually led to improved methods of extrapolating the low Reynolds number wind tunnel data to higher Reynolds number flight data (Paterson et.al., ref.8); (Blackerby and Cahill, ref.9). In England (Browne et.al., ref.10) a VC-10 was instrumented with pressure tubing, and an extensive comparison was made between the full-scale flight results and data from a 1:15 model in a wind tunnel. Extensive work, was done in flight, as witnessed by the symposium on Supercritical Wing Technology (ref.11). The experimental information collected was compiled and resulted in empirical "rules of thumb" (ref.12) for



extrapolation of wind tunnel data to flight. In general the static pressure distribution at tunnel conditions (with appropriate interpretation as shock location etc.) was scaled through creation of empirical parameters. One recent investigation by Cunningham and Spragle (ref.13) uses more recent data for both two- and three-dimensional configurations.

Delery and Marvin (ref.14) have made an extensive review of shock-wave boundary-layer interactions (experiments as well as computational methods), and in the present conference, Ayers gives a paper on flight research and testing (ref.15).

Over the years a variety of drag-reducing techniques have been investigated for use in transonic flows. One method explored early on was introduction of vortex generators. Already in the early 1940s active control through suction and blowing on shock wave/boundary layer interaction was explored (refs.16-17). Krogmann (ref.18) has recently reviewed the subject area both regarding active and passive control, and only limited reference will therefore be given here to other work.

#### PASSIVE SHOCK CONTROL

While the active suction may give a gross drag reduction, the energy required for pumping may preclude a net gain. However, several authors have observed that even without pumping (passive control) there is often a drag reduction, i.e. a direct gain. Nagamatsu et.al.(ref.19) tested a 14 % thick supercritical NACA profile made porous from 53 to 85 % chord through use of a large number of holes. The result was slightly increased drag at lower Mach numbers while the drag-rise Mach number was increased. Krogmann et al.(refs.20-21) investigated the flow on another supercritical profile, the VA-2. Their perforation was obtained both through use of holes as well as single and double slots in the surface at selected positions. Again the drag-rise Mach number was increased; the buffet boundary was moved.

The assumption is that the passive shock control decreases drag through an automatic adjustment in the shock region. At the foot of the shock boundary layer air is pushed in through the perforations, while it is blown out further upstream where the pressure is low. Thus the maximum Mach number is reduced.

Figure 1 (ref. 18) illustrates the principle of this interaction and also introduces the coordinate systems and the definitions to be used. It appears that the main effect of the perforation is to allow a strong shock to be split into several weaker shocks, thus in some cases avoiding shock-induced separations. In two-dimensional flows it is possible to determine the overall effect on performance, and Figure 2 (Krogmann), shows the effect of passive ( $C_q = 0$ ) and active shock control on the buffet boundaries of a supercritical profile. At least in this particular case, the main effect appears to be the surface perforation itself.

The size of the surface perforations relative to the local boundary layer thickness is important, as too large holes actually may cause a major disturbance through suction and blowing. Raghunathan and Mabey (ref.22) did an experiment on a 6% half circular arc airfoil to explore the effects of hole geometry; i.e. normal, forward- or backward facing holes. The forward-facing holes were found to give better results than the other. They also



investigated the effects of the perforation on the static pressure fluctuations. Savu (ref.23) did computations on the flow around a NACA 0012 profile with massive perforations, and conjectured the change in shock characteristics. Chen et.al.(ref.24) developed a full potential code to compute the flow over porous airfoils.

#### EXPERIMENT

Wind tunnel tests at transonic speeds are often cumbersome, as minor changes to a wind tunnel configuration easily may cause severe problems in the interpretation of data; both wall effects as well as free stream turbulence and disturbances tend to cause problems. Also, the added complication of manufacturing porous surfaces for small wind tunnel models, make wind tunnel tests of passive shock control hard. Computational tools under development often need good experimental data for comparison, and to avoid all uncertainties due to the wind tunnel environment, flight data has been utilized as a database in the present study.

The experiment was performed on a swept wing attack aircraft (ref.25), a SAAB 32A Lansen, and the results are available as a computerized database (refs.26-27) allowing a comprehensive description of aerodynamic flow on a swept wing in the entire subsonic flight regime. Figure 3 shows the geometry of the aircraft and the flight envelope while Figure 4 yields the wing geometry and coordinate systems.

The wing geometry was used as baseline for a series of transonic wings developed at the FFA in the 1970s - extensive studies of the force and moment characteristics as well as pressure distributions with a scale model at high Reynolds numbers were made.

#### INSTRUMENTATION AND EXPERIMENTAL SETUP

Comprehensive transonic measurements in flight require ample flight time, good description of reference conditions and a well organized data handling system. It is in general necessary to perform the measurements with only a few probes per flight to make sure that the shock pattern stays the same. One of the experiences using glued on tubing for pressure distributions in the VC-10 experiment was that the tubing indicated the correct pressure, but the value and the flow field were affected by the tube presence. In the present experiment the transonic flow mapping was performed over a large portion of the test, adding information a small piece at a time. In Figure 5, the sensor types used have been indicated. The modular approach, allows sensor complement, location and type to vary from flight to flight; as has been done recently on a Boeing 737 (ref.28). The validity of one sensor type often requires information obtained with another type of sensor. For example the static pressure measured with the modified Preston tube (refs.29-30) must be compared with the wall pressure taps at some locations. Also the cross-flow must be small, which requires information from dual hot films. These in turn require information on the static pressure for a proper evaluation. The solution to this apparent maze is use of redundant data and an efficient data handling system that solve most of the interrelations automatically. In general each aerodynamic parameter should be measured with at least two methods.

Another problem is the choice and repeatability of flight conditions. The ability to keep Mach number constant and have minimized control surface deflections while also keeping altitude requires a lot from pilot and aircraft. Also the weight of the aircraft and its trim should ideally be repeatable from flight to flight, to ensure the same angle of attack. The weather varies, both the turbulence characteristics and parameters like temperature and humidity.

The wing was equipped with a large number of static pressure taps - mostly in the leading-edge region (ref.24), but the distributions of pressure and local skin friction were also determined using modified Preston tubes.

This gave a coarse grid information in the chordwise as well as spanwise direction also as the Mach number increased, although the chordwise resolution was insufficient for proper shock documentation.

The main source of information used in the present study on shock/boundary-layer interaction is 51 static pressure taps close to the wing tip - see Figure 4. This row covers the region from  $\xi = 0.2$  to the trailing edge, and is supplemented by 13 static pressure taps in the leading-edge region. The pressure taps are located in a plane intersecting the leading edge at  $\eta = 0.912$  and the trailing edge at  $\eta = 0.812$ , being the non-dimensional spanwise location.

From previous experience it is known that the shock is located somewhere between  $\xi = 0.4$  and  $0.6$  depending on the flight altitude, and the pressure taps were positioned accordingly. To monitor spanwise variations two additional rows of pressure taps, inboard and outboard, were used in the shock region itself.

It is very hard to document whether or not flow is separated using only the static pressure as an indicator, and in the present study a three-step technique was employed:

- During one flight the row of pressure taps was used uncovered, to document  $C_p$ .
- During a second flight some of the taps were covered by razor blades with the edge pointing forward; acting as Stanton tubes.
- During a third flight some of the pressure taps were covered by razor blades facing backwards, acting similar to Stanton tubes and intended to detect backflow.

Figure 6 shows boundary-layer development in front of the shock. At  $\xi = 0.6$  a pressure rake was positioned, aligned with the flight direction. In most cases a limited shock-induced separation would be located close to  $\xi = 0.6$ , and it was considered important to have viscous layer information as far back as possible. Both total pressure and Mach number profiles were monitored; the wall static pressure was normally used for evaluation of integral properties but the static pressure 30 mm from the wall was also measured.

In the interaction region this may be questionable, but as the purpose of the investigation is to explore possible effects of

surface perforation, useful comparisons can be made. To verify whether or not the flow is separated is also a difficult task with the pressure rake data, and for this purpose extra flights were made with Stanton tubes (razor blades) over some of the pressure taps. Local skin friction may be determined if a universal calibration law is assumed valid.

One heated dual wall film probe was located in the shock region to monitor flow angularity and turbulence, but the data have not been evaluated so far.

The surface perforation was located at  $\xi = 0.42$  and  $\xi = 0.58$  respectively, as can be seen in Figure 4. They consisted of 2 and 3 mm diameter holes with a spacing of 15 mm; this is equivalent to the perforation used by Krogmann et.al.(ref.20). In the figure the various configurations used are defined ranging from 0 to 3.14 % porosity. The cavity used in this case was a reasonably well sealed box in the wing structure, extending from the front to the rear beam. Cavity pressure was monitored using five static pressure taps on the cavity walls.

#### FLOW CONDITIONS

Two flight altitudes were used for the flight experiments, 7 and 10 km, and Figure 7 may serve to illustrate the type of results obtained. At the same Mach number, the shock is moved forward roughly 3% chord due to changes in altitude. From the Figure it is clear that a high resolution is needed to find the pressure gradient in the pressure-rise region and to monitor the separation bubble beneath/behind.

One parameter used when comparing 2D and 3D flows at transonic Mach numbers is the Mach number component normal to the shock, MLN. It plays a dominant role when predicting separation limits. In the present case the three-dimensional shock pattern is not well defined in the spanwise direction. In fact, shock splitting etc. may occur, and therefore the experimental results have been evaluated using the Mach number normal to the local surface generator. Using the measured pressure coefficient, the Mach number component normal to the generator may be determined (comparable to a 2D flow) to find at what flight Mach number there is a possibility of a shock. Figure 8 shows the peak Mach number normal to the local generator, PMLN, as a function of flight Mach number for one choice of perforation. As can be seen only  $M > 0.87$  should be of interest in the present case. It can also be noted that shock-induced separation occurs at  $M = 0.895$  for  $H = 10$  km and  $M = 0.905$  at  $H = 7$  km for the present perforation. This figure may also serve to illustrate the repeatability of the data.

A note of caution is needed before discussing the general results from the tests. In a three-dimensional case of shock wave/boundary layer interaction almost any combination of flow pattern is possible, hysteresis, unsteadiness as well as interference from probes may actually dominate the flow, and Figure 9 may be used as a reminder of this. During nominally stationary conditions, the pilots of the

present tests are required to maintain an indicated speed and altitude. As a consequence of reasonable tolerances in these two parameters, the Mach number may vary. This does not normally create any problems, but in the present Figure an increase in flight Mach numbers of 0.005 has caused the flow to separate, causing a drop in the pressure coefficient upstream of the shock. The total pressure coefficients as well as the indicated Mach number profiles at  $\xi = 0.6$  are drastically changed, and the main question to ask in this case is whether or not the changes observed are typical of the corresponding Mach numbers.

The figure also demonstrates the difficulty of determining a proper Mach number profile from total pressure measurements, as the static pressure chosen for the data reduction may seriously affect the result. In this paper the value obtained from a wall pressure tap is used throughout the viscous layer. Also, as backflow cannot be measured, it is not reasonable to include the separated region in the integration of displacement and momentum thicknesses if the flow is separated, and this should be borne in mind when local values of  $\delta^*$ ,  $\theta$  and  $H$  are examined.

As the Mach number increases, the shock starts to grow in strength and moves back on the wing - as illustrated in Figure 10, where shock position is plotted against PMLN. Two positions are indicated for each case; location of the peak Mach number and the location of the sonic line. The movement is roughly 10% chord as the shock grows and separation occurs, and the rear region of ventilation holes close to  $\xi = 0.58$  is behind the sonic line for the attached case, in front of it for the separated.

Figure 11 may illustrate the boundary layer behind the shock location as function of the peak normal Mach number. The pressure rake was located at  $\xi = 0.6$ , and the momentum thickness is seen to increase dramatically. Also the shape factor  $H$  increases to around 3 before separation. For separated flow it was not possible to obtain information on the reversed flow, and thus the filled symbols of the figure are based on integration out from the zero-velocity point. As can be seen this agrees quite well with the decrease in peak Mach number due to separation. However, it means that the very high values of  $H$  sometimes associated with the shock-induced separation are not given here.

To evaluate the drag-reducing characteristics of the perforated surfaces, it was necessary to measure the boundary-layer characteristics downstream of the separated region. This was done for the following configurations:

Notation	PERFORATION	
	$\xi = 0.42$	$\xi = 0.58$
OPEN	3.1 %	3.1 %
CLOSED/OPEN	0 %	3.1 %
CLOSED/BASELINE	0 %	0 %

In Figure 11 a distinction is made between points with or without separation further forward using filled and open symbols respectively. There is a clear indication that the increase in  $H$  is delayed to higher flight Mach numbers, and also that the separation itself is delayed. However, Figure 11 does not contain the full story on drag effects - the static pressure may have changed in some cases.

Therefore the data were transferred to far-wake conditions using Squire-Young's formula, and the result is plotted in Figure 12. Here the configuration with perforation at the shock itself (i.e. normal blowing) is seen to delay drag-rise substantially, from  $M = 0.88$  to  $0.92$  for this span station, which is the most critical one. At lower Mach numbers the drag is not affected significantly by the downstream perforation, whereas also having upstream perforation appears to increase drag irrespectively of flight Mach number.

#### CONCLUSIONS

Passive shock control through surface perforation:

- It is possible to decrease drag through local perforation in the order of 2 % over a limited region at the shock. The gain is evident in a limited Mach number region only, and hence the wind tunnel data suggesting a shift in divergence Mach number appears appropriate.

- Perforating the surface far in front of the shock had negative effects, thus increasing drag without beneficial effects concerning the divergence Mach number. This is in agreement with Nagamatsu et. al.; although the shock may be weakened, the added boundary-layer flow upstream may have detrimental effects. In the present case it is probable that the large perforation size (compared to the boundary layer thickness) had a considerable effect.

#### REFERENCES

1. Gadberg, B.L. and Ziff, H.L.: "Flight Determined Buffet Boundaries of Ten Airplanes and Comparisons with Five Buffeting Criteria." NACA RM A50127 (1951).
2. Steger, J.L. and Bailey, H.E.: "Calculation of Transonic Aileron Buzz." AIAA Paper 79-0134, Jan. 1979.
3. Levy, Jr., L.L. and Bailey, H.E.: "Computation of Airfoil Buffet Boundaries." AIAA Journal, Vol 19, No 11, 1981, pp. 1488-90.
4. Spreiter, J.R. "Transonic Aerodynamics - History and Statement of the Problem." in Nixon, D. (Ed.) "Transonic Aerodynamics." Vol. 81, Progress in Astronautics and Aeronautics, AIAA, 1982.

5. Pearcey, H.H. and Holder, D.W.: "Examples of the Effects of Shock-Induced Boundary-Layer Separation in Transonic Flight." ARC R&M 3510 (1967).
6. Loving, D.L.: "Wind-Tunnel - Flight Correlation of Shock-Induced Separated Flow." NASA TN D-3580, 1966.
7. Blackwell, J.A., Jr.: "Preliminary Study of Effects of Reynolds Number and Boundary-Layer Transition Location on Shock-Induced Separation." NASA TN D-5003, 1969.
8. Paterson, J.H., Blackerby, W.T., Schwanebeck, J.C. and Braddock, W.F.: "An Analysis of Flight Test Data on the C-141A Aircraft." NASA CR-1558, 1970.
9. Blackerby, W.T. and Cahill, J.F.: "High Reynolds Number Tests of a C-141A Aircraft Semispan Model to Investigate Shock-Induced Separation." NASA CR-2604, 1975.10. Anonymous : "Supercritical Wing Technology - A Progress Report on Flight Evaluations." NASA SP-301, 1972.
10. Browne, G.C., Bateman, T.E.B., Pavitt, M. and Haines, A.B.: "A Comparison of Wing Pressure Distributions Measured in Flight and on a Windtunnel Model of the Super V.C.10. ARC R&M 3707, 1972.
11. Palmer, W.E. and Elliott, D.W.: "Summary of T-2C Supercritical Wing Program." in NASA SP-301, 1972.
12. Cahill, J.F. and Connor, P.C.: "Correlation of Data Related to Shock-Induced Trailing-Edge Separation and Extrapolation to Flight Reynolds Number. NASA CR-3178, September 1979.
13. Cunningham Jr., A.M. and Spragle, G.S.: "A Study of the Effects of Reynolds Number and Mach Number on Constant Pressure Coefficient Jump for Shock-Induced Trailing-Edge Separation. NASA CR-4090, August 1987.
14. Delery, J. and Marvin, J.G.: "Shock-Wave Boundary-Layer Interactions". AGARD AG-280 (1986).
15. Ayers, T.G.: "Flight Research and Testing." Transonic Symposium - Theory, Application, and Experiment., NASA Langley Research Center, Hampton, Virginia, April 19-21, 1988.
16. Regenscheit, B.: "Versuche zur Widerstandsverringierung eines Flügels bei hoher Mach'scher Zahl durch Absaugung der hinter dem Gebiet unstetiger Verdichtung abgelösten Grenzschicht." ZWB-FB-1424, Juli 1941, english translation : NACA TM 1168, July 1947.
17. Page, A. and Sargent, R.F.: "Effect on Airfoil Drag of Boundary Layer Suction Behind a Shock Wave." ARC R&M 1913, 1943.

18. Stanewsky, E. and Krogmann, P.: "Transonic Drag Rise and Drag Reduction by Active/Passive Boundary Layer Control". VKI Lecture Series "Aircraft Drag Prediction and Reduction", May 1985. (AGARD-R-723).
19. Nagamatsu, H.T., Dyer, R. and Ficarra, R.V.: "Supercritical Airfoil Drag Reduction by Passive Shock Wave/Boundary Layer Control in the Mach Number Range 0.75 to 0.90." AIAA Paper 85-0207.
20. Krogmann, P., Stanewsky, E. and Thiede, P.: "Effects of Local Boundary Layer Suction on Shock-Boundary Layer Interaction and Shock-Induced Separation." AIAA Paper 84-0098, AIAA 22nd Aerospace Sciences Meeting, Reno, Nevada, January 9-12, 1984.
21. Krogmann, P. and Thiede, P.: "Aktive und Passive Beeinflussung der Stoss-Grenzschicht-Interferenz an Überkritischer Tragflügeln." DFVLR IB 222 83 A 26, October 1983.
22. Raghunathan, S. and Mabey, D.G.: "Passive Shock-Wave/Boundary-Layer Control on a Wall-Mounted Model." AIAA Journal, Vol 25, No 2, February 1987, pp. 275-278.
23. Savu, G. and Trifu, O.: "Porous Airfoils in Transonic Flows." AIAA Journal, Vol. 22, No. 7, July 1984, pp. 989-991.
24. Chen, C.L., Chow, C.Y., Holst, T.L. and Van Dalsem, W.R.: "Numerical Simulation of Transonic Flow Over Porous Airfoils."
25. Bertelrud, A.: "The Role of Free Flight Experiments in the Study of Three-Dimensional Shear Layers". presented at "Perspectives in Turbulence Studies", International Symposium dedicated to the 75th Birthday of J.C. Rotta, Gottingen, May 11-12, 1987.
26. Bertelrud, A. and Olsson, J.: "Method of Analysing Data on a Swept Wing Aircraft in Flight." ICAS Paper 86-1.9.3 in ICAS Proceedings 1986, 15th ICAS Congress, London, September 1986.
27. Bertelrud, A.: "Pressure Distribution on a Swept Wing Aircraft in Flight." in AGARD AR-138 Addendum. (1984).
28. Bertelrud, A., Boeck, J., Heaphy, W. & Parks, M.: "A Real-Time Aerodynamic Analysis System for Use in Flight." AIAA Paper 88-2128, 4th Flight Test Conference, San Diego, May 1988.
29. Preston, J.H. "The Determination of Turbulent Skin Friction by Means of Pitot Tubes." J. Aeron. Soc., Vol. 58, pp. 108-121 (1954).
30. Bertelrud, A.: "Total Head/Static Measurements of Skin Friction and Surface Pressure." AIAA Journal, Vol. 15, March 1977, pp. 436-438.

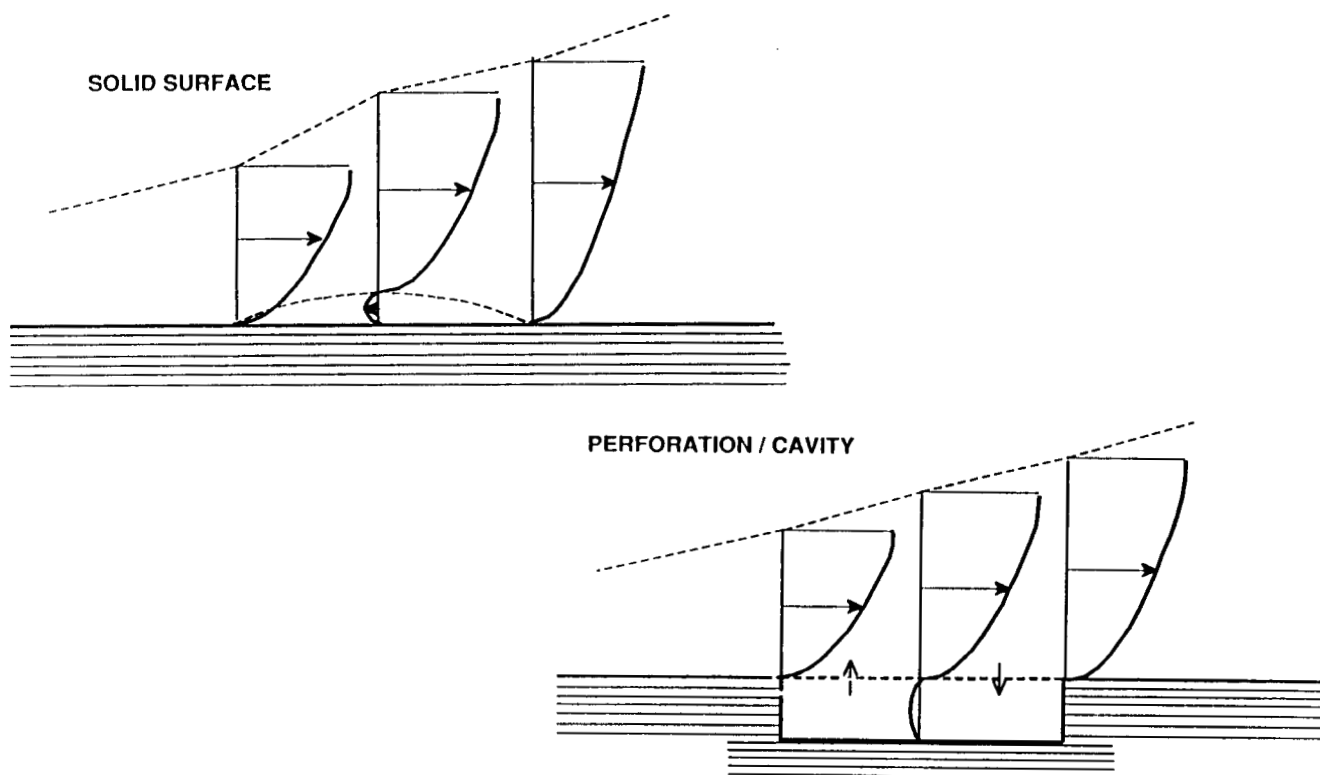


Figure 1 Principle of passive shock control (From ref. 18)

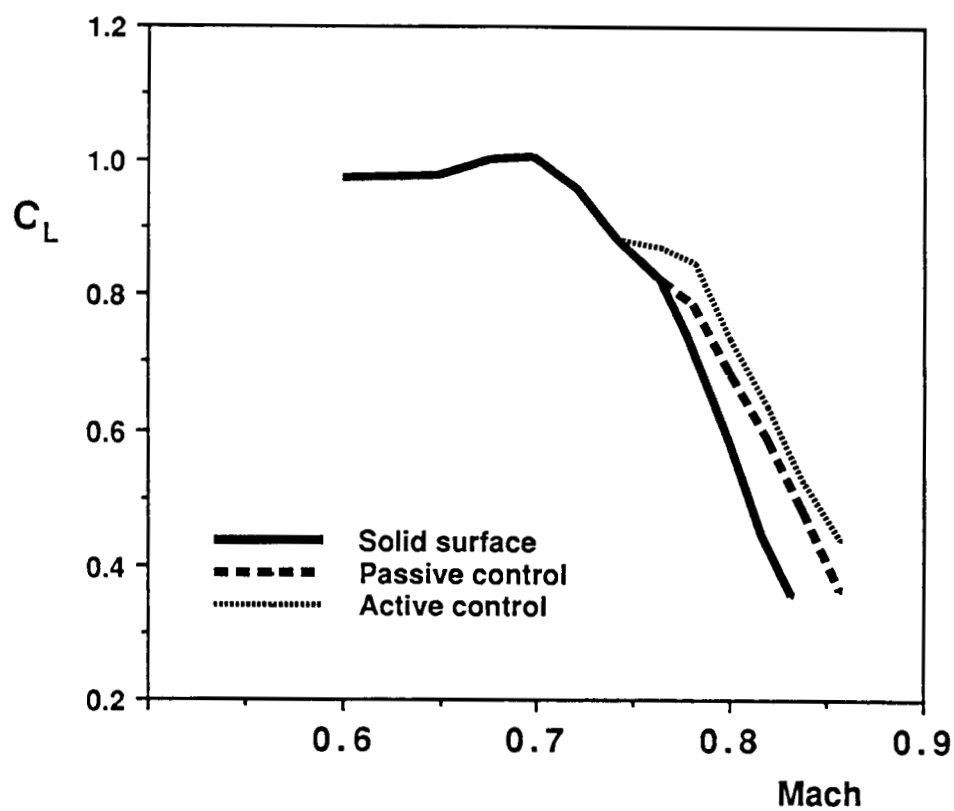


Figure 2 Effect of passive shock control on buffet boundary (From 18.)



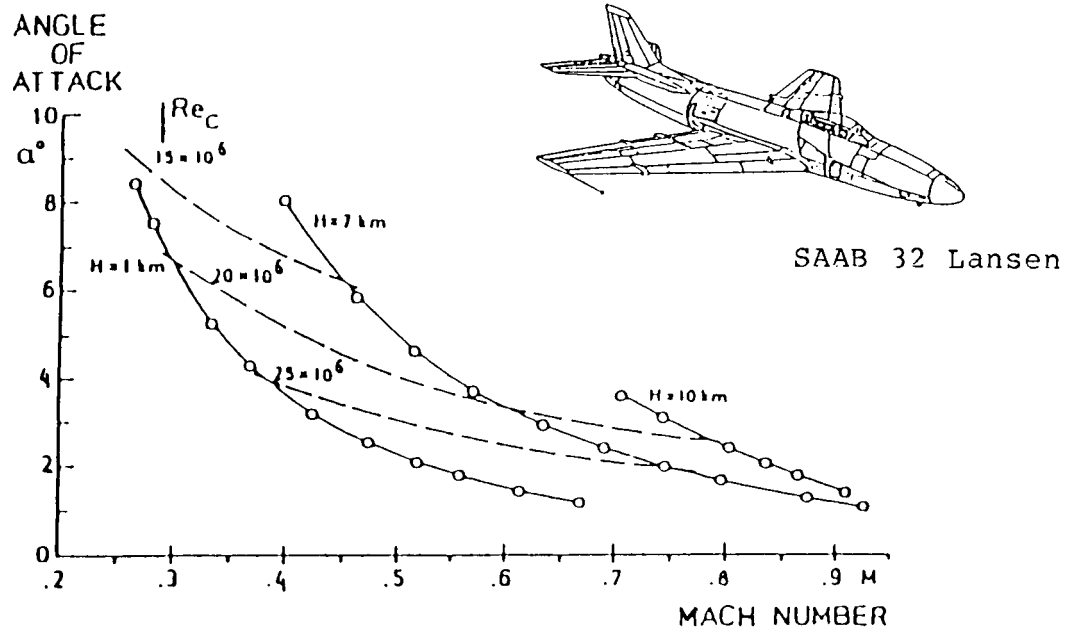


Figure 3 Geometry of the aircraft and the flight envelope.

## TEST AREA ON THE OUTER PART OF THE WING

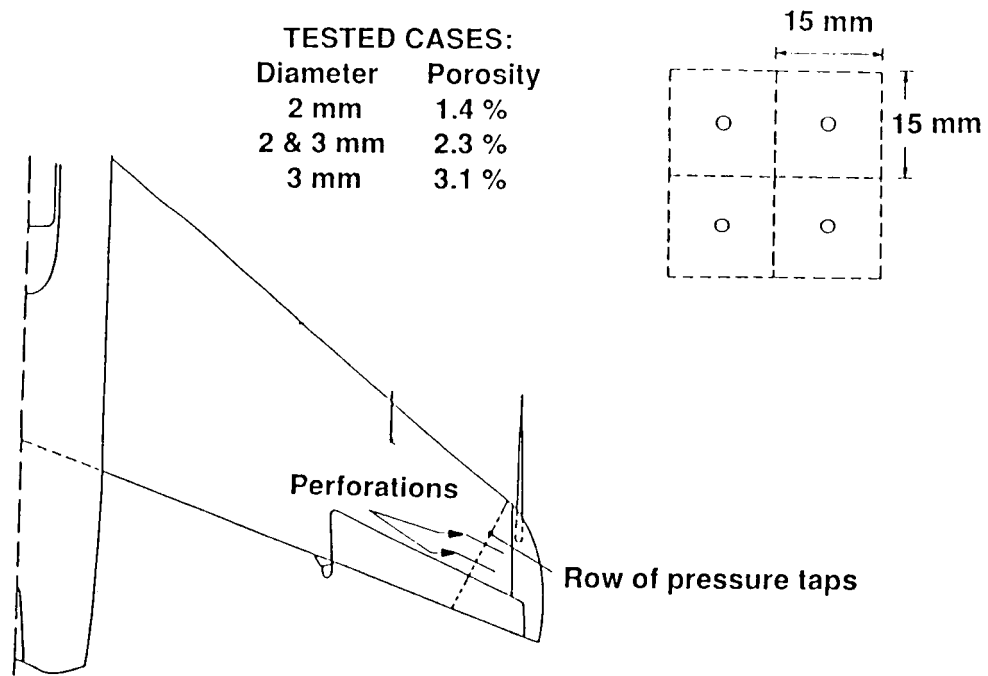


Figure 4 Wing geometry and coordinate system.

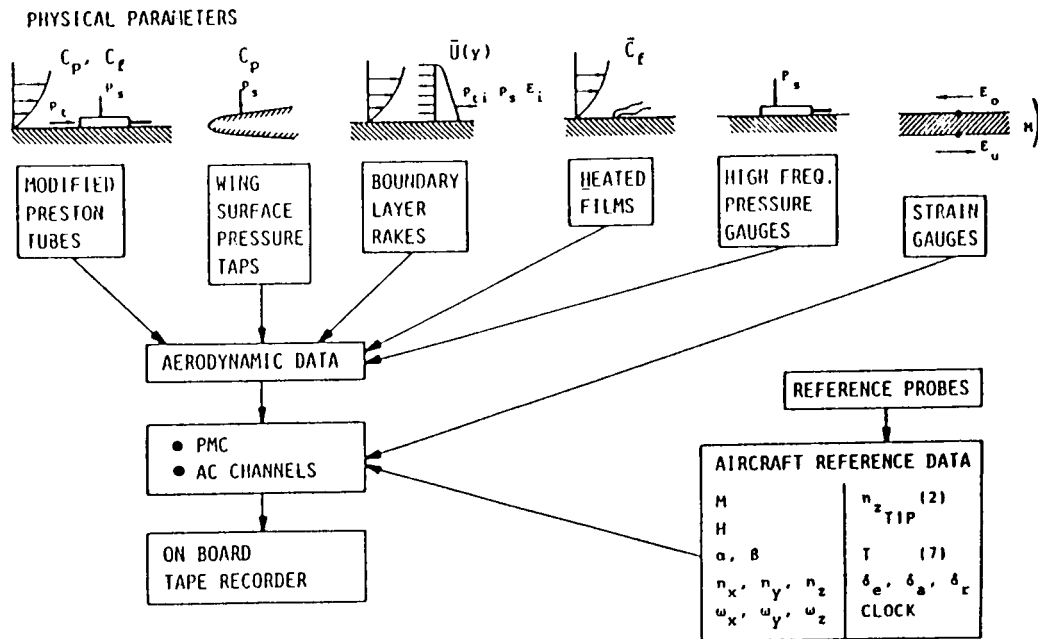


Figure 5 Sensor types and data acquisition system.

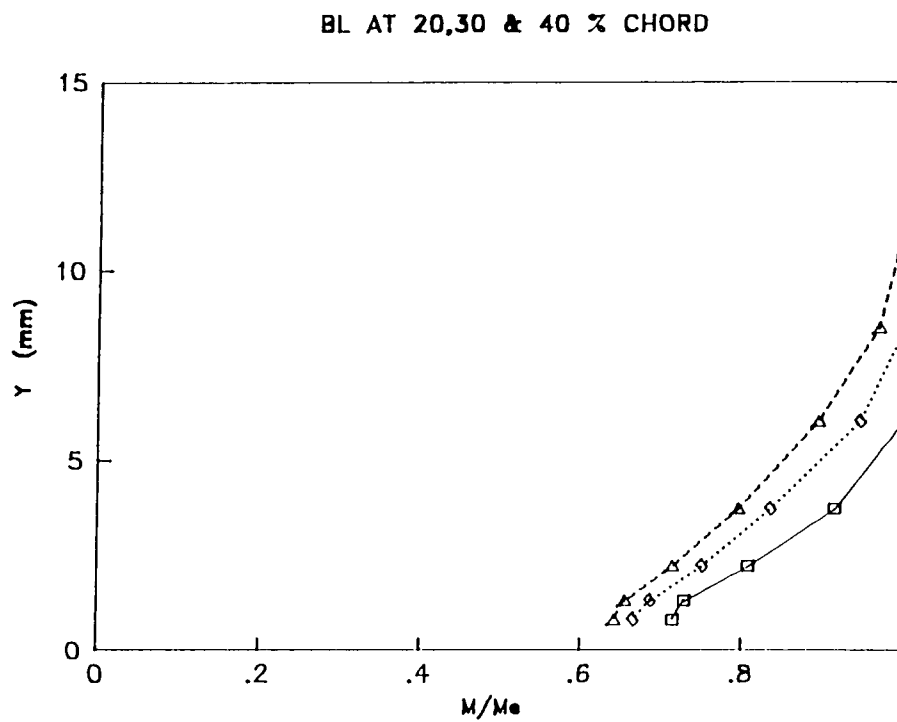
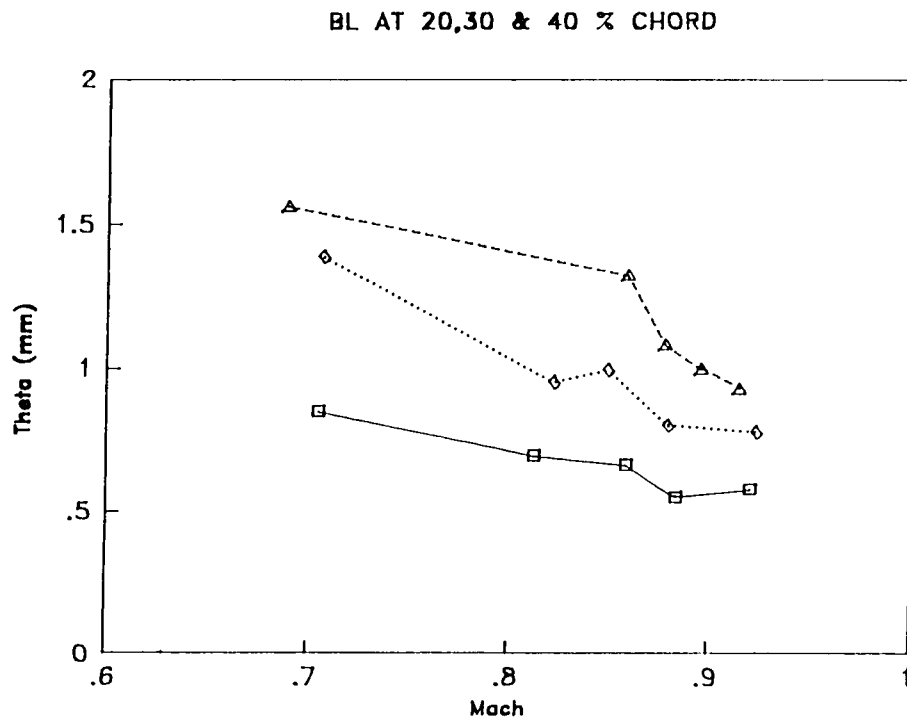


Figure 6 Boundary layer development in front of the shock. Baseline.

## SHOCK POSITION AT CONSTANT MACH NUMBER BASELINE

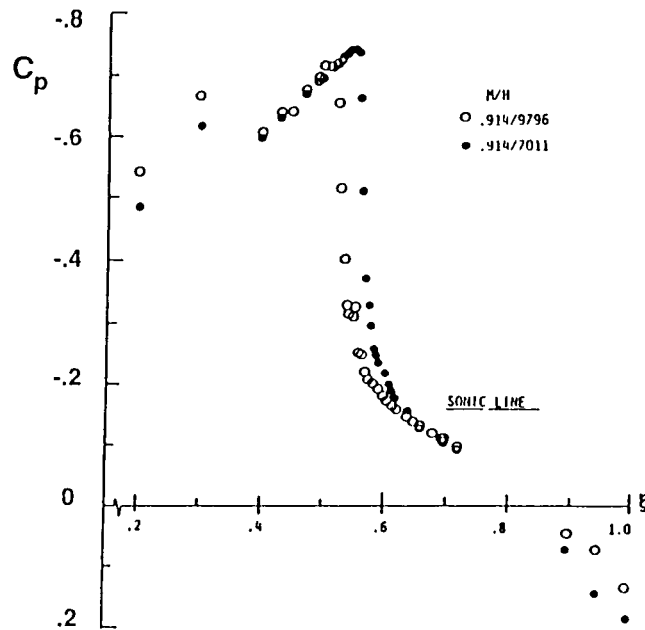


Figure 7 Shock movement due to change in altitude, baseline.

## PEAK NORMAL LOCAL MACH NUMBER (PMLN) 1.4 % POROSITY

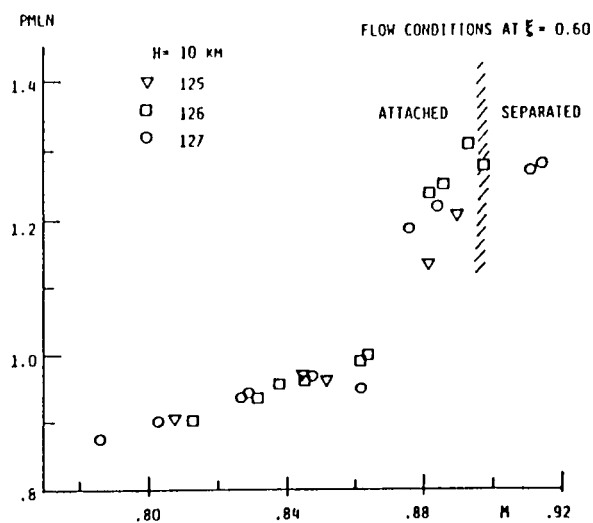


Figure 8 PMLN as function of flight Mach number.

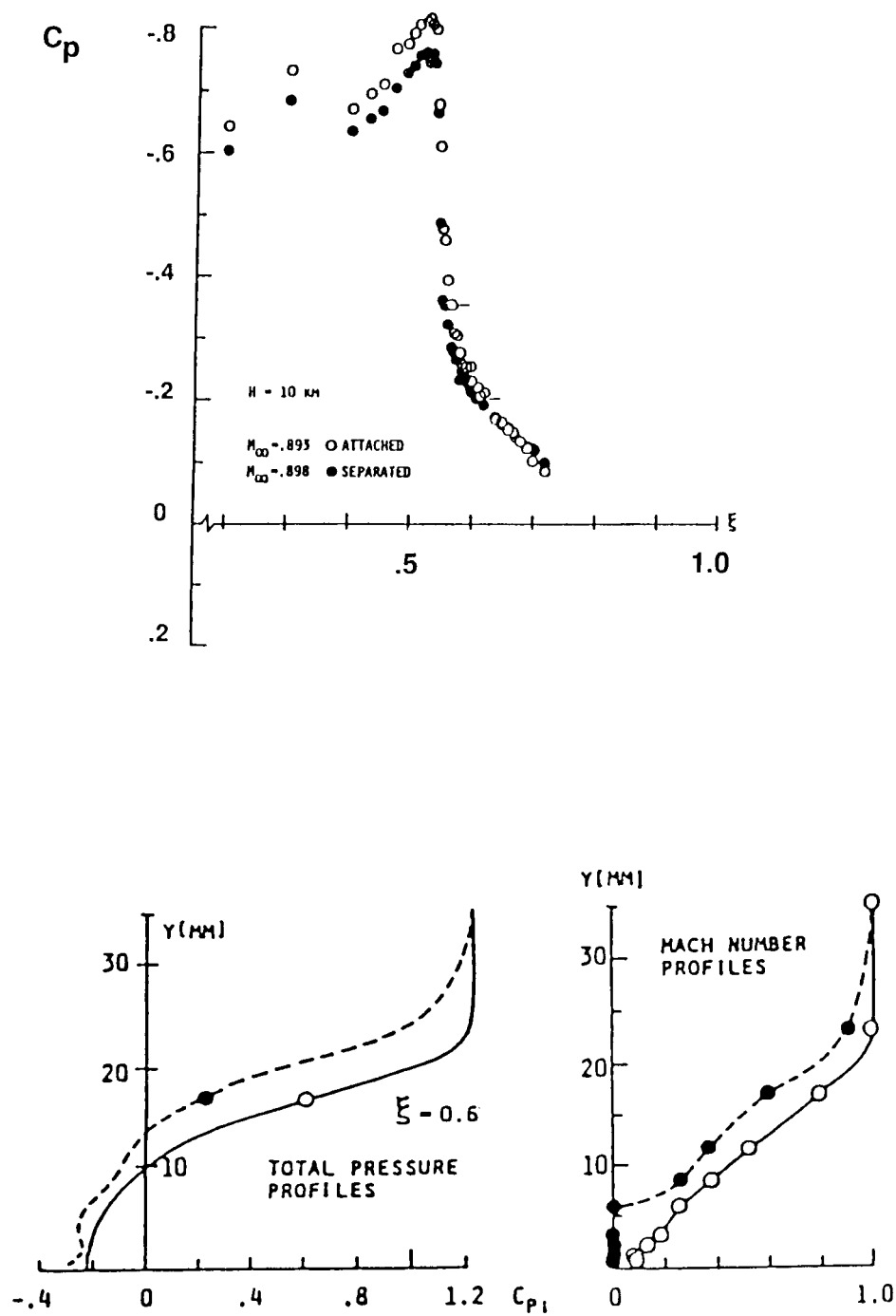


Figure 9 Flip-flop effect of separation, baseline.

## SHOCK POSITION AT CONSTANT ALTITUDE BASELINE

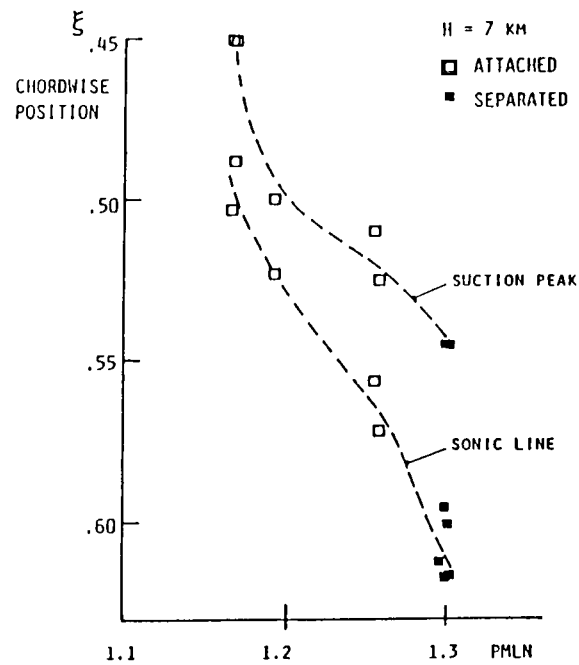


Figure 10 Shock movement due to changes in Mach number, baseline.

## BOUNDARY LAYER PARAMETERS AT 60 % CHORD

### 3.1 % POROSITY

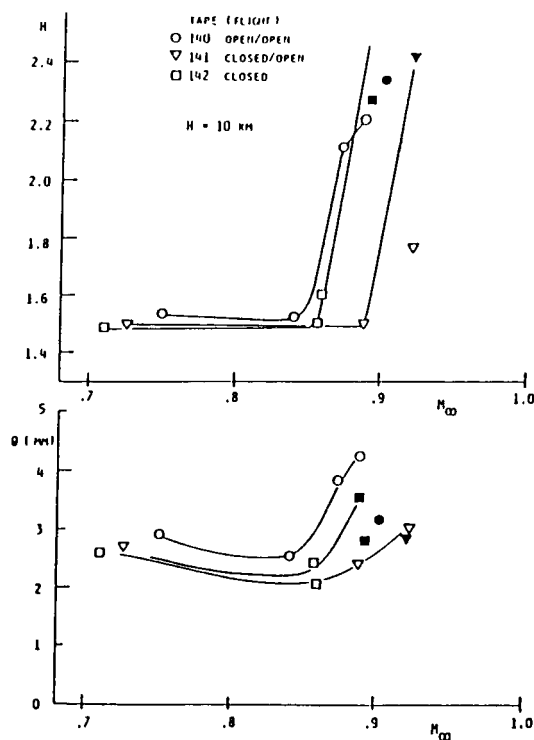


Figure 11 Momentum thickness and shape factor as function of PMLN at 60 % chord.

## MOMENTUM LOSS - DOWNSTREAM EFFECT

### 3.1 % POROSITY

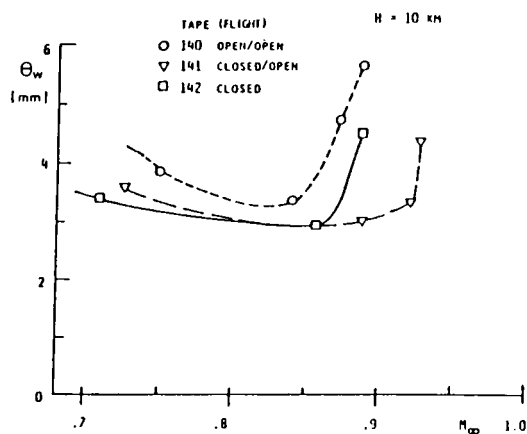


Figure 12 Momentum deficit interpreted as drag using the Squire-Young formula.

ORIGINAL PAGE IS  
OF POOR QUALITY

## TRANSONIC CFD APPLICATIONS AT BOEING

E. N. Tinoco  
Computational Fluid Dynamics Laboratory  
Boeing Commercial Airplane Company  
Seattle, Washington

### SUMMARY

The use of computational methods for three-dimensional transonic flow design and analysis at the Boeing Company is presented. A range of computational "tools" consisting of "production" tools for everyday use by project engineers, "expert user" tools for special applications by computational researchers, and a new "emerging" tool which may see considerable use in the near future are described. These methods include full potential and Euler solvers, some coupled to three-dimensional boundary layer analysis methods, for transonic flow analysis about nacelle, wing-body, wing-body-strut-nacelle, and complete airplane configurations. As the examples presented show, such a toolbox of codes is necessary for the variety of applications typical of an industrial environment. Such a toolbox of codes makes possible aerodynamic advances not previously achievable in a timely manner, if at all.

### INTRODUCTION

Computational Fluid Dynamics (CFD) is playing an ever increasing role in the design of air vehicles. CFD has joined the wind tunnel and flight test as a principal technology for aerodynamic design. When the next new Boeing airplane flies, whether an all new design, or a derivative of an existing production aircraft, CFD will play a role in its design. The proper and timely use of CFD will result in a superior product with reduced risk and lower cost. However, note success does not come automatically with CFD, the keys to success are the "proper and timely use."

CFD today covers a wide range of capabilities in terms of computational flow physics and geometrical complexity. Figure 1 illustrates the boundary in terms of the complexity of flow physics and configuration geometry that encompass what we believe is practical in industry. We realize that this boundary is continuously being challenged by researchers here and abroad.

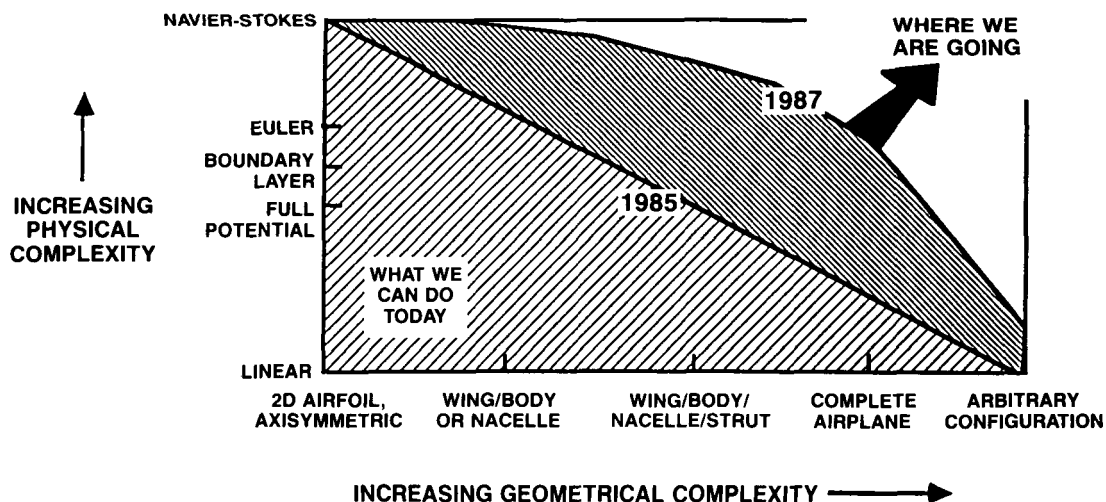


Figure 1. Status of CFD for Design Application.



The value of CFD in industry is in its application. CFD is used to lend understanding to the flow phenomena about a given geometry and to aid in the design of a piece of hardware, whether it be an all new wing, or a minor modification to an existing configuration. To be useful the computational method must faithfully represent the dominant flow physics, adequately represent the required geometrical complexity, be capable of providing solutions in a timely manner, and be affordable. This is a tall, and as yet unfilled, order by any single method. The approach at Boeing has been to assemble a toolbox with a collection of CFD tools that meets the above requirements to varying degrees. In this toolbox are "production" tools that are in wide use throughout the company by a variety of CFD users. These are well documented codes that have been specialized to a certain extent, and can be run by the nonexpert CFD users. There are "expert user" tools, which may have more general and advanced capabilities than the "production" codes, but are not as well developed, and may require special skill to run successfully. There are also "emerging" tools. New technologies under development, offer new capabilities, which may become "production" tools in the near future.

No CFD toolbox is complete without geometry and graphics tools. Geometry tools are essential for the preparation of the inputs to the various CFD codes. Three-dimensional graphics running on suitable workstations allow the inspection of surface and field grids prior to execution, and provide the keys to understanding the frequently massive output from a typical transonic CFD solution. The "timeliness" of CFD is very heavily tied into the quality of the geometry and graphics tools available. The primary tool fitting this need at Boeing is the interactive, three-dimensional geometry system known as the Aero Grid and Paneling System (AGPS), Reference 1. AGPS provides an efficient means of defining any three-dimensional surface or aircraft component. These surfaces can be combined to represent a complete aircraft configuration. AGPS has built-in and user-programmable features for extracting geometric data in the proper form for use by CFD codes. Paneling, surface grid generation, and grid distribution at block boundaries for input to three-dimensional grid generation codes are all possible. AGPS can also display CFD results in the form of three-dimensional objects with color representing the value of some flow property. Several other geometry and graphics codes are also essential parts of the toolbox.

Table 1. Transonic CFD Toolbox

PRODUCTION CODES	FORMULATION	GEOMETRY CAPABILITY
A502/PANAIR	Linear Potential	General Geometry
A488	Conservative Full Potential with Coupled 3-D Boundary Layer - Analysis	Wing-Body, Wing-Body-Strut-Nacelle
A555	Conservative Full Potential with 3-D Boundary Layer - Design	Wing-Body Wing-Body-Strut-Nacelle
A588	3-D Euler with Coupled 3-D Boundary Layer	Isolated Turbofan Nacelle Isolated Turbofan Nacelle-Strut
P318	Axisymmetric Full Potential with Boundary Layer	Isolated Axisymmetric Nacelle
P467	Full Potential with 3-D Boundary Layer	Axisymmetric Nacelle
P582	Full potential	General Geometry
WBPPW/BOPPE	Extended Transonic Small Disturbance with Coupled Boundary Layer	Wing-Body-Strut-Nacelle-Winglet
<b>EXPERT USER CODES</b>		
	Euler	Wing-Body-Tail Wing-Body-Tail-Aft Propfan UDF Nacelle-Strut Turbofan Nacelle
	Euler with Coupled 3-D Boundary Layer	Wing-Body-Tail Wing-Body-Strut-Aft Propfan Wing-Body-Winglet
<b>EMERGING CODE</b>		
TRANAIR	Full Potential	General Geometry

This paper will go on to describe the various CFD tools in use at Boeing, and in this manner will illustrate how transonic CFD methods are used. The perspective presented is mainly from the view of the Boeing Commercial Airplane Company. However, these methods are available, and are used by other members of The Boeing Company. The focus of this paper is on transonic CFD methods for three-dimensional flows. Table 1 lists some of the common CFD tools in use at Boeing today.

## SYMBOLS

$A$	= streamtube area
$b$	= wingspan
$C_d$	= section drag coefficient
$C_D$	= drag coefficient
$C_\ell$	= section lift coefficient
$C_L$	= lift coefficient
$C_{nf}$	= normal force coefficient
$C_p$	= pressure coefficient
$c$	= wing chord
FNPR	= fan nozzle pressure ratio
$M$	= Mach number
$T_c$	= Thrust coefficient
$x$	= streamwise coordinate
$y$	= lateral coordinate
$z$	= vertical coordinate
$\alpha$	= angle of attack
$\beta$	= side slip angle
$\delta^*$	= boundary layer displacement thickness
$\eta$	= span fraction

### Subscripts

$H$	= inlet highlite
$I$	= inlet
$\infty$	= freestream
$T$	= total

## PRODUCTION TOOLS

Production tools or codes are characterized by the following: they are used outside the research organization that created them; their documentation is adequate enough to allow use by other than their creators; stable versions of these codes exist for use outside the research environment that are not undergoing constant change; sufficient validation of these codes has been demonstrated such that outside users are willing to invest the necessary effort to use them.

Two production codes that see the most use in Boeing are A502/PANAIR, a linear panel method, and A488, a full-potential solver with coupled boundary layer analysis for wing-body and wing-body-strut-nacelle configurations. These two codes are accessed over 2,000 times a year each. Although A502/PANAIR (refs 2 and 3) is not a true transonic method, its ability to model complex detailed geometry, makes it the only currently usable tool in some instances. In the design of the Navy E-6A wingtip pod arrangement, shown in Figure 2, only A502/PANAIR could handle the complex geometry at the time. It was used in the design process to shape the pods and struts to minimize supercritical flow at cruise conditions. The resulting design was committed to manufacture and first saw real air when it flew on the aircraft. Only the emerging full-potential TRANAIR code promises the ability to deal with fine geometric details such as tip pods, stores, or missiles, etc. in a supercritical flow environment. TRANAIR will be discussed in more detail later in this paper.

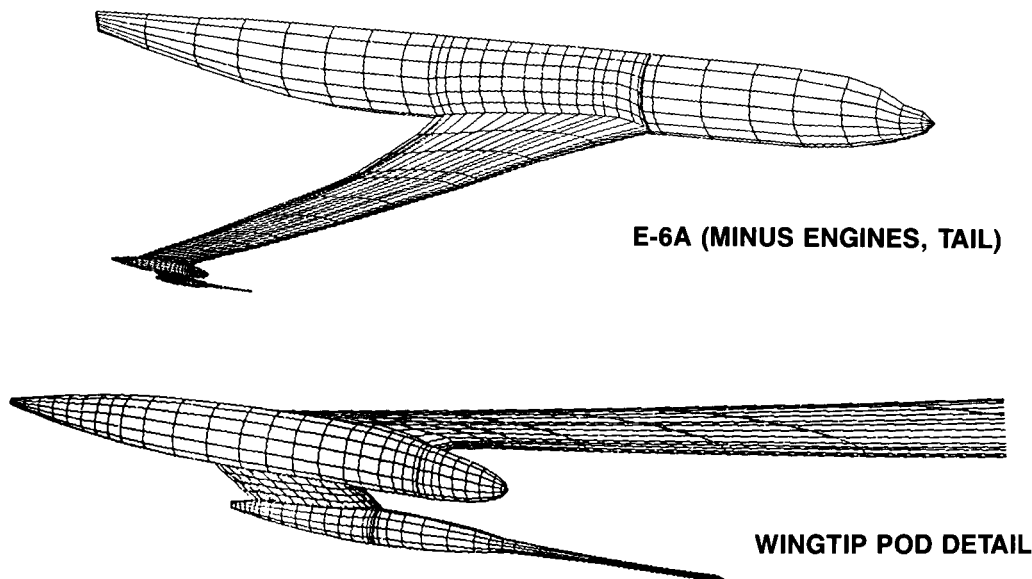


*Figure 2. E-6A Wingtip Pod—A CFD Design.*

For most analyses of wing-body, or wing-body-strut-nacelle configurations at Boeing, A488 is the code of choice. A488 couples a full-potential inviscid flow solver with a three-dimensional boundary layer solution for the wing. It has been undergoing continuous development and refinement for the last 10 years. The method was first demonstrated in 1978 (ref 4), and has evolved into a highly sophisticated analysis tool that will rival any Navier-Stokes solver for accuracy at a small fraction of the cost for analysis of attached flows. A488 has evolved into a system of some 50 programs tied together with job-control language. Use of the system requires user access to numerical lofts of the wing (in either of two commonly used geometry systems at Boeing), body, nacelle, and strut, or files consisting of normal station cuts for the body and nacelle, and waterline cuts for the strut. An input file is prepared containing flow condition information, i.e., Mach, angle of attack, Reynolds number, etc.; transition strip location as a function of span fraction, etc.; and file names of the various geometric components. An online program is executed that generates all the job-control logic and submits the problem for execution on a CRAY X-MP. The grid generation, and cycling between the inviscid and viscous solvers automatically proceeds for the prescribed number of iterations, as illustrated in Figure 3.

A488-CONSERVATIVE  
FULL-POTENTIAL  
WING-BODY-STRUT-NACELLE

A588-EULER  
NACELLE

EULER  
WING-BODY-TAIL

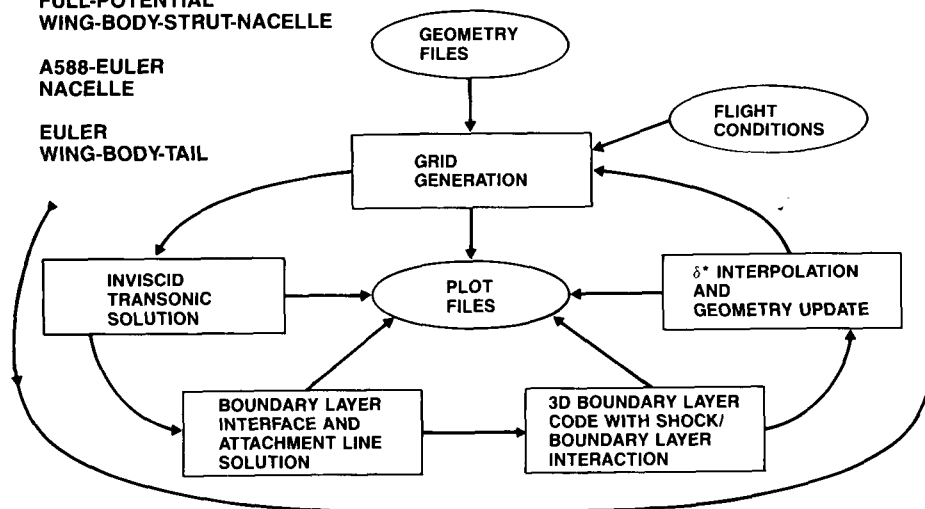


Figure 3. Integrated Transonic/Viscous Analysis System.

A flexible and efficient elliptic grid generation method (refs 5 and 6) is used to generate a surface-fitted C-type grid. The grid distribution along the strut-nacelle requires special consideration. For a general strut-nacelle installation, it is usually difficult to produce an exact surface-fitted grid with smooth and well distributed mesh spacing in the field. The approach taken here involves a simplification of the nacelle inlet geometry and a relaxation of the requirement that the grid lines lie along the corners formed by the nacelle-strut intersection and along the nacelle keel line, as illustrated in Figure 4. The tight clustering of grid lines close to the wing allows adequate grid resolution in the region between the wing lower surface and the nacelle. The exhaust plume is modeled as a solid surface. With the proper choice of the exhaust plume shape (ref 7), both power effects and core cowl shape effects can be simulated.

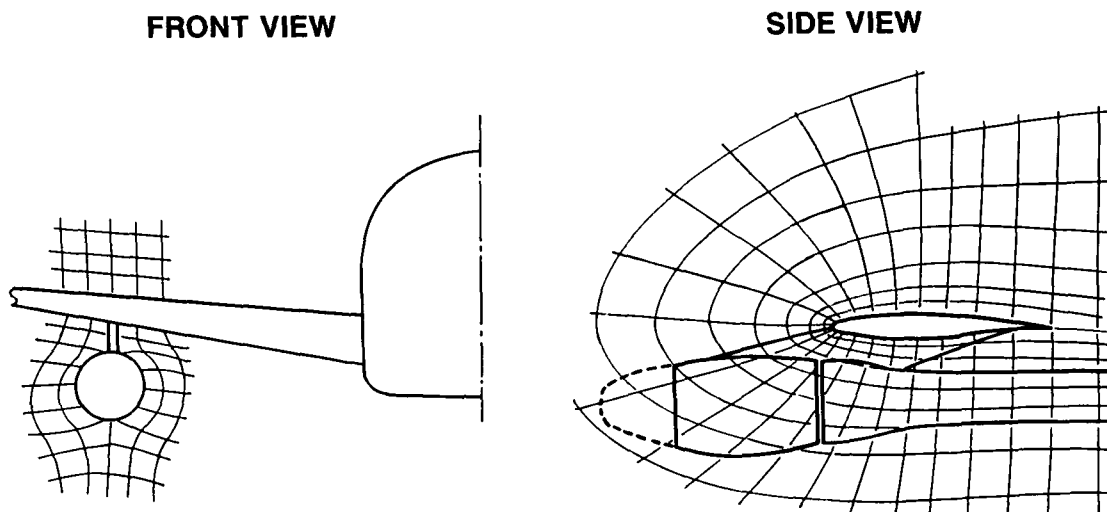


Figure 4. Grid Topology at Nacelle/Strut Station.

The current inviscid solver is based on the full-potential, fully conservative Jameson-Caughey finite volume algorithm, FLO28 (ref 8). Enhancements added to the method include: a convergence acceleration method using an extrapolation technique (ref 9), and GMRES (ref 10); second-order accurate differencing for better shock resolution; and, improvements to the calculation of surface pressures and the Kutta condition.

The boundary layer calculations are based on the method of McLean (ref 11). This is a three-dimensional finite difference formulation for both laminar and turbulent boundary layers. In addition, a semiempirical shock-boundary layer interaction model (ref 12) has been added. Here, the treatment of the effects of a shock on the boundary layer is improved by replacing the boundary layer equations in the shock zone with a set of empirical jump conditions for the changes in the boundary layer quantities through the shock. The boundary layer equations are still used upstream and downstream of the shock zone. The determination of the shock zone is based on the behavior of the shock-perpendicular Mach number. The method also includes an attachment line solution at the wing leading edge which is used to determine the starting conditions for the upper and lower surface boundary layer solution.

The interaction between the boundary layer and the inviscid flow is calculated by a classical direct-iteration scheme. In each cycle of the iterative procedure, the viscous flow is computed in the direct mode (i.e., given the velocity components from the inviscid outer solution calculate the boundary layer and output the displacement thickness), and a weighted average of the new and old displacement thickness is used to modify the surface shape for the next cycle. The field grid for the inviscid solver is automatically updated with each displacement thickness change.

A488 results have been compared with experimental data for a variety of vehicles. Figure 5 shows a comparison of A488 results with wing pressure distributions measured in flight on a 737-300. The computational model consisted of the wing, body, strut, and nacelle. The wing definition included the estimated aeroelastic twist for the condition flown. Although the character of the pressure distribution on the wing changes dramatically across the span, the computational results agree reasonably well with the measured data.

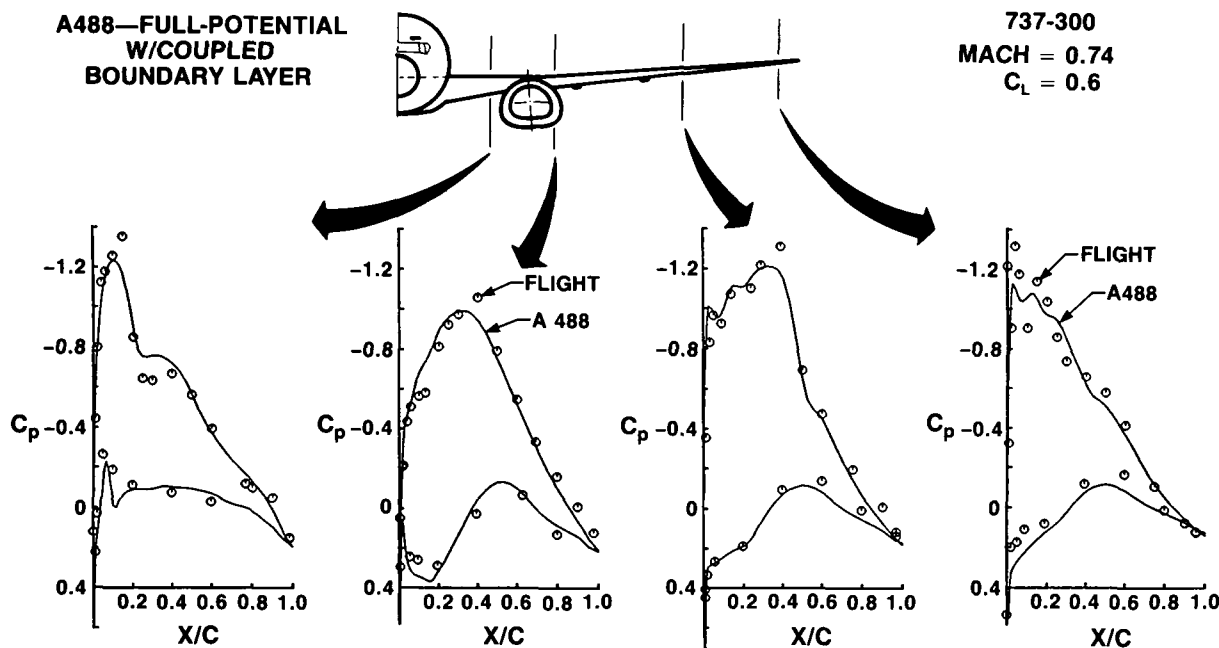


Figure 5. Comparison With Flight Pressure Distributions—737-300.

Figure 6 presents a comparison of spanwise distribution of section lift with wind tunnel data for an early developmental 757-200 wing-body-strut-nacelle configuration. This comparison illustrates the importance of accounting for the aeroelastic deflections that occur in the wind tunnel. The wind tunnel model was a full model with a steel wing and was tested in an atmospheric tunnel. At the dynamic pressure for Mach 0.80 and at the cruise lift, the estimated additional wing twist at the wingtip due to aeroelastics was 0.5 deg. Inclusion of the aeroelastic twist in the computational model definition was essential for good agreement with the experimental data.

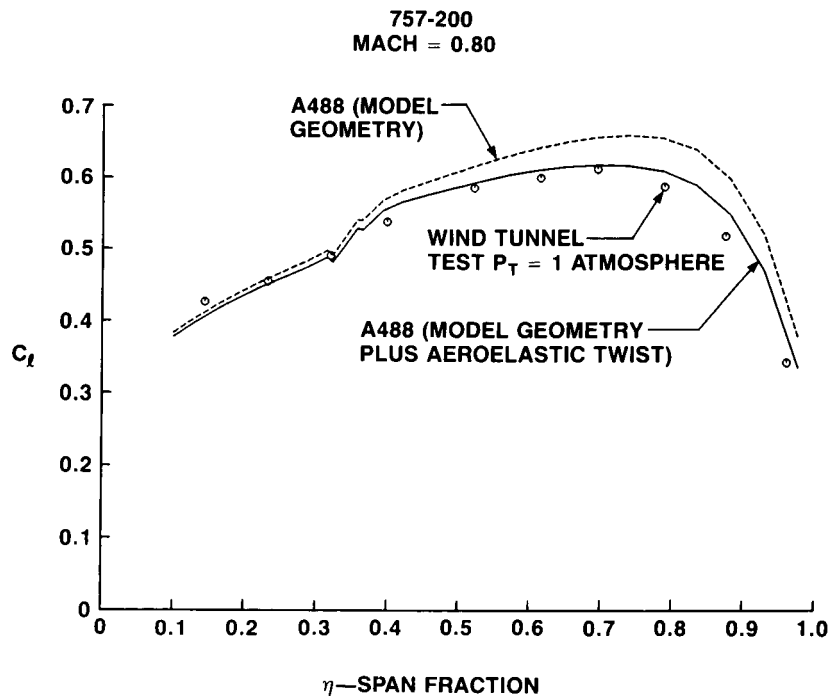


Figure 6. Comparison With Wind Tunnel Section Lift Distribution.

Figure 7 shows another comparison of A488 results with flight data. This time it shows a Grumman F-14 with the wing set at the 20-deg sweep position. These analyses were done in support of a variable sweep boundary layer transition flight experiment (ref 13). With the exception of the inner-most station, the computational results agree well with the measured data. The discrepancy at the most inboard station is believed to be due to the inability of the method, with its single block C-grid topology, to adequately represent the fuselage. The surface grid used for the analysis is shown in Figure 8. The general cross-section of the fuselage is represented but the engine inlet has been gridded over. This example illustrates the need for methods capable of handling more general and complex geometries.

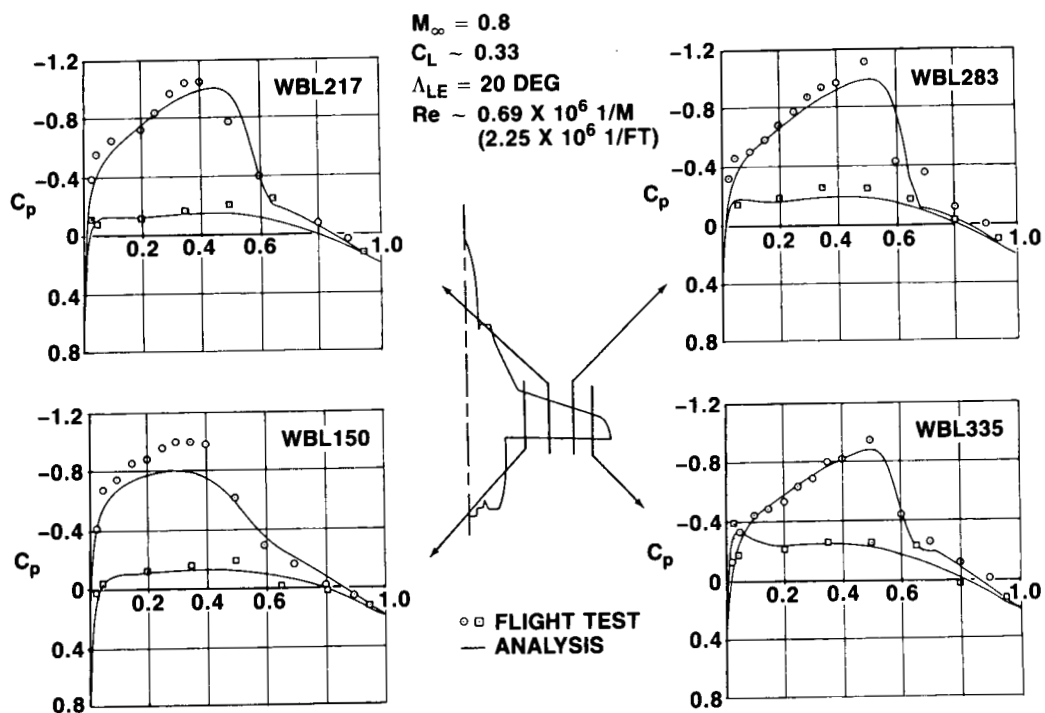


Figure 7. Comparison With Flight Pressure Distributions—F-14.

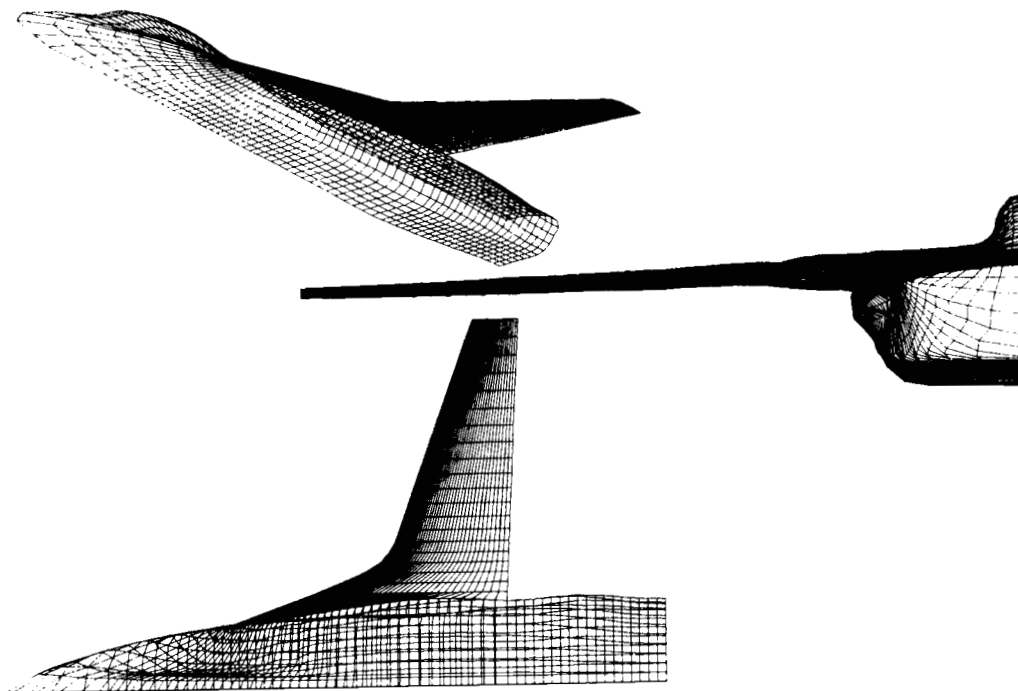


Figure 8. Surface Grid for F-14 in A488 Code.

In the solution process, detailed boundary layer characteristics are calculated. Using analyses at full-scale Reynolds number as a guide, trip strip patterns can be designed for low Reynolds number testing which will best result in a displacement thickness at the shock or trailing edge comparable to the expected full-scale value. The spanwise distribution of skin friction and profile drag can also be derived from the boundary layer calculations. The profile drag is based on applying the Squire Young formula (ref 14), along the wing trailing edge. Only the streamwise components of the trailing-edge velocity profiles are used in this formulation. A comparison with measured profile drag is shown in Figure 9. The distribution and level of profile drag are in good agreement with the test data. The skin-friction drag distribution is shown for reference. The experimental profile drag was derived from a series of wake traverses along the wingspan. For subcritical flows, the wake total pressure deficit is due only to the profile drag. For supercritical cases wave drag also adds to the total pressure deficit. Figure 10 shows a comparison for wave drag and profile drag. Measured and calculated profile and wave drags agree reasonably well. Examination of the spanwise variation of wing drag components helps identify the critical wing design regions and allows for better wing design.

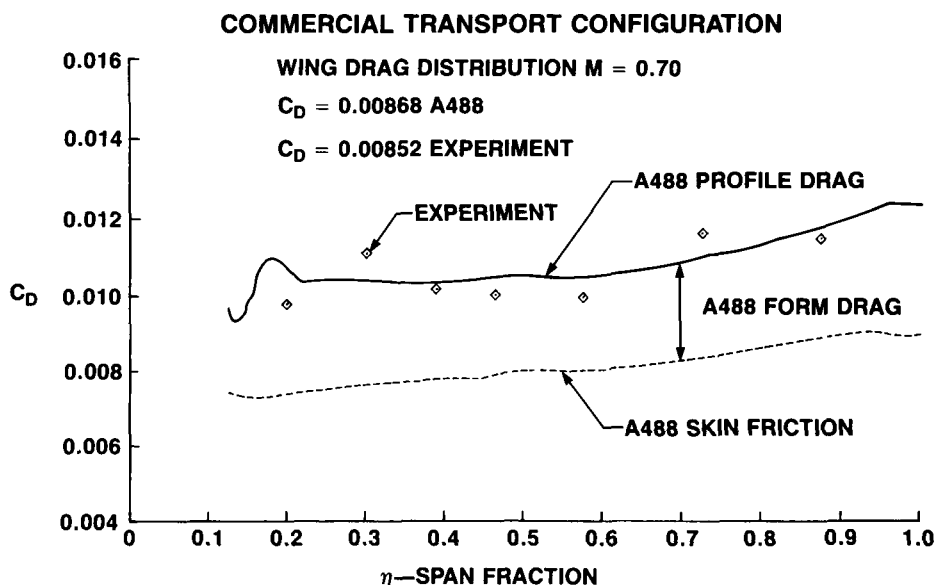


Figure 9. Wing Profile Drag Distribution—Test-Theory Comparison.

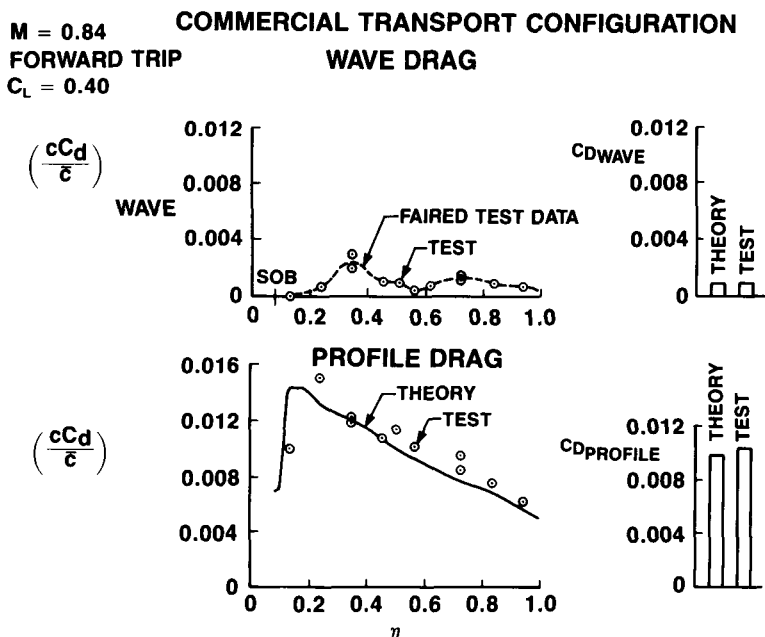


Figure 10. Spanwise Profile and Wave Drag Distributions,  $M = 0.84$ .



Accurate drag prediction is always of interest in industry. Although methods such as A488 can be used to develop drag polars (see Figure 11, for example), CFD has not yet matured to the level where it is capable of predicting complete airplane configuration drag to the accuracy needed for commercial transport development. The competitive nature of the commercial transport industry makes drag improvements of less than one percent airplane drag significant and worth seeking. CFD methods capable of reliably and accurately predicting drag values, even component drags, would be of great value to the aircraft designer. Methods like A488 may be able to do this for transport type wings with attached flow, but there is a lack of experimental data to adequately validate these methods. Adequate validation requires detailed test-theory comparisons at several combinations of Mach number, angle of attack, and Reynolds number. Not only are force data necessary for validation, detailed surface pressure data and wake measurements are also required.

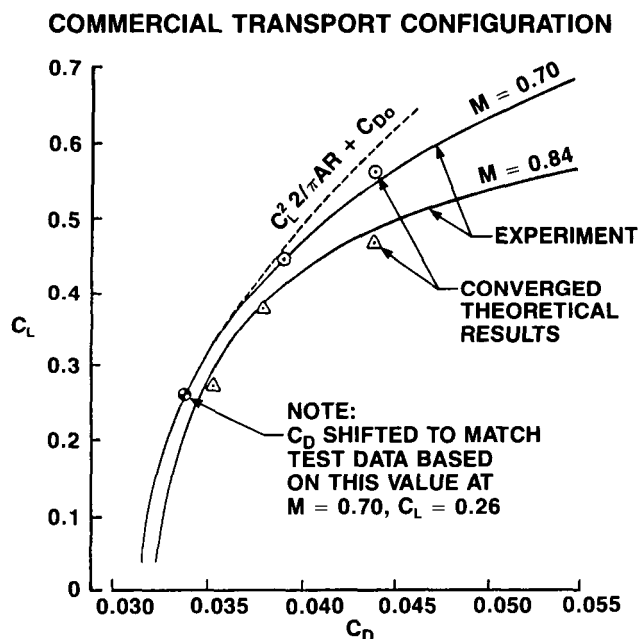


Figure 11. Comparison of Computational and Experimental Drag Polars.

The ability to adequately model the nacelle and strut is essential for many of our applications. The presence of the nacelle and strut can have a significant effect on surface pressures on the upper as well as the lower surface of the wing, as illustrated in Figure 12. We have had reasonable success in simulating engine installation details such as engine primary core cowl shape effects on wing lower surface pressure distributions (Fig 13), and engine power effects (Fig 14). Figure 13 shows the difference in wing lower surface pressure distribution that results when the engine primary core cowl is truncated to yield a desired inlet mass flow ratio in a wind tunnel flow through nacelle compared to what might be achieved by the actual engine geometry. Figure 14 shows the difference between the engine operating at cruise thrust or exhausting at "ram" fan nozzle pressure ratio, i.e., exhausting at free-stream Mach number. These effects are simulated by specification of the appropriate fan exhaust plume shape (ref 7).

ORIGINAL PAGE IS  
OF POOR QUALITY

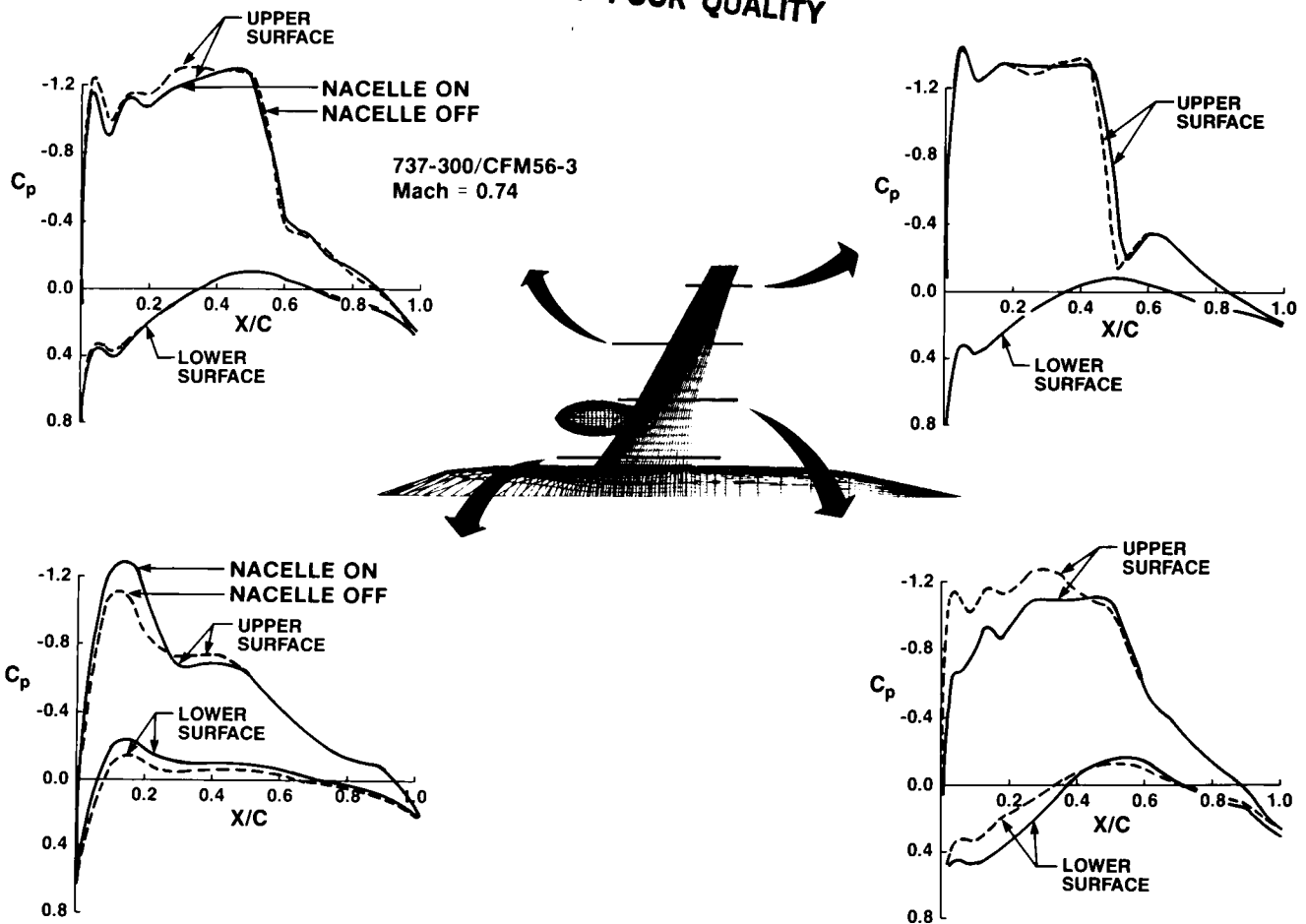


Figure 12. Influence of Nacelle on Wing Surface Pressures.

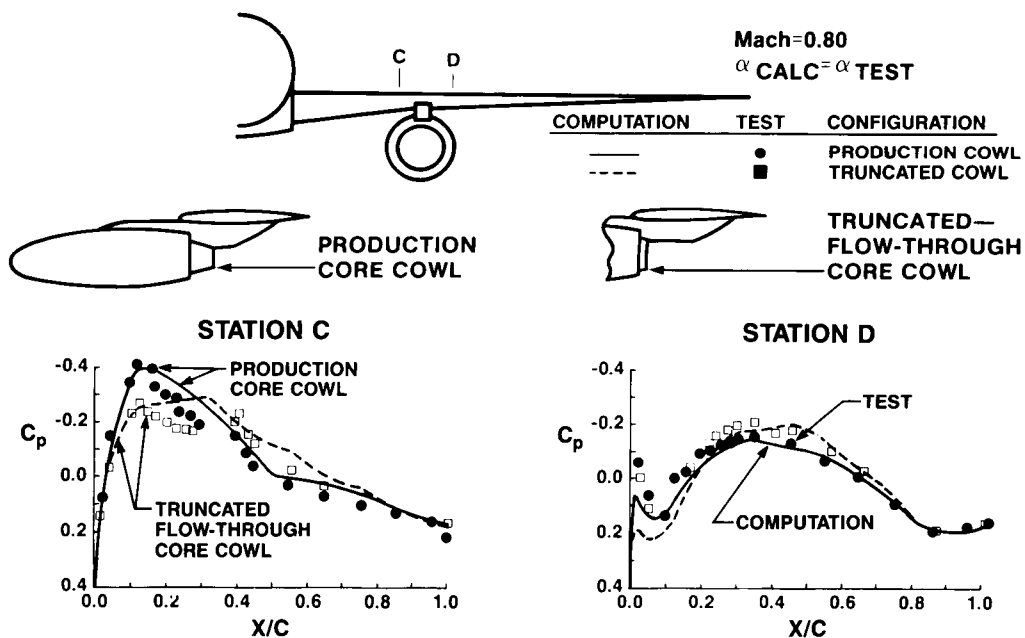


Figure 13. Core Cowl Geometry Effects.

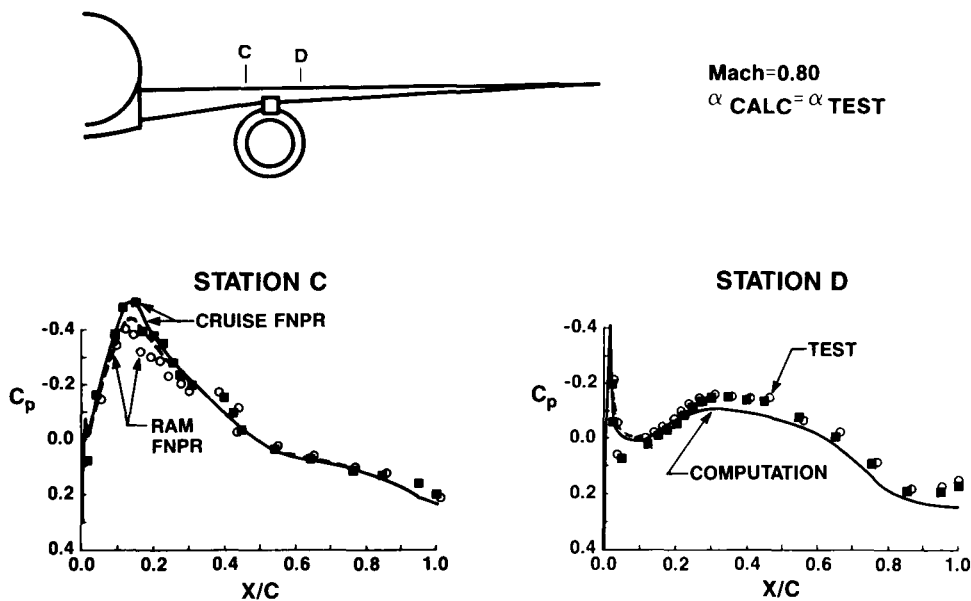
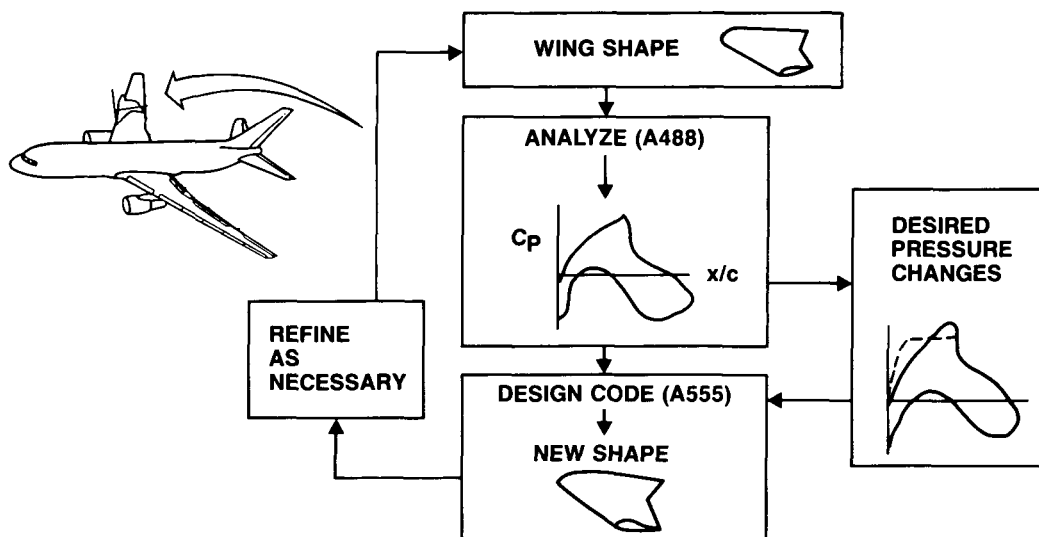


Figure 14. Power Effects on Wing Lower Surface.

Other applications of the A488 system have included evaluating out-of-contour fairings for a deeper landing gear-beam on the 737-400, wing modifications to several existing configurations, and aerodynamic analyses of several horizontal tails.

Originally developed in the early 1980s, but just recently elevated to production status is A555, an inverse design full-potential code with boundary layer effects. A555 is complementary to A488. Both use an enhanced version of FLO28 for their inviscid solver, and the same three-dimensional finite difference boundary layer code. The solutions are completely reversible, that is, one can take the pressure distribution from an A488 analysis, run it through A555 and recover the original A488 geometry. The use of A555 is illustrated in Figure 15. An initial seed geometry is first analyzed. If the resulting solution does not exhibit the desired

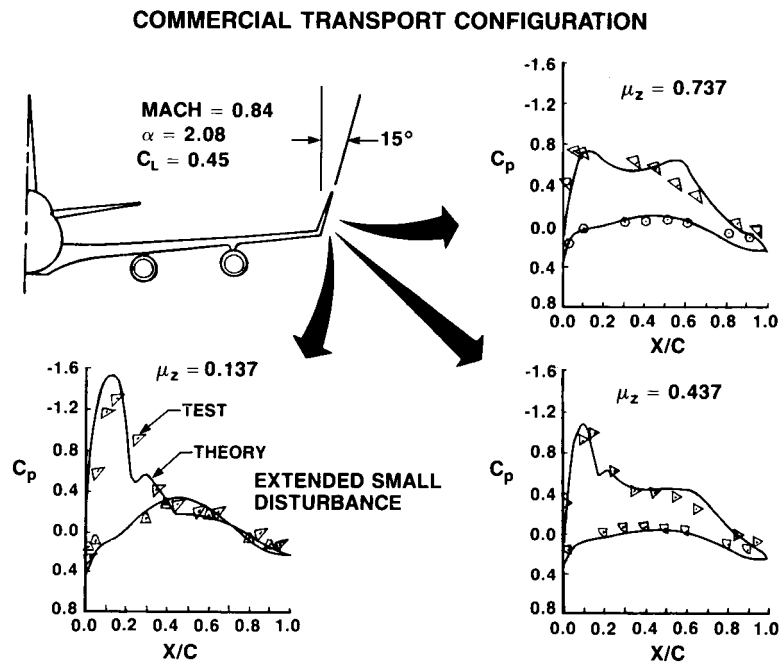


- Design and analysis with CFD
- Use wind tunnel to validate wing design

Figure 15. Wing Design Using CFD.

pressure distributions, the designer can specify a desired target pressure distribution. Several preprocessors are available to assist the designer in specifying distributions with the desired characteristics and proper smoothness. The inverse design code then produces a geometry which includes the boundary layer displacement thickness. The boundary layer solution supplies the displacement thickness to be removed, which after removal leaves the bare wing geometry. This resulting geometry is then modified as necessary to meet whatever manufacturing constraints might apply, and then reanalyzed. This cycle may be repeated several times until a wing design evolves having the desired pressure characteristics and meeting all the appropriate geometric constraints. The coordinated A488/A555 system has allowed wing designs to be developed in a timely manner that were not previously achievable.

Another transonic analysis code that is occasionally used at Boeing, because of its ability to model winglets in a simplified form, is the NASA WBPPW/Boppe code (ref 15). This code is based on an extended small disturbance transonic formulation, and features multiple-embedded grids. The code's use of linearized boundary conditions along with the multiple-embedded grids allows the user to avoid the complications of surface-fitted grid generation when analyzing configurations with winglets, pods, and pylons. A comparison of results from this code with experimental data acquired in the mid-1970s is shown in Figure 16. The ability to generate surface-fitted grids for wings with a full-chord winglet has recently been developed at Boeing allowing the use of full potential or Euler codes for winglet analysis.



The grid topology of the A488 system does not allow detailed analysis of the flow on the nacelle, only its effects on the wing. For detailed analysis of a turbofan nacelle we use A588, a three-dimensional Euler solver coupled to the same three-dimensional finite difference boundary layer code as used in A488. The Euler nacelle code, developed for powered turbofan nacelle analysis (ref 16), is based on FLO57 (ref 17). It features a time-dependent solution of the Euler equations in conservative form. A C-type body-fitted computational grid, illustrated in Figure 17, is used. The code solves a two-stream problem comprised of external and fan flows. Core flow is treated either as a solid-body extension of the input geometry or the core cowl geometry is simply extended and terminated at a point. The nacelle mounting strut can also be included in the analysis. Boundary conditions can be specified on the inlet face to control the inlet mass flow. Total pressure, total temperature, and swirl can be specified on the exit plane in the fan exhaust duct to describe the exhaust conditions. The code is capable of analyzing both angle of attack and yaw conditions.

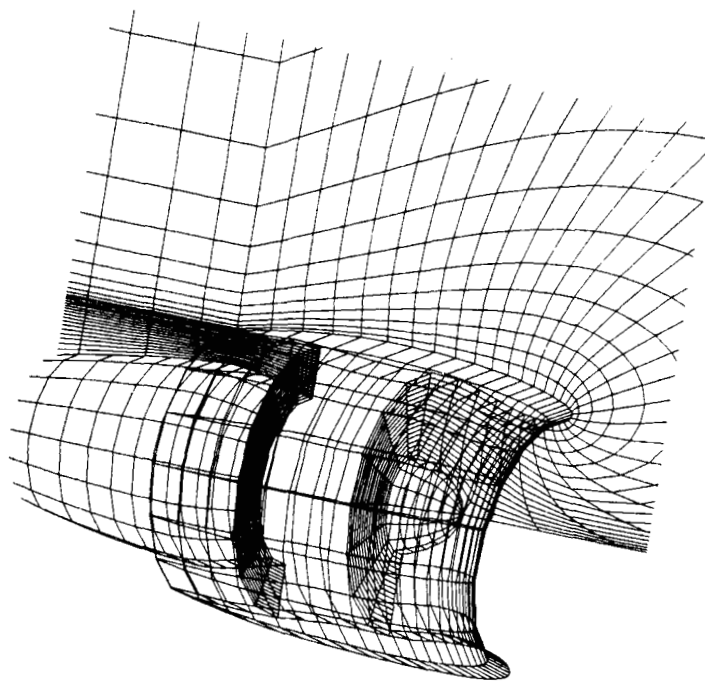


Figure 17. Computational Grid for Euler Powered Nacelle Code.

A588 has proven to be highly accurate in the calculation of the flow over isolated nacelles. Figure 18 shows the comparison of computed results with experimental data on a axisymmetric nacelle. The test data were acquired on a swept strut-mounted flow-through nacelle over a Mach number range from 0.70 to 0.925. A fixed mass flow ratio based on an experimental internal inlet pressure was specified for all the cases. The results shown in Figure 18 are typical of the very good agreement with test data that was obtained across the Mach number range.

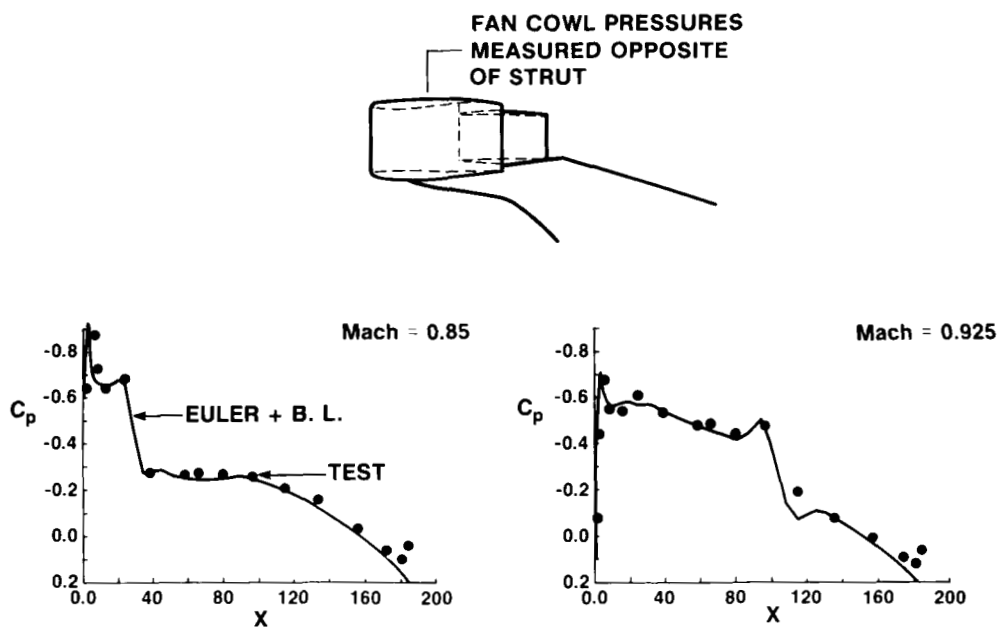


Figure 18. Comparison With Fan Cowl Pressures.

The second example of A588 analysis features a turbofan nacelle with a 5-deg drooped inlet. A comparison of the computed results and test data is shown in Figure 19. The test data were acquired on a swept strut-mounted flow-through nacelle. The inlet mass flow ratio for the test was calibrated in a model altitude test chamber. The test data were taken on the keel line, the right and left sides, and at about 30-deg right and left off the crown line along the side of the mounting pylon. The computations were done for the test Mach number, angle of attack, and inlet mass flow ratio. The discrepancy near the crown line can be attributed to a lack of modeling the mounting strut that was not included in this particular calculation. Note the variation of suction peak and shock strength around the circumference of the nacelle. The lack of perfect agreement with the suction peak around the circumference of the inlet might be attributed to a slight mismatch with the actual test angle of attack and mass flow, and to the geometric tolerances between the geometry tested and that used in the analysis. Note that the test data do not show perfect left/right symmetry. However, the overall agreement is good.

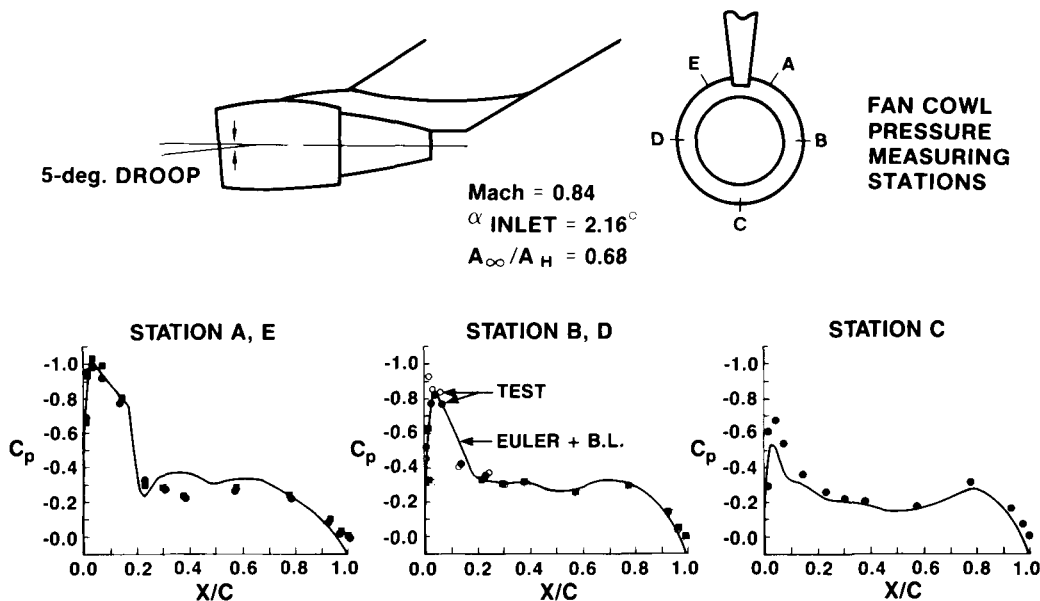


Figure 19. Fan Cowl Pressures on Nacelle at Angle of Attack.

A588 has demonstrated the ability to accurately predict nacelle drag, where drag is defined from the aerodynamicists view as the external fan cowl drag. The internal drag is accounted for by the propulsion engineer in the engine thrust-drag bookkeeping. For wind tunnel testing, the internal drag is determined in a model altitude test chamber. A comparison of A588 results (plus a handbook profile drag estimate for the mounting strut) with experimental data is shown in Figure 20. Note the excellent agreement for both drag level and drag rise. These types of comparisons have been made for a variety of nacelles. As long as the flow remains attached in the computational analysis, then usually any disagreement between test and A588 indicates a problem with the test data.

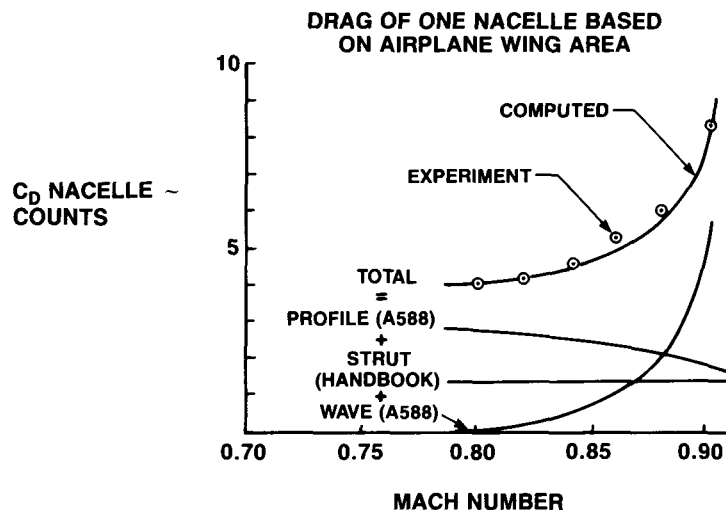


Figure 20. Fan Cowl Drag Rise—Comparison With Experiment.

Other useful production analysis codes include: P318, an axisymmetric full-potential code with boundary layer (ref 18); P467 axisymmetric geometry, three-dimensional full potential with the same three-dimensional boundary layer code used in A488; and P582, a three-dimensional full-potential cartesian grid code that can handle completely general geometries (ref 19). P318 is used because of its low cost to develop the initial lines of a nacelle, treating the crown, keel, and sides as separate geometry. The more complete A588 is then used to refine and validate the design. P582 has been used to analyze difficult geometries such as a tractor turboprop with an offset chin inlet (ref 20).

#### EXPERT USER TOOLS

Expert user tools or codes either have not yet matured enough in their development, or require skills generally not available outside the research environment for successful use. This category includes a series of codes based on the Euler formulation, specifically Jameson's FLO57 technology. The Euler formulation is of particular interest when dealing with rotational flows, i.e., flows of varying total temperature, total pressure, and swirl, and with flows in which trailing wakes from one surface may interact with another surface. These codes have been extended to handle complex transport type airplane configurations, illustrated in Figures 21 and 22, featuring wing, body, vertical, and horizontal tails, body-mounted engine nacelle and pylon, and propfan simulator disk, or wing mounted nacelle tractor propfans (refs 21 to 25). The complexity of the grid generation for these configurations currently precludes routine "production" use of this capability by users outside the research community. Another use of these Euler based codes has been in the analysis of a detailed propfan nacelle including pylon and simulator disk, illustrated in Figure 23, and engine exhaust flows (refs 26 and 27).

ORIGINAL PAGE IS  
OF POOR QUALITY

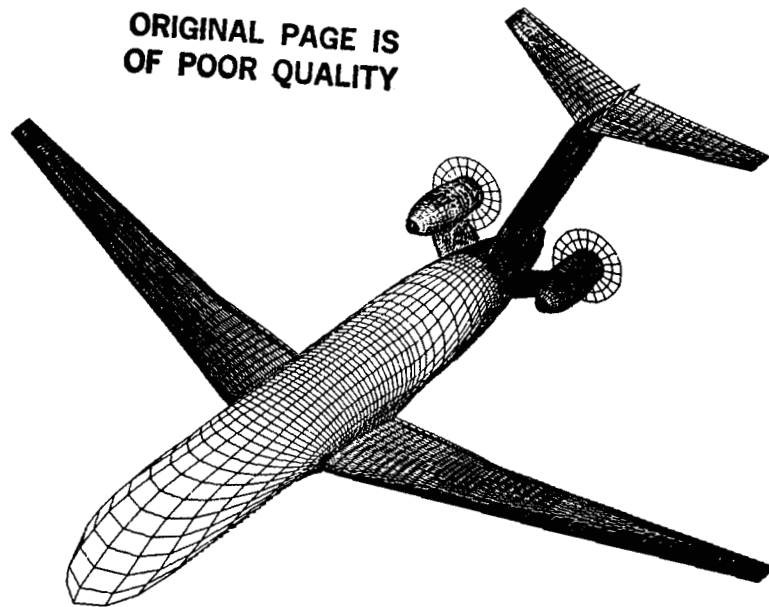


Figure 21. Surface Grid on Advanced Propfan Transport.

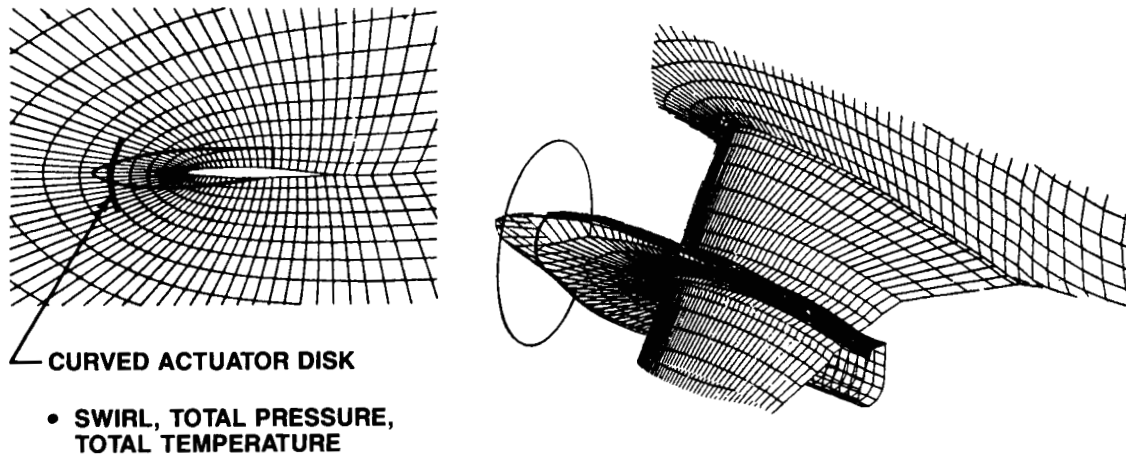


Figure 22. Grid for Wing-Mounted Tractor Propfan.



ORIGINAL PAGE IS  
OF POOR QUALITY

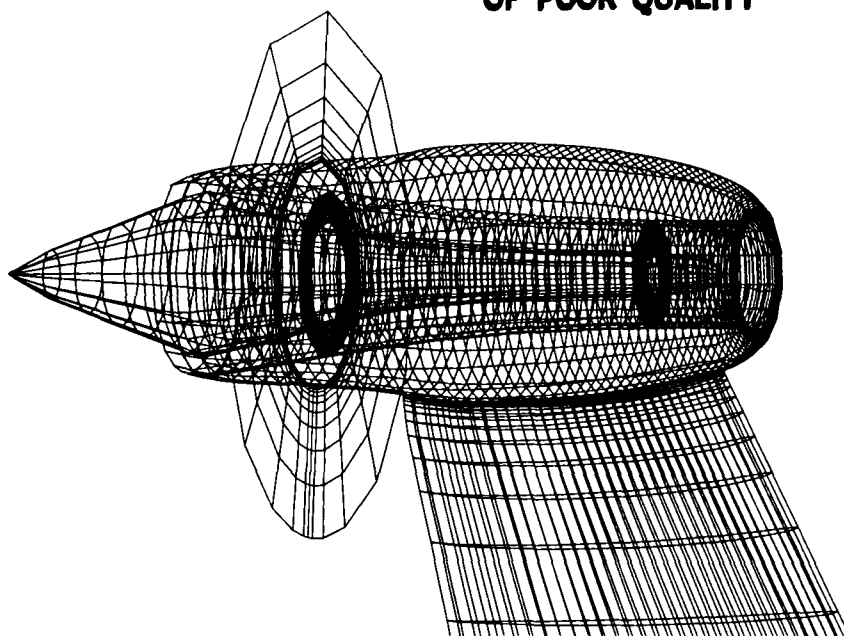


Figure 23. Grid for UDF Nacelle and Strut.

The basic solution technology for the unsteady Euler equations originated from Jameson's finite volume approach (FLO57) (ref 17) used in A588. In order to deal with much larger problems and more complex flows associated with complex aircraft configurations, considerable enhancements and improvements have been made to the basic technology which include; four- or five-stage Runge-Kutta time integration, a new dissipation model based on spectral radius scaling, a multigrid technique together with successive mesh refinement to speed up the convergence, and a multiblock treatment. The basic idea of the multiblock approach is to divide the complete flowfield into several blocks, such that the flowfield data within each block can fit in the existing central memory of a supercomputer. The complete flowfield data are stored on a solid state disk (SSD), and the computation is done in a block-by-block manner through the use of highly efficient input/output (I/O) data management. The flowfield in each block is advanced in time through one multigrid cycle. Within each grid level, a four or five-stage, explicit, Runge-Kutta time integration scheme, together with an implicit smoothing method, is used to update the flow variables to a new time level. The updated flowfield data are then moved to the SSD before another block of flowfield data is transferred to the central memory. The blocks of boundary data that are needed for the adjacent blocks in the flux and dissipation term calculations are saved in different locations on the SSD, so that they can be fetched during the calculation process. At the present time, the program is written such that the flowfield can be divided into an arbitrary number of blocks in both normal and spanwise directions to handle large problems. However, the general strategy is to keep the number of blocks to a minimum, for efficient vector processing. A solution for a wing-body-tail configuration (ref 23) is shown in Figures 24 and 25. The multiblock approach allows sufficient grid density to adequately capture the complex shock pattern on the wing, and the detailed interaction between the vertical and horizontal tail surfaces on the aftbody as indicated by the pressure contours shown in Figure 24. A comparison of the inviscid solution with experimental data shown in Figure 25, shows reasonable agreement.

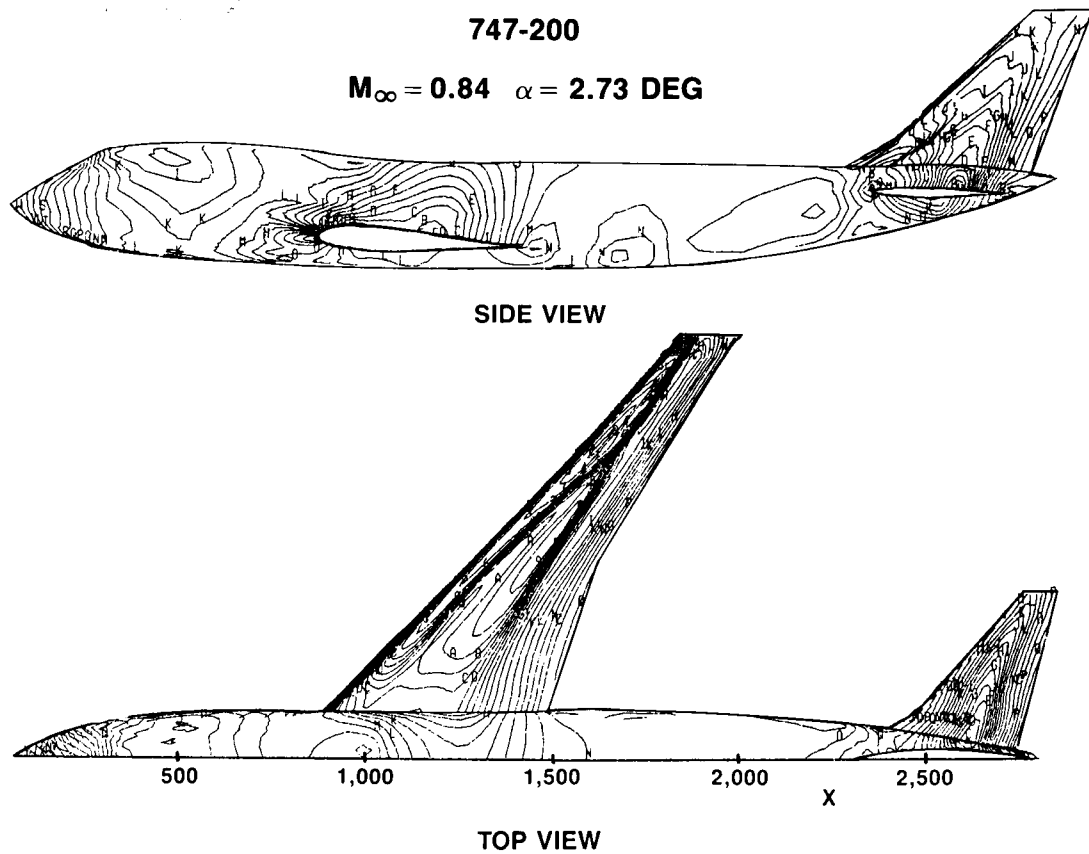


Figure 24. Surface Isobars for A 747-200 Configuration.

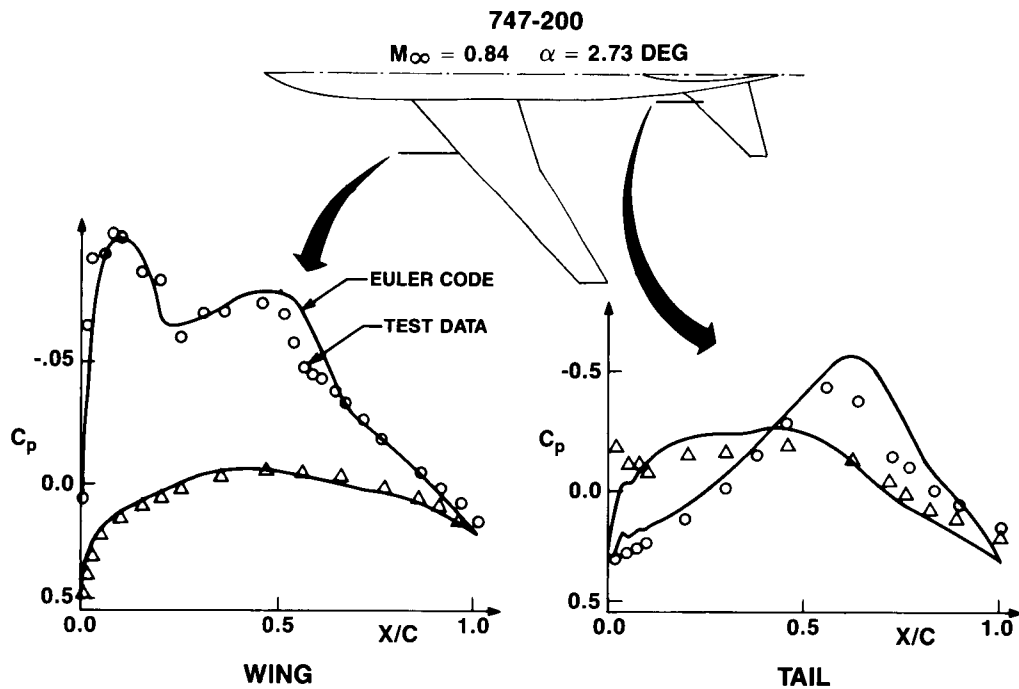


Figure 25. Comparison With Wing and Tail Pressure Distributions.

For a configuration with a propfan actuator disk, the program logic is greatly simplified if the propfan region including the propeller disk is kept in one block, such that the various boundary conditions on the propeller disk and exhaust plume can be implemented within a specified block. The propeller power loading is simulated by an actuator disk where the total pressure, total temperature, and swirl distributions are prescribed (ref 21). Another way of simulating propeller power effects is to prescribe the thrust, normal force, and sideforce in the propeller disk plane. The flow variables downstream of the disk are related to their corresponding upstream values through the use of continuity, momentum, and energy equations. The major advantages of this method are that the effects of angle of attack as well as the influence of side flow can easily be simulated through the input of normal and side force distributions along the propeller disk (ref 26).

A major application of this technology has been to the analysis of an advanced propfan powered aircraft, previously shown in Figure 21. A primary concern for a configuration with aft-mounted propfan engines is the power-induced interference effects on the aircraft's aerodynamics. While many of these characteristics can be investigated in the wind tunnel with powered propfan simulators, some conditions cannot. Small and powerful enough propfan simulators for testing at transonic conditions on a full model in yaw were not available to us at the time of this analysis. The asymmetric effects of a failed engine at cruise could only be investigated by computational methods. (This may still be the case today.) A full configuration analysis at both high and low speeds, and at yaw with various combinations of thrust on the right and left side engines was carried out to look at these issues. A grid of approximately 600,000 cells was used (ref 24). The CPU time on a CRAY X-MP for a solution was approximately two hours. The power induced effects at high speed on the pressure distributions on the vertical and horizontal tail surfaces are illustrated in Figures 26 and 27. For a low-speed, high-angle-of-attack case, the resulting moments and side force are shown in Figure 28. This type of information is very important to the stability and control engineer in estimating the handling characteristics of the aircraft.

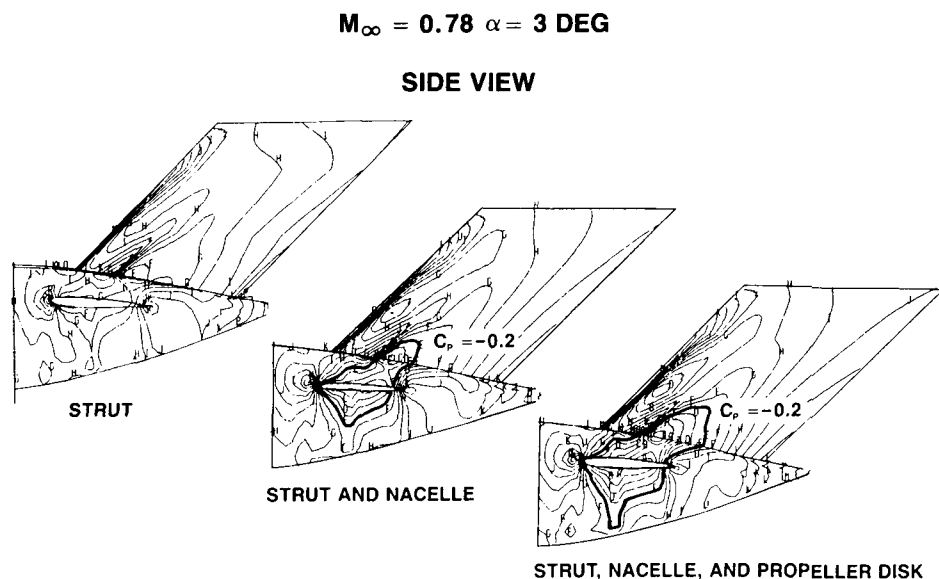


Figure 26. Effects of Propeller Power on Aftbody Isobars—Side View.

$$M_{\infty} = 0.78 \quad \alpha = 3 \text{ DEG}$$

TOP VIEW

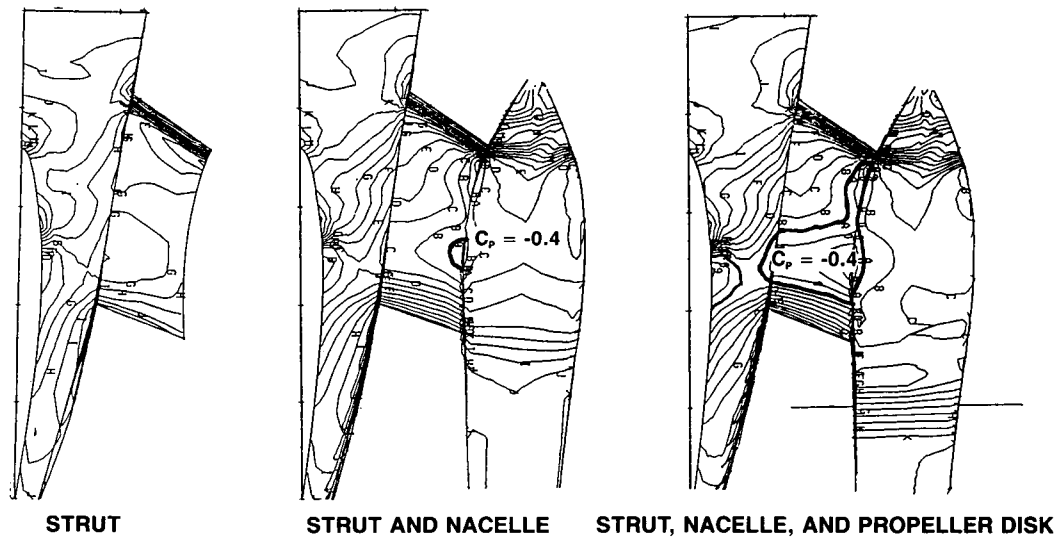


Figure 27. Effects of Propeller Power on Aftbody Isobars—Top View.

$$M_{\infty} = 0.3, \quad \alpha = 12.5 \text{ deg}, \quad \beta_{\text{yaw}} = 0 \text{ deg}$$

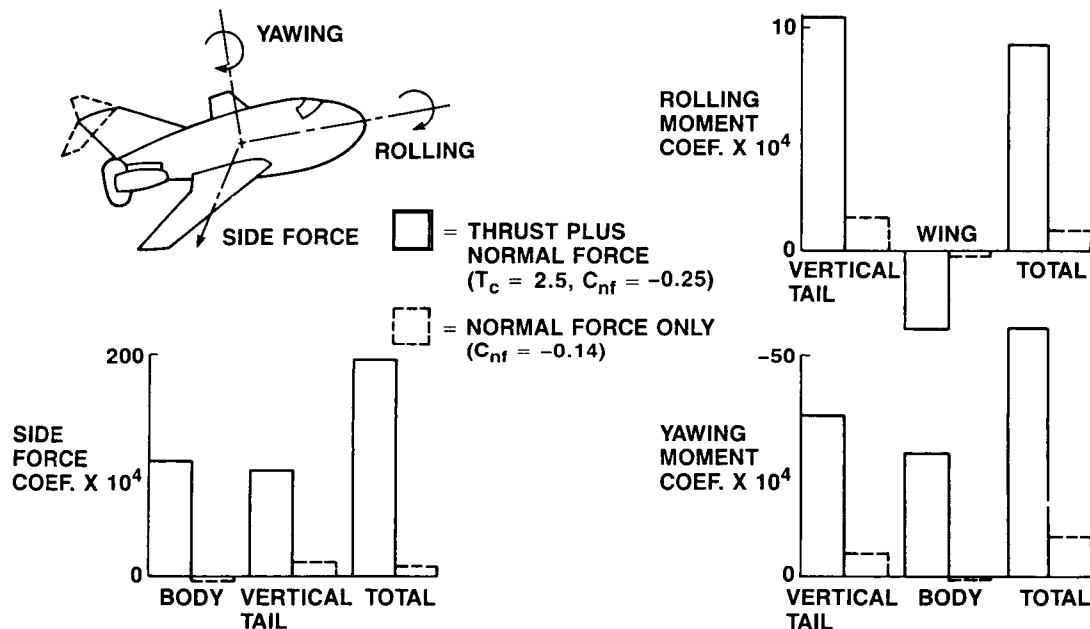


Figure 28. Effects of Asymmetric Thrust on Aircraft.

The Euler solver has also been incorporated into the boundary layer cycling package used in the A488 system previously described. In this implementation the boundary layer coupling can be applied to both wing and tail lifting surfaces. To improve the viscous coupling a contracting wake model has been added to the Euler solver (ref 25). This analysis package is being refined to include coupled solutions on full and partial chord winglet configurations.

The natural manner in which propulsion effects can be handled in the Euler formulation **makes this the** technology of choice for many problems. However, the level of expertise required to create the necessary surface-fitted grids will limit its use to a select few for the time being.

### EMERGING TOOLS

Two essential characteristics of a valuable CFD tool are timeliness and the ability to handle complex "real world" geometry. Requirements for CFD analysis extend far beyond the analysis of simple wing-body configurations. The multiblock Euler approach shows a promising capability to analyze rather complex geometries, but it is questionable whether the necessary surface-fitted grid generation could be done in a timely fashion. As finer details of the geometry become of interest, the grid generation problems become more difficult. Work on unstructured grids (refs 28 and 29) may offer a solution to dealing with complex geometries. For now, the structured surface-fitted grid Euler tools will continue to be special purpose tools used by expert users. But what about a "production" tool for timely analysis of transonic flows about complex geometries for use by CFDers outside the research community? Such a tool is emerging; it is called TRANAIR.

TRANAIR (refs 30 and 31) employs a new approach for solving the full-potential equation about arbitrary configurations. One of the most important features of this approach is its compatibility, in terms of user-provided inputs regarding the configuration boundary, with the existing A502/PANAIR panel method. More than two dozen CFDers throughout the Boeing Company are familiar with setting up inputs (panel models) for A502/PANAIR. There is already an extensive array of geometry tools, i.e., AGPS (ref 1), available for creating the necessary panel models, and there are no inherent limitations on the complexity of geometry that can be described. The inputs for analysis of complex configurations with geometric details of greatly varying length scales can be prepared in a timely manner. This is in sharp contrast to codes that use structured surface-fitted grids.

TRANAIR eliminates the need for the surface-fitted grid by using rectangular grids superimposed on the paneled boundary configuration, as illustrated in Figure 29. The flow both inside and outside the configuration is considered (although in aerodynamic applications, the internal flow is fictitious). A rectangular grid

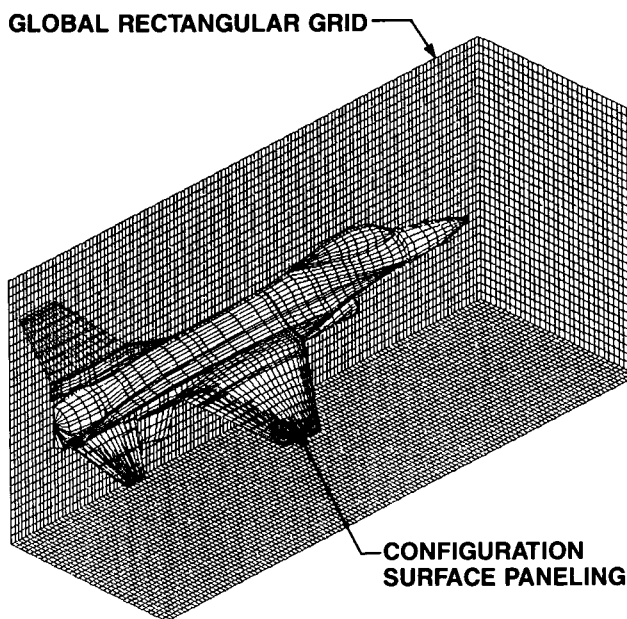


Figure 29. TRANAIR Grid Topology.

can always be superimposed on the configuration regardless of surface topology. The use of rectangular grids is not new. Rectangular grids have previously been used in small disturbance codes with linearized boundary conditions, and by Reyhner (ref 19), and others with "thick" geometries. What sets TRANAIR apart from previous codes is the use of finite element techniques to ensure that the discretization of the flowfield near the boundaries is flux conservative so that the conservation laws are imposed correctly and the global quantities of interest are predicted accurately, and now, the inclusion of automatic grid refinement near surface boundaries keyed to local panel density. The rectangular grid needs only to extend as far as the nonlinearities in the flowfield. The far field is handled by a discretized linear Prandtl-Glauert operator. The solution algorithm includes use of a Newton solver (nonlinear GMRES, ref 10) that uses the latest sparse matrix technology as a preconditioner. Future plans include the addition of hierarchical multigrid preconditioning.

The initial implementation of TRANAIR did not include the automatic grid refinement. Nevertheless, the computational results were very encouraging. The initial version of TRANAIR is well suited for compact objects such as fuselage forebody cabs, nacelles, etc. Figure 30 shows the paneling for a modern transport cab. The paneling is fine enough to resolve the crease line at the base of the windshield. A comparison of computed results from TRANAIR, A502/PANAIR, and experimental results is also shown in Figure 30. The TRANAIR results are in excellent agreement with the experimental data. As is typical of linear compressible flow theory, the A502/PANAIR results overpredict both the compression at the base of the windshield and the subsequent expansion.

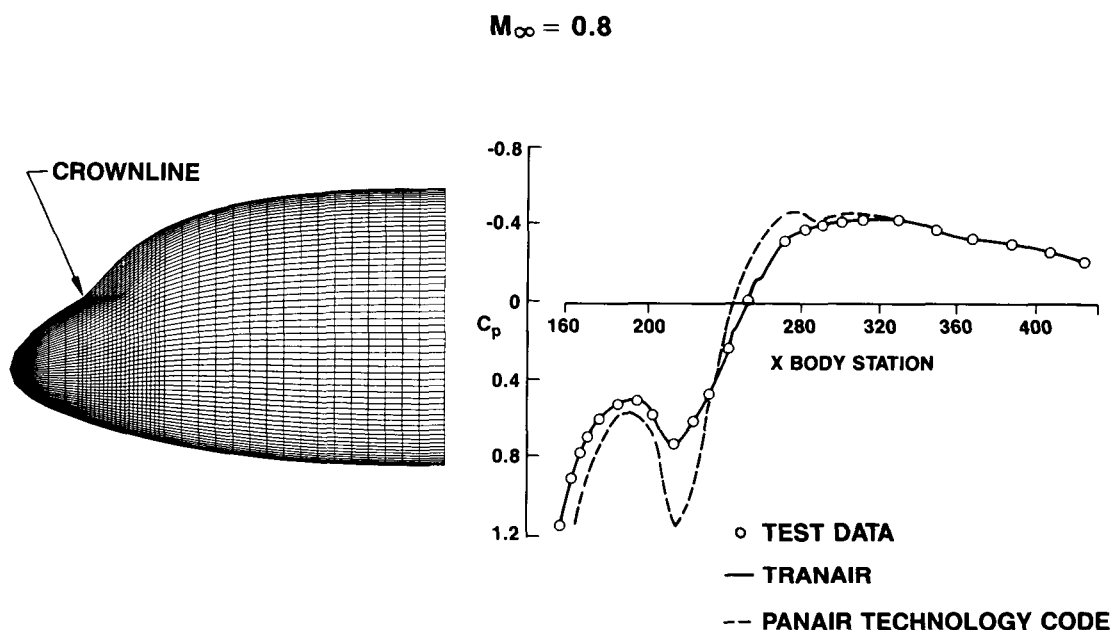


Figure 30. Transport Cab Analysis Test Theory Comparison.

A considerably more complex configuration that was analyzed with the initial TRANAIR was an F-16 fighter aircraft, shown in Figure 31. The configuration included the fuselage, canopy, wing, vertical and horizontal tail surfaces, and details of the inlet and exhaust regions. A total of 3000 panels were used to describe the surface geometry. A rectangular grid of 129 grid points in the x direction, 33 in the y direction, and 33 in the z direction was superimposed on the paneled configuration. The configuration was analyzed at both  $M = 0.6$  and  $0.9$ . In the subcritical solution, the residual error was reduced by 10 orders of magnitude in approximately 1350 CPU seconds on a CRAY X-MP. A comparison of the results for the Mach 0.6 case (not shown) with A502/PANAIR and experimental data on the wing showed excellent agreement except at the leading edge. For the supercritical Mach 0.9 case, the solution took 1500 CPU seconds to reduce the residual error by four orders of magnitude.

ORIGINAL PAGE IS  
OF POOR QUALITY

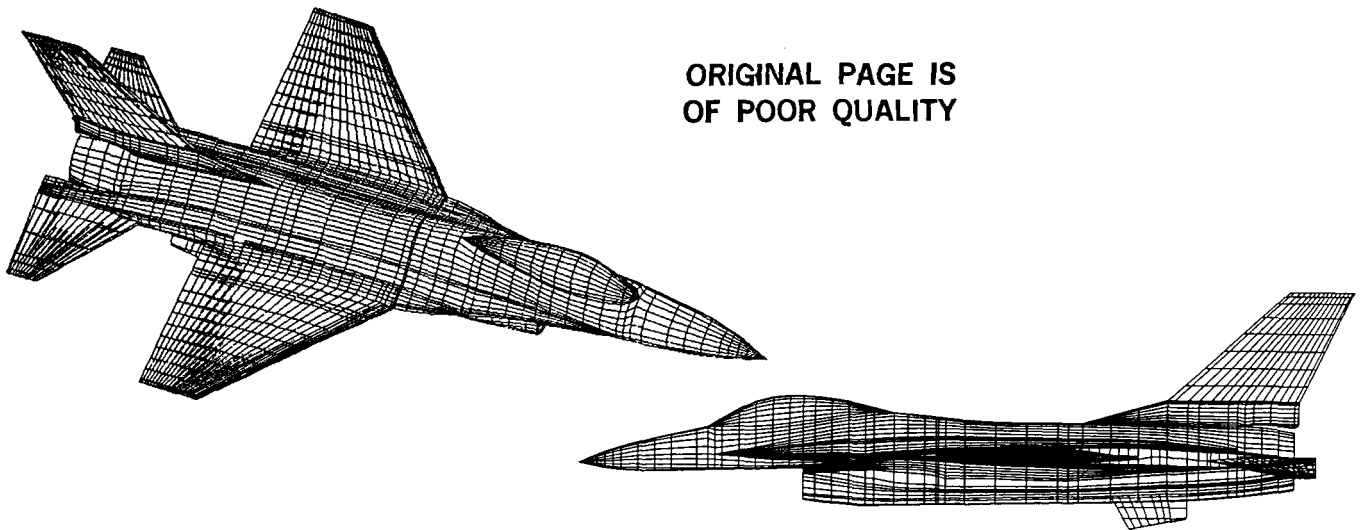


Figure 31. Surface Paneling for F-16 Fighter Aircraft.

A comparison of TRANAIR results for the Mach 0.90 analysis of the F-16 configuration with experimental data on the wing is shown in Figure 32. The agreement with experimental data is quite good except at the leading edge. The shock is well captured, albeit further aft than indicated by the experimental data. This is to be expected for an inviscid solution without viscous coupling. The discrepancy at the leading edge is easily understood when the coarseness of the global grid is taken into account (fig 33). The automatic grid refinement completely eliminates this shortcoming. Figure 34 shows the resulting grid after four levels of refinement. Note that the refinement takes place in three dimensional space. Each rectangular grid cell is divided into eight similar cells at each level of refinement. Figure 35 illustrates how the grid refinement ensures the resolution of detailed surface features. The user can specify the regions of space for refinement and the number of levels of refinement. The use of the automatic grid refinement allows use of a much sparser global grid with grid enrichment only where it is needed. As a consequence, the total number of grid cells can be kept to a reasonable number. At this time (December 1987) solutions for the F-16 with the grid refinement were not yet available. Additional TRANAIR F-16 results from the initial version without grid refinement can be found in reference 32.

$$M_{\infty} = 0.9 \quad \alpha = 4 \text{ DEG}$$

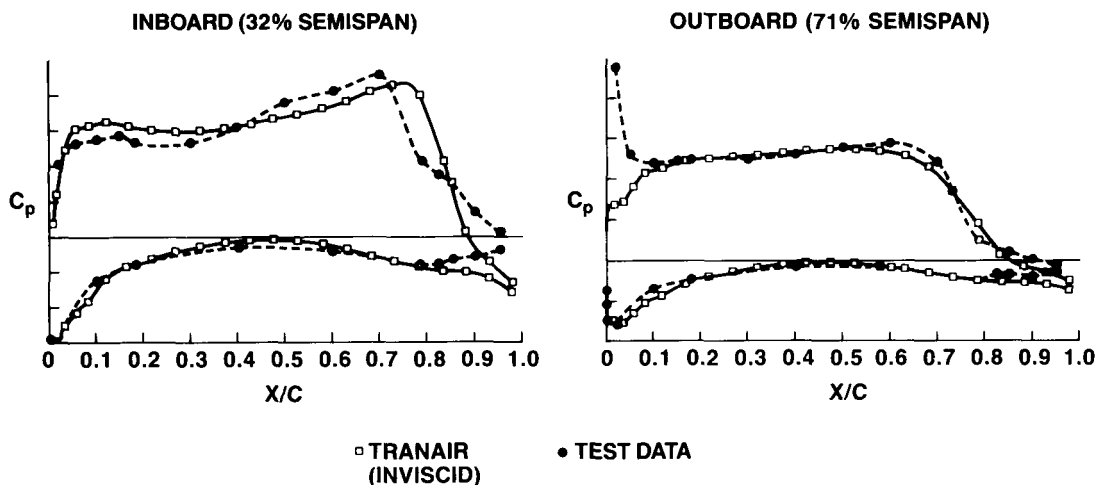


Figure 32. Comparison of Wing Surface Pressures on F-16 Configuration.

ORIGINAL PAGE IS  
OF POOR QUALITY

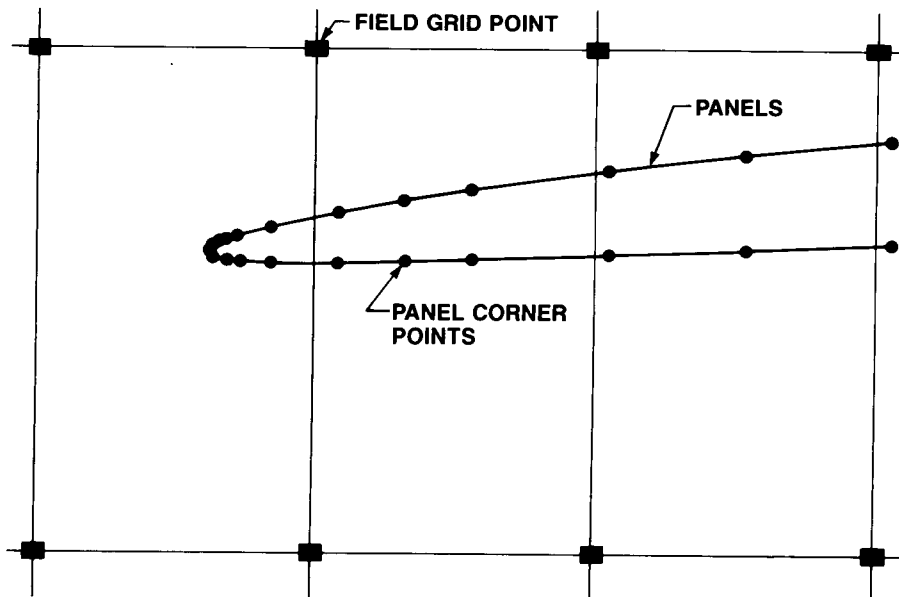


Figure 33. Relative Sizes of the Grid Cells and Surface Panels.

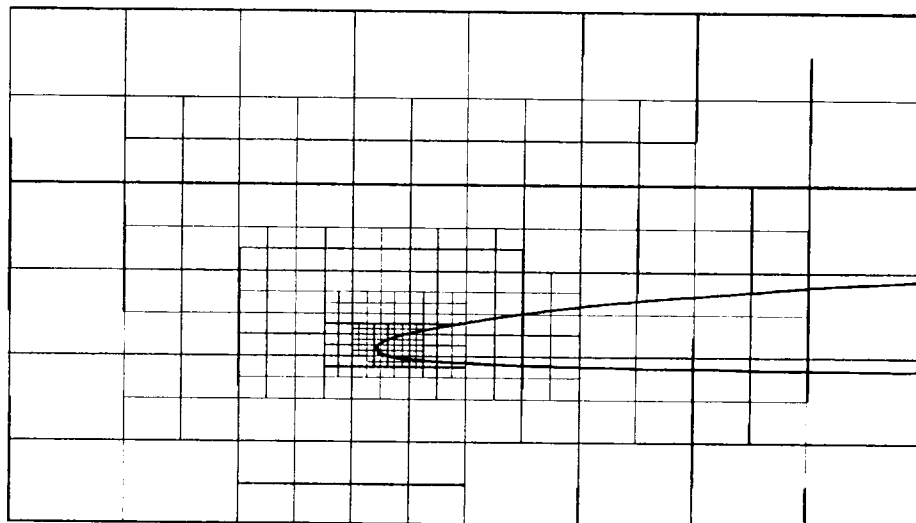


Figure 34. TRANAIR Automatic Grid Refinement Along Wing Leading Edge.

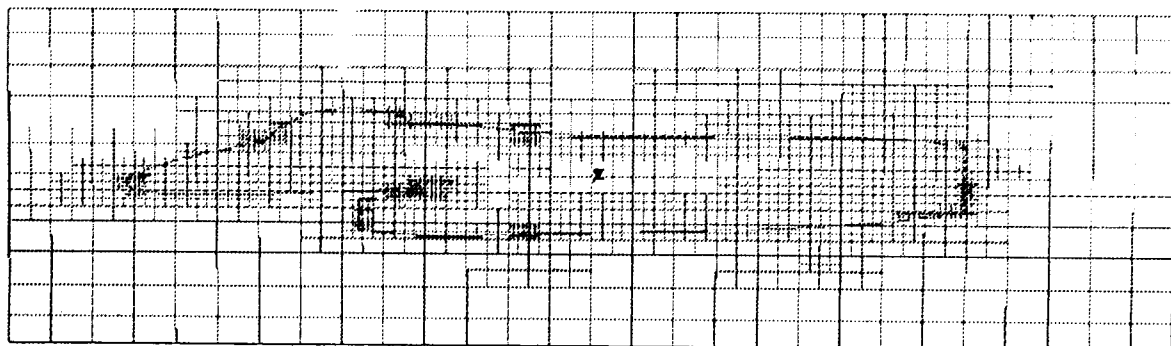


Figure 35. TRANAIR Automatic Grid Refinement on Fuselage—BBL = 20.



TRANAIR with grid refinement is scheduled to become available as a "production" code in 1988. Early indications are that subcritical TRANAIR solutions will be considerably cheaper than A502/PANAIR solutions for large cases, so we may see TRANAIR replacing that code. It is expected that automatic flowfield adaptive grid refinement will also become available in 1988 that will be very beneficial for supersonic solutions. Other anticipated improvements include a continued refinement of the algorithm to improve convergence rate, incorporation of the Hafez correction (ref 33) at the shock, possible wake capturing, and investigation of extending the method to the Euler equations. Plans are also being considered to incorporate some kind of viscous coupling similar to what is currently found in the A488 system and extending the code to the supersonic regime.

## FUTURE CHALLENGES

One of the hottest CFD research fields today is in Navier-Stokes solvers. Many problems, particularly very high speed flows, and flows with significant separation, require the physical representation of the Navier-Stokes equations. But where should Navier-Stokes fit in for transonic analysis of transport type configurations? Limited use of Navier-Stokes has been made in a zonal approach to deal with jet exhaust interactions (refs 7 and 34), and with open cavities (ref 35). More recently, significant progress has been made by others in the application of Navier-Stokes to complete transport wing-body type configurations (refs 36 and 37), and to a fighter type configuration (ref 38). However, in industry, one does not replace a proven tool by a more expensive higher technology tool unless it offers a clear benefit.

The Navier-Stokes applications shown to date are at least one or two orders of magnitude more expensive than the inviscid/coupled viscous A488 solutions. For attached flow conditions we have yet to see evidence that the current Navier-Stokes solutions are more accurate. In fact, the A488 solutions may be the more accurate because of the significantly higher grid density used by the finite difference three-dimensional boundary layer solver, and empirical modeling of the shock-boundary layer interaction zone. When the Navier-Stokes solvers exceed the accuracy of the coupled A488 system there will still be the question of cost. As previously mentioned, A488 sees very heavy usage. During the last few years the number of A488 accesses throughout the Boeing Company have averaged over 2000 times a year. This number includes runs that failed, restarts for additional iterations, and just grid generation runs. That still leaves on the order of a 1000 complete analysis runs a year. An order of magnitude cost increase for this volume of analysis is not tolerable. In some wing design exercises, a very short time span is available for designing a wing for a wind tunnel entry. During these periods, quick turnaround is needed which is not practical with methods taking hours of CPU time.

At flight conditions resulting in some flow separation, the coupled inviscid/coupled viscous boundary layer codes will generally fail to converge to a useful solution. For these conditions Navier-Stokes may be able to provide flow information not accessible by lesser methods. However, experience has shown that the off-design handling characteristics of most interest are quite sensitive to the exact details of the flow separation phenomena. Details such as laminar to turbulent boundary layer transition location, and the effects of vortex generators, leading-edge snags, wing fences, vortilons, etc., can have very dramatic effects on the pitchup characteristics of an aircraft. When will Navier-Stokes solvers be able to account for these types of details?

The preceding discussion is not meant to discourage the researchers developing Navier-Stokes technology, but rather to point out some of the "real world" challenges that must be overcome for these methods to be used on a routine basis in industry. Many of the concerns related to determining off-design handling qualities are also present in low Reynolds wind tunnel testing and can only be fully addressed in flight at the present time. We will maintain an active vigilance on the progress being made in Navier-Stokes technology and will try to incorporate the appropriate methods into our CFD toolbox at the proper time.

## CONCLUDING REMARKS

We have presented our current toolbox of CFD methods for three-dimensional transonic design and analysis and have illustrated their use through various applications. Production, expert user, and new emerg-

ing methods are all necessary parts of the toolbox. Just as a mechanic cannot work with a single wrench, we too need a mix of general purpose and special use tools. The competitive nature of the market place is forcing the Boeing Company to strive to a higher plane of excellence while reducing cost. In the aerodynamic design arena we are depending on CFD to provide the necessary leverage. However, to be of value CFD must be useful in a timely manner.

In early 1987, a critical wing design activity within Boeing reached an impasse with regard to satisfying airplane performance requirements, wing structural requirements, and other practicalities necessary for a successful overall design. It was determined that an improvement in the transonic technology level of the wing could be used to satisfy all the necessary requirements. But in order to implement a new level of wing technology consistent with a tight program schedule, new designs would have to be assessed in the remainder of 1987 using available wind tunnel test windows. Two-dimensional analysis and design tools (refs 39 and 40) were used to develop a series of airfoils to investigate different pressure distributions consistent with a more aggressive design philosophy. After a confirming wind tunnel test, three wings for a wing-body configuration employing variations of the most promising design pressure distribution were designed using A488 and A555 in a time period of a little over a month. Each design, maintaining realistic structural and manufacturing constraints, required many cycles through A488 and A555, sometimes two or three cycles in a single day, to develop. These wings were a break from the previous evolution of Boeing designs, although similar designs had been tested in the early 1970s without much success.

The confirming wind tunnel test, conducted in the fall of 1987, included the three new wings and a previously designed baseline wing. The A488 analysis had predicted how the four wings would rank with respect to each other at the design cruise point. The wind tunnel test results confirmed the A488 predictions. The new wings were approximately 10% thicker than the baseline wing, but delivered the same drag level and drag divergence Mach capability. There were differences in details that the codes were not able to predict, so further refinement of the computational methods is still desirable. The wind tunnel was, of course, able to give information over a wider range of conditions than CFD. This endeavor was a success and was carried out in a very short period of time because of the skill of the responsible project engineers, and because the necessary tools were in place. No new code development or validation was necessary. However, several desirable enhancements to A488 and A555 were identified from the experience. They are being incorporated into the codes to further improve their usability and accuracy.

CFD is an integral part of the aerodynamic design process at Boeing. Together with the wind tunnel, designs are now being developed in a timely manner that was not previously possible. That is the role of CFD in industry.

#### ACKNOWLEDGMENTS

This paper is based in part on work conducted for the Boeing Independent Research and Development Program. The author would like to thank Dr. Allen W. Chen for his contributions to many of the examples shown. Thanks also goes to Drs. N. J. Yu and H. C. Chen for their Euler work contributions, Drs. F. T. Johnson, S. S. Sammant, and J. E. Bussoletti for their TRANAIR contributions, and to the various project engineers responsible for some of the examples presented.

#### REFERENCES

1. Snepp, D. K. and Pomeroy, R. C., "A Geometry System for Aerodynamic Design," AIAA Paper 87-2902, September 1987.
2. Moran, J., Tinoco, E. N., and Johnson, F. T., "User's Manual—Subsonic/Supersonic Advanced Panel Pilot Code," NASA CR-152047, 1978.
3. Derbyshire, T. and Sidwell, K. W., "PAN AIR Summary Document, (Version 1.0)," NASA CR-3250, 1982.

4. daCosta, A. L., "Application of Computational Aerodynamics Methods to the Design and Analysis of Transport Aircraft," ICAS Paper 78.B2-01, September 1978.
5. Yu, N. J., "Grid Generation and Transonic Flow Calculations for Three-Dimensional Configurations," AIAA Paper 80-1391, July 1981.
6. Yu, N. J., "Transonic Flow Simulations for Complex Configurations with Surface Fitted Grids," AIAA-81-1258, June 1981.
7. Tinoco, E. N. and Chen, A. W., "CFD Applications to Engine/Airframe Integration," Numerical Methods for Engine-Airframe Integration, Vol. 102 of Progress in Astronautics and Aeronautics, AIAA, 1986.
8. Caughey, D. A. and Jameson, A., "Recent Progress in Finite Volume Calculations for Wing-Fuselage Combinations," AIAA Paper 79-1513, 1979.
9. Yu, N. J. and Rubbert, P. E., "Acceleration Schemes for Transonic Potential Flow Calculations," AIAA Paper 80-0338, January 1980.
10. Wigton, L. B., Yu, N. J., and Young, D. P., "GMRES Acceleration of Computational Fluid Dynamics Codes," AIAA Paper 85-1494, June 1985.
11. McLean, J. D. and Randall, J. L., "Computer Program to Calculate Three-Dimensional Boundary Layer Flows over Wings with Wall Mass Transfer," NASA CR-3123, 1978.
12. McLean, J. D. and Matoi, T. K., "Shock/Boundary-Layer Interaction Model for Three-Dimensional Transonic Flow Calculations," Turbulent Shear Layer/Shock Wave Interactions IUTAM Symposium Palaiseau 1985, Springer, Berlin Heidelberg 1986.
13. Rozendaal, R. A., "Variable Sweep Transition Flight Experiment (VSTFE)-Parametric Pressure Distribution Boundary Layer Stability Study and Wing Glove Design Task," NASA CR-3992, June 1986.
14. Squire, H. B. and Young, A. D., "The Calculation of the Profile Drag of Aerofoils," Aeronautical Research Committee, Reports and Memoranda No. 1838, London, November 1937.
15. Boppe, C. W., "Aerodynamic Analysis for Aircraft with Nacelles, Pylons, and Winglets at Transonic Speeds," NASA CR-4066, April 1987.
16. Chen, H. C., Yu, N. J., Rubbert, P. E., and Jameson, A., "Flow Simulations for General Nacelle Configurations Using Euler Equations," AIAA Paper 83-0539, 1983.
17. Jameson, A., Schmidt, W., and Turkel, E., "Numerical Solutions of the Euler Equations by Finite Volume Methods Using Runge-Kutta Time-Stepping Schemes," AIAA Paper 81-1259, 1981.
18. Colehour, J. L., "Transonic Flow Analysis Using a Streamline Coordinate Transformation Procedure," AIAA Paper 73-0657, July 1973.
19. Reyhner, T. A., "Three-Dimensional Transonic Potential Flow About Complex Three-Dimensional Configurations," NASA CR-3814, July 1984.
20. Sokhey, J. S., "Three-Dimensional Transonic Flow Analysis of Turboprop Inlet and Nacelle Configurations," AIAA Paper 84-0193, January 1984.
21. Yu, N. J., Samant, S. S., and Rubbert, P. E., "Flow Predictions for Propfan Configurations Using Euler Equations," AIAA Paper 84-1645, June 1984.
22. Samant, S. S., and Yu, N. J., "Flow Prediction for Propfan Engine Installation Effects on Transport Aircraft at Transonic Speeds," NASA CR-3954, January 1986.

23. Yu, N. J., Kusunose, K., Chen, H. C., and Summerfield, D. M., "Flow Simulations for a Complex Airplane Configuration Using Euler Equations," AIAA Paper 87-0454, January 1987.
24. Kusunose, K., Marcum, D. L., Chen, H. C., and Yu, N. J., "Transonic Analysis for Complex Airplane Configurations," AIAA Paper 87-1196, June 1987.
25. Chen, H. C., Yu, N. J., Marcum, D. L., Kao, T. J., and Kusunose, K., "Coupled Euler/Boundary Layer Analysis of a Complete Aircraft with Viscous Modeling on the Lifting Surface," AIAA Paper 87-2614-CP, August 1987.
26. Yu, N. J., and H. C. Chen, "Flow Simulations for Nacelle-Propeller Configurations Using Euler Equations," AIAA Paper 84-2143, August 1984.
27. Chen, H. C., Kusunose, K., and Yu, N. J., "Flow Simulations for Detailed Nacelle-Exhaust Flow Using Euler Equations," AIAA Paper 85-5003, October 1985.
28. Jameson, A. and Baker, T. J., "Improvements to the Aircraft Euler Method," AIAA Paper 87-0452, January 1987.
29. Lohner, R., Morgan, K., and Peraire, J., "Improved Adaptive Refinement Strategies for the Finite Element Aerodynamic Configurations," AIAA Paper 86-0499, January 1986.
30. Rubbert, P. E., Bussoletti, J. E., Johnson, F. T., Sidwell, K. W., Rowe, W. S., Samant, S. S., SenGupta, G., Weatherill, W. H., Burkhart, R. H., Everson, B. L., Young, D. P., and Woo, A. C., "A New Approach to the Solution of the Boundary Value Problem Involving Complex Configurations," Symposium on Future Directions in Computational Mechanics, Anaheim, California, December 1986.
31. Samant, S. S., Bussoletti, J. E., Johnson, F. T., Burkhart, R. H., Everson, B. L., Melvin, R. G., and Young, D. P., "TRANAIR: A Computer Code for Transonic Analyses of Arbitrary Configurations," AIAA Paper 87-0034, January 1987.
32. Erickson, L. L., Madson, M. D., and Woo, A. C., "Application of the TRANAIR Full Potential Code to Complete Configurations," ICAS-86-1.3.5, 1986.
33. Hafez, M. M., Murman, E. M., and South, J. C., "Artificial Compressibility Methods for Numerical Solution of Transonic Full Potential Equations," AIAA Paper 78-1148, 1978.
34. Roberts, D. W., "Prediction of Subsonic Aircraft Flows with Jet Exhaust Interaction," Aerodynamics of Power Plant Installation, AGARD-CP-301, Paper 32, May 1981.
35. Om, D., "Navier-Stokes Simulation for Flow Past an Open Cavity," AIAA Paper 86-2638, October 1986.
36. Obayashi, S., Fujii, K., and Takanashi, S., "Toward the Navier-Stokes Analysis of Transport Aircraft Configurations," AIAA Paper 87-0428, January 1987.
37. Takanashi, S., Obayashi, S., Matsushima, K., and Fujii, K., "Numerical Simulation of Compressible Viscous Flows Around Practical Aircraft Configurations," AIAA Paper 87-2410CP, August 1987.
38. Flores, J., Reznick, S. G., Holst, T. L., and Gundy, K., "Navier-Stokes Solutions for a Fighter-Like Configuration," AIAA Paper 87-0032, January 1987.
39. Drela, M. and Giles, M. B., "Viscous-Inviscid Analysis of Transonic and Low Reynolds Number Airfoils," AIAA Paper 86-1786, June 1986.
40. Giles, M. B., and Drela, M., "A Two-Dimensional Transonic Aerodynamic Design Method," AIAA Paper 86-1793, June 1986.

THE APPLICATION OF CFD FOR MILITARY  
AIRCRAFT DESIGN AT TRANSONIC SPEEDS

C. W. Smith  
W. W. Braymen  
I. C. Bhateley  
W. K. Londenber  
General Dynamics  
Forth Worth Division  
Ft. Worth, TX

ABSTRACT

Numerous computational fluid dynamics (CFD) codes are available that solve any of several variations of the transonic flow equations from small disturbance to full Navier-Stokes. The design philosophy at General Dynamics Fort Worth Division involves use of all of these levels of codes, depending on the stage of configuration development. Throughout this process, drag calculation is a central issue.

This paper provides an overview of several transonic codes and presents representative test-to-theory comparisons for fighter-type configurations. Correlations are shown for lift, drag, pitching moment, and pressure distributions. The future of applied CFD is also discussed, including the important task of code validation. With the progress being made in code development and the continued evolution in computer hardware, we can look forward to routine application of these codes for increasingly more complex geometries and flow conditions.

INTRODUCTION

It seems ironic -- the transonic flow regime is the most difficult for the aerodynamicist to analyze, but is the part of the flight envelope most critical to design success of military aircraft and fighters in particular. Calculating transonic characteristics with regions of mixed subsonic and supersonic flows, embedded shocks, and viscous interactions becomes complex even for simple geometries. When these complexities are combined with the need to consider complete configurations with blended wing/bodies, multiple lifting surfaces of low-aspect ratio, moderate-to-high sweep, high taper, leading- and trailing-edge flaps, and external stores, not to mention propulsion-induced aerodynamic interactions, the problem becomes overwhelming. Nevertheless, significant advancements have been made in CFD during the past ten years. Numerous codes are now available that solve any of several variations of the transonic flow equations from small disturbance to full Navier-Stokes. Solutions for simple to quite complex shapes can be obtained for a wide range of geometries modeled by these codes. Obviously, the more complex the flow algorithm or geometry, the more intensive the computation and associated computer time.

Cost has dictated that practicality be an important consideration in the selection of design tools. Evidence of this is the fairly common preliminary design practice of employing linear theory or modified-linear theory at transonic speeds where linear theory is clearly not applicable. This points to the need for transonic codes to be computationally efficient for routine use. Otherwise, they can never be employed in a design optimization study such as that required for an aeroelastically tailored wing, a process that often requires iteration of several thousand geometry combinations.

#### CURRENT DESIGN PHILOSOPHY

New design configurations generally evolve over a considerable length of time and involve aerodynamic analyses at the conceptual, preliminary, and detailed design levels, as shown in Figure 1. Therefore, analysis tools selected at each design stage must be compatible with the required accuracy and fit within the available budget. Normally, wind tunnel testing is integrated into the design process at the preliminary design stage to validate the aerodynamic predictions and contribute to configuration refinement. As better analytical tools are developed for application at each design stage, the amount of wind tunnel testing should decrease or one should, at least, be able to gain greater refinement while holding wind tunnel costs constant. There is a combination of analytical accuracy, cost, time required, and amount of wind tunnel testing that yields the best results at the lowest overall cost. Therefore, we must know which methods are most appropriate at any one time for any given application.

Design of multirole military aircraft requires evaluation of diversified flight regimes to determine optimum wing geometry. Consequently, the aircraft designers do not have the luxury of concentrating on a particular design point. To initiate a design study at General Dynamics, Fort Worth Division, a generalized conceptual design synthesis procedure (CDSP) (Reference 1) is used to determine the wing planform shape and size that best meets the multipoint design requirements. Gross effects of complex geometry characteristics, such as scheduled leading- and trailing-edge flaps, are included in the methodology. Once the planform is selected, linear theory, combined with empirical adjustments, is used to conduct a parametric study of camber and twist (or center of pressure for supersonic optimum camber) at selected design points. Effects of scheduled leading- and trailing-edge flaps are included and aeroelastic effects can be accounted for, if desired. A target drag level is established as a measure of merit at each design point. A plot, such as that shown in Figure 2, is constructed to show which camber designs meet or exceed the target drag levels. Attention is also given to pressure distribution characteristics. At this point, one or more candidate designs are selected for further detailed study. Refinement may consist of CFD code analyses as well as wind tunnel tests. Parametric variations are often accomplished at this stage but are restricted to a well defined "design space." As the design becomes more refined, the analysis codes used should become progressively more accurate.

Drag calculation is a central issue in the design philosophy. Although target pressures are often used in the wing optimization process, the drag level produced is the final measure of success. Therefore, the discussion of codes in this paper includes test-to-theory comparisons of drag as well as pressures. Multiple design point requirements and complex geometries of

fighter aircraft necessitate continued acquisition of parametric wind tunnel data. For example, General Dynamics has recently conducted a series of planform trades (Figure 3) that incorporate fully scheduled leading- and trailing-edge flaps that can be trimmed to high angles of attack. These data are also useful for CFD calibration as codes mature in the transonic regime. Before a code can be used with confidence, it is important to accomplish test-to-theory comparisons to assess its accuracy and to assure that the code is being used correctly. Some of the test-to-theory comparisons that have been accomplished at General Dynamics are presented in this paper. An overview of the codes for which comparisons are shown is presented below and is followed by the test-to-theory results.

## AN OVERVIEW OF METHODS

Figure 4 summarizes several codes that are presently used to solve various forms of the flow equations; flow field characteristics handled by the codes are also shown. Results from several of the codes (shaded area in Figure 4) have been selected as representative of test-to-theory comparisons of fighter-type configurations. The codes selected are the US8 modified-linear theory code (Reference 2), WBPPW small disturbance code (Reference 3), TWING and TAWFIVE full-potential codes (References 4 and 5, respectively), and PARC2D and PARC3D Euler/Navier-Stokes codes (Reference 6).

### Modified-Linear Theory

The US8 wing design code, developed at General Dynamics Fort Worth Division, is used for parametric wing design studies. The code employs an aerodynamic load matrix generated by the Carmichael panel method (Reference 7). In the Carmichael code, an arbitrary configuration is represented by up to 500 distributed singularities that satisfy the linearized potential equation. Experience has shown that better results are generally obtained for fighter-type configurations by representing both the body and lifting surfaces as wing-type members. Pressure loads are computed in US8 using the aerodynamic matrix in combination with configuration geometry (planform description and mean-line slopes). Lift, drag, and pitching moment characteristics are developed from these pressure loads. Calculation of the drag polar depends upon first determining the lower and upper bounds of drag. The upper bound of drag corresponds to the condition of zero leading-edge suction and is determined by integrating the products of the local pressure loads and local mean-line slopes. The lower bound of drag corresponds to 100 percent leading-edge suction and is calculated with the Sivells-Neely method (Reference 8) as a function of the span-load distribution. The actual predicted polar is determined using an empirically derived value of partial leading-edge suction, which positions the polar relative to the upper and lower bounds of drag. The polar break is also predicted by monitoring the leading-edge pressure values, and the drag polar above this break is degraded because of leading-edge suction loss.

### Transonic Small Disturbance

WBPPW (Wing-Body-Pod-Pylon-Winglet) is used to solve a modified form of the small-disturbance equation by incorporating higher order terms to improve swept shock resolution and to provide improved approximation to the full potential equation at the critical velocity where the equation changes type

(elliptic to hyperbolic). The equation is solved in non-conservative form using an implicit finite-difference scheme. The code uses an internally developed rectangular Cartesian grid system. The configuration is placed within a crude grid with boundaries representing infinity and the symmetry plane. Fine grids are placed around each component; on these grids the detailed computations are performed. The crude grid provides a communication link between the individual fine grids. Viscous effects, including calculation of skin friction drag, can be included for lifting surfaces by using an option that couples a modified-Bradshaw boundary-layer technique (Reference 9) with the basic finite-difference scheme.

### Full Potential

The TWING code (Transonic WING) solves the transonic full-potential equation in conservation form for an isolated wing on a wall. TWING utilizes a fully implicit, approximate-factorization algorithm. Since the code is written for an isolated wing, a two-dimensional grid-generation scheme is used at each span station with linear interpolation used to extend the grid to three dimensions. Wing geometry is input by the specification of breakpoint locations that define changes in leading-edge sweep, trailing-edge sweep, twist angle, inboard and outboard edges of part-span flaps, and flap deflections. Viscous effects are not included in the code.

TAWFIVE (Transonic Analysis of a Wing and Fuselage with Interacted Viscous Effects) solves the full potential equation using a conservative, implicit, finite-volume technique. The program is a combination of the Caughey-Jameson FLO-30 code (Reference 10) and a fully three-dimensional, compressible, boundary-layer method (References 11 and 12). An internal grid generator produces a Joukowski-parabolic conformally mapped grid for a wing-body configuration. This grid is best suited for wings of moderate sweep, aspect ratio, and taper ratio (transport-type wings). The geometry input consists of a series of airfoil sections to define the wing and a series of fuselage sections to define an arbitrary fuselage.

### Euler and Navier-Stokes

PARC2D and PARC3D solve the complete Navier-Stokes equations in conservative form using the Beam and Warming approximate factorization algorithm. In addition to solving the complete Navier-Stokes equations, the viscous terms can be selectively included so that either a thin-layer simulation can be performed or an inviscid (Euler) flow field can be calculated. For viscous simulations, turbulent flow is calculated by using Reynolds averaging and by employing an algebraic turbulence model. The algorithm is formulated for a curvilinear set of coordinates; therefore, quite complex geometries can be analyzed.

### TEST-TO-THEORY COMPARISONS

For test-to-theory discussions, the codes are divided into three classes: (1) linear theory and modified-linear theory, (2) small disturbance and full potential, and (3) Euler and Navier-Stokes. A few of the validation activities that are under way in the transonic flow regime are discussed in subsequent paragraphs.



Linear theory has well-known limitations and at first seems to be inappropriate for transonic application. However, when drags are calibrated with experimental results on similar configurations and pressure levels are monitored for separation based on previous experience, linear theory can become a powerful design tool for military multirole aircraft application. Design visibility for camber and twist can rapidly be obtained for multiple design conditions, e.g., cruise, transonic maneuver, acceleration, and often includes the important effects of scheduled leading- and trailing-edge flaps and trim. This process would be time-consuming using the second-level codes and an impossible task employing third level codes with today's hardware.

Second-level codes fit in the design process (Figure 1) very nicely as the next step after linear theory has been used. Optimization is still practical with these codes, but our approach is to use them as a refinement to the initial linear theory design.

Because of the time required to generate grids and solutions and considering computer costs, third level codes are generally used to address specific design problems and are employed as final refinements for particular geometry and flow condition combinations.

Test-to-theory comparisons were accomplished for the planform in Figure 5 with and without camber and flaps to assess how well each code predicts camber and flap effects, a key part of a wing design process. Lift, drag, and moment calculations for the uncambered wing are compared with test data in Figure 6 at Mach 0.9. The modified-linear theory actually shows the best overall correlation, although the drag levels have been calibrated with test data from a similar configuration. TWING results are somewhat better than those from TAWFIVE and WBPPW. Furthermore, converged solutions were obtained to a higher angle of attack for TWING than for TAWFIVE or WBPPW. TWING's success at the higher angles of attack can, in part, be attributed to an option in the code that allows for an approximation of a rotated differencing scheme in regions of local supersonic flow.

For this planform, the TAWFIVE code experienced difficulties in convergence at grid points near the tip. As revealed in Figure 7, the internally generated grid produced very sharp angles in the spanwise grid lines as the lines extend off the tip of the wing. This situation was circumvented by generation of an external grid. As shown in Figure 8, the spanwise grid lines are much smoother as the lines extend off the tip. A realistic representation of the fuselage was also incorporated in the grid system.

The ability to accurately predict drag and pitching moment increments attributed to camber is an important factor in the selection of a code used in the design environment. Comparisons shown in Figure 9 reveal that all the codes predict increments that compare reasonably well with the experimental data.

For a wing design code to be useful in fighter aircraft design, the code should accurately predict flap effects or at least indicate that calibration factors be developed to allow flap effects to be predicted with confidence. Incremental flap effects at 0.9 Mach number are compared with experimental results in Figures 10 and 11. Drag and moment trends are predicted quite well

with both linear theory and TWING for leading- and trailing-edge flap deflections of 10 degrees. TWING yields better drag increment predictions but linear theory provides somewhat better correlation of moments. Both over-predict the trailing-edge flap moment effect, which is common and can be accounted for with suitable calibration factors. Both codes provide comparable results for forces and moments. Of course, TWING has the advantage of providing more realistic simulation of the transonic flow field because of its ability to predict shocks.

Additional insight into the transonic codes is revealed in test-to-theory comparisons obtained for the F-16 configuration (Figure 12). The configuration was analyzed with wing-alone geometry in TWING and WBPPW while the simulation used in TAWFIVE consisted of the wing mounted on a semi-infinite axisymmetric cylinder. Symmetrical NACA 64A airfoils were employed between the centerline and Span Station 53.0 (the region of the theoretical planform covered by the strake and fuselage) in the TWING and WBPPW simulations. Typical force and moment plots obtained from these codes at Mach 0.9 are presented in Figure 13. Lift and drag were predicted reasonably well by all codes. Specifically, WBPPW and TAWFIVE predicted lift well but tended to predict higher drag levels. Drag was predicted very well by TWING for lift coefficients below 0.6. Good correlation of lift was obtained for angles of attack between 2 and 7 degrees. For angles of attack greater than 7 degrees, the experimental lift curve becomes dominated by flow separation and vortex lift. A variation between the codes was evident in the prediction of moments. Although TAWFIVE did a good job of predicting  $C_{M_O}$ , the predicted aerodynamic center is too far forward. In contrast, WBPPW does a better job of predicting the a.c., but misses the  $C_{M_O}$ . TWING predicts  $C_{M_O}$  reasonably well and the a.c. is very close to the test data below a lift coefficient of 0.5.

Pressure distributions for 4.1 degrees angle of attack are presented in Figure 14. The experimental pressures at the first span station ( $\eta = 0.32$ ) show considerable influence of the strake since this station is only four inches outboard of the wing/strake intersection. Local flow separation produced by the vortical flow results in the lack of a leading-edge pressure peak. Experimental data show a leading-edge pressure peak at all other span stations, and TWING predicts the peak pressures better than TAWFIVE. WBPPW does not predict a leading-edge pressure peak. The inability of TAWFIVE and WBPPW to adequately predict the leading-edge pressures results in a lower loading on the leading edge of the airfoil. This lower loading contributes to a more nose-down pitching moment inboard of  $\eta = 0.59$ . Outboard of this station, a more nose-up moment results from this lower loading. Over the plateau region of the pressure distributions (10- to 63-percent chord), all three codes compare reasonably well with both upper and lower surface experimental data. However, the inclusion of viscous effects would shift all of the upper surface curves down, thereby improving the TWING comparisons (except at the tip station). These plots also reveal that TWING consistently predicts the trailing-edge shock location better than either TAWFIVE or WBPPW.

Correlation of TWING predictions with test data is shown in Figure 15 for the F-16 wing with leading-edge flap deflections of 0, 5, and 10 degrees. Corresponding pressure comparisons are shown in Figure 16 at 6.06-degree angle of attack for 5-degree leading-edge flap deflection. Force and pressure comparisons again show that TWING predicts lift values and pressure levels

that agree reasonably well with experimental data in regions where viscous effects are not significant. Over-prediction of shock strength, exhibited in Figure 16, lends support to the rule of thumb suggested by Cosentino and Holst (Reference 13) that shock strengths are over predicted when the local Mach number ahead of the shock is greater than 1.3. Examination of the predicted pressures throughout the range where convergence was obtained with TWING indicates that, for local Mach numbers less than 1.2, shock strengths agreed quite well with experiment. Above Mach 1.3, the predicted shock waves were always too strong. For local Mach numbers between 1.2 and 1.3, shock wave agreement was not consistent.

F-16 results, presented here and those shown earlier for the generic wing-body, suggest that TWING generally provides better results for thin-wing, low-aspect ratio fighters than the other methods shown. Therefore, we decided to compare results to those obtained from an Euler code. The PARC Euler code was selected because of its present widespread industry usage. An F-16 wing-alone simulation was used in PARC to duplicate the geometry used in TWING. Comparisons of lift, moment, and drag are shown in Figure 17. PARC solutions were obtained only at 0-, 2-, and 4.1-degrees angle of attack. For these conditions, PARC and TWING produce comparable results, both of which are very good. Pressure data are compared in Figure 18 at 4.1-degrees angle of attack. Again, the comparisons with test data are in general quite good. TWING does a better job of predicting the leading-edge pressure peak while PARC is better at predicting the shock strength. The codes provide comparable results for shock location.

PARC2D was used to analyze an axisymmetric nozzle at Mach 1.2. A Navier-Stokes solution was obtained using the Beam and Warming implicit solution algorithm and a Baldwin-Lomax turbulence model. The analysis required approximately one CPU hour of CRAY X-MP/24 time. A comparison of predicted and test outer surface pressures is shown in Figure 19. Test and predicted values of drag and thrust are also shown. Both the pressures and forces correlate very well with the experiment.

General Dynamics has an ongoing cooperative effort with NASA Ames and the Air Force Flight Dynamics Laboratory to validate CFD codes through use of the extensive F-16 data base. As part of this effort an Euler analysis of the complete F-16 has been accomplished. Preliminary results were presented at a 1986 AGARD Symposium (Reference 14). Part of the grid system, which has over 500,000 grid points in 20 blocks, is shown in Figure 20. Detailed modeling of the inlet and nozzle with flow-through boundary conditions is essential for full aircraft simulation with power effects. Details of the inlet grid blocking are shown in Figure 21.

Calculations, which were made on the Fort Worth Division CRAY X-MP/24 and the NASA Ames CRAY 2, employed approximately thirty-five CPU hours. Computed velocity vectors on the surface of the forward fuselage are shown in Figure 22. Accuracy of the fuselage flow field calculations was further verified by an excellent comparison between computational results and experimental pressure coefficients from Reference 15. Sample comparisons at two fuselage stations are shown in Figure 22.

Since this was the first time that an analysis of this magnitude had been attempted, it was no surprise that problems were encountered. The code simply did not develop shock waves at the downstream edge of the supersonic bubble on the wing upper surface; consequently, pressures in this region were not accurately predicted. To address the problem, a denser grid system is being incorporated on the wing upper surface that will provide for better shock resolution. In addition, the code has been recently modified to allow for full Navier-Stokes solutions. Further computations are planned on the NASA/Ames Numerical Aerodynamics Simulator.

#### THE FUTURE OF APPLIED CFD

CFD capability is rapidly maturing and is now routinely used in the design process. Applications of first and second level codes have progressed to complex configurations at transonic speeds, but solutions of the more rigorous level three (Euler and Navier-Stokes) flow equations are time consuming and only practical for detailed design. With continued improvement in grid generation concepts and algorithms and the natural evolution in computer hardware, we can look forward to routine application in the preliminary design phase for complex geometries at increasingly more complex flow conditions. In the meantime, the applied aerodynamicist must rely on the faster codes for the important optimization tasks. We have advanced from total reliance on linear theory to more and more use of small-disturbance and full-potential codes. We must continue to improve the adaption of these intermediate level methods to aircraft design for optimization.

Code validation remains a major task, particularly for the more sophisticated codes applied to complex geometries. Studies to verify grid independence and to determine regions of applicability (Mach, angle of attack, Reynolds number, etc.) are expensive and time consuming but indispensable to achieve credibility.

Comparisons with experimental data must include forces and moments in addition to the common comparisons with flow fields and pressure distributions. We must work toward more quantifiable validation. Color pictures of flow fields are impressive but, by themselves, do not provide sufficient credibility for the design engineer.

For fighter applications, one of the most fruitful and most difficult areas for CFD application is at high angles of attack including the transonic regime. Current design practice requires significant wind tunnel refinement to achieve desired lateral/directional and longitudinal stability characteristics. These flows are heavily influenced by strong forebody vortex interaction with strakes, wings, and control surfaces. Accurate consideration of viscous effects (turbulence modeling), vortical flow and, most likely, dynamics are required in addition to complete 3-D geometry modeling. The capability to accurately model this flow regime will provide the design engineer with a good barometer of the CFD developer's progress.

Additional emphasis must be placed on the capability to predict drag accurately, for this will always be the performance bottom line. We must progress beyond the pressure monitoring approach, particularly in the

transonic regime, which is critical for cruise and maneuver design. The fidelity that comes with accurate drag predictions is required before CFD will reach its full potential as a design tool.

#### REFERENCES

1. A. G. Chavera, "The Conceptual Design Synthesis Program (CSDP)," General Dynamics Report FZA-552, 1 February 1986.
2. W. W. Braymen and C. Q. Pass, "Aerodynamic Wing Design and Analysis Methods," General Dynamics Report ERR-FW-2397, December 1983.
3. C. W. Boppe, "Transonic Flow Field Analysis for Wing-Fuselage Configurations," NASA CR-3243, May 1980.
4. G. B. Cosentino and T. L. Holst, "Numerical Optimization Design of Advanced Transonic Wing Configurations," NASA TM 85950, May 1984.
5. N. D. Melson and C. L. Streett, "TAWFIVE: A User's Guide," NASA TM 84619, September 1983.
6. G. K. Cooper, "The PARC Code: Theory and Usage," AEDC-TR-87-24, October 1987.
7. R. L. Carmichael, C. R. Castellano, and F. C. Chen, "The Use of Finite-Element Methods for Predicting the Aerodynamics of Wing-Body Combinations," Symposium on Analytical Methods in Aircraft Aerodynamics, Ames Research Center NASA SP-228, 28-30 October 1969.
8. J. C. Sivells and R. H. Neely, "Method of Calculating Wing Characteristics by Lifting-Line Theory Using Nonlinear Section Lift Data," NACA TN 1269, 1947.
9. P. Bradshaw and D. H. Ferriss, "Calculation of Boundary Layer Development Using the Turbulent Energy Equation. Compressible Flow on Adiabatic Walls," J. Fluid Mechanics, Vol. 46, 1971.
10. A. Jameson and D. A. Caughey, "A Finite-Volume Method for Transonic Potential Flow Calculations," Proceedings of AIAA 3rd Computational Fluid Dynamics Conference, June 1977.
11. P. D. Smith, "An Integral Prediction Method for Three-Dimensional Compressible Turbulent Boundary Layers," Royal Aeronautical Establishment R&M 3739, 1974.
12. H. W. Stock, "Integral Method for the Calculation of Three-Dimensional, Laminar and Turbulent Boundary Layers," NASA TM 75320, 1978.
13. G. B. Cosentino and T. L. Holst, "Numerical Optimization Design of Advanced Transonic Wing Configurations," NASA TM 85950, May 1984.

14. S. L. Karman, Jr., J. P. Steinbrenner, and K. M. Kisielewski, "Analysis of the F-16 Flow Field by a Block Grid Euler Approach," AGARD Paper No. 18, 58th Meeting of the Fluid Dynamics Panel Symposium, Aix En-Provence, France, April 1986.
15. G. H. Reue, M. E. Doberenz, and D. D. Wilkins, "Component Aerodynamic Loads From 1/9-Scale F-16A Loads Model," General Dynamics Report No. 16PR316, May 1976.

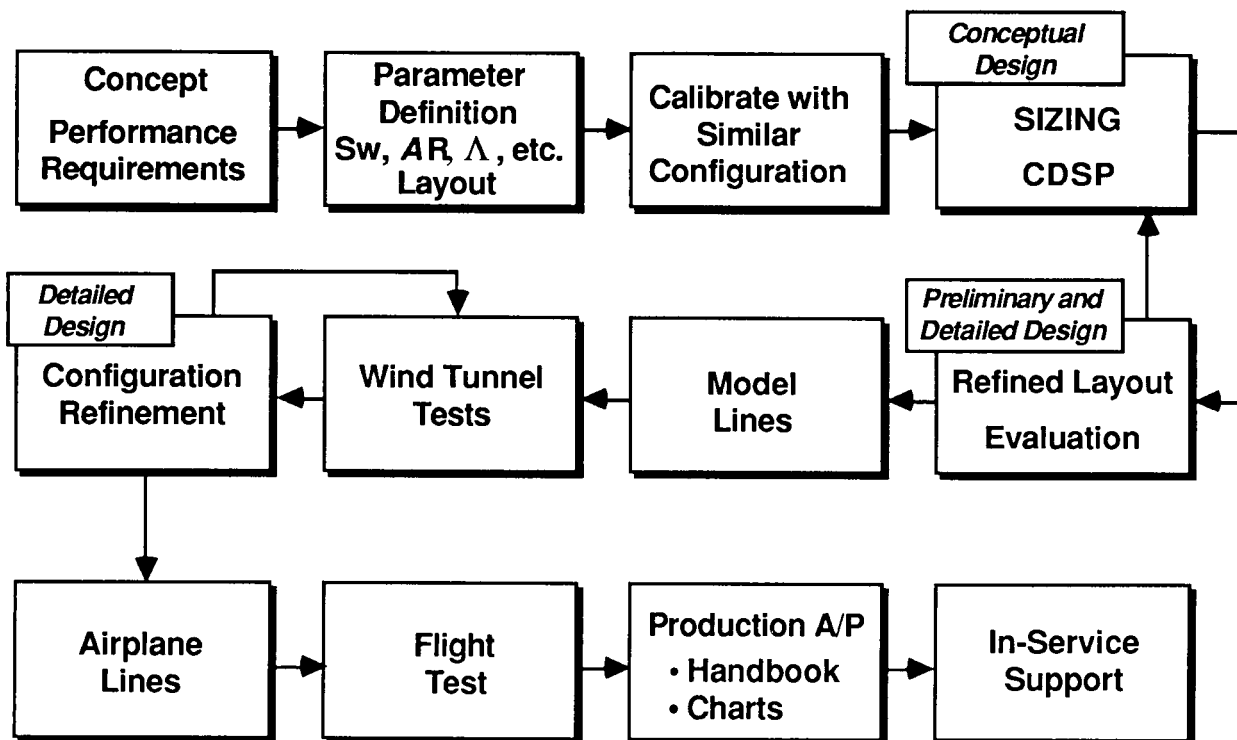


Figure 1. The Design Process

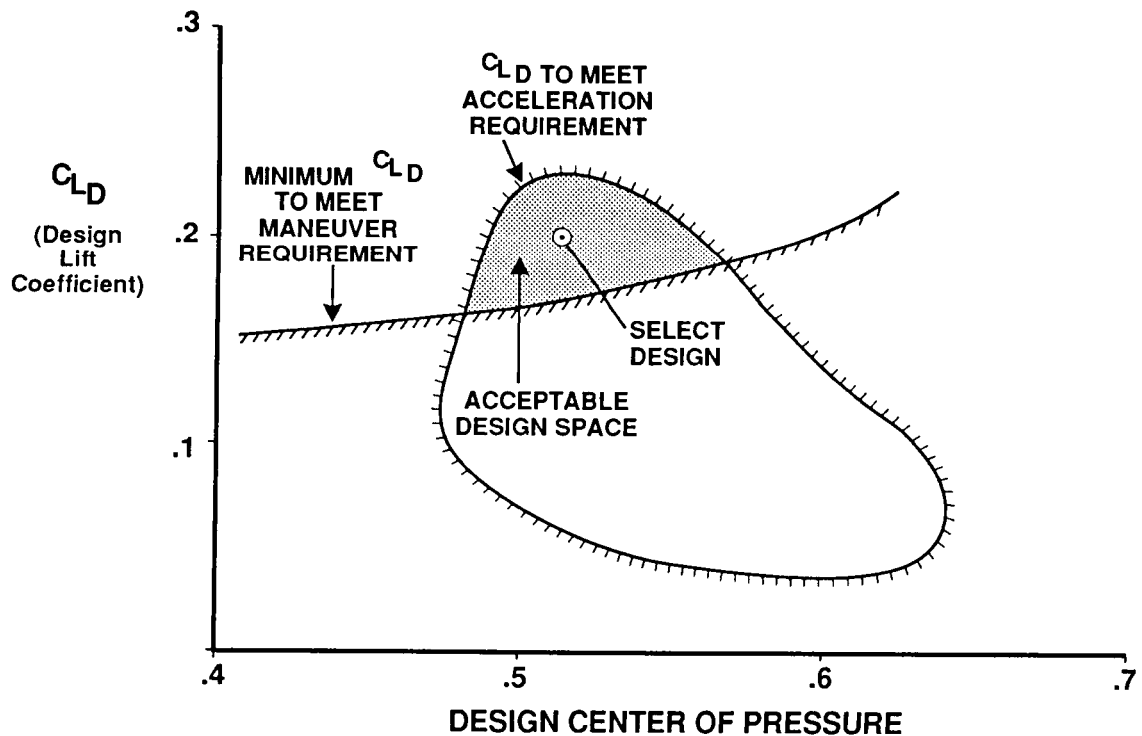


Figure 2. Illustration of Design Space

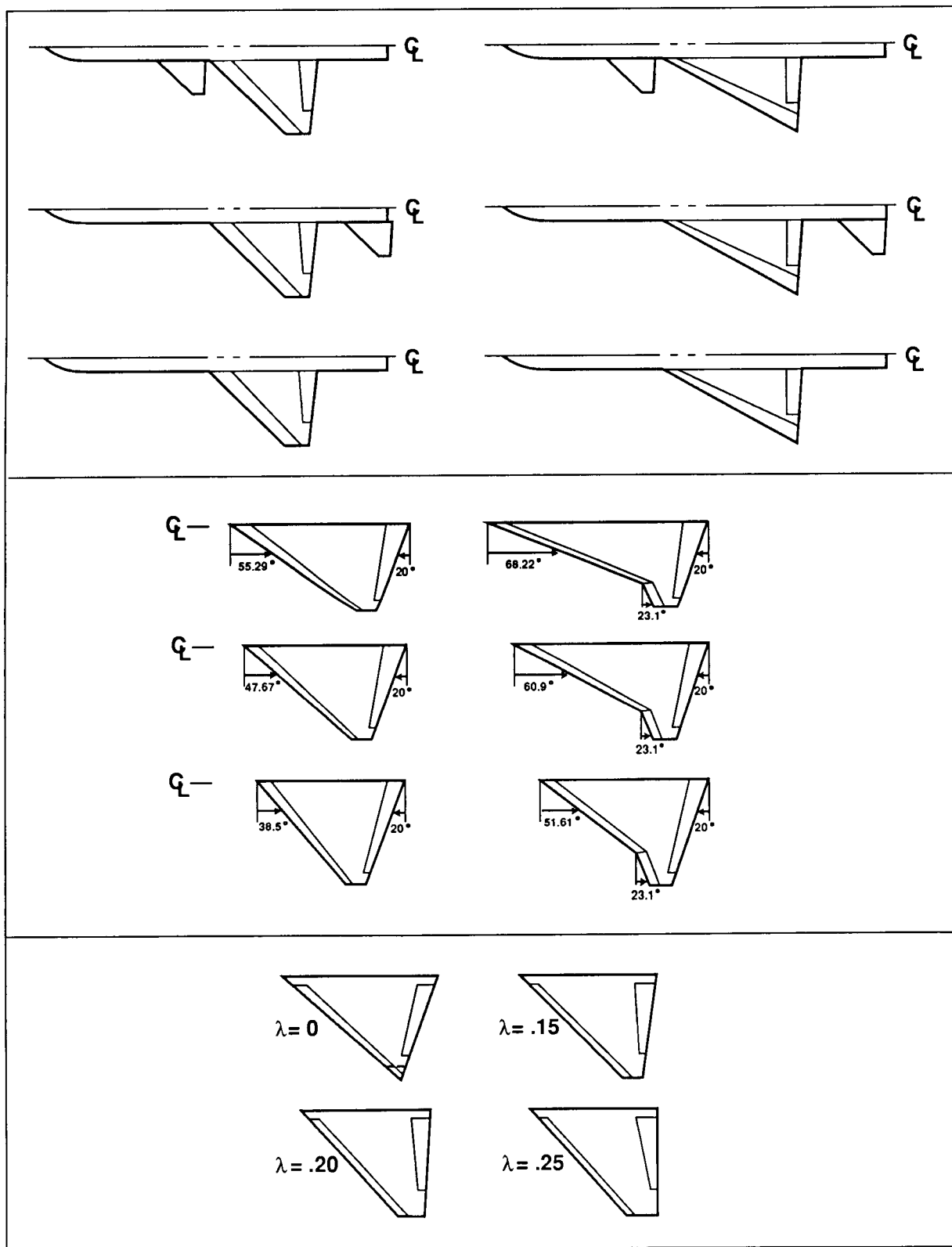


Figure 3. Parametric Models



EQUATION TYPE	EXAMPLE CODES	CAPABILITIES					
		COMPRESSIBLE	NONLINEAR	UNSTEADY	ROTATIONAL	VISCOUS	HEAT TRANSFER
• LINEAR VELOCITY POTENTIAL	WOODWARD, CARMICHAEL/US8 CUNNINGHAM, HESS, USSAERO, VSAERO, PAN AIR	✓					
• TRANSONIC SMALL DISTURBANCE	BAILEY/BALLHAUS, WBPPW, PANDORA, CANTATA	✓	✓				
• FULL POTENTIAL	FLO 22, FLO 27, FLO 28, FLO 30, TWING, TAWFIVE, GARABEDIAN/KORN (2-D)	✓	✓				
• EULER	FLO 57, FLO 58, SKOAL FALCON, PARC2D, PARC3D	✓	✓	✓	✓		
• NAVIER-STOKES	NS3D, ARC3D, PARC3D, FALCON, NS2D, ARC2D, PARC2D	✓	✓	✓	✓	✓	✓

Figure 4. Representative Codes

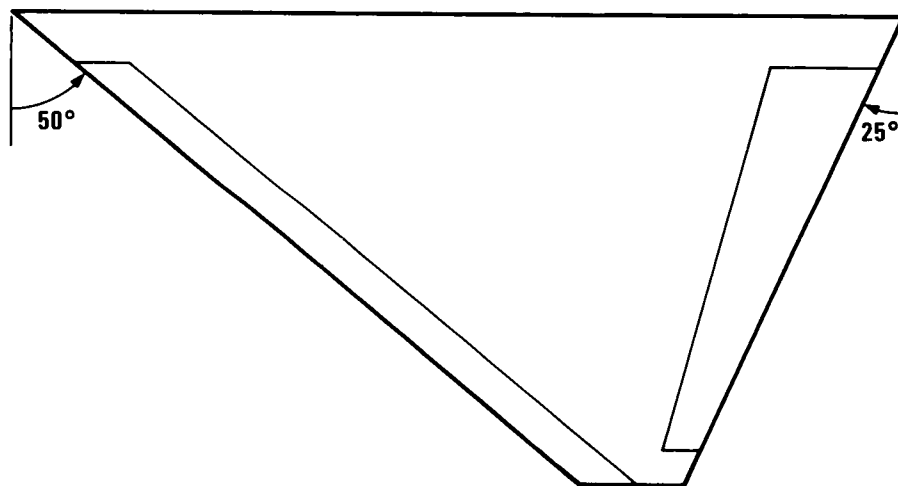


Figure 5. Selected Generic Planform

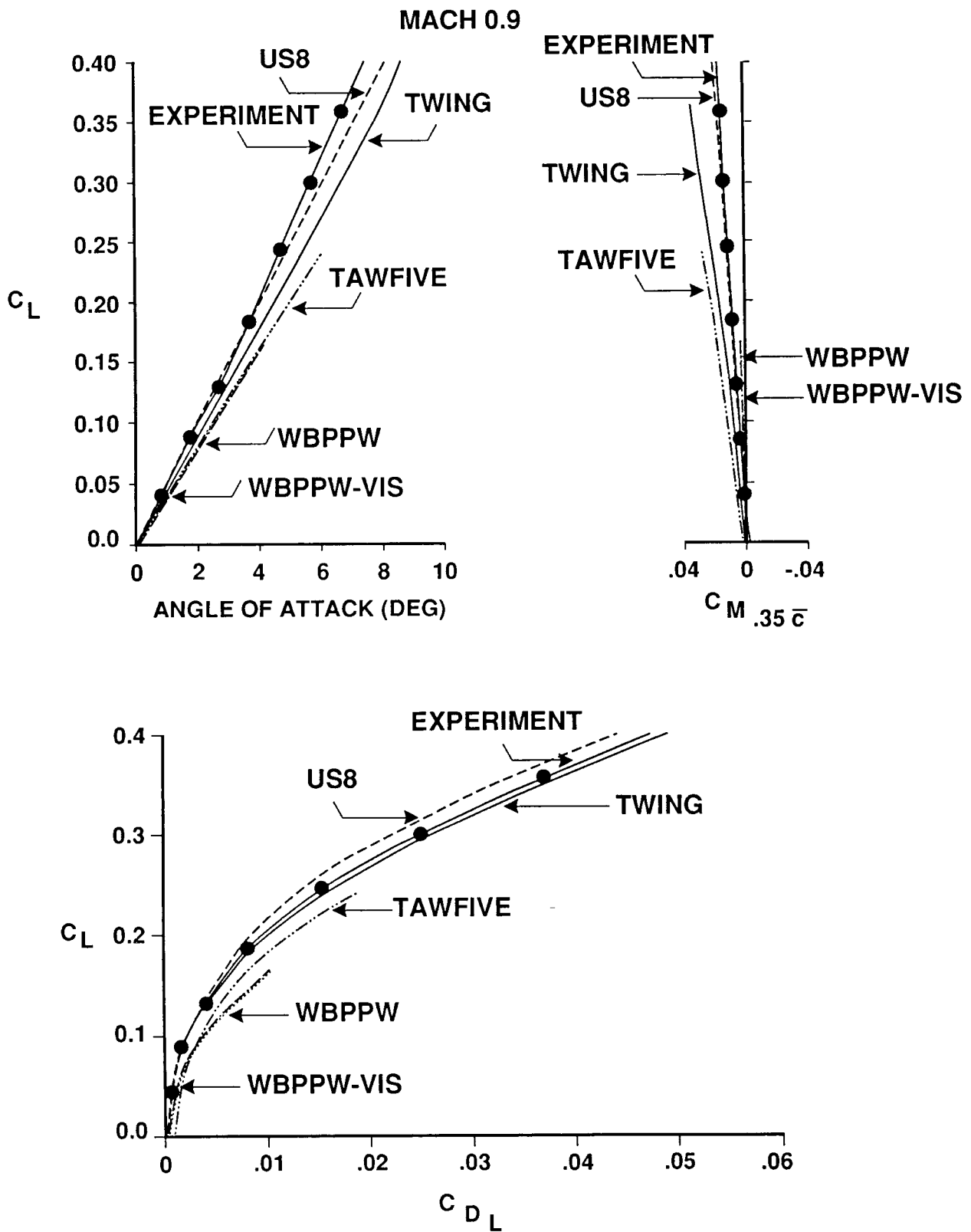


Figure 6. Test-to-Theory Comparisons of Uncambered Generic Wing at Mach 0.9

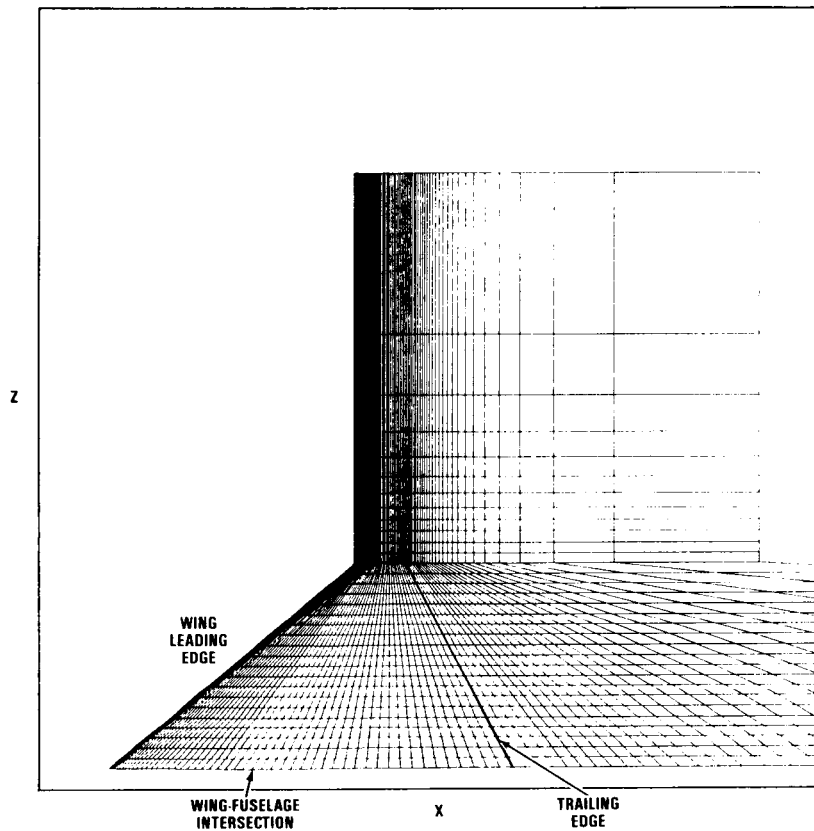


Figure 7. Generic Wing-Body Grid Generated Internally by TAWFIVE

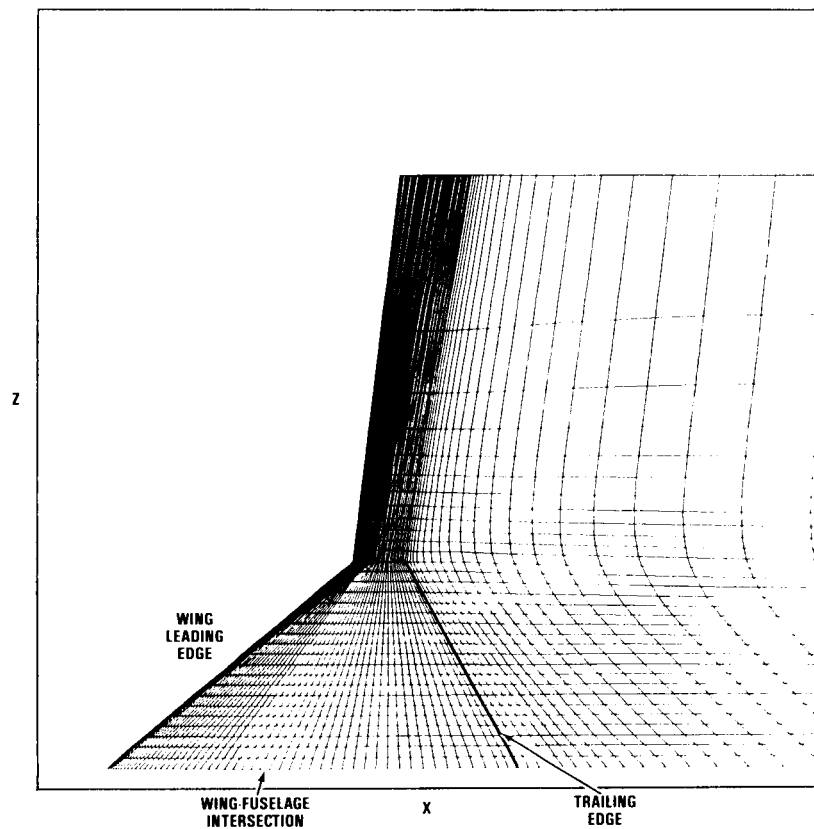


Figure 8. External Grid Used in TAWFIVE

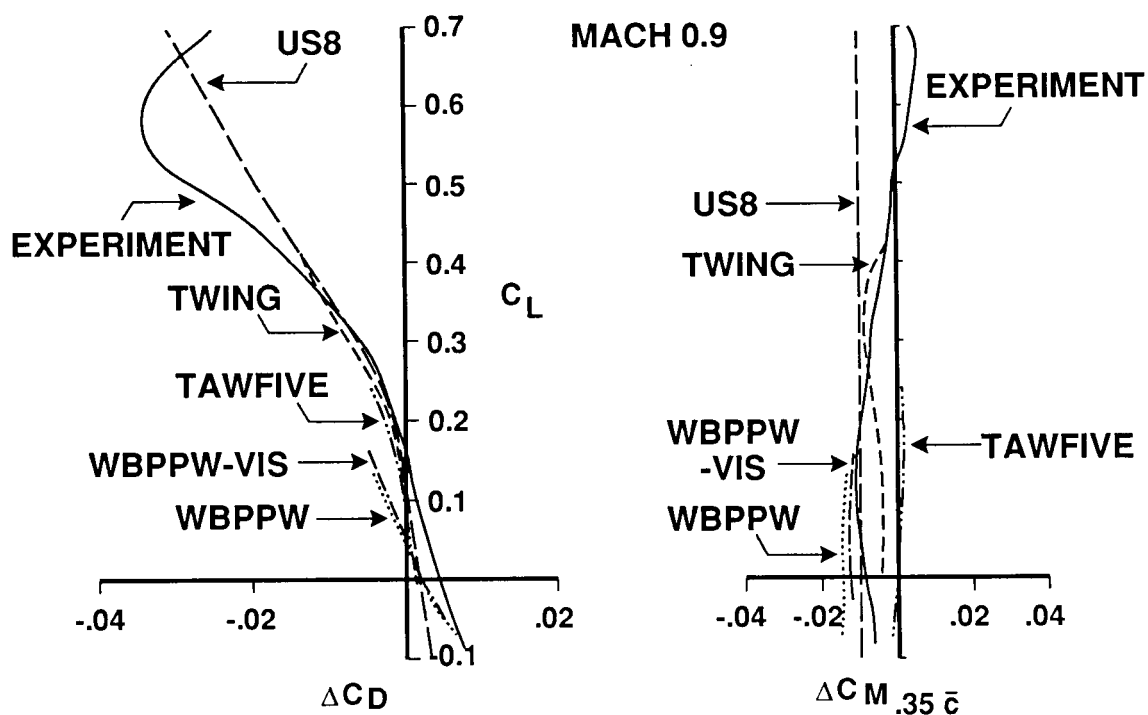


Figure 9. Camber Increment Comparisons

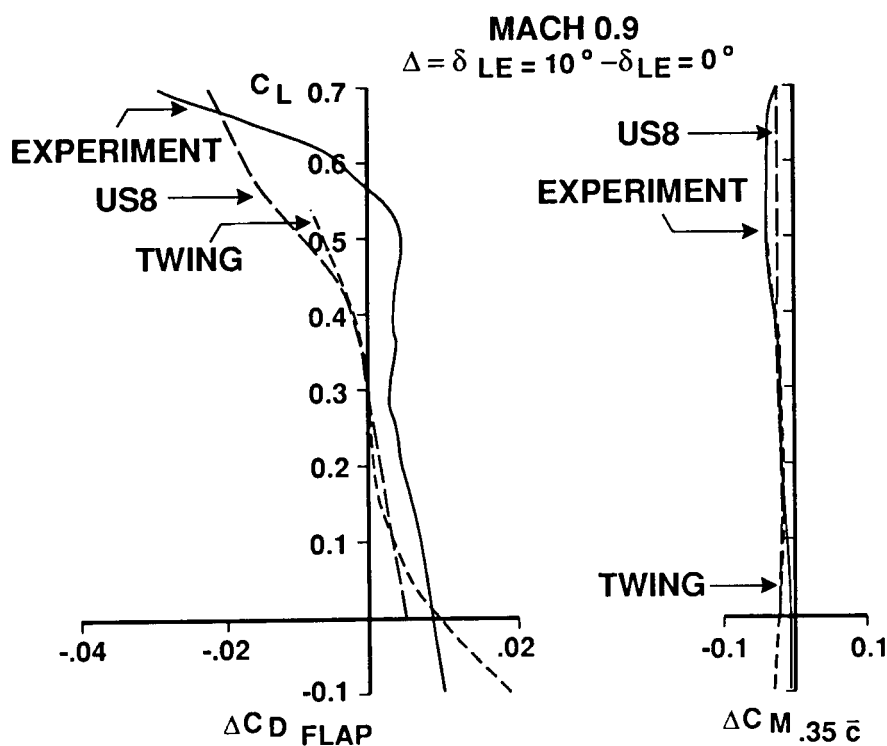


Figure 10. Comparison of Leading-Edge Flap Increments

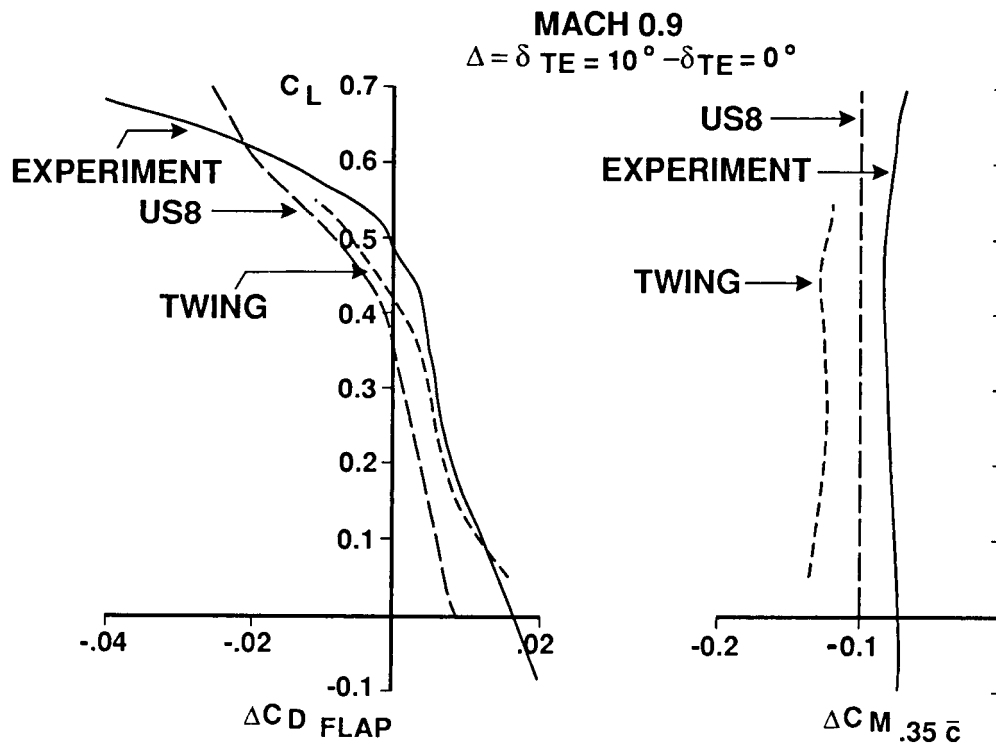


Figure 11. Comparison of Trailing-Edge Flap Increments

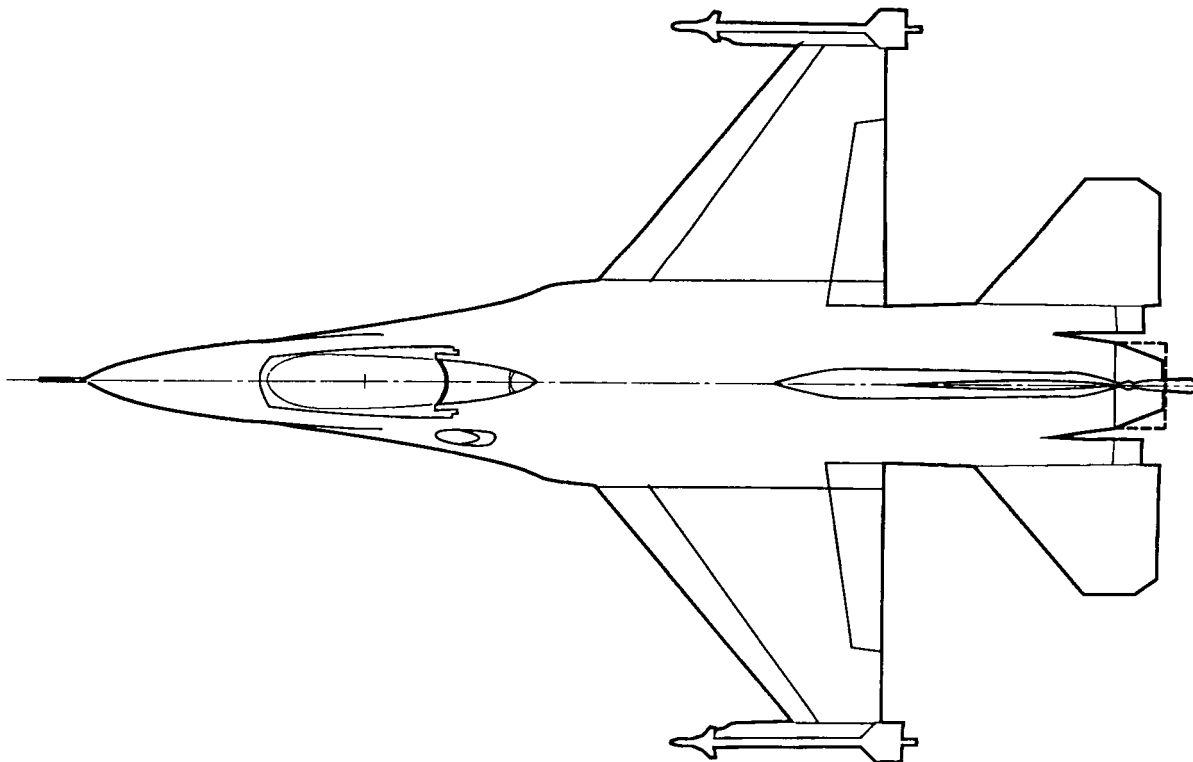


Figure 12. F-16 Configuration

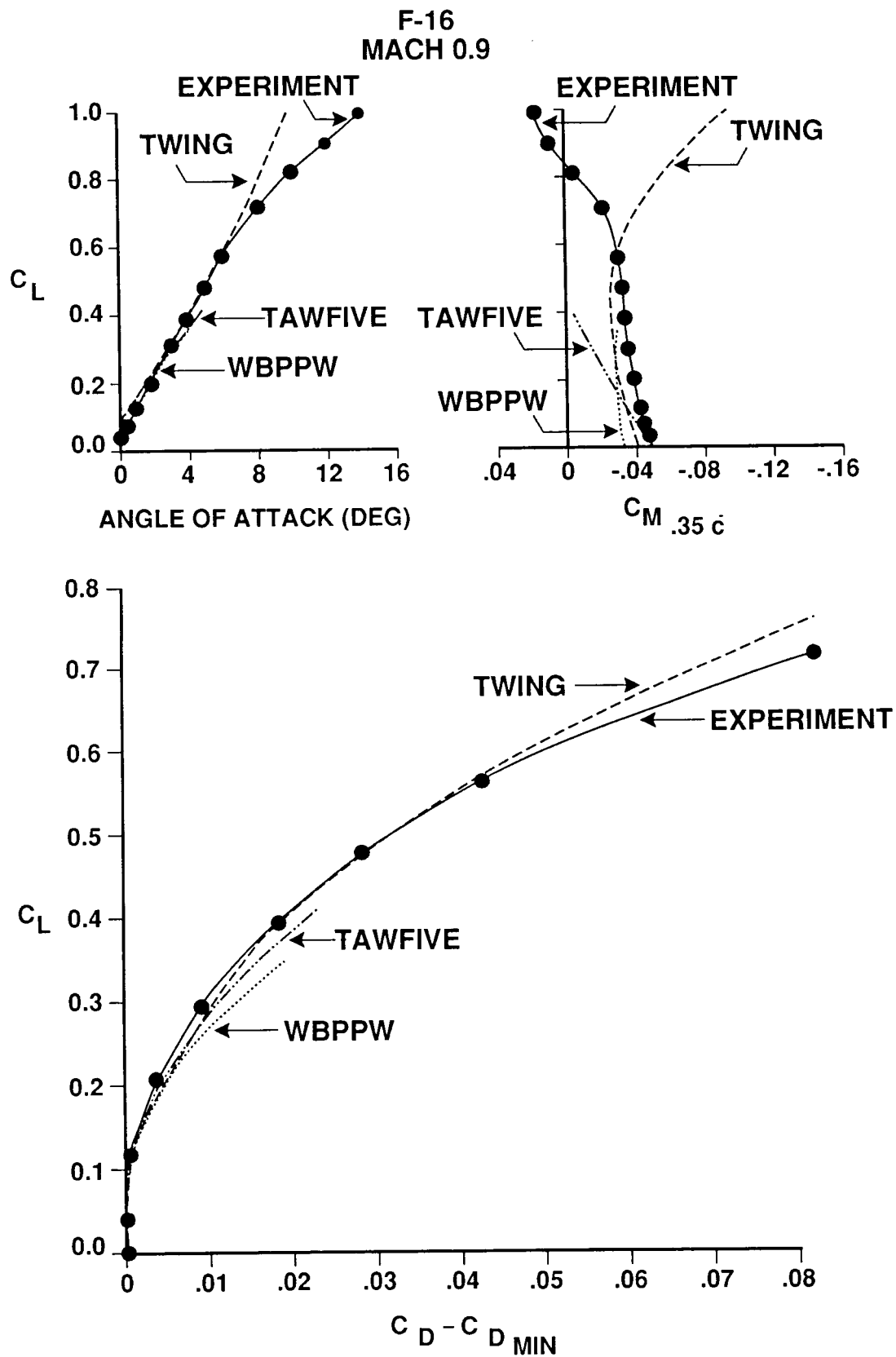


Figure 13. Test-to-Theory Comparison of F-16 Forces and Moments at Mach 0.9

ORIGINAL PAGE IS  
OF POOR QUALITY

F-16  
MACH = 0.9  
 $\alpha = 4.1^\circ$

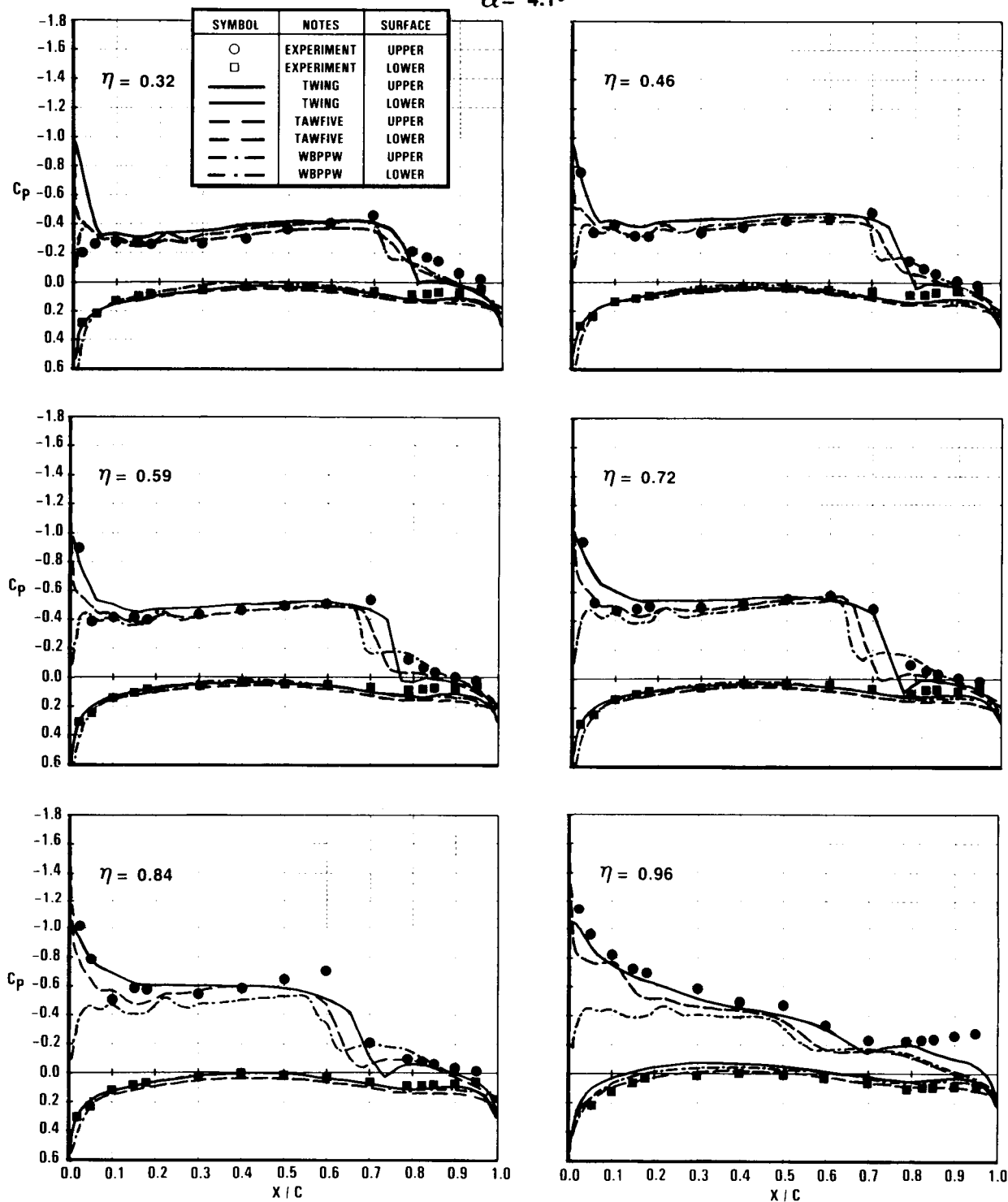


Figure 14. Comparison of F-16 Wing Pressures at Mach 0.9 and Angle of Attack of 4.1°

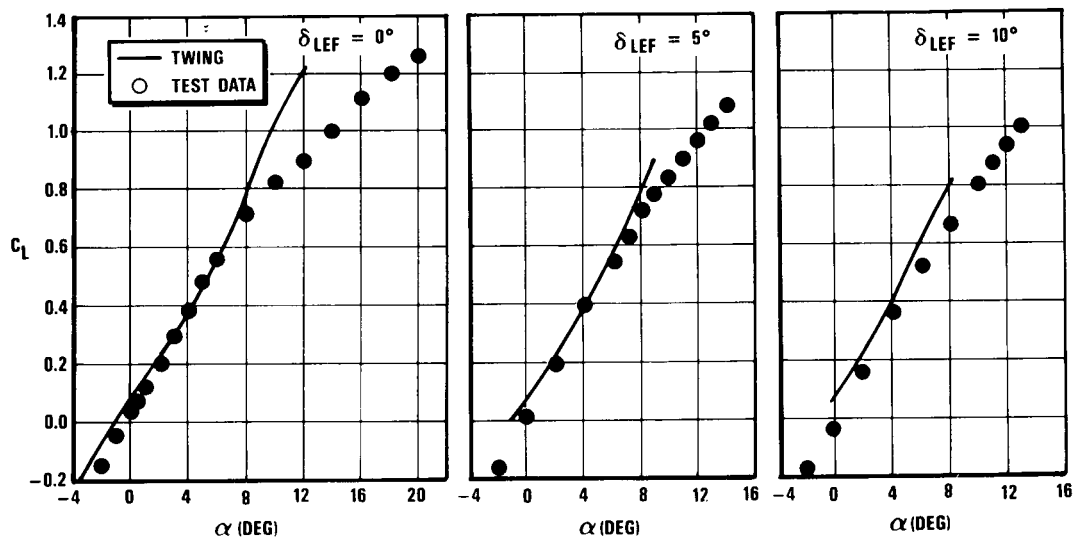


Figure 15. Comparison of F-16 Lift Curves at Mach 0.9 for Leading-Edge Flap Deflections of 0, 5, and 10 Degrees

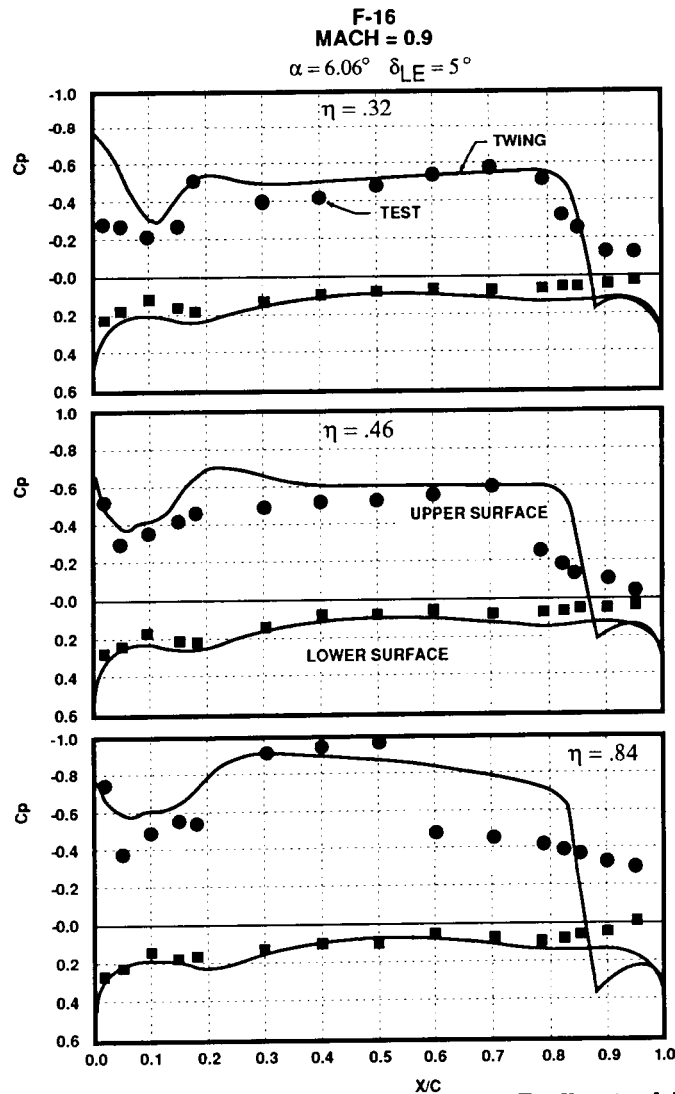


Figure 16. Comparison of F-16 Pressures with Deflected Leading Edge Flaps



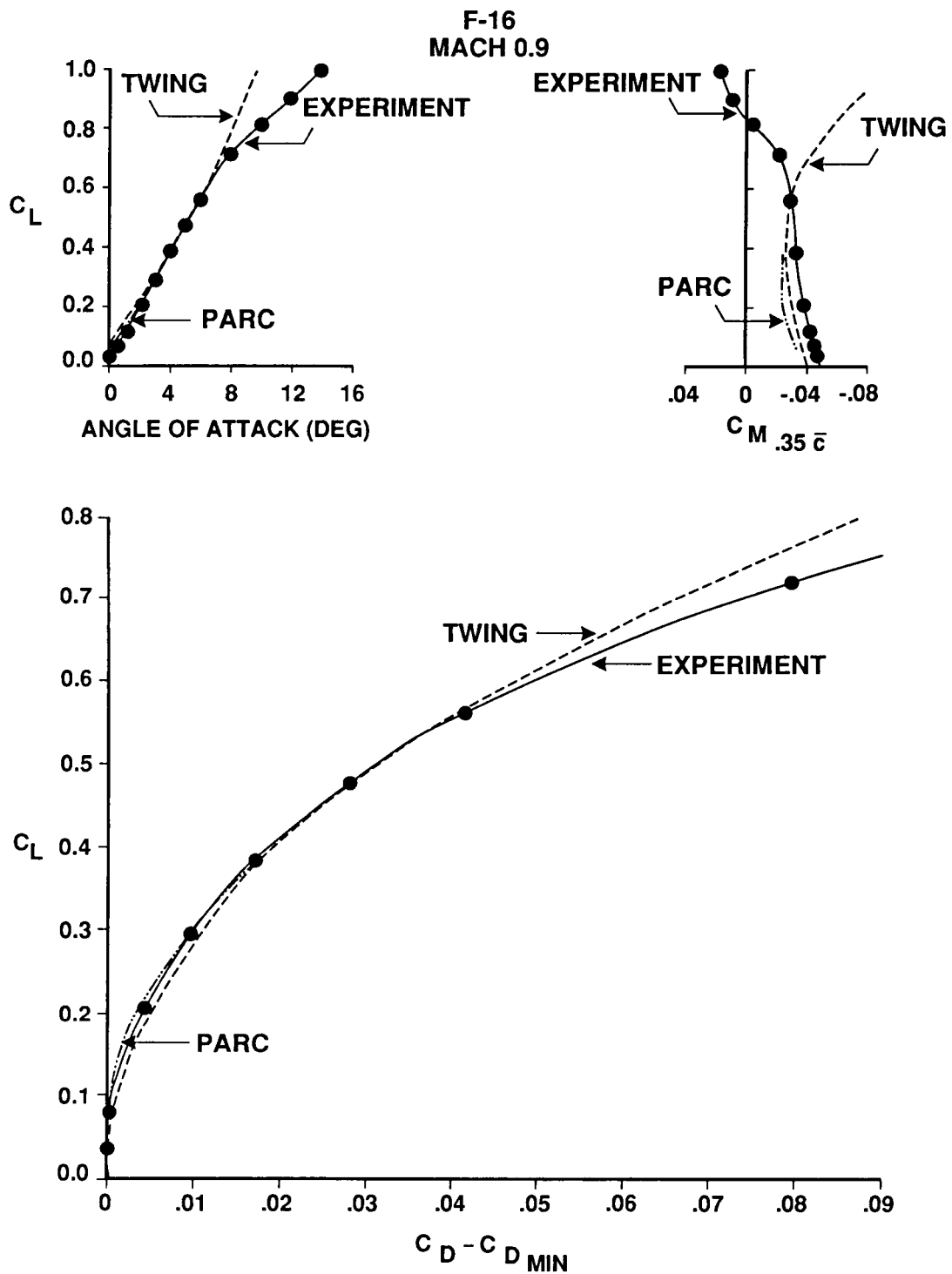


Figure 17. Comparison of PARC3D and TWING Force Predictions with F-16 Test Data at Mach 0.9

ORIGINAL PAGE IS  
OF POOR QUALITY

F-16  
MACH = 0.9  
 $\alpha = 4.1^\circ$

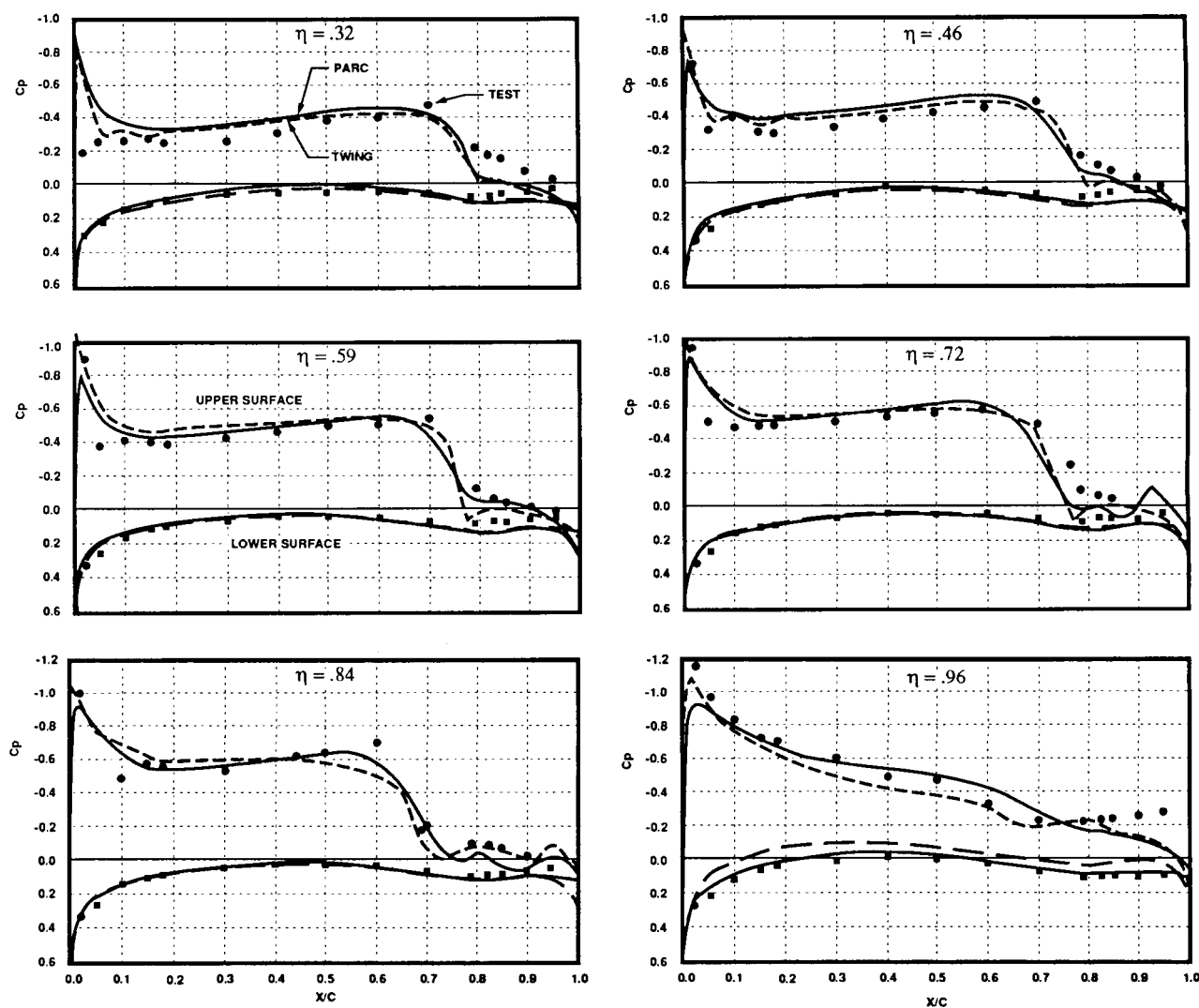


Figure 18. Comparison of PARC 3D and TWING Pressure Predictions with F-16 Test Data at Mach 0.9

ORIGINAL PAGE IS  
OF POOR QUALITY

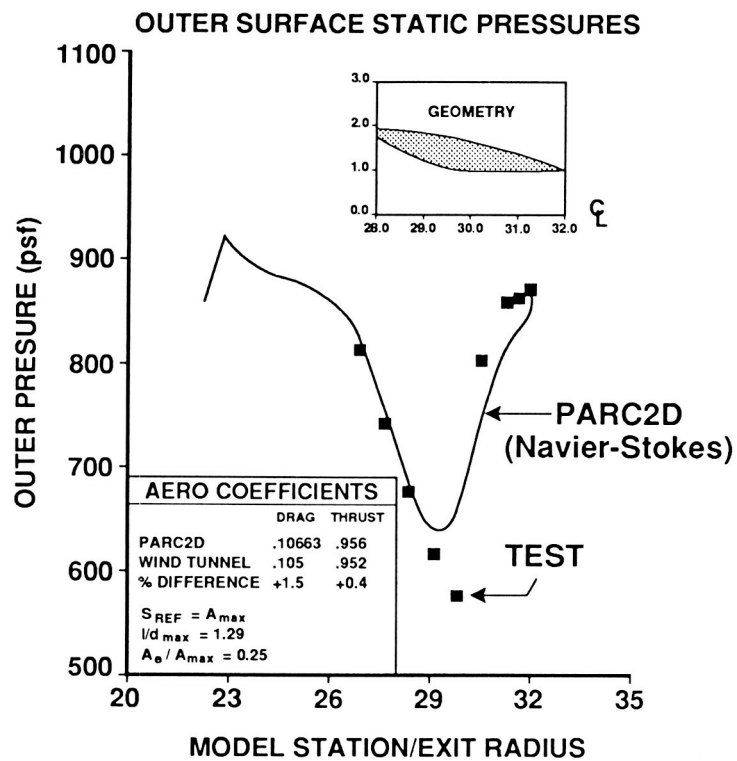


Figure 19. Test-to-Theory Comparison of Forces and Pressures on Axisymmetric Nozzle at Mach 1.2

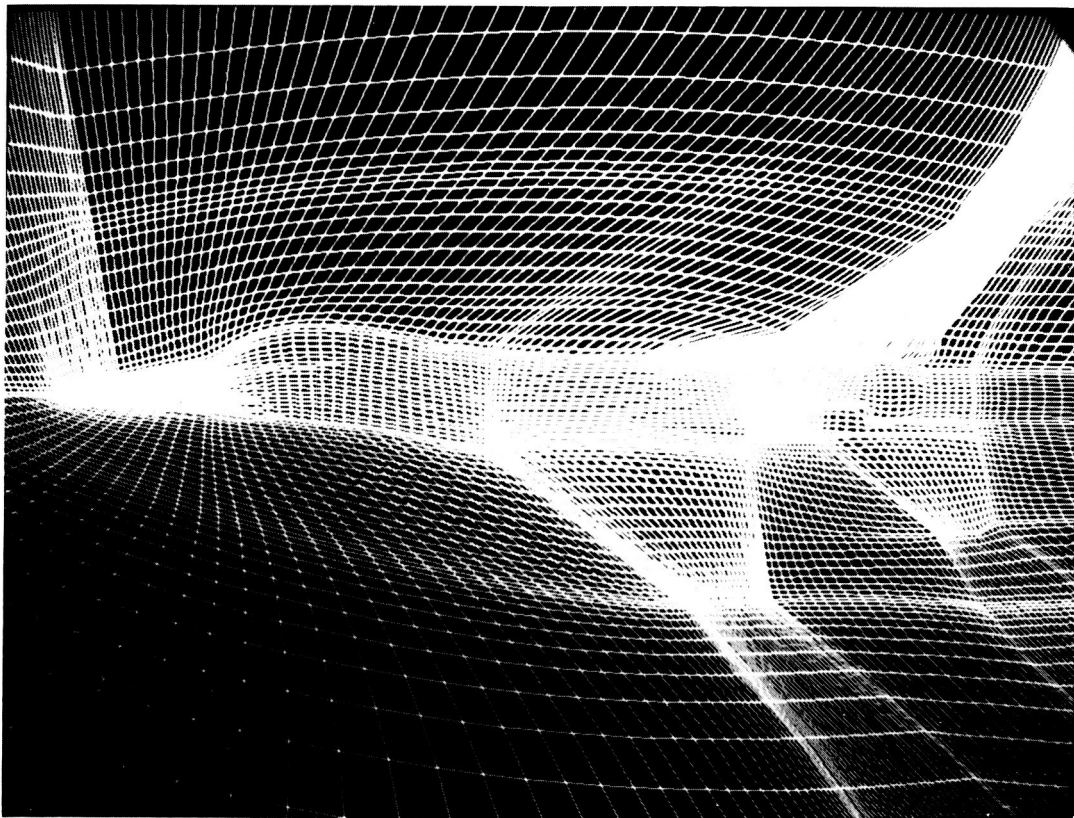
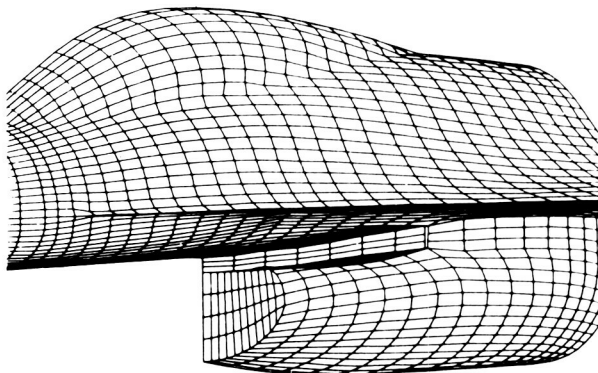
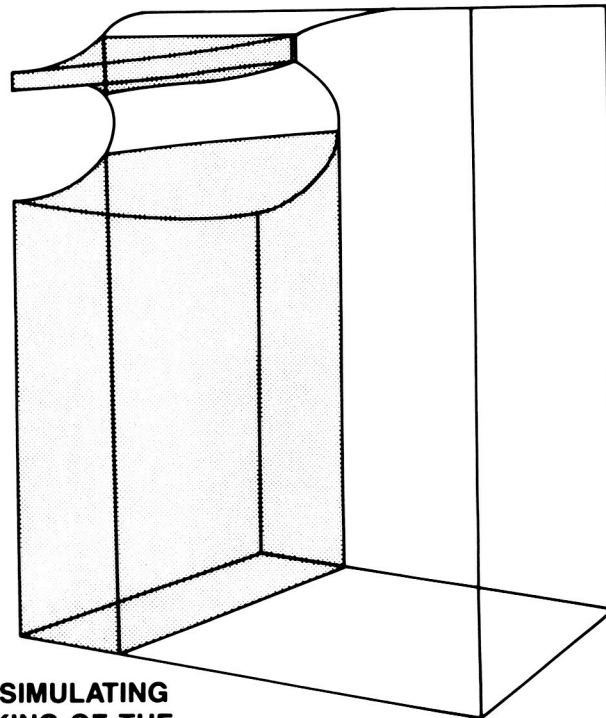


Figure 20. Grid System for Complete F-16 Representation

ORIGINAL PAGE IS  
OF POOR QUALITY



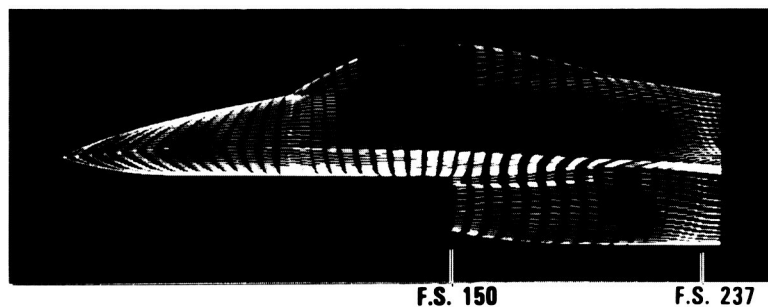
ACTUAL SURFACE GRIDS  
GENERATED FOR INLET-  
FUSELAGE SECTION



3 BLOCKS SIMULATING  
THE BLOCKING OF THE  
INLET-FUSELAGE REGION

Figure 21. Blocking Scheme Applied to F-16 Inlet Region

$M = .9$   $\alpha = 4^\circ$   
VELOCITY VECTORS



PRESSURE DISTRIBUTIONS

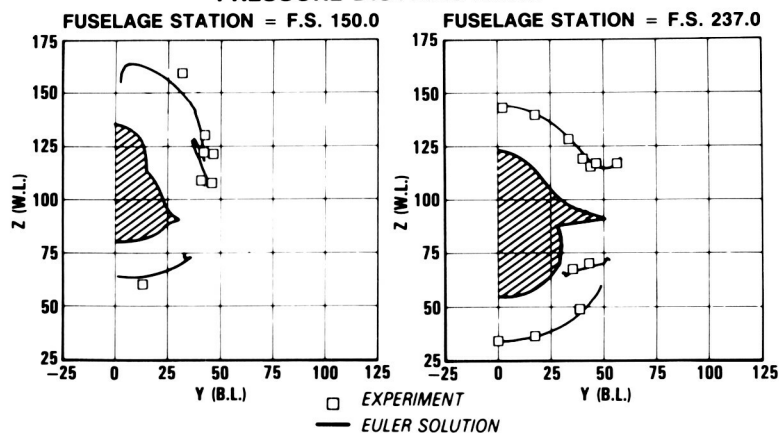


Figure 22. Euler Solution of F-16 Fuselage Flowfield

## APPLIED TRANSONICS AT GRUMMAN

W. H. Davis  
Grumman Aircraft Systems  
Bethpage, NY

## ABSTRACT

A review of several applications of Computational Fluid Dynamics (CFD) to various aspects of aerodynamic design recently carried out at Grumman is presented. The emphasis is placed on project-oriented applications where the ease of use of the methods and short start-to-completion times are required. Applications cover transonic wing design/optimization, wing mounted stores load prediction, transonic buffet alleviation, fuselage loads estimation, and compact offset diffuser design for advanced aircraft configurations. Computational methods employed include extended transonic small disturbance (automatic grid embedding) formulation for analysis/design/optimization and a thin layer Navier-Stokes formulation for both external and internal flow analyses.

## INTRODUCTION

The major drivers for the application of transonic CFD at Grumman are the engineering projects, either in direct support of an in-production aircraft or its upgrade, or in the advanced development world. This type of project-oriented application puts a premium on aspects of the CFD method not necessarily associated only with accuracy. While accuracy is of course important, the ability to respond in a time frame of days is usually critical. No matter how advanced a computational capability might be, if it requires two weeks to set up the geometry and computational grid, and another two weeks to obtain useful numerical results, then that capability is useless to the project if, for example, answers are required in two days to support an on-going flight test. This reality has led to a concentration, for transonic flows, on two computational formulations: transonic small disturbance (TSD) for complex configurations, and judicious use of thin-layer Navier-Stokes (TLNS) for complex flow/single component analyses.

The utility of such an approach is attested to by the broad range of engineering problems to which CFD has been applied at Grumman. Among these applications are developing contours for wing design, aiding in aircraft component integration, providing aerodynamic predictions for other disciplines, and as a diagnostic tool to aid in wind tunnel or flight testing (see also ref. 1,2). The intent of this paper is to demonstrate that wide range of application.

## WING-DESIGN/OPTIMIZATION

CFD codes employing the extended 3-D TSD formulation play a major role in external aerodynamic design/analysis at Grumman. The benefits are many. They include the ability to analyze complex realistic aircraft plus component configurations while requiring only short set up times (automatic grid generation). The low computer memory demand (less than 2 MW) and short computational times (under 5 minutes: CRAY XMP 1.4) allow many sequential runs to be turned around in a single day making them ideal for the demanding time constraints of project work. Finally, high confidence in code accuracy comes from 10 years of continuing development work and hundreds of test case comparisons with data.

The NASA-Grumman Wing Body Code (TSD formulation) has progressed from the work of Boppe (ref. 3,4) to extensions by Aidala (ref. 5) to include canards, and the more recent work of Rosen (ref. 6,7,8) to handle wing mounted stores (multiple fin capability) while employing a rotated finite difference scheme for added robustness. Short computational times also have allowed the development, under contract to NASA Langley Research Center, of an optimization/design version of the code, TRO-3D (ref. 9,10), based on Aidala's original work (ref. 5). Optimization by maximizing drag polar efficiency while holding both aerodynamic (lift, moment) and geometric constraints is available. Wing design is also on option by minimizing differences in computed and specified target pressure distributions while maintaining geometric constraints. The optimization module controls both geometry modification and aerodynamic analysis module. The key feature that distinguishes this method from others is the use of aero-function shapes rather than arbitrary functions for geometry modification during the optimization process.

Use of design variables having specific aerodynamic origins has two major benefits. It reduces the computational time for optimization by requiring fewer design variables than for previous schemes and results in pressures that would be more acceptable to an aerodynamicist. Neither of these effects would be expected with an arbitrary set of polynomial bumps used as design variables.

Design variable shapes having an aerodynamic origin were developed from both 2-D and 3-D codes (ref. 11,12). The inverse code translates the aerodynamic input (a pressure change) into a geometric shape perturbation (a geometry change). The 2-D inverse code provides efficient, reliable results with a grid density that can resolve the necessary geometric detail. A 3-D inverse code provides spanwise shape functions to be used with the wing-section shape functions. This approach allows the strengths of the inverse and optimization approaches to be combined. Design variable shapes having specific geometric origins were also developed. These include a leading edge nose radius shape and sets of shapes for leading and trailing edge camber used to model wing device deflections and shapes.

There is presently a catalogue of 25 aero-function shapes available (ref. 10). Not all of these shapes are required for every optimization case, and, in fact, as few as four shapes (design variables) can produce excellent results. One strength of these shapes is that their selection (or elimination) process becomes straightforward because the shapes produce

specific aerodynamic or geometric effects. Similarly, defining and enforcing geometric limits on the amount of additional wing thickness, twist camber device deflection, nose radius, etc. allowable in the final design is easily done as side constraints on the design variables rather than as constraint functions within the optimization algorithm. Full advantage of this last capability was taken during the following exercise.

A Natural Laminar Flow (NLF) Program sponsored jointly by NASA LaRC and NASA Ames-Dryden was initiated in 1984. A variable sweep transition flight test was proposed using the F-14 aircraft. NLF was to be attained by making changes to the baseline wing contours on the upper surface and outboard of the wing pivot point (fig. 1). Shape changes were to be affected by adding a foam and fiberglass glove over the wing in this region. These geometry changes were limited not only in extent but also to being volume-added-only; no cutting of the original wing contour was allowed. It was thought that the level flight condition at  $M_{\infty} = 0.7$ ,  $C_L = 0.4$ , altitude = 30,000 ft and wing sweep of 20 deg. would be particularly troublesome since the baseline pressure distribution in no way resembled the classic long chord run plateaus known to produce NLF. It was felt that the TRO-3D code, in the pressure design mode, could be applied in this case to determine if it was physically possible to attain NLF-type pressure distributions within these geometric constraints (ref. 13).

Two target pressure distributions were selected which were known to support laminar flow to 55 and 65 percent chord from 2-D tests and were applied, for each case, at three stations spanning the wing. Six design variables were chosen: angle of attack, inboard and outboard camber shapes developed specifically for 3-D root and tip effects, inboard and outboard chordwise load shift shapes developed from the 2-D inverse code, and a leading edge incremental radius shape. All shape changes were constrained to be positive (volume added) and to act only on the upper wing surface outboard of the glove. Four optimization cycles and a total of 38 calls to the analysis code were required. Detailed descriptions of all shape functions and their development are given in reference 10.

Results of both design cases are shown in Figures 2 and 3. Excellent agreement with target pressures are obtained in both cases considering that the targets were selected with no a priori knowledge that a unique geometry (meeting the particular design requirements) existed. Figure 4 shows airfoil geometries at three span stations for both cases. Thus, NLF type pressure distributions can be attained at this flight condition while maintaining the strict geometric constraints. Given the original F-14 wing/body geometry set which already existed, the total time required to complete this preliminary stage of the wing design was two days. NASA LaRC personnel continued refinement of the wing design using both 2-D and 3-D methods, in particular to take into account aerodynamic performance at off design flight conditions and to reduce added thickness in the trailing edge flap hinge region at 75% chord.

#### TRANSONIC STORES LOADS PREDICTION

The latest extension to the NASA-Grumman Transonic Wing-Body Code, funded by a contract through NASA Langley Research Center, includes the additional capability to handle isolated or under wing, pylon mounted stores with multiple fore and aft fins (ref. 8). The use of a 5-level embedded grid approach ending in a fine, body-fitted store C-grid and employing exact body boundary conditions, yields accurate store loads prediction and

store/configuration interaction effects. The incorporation of a rotated finite difference scheme in all grids substantially increases robustness allowing more accurate treatment of low aspect ratio, highly swept and tapered wings. Supersonic farfield boundary conditions also allow for a limited supersonic freestream capability. All grid generation and interaction is done automatically.

The aerodynamic prediction capability of the code for isolated stores is demonstrated in figure 5 for the GBU-15 configuration (ref. 14). Both absolute levels of lift and moment through the full configuration component build-up, are accurately calculated. The store body results include viscous crossflow estimates. A more complicated geometry, the Nielson wing body/pylon/store configuration (ref. 15) is shown in figure 6. The strong wing-store interaction effects evident in the store pressures (fig. 7) are accurately predicted by the code. This latest version of NASA-Grumman Transonic Wing-Body Code will be relied upon heavily for a large percentage of external aerodynamic CFD design/analysis applications at Grumman.

### F-14A<sup>+</sup> TRANSONIC BUFFET

The first stage of a major F-14A upgrade to an F-14D (engine plus avionics) required changes to incorporate the F110-GE-400 engine. This version, designated F-14A<sup>+</sup>, required aft-end nacelle contour modifications, including the fuselage sponson fairings, and the interfairing between the pancake centerbody and the nozzle (figure 8) to accept the new engine. These contour modifications were completed during wind tunnel testing in April 1985. The new engine also had modified shapes for the nozzle flap and forward composite regions.

During initial flight testing of the full scale development aircraft, the pilot reported the appearance of buffet at transonic conditions, in particular  $M_{\infty}=0.8-1.0$  at 7500 feet altitude. This flight condition is encountered only transiently during acceleration, thus the buffet was not considered a major problem. Nevertheless, an effort was made to understand the causes of the buffet and suggest methods to possibly alleviate it.

Subsequent flight testing uncovered several pertinent pieces of information about the buffet. The frequency of motion induced at the pilot seat was seven Hertz, corresponding to the fuselage first bending moment. The buffet was alleviated by two in-flight configuration changes: opening the nozzle flaps to the max A/B position and cracking open ( $10^\circ$  deflection) the speed brake (located on the aft region of the pancake). It is also interesting to note that the aft pancake shape of the production F-14A was actually modified during its initial development to alleviate a very early buffet problem. The F-14A production pancake shows this effect as trailing edge notches on either side of the centerbody.

Several mechanisms were suspected as the cause of the buffet, and each gave rise to a plan of investigation. For the purpose of this paper we concentrate on one such area: possible strong shock/boundary layer interaction in the aft-end region due to the configuration changes. A general picture of the complex 3-D aft-end flowfield was sought using CFD. The hope was to predict if and where strong shocks, leading to possible flow separation and buffet, might be occurring. Also the predicted effect of max A/B nozzle and brake deflection configuration changes on the shock pattern and strength



should not be inconsistent with the flight tests; i.e., both changes alleviated the buffet (in this case presumably by weakening the shocks).

The 3-D TSD code with pylon mounted stores capability, described in the previous section, was used to investigate the effects of the nacelles, pancake and nozzles, see figure 9. Actual nacelle lines were converted into equivalent axisymmetric shapes for modeling in the body conforming stores portion of the code. Centerbodies for both the pre-production and production F-14A pancake were modeled as a pylon with the wing acting as a symmetry plane. A freestream Mach number of 0.93 was selected for the analysis. Figures 10, 11 and 12 show planform views of the analytically predicted shock patterns. In figure 10, the F-14A cruise (nozzle flaps in the cruise position) with the pre-production pancake (top of figure) shows a strong shock at station 800. The production pancake (bottom of figure) sweeps the shock, weakening it, and removes area after the shock. Both effects may have contributed to the ability of the production pancake to reduce the F-14A pre-production buffet. Figure 11 shows that the F-14A<sup>+</sup> cruise shape throws a strong shock at the center of the pancake at station 750, which is not there for the F-14A cruise. The opening of the speed brake for the F-14A<sup>+</sup> cruise, figure 12, shows that the shock at station 750 goes away. In the same figure, the opening of the F-14A<sup>+</sup> nozzle flaps to the max A/B position has an even more dramatic effect in that all pancake and nozzle shocks are removed.

The TSD code for this case should not be expected to predict exact shock positions since the model is geometrically approximate. But general trends can be used diagnostically. The TSD calculations show that the appearance and disappearance (or weakening) of the shocks with various configuration changes, i.e., opening the nozzle to max A/B or cracking open the speed brake, correspond to the appearance and disappearance of the buffet from flight test results. This suggests that a strong nacelle/pancake shock around the 750 fuselage station may be the cause of the aft-end buffet through unstable shock induced flow separation.

This being the case, then the buffet might be reduced by stabilizing the shock (or reducing its strength). Vortex generators placed forward of the shock, energizing the boundary layer, would tend to stabilize the shock by reducing the tendency for shock induced flow separation. Generally, though, a complete alleviation of buffet by this means would not be expected. As flight Mach number, and thus shock strength, continues to increase, shock induced flow separation would again dominate the flow, overriding the beneficial boundary layer energizing effects of the vortex generators. Thus a delay of buffet onset is most reasonably to be expected if the vortex generators are at all effective.

Previous, low speed, wind tunnel tests at Grumman had shown that the counter-rotating vortex generator configuration was the most effective and had a downstream effective length of approximately 30 inches. Thus to affect the shock patterns of the F-14A<sup>+</sup> with the cruise nozzle flaps shown in the lower portion of figure 11, two rows of counter-rotating vortex generators were attached to the upper surface pancake region and continued onto the inner portion of the nacelle. These rows were placed at positions just forward of the predicted shock locations. The forward row was placed at fuselage station 740 and the aft row at fuselage station 770.

Subsequent flight tests showed that these vortex generators did indeed affect the buffet levels as anticipated. Figure 13 shows a plot of flight test results of maximum peak-to-peak g's (measured at the pilots seat) for the aircraft as Mach number is increased. The vortex generators have reduced F-

14A<sup>+</sup> buffet levels to those of the F-14A except at the higher Mach numbers. In fact, if a level of 0.2 g's is taken as reference for buffet onset, this boundary for the F-14A<sup>+</sup> at Mach 0.75 was pushed to Mach 0.88. This is still not quite at the F-14A level of Mach 0.95, but is a substantial improvement.

#### THIN LAYER NAVIER-STOKES

The CFD methods discussed so far offer powerful tools to the designer as long as the flow remains attached, but future requirements and constraints are emerging which force the designer into dealing with, at times, very large regions of flow separation. External vortices generated by sharp forebody chines or wing leading edges can produce dominant aerodynamic forces. While vortex formation at sharp edges and subsequent convection through the flowfield may be approached with the Euler formulation (this avenue is also being studied at Grumman, see references 16, 17, and 18), flow separation from smooth surfaces such as wings at high loading levels and forebodies at high angles of attack can have profound effects on aerodynamic performance.

Internal designs for inlets and nozzles can experience even more difficulty in this area. New aircraft configurations are forcing the use of highly offset compact diffusers which may exhibit flow separation and strong secondary flows leading to large total pressure losses and distortion. Prediction of these losses during the design process is critical to engine and aircraft performance.

Strong viscous effects with large total pressure losses can be simulated only with some form of the Navier-Stokes equations. Grumman has been working with the time-dependent three-dimensional thin-layer Navier-Stokes (TLNS) code ARC3D (ref.19) developed at NASA Ames Research Center. ARC3D is based on the Beam and Warming implicit approximate factorization algorithm and is a central difference 2nd order accurate, fully conservative finite difference code employing the Baldwin-Lomax turbulence model. Various single grid topologies have been explored for external flow over arbitrary forebodies and wings and for internal duct flows. Grids are all constructed using the transfinite interpolation method (ref. 20). An efficient code for generating such grids has been developed by B. Wedan of NASA Langley Research Center and forms the basis of our grid generation codes, both external and internal.

Unfortunately, accurate full configuration TLNS analysis on a routine basis for design purposes is not yet realizable because of grid size limitations and very large CPU times. But single component analyses using up to 120,000 points and requiring about one hour CPU time on a CRAY XMP 1.4 have shown quite good results in many cases and can be used sparingly in critical design situations. A growing set of favorable comparisons of analysis with data for forebody, wing, and internal flows is helping to develop confidence in ARC3D as a robust and reliable design/analysis tool. The following cases are examples of using the TLNS code to aid in design work.

#### FUSELAGE LOADS ESTIMATION

During an aircraft configuration development or modification, a Master Maneuver Program (MMP), developed at Grumman, is used to determine aircraft component loads. Control surface deflections, control laws, and wind tunnel

aerodynamic data, along with component flexibilities are used to fly the configuration through the time histories of multiple maneuvers. The result is a series of time histories of component loads.

MMP prediction of fuselage loadings, particularly during sideslip maneuvers, depends upon establishing side force distributions at a variety of flight conditions. Generally, due to limited wind tunnel data (i.e. total forces), these distributions are estimated. For example, one side force distribution for the A-6A had been approximated by scaling a baseline triangular distribution to match total side force and adjusted by adding a sine wave couple to correctly place the center of pressure as determined from wind tunnel total forces. This baseline triangular distribution had been constructed for Mach 1.07,  $3.3^\circ$  angle of attack, and  $4.9^\circ$  sideslip (rolling pullout maneuver).

In keeping with advances in CFD, a general cooperative effort between the Aerodynamics and Loads sections at Grumman has begun to look at the possibility of using CFD to augment loads estimation methodology. The A-6F, being a recent design effort, was taken as one focal point. The A-6F configuration is an evolutionary development of the in-production A-6E. The A-6F includes updated avionics and advanced engine for improved aircraft performance. Specifically, the transonic side force distribution was investigated since, again, limited wind tunnel data would require a dependence on estimating procedures. The ability of advanced CFD methods to match wind tunnel data and validate the estimated baseline triangular distribution was of particular interest.

The first attempt to estimate the fuselage side force distribution was made with VSAERO (ref. 21). This allowed wing/body configuration analysis in sideslip (fig. 14). Unfortunately, viscous effects, which can play a major role in slender body forces at angle of attack are only weakly modeled, and the limitation to subsonic flow restricted the usefulness of VSAERO. Since no experimental load distributions were available, the analytic results were compared to wind tunnel (wing/body model) total forces, moments and center of pressure location. Even in the low speed cases, the VSAERO calculations placed the center of pressure far forward of the experimental data even after making allowances for viscous crossflow effects. This is consistent with an under-estimation of viscous effects.

To more accurately assess these viscous effects, the TLNS code was used to analyze the A-6F body alone geometry. Since side forces at relatively low angle of attack were sought, wing effects were not considered crucial at this point. This approach would also allow the full Mach range of interest to be covered. The complete cycle, pre-processing/analysis/post-processing for the TLNS calculations, was completed within two days. Full 3-D grids were generated over the A-6F fuselage using the transfinite interpolator and a "QUICK" surface model (ref. 3) for the configuration (fig. 15) with inlets faired over. The grid contained 96,000 points, 60 axial (clustered to the nose), 40 circumferential, and 40 radial (clustered normal to the surface). Each calculation required 40 minutes of CPU time on a CRAY XMP 1.4 to reduce the L2 residual (ref. 17) three orders of magnitude.

Comparisons to wind tunnel data in figures 16 and 17 for total forces in sideslip give some confidence that the TLNS analytic results are believable. Figure 16 shows the beta (sideslip) derivative of side force plotted over the transonic Mach range. At low speeds both VSAERO and TLNS slightly overpredict the wing/body side force derivative ( $C_{Y\beta}$ ). The lack of a wing in the TLNS model does not seem to be critical to this side force calculation. At higher

speeds VSAERO actually predicts an increasing derivative, probably due to the combination of the subsonic limitation and weak viscous effects, while the TLNS more correctly follows the wind tunnel test trend of decreasing derivative with Mach number. The TLNS Code's over-prediction of this derivative may be due to an insufficient number of grid points for the calculation. At Mach 1.07 the expected decrement due to angle of attack is correctly predicted. Figure 17 shows the beta derivative of the yawing moment plotted over the transonic range. Both VSAERO and TLNS do quite well in reproducing the wind tunnel results. Finally, in all cases, the VSAERO predictions place the center of pressure of the fuselage side forces well ahead of the nose while the TLNS code correctly follows the wind tunnel results by placing the center of pressure consistently just slightly aft of the fuselage nose.

Confident now that in terms of total side forces and moments, VSAERO and the TLNS codes are accurate at low speeds and the TLNS code is consistent with data in the transonic regime, the side force distribution can now be examined. Figure 18 compares both VSAERO and TLNS estimates to the original baseline triangular distribution. Note that both TLNS and triangular distribution are for full flight conditions, while VSAERO estimates are for reduced Mach number. Three points can be made. First, as might be expected, all distributions are in general agreement showing a forward concentration of side load. Second, both VSAERO and TLNS distributions show higher forward loadings and somewhat steeper gradients than the triangular estimate. Third, the larger, more aft loading of TLNS compared to VSAERO is expected due to the higher Mach number used for the TLNS calculation. It remains to corroborate these differences with wind tunnel testing and to understand their significance with respect to component loading. But these preliminary results indicate that advanced CFD methods can be useful in enhancing transonic loads estimating methodology.

#### COMPACT/OFFSET DIFFUSER

Highly offset, compact diffusers for advanced aircraft propulsion systems offer several advantages. These tightly packaged systems offer lightweight, low volume designs. They do have their disadvantages though. Large secondary flows including separation can lead to excessive total pressure distortions at the engine face and possibly engine stall. Limited experimental work and a need for a basic understanding of the physical phenomena, as applied to design methodology, prompted an internally funded program in this area within the Propulsion Section at Grumman (ref. 22). Experimental work was aimed at extending the compact diffuser data base and providing a relevant focal point for CFD calculations.

The offset diffuser test configuration is shown in figure 19. The basic diffuser design has a rectangular inlet transitioning to a circular engine face including a central compressor bullet. An offset of 50% of axial length is applied in one plane only. Forty total pressure probes cover the exit plane with a moveable rake of probes employed at various axial stations along the duct to determine losses near the wall. Static pressure ports were stationed from inlet to exit along top and bottom centerline. A removeable wall section was designed to accommodate various boundary layer control (BLC) devices including suction, blowing, and vortex generators. The test rig was back-pressured to yield a range of inlet flow conditions; of particular interest here is a throat (inlet) Mach number of 0.72.

Preliminary estimates of surface static pressures, separation location, and BLC mass flow to alleviate flow separation were made using the VSAERO Code and details can be found in ref. 22. Of particular interest here is the use of the TLNS Code to predict total pressure losses, engine face distortion, and to give us a better understanding of the role of separation and secondary flows in the loss process. The surface grid for the computational model is shown in figure 20. The 3-D grid, generated by transfinite interpolation, is a symmetric O-H topology containing 112,000 points with a centerline collapsed singularity surface. The grid is clustered axially towards the engine face and radially towards the wall where grid orthogonality is maintained.

The symmetry plane velocity vector plot in figure 21 shows lower surface flow separation occurring at about 40% down the duct length (enlarged portion at left of the figure), very close to the test results, and, in fact, the VSAERO prediction. The upper surface centerline (enlarged portion at right of the figure) shows a thickening of the boundary layer but no separation. VSAERO predicts flow separation at this point. Test results are inconclusive as to the appearance of flow separation here but do show large total pressure losses (9%) in this region, which the TLNS calculation, as will be shown later, quite nicely corroborates.

Figure 22 shows crossflow velocities indicating that at approximately 60% down the duct the initial formation of a vortex appears in the lower quadrant. This vortex is probably driven by the three-dimensional flow separation which had occurred just upstream as shown in the previous figure. This vortex intensifies and is driven further down into the lower quadrant as the exit plane is approached. The development of the total pressure profile normal to the lower wall, as we move down the duct, is shown in the lower part of figure 22. Agreement is fair, with the poorest comparison near the wall. The data show a maximum total pressure loss of approximately 25% near the wall at station D. As we move downstream to the exit at station F, the total pressure has actually recovered approximately 38% of the maximum loss which occurred at the upstream station D. This is most probably due to mixing from the vortex in this region. The TLNS calculation shows this beneficial mixing effect at the outer edge of this region but fails as we move closer to the wall. This is probably due to inadequate grid resolution in this critical region. The total pressure calculations at the exit plane between the bullet and the upper wall compare quite well to the data.

Figure 23 compares total pressure contours at the exit plane for the test data, on the left, and the TLNS calculation, on the right. The overall agreement is quite good, with the lower quadrant vortex position appearing slightly low, giving rise to an over-prediction of losses near the outer wall and an under-prediction near the center bullet. The upper region losses and pattern are accurately predicted. Figure 23 shows that calculated total pressure recovery (an area weighted average of exit total pressures referenced to the incoming total pressure) agrees very well with test data, and that max-min distortion values (the difference between maximum and minimum total pressures at a given plane referenced to the area weighted average at that plane) differ only by 2%.

## CLOSING REMARKS

Advances in CFD algorithms along with computer size and speed have come at a fast pace in the past five years. This has made available a wide range of new tools to aid the engineer in either the design of new configurations or in understanding and diagnosing problem areas in current aircraft. The development of transonic methods, in particular, spans the range from transonic small disturbance to full potential, Euler and finally the Reynolds averaged form of the Navier-Stokes equations (generally in a thin-layer formulation). For design and diagnostic applications the engineering group at Grumman has concentrated efforts at both ends of that spectrum, TSD and TLNS. Using the TSD formulation, the setup and analysis of very complex configurations can be handled fast, a particularly important requirement within the real world of project-oriented tasks, and quite accurately. As long as flow separation does not dominate the aerodynamics, this will continue to be the favored approach.

For cases where strong viscous effects are dominant and may lead to flow separation, neither full potential nor Euler methods offer any advantage over TSD. In addition, the time consuming and not always straight forward process of generating a computational grid over very complex configurations, required for the higher order methods, can become prohibitive. The most effective approach is judicious use of the TLNS method. The reward, i.e., calculation of very complex flow fields, is a powerful incentive but is gained at some expense. Complex multiple component configurations cannot be handled, since even if a grid could be generated within a reasonable period of time, the huge number of grid points would result in prohibitive computational times and cost. But much valuable information for design or diagnosis can be obtained by using the TLNS method for selective component analysis, keeping setup and computational times down to a more cost effective level.

It would appear that this route ignores the middle of the CFD spectrum, but that is not entirely true. The Euler formulation is beginning to show promise for full configurations which aerodynamically rely on vortex formation from sharp leading edges for added performance. For this type of flow, the Euler method is probably superior to both TSD and TLNS. The irrotational TSD formulation precludes vortex formation, and Euler is much faster and less costly than TLNS. A major effort in this area is being carried on in the Grumman Research Department and will surely filter up to the engineering applications level as needs arise and validation cases mount up. But to date, the ends of the CFD spectrum, TSD and judicious use of TLNS, have proven quite useful.

## ACKNOWLEDGEMENT

The author expresses his appreciation to the many individuals at Grumman whose efforts are included in this work: Bruce Rosen (TSD stores/F-14 buffet); James Capodieci, Ray Mangan and Dick Kita (F-14 buffet); Marty Bourbin (A-6F loads); Ron Tindell and Dr. Tom Alston (offset diffuser). A final recognition goes to Charles W. Boppe for general technical and editorial guidance.

ORIGINAL PAGE IS  
OF POOR QUALITY

## REFERENCES

1. Boppe, C. W.: Computational Aerodynamic Design: X-29, The Gulfstream Series, and a Tactical Fighter. SAE Paper 851789, October 1985.
2. Boppe, C. W.: Elements of Computational Engine-Airframe Integration. Progress in Aeronautics, Volume 102, 1986.
3. Boppe, C. W.: Transonic Flow Field Analysis for Wing-Fuselage Configurations. NASA CR-3243, May 1980.
4. Boppe, C. W.: Aerodynamic Analysis for Aircraft with Nacelles, Pylons and Winglets at Transonic Speeds. NASA CR-4066, April 1987.
5. Aidala, P. V.: Numerical Aircraft Design Using 3-D Transonic Analysis with Optimization. Volume 2, Part 2: Fighter Design. AFWAL-TR-81-3091, Volume 2, Part 2, U.S. Air Force, August 1981.
6. Rosen B. S.: Computational Transonic Analysis of Canted Winglets. Journal of Aircraft, Volume 21, pp 873-878, November 1984.
7. Rosen, B. S.: Body Flow Field Simulation and Force/Moment Prediction at Transonic Speeds. AIAA Paper 85-0423, January 1985.
8. Rosen, B. S.: External Store Carriage Loads Prediction at Transonic Speeds. AIAA Paper 88-0003, January 1988.
9. Aidala, P. V., Davis, W. H., Mason, W. H.: Smart Aerodynamic Optimization. AIAA Paper 83-1863, July 1983.
10. Davis, W. H., Aidala, P. V., Mason, W. H.: A Study to Develop Improved Methods for the Design of Transonic Fighter Wings by the Use of Numerical Optimization. NASA-CR-3995, August 1986.
11. Davis, W. H.: TRO-2D: A Code for Rational Transonic Airfoil Design by Optimization. AIAA Paper 85-0425, January 1985.
12. Woodward, F. A.: Analysis and Design of Wing-Body Combinations at Subsonic and Supersonic Speeds. Journal of Aircraft, Volume 5, No. 6, November 1968.
13. Waggoner, E. G., Phillips, P. S., Viken, J. K., Davis, W. H.: Potential Flow Calculations and Preliminary Wing Design in Support of an NLF Variable Sweep Transition Flight Experiment. AIAA Paper 85-0426, January 1985.
14. Shadow, T. D.: Wind Tunnel Tests to Determine the Distributed Loads on a 0.25 Scale GBU-15 (CWW) Model at Transonic Mach Numbers. AEDC-TSR-80-P14, February 1980.
15. Stahara, S. S., Crisalli, A. J.: Data Report for a Test Program to Study Transonic Flow Fields about Wing-Body/Pylon/Store Combinations. AFOSR TR-79-1070, May 1978.

16. Melnik, R. E.: An Overview of Computational Fluid Dynamics Development and Application at Grumman. Presented at NASA Conference on Supercomputers in Aerospace, NASA Ames Research Center, Moffett Field, CA, March 10-12, 1987.
17. Volpe, G., Siclari, M. J., Jameson, A.: A New Multigrid Euler Method for Fighter-Type Configurations. AIAA Paper 87-1160-CP, June 1987.
18. Volpe, G., Siclari, M. J., Jameson, A.: Computation of Aircraft Flowfields by a Multigrid Euler Method. AIAA Paper 87-2268-CP, August 1987.
19. Pulliam, T., Steger, J.: Implicit Finite-Difference Simulations of 3-D Compressible Flow. AIAA Journal, Volume 18, No. 2, pp. 159-167, February 1980.
20. Eriksson, L. E.: Generation of Boundary-Conforming Grids Around Wing-Body Configurations Using Transfinite Interpolation. AIAA Journal, Volume 20, No. 10, pp 1313-1320, October 1982.
21. Maskew, B.: Prediction of Subsonic Aerodynamic Characteristics: A Case for Low-Order Panel Methods. Journal of Aircraft, Volume 19, No. 2, pp. 157-163, February 1982.
22. Tindell, R. H.: Highly Compact Inlet Diffuser Technology. AIAA Paper 87-1747, June 1987.



ORIGINAL PAGE IS  
OF POOR QUALITY

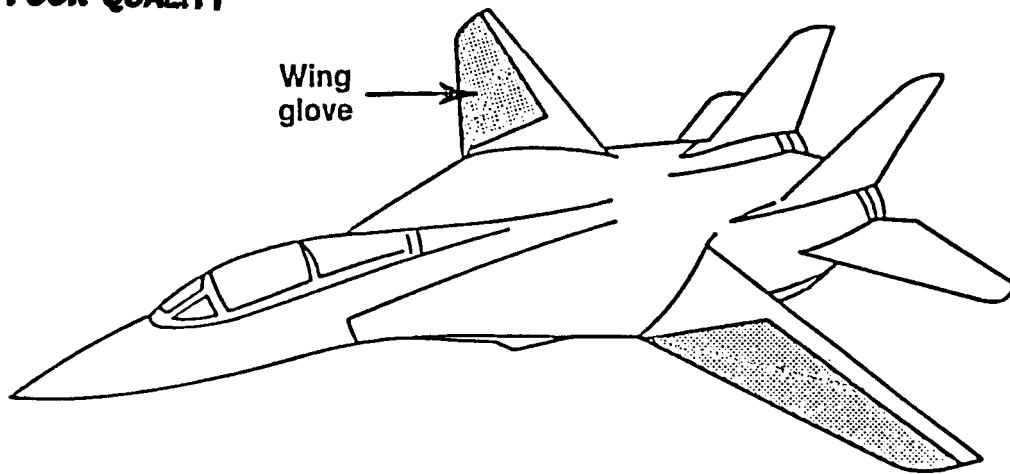


Figure 1. F-14/20° sweep configuration showing wing region available for NLF glove.

DESIGN TO TARGET WING PRESSURE DISTRIBUTION  
GEOMETRIC CONSTRAINTS  
M = 0.70  
CL = 0.40

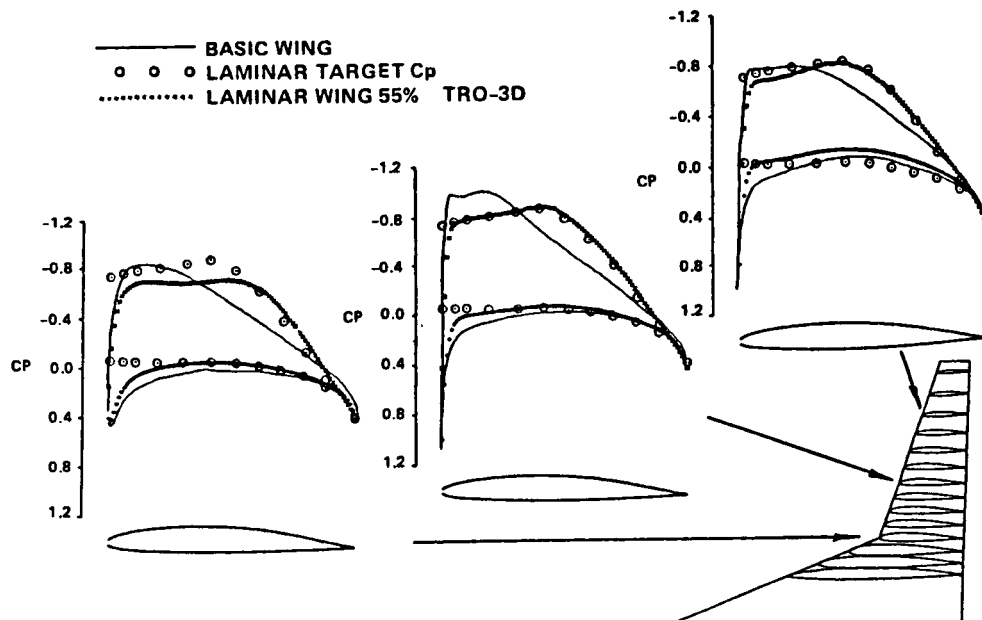


Figure 2. F-14/TRO-3D results for target pressure distribution with NLF to 55% chord.

DESIGN TO TARGET WING PRESSURE DISTRIBUTION  
 GEOMETRIC CONSTRAINTS  
 $M = 0.70$   
 $CL = 0.40$

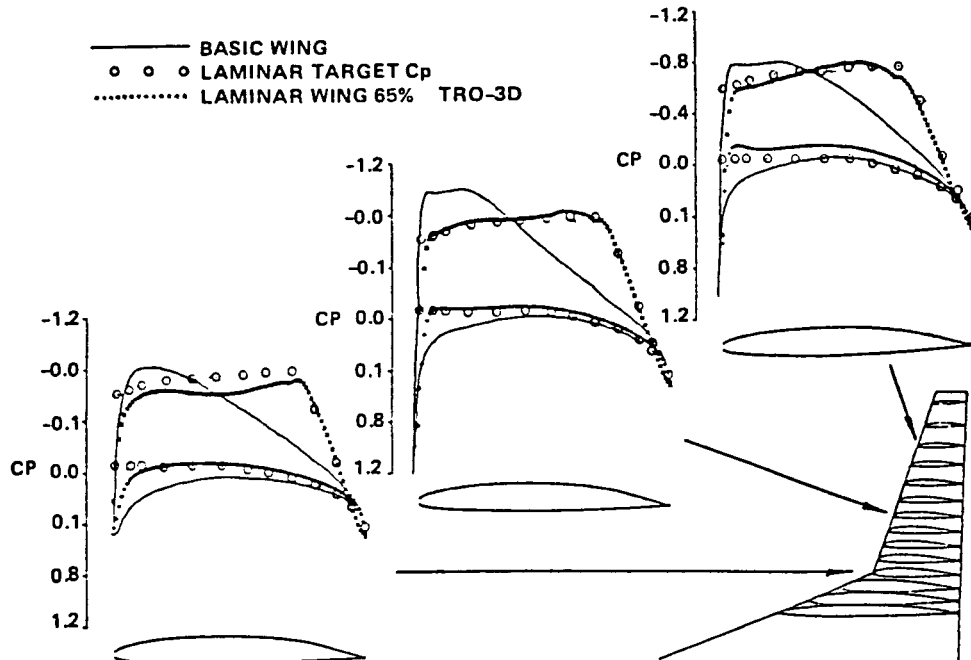


Figure 3. F-14/TRO-3D results for target pressure distribution with NLF to 65% chord.

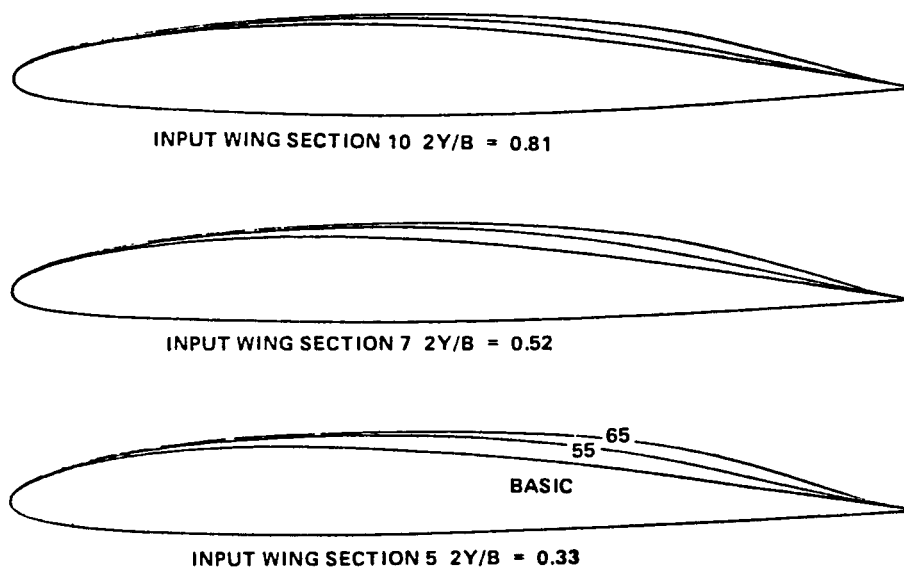


Figure 4. F-14/TRO-3D resulting airfoil shapes for NLF to both 55% and 65% chord.

$M = 0.95$   $\alpha = 6^\circ$

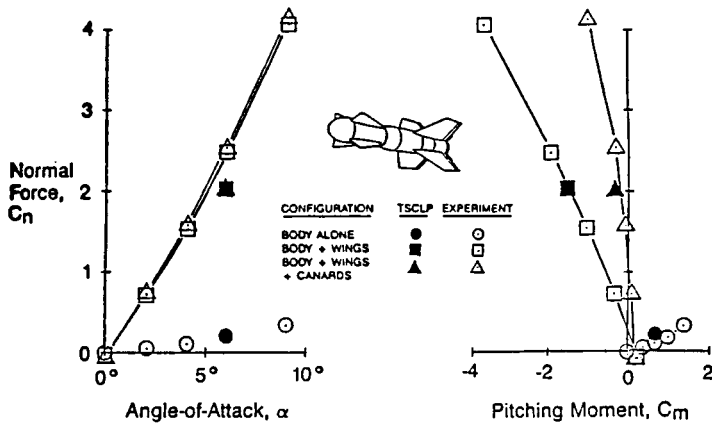


Figure 5. TSD: Force and moment correlation for GBU-15-CWW isolated store.

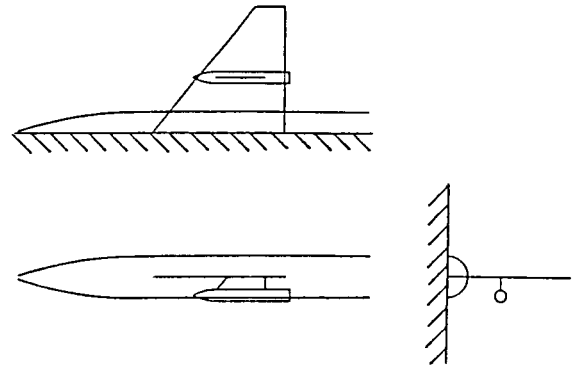


Figure 6. TSD: Geometry for Nielsen wing/fuselage/pylon/store.

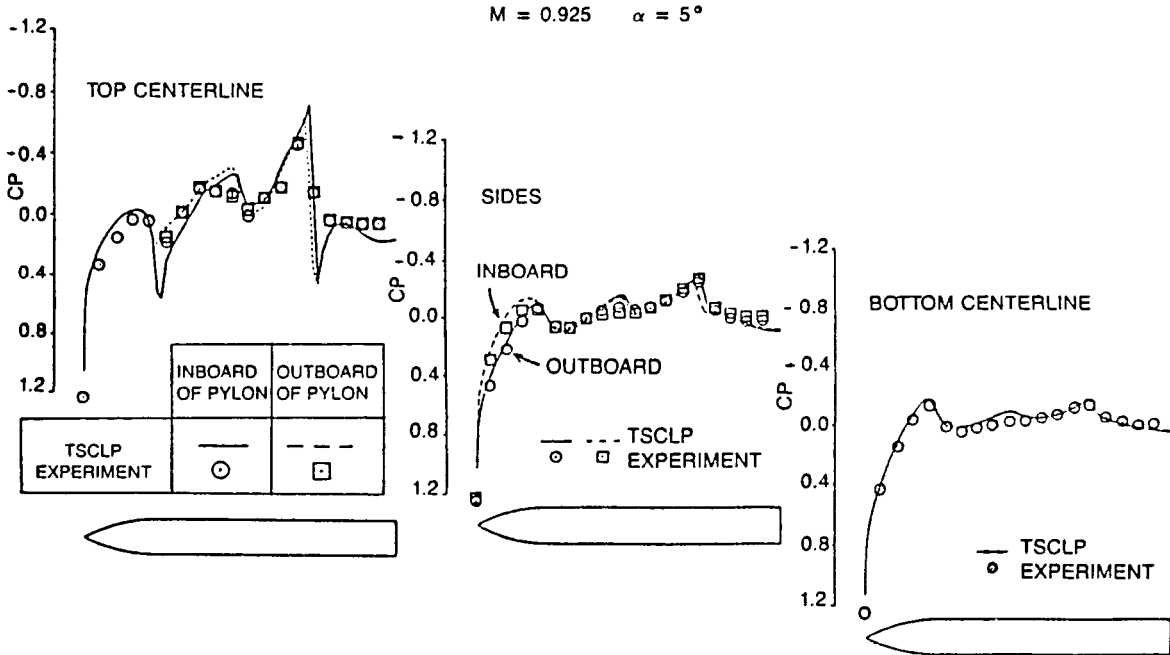


Figure 7. TSD: Store pressures for Nielsen wing/fuselage/pylon/store.

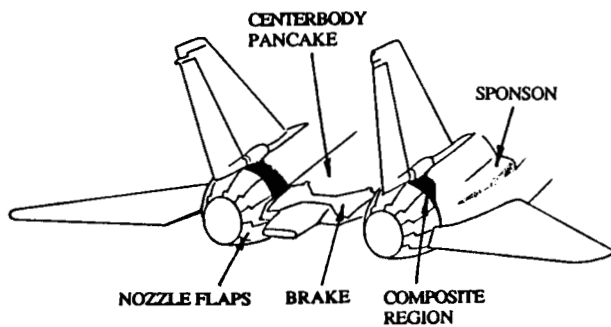


Figure 8. F-14A aft-end configuration.

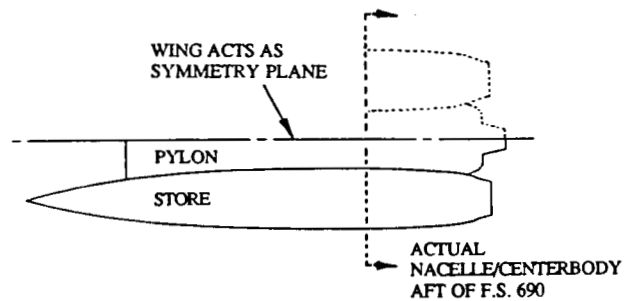


Figure 9. TSD model for F-14 aft-end buffet investigation.

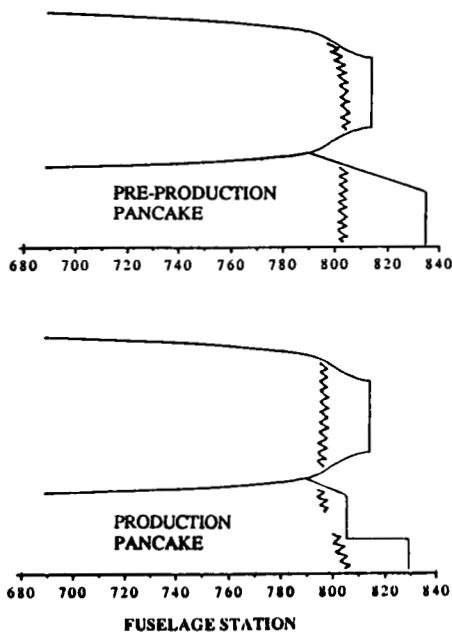


Figure 10. TSD predicted shock pattern. Effect of F-14A pre-production pancake modifications (cruise configuration at  $M_{\infty}=0.93$ ).

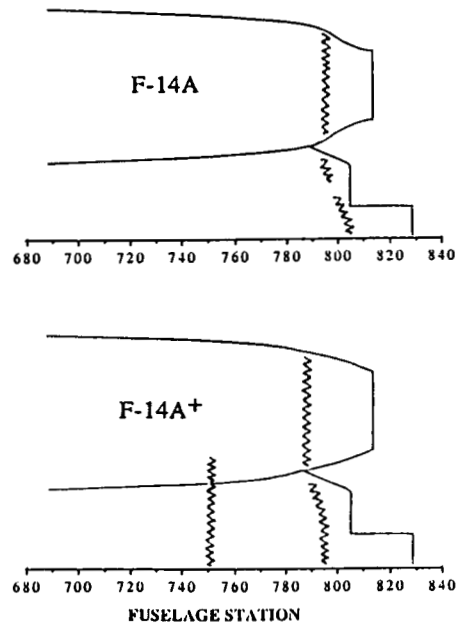


Figure 11. TSD predicted shock pattern. F-14A compared to F-14A<sup>+</sup> (cruise configuration at  $M_{\infty}=0.93$ ).

ORIGINAL PAGE IS  
OF POOR QUALITY

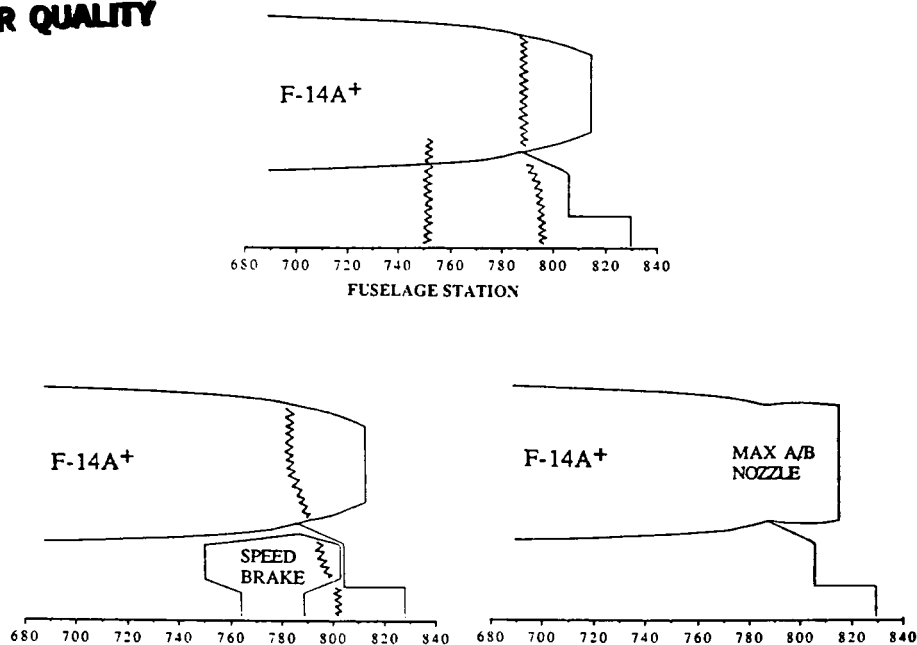


Figure 12. TSD predicted shock patterns. Effect of F-14A<sup>+</sup> configuration changes at  $M_\infty=0.93$ ).

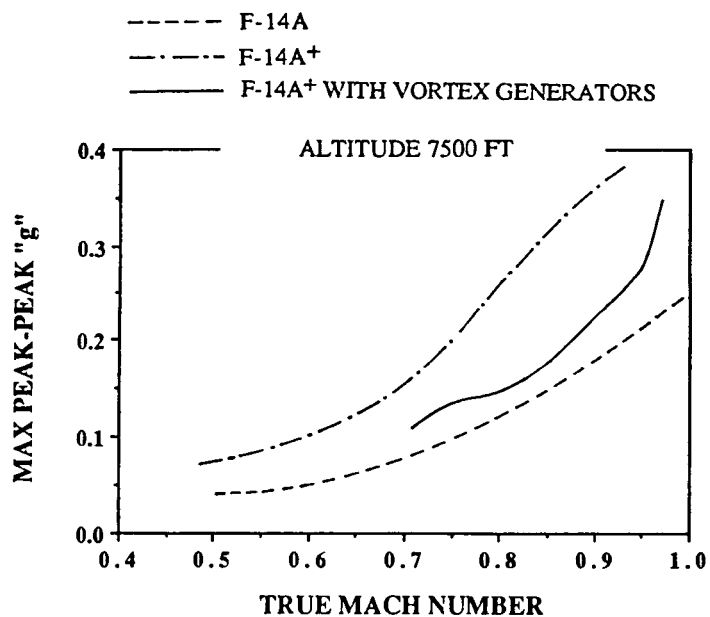


Figure 13. Flight test results. F-14A<sup>+</sup> transonic buffet: effect of vortex generators added to upper surface pancake and nacelles at F.S. 740 and 770.

ORIGINAL PAGE IS  
OF POOR QUALITY

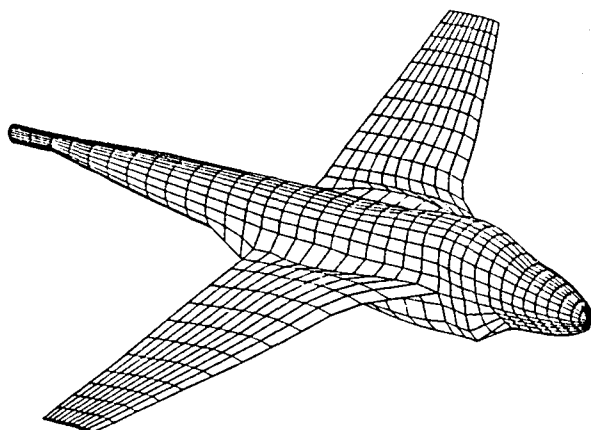


Figure 14. VSAERO panel model for A-6F side force distribution estimate.

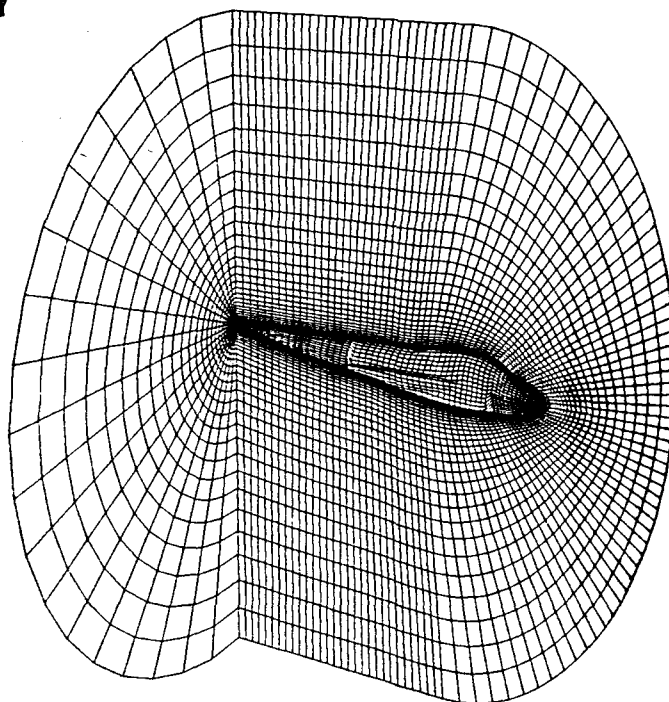


Figure 15. A-6F fuselage computational grid for TLNS calculation.

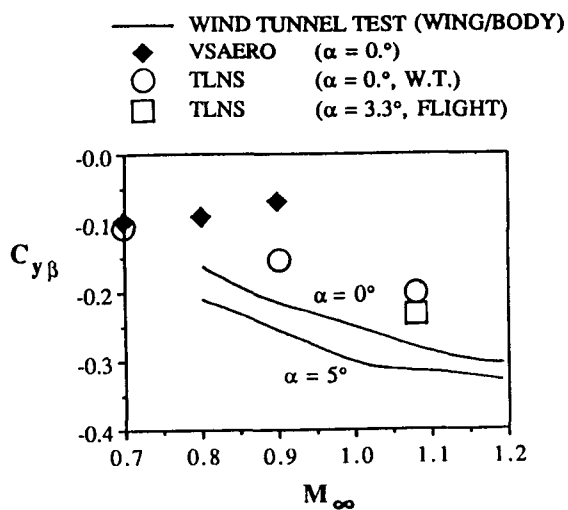


Figure 16. A-6F side force derivative in sideslip.

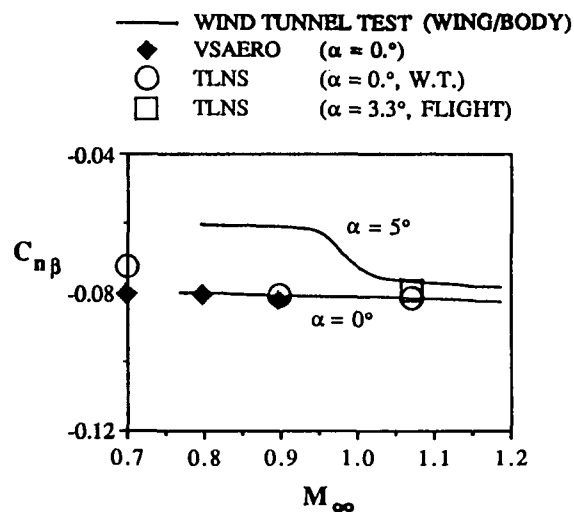


Figure 17. A-6F yawing moment derivative in sideslip.

ORIGINAL PAGE IS  
OF POOR QUALITY

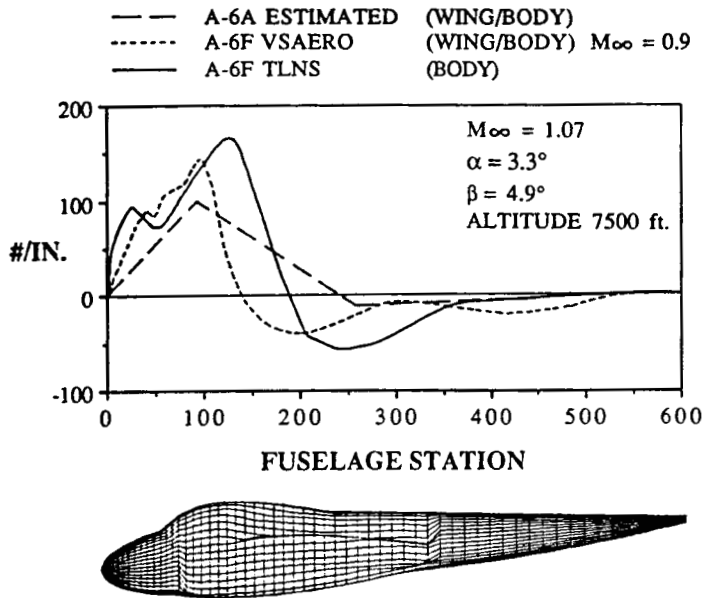


Figure 18. A-6F estimated side force distribution.

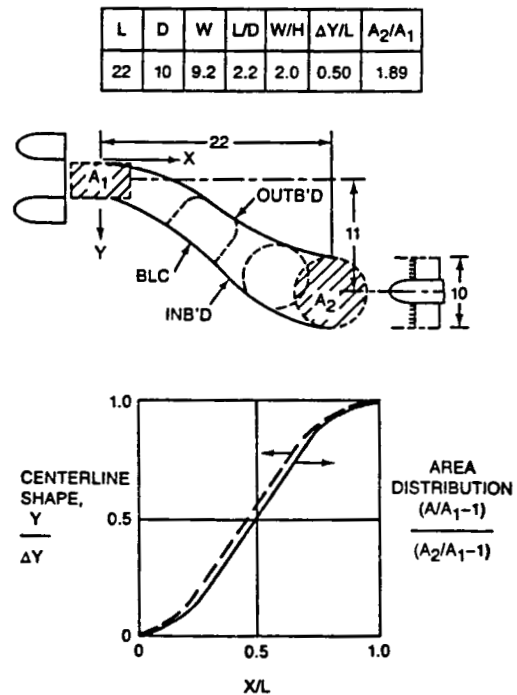


Figure 19. Offset diffuser test configuration definition.

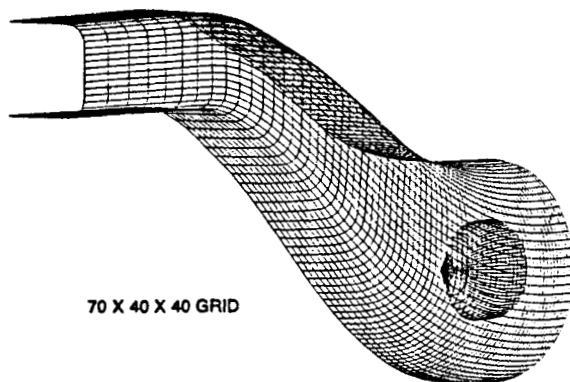


Figure 20. Offset diffuser computational surface grid for TLNS calculation.

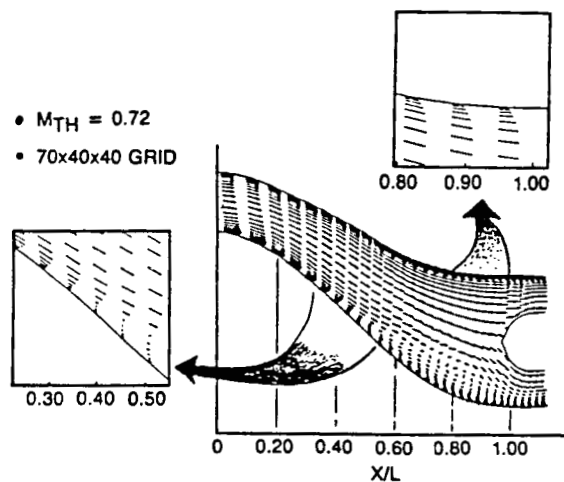


Figure 21. Offset diffuser symmetry plane velocity vectors from TLNS calculation.

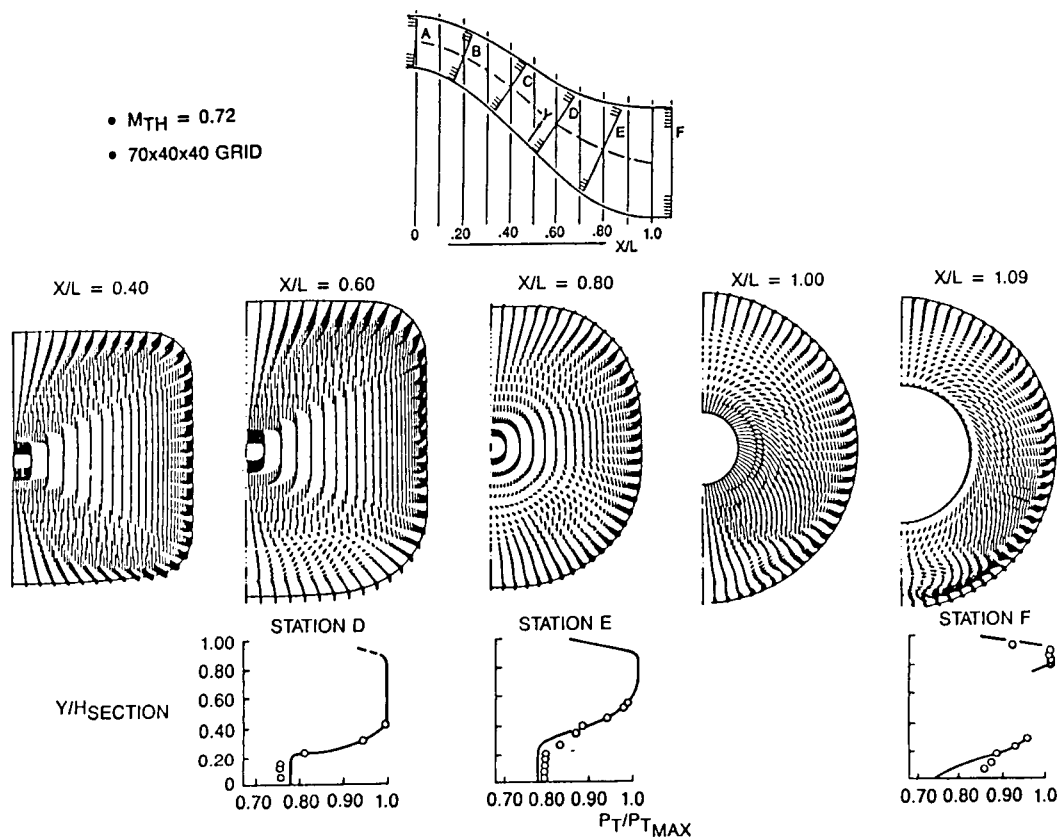


Figure 22. Offset diffuser cross-flow velocity vectors and wall total pressure losses, TLNS calculation compared to experimental data.

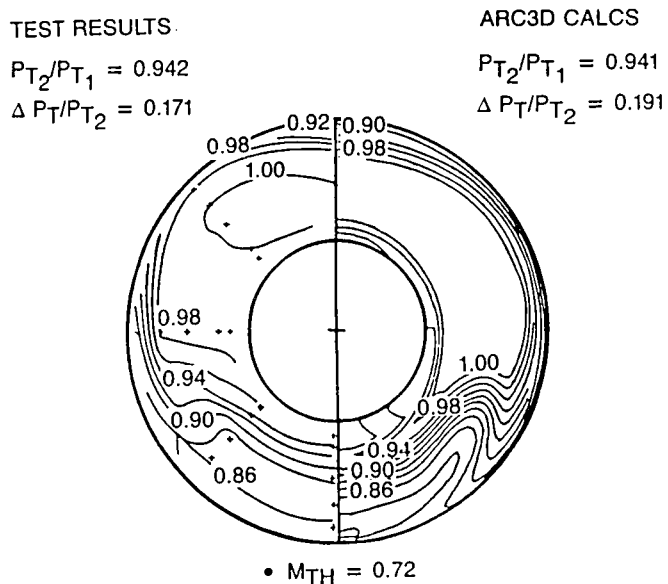


Figure 23. Offset diffuser exit total pressure profiles. TLNS calculation compared to experimental data.



**TRANSONICS AND FIGHTER AIRCRAFT:  
CHALLENGES AND OPPORTUNITIES FOR CFD**

Luis R. Miranda  
Lockheed Aeronautical Systems Company  
Burbank, California

**SUMMARY**

The application of computational fluid dynamics (CFD) to fighter aircraft design and development is discussed. Methodology requirements for the aerodynamic design of fighter aircraft are briefly reviewed. The state-of-the-art of computational methods for transonic flows in the light of these requirements is assessed and the techniques found most adequate for the subject application are identified. Highlights from some "proof-of-feasibility" Euler and Navier-Stokes computations about a complete fighter aircraft configuration are presented. Finally, critical issues and opportunities for design application of CFD are discussed.

**INTRODUCTION**

Progress in computational transonics, i.e. transonic CFD, has been most impressive in recent years. A measure of this can be obtained by comparing the papers being presented at this symposium with those given at the previous transonic symposium organized by the National Aeronautics and Space Administration (NASA) at the Ames Research Center in February 1981 (ref. 1). In that occasion, papers discussing CFD applications dealt with solutions of either the transonic small perturbation equation or the full potential equation about wing-alone or simple wing-body configurations. Presently, computations of solutions of the Euler equations about fairly complete aircraft configurations are becoming common. Furthermore, several pioneering computations of the Reynolds-averaged Navier-Stokes equations about wing-fuselage, and in some instances more complex configurations, are in progress, and some promising results have already been obtained. Yet, in spite of this rather sensational progress, the application of CFD to the design of fighter aircraft still poses a formidable challenge.

In this paper I intend to explain the magnitude of this challenge and share some of the experience and lessons learned in applying CFD at the Lockheed Aeronautical Systems Company (LASC). First, I will review the major requirements for the aerodynamic design of fighter aircraft. Then, I will briefly describe the computational methods and techniques that we have found most adequate for transonic applications. I will show highlights from Euler and Navier-Stokes flow computations about a complex fighter configuration to illustrate what is presently feasible with the state-of-the-art tools of CFD, but I will also discuss the principal problems and difficulties that the CFD practitioner faces today. This will help underscore the major developments that are needed to make CFD realize its full potential as an effective design tool for fighter aircraft. Finally, I will point out some opportunities for CFD applications that may greatly assist the designer even within the limits of present CFD shortcomings.

## FIGHTER AIRCRAFT DESIGN REQUIREMENTS

In general, advanced tactical aircraft must be designed to satisfy an extensive set of performance requirements. Figure 1 illustrates a typical design mission and the corresponding performance requirements for an advanced fighter. Usually, not one but several of these requirements become design drivers, as has already been discussed by Bradley in reference 2. For example, the following combination of performance requirements may dictate the design solution:

- o Transonic cruise
- o Sustained transonic maneuver
- o Supersonic cruise
- o Transonic acceleration

This multiple design point requirement is in contrast with transport aircraft, where usually a single performance consideration, i.e., cruise efficiency, becomes the paramount design driver. These multiple design points involve both attached and separated flow conditions (fig. 2), whereas cruise efficiency implies well behaved, attached flow. Furthermore, future fighter aircraft will be required to operate and, therefore, be controllable at very high angles of attack, beyond the onset of flow separation and maximum lift. Consequently, it will be crucial to determine how configuration details affect the onset of, and the behavior of the flow after separation. Major design features such as forebody shape, wing geometry, layout of control surfaces, etc., may be driven by the impact of these features upon the aerodynamic forces and moments at angles of attack beyond stall rather than by their effects in attached flow conditions.

A representative example of how relatively subtle configuration differences can greatly change the aerodynamic characteristics at high angles of attack is given by the effect of forebody shape on directional stability (fig. 3). The data presented in figure 3 were obtained from a number of fighter configurations with their vertical tails removed. All configurations are directionally unstable at low angles of attack and remain so until approximately 25 degrees. Above 25 degrees, cross-sectional shape effects become evident: the horizontal ellipse cross-sectional shape forebody turns directionally stable whereas the vertical ellipse forebody increases its instability.

In addition to the multiplicity and difficulty of flow conditions that the fighter aerodynamicist has to contend with, he must also deal with geometries that are complex and prone to generate strong interference effects among the configuration components (fig. 4). In many cases, the design depends on the maximization or tailoring of these interference effects as, for instance, in close-coupled canard configurations.

Airframe/propulsion integration is of paramount importance in fighter design, particularly with thrust-to-weight ratios equal to or greater than 1. This calls for flow computations at the inlet face, in inlet-diffuser geometries with duct offset and drastic cross-sectional shape variations, and about complex afterbody geometries.

Last but not least, all the related problems of weapons carriage and release, namely, store loads, separation characteristics, weapons bay cavity flows, etc., have to be addressed.

The designer of fighter aircraft must be able to deal with the nonlinear and difficult flow problems and complicated geometries discussed above because they are

predominant in fighter aerodynamics. In the past, his only means of doing this was the wind tunnel. But now, advanced CFD methodology is beginning to offer the possibility of dealing with the vexing problems of nonlinear aerodynamics. Although the jury is still out regarding the ultimate value of CFD as a fighter design tool, rapid progress is being made and valuable lessons are being learned in our efforts to apply CFD to fighter aircraft. The CFD methods and techniques that we have found to be most appropriate for fighter design application are discussed in the following section.

## COMPUTATIONAL TRANSONICS FOR FIGHTER AIRCRAFT

The experience at LASC with CFD methods for transonic flow analysis has covered a broad spectrum of the presently available methodology, as shown in table 1. Codes based on either the transonic small perturbation (TSP) equation or the full potential (FP) equation, though they may be suitable for some limited and specific applications, have been found to be inadequate for general fighter aircraft application. The reason for this is obvious: most fighter aerodynamic problems violate the assumptions of small perturbations (the fundamental assumption for the TSP equation) and irrotationality (inherent to both the TSP and FP formulations). Vortex flows play a preponderant role for highly swept leading edges and sharp edges, features which are commonly found on fighter configurations. An example of the difference between potential flow and Euler solutions for this class of problem is illustrated in figure 5. This example clearly underscores the inadequacy of potential flow methods for the analysis of free vortex flows.

The need to deal with vortex flows, strong shock waves, and, eventually, separated flows, has led us to concentrate on Euler and Reynolds-averaged Navier-Stokes (R-A N-S) methods in our transonic CFD work. At the present time, our experience with Euler codes is much more extensive than with R-A N-S codes. But thanks to the recent availability of supercomputers with very large memory capacity, we are rapidly expanding our R-A N-S experience base.

The majority of practical methods for solving the Euler and Navier-Stokes equations are based on either finite difference or finite volume numerical approaches. Finite difference schemes result from the discretization of the partial differential formulation of the equations of fluid flow. Finite volume schemes are derived by discretizing the integral formulation of the flow equations. Although in principle both approaches are equivalent, their actual numerical implementations involve differences which make finite volume methods more robust for obtaining flow solutions about the type of geometries characteristic of fighter aircraft. This is because finite difference methods, due to the differential nature of their formulation, are more sensitive to boundary singularity problems, such as sharp edges and surface slope discontinuities. Accordingly, we have emphasized the development and application of explicit, time-stepping, finite-volume techniques for the solution of both the Euler and Navier-Stokes equations. These techniques are based on the work of Jameson et al (refs. 3-4).

Experience with realistically complex and complete aircraft geometries has taught us that codes requiring single global computational grids are woefully inadequate. For general applications, codes must be able to handle multiple zonal grid blocks (fig. 6). Otherwise, computer memory requirements increase substantially, and more seriously, the grid generation task, which is already difficult and time-consuming, becomes much more complicated, and in some instances, practically impossible.

The two approaches commonly used for generating multiple zonal grid blocks are 1) grid embedding, and 2) grid patching (fig. 7). In the grid embedding approach, computational grids are generated about the principal configuration components (e.g., wing, nacelle, fuselage, etc.) as if they were in isolation, and then they are assembled together in an overlapping fashion. In the grid patching approach, the various zones are separated by interfacing surfaces and there is no grid overlap between the zones. Although grid embedding facilitates the use of boundary conforming orthogonal grids, it has some serious drawbacks: it requires special interpolation schemes for the overlapped regions, it leads to cumbersome data structures, and it makes conservation of the pertinent flow quantities difficult to preserve. Grid patching, on the other hand, makes boundary conforming grids with reasonable orthogonality more difficult to achieve, but instead, it possesses some very good attributes for practical application such as well ordered data structures, good conservation properties, and good convergence and accuracy characteristics. Because of these attributes, we have elected to work with grid patching instead of grid embedding.

The above considerations have guided the development at LASC, and under partial funding from the USAF Flight Dynamics Laboratory, of the TEAM (Three-dimensional Euler Aerodynamic Method) and TRANSAM (Three-dimensional Reynolds-Averaged Navier-Stokes Aerodynamic Method) codes (refs. 5-8). These codes incorporate cell-centered finite volume flow solvers with explicit multistage Runge-Kutta time marching. They can operate on multiple block zonal grids of arbitrary topology with the three different types of zonal interfaces illustrated in figure 8. The treatment of the zonal interfaces has been formulated along the lines proposed by Rai (ref. 9).

The TEAM code solves the Euler equations for inviscid flow. These equations contain all of the continuum flow physics except for viscosity. Rotational flows, such as vortex flows, and strong shock waves can be simulated with the Euler equations. The TRANSAM code is an extension of the modularized TEAM computational system to which momentum fluxes due to both viscous and Reynolds, namely, turbulent flow stresses have been added. Either the full Reynolds-averaged or the thin shear layer approximations to the Navier-Stokes equations can be solved at the user's option; the user can also choose between algebraic and two-equation turbulence models. Because of its zonal architecture, different equation sets can be solved in different zones. For instance, the thin shear-layer equations can be solved in zones close to solid boundaries where boundary-layer behavior is to be expected; all the shear stress terms can be accounted for in zones where fully separated flow is likely to occur; and, finally, the Euler equations can be used to model the flow for the remaining, essentially inviscid, zones. This approach yields substantial savings in both computer execution time and memory requirements.

#### ADVANCED CFD APPLICATION HIGHLIGHTS

With the TEAM and TRANSAM codes it is now feasible to perform both inviscid (TEAM) and viscous (TRANSAM) flow computations about arbitrarily complex and complete aircraft configurations at subsonic, transonic, and supersonic mach numbers. "Proof-of-feasibility" computations have recently been performed at LASC using the supersonic vertical/short take-off and landing (V/STOL) fighter concept of reference 10, which is known as the Advanced Nozzle Concept (ANC) configuration. This configuration was selected for these "proof-of-feasibility" computations due to its challenging geometric complexity (fig. 9). The computations were done on the LASC Cray X-MP/24 supercomputer.

A partial view of the grid used for the inviscid Euler computations is shown in

figure 10. A total of 288,750 finite volume cells was required to cover half the configuration, which is symmetrical about the x-z plane. These cells were distributed in 25 different zones; the largest zonal block containing 35,464 cells, and the smallest one 252 cells.

The surface pressure distribution computed by the TEAM code, at an angle of attack of 4.8 degrees and mach number of 1.2, is shown in color-coded displays in figures 11 and 12. The computational mesh on the airplane surface is also visible in these figures. In the TEAM computations the nacelles were treated as flow-through ducts, in other words, power effects were not simulated. The differences between the numerically computed and wind tunnel measured values were 5 percent for lift and 8 percent for pitching moment. Drag correlation has not yet been attempted due to the lack of modeling of the wind tunnel model support system. Reasonable correlation was obtained for the one wing station, just outboard of the nacelles, for which some rather sparse experimental surface pressure distribution data were available.

For the Navier-Stokes computations, 521,224 cells were required to cover half the configuration. These cells were distributed in 27 different zones; the largest zonal block containing 42,312 cells, and the smallest one 480 cells. The total number of cells was constrained by computer memory and processing time considerations. A larger number of cells is desirable for an accurate viscous computation. In particular, because of computer capacity constraints, the grid coverage over most of the fuselage is considered quite inadequate for viscous flow simulation.

The surface pressure distribution computed by the TRANSAM code at the same flow condition shown previously for the Euler case (angle of attack of 4.8 degrees and mach number of 1.2) is presented in color-coded displays in figures 13 and 14, which also illustrate the computational surface grid. Representative boundary layer velocity profiles for the wing upper surface are shown in figure 15. The Reynolds number, based on the wing mean aerodynamic chord, was 6.5 million. The thin shear layer approximation to the Navier-Stokes equations was used for this computation. Fully turbulent flow was assumed, turbulence being modeled with a modified Baldwin-Lomax eddy viscosity. Little difference can be observed between the viscous and inviscid computations for this case. Some minor improvement was observed in the correlation of computed lift and pitching moment with experimental data.

These computations will be continued as soon as a Solid-state Storage Device (SSD) is attached to the LASC Cray supercomputer, adding 128 megawords of fast access memory. This will allow increasing the grid density for adequate simulation of viscous and separated flow characteristics. Similar computations to study the adequacy of TRANSAM for high angle of attack flows about fighter configurations are planned for the NASA Ames Research Center Numerical Aerodynamic Simulator (NAS).

#### CRITICAL ISSUES FOR DESIGN APPLICATION

The potential capability of CFD methodology, which the preceding examples give a glimpse of, is remarkable. The challenge is to convert this capability from potential into actual within the constraints imposed by the design environment. To do this successfully, much work remains to be accomplished. Our recent experience underscores the critical importance of the following four major issues:

- 1) Grid sensitivity: Results of Euler and Navier-Stokes computations - even those based on supposedly robust schemes such as finite volume - display a

high degree of sensitivity to the characteristics of the computational grid: density, distribution, and skewness. In many cases this sensitivity is more pronounced than that due to the type of mathematical model being used, e.g., Navier-Stokes versus Euler equations. Grid characteristics also affect the convergence of the solution process for time-stepping methods.

Two examples are used here to underline the impact of grid features on the quality of the solution. The first one (fig. 16) shows the effect of grid density (coarse versus fine) on the surface pressure distribution on the Onera M6 wing near the tip. The second one, internal flow computations for a subsonic diffuser (fig. 17), illustrates the effect of grid point distribution. Three computations were carried out with an inlet Mach number of 0.72: an Euler (TEAM) and two turbulent Navier-Stokes (TRANSAM) computations. The latter were done at a Reynolds number of about 1.7 million (based on duct diameter) using an algebraic eddy viscosity model. The first viscous computation was performed on the same grid used for the inviscid computation. This grid had some clustering of points near the solid boundaries; otherwise, it was uniformly spaced. Grid clustering near the walls was increased twofold for the second viscous computation, but the total number of cells was kept constant (31 in the radial direction). The corresponding velocity profiles (fig. 17) show the strong influence of grid spacing; it is quite obvious that the results from the first viscous computation are physically unrealistic.

To resolve the grid sensitivity problem we must come up with means of a) determining the adequacy of a computational grid for reliable results, and b) adjusting the grid to become adequate in the areas found deficient. Computationally-adaptive grids offer much promise in this respect although the development of robust algorithms for three-dimensional and multiblock zonal application will not be easy.

- 2) **Turbulence modeling:** Turbulence modeling is the Achilles' heel of Reynolds-averaged Navier-Stokes codes. Reference 11 provides a concise but comprehensive survey of the state-of-the-art in turbulence modeling. This survey makes obvious that many difficulties remain. Experience with separated flows indicates that the presently available algebraic turbulence models are inadequate to predict strongly separated flows with reasonable accuracy and consistency. Usually, extensive code calibration is required to reproduce experimental results. Furthermore, these calibrations tend to be restricted to relatively narrow classes of problems. The degree by which more sophisticated models (such as the two-equation or Reynolds stress models) will improve the accuracy of separated flow computations remains to be determined.
- 3) **Timeliness:** The time from "blueprint" to first satisfactory nonlinear CFD solution is presently totally inadequate for design application. The Euler and Navier-Stokes solutions about the supersonic V/STOL fighter shown above required about six months of effort to obtain. Similar computations conducted on an F-16 configuration (ref. 12) have taken about a year to complete. The principal cause for this is the difficulty of generating adequate computational grids for complex three-dimensional configurations. Fortunately, significant progress is being made in this area. Advanced graphics software and hardware developments, e.g., color graphics workstations, are beginning to aid and speed up the grid generation process. Finite-volume zonal methods, like the ones discussed in this paper, facilitate the grid generation task. Application of artificial intelligence and expert systems technology will probably help accelerate grid generation.

In addition, alternate approaches to the treatment of complex geometries are being actively pursued, examples of which are the work discussed in references 13 and 14. These alternate methods allow the use of either cartesian non-boundary-conforming or non-structured grids.

For Navier-Stokes codes the timeliness issue is further aggravated by the extensive calibration and numerical experimentation which are required to overcome the shortcomings of present turbulence models.

- 4) **Validation:** A code can be considered validated when its accuracy and range of validity have been determined sufficiently well to be applied, without calibration, to the problem of interest with a high degree of confidence. Validation of flow field solvers, such as the Euler and Navier-Stokes codes, requires experimental data of special type and quality which presently are very scarce. Consequently, very few, if any, of the advanced CFD codes can be considered to be validated in the true sense of the word. Yet, validation is a most important factor in determining the acceptance of a CFD code by the design community.

#### OPPORTUNITIES FOR CFD APPLICATION

In the light of the previous considerations, it may be argued that, at the present time, nonlinear CFD methodology is more postdictive than predictive in nature. This may be so due to the difficult problem posed by fighter aircraft design requirements. Lest we forget, wind tunnels also face difficulties that, although different in nature, are equally serious: wall and support interference, Reynolds number effects, difficulty or impossibility of simulating unsteady motions, etc. Furthermore, CFD should be viewed not as a tool to replace the wind tunnel, but rather as a tool to complement the wind tunnel. With this in mind, there are many opportunities for valuable application of CFD to fighter design, even within its present limitations. Some of these opportunities are

- o **Design:** It has already been pointed out how the design of a fighter aircraft depends on predicting aerodynamic characteristics for flow conditions for which the present accuracy of CFD is questionable. Yet, in the design or synthesis process, oftentimes it is sufficient to determine qualitatively, rather than quantitatively, which of the design options under consideration is the best. In this sense, CFD methodology is quite capable. The timeliness issue is the only major obstacle to its full suitability as a synthesis tool.
- o **Wind tunnel corrections:** Correcting wind tunnel data for wall and model support interference is well within the realm of CFD capability. With due calibration, correcting for Reynolds number effects should also be quite accurate.
- o **Experimental data enrichment:** Postdiction can be quite useful when properly used. CFD can provide flow field description and details that are beyond the practical capability of even the most advanced experimental techniques. Thus, after careful calibration, it can be used to enrich and expand the experimental database and to help diagnose unusual problems uncovered by testing.
- o **Airloads prediction:** This is one application area where CFD can be used to great advantage. Nonlinear CFD methodology offers significant improvement in

accuracy over classical linearized methods, as the example of figure 18 indicates. With a reasonable amount of calibration based on simpler wind tunnel models, it should be possible to obtain loads data for structural design of adequate accuracy and detail at a much earlier stage in the design process than that provided by the expensive pressure loads models currently used.

- o Configuration modification evaluation: The ability of CFD to predict incremental values more accurately than absolute levels is well recognized, and it has been demonstrated on many occasions. Therefore, CFD is a most useful tool in assessing the effects of configuration perturbations, particularly after calibrating the method on the baseline geometry.

These application opportunities by themselves make CFD a valuable tool for fighter design and development. But to take full advantage of them, it is imperative that the time and labor required for the computational grid generation process be greatly reduced.

#### CONCLUDING REMARKS

CFD is becoming an increasingly powerful tool for the aerodynamic design and analysis of aerospace systems. Fighter aircraft, because of the multiple design point requirements involving difficult flow conditions, present a formidable CFD application challenge. Several "proof-of-concept" computations are beginning to demonstrate the ultimate potential of CFD, but much remains to be accomplished before CFD can be accepted as a fighter aircraft design and development tool with a high level of confidence.

Our experience has helped identify the multiblock zonal, finite volume, time marching flow solvers as the presently preferred approach for fighter aircraft design and development application. It has also highlighted four crucial issues that must be successfully resolved to turn CFD into a practical and reliable design and development tool: grid sensitivity, turbulence modeling, timeliness, and validation. The task is not easy, but it is feasible and the benefits are high.

#### ACKNOWLEDGEMENTS

The author is indebted to the staff of the Computational and Advanced Aerodynamics Department at the Lockheed Aeronautical Systems Company - Burbank for providing technical assistance and consultation. Especially, the contributions of K. K. Mani, who performed the Euler computations on the ANC configuration, C. R. Olling, responsible for the corresponding Navier-Stokes solutions, and P. Raj were crucial to the preparation of this paper. K. Henry assisted in the preparation of the text and technical art material.



## REFERENCES

1. Nixon, D. (editor) : Transonic Aerodynamics. Progress In Aeronautics and Astronautics, Volume 81, 1982.
2. Bradley, R. G.: Practical Aerodynamic Problems - Military Aircraft. Progress in Aeronautics and Astronautics, Volume 81, 1982, pp. 149-187.
3. Jameson, A., Schmidt, W., and Turkel, E.: Numerical Solutions of the Euler Equations by Finite Volume Methods Using Runge-Kutta Time-Stepping Schemes. AIAA Paper 81-1259, 14th Fluid and Plasma Dynamics Conference, Palo Alto, California, June 23-23, 1981.
4. Jameson, A., and Baker, T. J.: Solution of the Euler Equations for Complex Configurations. Proceedings AIAA 6th Computational Fluid Dynamics Conference, Danvers, Massachusetts, 1983, pp. 293-302.
5. Miranda, L. R.: CFD Applications: The Lockheed Perspective. NASA Conference Publication 2454, pp. 77-85, Moffett Field, California, March 10-12, 1987.
6. Raj, P., and Long, L. N.: An Euler Aerodynamic Method for Leading-Edge Vortex Flow Simulation. NASA Conference Publication 2416, pp. 263-282, Hampton, Virginia, October 8-10, 1985.
7. Raj, P., Sikora, J. S., and Keen, J. M.: Free-Vortex Flow Simulation Using a Three-Dimensional Euler Aerodynamic Method. ICAS Paper 86-1.5.2, 15th Congress of the International Council of the Aerospace Sciences, London, United Kingdom, September 7-12, 1986.
8. Raj, P., and Brennan, J. E.: Improvements to an Euler Aerodynamic Method for Transonic Flow Analysis. AIAA Paper 87-0040, AIAA 25th Aerospace Sciences Meeting, Reno, Nevada, January 12-15, 1987.
9. Rai, M. M.: A Conservative Treatment of Zonal Boundaries for Euler Equation Calculations. AIAA Paper 84-0164, Reno, Nevada, 1984.
10. Zilz, D. E., and Devereaux, P. A.: Propulsion and Airframe Aerodynamic Interactions of Supersonic V/STOL Configurations. NASA Contractor Report 177343, September 1985.
11. Lakshminarayana, B.: Turbulence Modeling for Complex Shear Flows. AIAA Journal, Vol. 24, No. 12, December 1986, pp. 1900-1917
12. Flores, J., Reznick, S. G., Holst, T. L., and Gundy K.: Transonic Navier-Stokes Solutions for a Fighter-like Configuration. AIAA Paper 87-0032, Reno, Nevada, January 12-15, 1987.
13. Samant, S. S., Burkhart, R. H., Bussoletti, J. E., Everson, B. L., Johnson, F. T., Young, D. P., Erickson, L. L., Madson, M., and Woo, A. C.: TRANAIR: A Computer Code for Transonic Analyses of Arbitrary Configurations. AIAA Paper 87-0034, Reno, Nevada, January 12-15, 1987.
14. Jameson, A., and Baker, T.: Improvements to the Aircraft Euler Method. AIAA Paper 87-0452, Reno, Nevada, January 12-15, 1987.

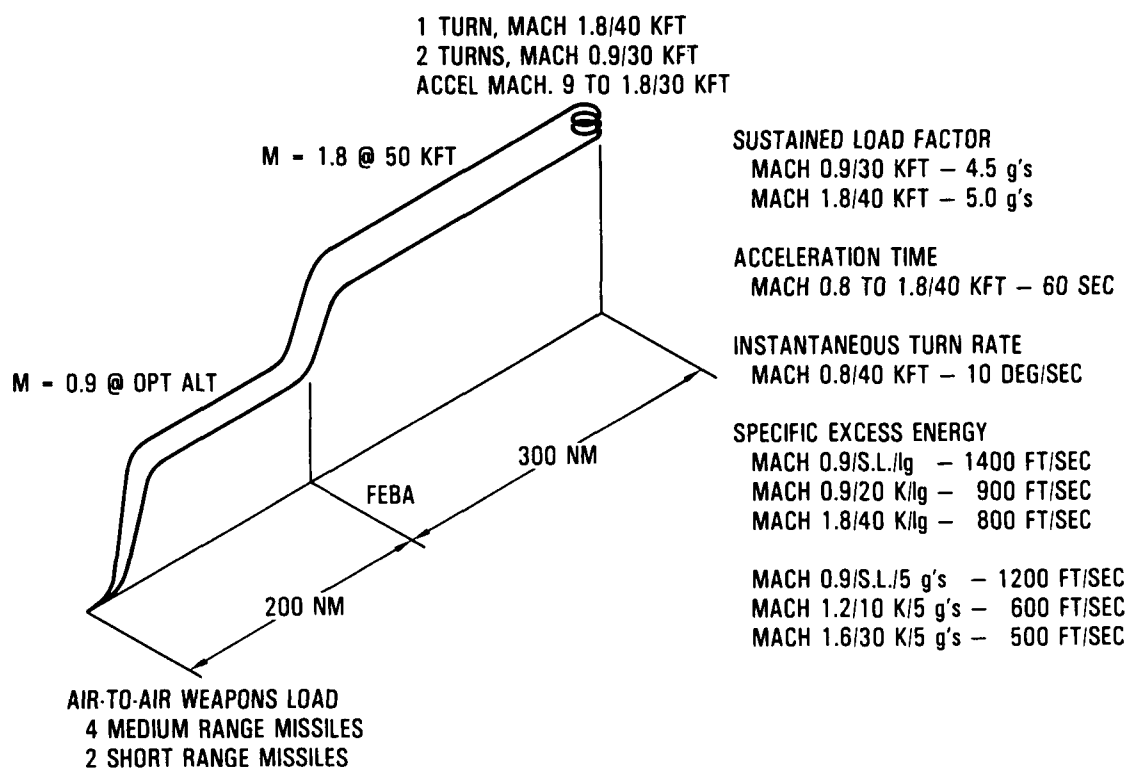


Figure 1 Typical Fighter Design and Performance Requirements.

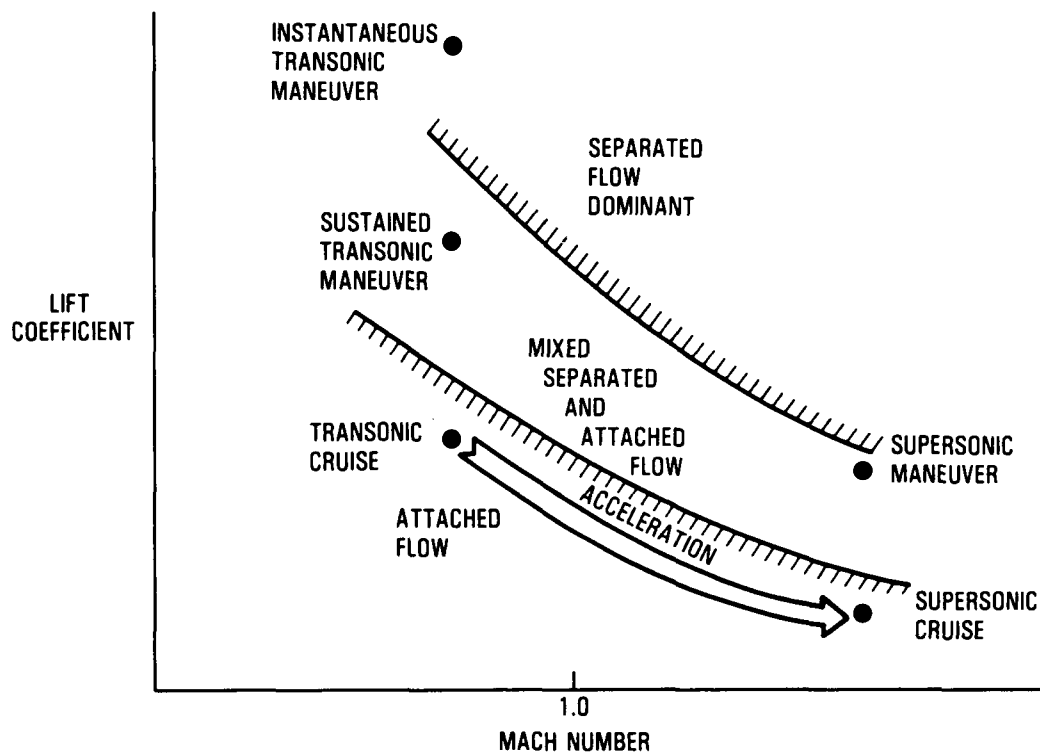


Figure 2 Multiple Design Points and Flow Conditions for Advanced Fighter Aircraft.

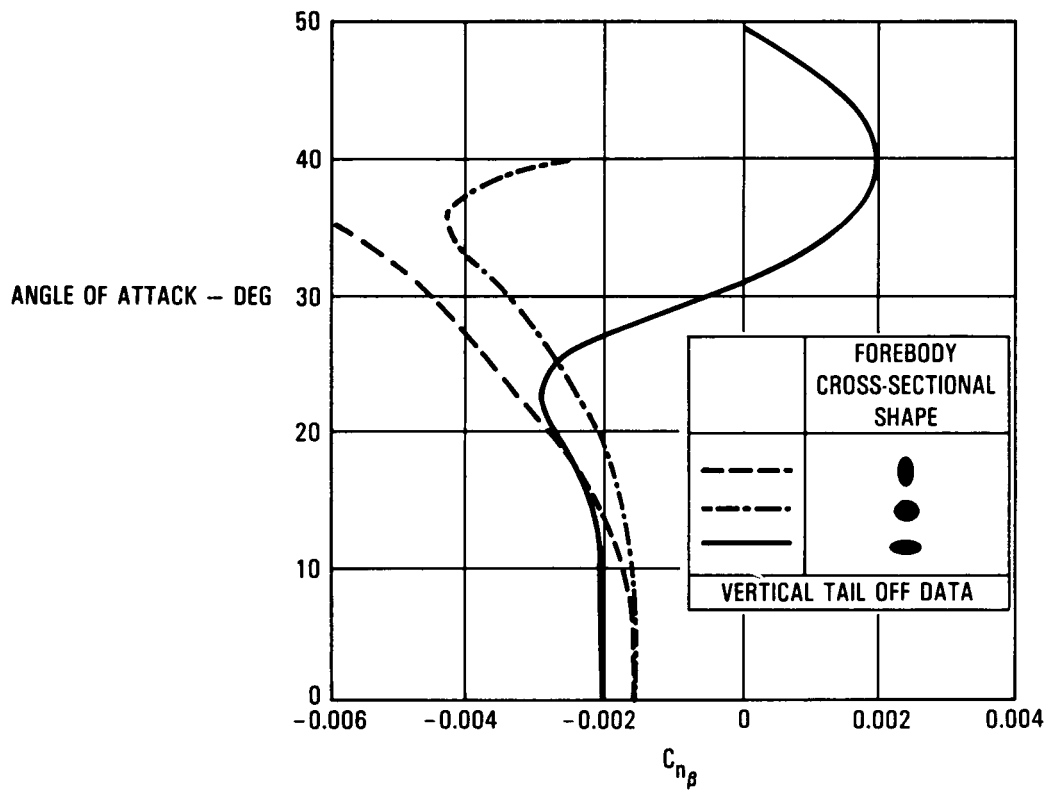


Figure 3 Effect of Forebody Cross-sectional Shape on Directional Stability.

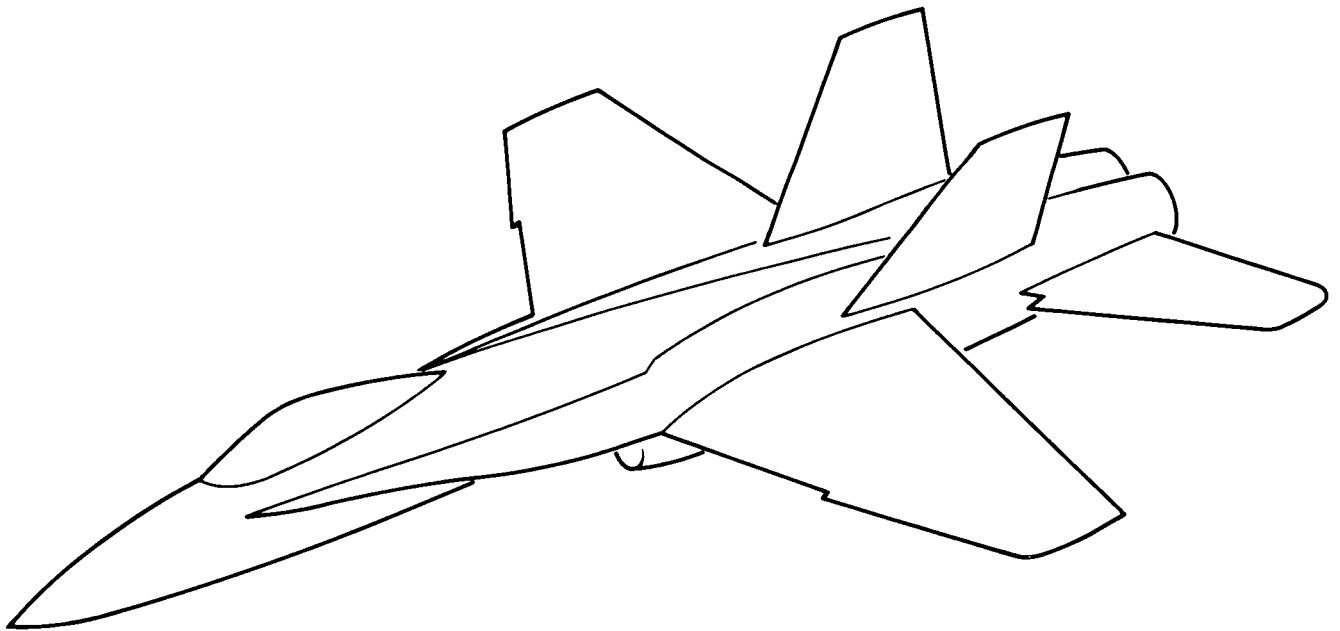


Figure 4 Representative Advanced Fighter Aircraft Configuration.

TABLE 1.- TRANSONIC CFD METHODOLOGY

FLOW EQUATION	CODE USED AT LOCKHEED	SOLUTION APPROACH
TRANSONIC SMALL PERTURBATION	BOPPE (1976)*	Non-conservative finite difference on cartesian, i.e., non-body- conforming grid.
FULL POTENTIAL	FLO-22.5 (1978)*	Non-conservative finite difference on body-conforming grid.
EULER	TEAM (1984)*	Time-marching finite volume. Zonal multiblock body-conforming grid.
REYNOLDS-AVERAGED NAVIER-STOKES	TRANSAM (1986)*	Time-marching finite volume. Zonal multiblock body-conforming grid.   Algebraic or 2-eqn. turb. model.

\* Year of first application.

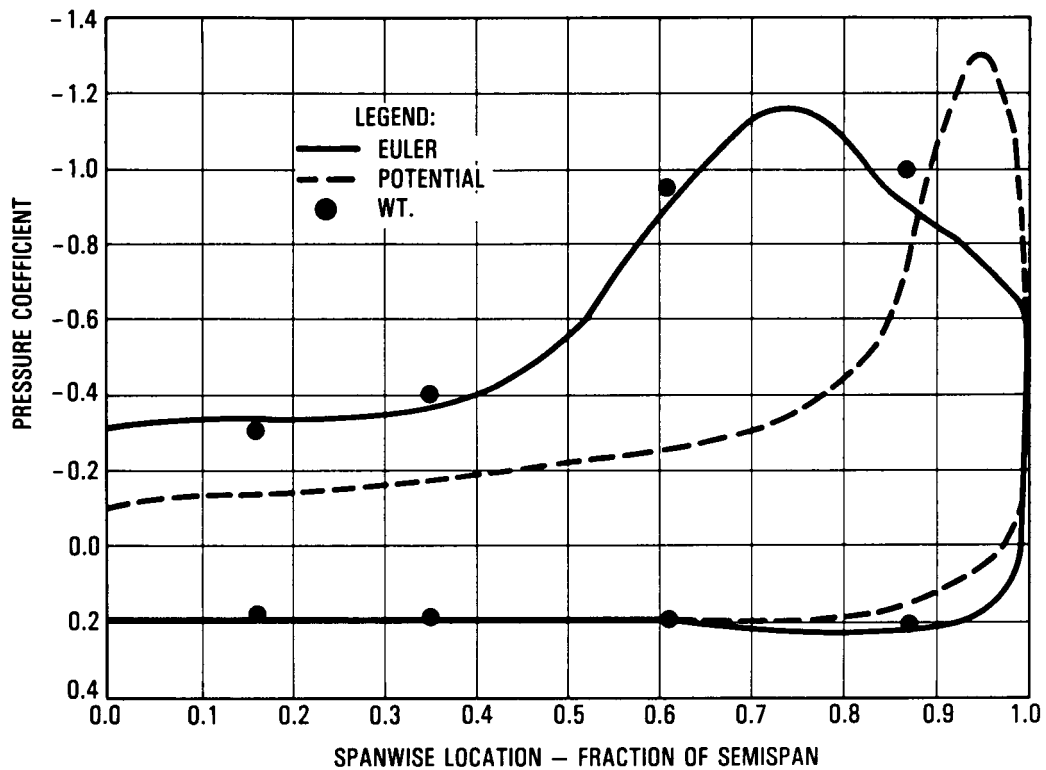


Figure 5 Euler vs. Potential Flow Solution about Arrow Wing-body with Sharp Leading Edge at Mach = 0.85 and Alpha = 15.8 Degrees.

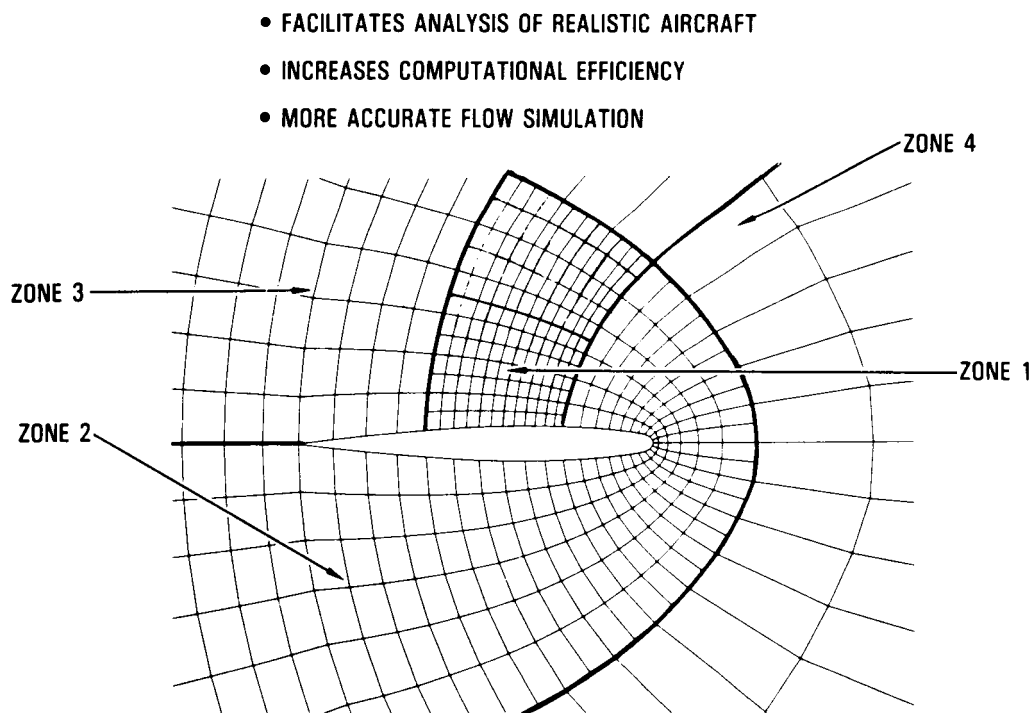
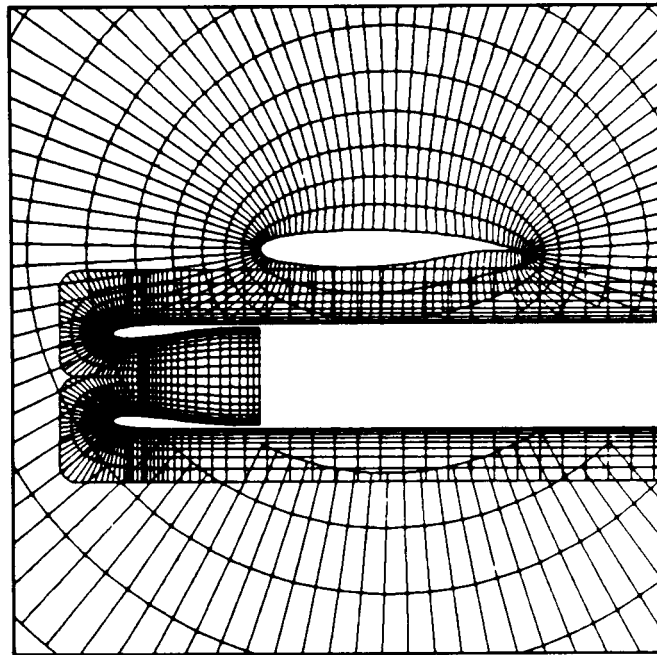


Figure 6 Multiple Zonal Grid Blocks.

# GRID EMBEDDING



# GRID PATCHING

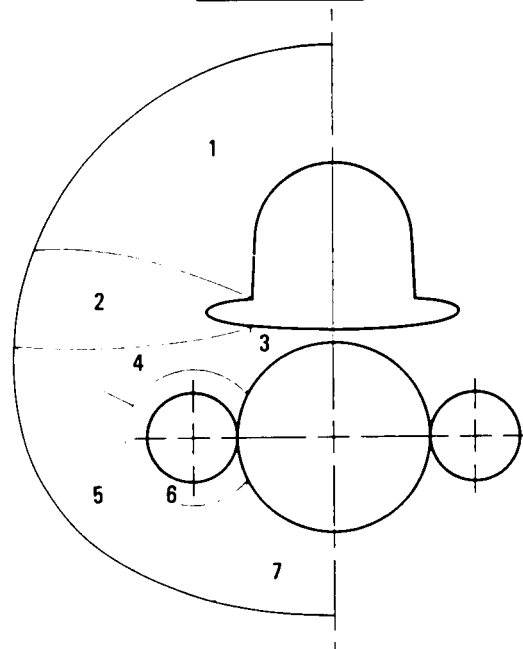


Figure 7 Approaches for Generating Zonal Grids: Grid Embedding versus Grid Patching.

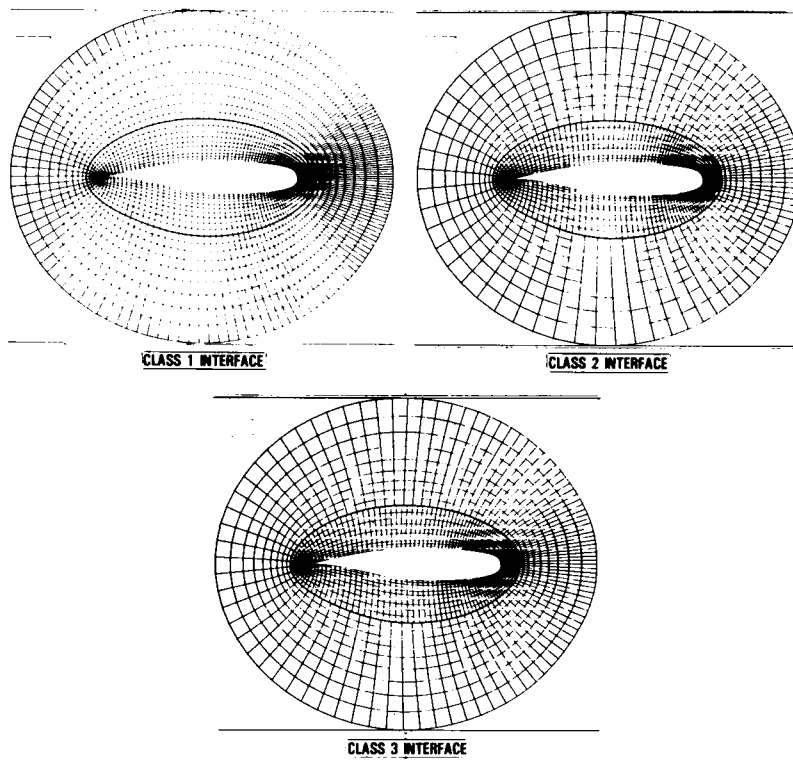


Figure 8 Three Classes of Zonal Interfaces Handled by the TEAM and TRANSAM Codes: 1) One-to-One Correspondence, 2) Integer Correspondence, and 3) Noninteger (Arbitrary) Correspondence.

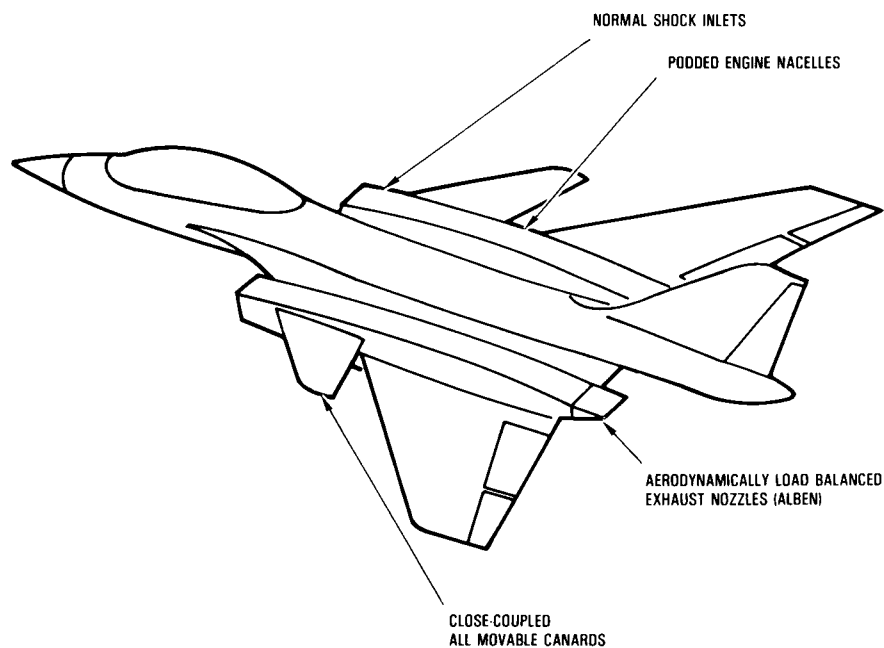


Figure 9 Supersonic V/STOL Advanced Nozzle Concept Fighter Configuration.

ORIGINAL PAGE  
COLOR PHOTOGRAPH

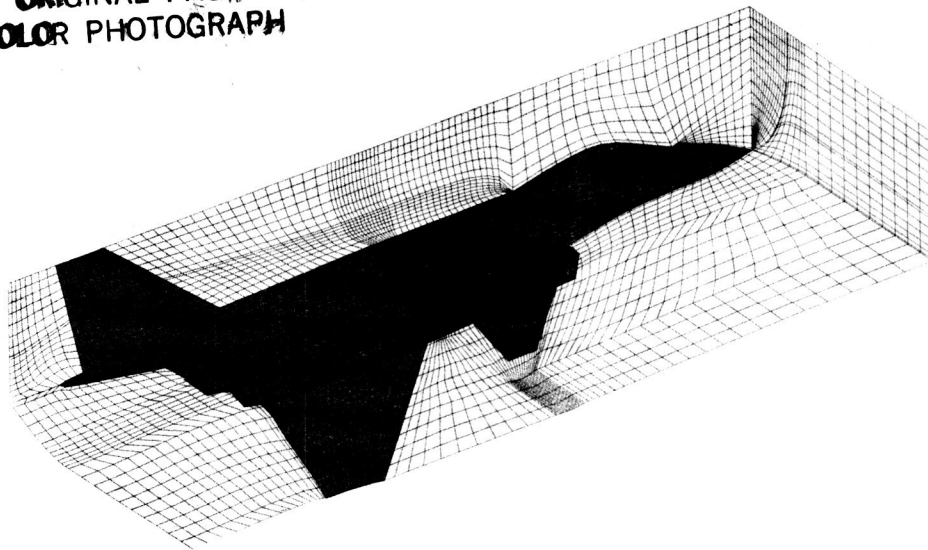


Figure 10 Partial View of Grid about ANC Configuration for Euler Computation.

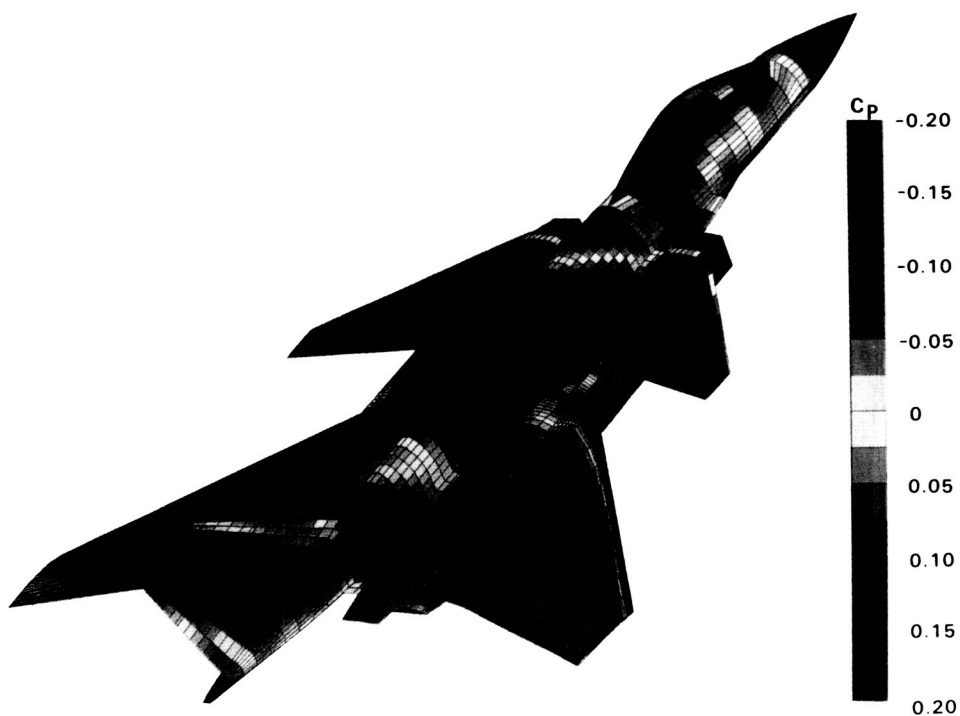


Figure 11 Surface Pressure Distribution Computed by the TEAM Code (Euler Solution) at Angle of Attack = 4.8 Degrees and Mach Number = 1.2 - Upper Rear Quarter View.



ORIGINAL PAGE  
COLOR PHOTOGRAPH

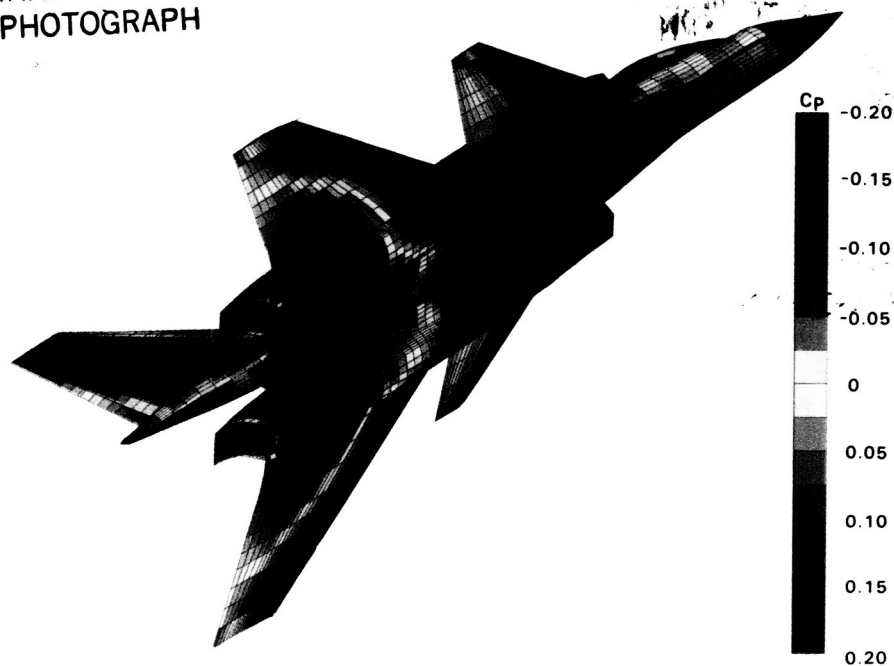


Figure 12 Surface Pressure Distribution Computed by the TEAM Code (Euler Solution) at Angle of Attack = 4.8 Degrees and Mach Number = 1.2 - Lower Rear Quarter View.



Figure 13 Surface Pressure Distribution Computed by the TRANSAM Code (Navier-Stokes Solution) at Angle of Attack = 4.8 Degrees, Mach Number = 1.2, and Reynolds Number = 6.5 Million - Upper Rear Quarter View.

ORIGINAL PAGE  
COLOR PHOTOGRAPH

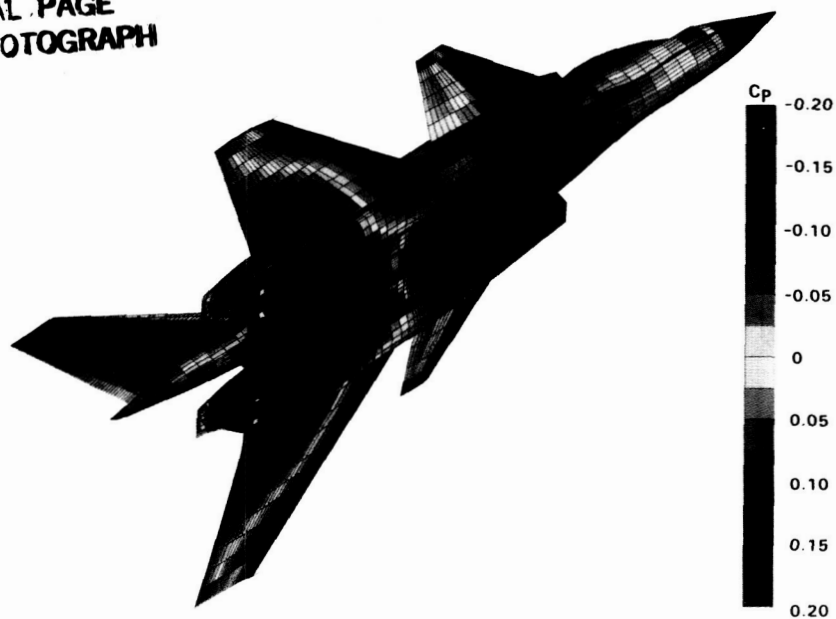


Figure 14 Surface Pressure Distribution Computed by the TRANSAM Code (Navier-Stokes Solution) at Angle of Attack = 4.8 Degrees, Mach Number = 1.2, and Reynolds Number = 6.5 Million - Lower Rear Quarter View.

LEGEND:

—  $X/C = 0.05$   
 ---  $X/C = 0.48$   
 - - -  $X/C = 0.91$

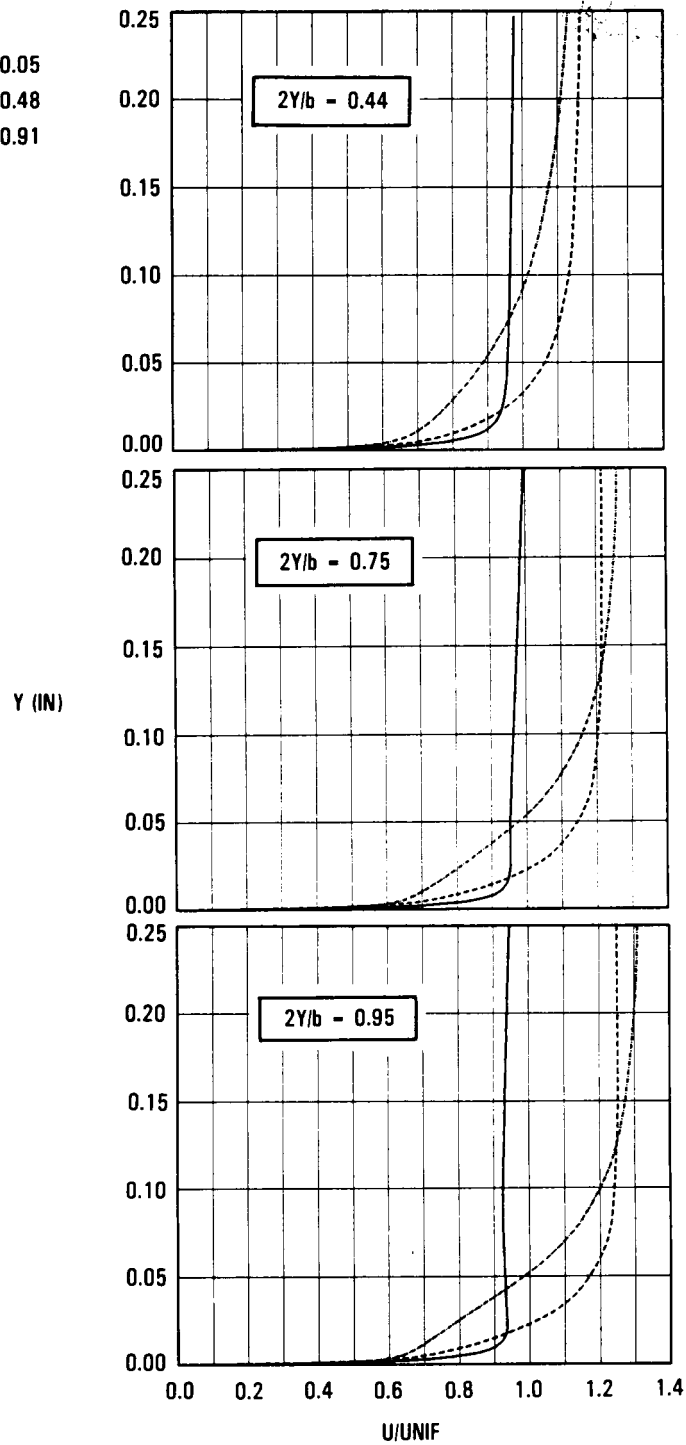


Figure 15 Wing Upper Surface Boundary Layer Velocity Profiles Computed by TRANSAM at Angle of Attack = 4.8 Degrees, Mach Number = 1.2, and Reynolds Number = 6.5 Million.

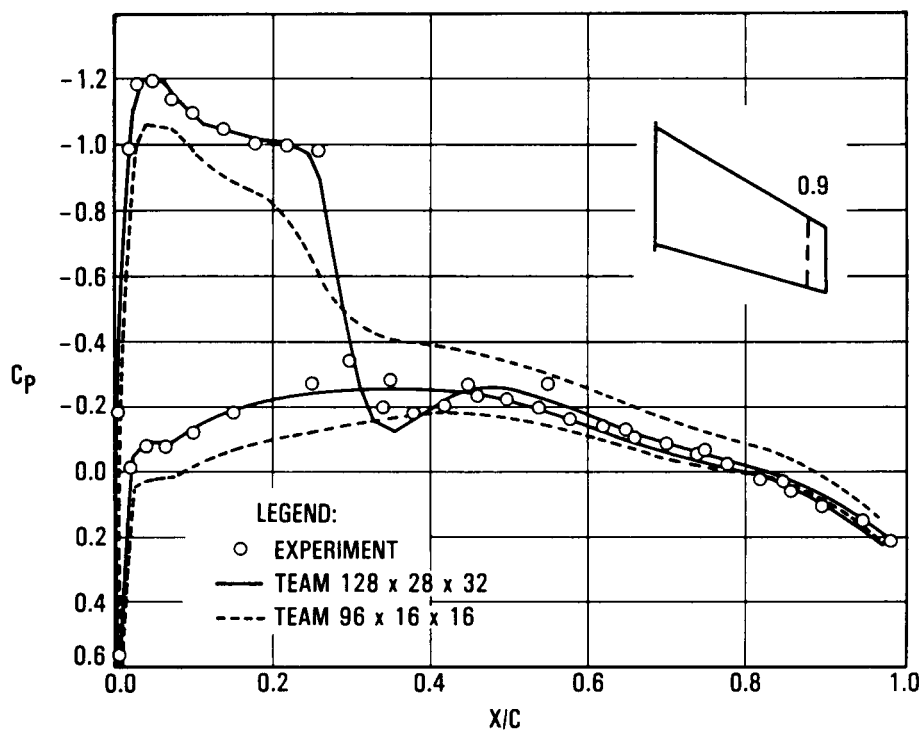


Figure 16 Effect of Grid Density on Euler Computation of Surface Pressure Distribution on the Onera M6 Wing Near the Tip. Mach = 0.84, and Angle of Attack = 3.08 Degrees.

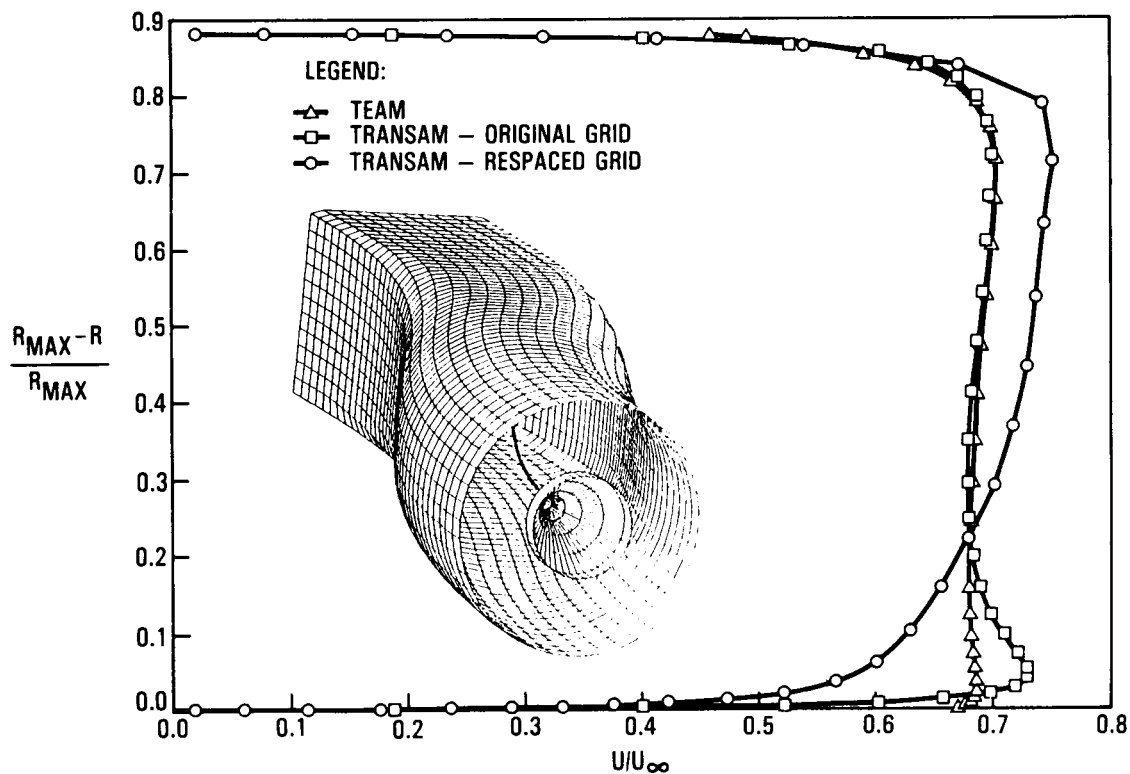


Figure 17 Computation of Internal Flow in a Subsonic Diffuser: Effect on Grid Point Distribution on Navier-Stokes Solution. Inlet Mach Number = 0.72.

ORIGINAL PAGE IS  
OF POOR QUALITY

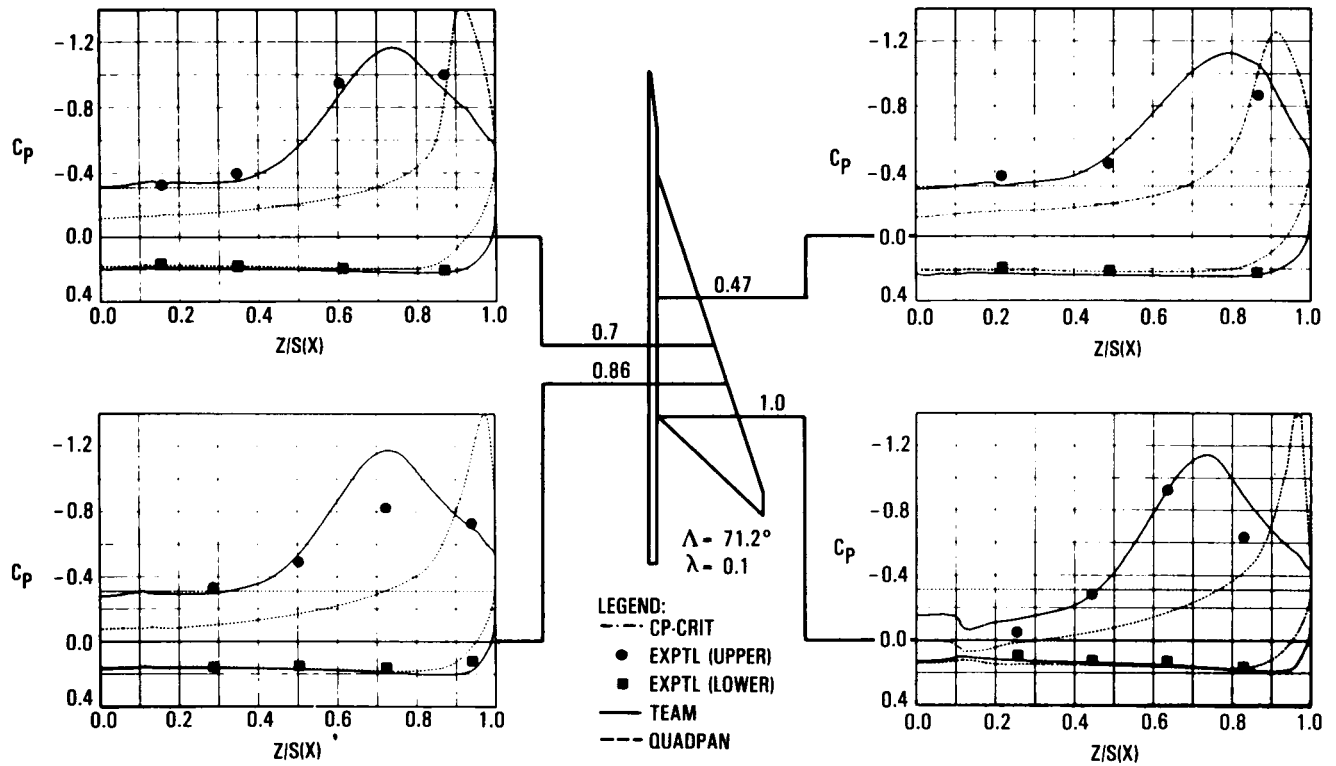


Figure 18 Cross-plane Pressure Correlation for Arrow Wing-body Configuration at Mach = 0.85 and Angle of Attack = 15.8 Degrees.

COMPUTATION OF AIRCRAFT COMPONENT FLOW FIELDS AT TRANSONIC  
MACH NUMBERS USING A THREE-DIMENSIONAL NAVIER-STOKES ALGORITHM

George D. Shrewsbury, Joseph Vadyak, David M. Schuster, and Marilyn J. Smith  
Advanced Flight Sciences Department  
Lockheed Aeronautical Systems Company  
Marietta, Georgia

### INTRODUCTION

A computer analysis has been developed for calculating steady (or unsteady) three-dimensional aircraft component flowfields. This algorithm, called ENS3D, can compute the flowfield for the following configurations: 1) diffuser-duct/thrust-nozzle, 2) isolated wing, 3) isolated fuselage, 4) wing/fuselage with or without integrated inlet and exhaust, 5) nacelle/inlet, 6) nacelle (fuselage) afterbody/exhaust-jet, 7) complete transport engine installation, and 8) multicomponent configurations using zonal grid generation techniques.

Solutions can be obtained for subsonic, transonic, supersonic, or hypersonic freestream speeds. The algorithm can solve either the Euler equations for inviscid flow, the thin-shear-layer Navier-Stokes equations for viscous flow, or the full Navier-Stokes equations for viscous flow. The flowfield solution is determined on a body-fitted computational grid. A fully-implicit alternating-direction-implicit method is employed for solution of the finite-difference equations. For viscous computations, either a two-layer eddy-viscosity turbulence model or the k-e two-equation transport model can be used to achieve mathematical closure.

### APPROACH

The flowfield solution for a given configuration is determined on a body-fitted three-dimensional curvilinear computational mesh. The computational mesh for each different configuration is determined by a separate grid generation algorithm. Ten grid generation programs are currently used in conjunction with the flow analysis program. Figure 1 illustrates the family of algorithms used to analyze the respective geometry configurations. Most of the existing mesh generation algorithms rely on numerical grid techniques which are based on solving a system of coupled elliptic partial differential equations. Isolated component geometries are typically analyzed using a single block grid approach. Multi-component configurations are typically analyzed using a multi-block H-grid approach where the global computational grid is comprised of a series of cartesian-like sub-grids which are patched together along common interface boundaries.

Once the computational grid is generated, the flowfield is obtained using the ENS3D algorithm by solving either the full three-dimensional Reynolds-averaged Navier-Stokes equations or simplified versions thereof, namely the thin-shear-layer Navier-Stokes equations, or the Euler equations. The thin-shear-layer Navier-Stokes equations retain the viscous and thermal diffusion terms only in the curvilinear coordinate direction normal to the body surface. The retained diffusion terms are generally the most dominant, however, and this approximation allows reduced computer execution times to be achieved without, in many cases, neglecting the most salient viscous flow features. The Euler equations are, of course, applicable to inviscid flow modeling where the vehicle boundary layers remain attached and thin.

The governing equations are cast in strong conservation-law form to admit solutions in which shocks are captured. Second-order differencing is used in computing the metric parameters which map the physical domain to the computational domain. A time-marching fully-implicit approximate factorization scheme is used for solution of the finite-difference equations. Either steady-state or time accurate solutions can be obtained, with second-order or fourth-order spatial accuracy and first- or second-order temporal accuracy. The convective (inviscid) terms in the governing equations are differenced using either central or upwind differencing. The upwind differencing option considers the range of influence and domain of dependence at a solution mesh point, and is used for supersonic flow calculations. The viscous diffusion terms employ central differencing. The algorithm includes the grid speed terms in the contravariant velocity calculations, thereby permitting the computation of unsteady flows with a time-varying grid that can account for elastic deformations of the aircraft structure. Although the interior points are updated implicitly, an explicit boundary condition treatment is employed which allows for the ready adaption of the program to new configurations. To aid convergence, non-reflecting subsonic outflow boundary conditions are employed along with a spatially varying time step for steady-flow solution cases. For the central difference option, the algorithm can use either a constant coefficient artificial dissipation model or a variable coefficient model where the coefficient's magnitude is based on the local pressure gradient. For the upwind differencing option, the algorithm is naturally dissipative. Laminar viscosity is computed for viscous cases using Sutherland's law. For turbulent viscous flows, the effective eddy viscosity is currently computed using either the Baldwin-Lomax two-layer algebraic turbulence model or the k-e two-equation transport model. For cases with separation, a streamwise eddy viscosity relaxation scheme is also used in conjunction with the Baldwin-Lomax turbulence model. This accounts for turbulence history effects and improves the simulation of separated flowfields.

In an effort to reduce the required computer execution time, versions of the flow simulation algorithm were developed for use on Class VI vector supercomputers. The ENS3DC version was written for the CDC CYBER-205 and employs a fully vectorized block tridiagonal simultaneous equation solution scheme and vectorized coefficient calculations to improve algorithm efficiency. ENS3DV is a similar version written for a Lockheed CRAY X-MP/24 using one of two central processors available on this machine. ENS3DVM is a modified version of ENS3DV which employs the multitasking process to operate both of the central processors available on the CRAY X-MP/24 simultaneously on the same source code. The use of these vectorized versions has dramatically reduced the required execution time. For instance, the ENS3DV version is about 10 times as fast as the ENS3D version when measuring CPU time on a single processor of the CRAY X-MP/24. The ENS3DVM version yields a factor of approximately 2 improvement in speed over the ENS3DV version when measuring wall clock execution time in a dedicated environment on the CRAY X-MP/24. Additional versions of the program exist for performing flowfield calculations at hypersonic Mach numbers. These versions account for real gas effects by using parametric curve fits to calculate pressure, temperature, and sonic speed as function of density and internal energy for equilibrium air. Another version of the program solves a system of species continuity equations in addition to the five mean flow equations and thereby permits flowfield calculations with finite-rate thermochemical effects. This version is used to model H<sub>2</sub> - air combustion flows for hypersonic cruise vehicles. Applications of the ENS3D algorithm are presented in reference 1.

## SAMPLE RESULTS

Correlation studies have been performed for all of the computational options. These studies are documented in References 1,2,3,4,5, and 6. Selected results are presented below to illustrate application of the analysis.

### Afterbody/ Exhaust-Jet Flow Simulations

The AGRID and ENS3D algorithms were used in performing correlation studies for afterbody/exhaust-jet configurations. The AGRID algorithm can generate the three-dimensional body-fitted grid for arbitrary nacelle (fuselage)/ exhaust-jet configurations. The grid is obtained using two-dimensional grid generation techniques for a series of meridional planes splayed circumferentially around the body. The AGRID and ENS3D algorithms are capable of simulating the flowfield for: (1) afterbody/plume-simulator, (2) turbojet (single exhaust jet), and (3) turbofan (coaxial exhaust jet) configurations at arbitrary speed and incidence.

### Turbulent Thin-Shear-Layer

Navier-Stokes computations were performed for an afterbody/plume-simulator configuration for free-stream Mach numbers  $M_\infty$  of 0.4 and 0.9, zero incidence ( $\alpha = 0^\circ$ ), and Reynolds numbers  $Re$  of 1,300,000 and 1,900,000, respectively. This configuration was tested by Reubush (reference 7) at NASA-Langley and has a circular arc afterbody contour with a fineness ratio (ratio of afterbody length to maximum afterbody diameter) of 2.0 and a closure ratio (ratio of nozzle exit diameter to maximum afterbody diameter) of 0.7. Figure 2 illustrates the computed surface pressure coefficient  $C_p$  plotted as a function of the nondimensional distance  $X/d_m$  (distance/afterbody diameter) measured along the afterbody. Also shown are the corresponding experimental data (reference 7). These results correspond to an attached flow case.

Figure 3 illustrates the computed pressure distribution for another afterbody/plume-simulator configuration for a free-stream Mach number  $M_\infty$  of 0.9, zero incidence ( $\alpha = 0^\circ$ ), and a turbulent flow Reynolds number of 1,900,000. These results correspond to a shock-induced separated flow case and are for an afterbody with a fineness ratio of 1.0 and a closure ratio of 0.5. Also shown in the figure are the corresponding experimental data (reference 7). Good agreement is observed between the results of the analysis and experiment. This calculation required using eddy viscosity relaxation in conjunction with the Baldwin-Lomax turbulence model.

Figure 4 illustrates the computed surface pressure distribution for a turbojet afterbody with  $M_\infty = 0.9$ ,  $\alpha = 0^\circ$ , and  $Re = 1,900,000$ . Uniform jet inflow conditions with a turbulent nozzle wall boundary layer velocity profile were specified. The jet inflow conditions correspond to a jet total to free-stream static pressure ratio of 2.0. Also shown along with the results of the turbulent thin-shear-layer Navier-Stokes calculations are the corresponding experimental data (reference 8).

### Turbofan Engine Installation Flow Simulations

The NGRID, AGRID, and ENS3D algorithms were used in performing flow simulations for complete turbofan engine installations. The NGRID algorithm can generate the three-dimensional body-fitted grid for arbitrary nacelle/inlet forebody configurations. Like AGRID, NGRID generates the nacelle forebody grid by using two-dimensional grid generation techniques for a series of meridional



planes arranged around the body. The NGRID and AGRID codes can be linked together to generate grids for complete engine installations.

Flow computations (reference 2) have been performed for an asymmetric turbofan engine installation. The configuration under study is a recent Lockheed drooped-inlet design in which the inlet contour has circumferential variation both in section shape and in length from the hilite point to the compressor face. The front of the inlet is tilted downward with respect to the engine centerline for the purpose of aligning the inlet with the local flow direction underneath the wing. Figure 5 illustrates the engine installation contours, and a portion of the computational meridional plane grid for the top ( $\theta = 0^\circ$ ) circumferential station (upper symmetry meridian). The nacelle has one plane of geometric symmetry. The configuration has an asymmetric circular arc afterbody contour for the outer (fan) cowl. The contour around the primary (gas generator) nozzle is also a circular arc but is axisymmetric. Turbulent flow calculations have been performed for the turbofan engine configuration illustrated in Figure 5. Figure 6 presents the symmetry plane velocity vector field for a turbulent thin-shear-layer Navier-Stokes calculation. The flow conditions correspond to a free-stream Mach number of 0.8, an angle of attack of  $0^\circ$ , an effective compressor face Mach number MCF of 0.35, Reynolds number  $Re$  of 2,400,000/ft, a primary jet Mach exit number MJF of 1.0, and a fan jet Mach exit number MJF of 1.0. The mixing layers between the primary jet and fan jet, and fan jet and external flow are illustrated in the figure. The exhaust jet velocity profiles were specified to be in the axial direction and were composed of a uniform jet core velocity profile and a turbulent boundary layer velocity profile next to a given solid surface.

For an asymmetric nacelle, the flow will be three-dimensional even at zero incidence. Computed surface pressure distributions for the top ( $\theta = 0^\circ$ ) and bottom ( $\theta = 180^\circ$ ) meridians of the asymmetric engine installation are presented in Figure 7. Asymmetry exists in the computed solution with the lower external surface producing a higher suction level than the top meridian at this angle of attack. Transition was specified as occurring at the suction peak.

#### Transport Wing Flow Simulations

The WGRID and ENS3D algorithms were used in performing correlation studies for isolated wing configurations. The WGRID code can generate the three-dimensional, body-fitted grid for wings with arbitrary planforms and section shapes. The computational mesh is obtained using two-dimensional, numerical, grid-generation techniques for a series of spanwise stations that are arranged along the span. An option exists within the WGRID and ENS3D algorithms to compute the flowfield for a wing contained between two parallel walls. Either an O-grid or C-grid topology can be used in analyzing isolated wing flowfields.

Flow computations, both inviscid Euler and viscous thin-shear-layer Navier-Stokes, have been performed for the Onera M-6 swept and tapered wing (reference 9). Figure 8a illustrates the wing section and the spanwise plane C-grid used in performing the Euler computations. The grid used for viscous computations has finer mesh spacing in the normal direction and had an increased number of normal stations.

Figure 8b compares Onera M-6 wing experimental data and the results of the ENS3D algorithm executed in the Euler equation mode for  $M_\infty = 0.84$ , and  $\alpha = 0^\circ$ . Correlation results were determined for a number of semispan locations. The analysis and experimental data semispan locations are denoted by  $\eta_{th}$  and  $\eta_{exp}$ ,

respectively. Except for a slight under-prediction of the suction peak, good agreement was obtained.

Figure 8c presents additional correlations between the analysis executed in the thin-shear-layer Navier-Stokes mode and experimental data for  $M_\infty = 0.7$ ,  $\alpha = 1^\circ$ , and  $Re = 11,740,000$ . This calculation used the finer grid and a fully turbulent flow approximation. Again, except for under-prediction of the suction peak, good agreement was obtained.

#### Advanced Transport Vehicle and Generic Fighter Simulations

The WGRID, WBGRID, and ENS3D algorithms were used in performing simulations for an advanced transport vehicle and a high technology generic fighter configuration. The WBGRID code is able to generate the grid for a variety of wing/fuselage configurations. The mesh is obtained using two-dimensional numerical grid generation techniques for the symmetry and freestream sidewall planes and three-dimensional numerical grid generation techniques for stations in between these spanwise stations.

Viscous flow simulations have been performed for a blended wing-body advanced transport vehicle configuration. Figure 9a presents the surface grid for this vehicle. The wing is swept and tapered. The fuselage section ordinates were obtained by linearly interpolating between those on the symmetry plane and those at the wing break. Figure 9a also shows a portion of the spanwise plane field C-grid near the wing break.

Thin-layer Navier-Stokes computations were performed for this configuration for  $M_\infty = 0.8$ ,  $\alpha = 0^\circ$ , and  $Re = 4 \times 10^6$ . A fully turbulent flow approximation was used in the analysis.

Figure 9b presents the computed surface static pressure field for this vehicle. The highest pressure is denoted by red and the lowest is denoted by blue. The highest pressure is at the vehicle's nose and at the wing's leading edge, whereas maximum suction occurs near mid-chord on the wing. This figure also shows the field pressure distribution on a portion of a spanwise station near the wing break.

Figure 9c presents the computed surface pressure coefficient  $C_p$  plotted as a function of fractional chord  $x/c$  for the 7.07% ( $\eta = .07$ ) and 60.0% ( $\eta = .60$ ) semispan locations. The vehicle is designed to have nearly shock-free compressions. Greater loading occurs on the wing than on the fuselage, although the fuselage does contribute to the total lift of the vehicle.

Thin-layer and full Navier-Stokes viscous flow simulations have been performed for a Lockheed generic fighter configuration. Figure 10a illustrates this vehicle along with the grid used in the computations. The vehicle has a straked forebody with a sharp leading edge. The wing has biconvex airfoil sections of low thickness with sharp leading edges.

Figure 10b illustrates the computed pressure distribution for a thin-layer Navier-Stokes calculation at  $M_\infty = 0.8$ ,  $\alpha = 1^\circ$ , and  $Re = 4 \times 10^6$ . Again, a fully turbulent flow approximation was used. This figure presents the computed surface pressure coefficient  $C_p$  as a function of fractional chord  $x/c$  for the 6 percent ( $\eta = 0.06$ ) and 72 percent ( $\eta = 0.72$ ) semispan locations. The  $\eta = 0.06$  station corresponds to the fuselage. Compression occurs at the leading edge with a double peak expansion occurring on the fuselage's upper surface. An engine pod assembly was attached to the vehicle's lower side which gives rise to

an expansion and subsequent recompression around the pod as shown in the figure. The  $\eta = 0.72$  location corresponds to a wing station.

### Hypersonic Cruise Vehicle with Power Addition Effect Simulations

The ENS3D algorithm has also been employed to analyze hypersonic cruise vehicles with power addition effects at subsonic, transonic, supersonic, and hypersonic Mach numbers. One of the major concerns associated with hypersonic vehicles operating in the transonic range is the prediction of the complex afterbody flowfields associated with the hypersonic airframe/propulsion integration problem. The majority of hypersonic vehicle designs use a highly upswept afterbody as a nozzle surface for operation at hypersonic conditions. The afterbody is designed so that the propulsion system exhaust plume expands into the upswept afterbody creating an efficient nozzle system. At transonic speeds however, the exhaust plume does not fill this region and the flow separates. This results in increased drag and pitching moment changes which can severely impact the performance of the vehicle as it accelerates to hypersonic flight. Therefore, accurate computational aerodynamics methods are required to predict these flows, thus enabling the aerodynamicist to evaluate and modify the design in a timely and cost-effective manner.

The configuration investigated employed an upswept conical afterbody with a semi-circular exhaust nozzle. This design is representative of a number of scramjet installations currently under consideration for hypersonic cruise vehicles. The configuration forebody was effectively uncambered to eliminate any pressure gradients leading up to the nozzle exit. The wing design was a symmetrical bi-convex airfoil section and the planform was designed to shield the afterbody from the upper surface flow. A computer rendition of this configuration is shown in Figure 11.

A single-block fuselage grid topology was chosen to model the hypersonic configuration. The topology was modified at the wing trailing edge to allow grid lines on the wing surface to leave the trailing edge onto a wake surface rather than abruptly collapsing to the symmetry plane. This eliminates problems with grid skewness at the wing trailing edge, but forces the user to model the upper and lower halves of the geometry with the same number of spanwise points.

Figure 12 shows an isometric view of the surface grid. Two axial grid planes have been added to this figure to show the circumferential grid topology used to model the geometry and the general distribution of the flowfield grid points. This grid consists of 82 points in the streamwise direction, 42 points circumferentially and 27 points normal to the body surface. This gives a total of approximately 93,000 total points which requires 3.4 million words of storage in the ENS3D algorithm. ENS3D is run on Lockheed's Cray X-MP/24 and this grid size is very close to the limit which can be run on this computer.

Figure 13 shows a side view of the surface grid with the upper and lower symmetry plane grids added. This view shows the streamwise grid topology and the axial distribution of grid points. Axial stations have been clustered in the jet/afterbody region which is the primary zone of interest in this study. This sacrifices resolution on the forebody, but since only the overall effect of the forebody on the afterbody flow is desired, this grid density is sufficient to capture the required flowfield qualities. The figure also shows that the jet exit has been modeled as a slanted surface rather than a vertical exhaust plane. This was done so as to eliminate abrupt changes in the grid metrics which could cause convergence problems in ENS3D.

ENS3D computations were conducted for this configuration at a  $M_\infty = 0.7$ ,  $\alpha = 0^\circ$ ,  $Re = 7,000,000$ , and a jet pressure ratio of 2.0, which corresponds to a choked jet. Figure 14 shows a color Mach number contour of an ENS3D solution on the model afterbody at the centerline. The figure clearly shows that the flow has separated from the afterbody and the deflection of the jet behind the vehicle is also shown. Figure 15 shows the Mach number contour on a transverse cut through the afterbody. This figure shows that the maximum Mach number is not attained on the vehicle centerline, but rather near the wing/body intersection, thus indicating the highly three-dimensional nature of this flowfield.

#### COMPUTER RESOURCE REQUIREMENTS

The ENS3D flow simulation algorithm is best suited for execution on Class-VI vector supercomputers. A vectorized version (ENS3DV) and a vectorized/multitasked version (ENS3DVM) are the most efficient versions of the algorithm and were written for use on the CRAY X-MP and CRAY-2 computer systems. The multitasked ENS3DVM version reduces the wall clock execution time required by the ENS3DV version by a factor approximately equal to the number of central processors available on the machine if the program is executed in a dedicated environment. Although the wall clock execution time is reduced using the multitasked ENS3DVM version, the total CPU time remains approximately the same as using the single processor ENS3DV version since multitasking simply splits the computational work load over a number of processors. The machine billing algorithm generally uses the total CPU time and allocated memory in determining the cost of a given execution.

The execution speed of the ENS3DV version of the algorithm is problem dependent. Two primary vector lengths are incorporated into the algorithm: (1) the number of wraparound or axial grid stations ( $I_m$ ), and (2) the number of block tridiagonal inversions to be performed simultaneously ( $N_I$ ). For a fixed total grid size and fixed number of time steps, increasing  $I_m$  and/or  $N_I$  will reduce the required execution time. This is because on all vector computers increasing the vector length reduces the number of internal clock periods per result, thereby increasing execution speed. The effect of increasing  $N_I$  while fixing the grid size and number of time steps is illustrated for a sample problem in Figure 16. The problem under study is the solution of a steady viscous turbulent flowfield for a sample configuration. A grid size of approximately 40,000 points was employed and 800 time steps were used in the execution to achieve a converged solution. At the same time, a spatially variable time step was used to accelerate convergence. Shown in the figure are single central processor execution times as a function of  $N_I$  for both turbulent thin-shear-layer and turbulent full Navier-Stokes executions. In all cases, increasing  $N_I$  reduces the required CPU time. Increasing  $N_I$ , however, increases the amount of temporary storage. The product of storage and execution time can increase with higher vector lengths to actually increase the number of system billing units (SBU) which is a measure of the total job cost. The results presented in Figure 16 are for a Lockheed CRAY X-MP/24 computer. Billing algorithms can be site dependent and may weight processor time and memory differently.

The ENS3DV algorithm requires a memory allocation of roughly 34 times the number of computational grid points plus some temporary storage overhead, which increases as does  $N_I$ , as described previously.

#### CONCLUSIONS

An analysis has been presented for calculating the flowfield for a variety of aircraft components. Solutions have been obtained by solving the viscous

Navier-Stokes equations on body-fitted curvilinear grids using a fully-implicit approximate factorization algorithm. Enhancements currently being incorporated into the algorithm include: discrete bow shock wave fitting, upwind differencing for supersonic flow calculations, a solution adaptive grid scheme, and turbulent viscosity field calculation using a transport equation model.

#### REFERENCES

1. Vadyak, J., Smith, M. J., Schuster, D. M., Shrewsbury, G. D., "Simulation of Aircraft Component Flowfields Using a Three-Dimensional Navier-Stokes Algorithm," 3rd Cray International Science and Engineering Symposium, Cray Research, Inc., Minneapolis, Minnesota, September, 1987.
2. Vadyak, J., "Simulation of Nacelle-Afterbody/Exhaust-Jet Flowfields Using a Three-Dimensional Navier-Stokes Algorithm," AIAA Paper No. 85-1283, July, 1985.
3. Vadyak, J. and Smith, M. J., "Simulation of Engine Installation Flowfields Using a Three-Dimensional Euler/Navier-Stokes Algorithm," AIAA Paper No. 86-1537, June, 1986.
4. Vadyak, J., "Simulation of Transonic Three-Dimensional Nacelle/Inlet Flowfields Using an Euler/Navier-Stokes Algorithm," AIAA Paper No. 85-0084, January, 1985.
5. Vadyak, J., "Simulation of Diffuser Duct Flowfields Using a Three-Dimensional Euler/Navier-Stokes Algorithm," AIAA Paper No. 86-0310, January, 1986.
6. Vadyak, J., Smith, M. J., Schuster, D. M., and Weed, R., "Simulation of External Flowfields Using a 3-D Euler/Navier-Stokes Algorithm," AIAA Paper No. 87-0484, January 1987.
7. Reubush, D. E., "Experimental Study of the Effectiveness of Cylindrical Plume Simulators for Predicting Jet-On Boattail Drag at Mach Numbers up to 1.3," NASA TN D-7795, 1974.
8. Reubush, D. E., and Runckel, J. F., "Effect of Fineness Ratio on Boattail Drag of Circular-Arc Afterbodies having Closure Ratios of 0.50 with Jet Exhaust at Mach Numbers up to 1.30," NASA TN D-7192, 1973.
9. Schmitt, V., and Charpin, F., "Pressure Distribution on the Onera M-6 Wing at Transonic Mach Numbers," AGARD-AR-138, 1979.

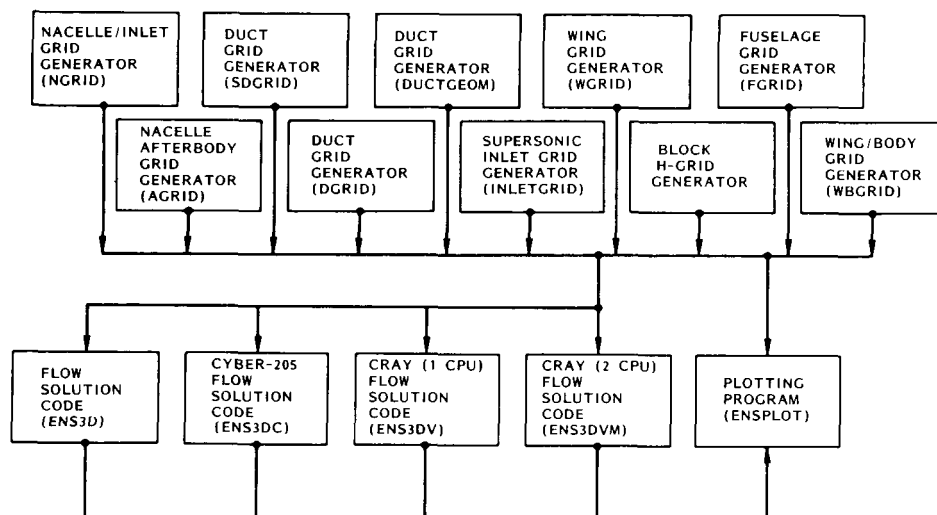


Figure 1. Family of 3-D Flow Analysis Algorithms

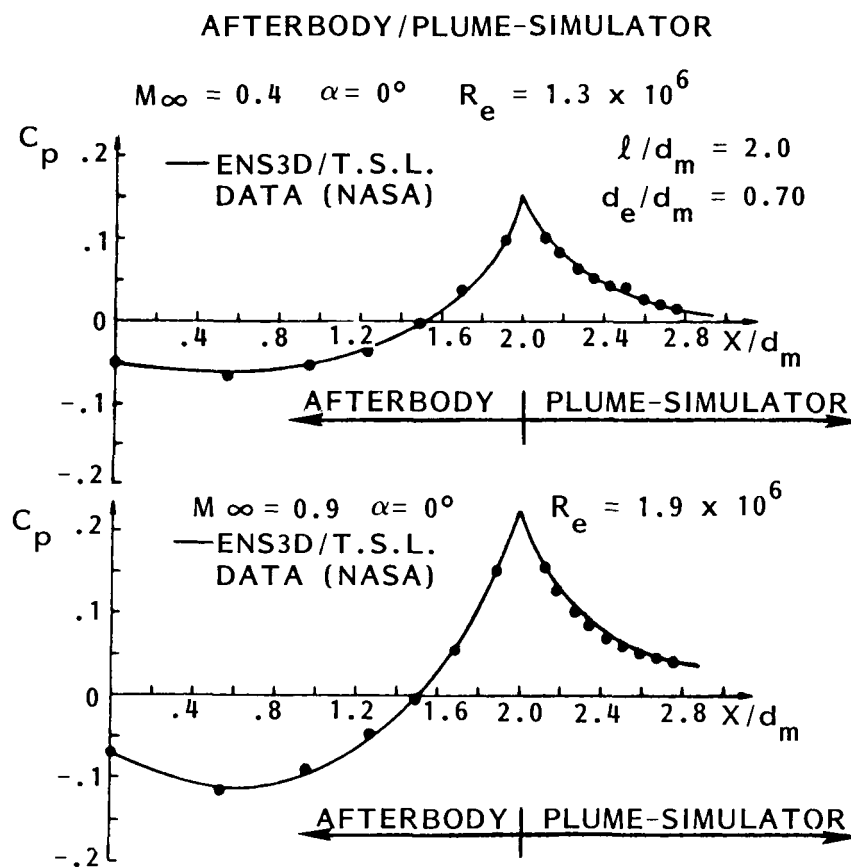


Figure 2. Afterbody/Plume-Simulator Pressure Distributions (Attached Flow)

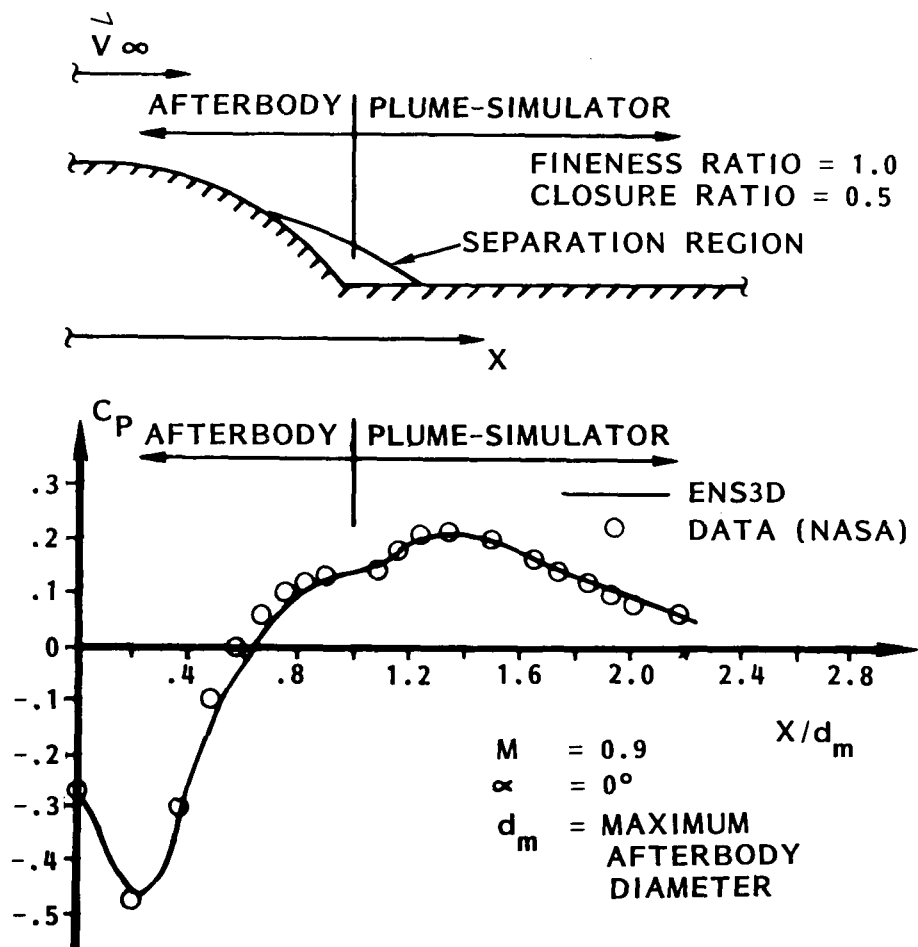


Figure 3. Afterbody/Plume-Simulator Pressure Distribution (Separated flow)

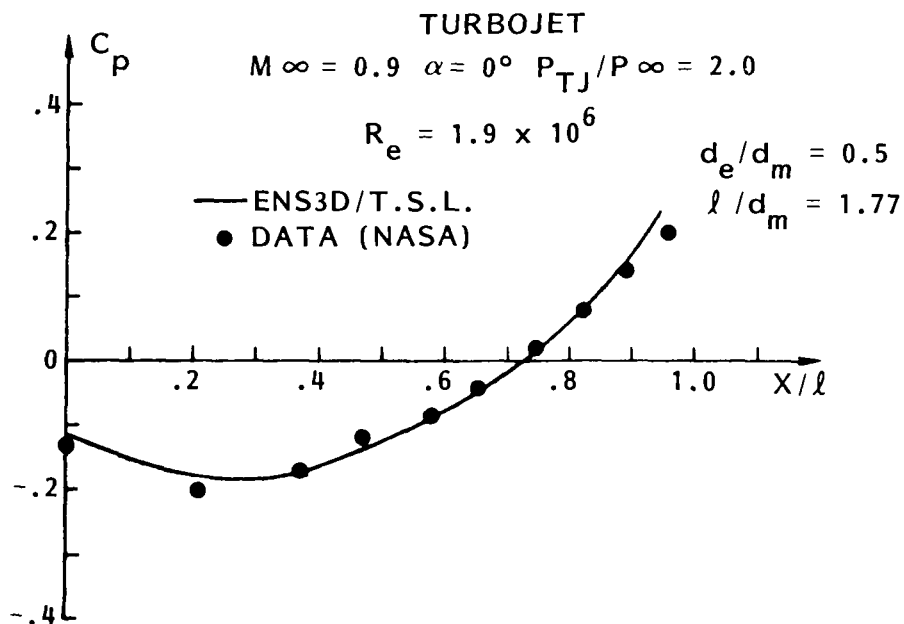
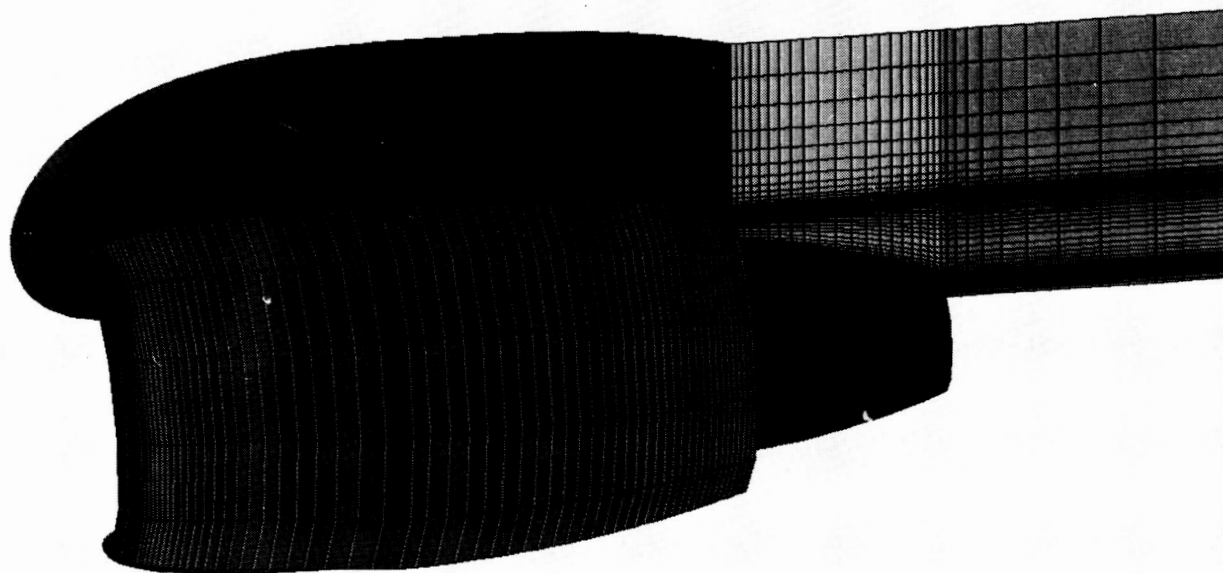


Figure 4. Turbojet Afterbody Pressure Distribution

ORIGINAL PAGE IS  
OF POOR QUALITY



ENGINE ZONAL GRID  
ELEV= 20.00 YAW= 80.00

Figure 5. Turbofan Engine Grid



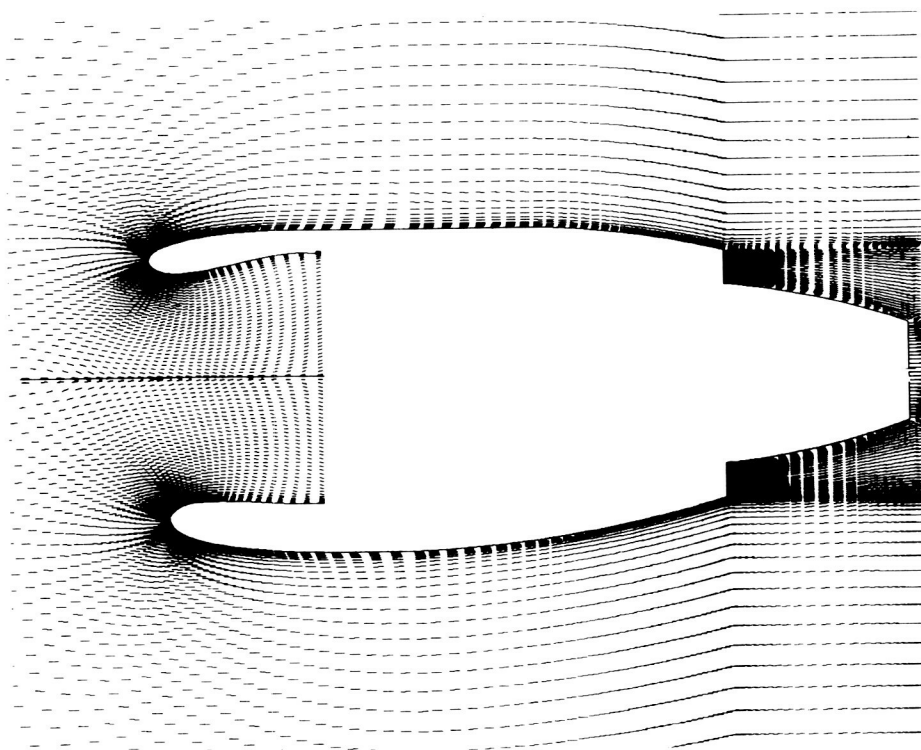


Figure 6. Turbopan Engine Symmetry Plane Velocity Vectors

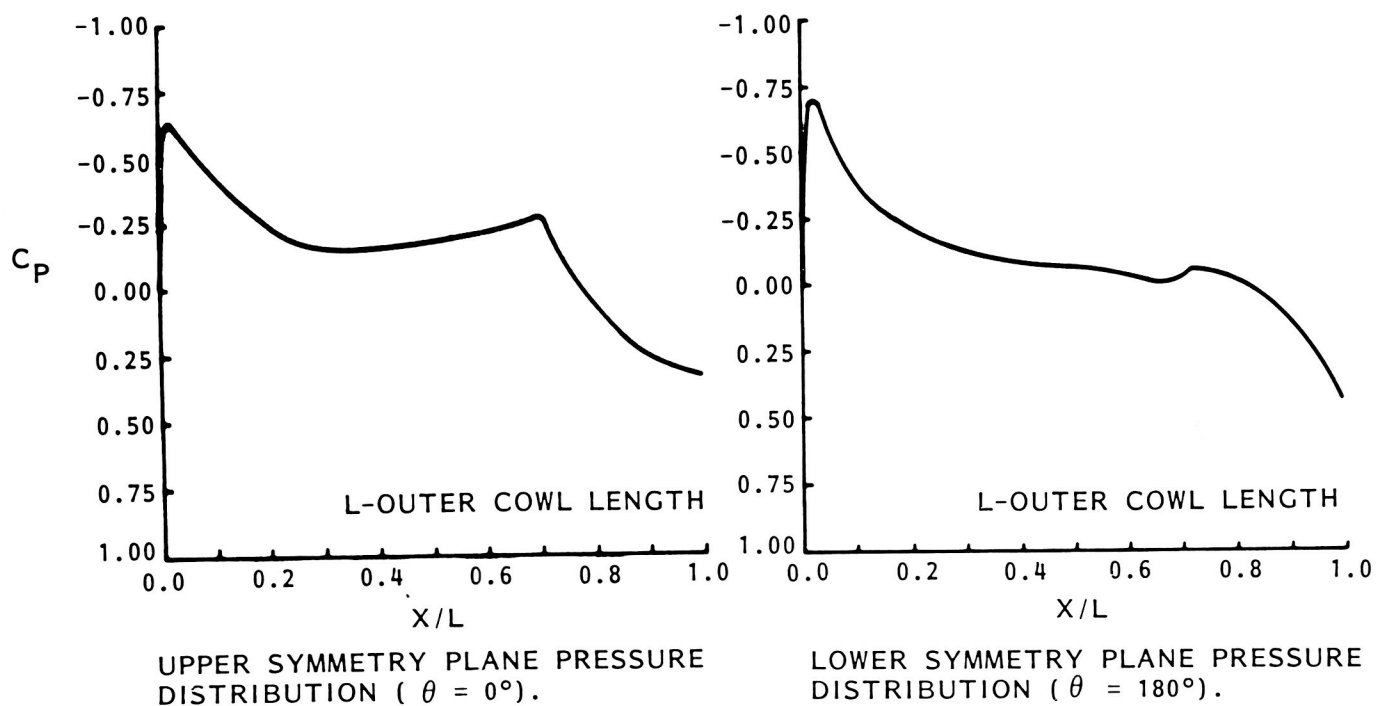
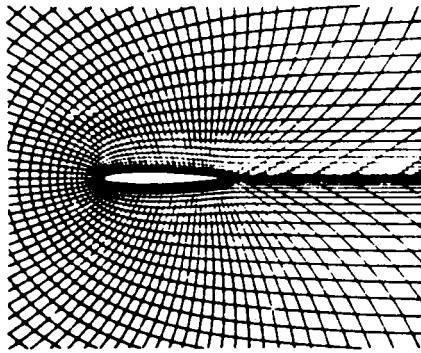
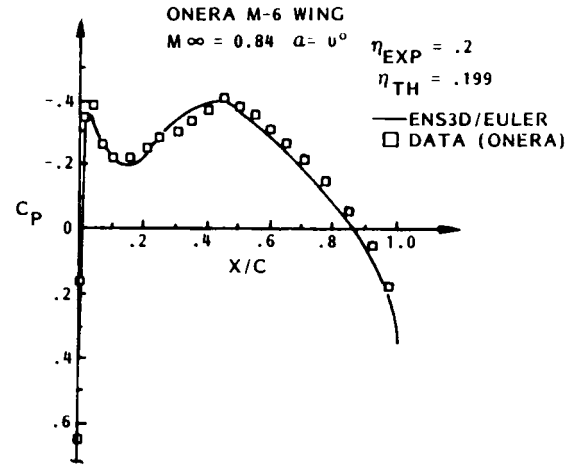


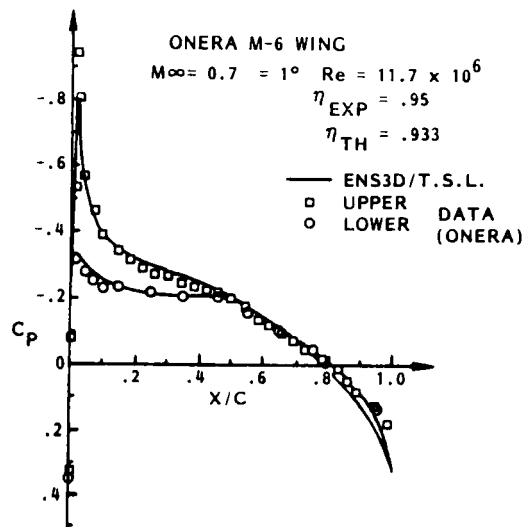
Figure 7. Turbopan Engine Pressure Distributions



(a) SPANWISE PLANE GRID.



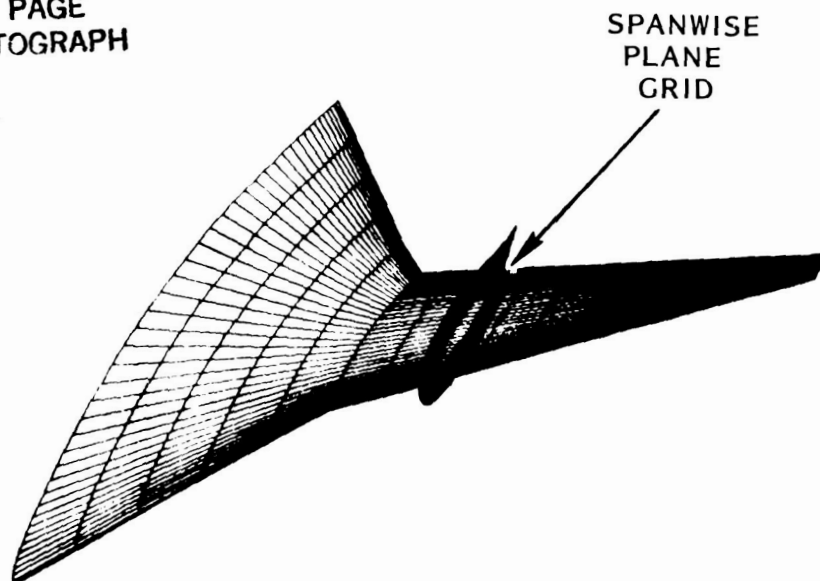
(b) PRESSURE DISTRIBUTION FOR EULER SOLUTION.



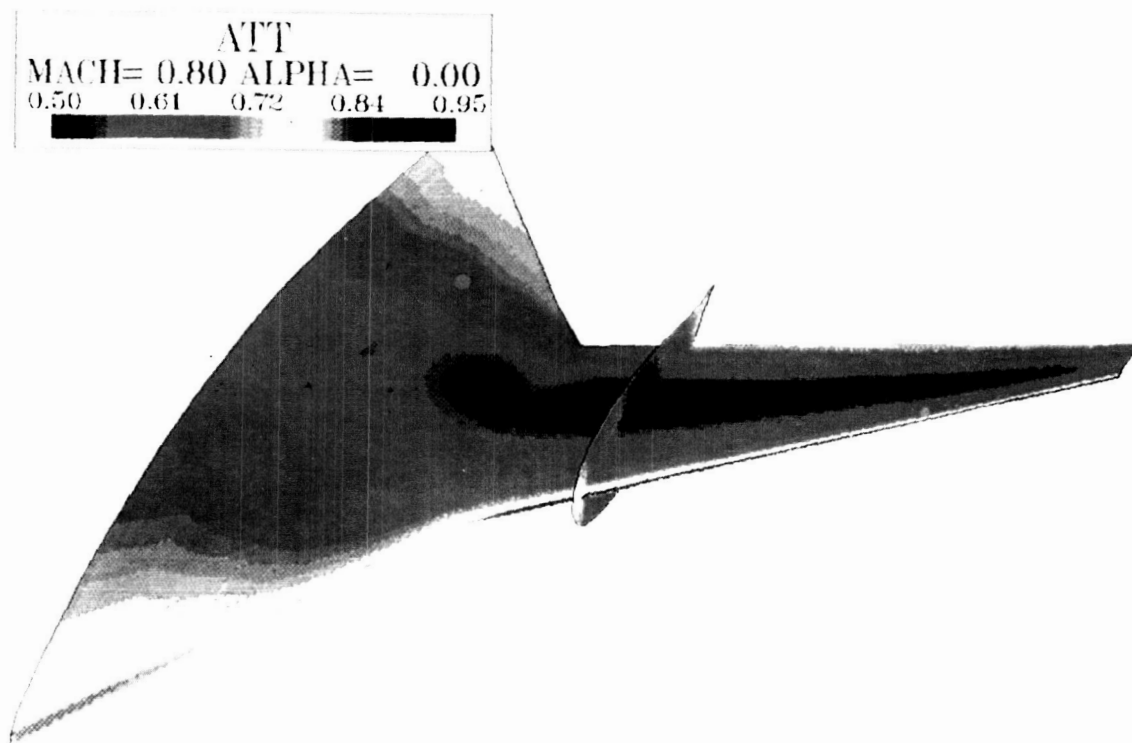
(c) PRESSURE DISTRIBUTION FOR THIN-SHEAR-LAYER NAVIER-STOKES SOLUTION.

Figure 8. Grid and Pressure Distribution for Onera M-6 Wing

ORIGINAL PAGE  
COLOR PHOTOGRAPH

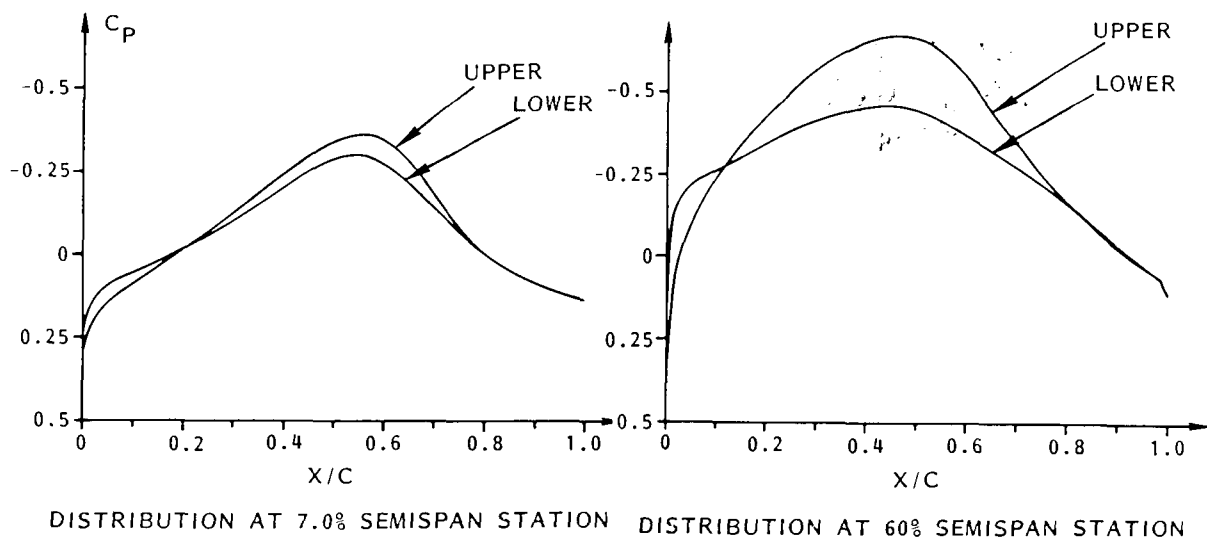


a.) Surface Grid for Advanced Transport Vehicle



b.) Surface Pressure Distribution for Advanced Transport.

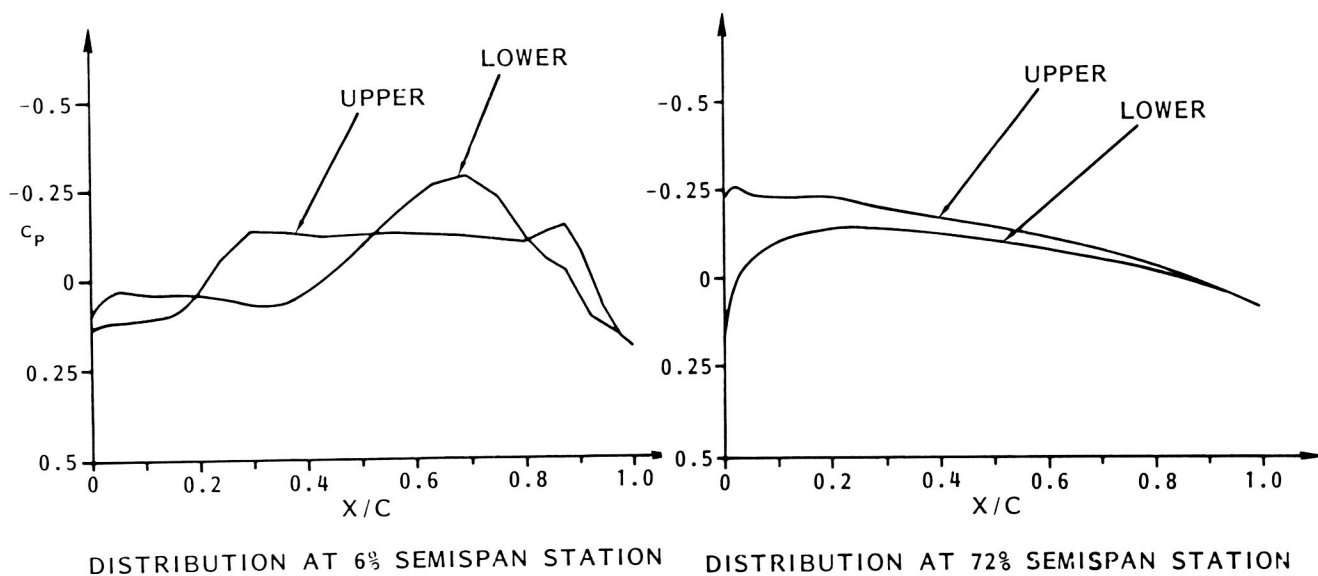
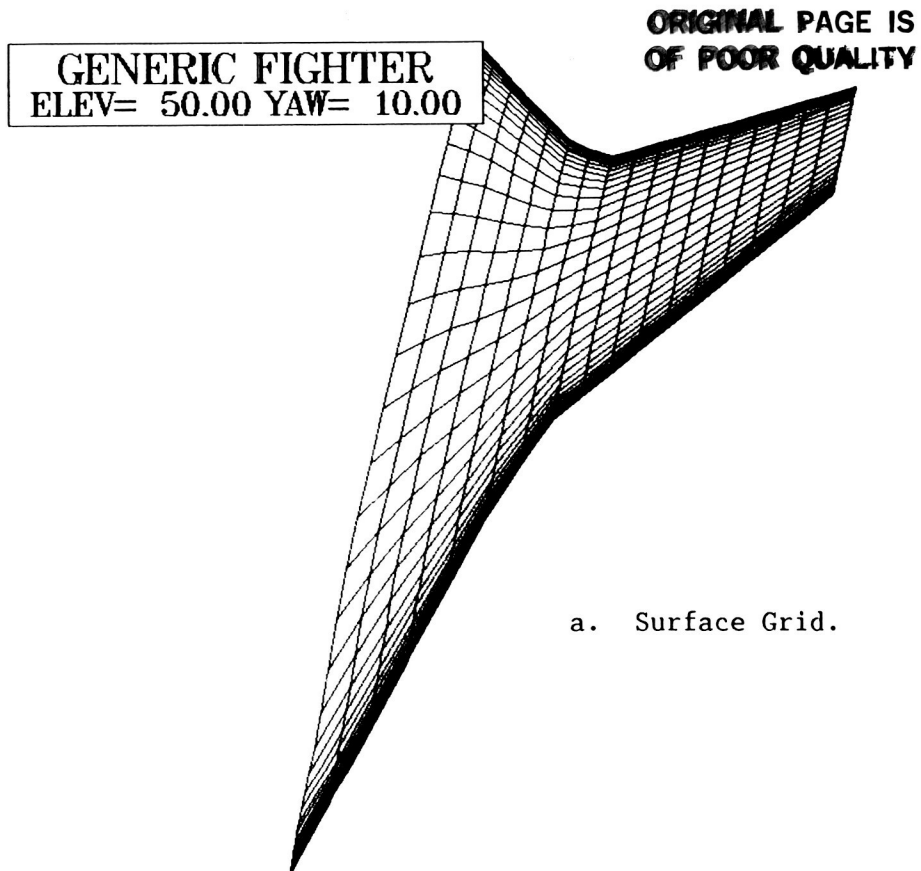
Figure 9. Grid and Pressure Distribution for Advanced Transport Vehicle



c) Surface Pressure Coefficient  
Distribution for Advanced Transport at  
 $M_\infty = 0.8$  and  $\alpha = 0^\circ$ .

Figure 9. Grid and Pressure Distribution for Advanced Transport Vehicle

ORIGINAL PAGE IS  
OF POOR QUALITY



b. Surface Pressure Coefficient distribution for  
 $M_\infty = 0.8$  and  $\alpha = 1^\circ$ .

Figure 10. Grid, Pressure Distribution, and Velocity Field for  
Advanced Fighter



Figure 11. Generic Hypersonic Configuration

# HYPERSONIC MODEL

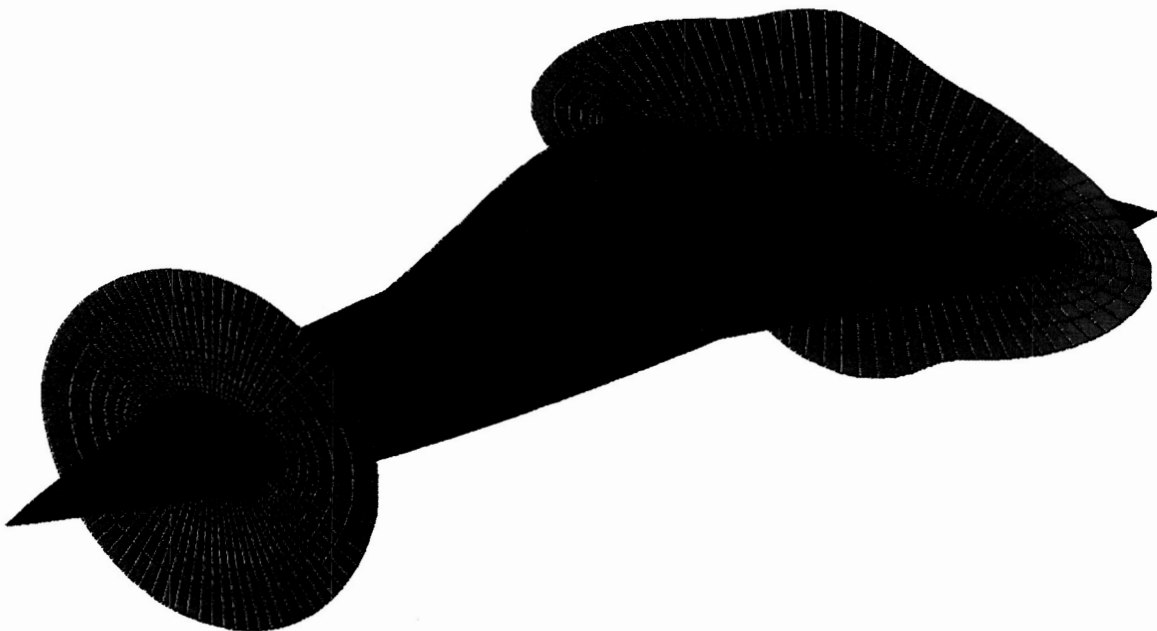


Figure 12. Surface and Circumferential Grids

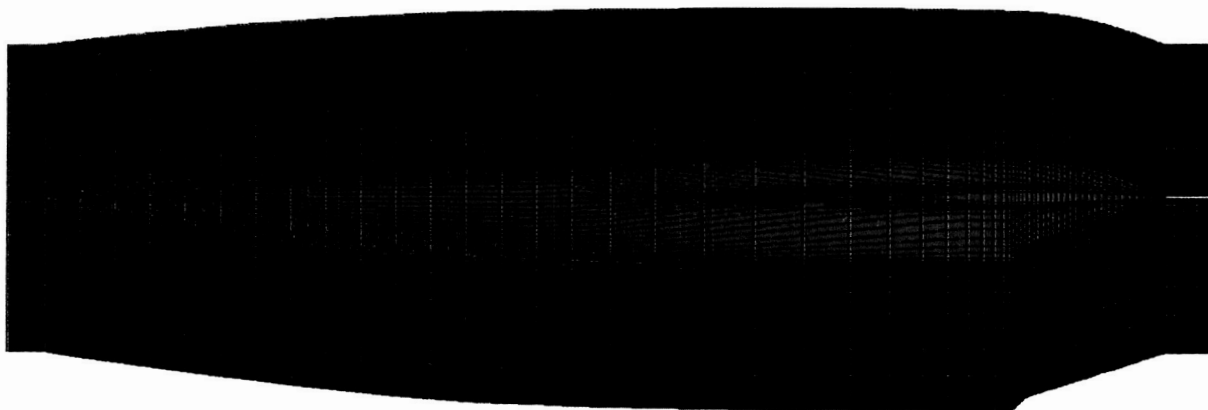


Figure 13. Symmetry Plane Grid

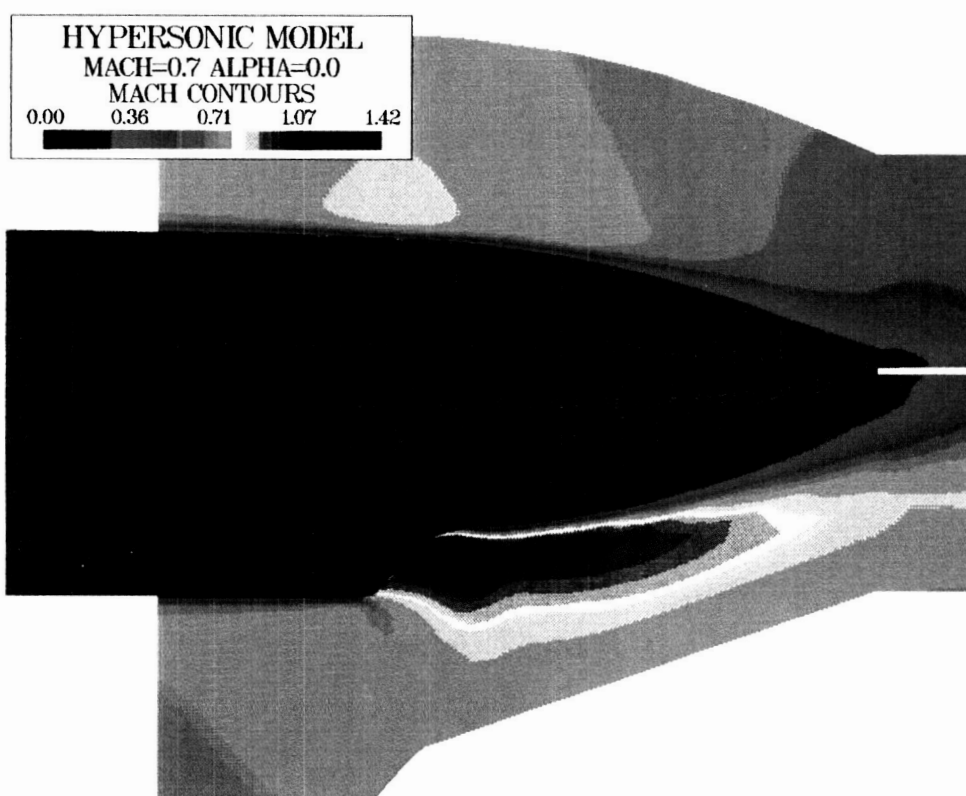


Figure 14. Mach Number Contours on 20 Degrees Upswept Afterbody, NPR 2.0

ORIGINAL PAGE  
COLOR PHOTOGRAPH

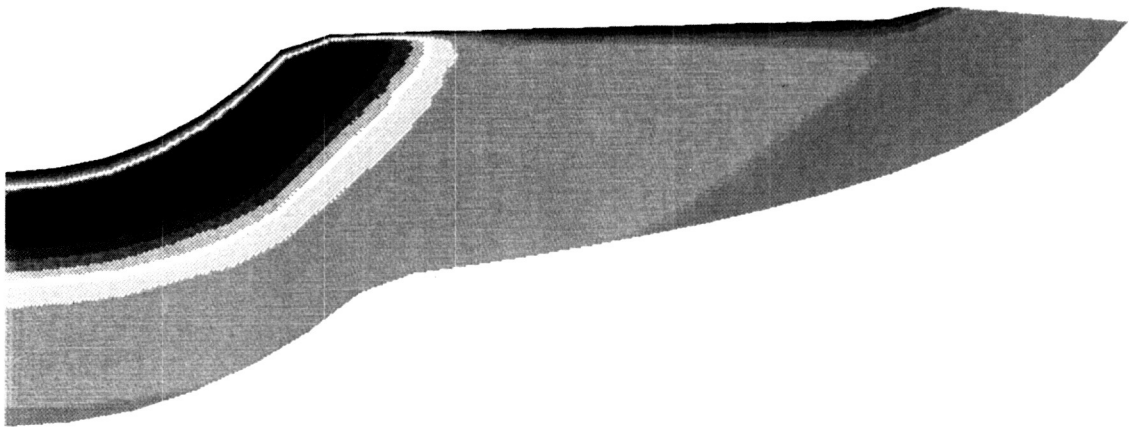
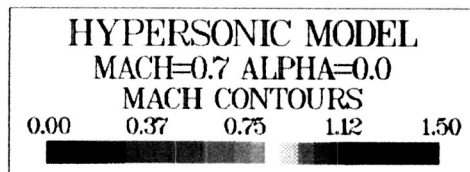
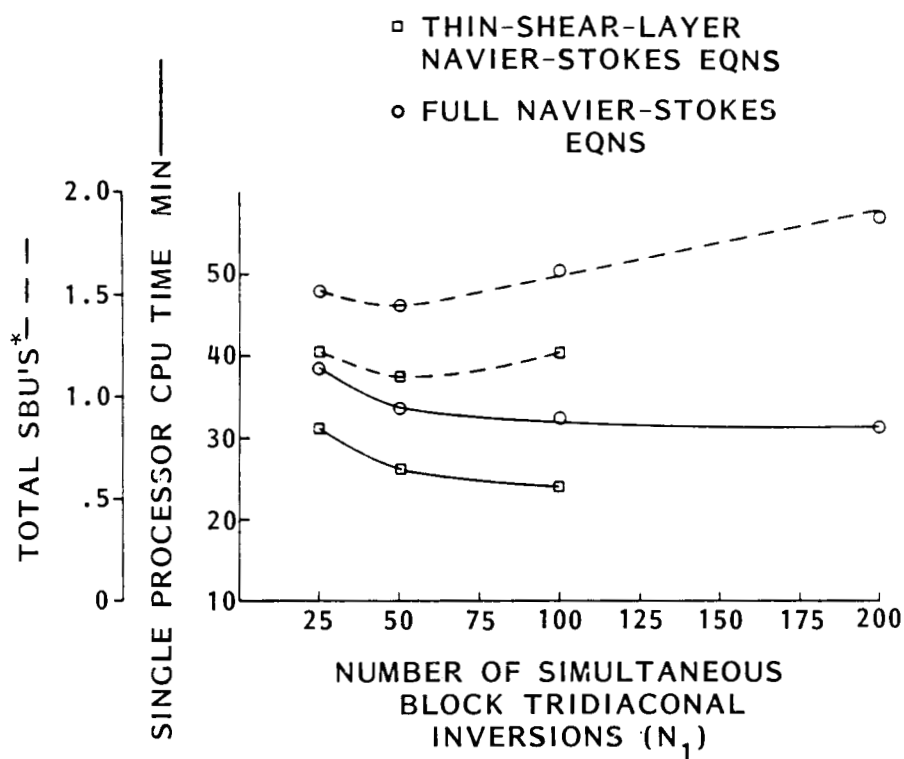


Figure 15. Spanwise Mach Number Contour in Jet/Afterbody Region,  
NPR 2.0





\*AN SBU IS BASED ON CPU TIME AND  
ALLOCATED MEMORY

Figure 16. ENS3DV (Single Processor) CRAY CPU Time and SBU Usage as a Function of Number of Simultaneous Inversions [CFT 1.14 Compiler on CRAY X-MP/24]

## TRANSONIC AERODYNAMIC DESIGN EXPERIENCE

E. Bonner  
Rockwell International Corporation  
North American Aircraft Operations  
Los Angeles, California

## SUMMARY

Advancements have occurred in transonic numerical simulation that place aerodynamic performance design into a relatively well developed status. Efficient broad band operating characteristics can be reliably developed at the conceptual design level. Recent aeroelastic and separated flow simulation results indicate that systematic consideration of an increased range of design problems appears promising. This emerging capability addresses static and dynamic structural/aerodynamic coupling and nonlinearities associated with viscous dominated flows.

## INTRODUCTION

Substantial advancements have occurred in transonic numerical design and analysis since the last Transonic Perspective<sup>1</sup> was held at the Ames Research Center in the spring of 1981. The modeling of general wing-body arrangements is well developed at the full potential/Euler level and has been coupled to boundary layer equations to approximate the effects of viscosity. The interaction of multiple surfaces can be systematically treated. In short, most of the identified deficiencies at the time<sup>2</sup> have been eliminated. Recently, modeling of extensively separated flows has been successfully demonstrated using Reynolds-averaged Navier-Stokes analysis. This is encouraging and provides impetus to numerically investigate increasingly complex design conditions.

One of the pacing technologies in numerical design and analysis is grid generation. The wide variety of geometry and flow gradients emphasizes multiblock/multigrid simulations in the interest of generality and computational efficiency through accelerated solution convergence. Grid size constraints places emphasis on adaptive strategies in order to resolve viscous regions, local interactions, etc.

The development of unified solution algorithms for nonlinear equations<sup>3,4</sup> allows consideration of subsonic (elliptic), transonic (mixed elliptic - hyperbolic) and supersonic (hyperbolic) flows for both steady and unsteady problems.

## SYMBOLS

AR	Aspect Ratio
c	Local Chord
b	Wing Span
$C_D$	Drag Coefficient
$C_L$	Lift Coefficient
$C_{L\alpha}$	Theoretical Lift Curve Slope - Per Radian
$C_p$	Static Pressure Coefficient, $\frac{P-P_\infty}{q_\infty}$
I	Inviscid
M	Mach Number
L/D	Lift-Drag Ratio
NT	Number of Time Steps
P	Static Pressure
q	Dynamic Pressure
RANS	Reynolds-averaged Navier-Stokes
$R_n$	Mean Aerodynamic Chord Reynolds Number
S	Suction Parameter (see Equation 1)
SFP	Supersonic Full Potential
TWT	Rockwell Trisonic Wind Tunnel
UPWT	Langley Unitary Plan Wind Tunnel
V	Viscous
x,y,z	Axial, Lateral, Vertical Cartesian Coordinates
$\alpha$	Angle of Attack
$\delta$	Flap Deflection Angle
$\theta$	Twist Angle
$\Lambda$	Sweep Angle

### Subscripts:

F	Friction
LE	Leading Edge
t	Tip
$\infty$	Free Stream

## DISCUSSION

Representative computational simulations will be presented to illustrate the current state-of-the-art in transonic aerodynamic numerical design. Related results at subsonic and supersonic speeds will also be given since these conditions are often relevant to transonic flows vis-a-vis imposed geometric constraints.

Two specific cases will be selected for detailed discussion. The first addresses conceptual numerical design capability. The second describes the simulation generality which is possible using unified solution algorithms. The discussion is concluded by citing a number of related developments to further define the scope and success of recent transonic numerical efforts.

### Advanced Concept

A multistage process is used to achieve a conceptual aerodynamic design defined here as that activity which is used to numerically screen and define the arrangement and flow characteristics prior to committing to a subscale test. The procedure is summarized on figure 1 in conjunction with the approximating equations used and proceeds from left to right. Linear theory is used to establish necessary far field thickness and lifting constrained optimums and associated geometry. A transonic nonlinear analogue is currently under development<sup>5</sup>. Linear results are necessary but not sufficient in nature since they do not explicitly deal with embedded shock waves and viscous effects. Full potential and Euler/boundary layer simulations are subsequently used to resolve the wave system and manage its interaction with the boundary layer. Transonic aerodynamic deficiencies can be commonly traced to a failure to deal with this consideration adequately. Finally, there is a design space in which viscous effects dominate to the extent that force and moment nonlinearities dictate structural and stability/control system requirements. These flows are typically extensively separated and are statically or dynamically coupled with the structure. Because of the complex nature of such conditions, the slowest progress from both a numerical and test standpoint has resulted for this class of problems.

In order to illustrate the process of figure 1, the following example<sup>6</sup> is presented for the tactical fighter concept of figure 2 which had transonic acceleration, supersonic cruise, and subsonic/transonic/supersonic maneuver design points. These diverse operating conditions were reconciled using 25 percent chord full span deflectable leading and trailing edge wing flaps to provide variable camber and an aeroelastically tailored structure to increase nose-down twist with pitch angle. Subsonic/transonic maneuver design pretest expectations in terms of wing surface pressure coefficient distributions are presented on figures 3 and 4, respectively. The secondary peaks are due to the discrete deflections of the two-element leading edge and single-element trailing edge flaps. The leading edge peak was not fully suppressed in order to reduce these local accelerations. Full potential simulation with and without boundary layer modeling indicated that trailing edge type separation would exist. At

M=0.9 a shock wave of increasing spanwise strength occurred downstream of the trailing edge flap hingeline. The flow is separated at the foot of the shock in the outboard region and is partially a consequence of supersonic efficiency considerations which limit the geometric camber between the flaps. The approach here is thus one of accepting trailing edge separation and limiting its extent through pressure gradient location. Post-test comparison with measurements presented on figures 3 and 4 indicate that this objective was realized. Surface flow data (not shown) further corroborated the anticipated separation extent.

Measured performance results in terms of the aerodynamic lifting efficiency parameter

$$S = \frac{C_L^2 / C_{L\alpha} - (C_D - C_{DF})}{C_L^2 / C_{L\alpha} - C_L^2 / \pi AR} \quad (1)$$

are presented on figure 5. Two cases are shown. The first design placed increased emphasis on acceleration/cruise while the second placed increased emphasis on maneuver. Both were designed numerically. Theoretical upper bound lifting efficiency corresponds to  $S=1$  and is associated with an elliptic span load.  $S=0$  corresponds to the zero suction drag of a flat plate of the same gross planform. The test derived  $M=0.6$  variation with lift coefficient indicates the onset and growth of separation at subsonic conditions. Comparison with the transonic characteristics at  $M=0.9$  indicates the impact of the formation and strengthening of embedded shock waves and associated upper surface separation. The test results compared to upper bound levels verify that the numerical design is operating efficiently over a broad band of operating lift coefficient at both subsonic and transonic conditions. A corollary result is that numerical pressure gradient/boundary layer control through camber and twist management is an effective strategy. The impact of twist/camber variations at supersonic speeds is presented on figure 6. Also shown is the effect of transonic considerations associated with reduced leading edge sweep and increased leading edge radius, camber and twist relative to an unconstrained supersonic design. The impact of the twist/camber changes between the first and second transonic design of figure 5 were secondary at this condition and consequently not shown. Numerical pretest expectations are in good agreement with measurements in all cases.

In summary, numerical design was very effective in developing high aerodynamic efficiency for an advanced concept over a broad Mach number/lift coefficient operating envelope and was realized with a minimal number (specifically two) of test entries. The impact of computational fluid dynamics on the design effort is summarized on figure 7 which compares the present advanced concept results with representative inventory tactical aircraft of the same class. Transonic improvements are attributed to increased lifting efficiency and supersonic improvements to increased volumetric efficiency. These and similar results not presented here indicate that numerical aerodynamic performance design has progressed to a relatively mature status. Adequate prediction of transonic drag does, however, remain an area of research, particularly for conditions which have separation present.

## Research Wing-Body

A series of numerical computations will now be compared to test results for the wing-body arrangement of figure 8 to illustrate the current capability to systematically simulate a wide variety of conditions encompassing subsonic, transonic, and supersonic conditions for both attached and separated flows using a unified solution algorithm<sup>3,4</sup> and grid topology. The analysis is equally capable of treating unsteady as well as steady flows. Only results for the latter will be presented. The geometry under consideration is undesigned and consequently the subject pertinent to aerodynamic development is how reliably are the characteristics associated with this arrangement numerically captured. This, of course, is a prerequisite to their modification through numerical design.

The multiblock six-zone H grid topology of figure 9 was used for the numerical simulation. An isometric upper half plane of the computational domain is presented in figure 9a. A typical cross-section cut is presented on figure 9b to further define the blocking and clustering. Nominally 89,000 grid points were employed (maximum available on CRAY XMP/14) for an in core simulation. Euler results<sup>7</sup> for six degrees angle-of-attack at  $M=0.9$  and  $1.2$  are presented on figure 10 for various wing span stations and fuselage polar angle locations of  $+15^\circ$  above the plane of the wing where the wing-body interaction is strong. Comparison with measured surface pressure coefficient results is excellent. At  $M=0.9$ , a strong shock exists on the fuselage above the plane of the wing. Embedded leading and trailing edge shock exists on the suction side of the wing which increase in strength spanwise until they coalesce and further increase in strength until shock-induced separation occurs very near the wing tip. The flow at  $M=1.2$  has an upper surface trailing edge shock and is sufficiently weak that the flow is attached. All major features of the flow have been accurately forecast except, of course, the shock-induced tip separation. Ample warning was provided even in this area that the shock was strong and that separation was consequently a possibility. From a design viewpoint, it can either be accepted or explicitly dealt with through redesign. The Euler numerical results typically required 20 minutes of CRAY CPU time per case. It should be pointed out that a 33,660 grid point single zone C-H grid full potential simulation at  $M=0.9$  produced similar prediction success in 80 CPU seconds. No important rotational flow effects consequently existed for this case. A similar conclusion at supersonic speeds is provided by the space marching full potential and Euler results of figure 6.

The multiblock grid of figure 9 was subsequently used for turbulent Navier-Stokes simulation of the research wing-body arrangement. Typical impact of angle-of-attack on measured wing surface pressure coefficient characteristics is presented on figure 11. The inboard upper surface loading increases with the leading edge suction peak exhibiting pronounced broadening which is indicative of the formation of a vortex in this region. The outboard wing exhibits a pronounced decrease in loading and a flat upper surface pressure level typical of wing stall. Clearly this is a relatively complex viscous dominated flow which provides a difficult practical test for Reynolds-averaged Navier-Stokes

simulation. Two cases were selected for evaluation --  $M=0.6$ ,  $\alpha=14^\circ$ , and  $M=0.9$ ,  $\alpha=10^\circ$ , corresponding to the highest angle-of-attack tested at each Mach number. Both exhibit the previously discussed inboard vortex/outboard separation behavior.

A zero equation (Baldwin-Lomax) turbulence model was used in zones 1 and 4 of figure 9b for the viscous simulation. The numerical analysis is compared to measured surface pressure results on figures 12 and 13. The major features of the flow are well reproduced for both cases. In particular, the formation of the inboard wing vortex and the outboard wing stall are captured. Considering the relatively coarse (limited by available core) grid being used to simulate the phenomena, the results are quite good. The potential for using such analysis for structural design and high angle-of-attack viscous dominated nonlinear modeling appears promising. The Navier-Stokes solution discussed previously required between 1-1/2 to 2-1/2 CRAY CPU hours to nominally converge. Although this level of computer resources is considerable, it is not unreasonable from an aerodynamic design point of view. This is particularly true if such simulations are used discriminately and projected to advanced state-of-the-art computers such as the CRAY 2.

In summary, numerical simulation of a research wing-body arrangement was successfully demonstrated at subsonic, transonic, and supersonic speeds. Both attached and separated flow conditions were considered. These results were achieved with a unified solution algorithm and multizone grid topology. The associated computer resources were consistent with advanced concept development activities. The viscous modeling success indicates that systematic consideration of strong viscous interaction design problems appears promising.

#### Related Advancements

Finally, a series of developments will be cited to further define the scope and success of recent transonic numerical efforts. Table I summarizes these activities. Detailed results are provided in the indicated references and will not be repeated here for brevity. Examination of the analyses and comparison with test measurements where pertinent establish that advancement is occurring in a variety of areas covering grid generation, multiple surface interactions, steady and unsteady aeroelasticity, and strongly shocked and separated flows. This research considered a hierarchy of fluid dynamic equations covering full potential, Euler, and Reynolds-averaged Navier-Stokes approximations. Unification of the grid topology and flow solvers is being emphasized in order to reduce the effort associated with development of simulations covering a wide design space.

## CONCLUDING REMARKS

Substantial progress has occurred in transonic numerical simulation and design since the last Transonic Perspective. Aerodynamic numerical performance design is in a relatively well developed state as evidenced by the ability to reliably develop efficient broad band characteristics at the conceptual design level. Recent aeroelastic and separated flow simulation results indicate that a capability to consider an important new range of design problems is emerging. Grid generation remains a pacing technology for numerical aerodynamic design efforts. It becomes increasingly demanding for complex geometry/viscous flow resolution. Overall grid size limits must be compatible with conceptual development activity in terms of time and resources available if advanced numerical analyses are to have the desired early design impact.



## REFERENCES

1. Transonic Aerodynamics, Progress in Astronautics and Aeronautics, Volume 81, David Nixon Editor, 1981
2. IBID, chapter X
3. Shankar, V., and Chakravarthy, S., "Development and Application of Unified Algorithms for Problems in Computational Science," NASA CP-2454 Supercomputing in Aerospace Sciences Symposium Proceedings, pp. 87-107, Ames Research Center, March 10-12, 1987
4. Chakravarthy, S. and Szema, K. Y., "Advances in Finite Difference Techniques for Computational Fluid Dynamics," Chapter in State of the Art Survey in Computational Mechanics, edited by A. K. Noor and J. T. Oden, to be published by ASME, April 1988
5. Malmuth, N. D., and Cole, J. D., "Wave Drag Due to Lift for Transonic Airplanes," NASA CP3020, 1989
6. Bonner, E., "Nonlinear Aerodynamic Wing Design," NASA CR 3950, December 1985
7. Woan, C. J., and Chakravarthy, S. R., "Transonic Euler Calculation of a Wing-Body Configuration Using a High Accuracy TVD Scheme," Proposed Paper AIAA 6th Applied Aerodynamics Conference, June 6-8, 1988

TABLE I  
ADDITIONAL TRANSONIC SIMULATION RESULTS

<u>Simulation</u>	<u>Formulation</u>	<u>Reference</u>
Grid Generation	Multiblock	AIAA 88-0312 88-0521
Multiple Surface Interactions	Full Potential	AIAA 86-1795
Wing-Body Static Elasticity	Full Potential	AIAA 87-0707
Wing-Body Dynamic Elasticity	Full Potential	AIAA 87-1238
Subcritical, Critical & Supercritical Inlet Flow	Euler	Unpublished
Boattail, Ramp, & Back Step Separation	Reynolds-averaged Navier-Stokes	NASA CP-2454 pp. 87-107
Attached & Separated Nozzle Flow	Reynolds-averaged Navier-Stokes	Proposed Paper AIAA 6th Applied Aerodynamic Conference, June 1988
Cavity Flow	Reynolds-averaged Navier-Stokes	AIAA 87-0117
Attached & Separated Duct Flow	Reynolds-averaged Navier-Stokes	Unpublished

## SYMBOLS

AR	Aspect Ratio
c	Local Chord
b	Wing Span
$C_D$	Drag Coefficient
$C_L$	Lift Coefficient
$C_{L\alpha}$	Theoretical Lift Curve Slope - Per Radian
$C_p$	Static Pressure Coefficient, $\frac{P-P_\infty}{q_\infty}$
I	Inviscid
M	Mach Number
L/D	Lift-Drag Ratio
NT	Number of Time Steps
P	Static Pressure
q	Dynamic Pressure
RANS	Reynolds-averaged Navier-Stokes
$R_n$	Mean Aerodynamic Chord Reynolds Number
S	Suction Parameter (see Equation 1)
SFP	Supersonic Full Potential
TWT	Rockwell Trisonic Wind Tunnel
UPWT	Langley Unitary Plan Wind Tunnel
V	Viscous
x,y,z	Axial, Lateral, Vertical Cartesian Coordinates
$\alpha$	Angle of Attack
$\delta$	Flap Deflection Angle
$\theta$	Twist Angle
$\Lambda$	Sweep Angle

### Subscripts:

F	Friction
LE	Leading Edge
t	Tip
$\infty$	Free Stream

TABLE I  
ADDITIONAL TRANSONIC SIMULATION RESULTS

<u>Simulation</u>	<u>Formulation</u>	<u>Reference</u>
Grid Generation	Multiblock	AIAA 88-0312 88-0521
Multiple Surface Interactions	Full Potential	AIAA 86-1795
Wing-Body Static Elasticity	Full Potential	AIAA 87-0707
Wing-Body Dynamic Elasticity	Full Potential	AIAA 87-1238
Subcritical, Critical & Supercritical Inlet Flow	Euler	Unpublished
Boattail, Ramp, & Back Step Separation	Reynolds-averaged Navier-Stokes	NASA CP-2454 pp. 87-107
Attached & Separated Nozzle Flow	Reynolds-averaged Navier-Stokes	Proposed Paper AIAA 6th Applied Aerodynamic Conference, June 1988
Cavity Flow	Reynolds-averaged Navier-Stokes	AIAA 87-0117
Attached & Separated Duct Flow	Reynolds-averaged Navier-Stokes	Unpublished

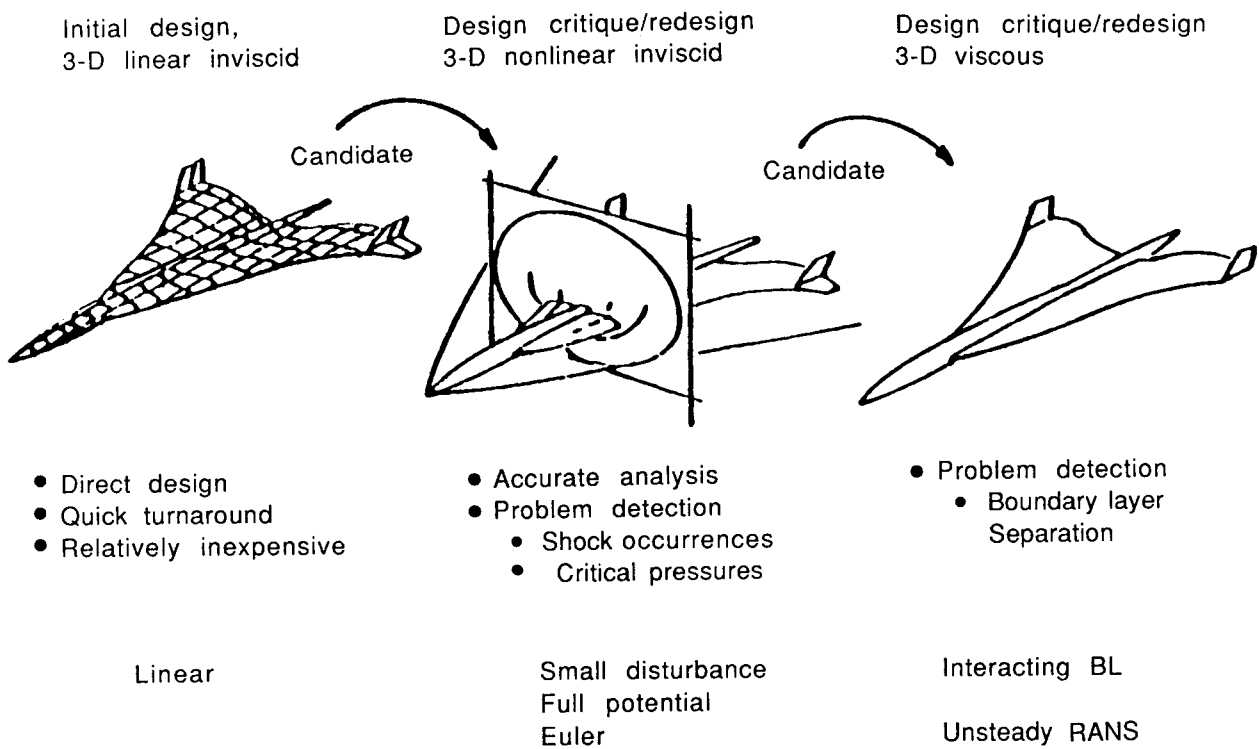


Figure 1. Numerical Design Approach

<u>GEOMETRIC PARAMETER</u>	<u>WING (TRAP)</u>	<u>VERTICAL (TRAP)</u>
ASPECT RATIO	3	1
TAPER RATIO	0.2	0.2
LE SWEEP	48°	55°
DIHEDRAL	0	70°
THICKNESS RATIO	0.04	0.04

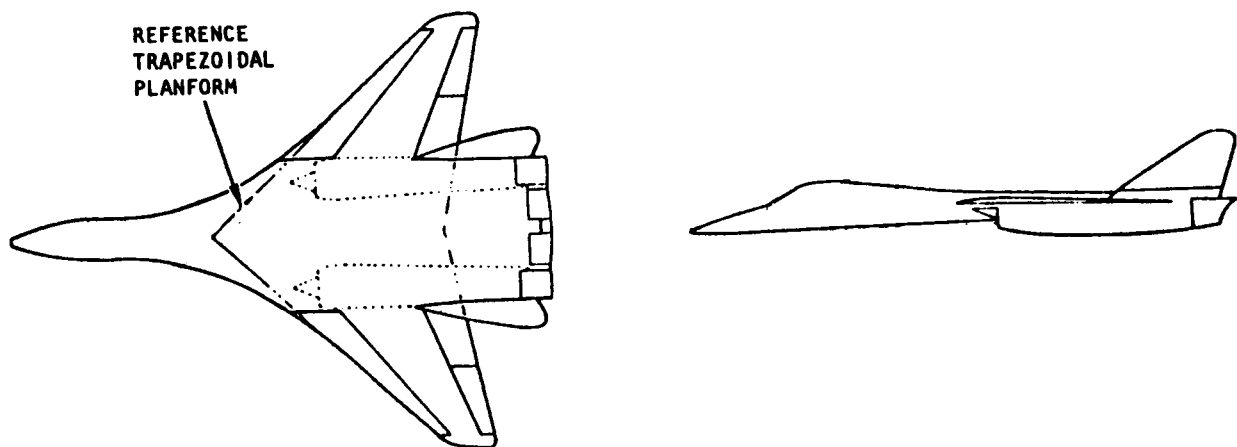


Figure 2. Advanced Concept

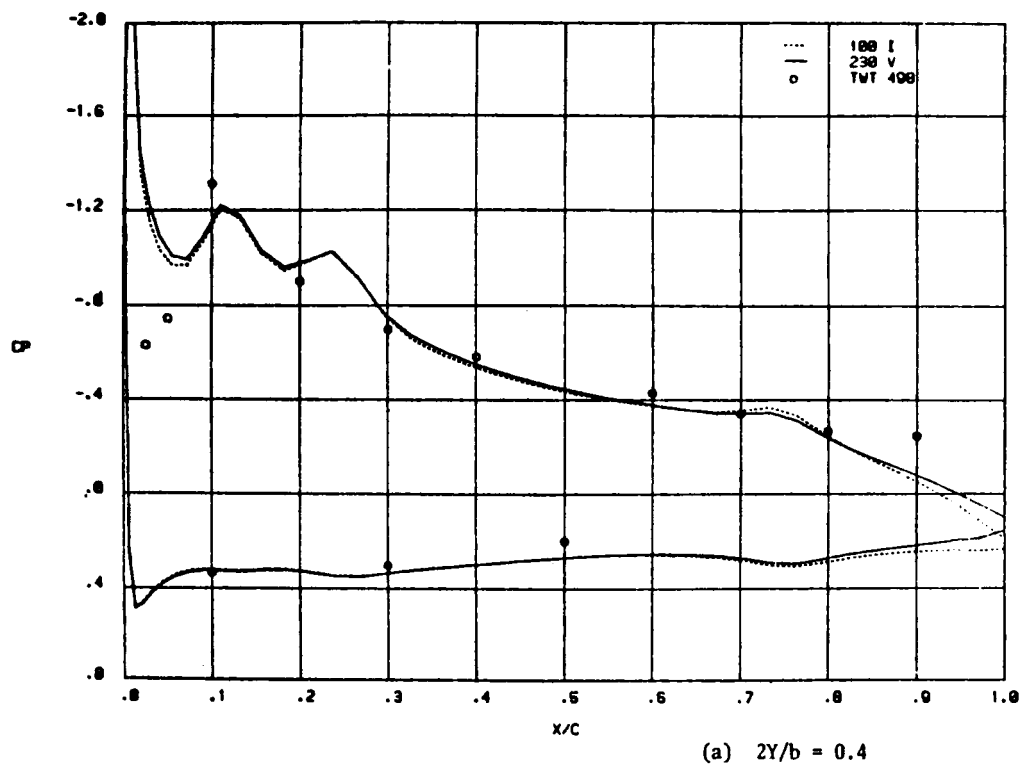


Figure 3. Advanced Concept Subsonic Wing Pressure Distributions  
At  $M = 0.6$ ,  $\alpha = 14^\circ$ ,  $R_n = 5 \times 10^6$

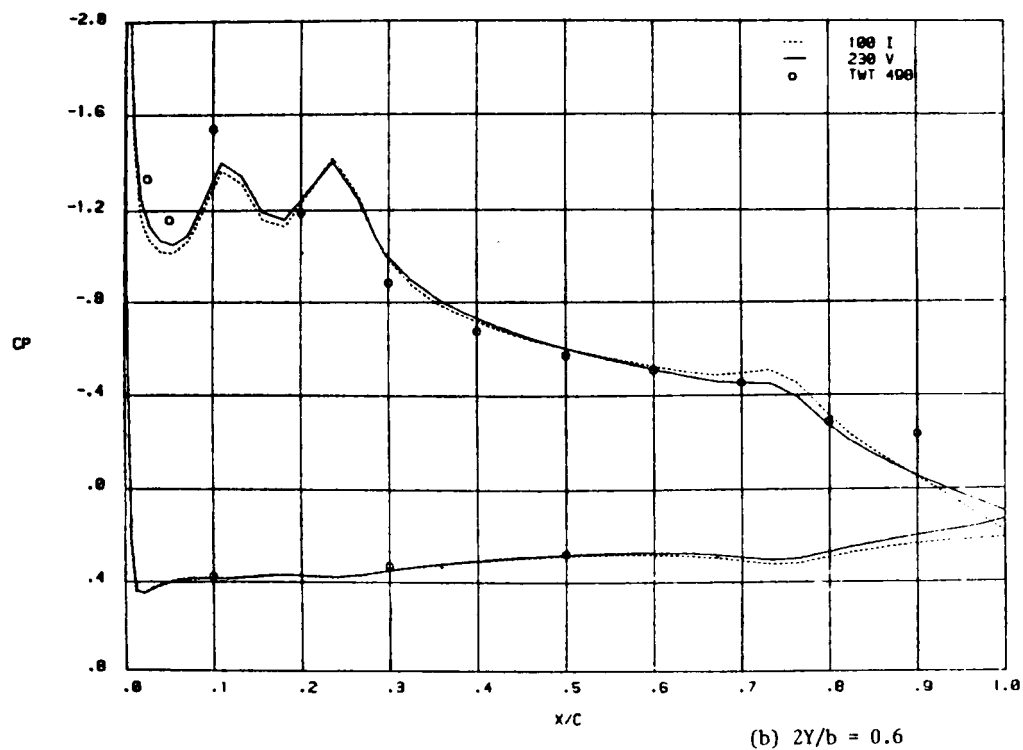


Figure 3. Continued

ORIGINAL PAGE IS  
OF POOR QUALITY

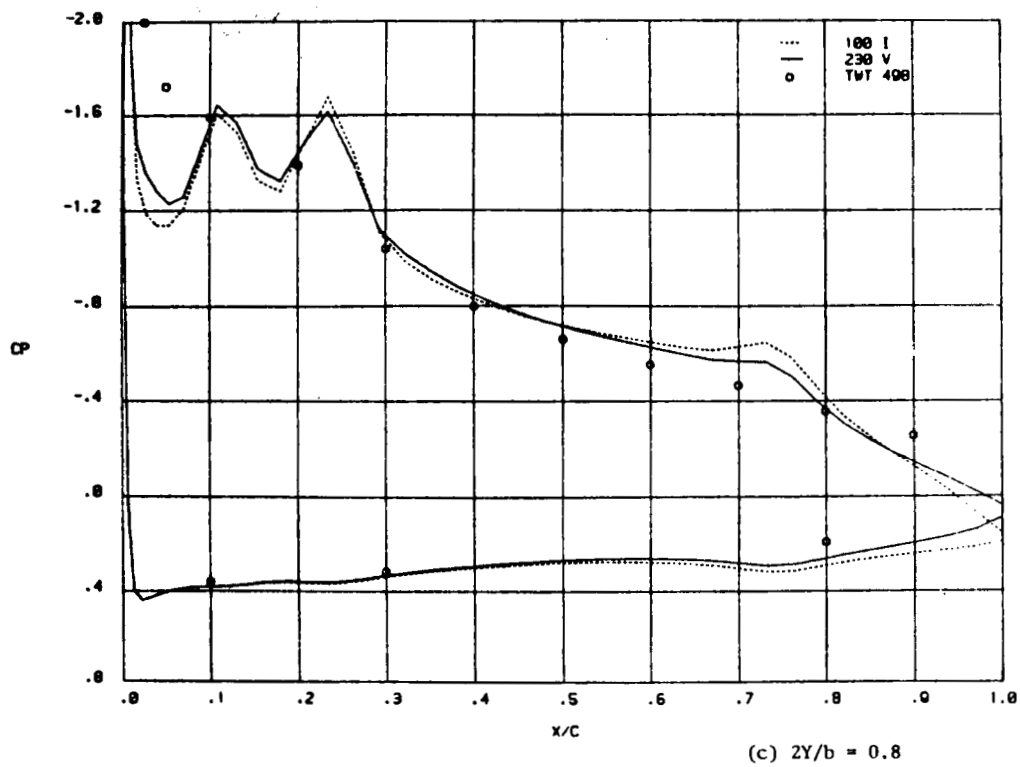


Figure 3. Concluded

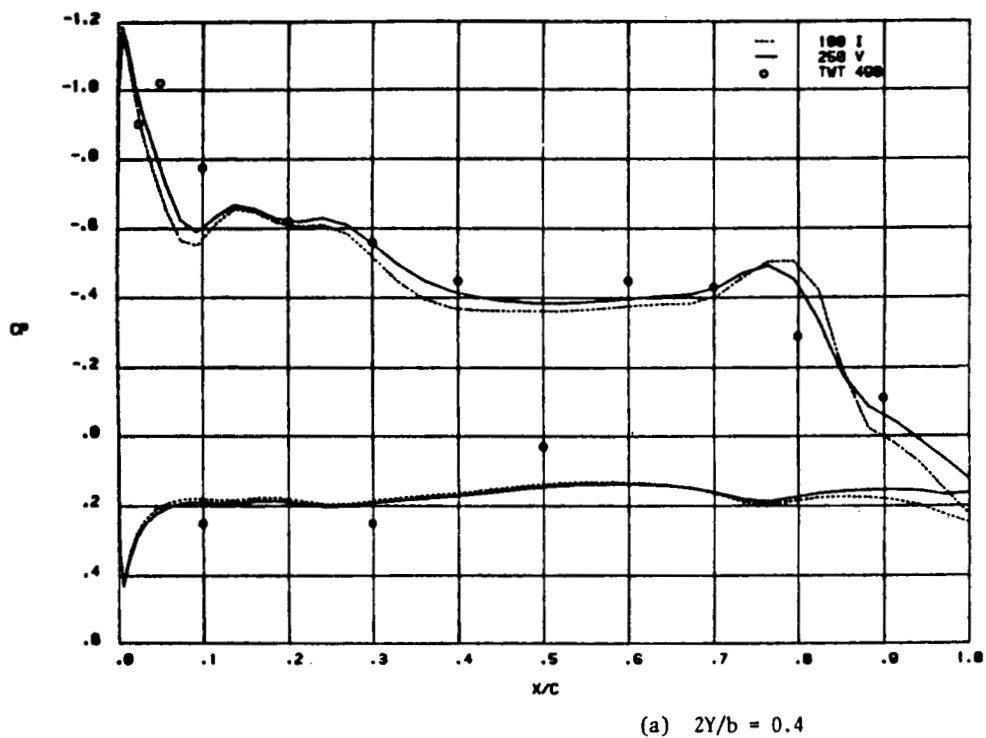
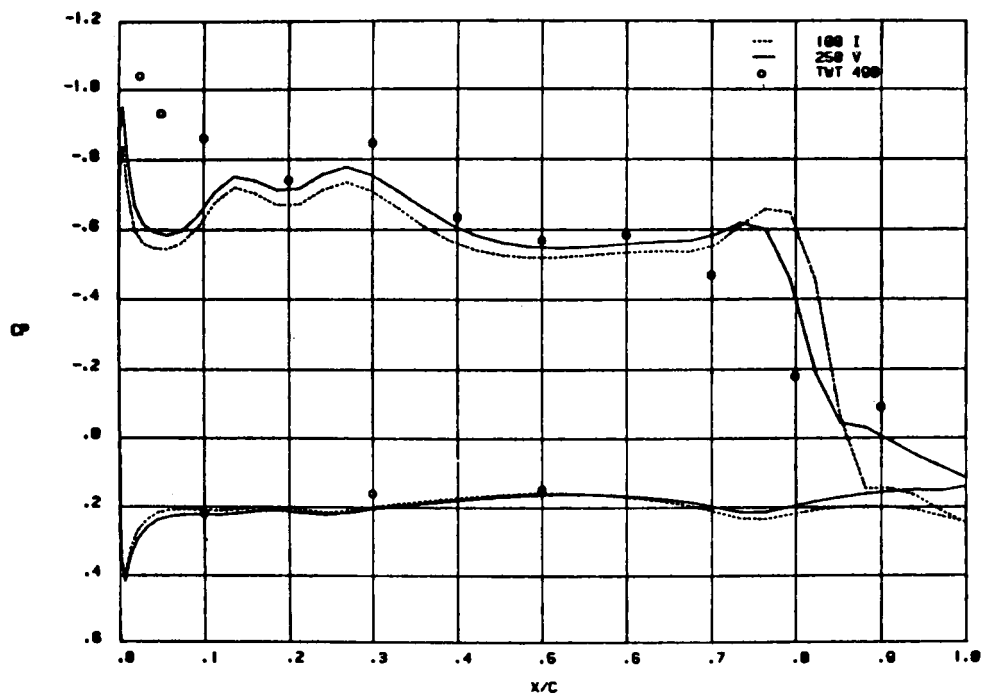


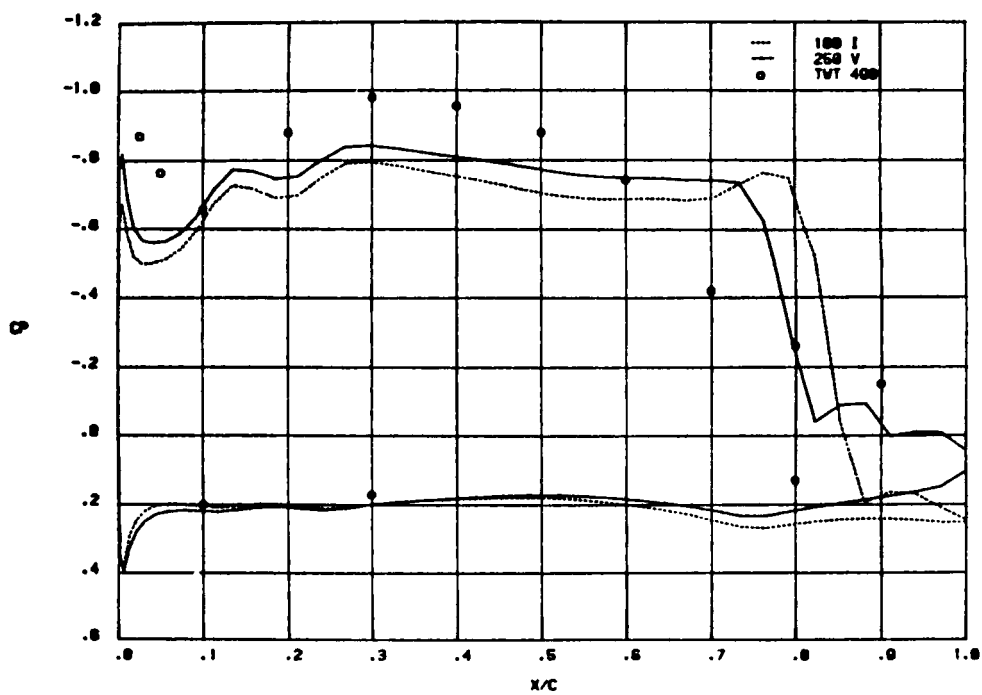
Figure 4. Advanced Concept Transonic Wing Pressure Distributions  
At  $M = 0.9$ ,  $\alpha = 8.25^\circ$ ,  $R_n = 5 \times 10^6$

ORIGINAL PAGE IS  
OF POOR QUALITY



(b)  $2Y/b = 0.6$

Figure 4. Continued



(c)  $2Y/b = 0.8$

Figure 4. Concluded



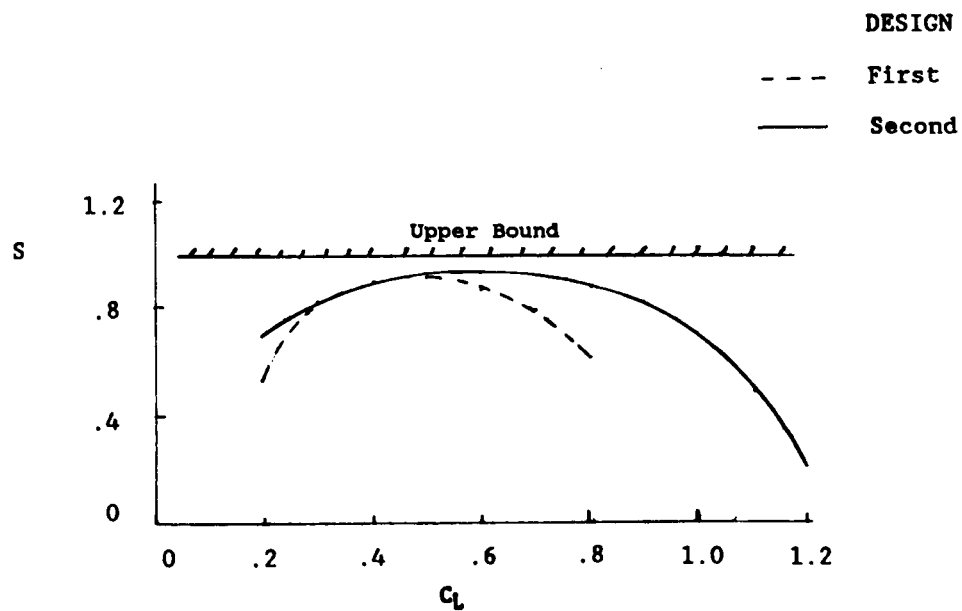


Figure 5. Advanced Concept Test Derived Subsonic/Transonic Lifting Efficiency

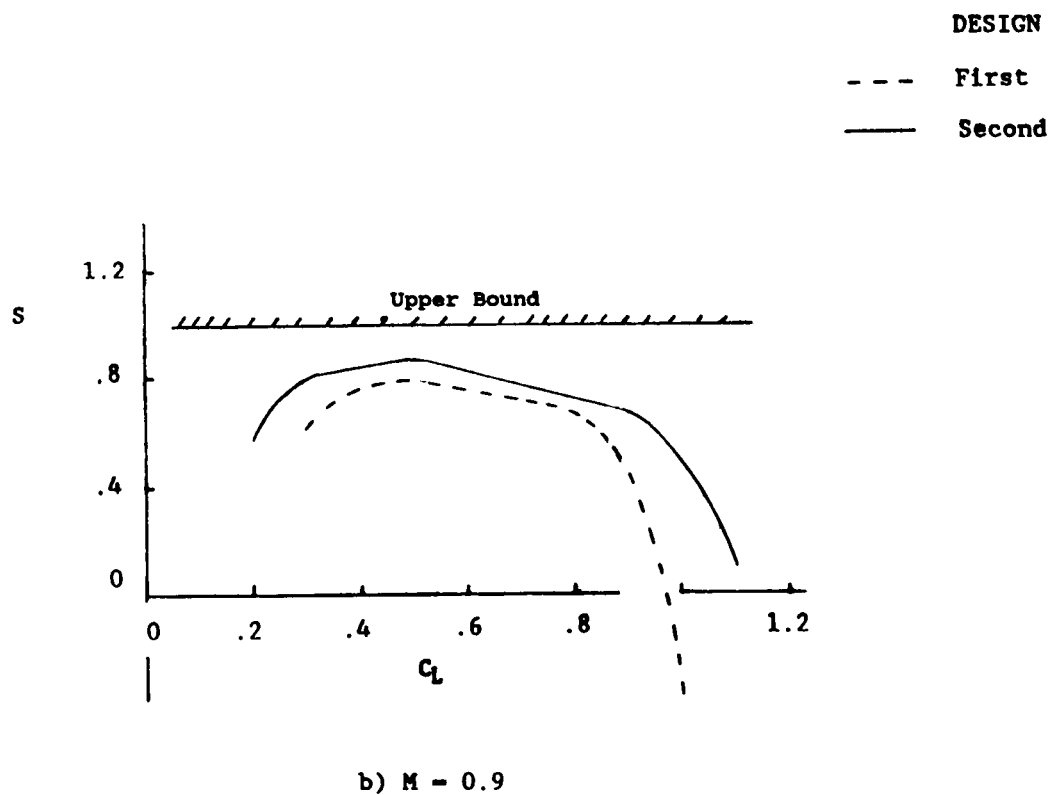


Figure 5. Concluded

ORIGINAL PAGE IS  
OF POOR QUALITY

$A^{\circ}_{LE}$	TEST	LINEAR	SFP	EULER
55	-UPWT	X	□	△
48	--UPWT	Y	○	

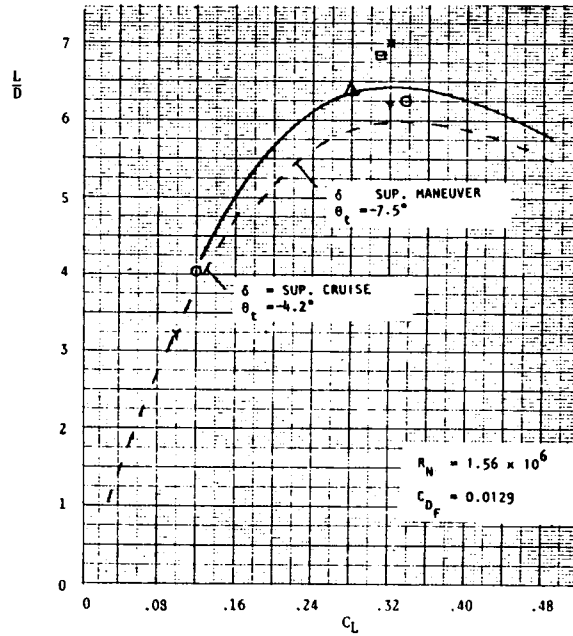


Figure 6. Advanced Concept Measured and Predicted Aerodynamic Efficiency At  $M=1.6$

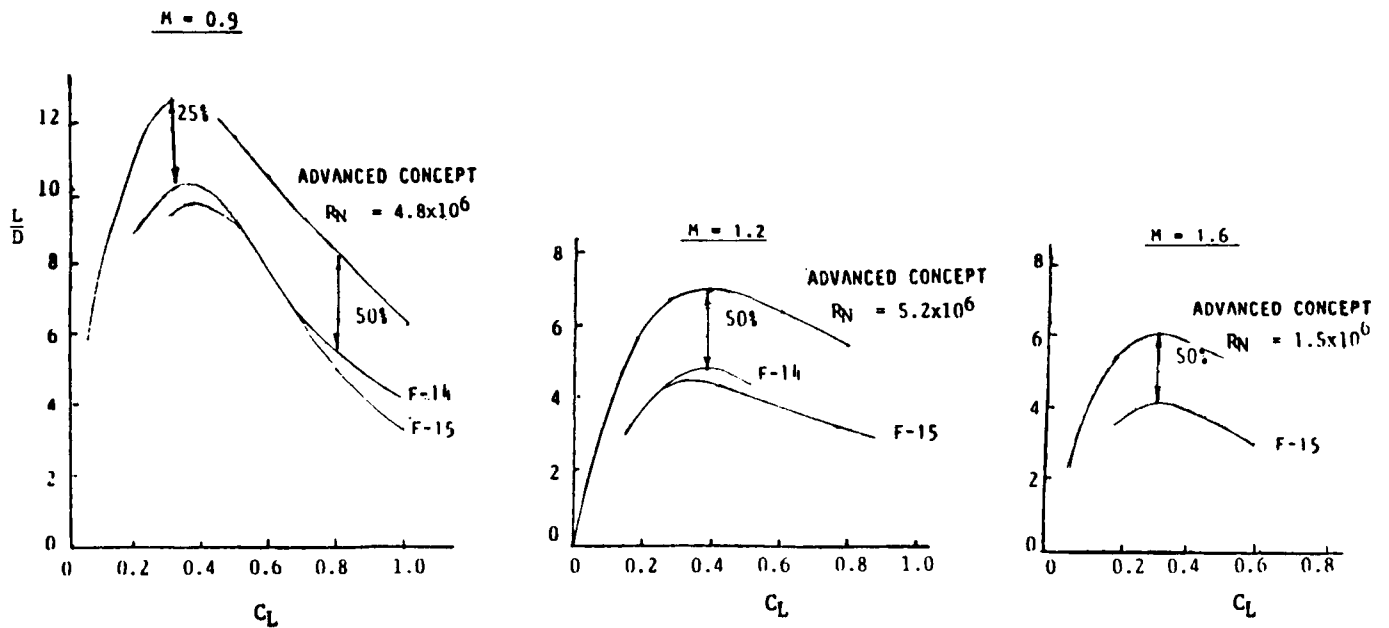


Figure 7. Impact of Numerical Design On Aerodynamic Development

tion  
o  
deg  
deg  
wist, deg

NACA 65A006

4  
0.6  
0  
0  
0

.25-chord line

$c' = 6.125$

20.0

45°

7.5

Maximum diameter = 3.334

33.333

4.5

12.0

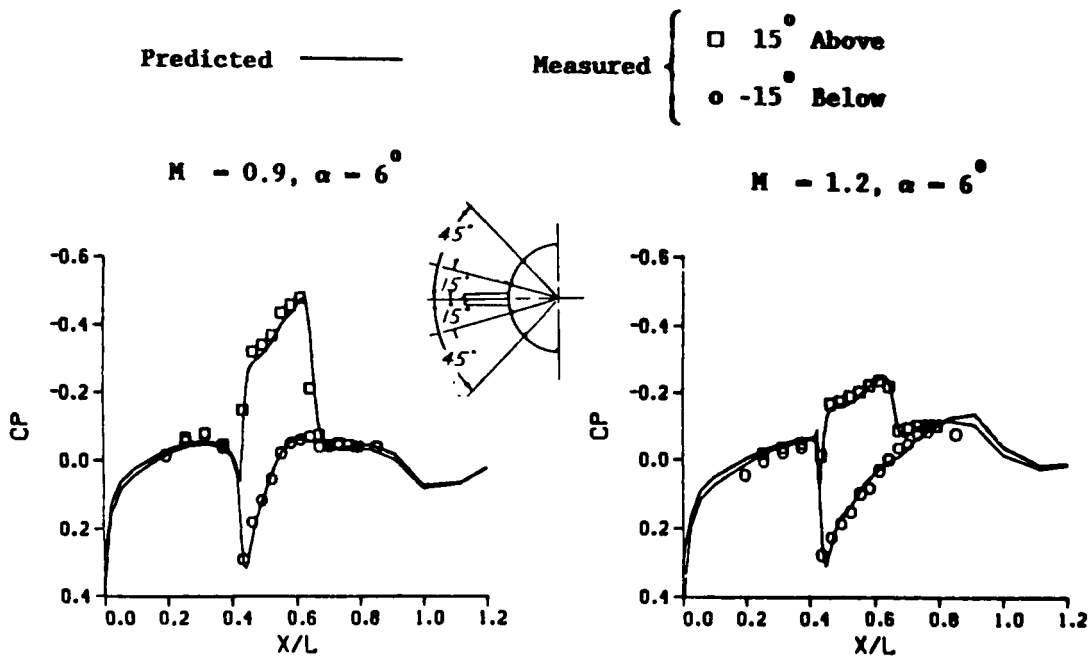
5.5

Sting

A 3D perspective drawing of a rectangular prism, or box, with a grid pattern on its visible faces. The grid consists of lines forming a mesh. The box is oriented such that its edges are parallel to the axes of a 3D coordinate system. In the bottom left corner, there is a small diagram of the coordinate system with three axes labeled 'x', 'y', and 'z'. The 'z' axis points upwards, the 'y' axis points to the left, and the 'x' axis points towards the bottom right.

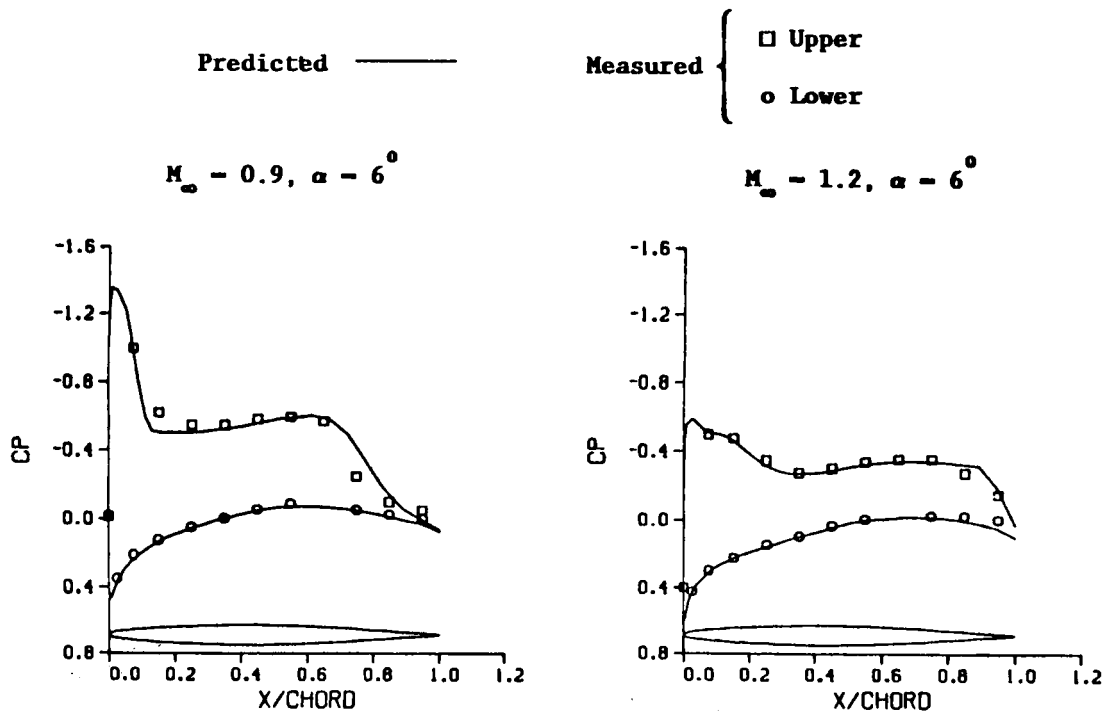
### b) Crossection

**ORIGINAL PAGE IS  
OF POOR QUALITY**



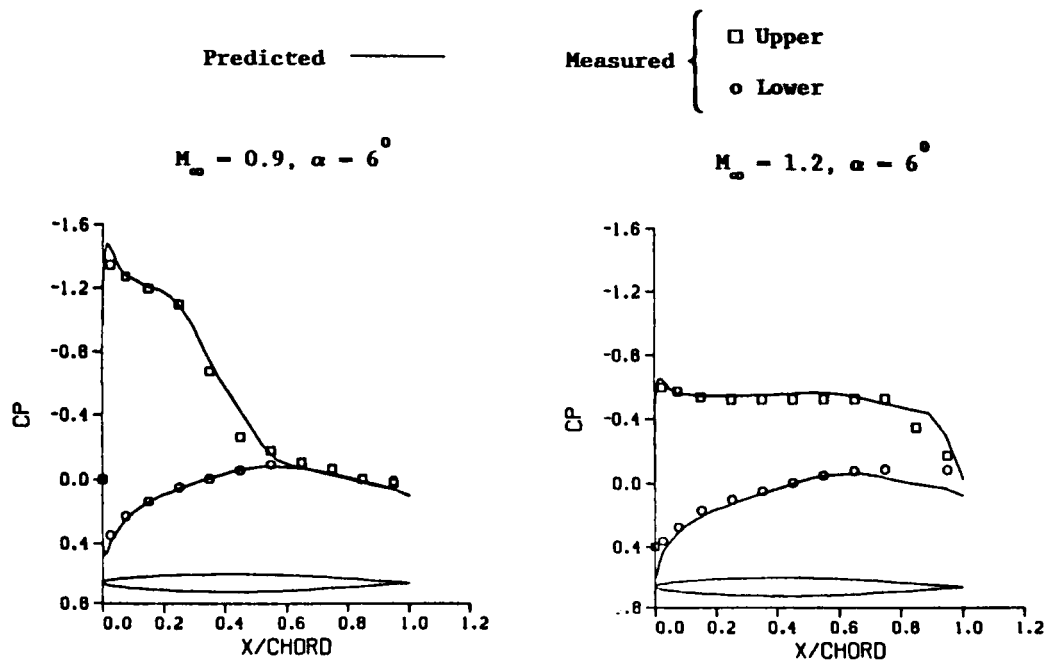
a) Fuselage,  $\theta = \pm 15^\circ$

Figure 10. Research Wing-Body Unified TVD Euler Solution  
at Transonic and Supersonic Conditions



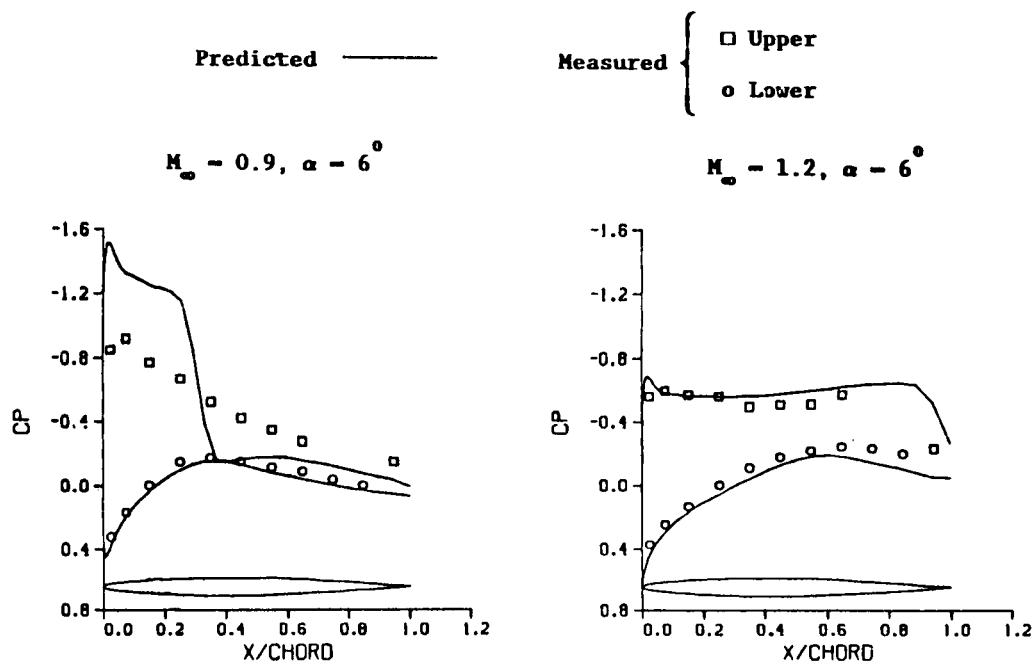
b) Wing,  $2y/b = 0.4$

Figure 10. Continued



c) Wing ,  $2y/b = 0.8$

Figure 10. Continued



d) Wing ,  $2y/b = 0.95$

Figure 10. Concluded

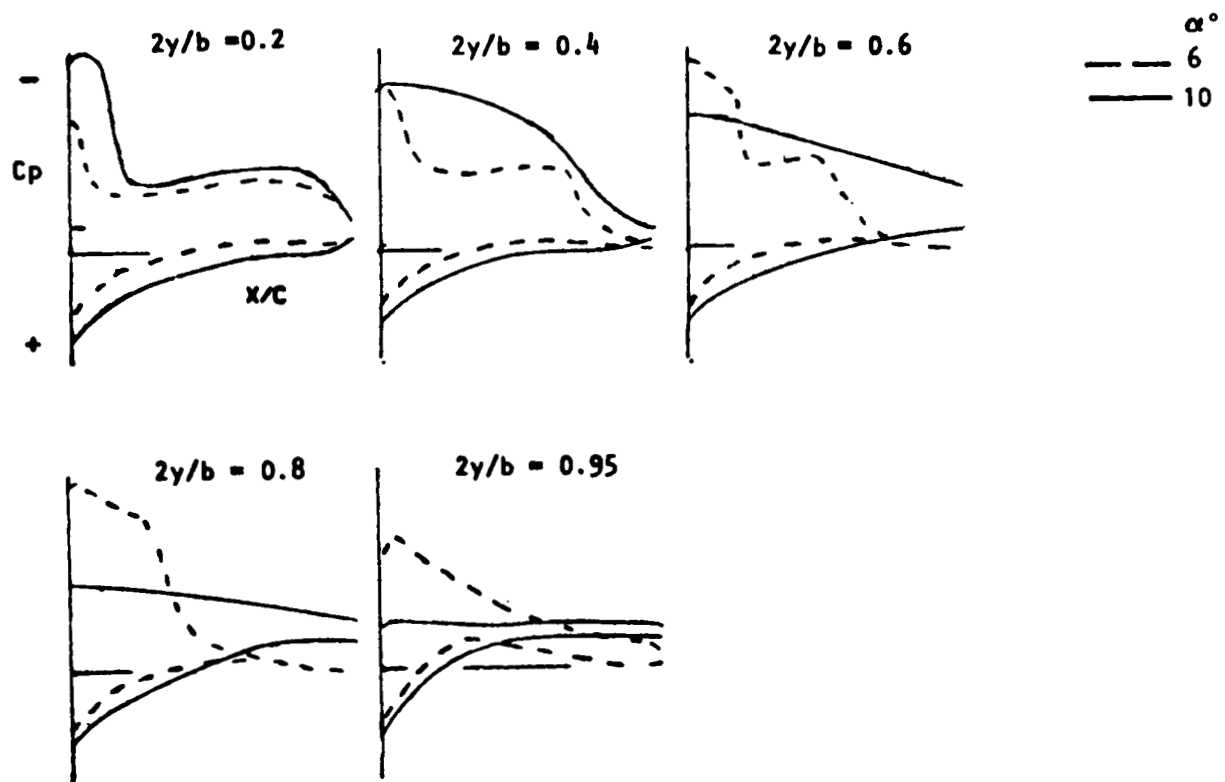


Figure 11. Effect of Viscosity on Measured Surface Pressure Characteristics for Research Wing-Body

ORIGINAL PAGE IS  
OF POOR QUALITY

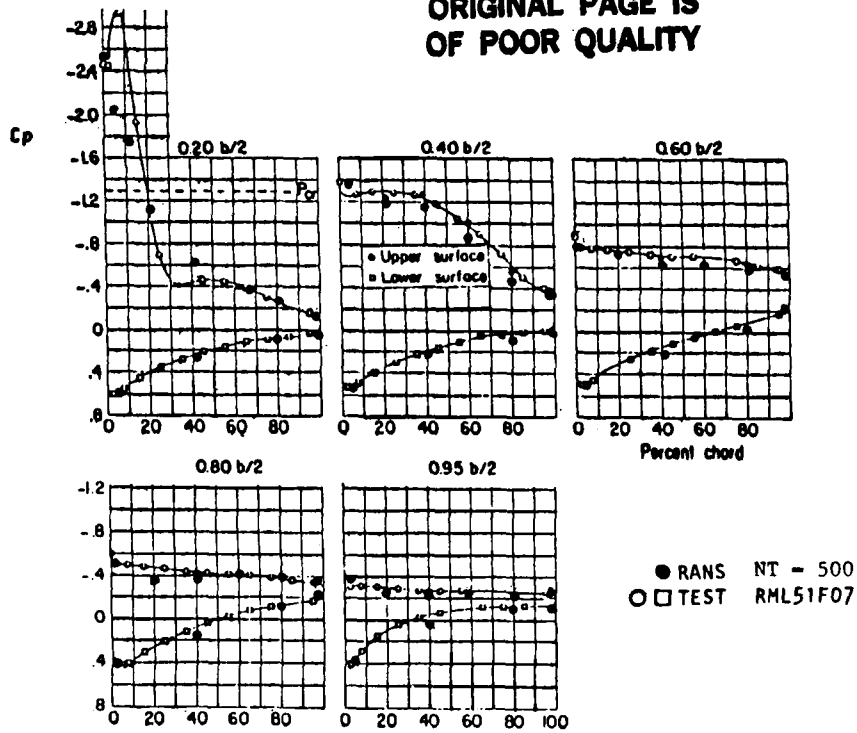


Figure 12. Reynolds Averaged Navier Stokes Separated Flow Simulation  
for Research Wing-Body at  $M = 0.6$ ,  $\alpha = 14^\circ$ ,  $R_n = 1.74 \times 10^6$

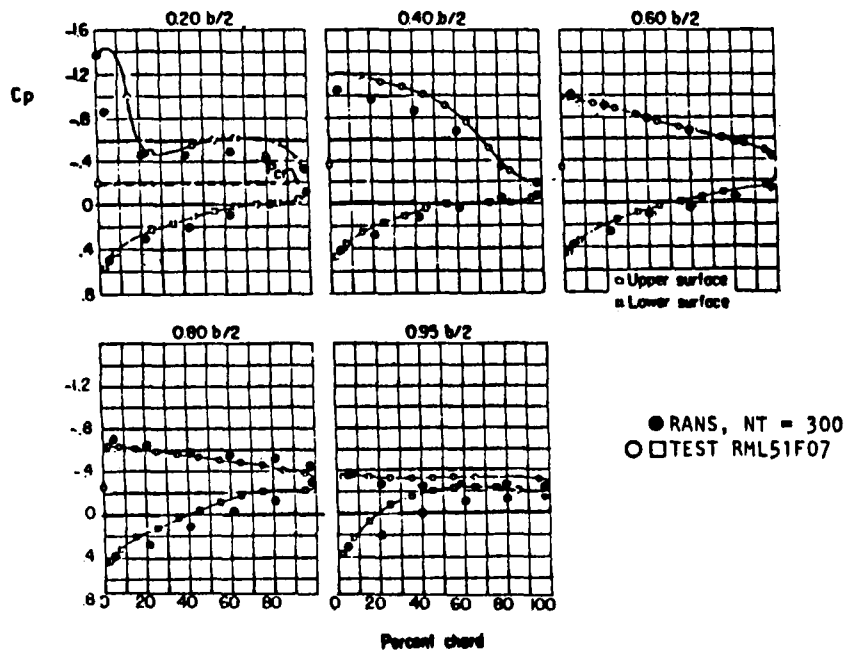


Figure 13. Reynolds Averaged Navier Stokes Separated Flow Simulation  
for Research Wing-Body at  $M = 0.9$ ,  $\alpha = 10^\circ$ ,  $R_n = 2.1 \times 10^6$

## EULER SOLVERS FOR TRANSONIC APPLICATIONS

Bram van Leer  
University of Michigan  
Ann Arbor, Michigan

## 1. INTRODUCTION

The 1980s may well be called the Euler era of applied aerodynamics. Computer codes based on discrete approximations of the Euler equations are now routinely used to obtain solutions of transonic flow problems in which the effects of entropy and vorticity production are significant. Such codes can even predict separation from a sharp edge, owing to the inclusion of artificial dissipation, intended to lend numerical stability to the calculations but at the same time enforcing the Kutta condition.

One effect not correctly predictable by Euler codes is the separation from a smooth surface, and neither is viscous drag; for these we need some form of the Navier-Stokes equations. It, therefore, comes as no surprise to observe that the Navier-Stokes era has already begun before Euler solutions have been fully exploited. Moreover, most numerical developments for the Euler equations are now constrained by the requirement that the techniques introduced, notably artificial dissipation, must not interfere with the new physics added when going from an Euler code to a full Navier-Stokes approximation.

In order to appreciate the contributions of Euler solvers to the understanding of transonic aerodynamics, it is useful to review the components of these computational tools. Space discretization, time- or pseudo-time marching and boundary procedures are their essential constituents, to be discussed in Sections 2-4. The subject of grid generation and, in particular, grid adaptation to the solution, is worthy of a separate review and will be touched upon only where relevant; the influence of computer architecture on the choice of discretization is covered similarly. Section 5 rounds off with a list of unanswered questions and an outlook for the near future.

## 2. SPACE DISCRETIZATION

While finite-element discretizations are gaining ground, the majority of codes for inviscid compressible flow adhere to the finite-volume formulation. Two classes of finite-volume codes must be distinguished: those based on cell-centered data that represent cell averages of the conserved state quantities (refs. 1-3), and those based on cell-vertex data representing point samples of the state quantities (refs. 4-6). Cell-vertex schemes have been the lesser studied but bear the promise of a greater accuracy for a given grid (ref. 7), especially if the grid is unstructured. To appreciate the difference between the two sorts of data, consider the integral form of the Euler equations in two dimensions:

$$\frac{\partial u_{i,j}}{\partial t} = -\frac{1}{V_{i,j}} \oint_{B_{i,j}} (f dy - g dx).$$



On the left-hand side, we see the time derivative of the state vector  $u$ , averaged over the cell volume  $V_{i,j}$ ; the right-hand side shows the boundary integral of the normal flux. The right-hand side is called the residual, at least if a steady solution is sought. In order to compute it, we only need data on the cell boundary; therefore, providing cell-vertex data is very efficient. In contrast, if cell-averaged data are given, boundary data must be obtained by interpolation. On the other hand, the left-hand side of (1) shows that cell-averaged data are the right choice for bookkeeping in time, i.e. when computing transient flows. An approach in which the discrete solution is described by a combination of cell-vertex and cell-boundary data is only known for one-dimensional flow (ref. 8).

Among schemes based on cell averages, one may again distinguish two approaches to the problem of finding boundary fluxes. In the "projection-evolution" approach (refs. 8, 9), boundary data are obtained by interpolation on both sides of a cell interface; the two state vectors then merge into one single flux vector by an "approximate Riemann solver" (ref. 10), which more or less describes the interaction of two fluid cells at their interface. Almost all upwind-biased schemes follow this format. In the projection or interpolation phase, non-oscillatory interpolation guarantees the absence of numerical oscillations in the final discrete solution (refs. 9, 11). The latest development in interpolation is the reconstruction of discontinuous solutions (refs. 12, 13).

The other approach (ref. 1) is to compute at each interface a straight flux average, leading to central differencing, and two different dissipative terms, one to stabilize the solution against pattern instabilities (zebra, checkerboard), the other one to help out near shock waves. The "artificial viscosity" approach has been shown to contain the same ingredients as the "projection-evolution" approach, but implemented differently (refs. 9, 10). For a comparison, see figure 1.

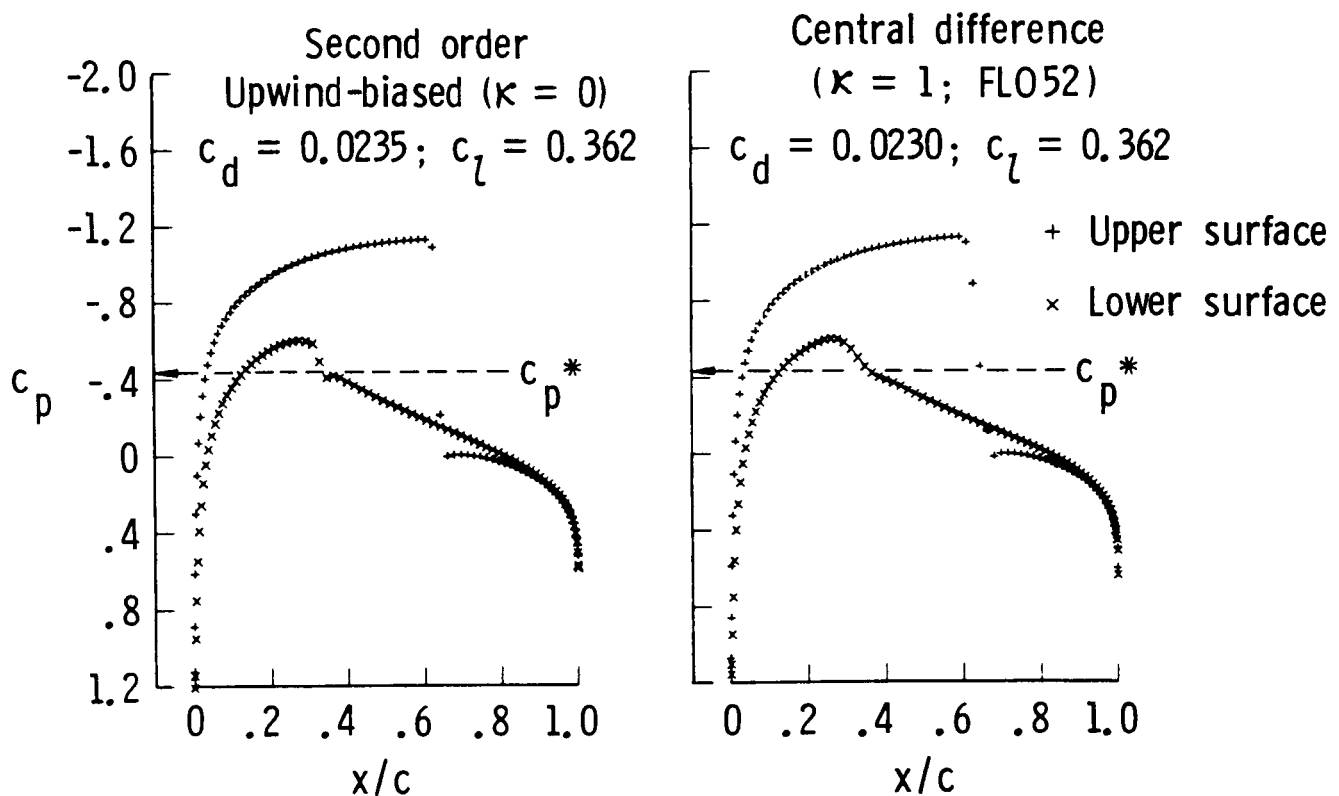


Figure 1. Pressure-coefficient distributions on a NACA 0012 airfoil for  $M_\infty = 0.80$ ,  $\alpha = 1.25$  deg, computed with codes based on upwind-biased (left) and central differencing (right). From ref. 2.

For cell-vertex schemes, a theory of monotone interpolation has not yet been developed, so artificial viscosity is still the only instrument to smooth numerical solutions. It is worth noticing that cell-vertex schemes are less prone to pattern instabilities than cell-average schemes (ref. 12).

No discrete solution can exist without specifying a computational grid. Structured grids as building blocks in a strategy of domain decomposition (ref. 14) seem to be in the lead here, with nested grid refinement (ref. 6) as a welcome accessory technique. Fully unstructured grids, such as traditionally used in the finite-element method, form the alternative (ref. 15) (see figure 2); to retain sufficient accuracy, use of cell-vertex schemes is mandatory (see figure 3).

### 3. MARCHING IN TIME OR TO A STEADY STATE

Unlike the transient-flow problems of high-energy physics and astrophysics, problems of time-dependent transonic flow are of a gentler nature, the time dependence usually arising in the form of a slow oscillation about some mean state (ref. 16). The length of the characteristic time suggests the use of time steps greater than permitted by explicit time-accurate schemes, so implicit methods have been favored in this area. More generally speaking, the most effective methods are those that are also used to march to a steady state. More rapidly varying flows, such as encountered in turbo-machinery (rotor-stator interaction, ref. 17), require the full temporal resolution of an explicit marching scheme.

The effort spent on developing time-accurate marching methods for aerospace applications is scant, which clearly illustrates that this field is dominated by steady-flow problems. Still in use is MacCormack's predictor-corrector central-difference scheme (ref. 18); an upwind-biased non-oscillatory predictor-corrector scheme was presented and tested in (ref. 19). These schemes are examples of a "package deal": space and time discretization are inseparable. A more general strategy is to use a multi-stage Runge-Kutta-type scheme for the time integration, matched with the chosen spatial differencing operator to form a stable overall method.

Interesting enough, multi-stage Runge-Kutta methods have predominantly been used to march to steady solutions (ref. 1), without regard to their potential time accuracy. When developing Runge-Kutta methods for problems of time-dependent transonic flow, the same standards of accuracy and robustness must apply as those that led to the Piecewise Parabolic Method (PPM) (ref. 20) and other schemes suited equally well for smooth flow as for shocked flow. A breakthrough in this respect are the recently derived Total Variation Diminishing (TVD) multi-stage schemes (ref. 21), which preserve the TVD property of the spatial operator while advancing in time.

Regarding methods for marching to a steady state, explicit and implicit methods have been going up and down in popularity as on a wheel of fortune. Some of these changes were driven by developments in computer technology, others by advancement in numerical analysis. In the mid-seventies, Approximate Factorization (AF) emerged as an efficient method for solving steady inviscid problems (ref. 22). This is a relative of Alternating-Direction Implicit methods and requires considerable storage for maximum efficiency, namely, storage of the block-LU decomposition resulting from a line-inversion (this decomposition may be "frozen" for many iteration cycles). Jameson et al. (ref. 1) avoided storage problems by developing an explicit marching strategy based on a multi-stage time-discretization, use of "local" time-steps (constant Courant number rather than constant time step for the whole grid), residual smoothing and enthalpy

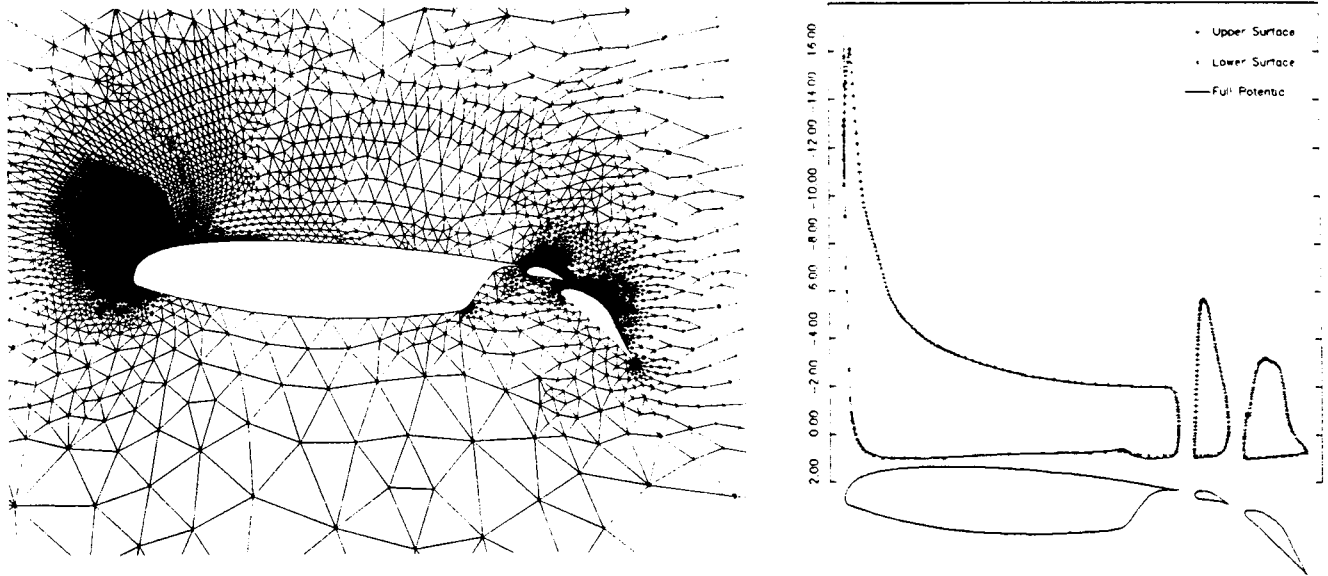


Figure 2. Unstructured, adaptively refined grid (left) and corresponding pressure-coefficient distributions (right) for a multi-element airfoil obtained with a cell-vertex scheme. Also included are results obtained with a finite-difference approximation of the full potential equation. From ref. 15.

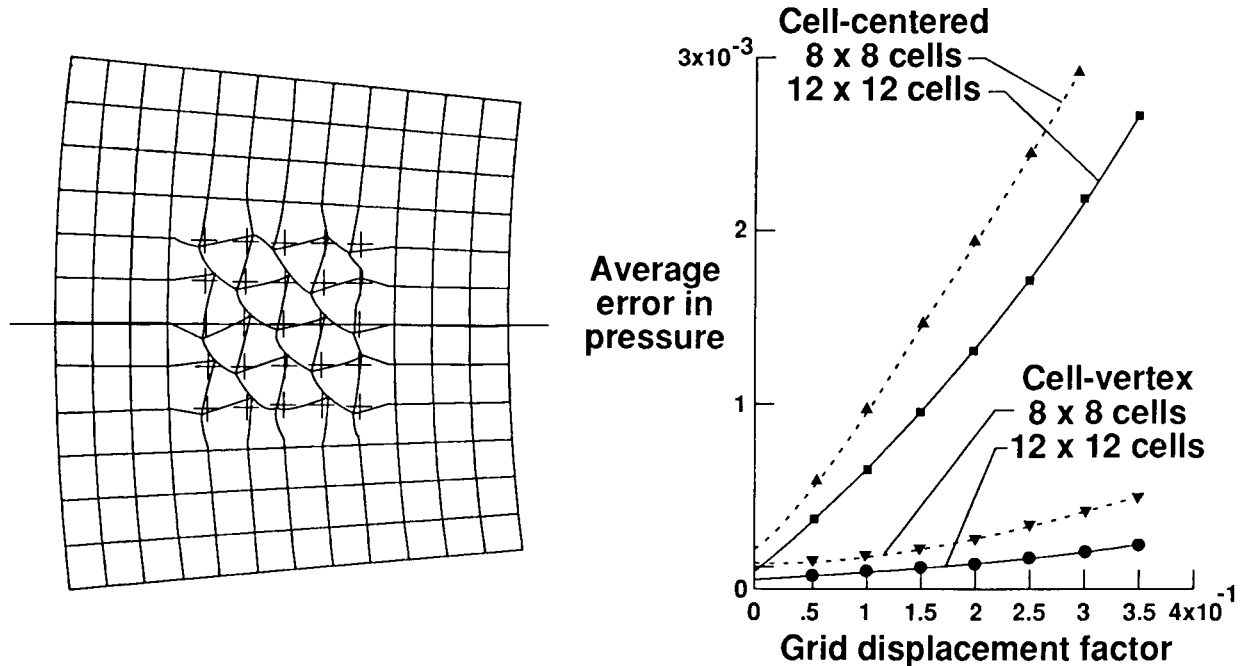


Figure 3. Grid distortion (left) and associated numerical error (right) in the computation of subsonic Ringleb flow with a cell-centered and a cell-vertex scheme. From ref. 7.

damping (using the fact that the specific total enthalpy becomes uniform in the steady state). Both AF and multi-stage marching schemes were combined with spatial discretizations based on central differencing and explicit artificial viscosity.

Next, the introduction of upwind-biased fluxes in schemes for finding steady Euler solutions (refs. 23, 24) led to a revival of the classical relaxation schemes such as Gauss-Seidel and line/Gauss-Seidel. It turns out that these methods, developed for finding solutions of elliptic equations, or steady solutions of parabolic equations, are the perfect match to upwind residual approximations, owing to the inherent dissipativity of the latter. On a scalar computer, Alternating Line/Gauss-Seidel (ALGS) relaxation easily outperforms AF (ref. 25), while requiring the same computational effort (two block-tridiagonal systems solved per iteration); see figure 4a.

Almost at the same time, the introduction of vector computing again reversed the order of preference among the known relaxation methods: although it requires considerably more iterations, AF outperforms ALGS when comparing CPU times, because it vectorizes better (ref. 25); see figure 4b. Such a radical changing of the guards suggests a search for new methods that exploit vector arithmetics even more strongly. This is not a trivial job, as there is something unnatural about the combination of vectorization and hyperbolicity. Hyperbolic equations model the propagation of signals moving in a continuum of directions, which is rather well imitated by a series of Gauss-Seidel sweeps in alternate discrete directions. The very fact of sequential dependence in Gauss-Seidel updating prohibits code vectorization to a great extent. It is worth mentioning here that recently it was proved that Symmetric Line/Gauss-Seidel relaxation (SLGS) is not unconditionally stable for upwind-biased Euler residuals (ref. 26). This accounts for some earlier, unexplained non-convergence of numerical results (ref. 23).

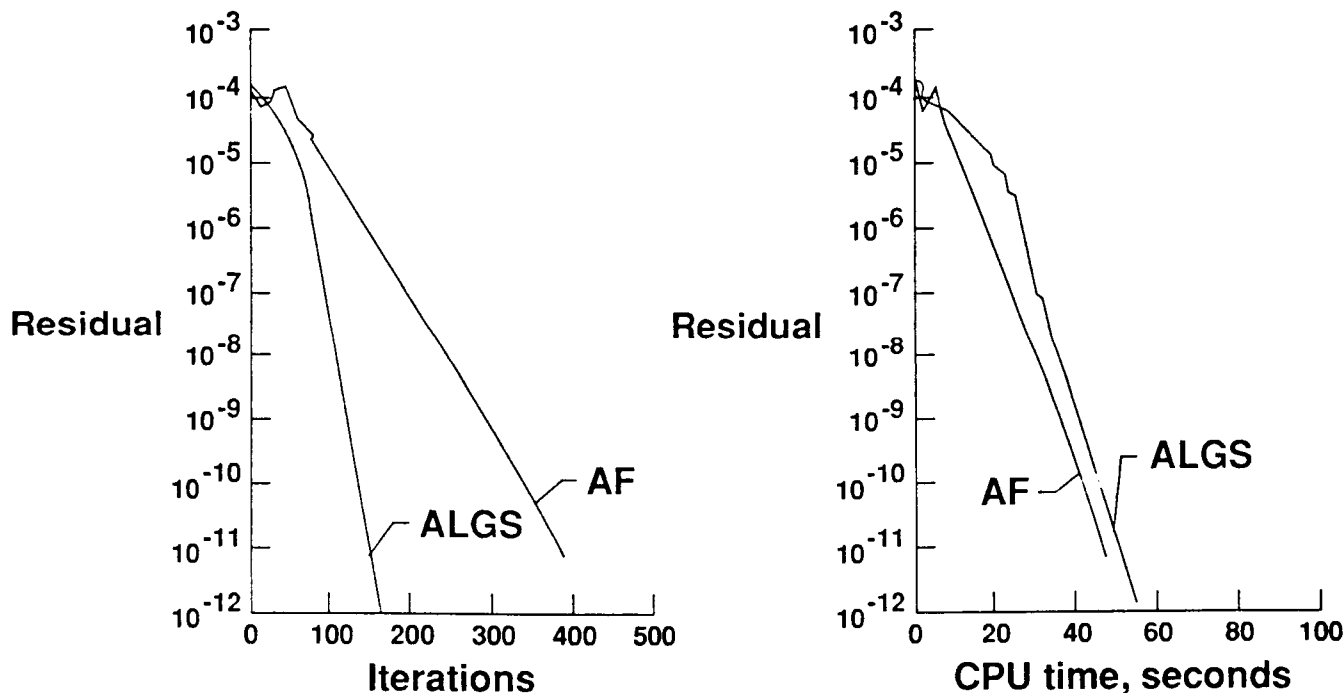


Figure 4. A comparison of iteration strategies for the computation of a transonic flow (NACA 0012,  $M_\infty = 0.8$ ,  $\alpha = 1.25$  deg,  $161 \times 41$  C-mesh, first-order upwind differencing). Left(a): convergence of Alternating-Line Gauss-Seidel (ALGS) relaxation and Approximate Factorization (AF) in terms of number of iterations; right(b): in terms of CPU seconds on a Cyber 205 vector computer. From ref. 25.

Meanwhile, multigrid relaxation, a fully matured technique for solving elliptic equations, has been shown to be a valuable accessory technique for removing long-wave components in distributions of Euler residuals (refs. 27-29). This, again, is causing a shift of interest from implicit to explicit relaxation methods, with the boom still to come. For a better understanding, it should be said that the basic marching scheme in a multigrid strategy must be a good relaxation scheme only for the short-wave components in a residual distribution; such a scheme is called a "smoother." In a discrete distribution, wave lengths scale with the cell size, so when going to coarser and coarser grids, the shortest wave that can be represented on the grid eventually becomes as long as the largest scale in the problem. Explicit marching schemes for the Euler equations can be designed to damp just the shortest waves without going beyond the stable range of the time-step, and therefore seem to be the perfect match to multigrid relaxation. In contrast, implicit schemes, such as line relaxation, will also attack long one-dimensional waves, which would seem unnecessary in a multigrid framework.

The highest possible achievement of a multigrid scheme is the so-called "multigrid convergence": convergence in a fixed number of multigrid cycles, regardless of the cell size of the finest grid. Such convergence has actually been realized in solving a simple channel-flow problem (refs. 30, 31); see figure 5. The fly in the ointment is that classical multigrid has also been shown *not* to work in very similar inviscid problems. This is caused by loss of information during coarsening when long waves in one direction are coupled to short waves in another direction, a situation that can arise when the grid is aligned with a stratified flow over an appreciable distance, as in channel flow (ref. 32), or when it is strongly stretched (ref. 33). Under these circumstances, one-

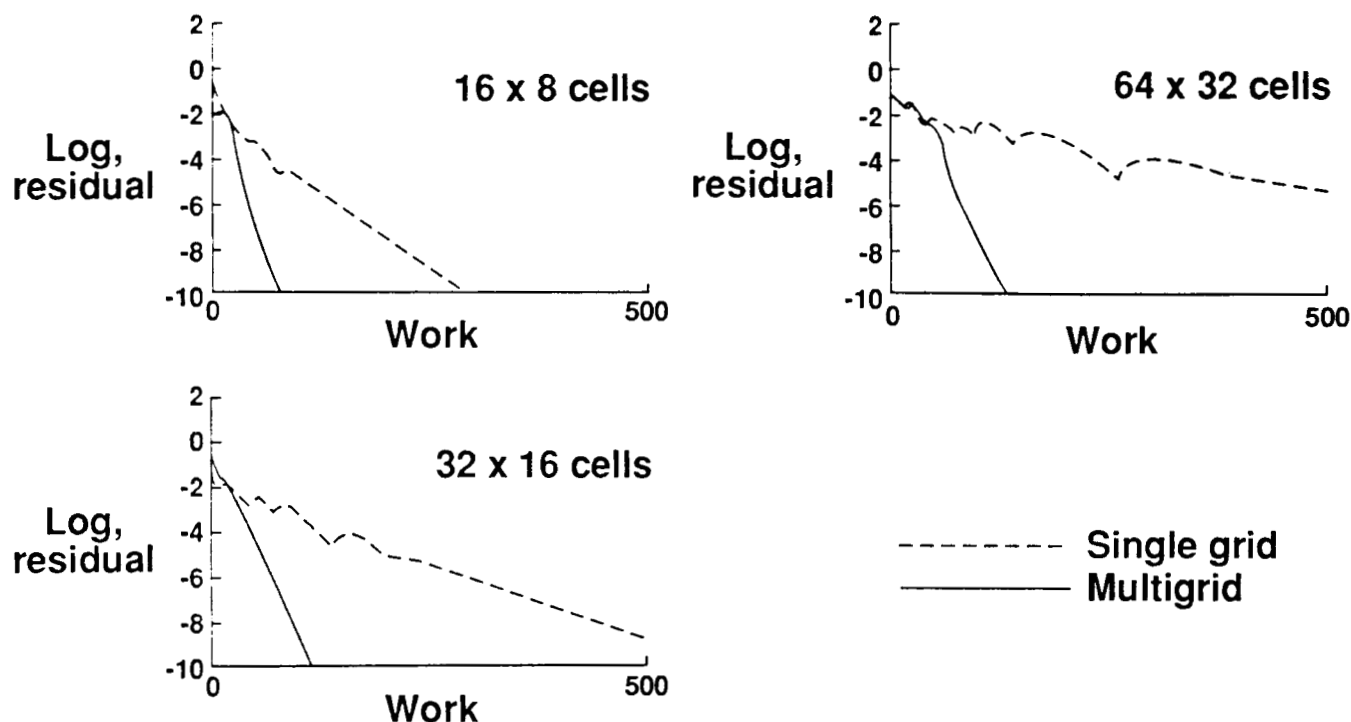


Figure 5. Convergence histories for the computation of the flow at  $M_\infty = 0.85$  over a circular bump (thickness .042 of chord) in a channel, using first-order upwind differencing and multigrid relaxation on three different grids. In all cases, the slower convergence is for the single-grid scheme; the total work for the multigrid scheme stays constant for grids on which the flow features are sufficiently resolved. From ref. 30. (Copyright ©1985. Academic Press, Inc.)

dimensional coarsening rather than multidimensional coarsening should be considered. It turns out that the need for semi-coarsening was already demonstrated in an early multigrid application to the potential equations (ref. 34); a full utilization of semi-coarsening has recently been proposed and analyzed by Mulder (ref. 35). The latter method has an appreciable degree of parallelism (yet to be exploited) and shows convergence rates for subsonic, transonic and supersonic channel flows between .3 and .4 per multigrid cycle.

With multigrid relaxation finally outgrowing its "elliptic" origin and becoming robust for the Euler equations, a new wave of advanced explicit algorithms is awaited with impatience. These algorithms do away with models of coordinate-wise wave propagation on which all present discretizations, including the upwind-biased ones, are based; instead, discrete models of the infinite variety of multidimensional wave motions are adopted. The basic concepts have been formulated (refs. 36, 37), but it is at present not clear how to incorporate these into robust marching methods. Yet, this development promises significant gains in accuracy, efficiency (see figure 6), and generality, while retaining programming simplicity and matching the computer architectures of today and tomorrow.

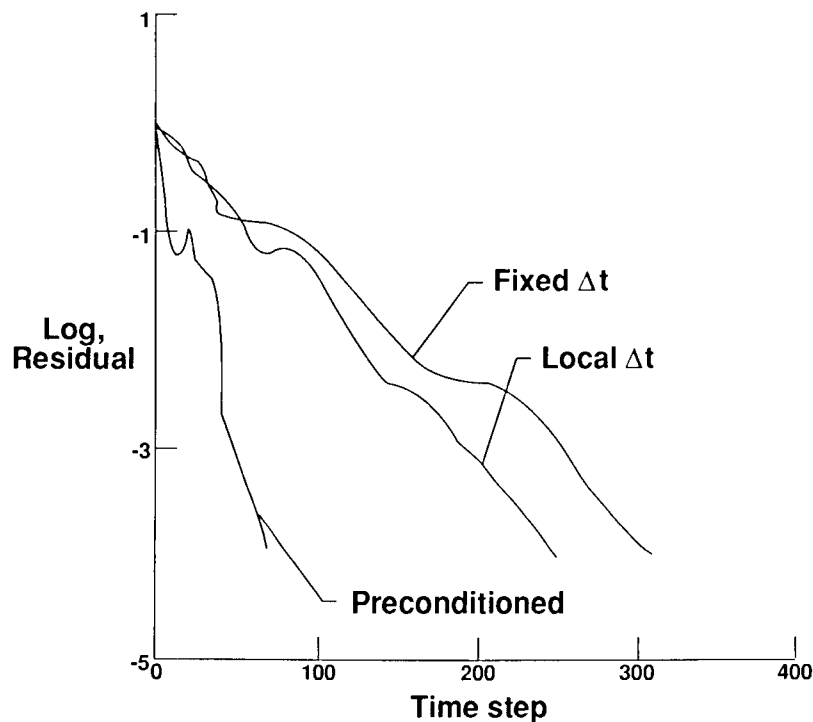


Figure 6. Effect of preconditioning on the computation of one-dimensional transonic nozzle flow with a first-order upwind scheme. Shown are the convergence histories resulting from the use of (1) the same time-step in all cells, (2) the maximum time-step in each cell (the so-called "local" time-step) and (3) the maximum time-step for each characteristic wave in each cell. The latter technique requires decomposition of the residual into wave contributions, which is needed anyway for upwind differencing, and leads to significant savings.

In the area of implicit methods, on the other hand, the tendency is to move toward greater complexity. With in-core storage capacity orders of magnitude larger than a decade ago, genuine Newton methods have been formulated and implemented using direct rather than iterative solution techniques for the large linear systems arising in the process (ref. 38); see figure 7. These methods are almost competitive with relaxation methods for the number of unknowns typically encountered in two-dimensional calculations, and a lot more robust. The main contribution to the complexity is the derivation of the full Jacobian of today's sophisticated numerical flux functions such as Roe's (ref. 39). If progress is to be made in this direction, automation of the algebra of differentiation, or, alternatively, reliance on numerical differentiation, seems to be inevitable. Any increase in generality, such as applicability on unstructured or locally refined grids, will involve a major programming effort.

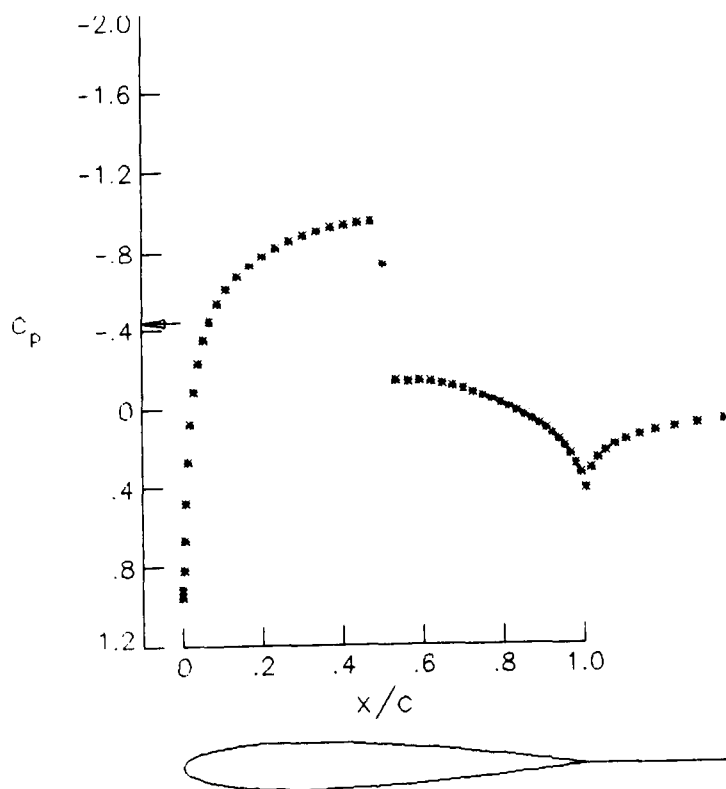


Fig. 3a.

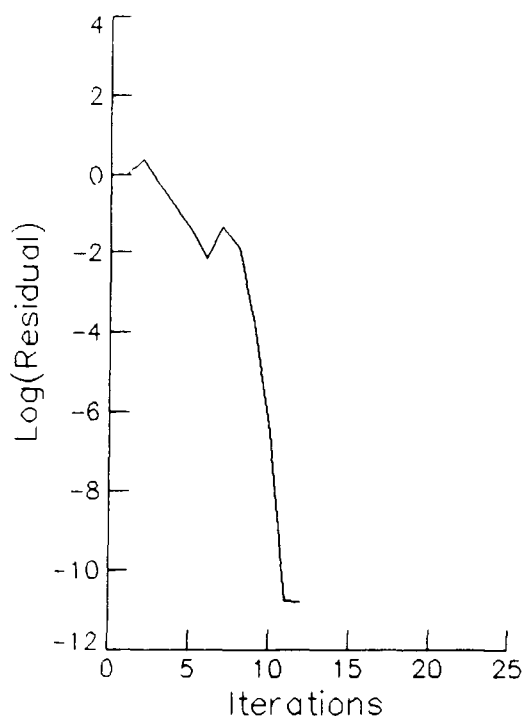


Fig. 3b.

Results using Ordering A (  $M = 0.8$ ,  $\alpha = 0$  )

160 X 32 GRID       $M = .800$        $\text{ALPHA} = 0.000$        $CD, CL = .01103$        $0.0000$   
 MIN VALUE =  $-.94$        $\text{MAX} = .9535$

Figure 7. Pressure-coefficient results and convergence history of a transonic-airfoil computation (NACA 0012,  $M_\infty = 0.80$ ,  $\alpha = 0$  deg) with a full Newton method. Note the quadratic convergence of the residual in the final phase. From ref. 38.

The abundance of core memory in modern computers is also a stimulus for the development of marching methods based on multiple iterates. Most classical iteration schemes make due with information exclusively from iteration level  $k$  when advancing to level  $k+1$ , thus ignoring the information contained in the first  $k-1$  iterates. Obviously, this information might give clues as to the best way to proceed beyond level  $k$ . Since each iterate of a numerical solution can be represented by a large vector, and the aim of iterative methods is to make this vector converge to some unknown final value, this subject is commonly referred to as "convergence acceleration of vector sequences" (ref. 40). The label suggests that the convergence of the vectors can be studied without in-depth knowledge of the physics represented by the vectors. This is probably as true as the statement that all CFD problems are similar to solving Laplace's equation on a rectangle. Some recent applications of acceleration methods like GMRES (Generalized Minimum Residual Method), MPE (Minimum Polynomial Extrapolation), reduced-rank extrapolation and Wynn's  $\epsilon$ -algorithm (see figure 8) can be found in references 41-45.

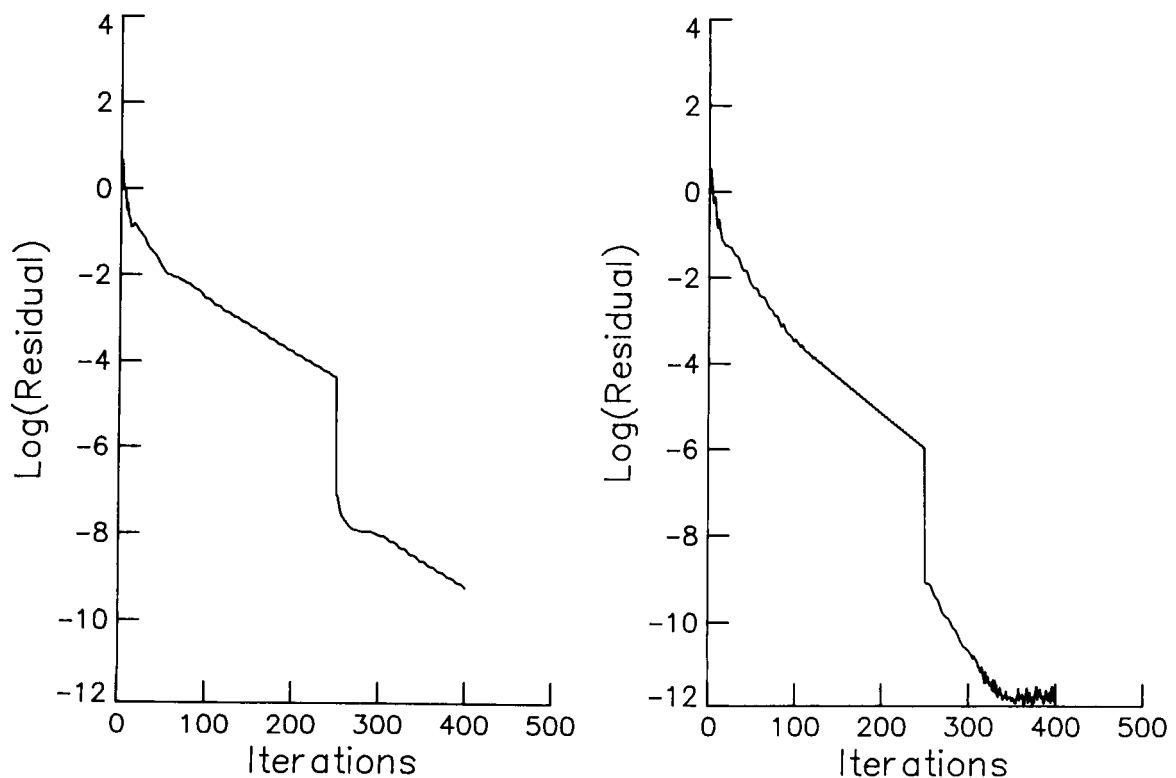


Figure 8. Convergence acceleration for two transonic-airfoil computations by the use of Wynn's  $\epsilon$ -algorithm. The residual decreases sharply upon application of the acceleration technique after 250 iterations. Left: Korn airfoil,  $M_\infty = 0.75$ ,  $\alpha = 0$  deg; right: NACA 0012,  $M_\infty = 0.80$ ,  $\alpha = 1.25$  deg. From ref. 45.

One aspect not addressed at all in these papers is the inherent nonlinearity of the CFD problem to be solved. When solving problems of steady transonic flow there actually are two separate but related questions:

1) how to efficiently march from an arbitrary initial guess to within the range of attraction of the steady solution;



2) how to quickly converge to the steady solution from a nearby state.

Vector-sequencing strategies address the second problem, which is the easier of the two owing to the validity of linearization. The only current methodology that also addresses the first problem is full multigrid.

#### 4. BOUNDARY PROCEDURES

How to derive non-reflective far-field boundary conditions has been pretty well understood since the appearance of a key paper by Engquist and Majda (ref. 46). For the Euler equations, a safe technique is to discretize the characteristic equations for waves moving outward normal to the boundary; supplemental conditions regarding the far field may be provided in the form of free-stream values. Greater accuracy, faster convergence and a smaller computational domain are the benefits of a more accurate description of the far field, based on various kinds of expansions of the solution (see, e.g. ref. 47). The most remarkable reduction in the computational domain has been demonstrated by Ferm and Gustafsson (ref. 48); see figure 9.

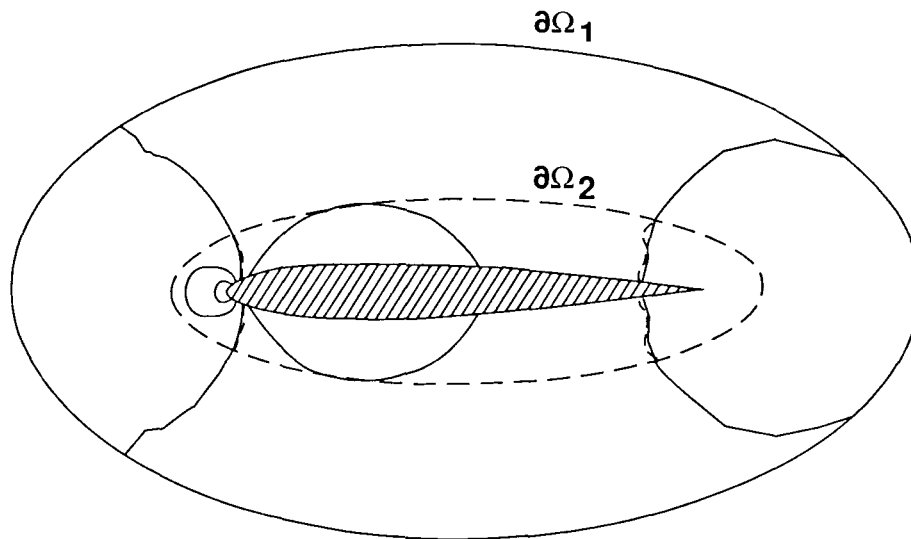


Figure 9. Isobars for the incompressible flow over NACA 0012 airfoil, computed with Ferm and Gustafsson's (ref. 48) "fundamental boundary conditions." Solid-line contours are from the solution on the larger domain ( $\partial\Omega_1$ ), dashed lines are for the smaller domain ( $\partial\Omega_2$ ).

#### 5. CONCLUSIONS

During the past decade, Euler solvers have come of age. Accuracy and efficiency of today's finite-volume Euler codes are sufficient to deliver detailed two-dimensional and useful three-dimensional flow solutions.

The accuracy achieved is somewhat surprising, as the ingredients for the spatial discretiza-

tions are almost exclusively based on a one-dimensional analysis, applied coordinate-wise. The insufficiency of this strategy shows up, for instance, as a loss of resolution of shock waves and shear waves oblique to the grid. Keeping in mind the even higher resolution required for a Navier-Stokes solution, it appears necessary to develop truly multi-dimensional numerical building blocks for use in future Euler codes.

Independently, the development of grid-adaptation techniques will support solutions of high accuracy at a reasonable cost. To comply with complicated geometries, the use of unstructured triangular and tetrahedral meshes is gaining ground; this in turn is stimulating the development of cell-vertex-based spatial discretizations, which are relatively insensitive to grid deformations.

On the efficiency front, multigrid relaxation and vector-sequence convergence acceleration are the two auxiliary techniques that bear the most promise of making three-dimensional calculations feasible and robust. The explicit marching schemes on which these techniques build, however, remain to be optimized as regards their capacity to smooth short waves and to overcome stiffness of the equations. Again, a truly multi-dimensional approach is needed.

Among implicit methods, Newton's method with full Jacobian evaluation and direct solution of the linearized system, is now competitive in obtaining two-dimensional flow fields; at present, the extension to three dimensions does not seem feasible.

## REFERENCES

1. Jameson, A.; Schmidt, W.; and Turkel, E., "Numerical Solution of the Euler Equations by Finite-Volume Methods Using Runge-Kutta Time-Stepping Schemes," AIAA Paper 81-1259, 1981.
2. Anderson, W. K.; Thomas, J. L., and van Leer, B., "Comparison of Finite-Volume Flux-Vector Splittings for the Euler Equations," AIAA Paper 85-0122, 1985; also, AIAA J., Vol. 24, 1986, pp. 1453-1460.
3. Chakravarthy, S. R. and Osher, O., "A New Class of High-Accuracy TVD Schemes for Hyperbolic Conservation Laws," AIAA Paper 85-0363, 1985.
4. Hall, M. G., "Cell-Vertex Multigrid Schemes for Solution of the Euler Equations," in Numerical Methods for Fluid Dynamics III, eds. K. W. Morton and M. J. Baines, Clarendon, Oxford, 1986.
5. Jameson, A., "A Vertex-Based Multigrid Algorithm for Three-Dimensional Compressible Flow Calculations," in Numerical Methods for Compressible Flow - Finite Difference, Element and Volume Techniques, eds. T. E. Tezduar and T. J. R. Hughes, ASME Publication AMD 78, 1986.
6. Powell, K. G., "Vortical Solutions of the Conical Euler Equations," Doctoral Thesis, Department of Aeronautics and Astronautics, MIT, Cambridge, MA, 1987.
7. Lin, H.-C., "Accuracy of Various Schemes for Numerical Solution of the Euler Equations Governing Inviscid Compressible Flow," M. Sc. Thesis, Cranfield Institute of Technology, Cranfield, England, 1987.

8. Van Leer, B., "Towards the Ultimate Conservative Difference Scheme. IV. A New Approach to Numerical Convection," J. Comp. Physics, Vol. 23, p. 276, 1977.
9. Van Leer, B., "Upwind-difference Methods for Aerodynamic Problems Governed by the Euler Equations," in Lectures in Applied Mathematics, Vol. 23, Part 2, AMS, Providence, 1985, pp. 327-336.
10. Van Leer, B.; Thomas, J. L.; Roe, P. L., and Newsome, R. W., "A Comparison of Numerical Flux Formulas for the Euler and Navier-Stokes Equations," AIAA Paper 87-1104-CP, 1987.
11. Harten, A.; Osher, S.; Engquist, B.; and Chakravarthy, S. R., "Some Results on Uniformly High Order Accurate Essentially Non-Oscillatory Schemes," in Advances in Numerical and Applied Mathematics, eds. J. C. South, Jr. and M. Y. Hussaini, ICASE Report 86-18, 1986.
12. Van Leer, B., "The Computation of Steady Solutions to the Euler Equations. A Perspective," Introductory Review for the GAMM Workshop on Numerical Simulation of Compressible Euler Flows, Rocquecourt, France, June 10-13, 1986.
13. Harten, A., "ENO Schemes with Subcell Resolution," ICASE Report 87-56, 1987.
14. Weatherill, N. P.; Shaw, J. A.; and Forsey, C. R., "Grid Generation and Flow Calculations for Complex Aerodynamic Shapes," in Numerical Methods for Fluid Dynamics II, eds. K. W. Morton and M. J. Baines, Clarendon, Oxford, England, 1986, pp. 595-608.
15. Mavriplis, D., "Accurate Multigrid Solution of the Euler Equations on Unstructured and Adaptive Meshes," AIAA Paper 88-3707, 1987.
16. Anderson, W. K.; Thomas, J. L.; and Rumsey, C. L., "Extension and Application of Flux-Vector Splitting to Unsteady Calculations on Dynamic Meshes," AIAA Paper 87-1152-CP, 1987.
17. Rai, M. M., "A Relaxation Approach to Patched-Grid Calculations with the Euler Equations," AIAA Paper 85-0295, 1985.
18. McCormack, R. W., "The Effect of Viscosity on Hypervelocity Impact Cratering," AIAA Paper 69-354, 1969.
19. Van Albada, G. D.; van Leer, B.; and Roberts, Jr., W. W., "A Comparative Study of Computational Methods in Cosmic Gas Dynamics," Astronomy and Astrophysics, Vol. 108, 1982, pp. 76-84.
20. Colella, P. and Woodward, P. R., "The Piecewise Parabolic Method for Gas Dynamical Simulations," J. Comp. Physics, Vol. 54, 1984, pp. 174-201.
21. Shu, C.-W. and Osher, S., "Efficient Implementation of Essentially Non-Oscillatory Shock Capturing Schemes," ICASE Report 87-33, 1987.

22. Beam, R. M. and Warming, R. F., "An Implicit Finite-Difference Algorithm for Hyperbolic Systems in Conservation Law Form," J. Comp. Physics, Vol. 22, 1976, pp. 87-110.
23. Van Leer, B. and Mulder, W. A., "Relaxation Methods for Hyperbolic Equations," in Numerical Methods for the Euler Equations of Fluid Dynamics, eds. F. Angrand, A. Dervieux, J. A. Désidéri and R. Glowinski, SIAM, Philadelphia, 1985, pp. 312-333.
24. Chakravarthy, S. R., "Relaxation Methods for Unfactored Implicit Upwind Schemes," AIAA Paper 84-0165, 1984.
25. Thomas, J. L.; van Leer, B.; and Walters, R. W., "Implicit Flux-Split Schemes for the Euler Equations," AIAA Paper 85-1680, 1985.
26. Mulder, W. A., "A Note on the Use of Symmetric Line Gauss-Seidel for the Steady Upwind Differenced Euler Equations," Report CLaSSiC 87-20, Stanford University, Stanford, California, 1987.
27. Jameson, A., "Numerical Solution of the Euler Equations for Compressible Inviscid Fluids," in Numerical Methods for the Euler Equations of Fluid Dynamics, eds. F. Angrand, A. Dervieux, J. A. Désidéri, and R. Glowinski, SIAM, Philadelphia, 1985, pp. 199-245.
28. Anderson, W. K.; Thomas, J. L.; and Whitfield, D. L., "Multigrid Acceleration of the Flux Split Euler Equations," AIAA Paper 86-0274, 1986.
29. Mulder, W. A., "Computation of the Quasi-Steady Gas Flow in a Spiral Galaxy by Means of a Multigrid Method," Astronomy and Astrophysics, Vol. 156, 1986, pp. 354-380.
30. Mulder, W. A., "Multigrid Relaxation for the Euler Equations," J. Comp. Physics, Vol. 60, 1985, pp. 235-252.
31. Henker, P. W. and Spekreyse, S. P., "Multigrid Solution of the Steady Euler Equations," Report NM-R8505, Centre for Mathematics and Computer Science, Amsterdam, Netherlands, 1985.
32. Koren, B., "Euler Flow Solutions for a Transonic Windtunnel Section," Report NM-R8601, Centre for Mathematics and Computer Science, Amsterdam, Netherlands, 1985.
33. South, Jr., J. C. and Brandt, A., "Application of a Multi-Level Grid Method to Transonic Flow Computations," ICASE Report 76-8, 1976.
34. Arlinger, B., "Multigrid Technique Applied to Lifting Transonic Flow Using Full Potential Equation," Saab-Scania Report L-0-1 B439, 1978.
35. Mulder, W. A., "A New Multigrid Approach to Convection Problems," CAM Report 88-04, University of California, Los Angeles, California, 1988.

36. Roe, P. L., "Discrete Models for the Numerical Analysis of Time-Dependent Multi-Dimensional Gas Dynamics," J. Comp. Physics, Vol. 63, 1986, pp. 458-476.
37. Hirsch, C.; Lacor, C.; and Deconinck, H., "Convection Algorithms Based on a Diagonalization Procedure for the Multidimensional Euler Equations," AIAA Paper 87-1163-CP, 1987.
38. Venkatakrishnan, V., "Newton Solution of Inviscid and Viscous Problems," AIAA Paper 88-0413, 1988.
39. Barth, T. J., "An Analysis of Implicit Local Linearization Techniques for Upwind and TVD Algorithms," AIAA Paper 87-0595, 1987.
40. Smith, D. A.; Ford, W. F.; and Sidi, A., "Extrapolation Methods for Vector Sequences," SIAM Review, Vol. 29, 1987.
41. Saad, Y. and Schultz, M. H., "GMRES: A Generalized Minimal Residual Algorithm for Solving Nonsymmetric Linear Systems," Research Report YALEU/DCS/RR-254, Yale University Department of Computer Science, 1983.
42. Wigton, L. B.; Yu, N. J.; and Young, D. P., "GMRES Acceleration of Computational Fluid Dynamics Codes," AIAA Paper 85-1494-CP, 1985.
43. Hafez, M.; Parlette, E.; and Salas, M., "Convergence Acceleration of Iterative Solutions of Euler Equations for Transonic Flow Computations," Computational Mechanics, Vol. 1, 1986, pp. 165-176.
44. Mallet, M.; Periaux, J.; and Stoufflet, B., "Convergence Acceleration of Finite Element Methods for the Solution of the Euler and Navier-Stokes Equations of Compressible Flow," in Proceedings of the 7th GAMM Conference on Numerical Methods in Fluid Dynamics, 1987.
45. Hafez, M.; Palaniswamy, S.; Kuruville, G.; and Salas, M., "Applications of Wynn's  $\epsilon$ -Algorithm to Transonic Flow Calculations," AIAA Paper 87-1143-CP, 1987.
46. Engquist, B. and Majda, A., "Absorbing Boundary Conditions for the Numerical Simulation of Waves," Math. Comp., Vol. 31, 1977, pp. 629-651.
47. Thomas, J. L. and Salas, M. D., "Far-Field Boundary Conditions for Transonic Lifting Solutions to the Euler Equations," AIAA Paper 85-0020, 1985; also, AIAA J., Vol. 24, 1986, pp. 1074-1080.
48. Ferm, L. and Gustafsson, B., "Far-Field Boundary Conditions for Steady-State Solutions to Hyperbolic Equations," in Nonlinear Hyperbolic Problems, Lecture Notes in Mathematics, 1270, 1988, Springer-Heidelberg.

# An Embedded Mesh Procedure for Leading-Edge Vortex Flows

Kenneth G. Powell  
The University of Michigan  
Department of Aerospace Engineering

Earll M. Murman  
Massachusetts Institute of Technology  
Department of Aeronautics and Astronautics

## Abstract

A new cell-vertex scheme is outlined for solving for the flow about a delta wing with  $M_\infty > 1$ . Embedded regions of mesh-refinement allow solutions to be obtained which have much higher resolution than those achieved to date. Effects of mesh-refinement and artificial viscosity on the solutions are studied, to determine at what point leading-edge vortex solutions are "grid-converged." A macroscale and a microscale for the size of the vortex are defined, and it is shown that the macroscale (which includes the wing surface properties) is converged on a moderately refined grid, while the microscale is very sensitive to grid spacing. The level of numerical diffusion in the core of the vortex is found to be substantial. Comparisons with experiment are made for two cases which have transonic cross-flow velocities.

## Introduction

Compressible flow past sharp-edged delta wings can lead to a variety of flow patterns. Stanbrook and Squire [1] originally postulated the classification of flow patterns as a function of angle of attack normal to the leading-edge

$$\alpha_N = \tan^{-1}(\tan \alpha \sec \Lambda)$$

and Mach number normal to the leading-edge

$$M_N = M_\infty \sqrt{1 - \sin^2 \Lambda \cos^2 \alpha}.$$

Their data suggested a boundary near  $M_N = 1$ . To the left of the boundary ( $M_N < 1$ ) the leading-edge is swept behind the Mach cone and the flow is separated at the leading-edge. To the right ( $M_N > 1$ ) the flow is attached, with a Prandtl-Meyer expansion at the leading-edge. Szodroch and Peake [2] and Miller and Wood [3] carried the classification further, defining several regimes in the  $(M_N, \alpha_N)$  plane. Miller and Wood [3], for example, produced the chart of flow regimes diagrammed in Figure 1. Vorropoulos and Wendt [4] postulated the possibility of leading-edge vortex flow with a reverse cross-flow shock under the vortex (See Figure 2), based on evidence from their laser-doppler results. This flow regime was at low normal Mach number and angle of attack. It is exactly this richness of flow phenomena that makes the compressible leading-edge vortex problem such an exciting one. The possibility of finding new complex flow topologies for this geometrically simple problem is a challenge, both for experimentalists and theoreticians. A good deal of numerical research has been carried out for this class of problems, as outlined below.

Solutions of the Euler equations using centered-difference conservative schemes have been carried out by Rizzi [5], Rizzi and Eriksson [6], Murman *et al* [7] and Newsome [8], among others. Upwind conservative schemes have been used by Newsome and Thomas [9] and Chakravarthy and Ota [10]. Characteristic-based non-conservative schemes have been used by Marconi [11]. All of these give reasonable estimates for the pressure coefficient on the wing, although they tend to overpredict the suction peak due to the vortex.

Some of these methods use the full three-dimensional form of the equations; others use a conical self-similarity assumption to reduce the problem to one with two independent spatial variables. The latter approach has justification through the experimental evidence described above: classification of the flows in the two-parameter  $(M_N, \alpha_N)$  space suggests conical self-similarity. Three-dimensional solutions for these problems suffer from a lack of resolution (Rizzi [5] has reported that at least  $10^6$  grid points are necessary to resolve the flow details), and even the conical solutions are not grid-converged [12]. To help understand and solve this problem, a solution method must be developed that allows a higher level of resolution than has been achieved previously.

The solution method described in this paper is a new cell-vertex scheme that allows for multiple levels of embedded grids. Cell-vertex schemes for logically rectangular meshes have been developed by Ni [13], Hall [14] and Siclari [15]. The embedded-grid scheme is adopted to provide good resolution in the leading-edge vortex region of the flow without the necessity of many grid points in the rest of the flow. The cell-vertex approach is adopted for its second-order accuracy, even at embedding interfaces and regions of highly stretched grid. Recent studies by Shapiro and Murman [16] have shown that a cell-vertex finite-volume scheme is identical to a finite element method with constant test functions, and that its accuracy is equal to a Galerkin method for all practical purposes. The scheme as a whole allows highly accurate solutions to be obtained efficiently. Results from the scheme are used to show effects of grid refinement on leading-edge vortex solutions, and to determine the level of refinement necessary to resolve flow details.

## Governing Equations

The three-dimensional Euler equations may be written in vector form as

$$\frac{\partial}{\partial t} \begin{bmatrix} \rho \\ \rho u \\ \rho v \\ \rho w \\ \rho E \end{bmatrix} + \frac{\partial}{\partial x} \begin{bmatrix} \rho u \\ \rho u^2 + p \\ \rho uv \\ \rho uw \\ \rho u h_0 \end{bmatrix} + \frac{\partial}{\partial y} \begin{bmatrix} \rho v \\ \rho uv \\ \rho v^2 + p \\ \rho vw \\ \rho v h_0 \end{bmatrix} + \frac{\partial}{\partial z} \begin{bmatrix} \rho w \\ \rho uw \\ \rho vw \\ \rho w^2 + p \\ \rho w h_0 \end{bmatrix} = 0$$

where  $h_0$  is the stagnation enthalpy,

$$h_0 = E + \frac{p}{\rho}.$$

The ideal gas law

$$p = (\gamma - 1) \rho \left[ E - \frac{u^2 + v^2 + w^2}{2} \right]$$

closes the set of equations. Introducing the conical variables

$$\begin{aligned} r &= \sqrt{x^2 + y^2 + z^2} \\ \eta &= \frac{y}{x} \\ \zeta &= \frac{z}{x} \end{aligned}$$

and assuming conical self-similarity (that the solution is independent of  $r$ ), the Euler equations become

$$\frac{r}{\kappa} \frac{\partial}{\partial t} \begin{bmatrix} \rho \\ \rho u \\ \rho v \\ \rho w \\ \rho E \end{bmatrix} + \frac{\partial}{\partial \eta} \begin{bmatrix} \rho \bar{v} \\ \rho u \bar{v} - \eta p \\ \rho v \bar{v} + p \\ \rho w \bar{v} \\ \rho h_0 \bar{v} \end{bmatrix} + \frac{\partial}{\partial \zeta} \begin{bmatrix} \rho \bar{w} \\ \rho u \bar{w} - \zeta p \\ \rho v \bar{w} \\ \rho w \bar{w} + p \\ \rho h_0 \bar{w} \end{bmatrix} + 2 \begin{bmatrix} \rho u \\ \rho u^2 + p \\ \rho uv \\ \rho uw \\ \rho u h_0 \end{bmatrix} = 0,$$

where

$$\begin{aligned} \bar{u} &= u + \eta v + \zeta w \\ \bar{v} &= v - \eta u \\ \bar{w} &= w - \zeta u \end{aligned}$$

and

$$\kappa = \sqrt{1 + \eta^2 + \zeta^2}.$$

These conical Euler equations may be expressed in terms of the state vector  $\mathbf{U}$ , the Cartesian flux vector  $\mathbf{F}$  and the conical flux vectors  $\hat{\mathbf{G}}$  and  $\hat{\mathbf{H}}$  as

$$\frac{r}{\kappa} \frac{\partial \mathbf{U}}{\partial t} + \frac{\partial \hat{\mathbf{G}}}{\partial \eta} + \frac{\partial \hat{\mathbf{H}}}{\partial \zeta} + 2\mathbf{F} = 0.$$

The unsteady terms have been included so that an iterative procedure may be employed to reach a conically self-similar steady-state. The equations are solved on the unit sphere by setting  $r = 1$ .

The physical boundary conditions consist of a no-flux condition at the wing, free-stream conditions outside the bow shock, and a Kutta condition at the leading-edge of the wing. Implementation of these boundary conditions will be discussed in the next section.

## Solution Procedure

The solution scheme used is a finite-volume, multi-stage scheme in which the state variables are stored at the nodes. It allows for regions of local mesh refinement. The grid generation, spatial discretization, added artificial viscosity, temporal discretization and boundary and interface procedures are described below, along with the data structure that underlies the algorithm.

### Grid Generation

For the cases presented here, the grid generation is carried out by a Joukowski transformation. The  $(\eta, \zeta)$  plane is mapped to a complex  $\chi$  plane, in which the wing becomes a circle, by the transformation

$$\eta + i\zeta = \chi + \tan^2 \frac{(\frac{\pi}{2} - \Lambda)}{2\chi}$$

where  $\Lambda$  is the leading-edge sweep of the wing. In the  $\chi$  plane,  $i = \text{constant}$  lines are equiangularly spaced rays emanating from the origin and  $j = \text{constant}$  lines are concentric rings. Grid points are generated along rays in the  $\chi$  plane by an exponential stretching. This procedure yields near-conformal grids with good resolution near the wing. The embedded regions are generated by sub-dividing each cell in the region. This is done by adding a node on each face of the cell to be divided, and one in the center of the cell. Bilinear interpolations are used to find the coordinates of the new points. A typical grid is shown in Figure 3. Indexing the grid in an  $(i, j)$  manner is no longer convenient; the data structure chosen for the scheme is described below. Although in the work presented here the embedded regions are determined *a priori*, the formulation and code are directly extendable to adaptive determination of the embedded regions.

### Discretization of Equations

The finite volume discretization of the partial differential equations is formulated by integrating the conical Euler equations over a cell. This gives

$$\iint_{\Omega} \frac{r}{\kappa} \frac{\partial \mathbf{U}}{\partial t} d^2x + \iint_{\Omega} \left[ \frac{\partial \hat{\mathbf{G}}}{\partial \eta} + \frac{\partial \hat{\mathbf{H}}}{\partial \zeta} \right] d^2x + \iint_{\Omega} 2\mathbf{F} d^2x = 0.$$

Using Gauss' theorem and the mean value theorem, this may be rewritten as

$$A \overline{\frac{r}{\kappa} \frac{\partial \mathbf{U}}{\partial t}} + \oint_{\partial\Omega} [\hat{\mathbf{G}} d\zeta - \hat{\mathbf{H}} d\eta] + 2A\overline{\mathbf{F}} = 0$$

where an overbar denotes a cell-average and  $A$  is the cell area.

The line integral of the fluxes is carried out by a trapezoidal integration about the cell, i.e.

$$\oint_{\partial\Omega} [\hat{\mathbf{G}} d\zeta - \hat{\mathbf{H}} d\eta] = \sum_{\text{faces}} \left[ \frac{1}{2} (\hat{\mathbf{G}}_1 + \hat{\mathbf{G}}_2) (\eta_2 - \eta_1) - \frac{1}{2} (\hat{\mathbf{H}}_1 + \hat{\mathbf{H}}_2) (\zeta_2 - \zeta_1) \right],$$

where the subscripts denote the two nodes that define the face, ordered so that the integral is carried out in a counter-clockwise sense.

The cell-average of the source term is calculated by averaging the source term at the four nodes defining the cell. This gives the residual at the center of the cell,  $\partial \mathbf{U} / \partial t$ . This cell-average of the residual is distributed to the four nodes defining the cell with a simple  $(\frac{1}{4}, \frac{1}{4}, \frac{1}{4}, \frac{1}{4})$  weighting.



The artificial viscosity is a blend of a nonlinear second-difference and a linear fourth-difference. It is constructed from a weighted Laplacian,  $\bar{L}$ , and an unweighted Laplacian squared,  $L^2$ , respectively. The weighting function  $\mathcal{W}$  is a normalized Laplacian of the pressure,

$$\mathcal{W} = \left| \frac{L(p)/p}{\|L(p)/p\|_\infty} \right|,$$

where  $\|\cdot\|_\infty$  denotes the  $L_\infty$  norm, so that  $0 < \mathcal{W} < 1$ . This weighting is chosen for the efficient capturing of shocks and vortices. It causes the second-difference term to be first-order in high-gradient regions and small elsewhere; the fourth-difference term is third-order everywhere. Thus the artificial viscosity is given by

$$\begin{aligned} D(\hat{\mathbf{U}}) &= \epsilon_2 D_2(\hat{\mathbf{U}}) - \epsilon_4 D_4(\hat{\mathbf{U}}) \\ &= \epsilon_2 \bar{L}(\mathcal{W}, \hat{\mathbf{U}}) - \epsilon_4 L^2(\hat{\mathbf{U}}) \end{aligned}$$

where  $\hat{\mathbf{U}}$  is a modified state vector, with the energy term  $\rho E$  replaced by  $\rho h_0$ , so that the discrete equations permit a solution with constant total enthalpy. The Laplacians are calculated in a way that automatically enforces conservation at physical and numerical boundaries.

The temporal discretization is a four-stage scheme with coefficients  $(\frac{1}{4}, \frac{1}{3}, \frac{1}{2}, 1)$ . The time step is calculated on a local basis to satisfy the CFL criterion for stability.

## Boundary Conditions

There are boundary conditions to be enforced at the physical boundaries

1. No flux through the wing
2. Free-stream conditions upstream of the bow-shock
3. Kutta condition at the leading-edges

and at the numerical boundaries

1. no flow through the symmetry plane
2. consistency and conservation at the embedding interfaces

The wing boundary condition is met by retaining only the pressure terms in the flux calculation on cell faces which abut the wing. No pressure extrapolation is necessary since the state variables are stored at the nodes. The outer boundary condition is implemented by ensuring that the outer boundary of the domain is outside the bow shock and enforcing free-stream conditions there. The Kutta condition is enforced implicitly by ensuring that the artificial viscosity is present near the leading-edges. This is done by arbitrarily setting the pressure switch  $\mathcal{W}$  to one at several nodes in the vicinity of the leading-edges. Numerical experience demonstrates that this is adequate to ensure smooth separation [12].

The symmetry plane is introduced so that the flow past a wing at zero yaw may be solved on a half-plane. The condition to be enforced at the symmetry line is that the through-flow velocity,  $v$ , is zero. This is implemented by setting  $v$  to zero initially and zeroing the distributed flux for the  $y$ -direction momentum equation at each iteration. Interfaces between two levels of grid refinement lead to cells of more than four nodes and faces. The embedding philosophy used here restricts the grid to a series of nested rectangles in which there is refinement by a factor of two in each direction at the interfaces. With this restriction, only one type of interface cell is generated — a cell with five faces and five nodes. These cells are the coarse cells which abut the embedding interface. This makes the interface treatment very simple. The flux integration for these cells is carried out exactly as above, with five faces for the cell instead of the usual four. The distribution step is modified, however, so that the “extra” node is updated. The distribution used is diagrammed in Figure 4.

## Data Structure

Because of the embedded regions of the grid, it is inconvenient to index the grid in a typical  $(i,j)$  fashion. Instead, nodes, cells, and faces are singly indexed, and pointer vectors are constructed with the necessary information for interrelating them. The pointer vectors used for the scheme are:

1. A cell-to-node pointer, relating a cell to the four corner nodes that define it
2. A cell-to-face pointer, relating a cell to its four faces
3. A face-to-node pointer, relating a face to the two nodes defining it
4. A node-to-node pointer, relating a node to its (at most) four neighbors

Each pointer has a specific use. The cell-to-node pointer is used in the flux distribution and the damping calculation. In each of these steps, cells are visited, and changes in the cell are distributed to the nodes of the cell. The cell-to-face pointer is used in the flux summation step — each cell is visited, and the fluxes from the four faces defining the cell are summed. The face-to-node pointer is used in the calculation of the face fluxes — each face is visited, and the coordinates and the values of the flux vectors at the nodes defining the face are used to carry out the trapezoidal integration. The node-to-node pointer is used to calculate grid metrics and cell areas, and to extrapolate quantities (such as the time step and the weighting function  $W$ ) to the boundaries and interfaces.

In addition to these, pointers which contain boundary information are necessary. They are

1. A vector containing the index of each face on the wing
2. A vector containing the index of each node on the wing
3. A vector containing the index of each node on the symmetry boundary
4. A vector containing the index of each node on the far-field boundary
5. A vector containing the index of each node at which the weighting factor for the damping is to be overridden
6. A vector containing the index of each coarse cell which abuts an embedding interface
7. A vector relating each of these interface cells to its “extra” node
8. A vector relating each of these interface cells to its “extra” face
9. A vector containing the orientation of each of these “extra” faces (i.e. which side of the cell the face is on)

The boundary conditions at physical and numerical boundaries are enforced using these pointers.

## Effects of Numerical Parameters on Solutions

The embedded mesh procedure outlined above forms a practical method to carry out a careful study of the effects of mesh refinement on leading-edge vortex solutions to the Euler equations. This study is carried out for a  $75^\circ$  swept wing at  $10^\circ$  angle of attack in a Mach 1.1 stream. The cross-flow streamlines for this case are shown in Figure 5. The vortex is the dominant feature of the flow. The cross-flow stagnation points at the leeward and windward symmetry points and on the outboard portion of the windward side of the wing are also evident. The cross-flow is transonic for this case.

The grid is varied from an equivalent global resolution of  $64 \times 64$  to  $256 \times 256$ . The results for the coarsest grid are shown in Figures 6–9. Figure 6 shows the grid, with refinement on the leeward side on the wing. Figure 7 shows contours of the pressure coefficient. The compression on the leeward side of the wing, the expansion about the leading-edge and the low-pressure region in the core of the vortex may be seen. Figure 8 presents contours of the cross-flow Mach number. The large gradients of cross-flow Mach number in the core and feeding-sheet may be seen. Figure 9 presents contours of total pressure loss ( $1 - p_0/p_\infty$ ). There is a large loss in total pressure in the vortex, reaching a value of 34% in the core.

Figures 10–13 are the results on a grid with equivalent  $128 \times 128$  resolution. The gradients of pressure in the core (Figure 11) are better resolved, and a cross-flow shock is apparent underneath the vortex. The cross-flow Mach number contours are shown in Figure 12. Again the gradients are much better resolved, and the shock may clearly be seen. The contours of total pressure loss are shown in Figure 13. The lossy region appears smaller on this grid, but the level of loss has not gone down. Here it is 38%.

A further grid refinement is shown in Figures 14–17. The pressure contours are shown in Figure 15. The shock is slightly sharper than on the previous grid and the suction in the core slightly better resolved, but otherwise the solution has not changed appreciably. The cross-flow Mach number contours (Figure 16) show the same trends. The

total pressure loss distribution has changed fairly drastically (Figure 17). The roll-up of the sheet into a core of distributed total pressure loss may be seen. The level of the loss is relatively unchanged, however, with a core loss of 35%.

The loss levels and two scales for the sizes of the vortices in the different cases are tabulated in Table 1. "Core sizes" are determined by summing the area of all cells in which the total pressure loss  $(1 - p_0/p_{0\infty})$  is greater than 10%. They are normalized by the core size for the  $128 \times 128$  case. "Vortex width" and "Vortex height" are determined by measuring the width and height of the 2% contour at the center of the vortex. They are also normalized by the values for the  $128 \times 128$  case. The "core size", a microscale for the vortex, changes dramatically with the grid refinement. The "vortex width" and "vortex height" are nearly converged on the  $128 \times 128$  grid, however.

A similar table may be compiled for the effects of artificial viscosity on the loss. The values presented below are for a  $128 \times 128$  grid and are normalized by the case for which  $\epsilon_2 = 0.003$  and  $\epsilon_4 = 0.0010$ . Again the microscale for the vortex changes with the level of artificial viscosity, while the core loss level and the macroscale for the vortex remain approximately constant. The level of artificial viscosity does not greatly affect flow variables outside the core.

It is interesting to note that, although the magnitude of the total pressure loss is independent of the *level* of artificial viscosity, it does depend on the *form* of the artificial viscosity. This dependence on the form of the viscosity was discovered in an attempt to lower the damping on the continuity equation. Figure 18 shows the total pressure loss contours for the  $M_\infty = 1.1$ ,  $\alpha = 10^\circ$ ,  $\Lambda = 75^\circ$  case on an equivalent  $128 \times 128$  grid where the second-difference damping terms in the continuity equation have been removed. For this case, the loss in the core is 27%.

The effect that zeroing the continuity damping has on the form of the damping for the system of equations may be seen most easily by analyzing a one-dimensional steady model problem. The equivalent continuity and momentum equations are, including the second-difference damping,

$$\begin{aligned}\frac{\partial}{\partial x}(\rho u) &= \epsilon_\rho \frac{\partial^2 \rho}{\partial x^2} \\ \frac{\partial}{\partial x}(\rho u^2 + p) &= \epsilon_{\rho u} \frac{\partial^2}{\partial x^2}(\rho u),\end{aligned}$$

where  $\epsilon_\rho$  and  $\epsilon_{\rho u}$  are damping coefficients for the two equations. Using the chain rule, the momentum equation may be written

$$\rho u \frac{\partial u}{\partial x} + u \frac{\partial}{\partial x}(\rho u) + \frac{\partial p}{\partial x} = \epsilon_{\rho u} \left( u \frac{\partial^2 \rho}{\partial x^2} + \rho \frac{\partial^2 u}{\partial x^2} + 2 \frac{\partial \rho}{\partial x} \frac{\partial u}{\partial x} \right)$$

which, when combined with continuity, becomes

$$\rho u \frac{\partial u}{\partial x} + \frac{\partial p}{\partial x} = \rho \epsilon_{\rho u} \frac{\partial^2 u}{\partial x^2} + u(\epsilon_{\rho u} - \epsilon_\rho) \frac{\partial^2 \rho}{\partial x^2} + 2\epsilon_{\rho u} \frac{\partial \rho}{\partial x} \frac{\partial u}{\partial x}.$$

Comparison with the one-dimensional steady Navier-Stokes equation shows that this equation has two spurious terms: the term  $u(\epsilon_{\rho u} - \epsilon_\rho) \partial^2 \rho / \partial x^2$ , due to the difference in the two damping coefficients, and the cross-term  $2\epsilon_{\rho u} \partial \rho / \partial x \partial u / \partial x$ . The first term is a spurious diffusive term; the second is a spurious convective term.

If  $\epsilon_{\rho u} = \epsilon_\rho$ , the first spurious term drops out. This suggests a way to zero the continuity damping while retaining the proper form of damping for the system of equations. By subtracting these terms from the momentum and energy equations, the system will have the same form as it would in the case  $\epsilon_{\rho u} = \epsilon_\rho$ . Figure 19 shows the total pressure loss contours with the damping altered in this way. The core total pressure loss is 38%, as it was in the case without lowering the continuity equation damping.

An estimate of the level of artificial viscosity in the vortex core may be determined by calculating an "equivalent Reynolds number" for the computation. In regions in which the second-difference viscosity dominates the fourth-difference viscosity, the damping terms for the conical Euler equations have the form

$$\begin{aligned}D(\hat{\mathbf{U}}) &\sim \epsilon_2 \bar{L}(\mathcal{W}, \hat{\mathbf{U}}) \\ &\sim \epsilon_2 \mathcal{W} L(\hat{\mathbf{U}}) \\ &\sim 4\epsilon_2 \mathcal{W} \Delta^2 \nabla^2 \hat{\mathbf{U}}\end{aligned}$$

where  $\Delta$  is an estimate of the grid spacing, and the factor of four arises from the non-normalized stencil used for the Laplacian operator  $L$ . Since this damping operator is multiplied by the CFL number in the temporal updating, the

actual damping terms added to the conical Euler equations have the form

$$\frac{\lambda}{\Delta t} D(\hat{\mathbf{U}}) \sim 4\epsilon_2 \mathcal{W} \Delta \nabla^2 \hat{\mathbf{U}}$$

where  $\Delta$  is taken to be the average of the lengths of the faces emanating from the node. Thus an equivalent Reynolds number can be defined as

$$\frac{1}{Re_{eq}} = 4\epsilon_2 \mathcal{W} \Delta$$

Contours of the log of the equivalent Reynolds number are shown in Figures 20–22 for the three different levels of grid refinement. The equivalent Reynolds number increases with grid refinement, reaching values of  $10^3$  in the core for the  $256 \times 256$  case. The equivalent Reynolds number is surprisingly high at the leading-edge, due to the small size of the cells, but surprisingly low in the vortex core. Care must clearly be taken in computing solutions to the Navier-Stokes equations for leading-edge vortices in high Reynolds number flow.

This study has shown that the level of total pressure loss in computed vortex cores depends on the form of the diffusive terms, but not on the magnitude of the diffusive terms. Analytical evidence to this effect has been demonstrated by the authors [17]. Numerous calculations performed by the authors show that the magnitude of total pressure loss depends strongly on the aerodynamic and geometric parameters [12]. Surface pressure coefficients and other variables outside of the core should converge with the macroscale for the vortex. For high-Reynolds number attributes of the vortex on a scale smaller than the macroscale, however, the grid resolution must be such that the equivalent Reynolds number due to truncation error and artificial viscosity is substantially higher than the Reynolds number of interest.

## Comparison with Experiment

In this section, two cases are compared with experimental data. Both are  $75^\circ$  swept wings. They are

1.  $M_\infty = 1.95$ ,  $\alpha = 25^\circ$ ,  $\beta = 0^\circ$
2.  $M_\infty = 1.70$ ,  $\alpha = 12^\circ$ ,  $\beta = 8^\circ$

Computed results for the first case are shown in Figures 23 and 24. Figure 23 shows the cross-flow streamlines for this case and Figure 24 shows the total pressure loss contours. Three cross-flow shocks are apparent in the vicinity of the vortex, and the vortex takes on an almost triangular cross-section. Figures 25 and 26 show a comparison of computed and measured pitot pressures. The pitot pressures compare extremely well in the vortex and above it; below it, viscous effects, which are not modeled in the code, dominate. Figure 27 shows a comparison of computed and measured flow angles along the leeward symmetry line. The agreement is surprisingly good, particularly near the wing.

The second case is shown in Figures 28–33. This case was run on a grid with  $256 \times 128$  equivalent refinement, shown in Figure 28. The cross-flow streamline plot (Figure 29) shows two vortices: a long, narrow vortex on the port side and a nearly axisymmetric vortex on the starboard side of the wing. There is a saddle point on the windward side of the wing near the port leading-edge, and one on the leeward side near the center of the wing. All the cross-flow streamlines to port of the two saddle points converge in the port vortex; all others converge in the starboard vortex. The total pressure loss contours (Figure 30) show the difference in strength and shape of the two vortices. The port vortex is stronger, with a core total pressure loss of 66%. The starboard vortex has a core loss of 43%. There is also evidence of a weak shock above the port vortex. The pressure coefficient contours (Figure 31) also show evidence of this shock. The pressure on the wing (Figure 32) compares well with experiment. Both vortices are predicted too far outboard, and the suction peaks are overpredicted. The solution does capture the unusual double expansion-recompression pattern under the port vortex, however. This unusual pattern is more clearly seen in the cross-flow Mach number distribution (Figure 33). Under the port vortex, the flow expands to a cross-flow Mach number of 1.6, recompresses to 1.2, then expands again, reaching a value of 1.3, then recompresses outboard to the port leading-edge. The cross-flow Mach number reaches a value of 1.7 above the port vortex, and goes slightly supersonic above and below the starboard vortex.

## Conclusions

A new cell-vertex scheme which allows for nested regions of embedded grid has been presented. The scheme has been used to solve several cases of compressible, supersonic flow past a delta wing. The grid-embedding capacity of the code has been used to study the effects of resolution on leading-edge vortex solutions. A macroscale and a microscale for the vortex have been proposed, and it has been shown that the macroscale converges on a moderately refined grid, while the microscale does not. It has been shown that even on a relatively fine grid, the level of artificial viscosity in the core of the vortex is substantial. Thus, if details inside the core are desired, it is necessary to use a very fine grid in that region to ensure that the equivalent Reynolds number due to truncation error and artificial viscosity is substantially higher than the Reynolds number of interest.

The scheme has been used to compute two flows for which experimental data existed. Measurements of pitot pressure from the first experiment were modeled well, as was the flow angularity. Measured surface pressure coefficients from the second experiment were modeled fairly well, with discrepancies due to viscous effects.

## References

- [1] A. Stanbrook and L. C. Squire, "Possible Types of Flow at Swept Leading-Edges," *Aeronautical Quarterly*, Vol. 15, 1964.
- [2] J. Szodruch and D. Peake, "Leeward Flow over Delta Wings at Supersonic Speeds," NASA TM 81187, 1981.
- [3] D. S. Miller and R. M. Wood, "Lee-Side Flow over Delta Wings at Supersonic Speeds," NASA TP 2430, 1985.
- [4] G. Vorropoulos and J. F. Wendt, "Laser Velocimetry Study of Compressibility Effects on the Flow Field of a Delta Wing," In *AGARD-CP-342*, 1983.
- [5] A. Rizzi, "Three-Dimensional Solutions to the Euler Equations with One Million Grid Points," *AIAA Journal*, Vol. 23, 1985.
- [6] A. Rizzi and L. E. Eriksson, "Computation of Flow around Wings Based on the Euler Equations," *Journal of Fluid Mechanics*, Vol. 148, 1984.
- [7] E. M. Murman, K. G. Powell, D. S. Miller, and R. M. Wood, "Comparison of Computations and Experimental Data for Leading-Edge Vortices — Effects of Yaw and Vortex Flaps," AIAA Paper 86-0439, 1986.
- [8] R. W. Newsome, "A Comparison of Euler and Navier-Stokes Solutions for Supersonics Flow over a Conical Delta Wing," AIAA Paper 85-0111, 1985.
- [9] R. W. Newsome and J. L. Thomas, "Computation of Leading-Edge Vortex Flows," In *Vortex Flow Aerodynamics — Volume I*, NASA CP 2416, 1985.
- [10] S. K. Chakravarthy and D. K. Ota, "Numerical Issues in Computing Inviscid Supersonic Flow over Conical Delta Wings," AIAA Paper 86-0440, 1986.
- [11] F. Marconi, "The Spiral Singularity in the Supersonic Inviscid Flow over a Cone," AIAA Paper 83-1665, 1983.
- [12] K. G. Powell, *Vortical Solutions of the Conical Euler Equations*, ScD thesis, Massachusetts Institute of Technology, 1987.
- [13] R. H. Ni, "A Multiple-Grid Scheme for Solving the Euler Equations," *Journal of Fluid Mechanics*, Vol. 20, 1981.
- [14] M. G. Hall, *Cell-Vertex Schemes for Solution of the Euler Equations*, Technical Memo Aero 2029, Royal Aircraft Establishment, 1985.
- [15] M. J. Siclari and P. Del Giudice, "A Hybrid Finite Volume Approach to Euler Solutions for Supersonic Flows," AIAA Paper 88-0225, 1988.
- [16] R. A. Shapiro and E. M. Murman, "Adaptive Finite Element Methods for the Euler Equations," AIAA Paper 88-0034, 1988.
- [17] K. G. Powell and E. M. Murman, "A Model for the Core of a Slender Viscous Vortex," AIAA Paper AIAA-88-0503, 1988.

Equivalent Grid	Loss Level	Core Size	Vortex Width	Vortex Height
64 × 64	33.9%	2.55	1.39	1.43
128 × 128	37.6%	1.00	1.00	1.00
256 × 256	35.1%	0.26	0.96	1.05

Table 1: Effects of grid refinement on loss

$\epsilon_2$	$\epsilon_4$	Loss Level	Core Size	Vortex Width	Vortex Height
0.003	0.0010	37.4%	1.00	1.00	1.00
0.003	0.0003	37.6%	0.32	1.10	1.13
0.003	0.0030	38.2%	1.74	1.08	1.02
0.001	0.0010	37.2%	0.71	0.97	1.01
0.010	0.0010	37.6%	1.67	1.11	1.08

Table 2: Effects of artificial viscosity level on loss

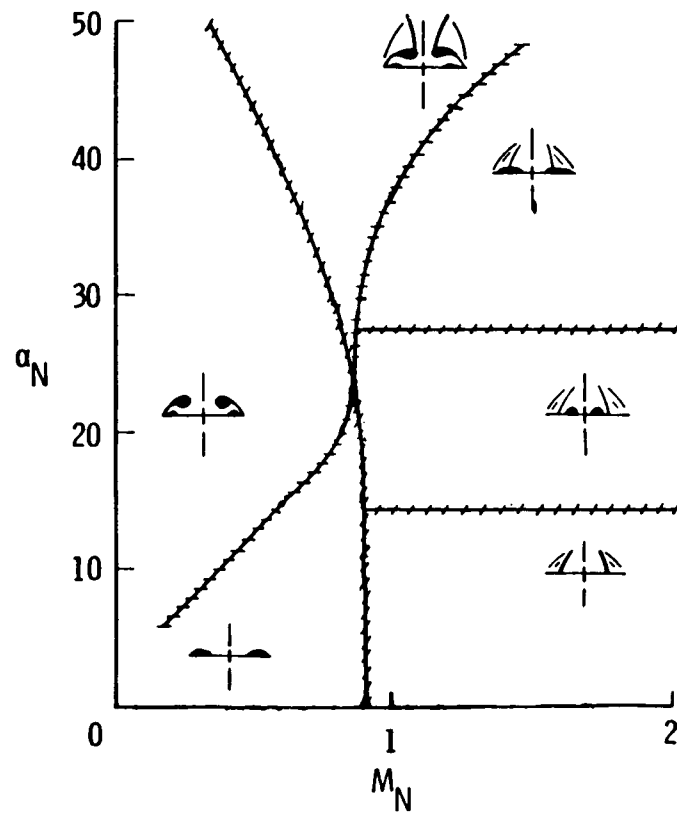


Figure 1: Flow Regime Diagram

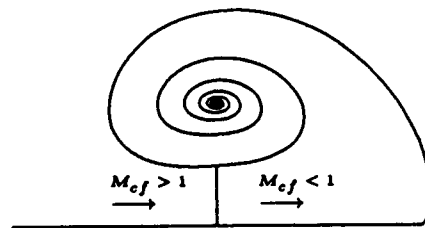


Figure 2: Reverse Cross-Flow Shock under Vortex



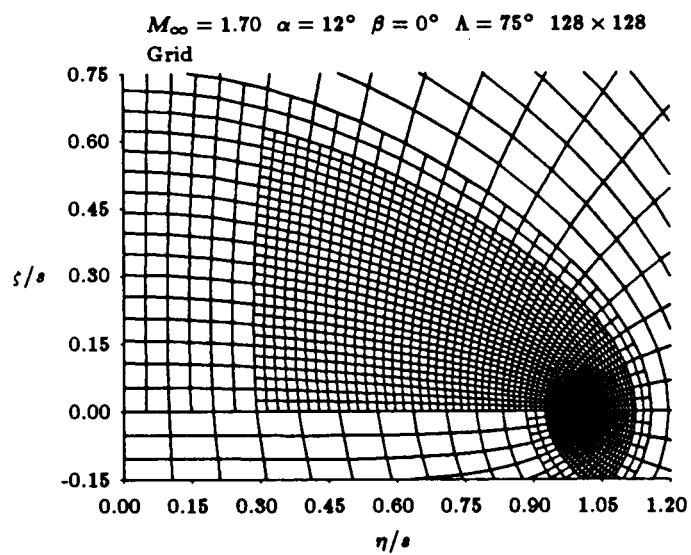


Figure 3: Embedded Grid — Equivalent  $128 \times 128$  Refinement

$$a = \frac{1}{4+2\sqrt{2}}$$

$$b = \frac{\sqrt{2}}{4+2\sqrt{2}}$$

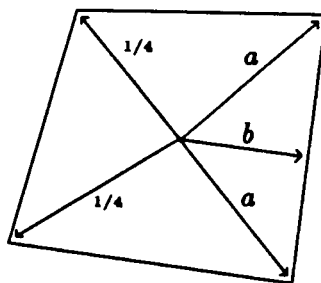


Figure 4: Interface Distribution Scheme

**ORIGINAL PAGE IS  
OF POOR QUALITY**

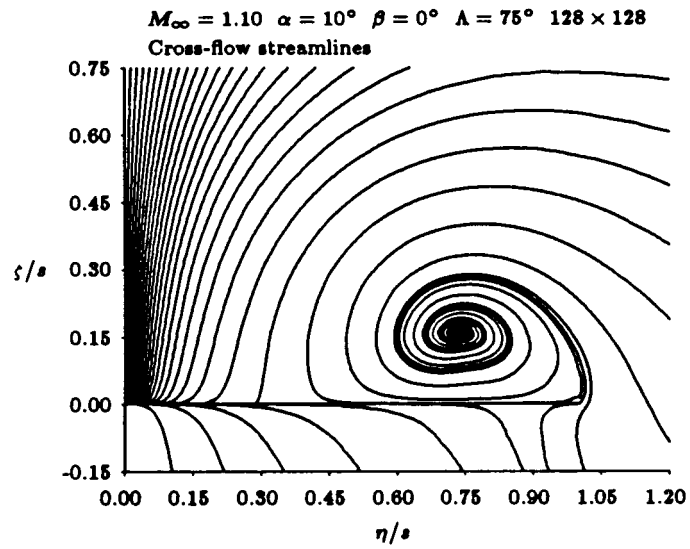


Figure 5: Cross-Flow Streamlines

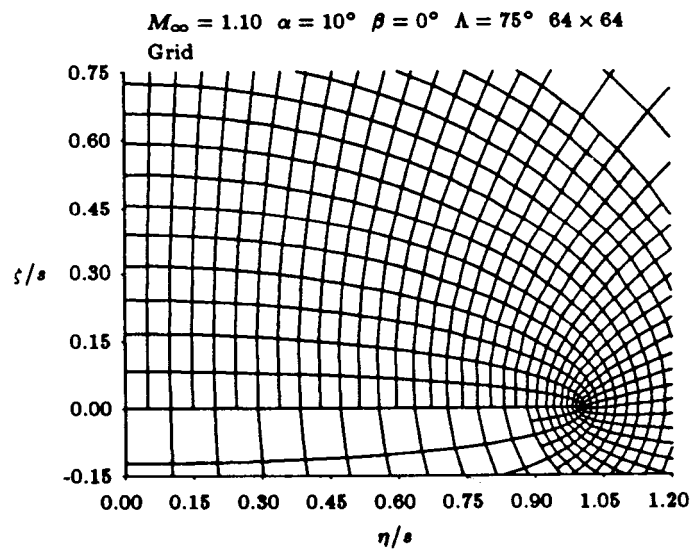


Figure 6: Grid —  $64 \times 64$  Resolution

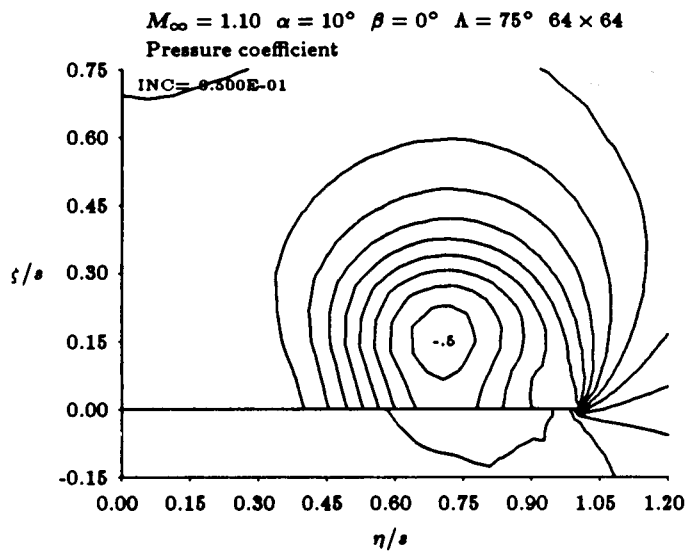


Figure 7: Pressure Coefficient —  $64 \times 64$  Resolution

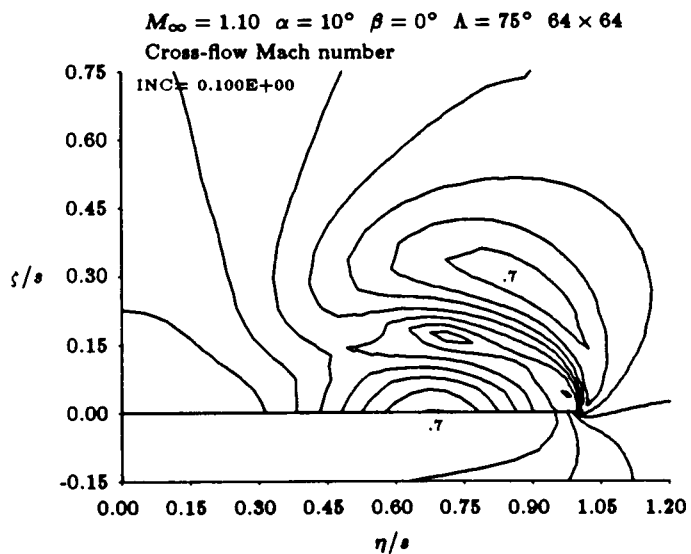


Figure 8: Cross-flow Mach Number —  $64 \times 64$  Resolution

ORIGINAL PAGE IS  
OF POOR QUALITY

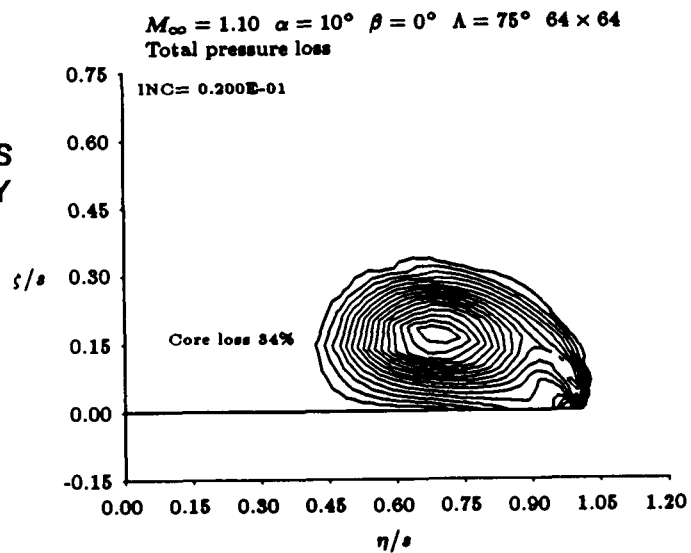


Figure 9: Total Pressure Loss —  $64 \times 64$  Resolution

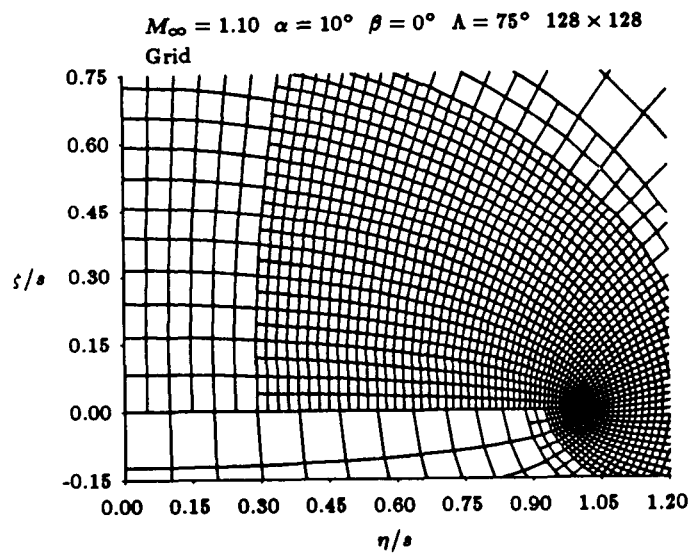


Figure 10: Grid —  $128 \times 128$  Resolution

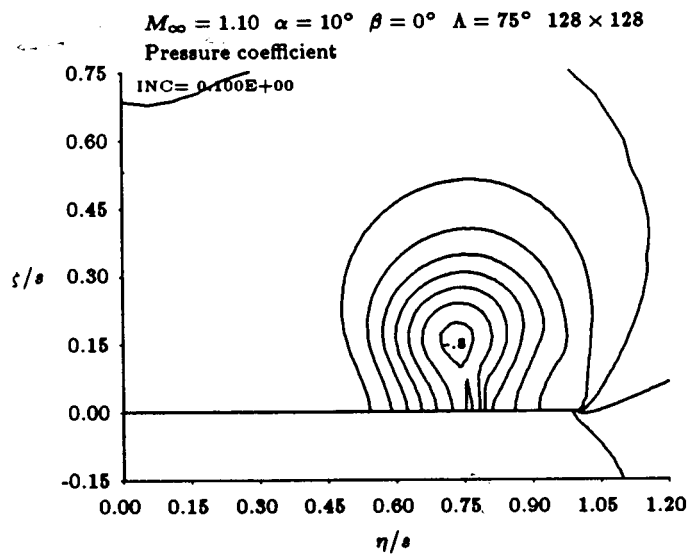


Figure 11: Pressure Coefficient —  $128 \times 128$  Resolution

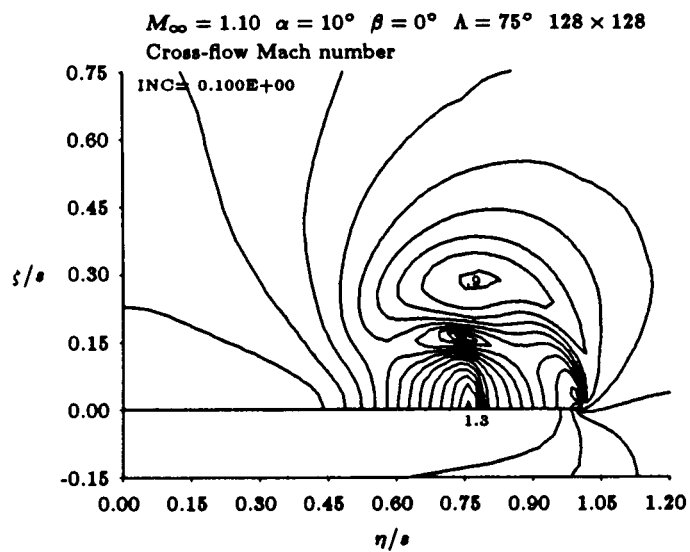


Figure 12: Cross-flow Mach Number —  $128 \times 128$  Resolution

ORIGINAL PAGE IS  
 OF POOR QUALITY

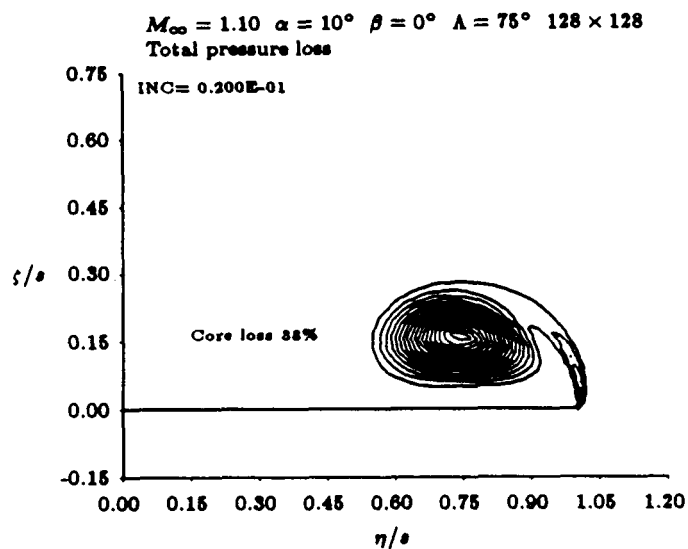


Figure 13: Total Pressure Loss —  $128 \times 128$  Resolution

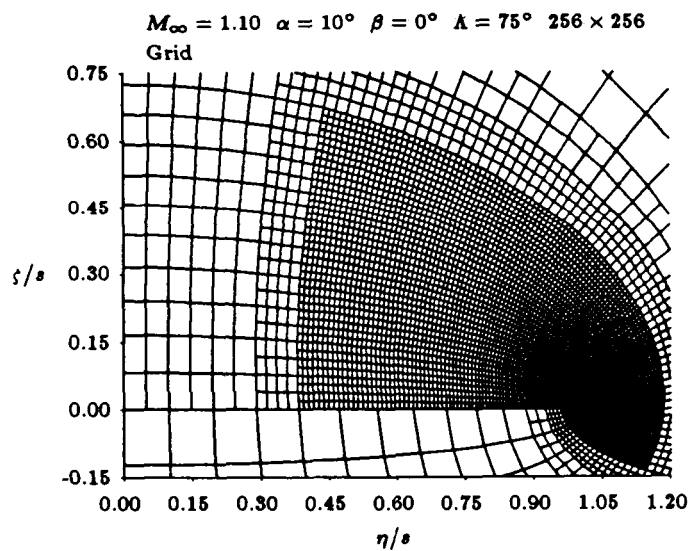


Figure 14: Grid —  $256 \times 256$  Resolution

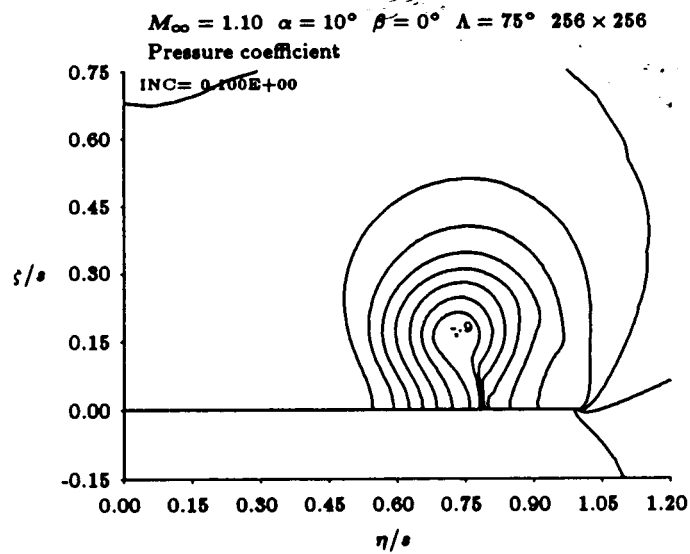


Figure 15: Pressure Coefficient —  $256 \times 256$  Resolution

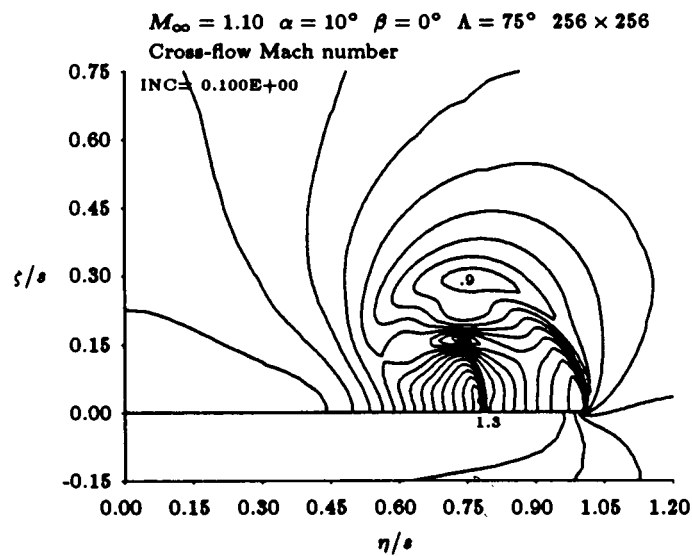


Figure 16: Cross-flow Mach Number —  $256 \times 256$  Resolution

ORIGINAL PAGE IS  
OF POOR QUALITY

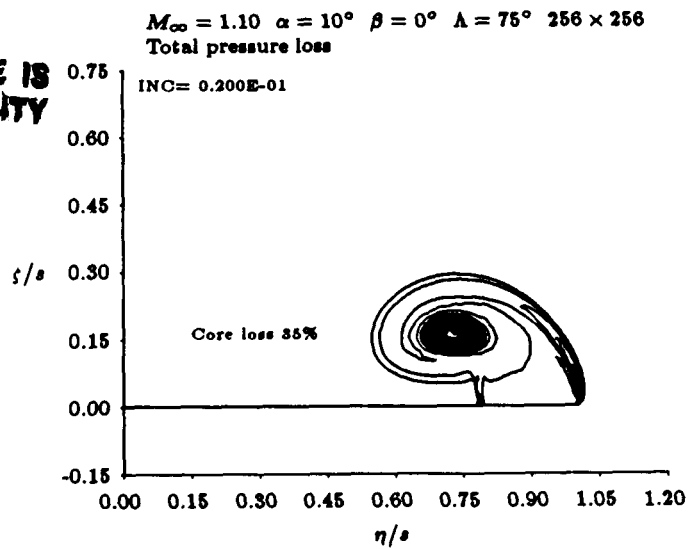


Figure 17: Total Pressure Loss —  $256 \times 256$  Resolution

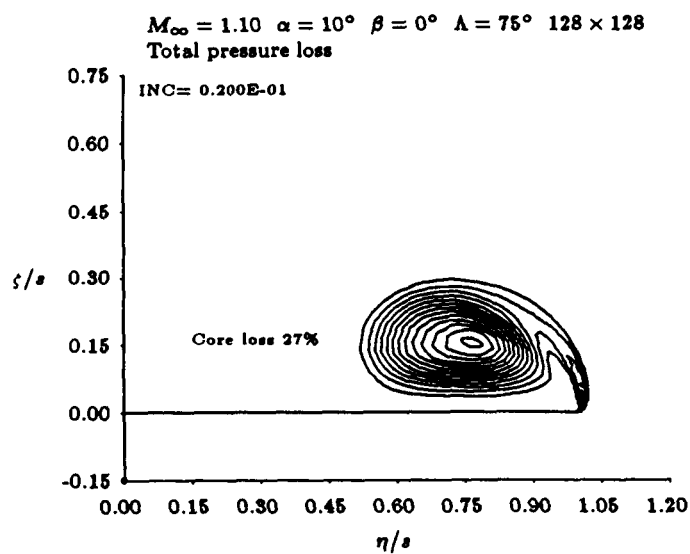


Figure 18: Total Pressure Loss — Zero second-difference continuity damping



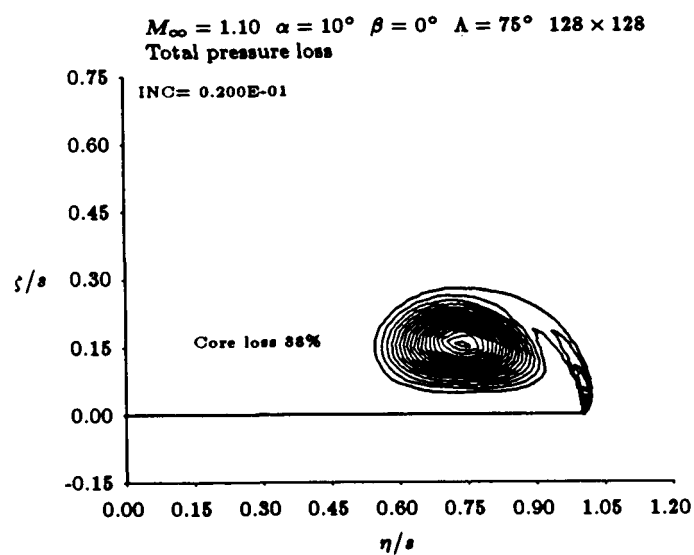


Figure 19: Total Pressure Loss — Zero second-difference continuity damping

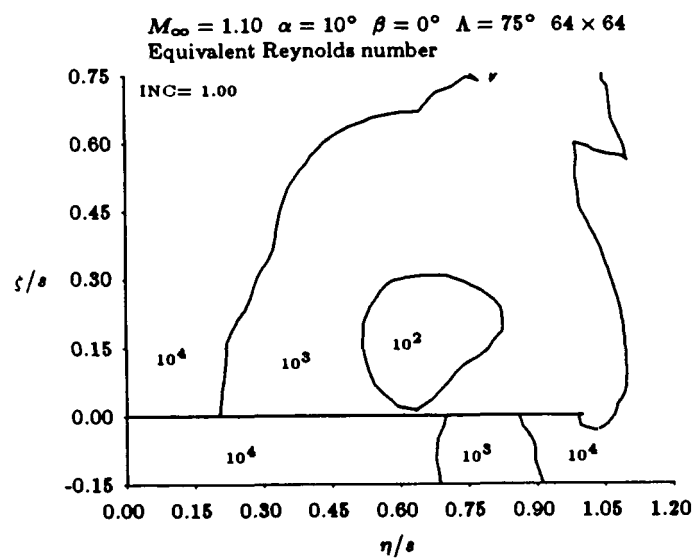


Figure 20: Equivalent Reynolds Number —  $64 \times 64$  refinement

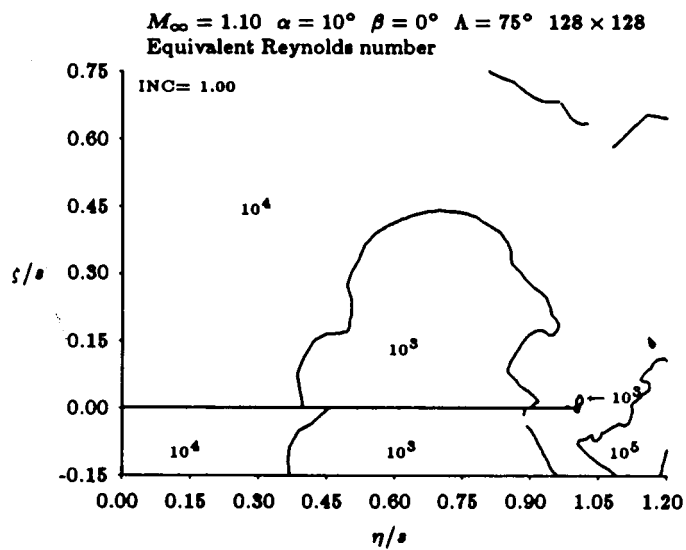


Figure 21: Equivalent Reynolds Number —  $128 \times 128$  refinement

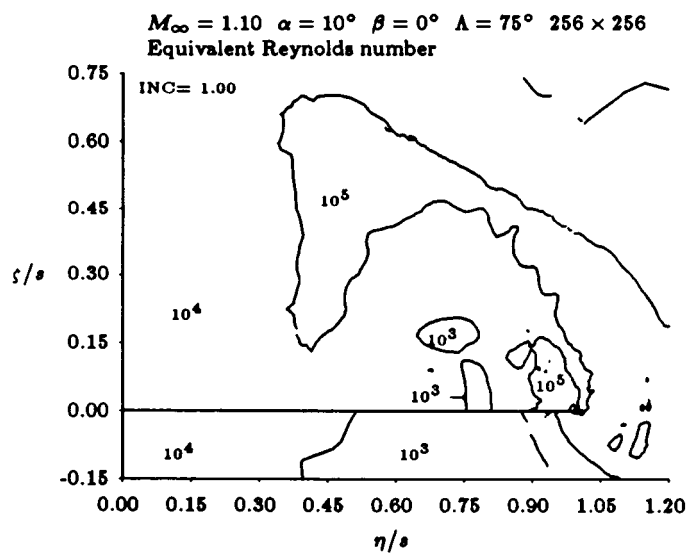


Figure 22: Equivalent Reynolds Number —  $256 \times 256$  refinement

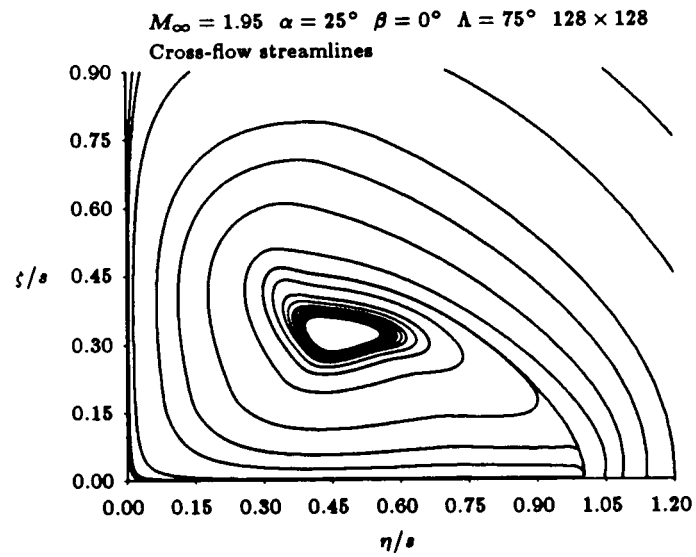


Figure 23: Cross-flow Streamlines —  $M_\infty = 1.95$ ,  $\alpha = 25^\circ$ ,  $\Lambda = 75^\circ$

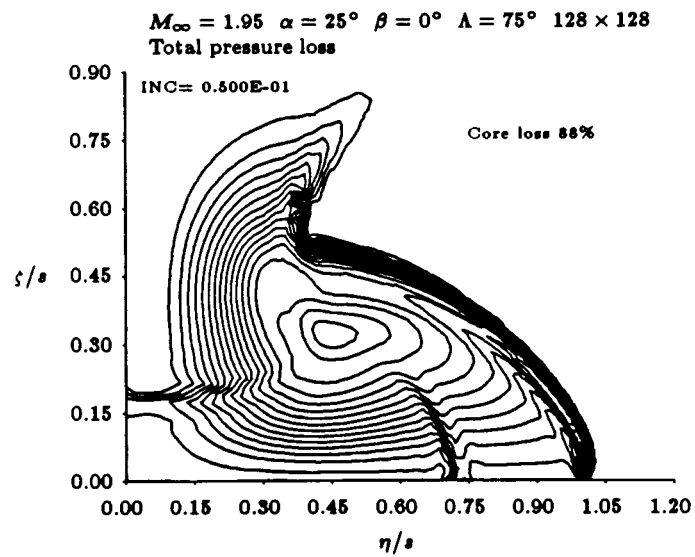


Figure 24: Total Pressure Loss —  $M_\infty = 1.95$ ,  $\alpha = 25^\circ$ ,  $\Lambda = 75^\circ$

ORIGINAL PAGE IS  
OF POOR QUALITY

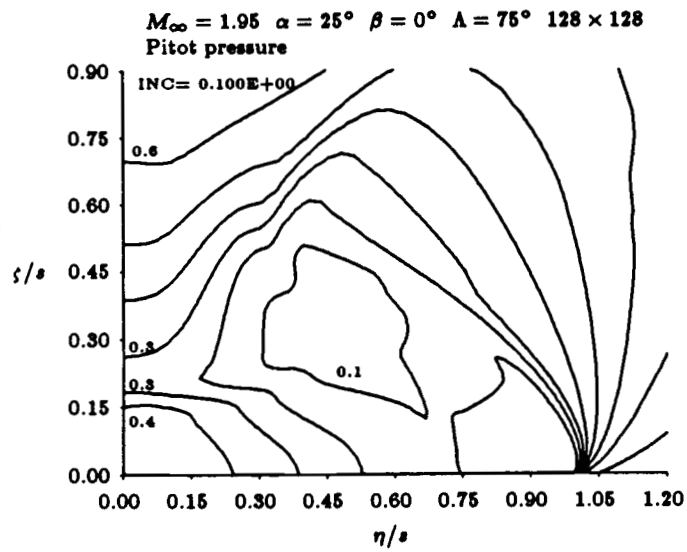


Figure 25: Computed Pitot Pressures —  $M_\infty = 1.95$ ,  $\alpha = 25^\circ$ ,  $\Lambda = 75^\circ$

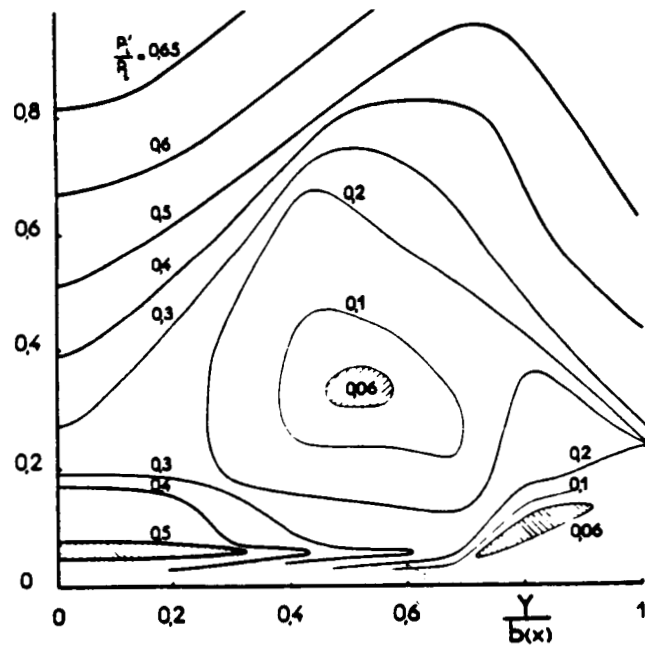


Figure 26: Measured Pitot Pressures —  $M_\infty = 1.95$ ,  $\alpha = 25^\circ$ ,  $\Lambda = 75^\circ$

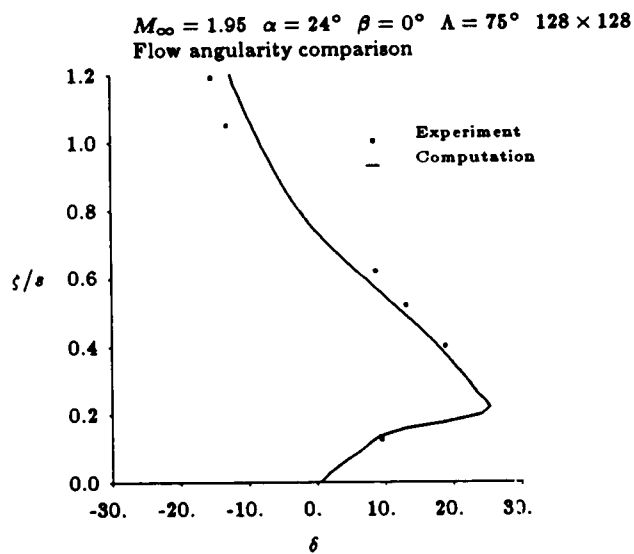


Figure 27: Flow Angularity Comparison —  $M_\infty = 1.95$ ,  $\alpha = 25^\circ$ ,  $\Lambda = 75^\circ$

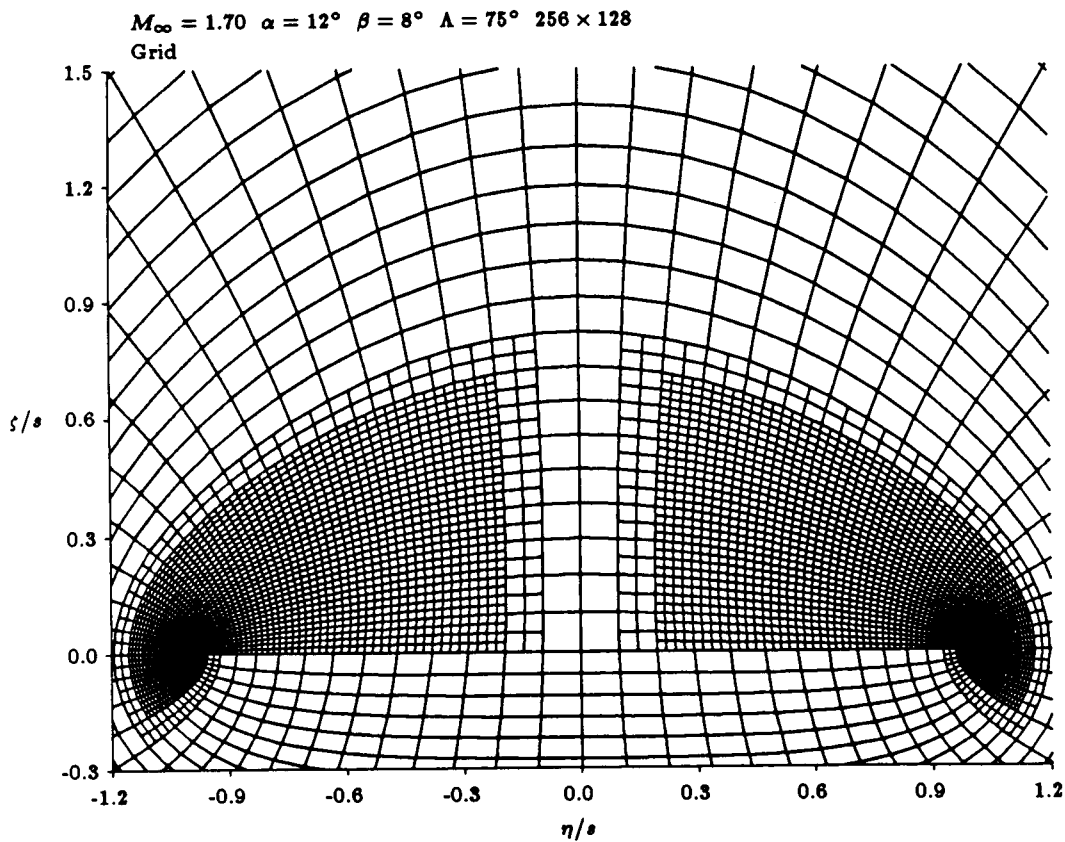


Figure 28: Grid —  $M_\infty = 1.7$ ,  $\alpha = 12^\circ$ ,  $\Lambda = 75^\circ$ ,  $\beta = 8^\circ$

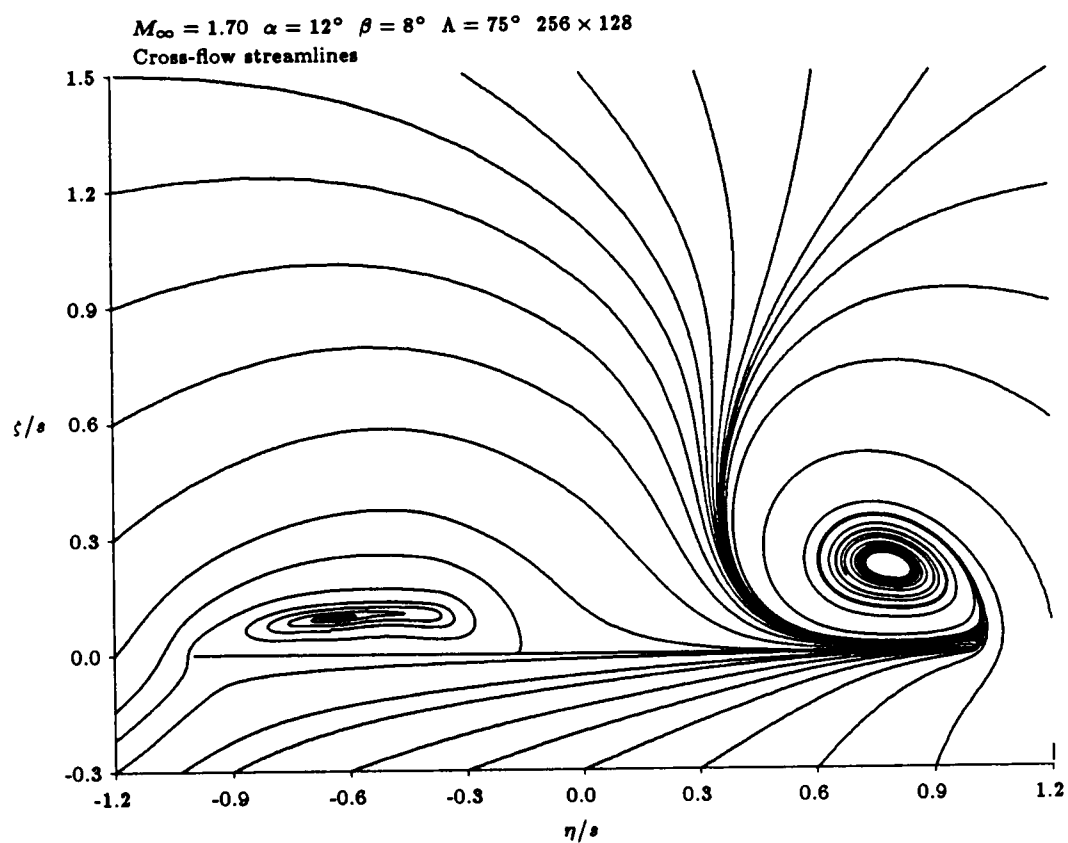


Figure 29: Cross-flow Streamlines —  $M_\infty = 1.7$ ,  $\alpha = 12^\circ$ ,  $\Lambda = 75^\circ$ ,  $\beta = 8^\circ$

ORIGINAL PAGE IS  
OF POOR QUALITY

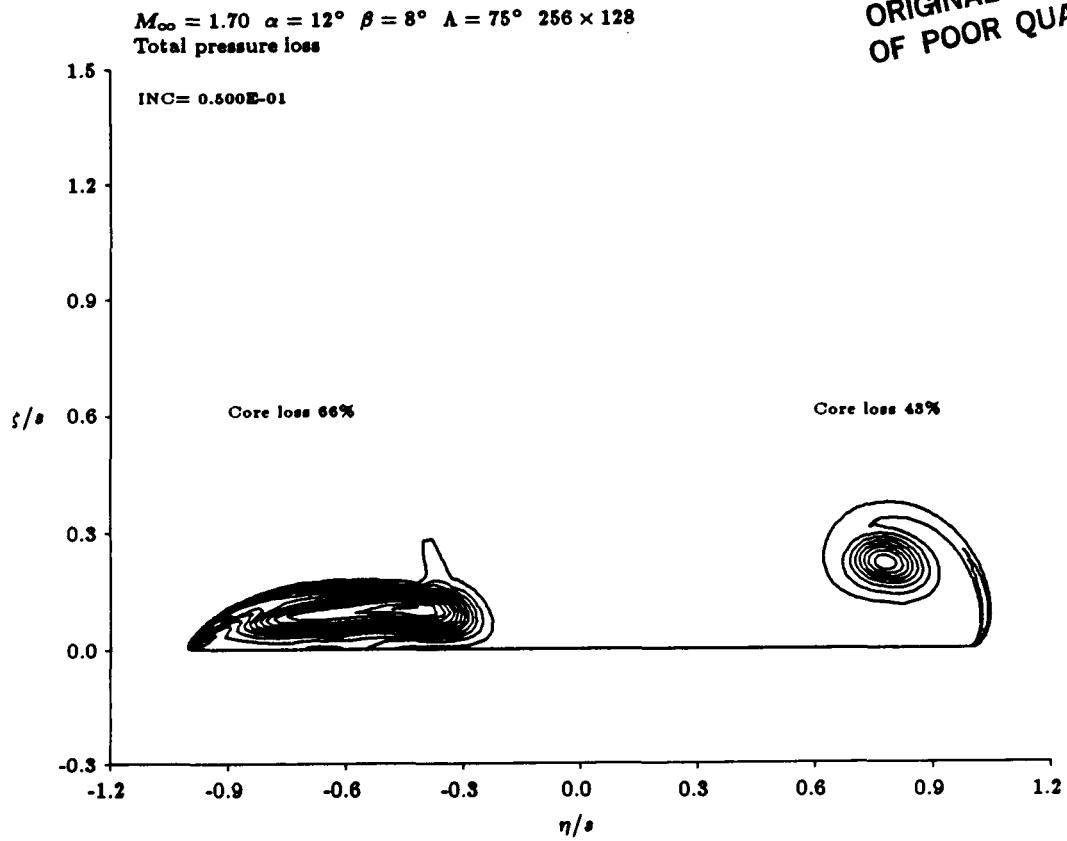


Figure 30: Total Pressure Loss —  $M_\infty = 1.7$ ,  $\alpha = 12^\circ$ ,  $\Lambda = 75^\circ$ ,  $\beta = 8^\circ$

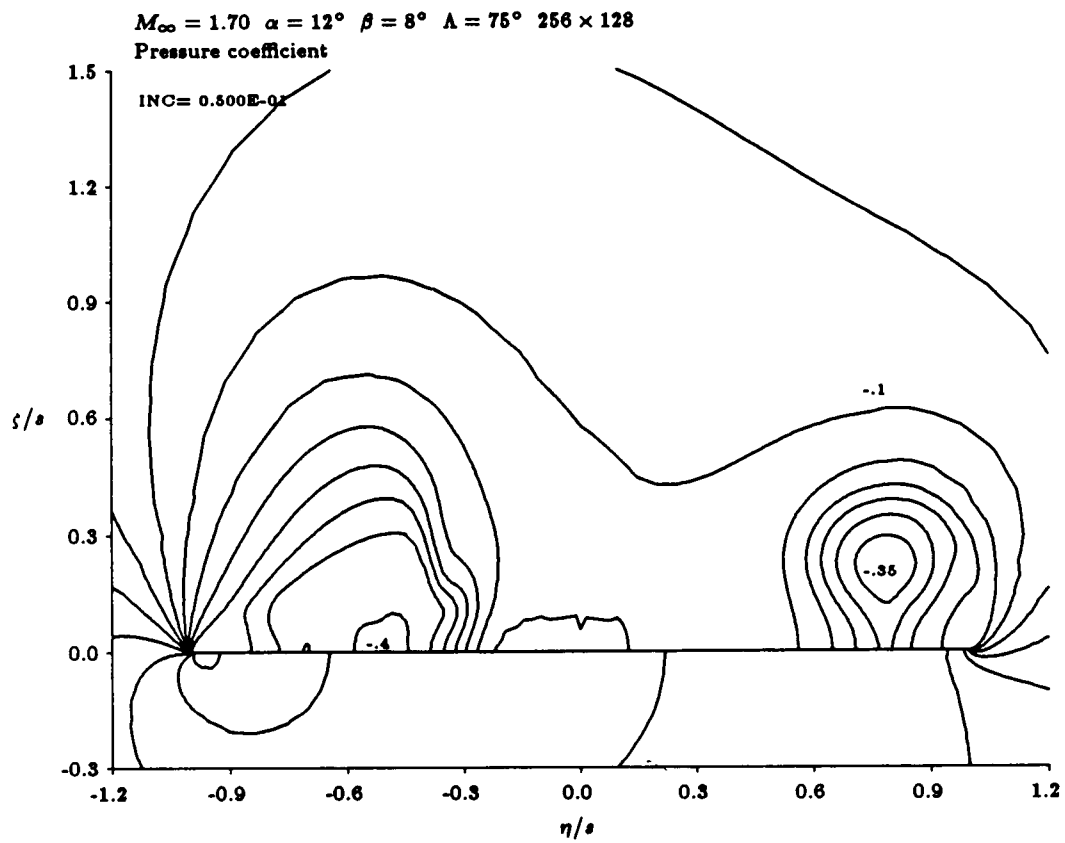


Figure 31: Pressure Coefficient —  $M_\infty = 1.7$ ,  $\alpha = 12^\circ$ ,  $\Lambda = 75^\circ$ ,  $\beta = 8^\circ$



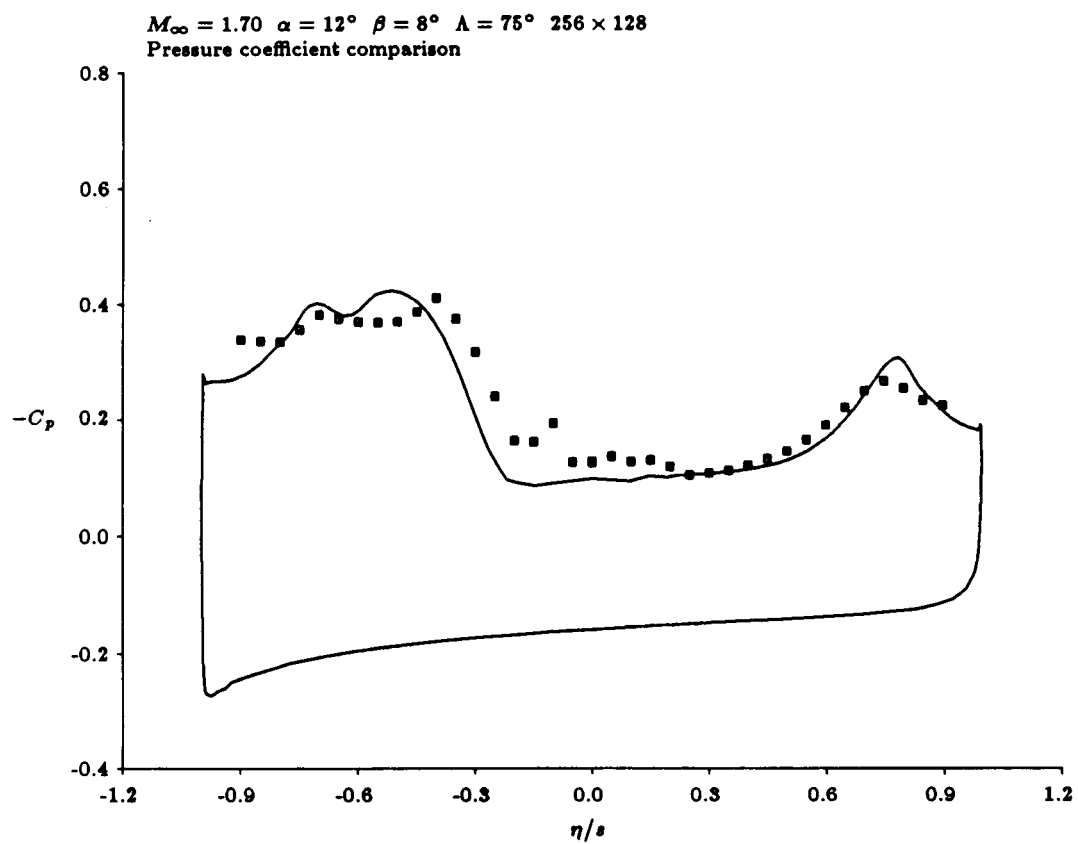


Figure 32: Pressure Coefficient —  $M_\infty = 1.7$ ,  $\alpha = 12^\circ$ ,  $\Lambda = 75^\circ$ ,  $\beta = 8^\circ$

ORIGINAL PAGE IS  
OF POOR QUALITY

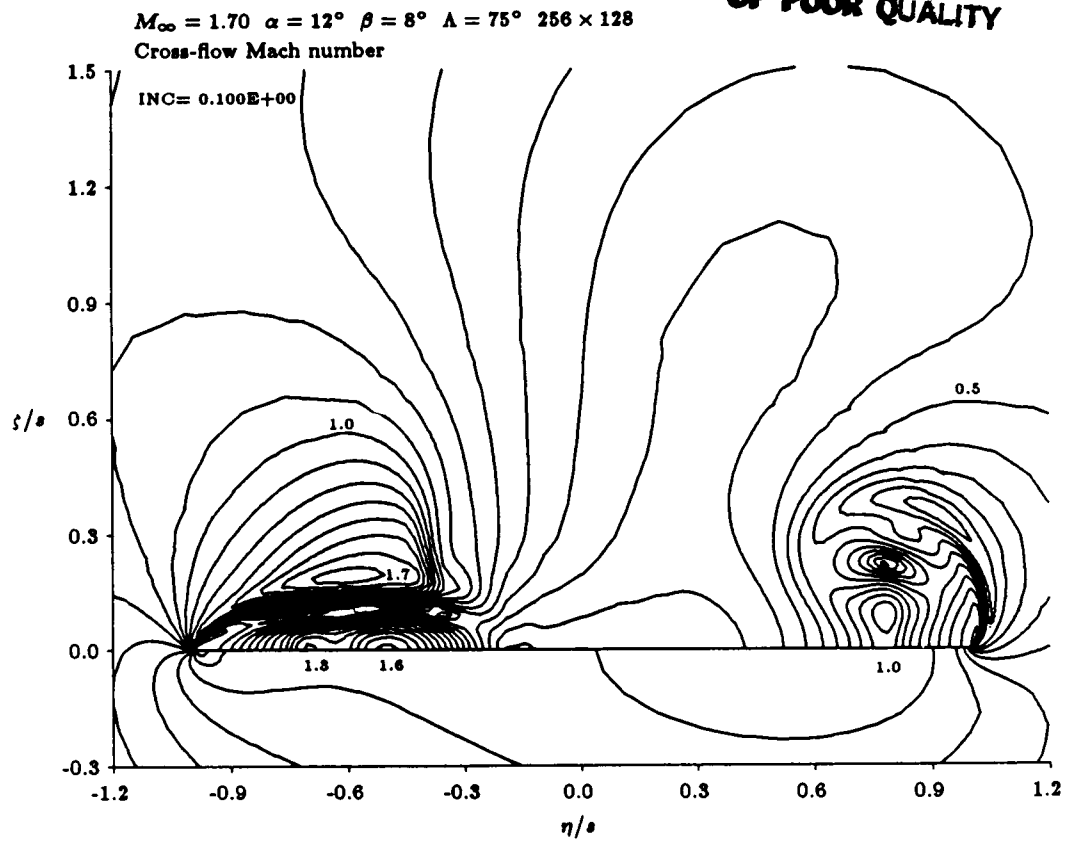


Figure 33: Cross-flow Mach Number —  $M_\infty = 1.7$ ,  $\alpha = 12^\circ$ ,  $\Lambda = 75^\circ$ ,  $\beta = 8^\circ$

## ASYMPTOTIC METHODS FOR INTERNAL TRANSONIC FLOWS

T.C. Adamson, Jr.  
A.F. Messiter  
The University of Michigan  
Ann Arbor, Michigan

## SUMMARY

For many internal transonic flows of practical interest, some of the relevant nondimensional parameters typically are small enough that a perturbation scheme can be expected to give a useful level of numerical accuracy. A variety of steady and unsteady transonic channel and cascade flows is studied with the help of systematic perturbation methods which take advantage of this fact. Asymptotic representations are constructed for small changes in channel cross-section area, small flow deflection angles, small differences between the flow velocity and the sound speed, small amplitudes of imposed oscillations, and small reduced frequencies. Inside a channel the flow is nearly one-dimensional except in thin regions immediately downstream of a shock wave, at the channel entrance and exit, and near the channel throat. A study of two-dimensional cascade flow is extended to include a description of three-dimensional compressor-rotor flow which leads to analytical results except in thin edge regions which require numerical solution. For unsteady flow the qualitative nature of the shock-wave motion in a channel depends strongly on the orders of magnitude of the frequency and amplitude of impressed wall oscillations or fluctuations in back pressure. One example of supersonic flow is considered, for a channel with length large compared to its width, including the effect of separation bubbles and the possibility of self-sustained oscillations. The effect of viscosity on a weak shock wave in a channel is discussed.

## 1. INTRODUCTION

Systematic asymptotic methods of analysis have been in use for roughly thirty years, in a wide variety of perturbation problems. Although they have proven to be quite useful in general, there are several classes of problems in fluid mechanics in which they are particularly powerful, not only because they provide relatively simple formulations for quite complex flows, but also because they emphasize and illuminate regions of particular physical and mathematical importance. This has been true in flow problems involving viscous-inviscid interactions, for example, and in the subject area of this paper, internal inviscid transonic flows (refs. 1-33).

There are several reasons for the success of asymptotic methods in internal transonic flows. One is that small changes in cross-sectional area cause relatively large changes in flow velocity, and so perturbation methods are particularly appropriate. Most important, however, is the well-known fact that the nonlinear small-disturbance equation, which generally holds in some part of a transonic flow field, is valid in regions for which the characteristic length in the flow direction is small compared to that in the lateral direction. Thus, in transonic flow over an isolated airfoil, lengths in the flow direction are scaled by the chord but the proper scale in the transverse direction is large in comparison with the chord. In internal flows, however, the lengths in the transverse direction are constrained by the channel walls. Hence, regions where the nonlinear equation may be required are small in the flow direction, i.e. they are "inner" regions; by far the major part of the flow field is governed by simpler equations, one-dimensional to lowest order. It will be seen that inner solutions are needed at the throat of a channel, immediately downstream of a shock wave, at the entrance and exit of a diffuser, and at the leading and trailing edges of cascades. Still further simplifications follow in certain important limiting cases for which the inner regions (except perhaps at the throat) are described by linearized two-dimensional equations. Finally, it may be noted that in transonic channel flows with shock waves,

PRECEDING PAGE BLANK NOT FILMED

PRECEDING PAGE BLANK NOT FILMED

only small changes in downstream pressure or wall shape are sufficient to give large changes in position of the shock wave. Hence, the fact that perturbation theory is employed does not restrict the physical problem to one in which only small changes in every variable are allowed. Problems of significant technical interest can be considered using asymptotic techniques.

Of the early attempts to obtain solutions for transonic channel flows, two groups of studies have special bearing on the subject of this paper, the use of systematic asymptotic methods of formulation. The first of these covers work initiated in a paper by Tomotika and Tamada (ref. 1), in which similarity solutions to the nonlinear small-disturbance equation are introduced. As is usual with similarity solutions, it is not possible to select arbitrary wall shapes at which boundary conditions may be imposed; instead one accepts the solution as given and chooses one of the streamlines as a wall. However, the solutions given by Tomotika and Tamada were very informative in illustrating the way in which a flow accelerates from subsonic through sonic to supersonic conditions (Meyer flow) and the way in which supersonic pockets form along the walls and grow as the pressure ratio across the channel increases (Taylor flow). It was found by Sichel (ref. 2), in his study of nozzle flows, and also by Ryzhov (ref. 3), that this similarity transformation can be used when the longitudinal viscosity is such that a shock wave of non-negligible thickness is formed. Indeed, the transformation holds for nozzle flows in which the shock wave is infinitesimally thin as well (ref. 4). Because the flow is deflected slightly as it passes through a nearly normal shock wave, the streamlines through a thin shock have a kink at the wave and through a thick shock are bent while passing through the wave. Hence, the interpretation of a streamline as being equivalent to a wall is not obvious, especially if a channel with varying back pressure and thus varying shock-wave positions is being considered. In these studies no order estimates of characteristic lengths are given and, indeed, there was some controversy among workers in the field about the extent of the flow field over which these solutions held.

It was found that the similarity transformation of Tomotika and Tamada could be extended to unsteady flows with a relatively simple modification (ref. 5), and this fact was exploited to cover unsteady flows with either thick or thin shock waves (ref. 4). In the latter reference, an inner region in which the structure of the shock wave was calculated was employed for the case where the shock was thin. In all other aspects, the solutions are similarity solutions so that streamlines move with time and at the shock wave again have a bend which now moves with the wave. Nevertheless, unsteady Meyer and Taylor flows are shown as is the structure of moving shock waves, all with very little computational effort; thus, such solutions are very informative but not particularly useful insofar as use in channel design is concerned.

The second group of papers which are particularly relevant begins with a paper by Szaniawski (ref. 6), in which he introduced a power-series solution to the general steady-flow potential equation. The small parameter in terms of which the series is written, although undefined, could be inferred to be of the order of the relative change in the cross-sectional area between the channel exit and the throat. The coefficients consist of polynomials in  $y^2$ , each power of which is multiplied by an arbitrary function of  $x$ , where  $x$  and  $y$  are coordinates in the longitudinal and transverse directions respectively. The new and important feature of this solution was that arbitrary wall shapes could be considered; at each order of approximation the governing equations and boundary conditions give equations which determine the unknown function of  $x$  in the polynomial solution. However, neither the conditions under which this solution holds nor its relation to the previously mentioned similarity solutions was considered, although it appeared that the region of validity of the solutions was not limited in the  $x$  direction. An extension to flows with shock waves was also presented (ref. 7).

It was shown later (ref. 8) that the Szaniawski series could be derived in a systematic fashion using asymptotic methods, that this solution should be considered as an outer solution which might not remain uniformly valid as a sonic throat was approached, and finally, that there exists an inner region about the throat, in which the aforementioned similarity regions could hold. More importantly, it was shown in this derivation that in the outer region, where  $x$  and  $y$  are of the same order, the governing

equations for each order of approximation are linear, so that solutions for flows with arbitrary wall shapes are easily found; again, it is only in a very thin throat region that the nonlinear equation need be considered. In reference 8, inner and outer solutions were matched and it was demonstrated that unsteady flows could be analyzed using the same asymptotic methods; no shock waves were considered. Finally, in reference 9 a steady flow with a shock wave was considered and it was demonstrated that another inner region enclosing the shock wave was necessary, since solutions immediately downstream of the shock wave do not match with channel-flow solutions at that location. Applications to unsteady flows with shock waves were outlined in reference 10. The extension of these ideas to cover many different steady and unsteady transonic internal flows is described in the following sections.

## 2. PERTURBATION PROCEDURES

An analytical description of two- and three-dimensional, steady and unsteady, transonic channel and cascade flows requires introduction of an intimidating variety of nondimensional parameters. A few of these parameters are numerically small, and one is led to consider the possibility of deriving asymptotic solutions which are expected to be valid in some limit as these parameters approach zero. In selecting appropriate limiting cases for study, it is necessary to make choices about the relative orders of magnitude of the small parameters. One dimensionless quantity, say  $\epsilon$ , is identified as the basic small parameter, and then various cases can be studied depending on the orders of magnitude of the other parameters relative to  $\epsilon$ , in the limit as  $\epsilon \rightarrow 0$ . Although the number of parameters is thereby reduced only by one, it is often possible to obtain analytical solutions and thus to show the dependence on the remaining parameters explicitly. In principle these solutions can be carried out to higher order, to provide numerical accuracy over a wider parameter range.

Many of the examples to be considered are concerned with two-dimensional transonic flow through a converging-diverging channel with small area change, typically with a shock wave in the diverging part. A steady flow is characterized by two nondimensional small parameters, which measure the relative change in channel cross-section area and the typical difference between the local flow Mach number and one. The width and length of the channel are taken to be of the same order, and a parameter  $\epsilon^2$  is introduced as a measure of the area change. If the flow is to accelerate through sonic speed at the throat (choked flow), the Mach number  $M_\infty$  in the undisturbed flow ahead of the channel is given by  $1 - M_\infty = O(\epsilon)$ ; an area change  $O(\epsilon^2)$  then gives a change  $O(\epsilon)$  in Mach number.

Unsteady motions might be caused by oscillations of the channel walls or by oscillations in the downstream pressure. If the motion is caused by wall oscillations, one additional small parameter is the nondimensional amplitude  $\alpha$  of the wall oscillations. A second new parameter which may be small is the reduced frequency  $\tau^{-1} = \omega L/a^*$ , where  $L$  is the channel half-width,  $\omega$  is the angular frequency, and  $a^*$  is the critical sound speed in the undisturbed flow. Thus  $\tau^{-1}$  is proportional to the ratio of the flow residence time to the period of the impressed oscillations. Asymptotic solutions can be derived for  $\epsilon \rightarrow 0$ ,  $\tau^{-1} \rightarrow 0$ , and  $\alpha \rightarrow 0$ , corresponding to selected relationships for the orders of magnitude of  $\tau^{-1}$  and  $\alpha$  in terms of  $\epsilon$ .

Since nondimensional velocity changes are  $O(\epsilon)$ , the entropy change across a shock wave is  $O(\epsilon^3)$ . If a shock wave is present and is nearly plane, the nondimensional vorticity is smaller than  $O(\epsilon^3)$ , and a velocity potential can be used to describe the first few terms in asymptotic expansions of the flow variables. If the coordinates are made nondimensional with  $L$ , the time with  $\omega^{-1}$ , and speeds with  $a^*$ , the full potential equation is

$$a^2 \nabla^2 \phi - \vec{q} \cdot \nabla \frac{q^2}{2} - \frac{2}{\tau} \vec{q} \cdot \vec{q}_t - \frac{1}{\tau^2} \phi_{tt} + \frac{1}{\tau} F'(t) = 0 \quad (2.1)$$

where

$$F(t) = \frac{1}{\tau} \phi_t + H = \frac{1}{\tau} \phi_t + \frac{1}{2} q^2 + \frac{a^2}{\gamma - 1} \quad (2.2)$$

Here  $H$  is the nondimensional total enthalpy and  $a^2 = p/\rho$ , where the sound speed  $a$ , the pressure  $p$ , and the density  $\rho$  have been made nondimensional with the corresponding critical values in the undisturbed flow. Upstream of a shock wave  $F(t) = H_\infty = (1/2)(\gamma+1)/(\gamma-1)$ , and  $F(t)$  has the same value downstream if the flow is steady. Across a moving shock wave defined by  $S(x,y,t) = 0$ , the jump in  $H$  is given by

$$H_d - H_u = c (q_{nd} - q_{nu}) \quad (2.3)$$

where  $x, y$  are coordinates along and normal to the undisturbed flow direction, with  $x = 0$  at the channel throat and  $y = 0$  along the channel center line;  $q_n = \vec{q} \cdot \nabla S / |\nabla S|$  is the velocity component normal to the shock wave;  $c = -\tau^{-1} S_t / |\nabla S|$  is the shock speed; and the subscripts  $u, d$  refer to conditions immediately upstream and downstream of the shock. The Prandtl relation at the shock wave gives

$$(q_{nu} - c)(q_{nd} - c) = \{H_\infty - c(q_{nu} - c/2)\} \{2(\gamma-1)/(\gamma+1)\} \quad (2.4)$$

For a symmetric channel the walls are given by

$$y_w = \pm \{1 - \epsilon^2 f(x) + \alpha G(x,t)\} \quad (2.5)$$

(if wall oscillations, when present, also are symmetric), and the boundary condition at the walls is

$$v_w = \tau^{-1} \partial y_w / \partial t + u_w \partial y_w / \partial x \quad (2.6)$$

where  $u_w = u(x, y_w, t)$  and  $v_w = v(x, y_w, t)$ .

Throughout most of the channel the perturbations from a uniform flow at the critical sound speed are described by a perturbation potential  $\phi$ . In the cases to be considered,  $\phi$  can be expanded in the form

$$\phi = \epsilon \phi_1(x,t) + \epsilon^2 \phi_2(x,y,t) + \epsilon^3 \phi_3(x,y,t) + \dots \quad (2.7)$$

where it has been anticipated that the first term describes a one-dimensional flow and that two-dimensionality appears in the second approximation. As discussed later, it can be shown that this kind of representation fails in thin regions immediately behind a shock wave and at a channel entrance or exit, and in a different way close to the throat. The approximate pressure can be found, if only terms larger than  $O(\epsilon^3)$  are needed, by expanding the isentropic relation  $p = a^{2\gamma/(\gamma-1)}$ . The leading terms are

$$p = 1 - \epsilon \gamma \phi_{1x} - \epsilon^2 \gamma \phi_{2x} - \gamma \epsilon \tau^{-1} \phi_{1t} + \dots \quad (2.8)$$

provided that a term proportional to  $F(t) - H_\infty$  can be neglected; this term is  $O(\alpha)$ , as noted below.

The shock-wave position  $x = x_s(y,t)$  is expanded, for the cases considered here, in the form

$$x_s(y,t) = x_{so}(t) + \varepsilon x_{s1}(t) + \dots \quad (2.9)$$

where it has been anticipated that in most applications the first two terms will be independent of  $y$ ; typically it is found that  $\partial x_s / \partial y = O(\varepsilon^{3/2})$ . For unsteady flows, the shock-wave motion is found to be quasi-steady for frequencies low enough that  $\tau^{-1} \ll \varepsilon^2$ , and the time required for disturbances from the channel exit to reach the shock wave is short in comparison with one period when  $\tau^{-1} \ll \varepsilon$ . Thus two important special cases arise for  $\tau^{-1} = O(\varepsilon^2)$  and  $\tau^{-1} = O(\varepsilon)$ ; these will be referred to as "low" and "moderate" frequencies in the following. The wall oscillations with amplitude  $O(\alpha)$  are equivalent to time-dependent area changes  $O(\alpha)$ , which imply changes  $O(\alpha/\varepsilon)$  in the flow velocity;  $\alpha$  is taken to be at most  $O(\varepsilon^2)$ . For  $\tau^{-1}$  equals  $O(\varepsilon^2)$  or larger, the shock wave velocity is also  $O(\alpha/\varepsilon)$ , and so the shock-wave displacement is  $O(\tau\alpha/\varepsilon)$ . Thus the amplitude of the shock-wave oscillation is  $O(1)$  if  $\alpha = O(\varepsilon\tau^{-1})$  and small if  $\alpha \ll \varepsilon\tau^{-1}$ . It now also can be seen, from equations (2.2) and (2.3), that the neglected term proportional to  $F(t) - H_\infty$  in equation (2.8) is  $O(\alpha)$ .

In the three-dimensional examples to be considered, the variation of Mach number is taken to be  $O(\varepsilon)$  in a transverse direction as well as in the flow direction. For a cascade the blade stagger, as well as the ratio of spacing to chord, is taken to be  $O(1)$ . In one example of unsteady supersonic channel flow, the ratio of channel length to width is  $O(\varepsilon^{-1/2})$ ; although boundary layers are thin, the displacement thickness due to separation bubbles in this example is of the same order as the variation in channel width. The viscosity in general is taken to be small enough that the shock-wave thickness is small in comparison with any relevant streamwise length; in cases where shock-wave structure is considered, the Reynolds number is such that the shock-wave thickness is  $O(\varepsilon)$ .

### 3. STEADY FLOWS

#### Two-dimensional Inviscid Channel Flow

To provide an introduction for applications to other flows, the results of reference 9 are summarized here, with some minor changes in notation. Substitution of the expansion (2.7) into the potential equation (2.1) and boundary condition (2.6) leads to a first approximation defined by

$$\phi_{1yy} = 0, \quad \phi_{1y}(x, \pm 1) = 0 \quad (3.1)$$

The solution has the form  $\phi_1 = \phi_1(x)$ , as already anticipated in (2.7). The second approximation is defined by

$$\phi_{2yy} = (\gamma+1) \phi_{1x} \phi_{1xx}, \quad \phi_{2y}(x, \pm 1) = \mp f'(x) \quad (3.2)$$

With the further requirement that the flow be choked, so that  $\phi_{1x}(0) = 0$ , for  $f'(0) = 0$ , the solution for  $\phi_1$  can be completed:

$$\phi_{1x}(x) = \pm \left( \frac{2}{\gamma+1} \right)^{1/2} \{f(0) - f(x)\}^{1/2} \quad (3.3)$$

If  $f = 0$  at the channel entrance and the undisturbed velocity  $u = u_\infty$  is expanded as  $u_\infty = 1 + \varepsilon u_{1\infty}$

+  $\epsilon^2 u_{2\infty} + \dots$ , the constant  $f(0)$  is related to  $u_{1\infty}$  by (for subsonic incoming flow)  $u_{1\infty} = -\{2f(0)/(\gamma+1)\}^{1/2}$ .

The solution for  $\phi_2$  contains a function  $h_2(x)$  that is still unknown:

$$\phi_2(x,y) = \frac{1}{2} f'(x) \left( \frac{1}{3} - y^2 \right) + h_2(x) \quad (3.4)$$

The differential equation and boundary condition for the third approximation then allow completion of the solution for the second approximation. The function  $h_2'(x)$  is found to be

$$h_2'(x) = (3 - 2\gamma) \phi_{1x}^2 / 6 + c_2 / \{(\gamma+1) \phi_{1x}\} \quad (3.5)$$

where the constant  $c_2$  is discontinuous at a shock wave. For choked flow,  $c_{2u} = 0$ . The Prandtl relation (2.4) gives

$$u_{1u} + u_{1d} = 0, \quad u_{2u} + u_{2d} = -u_{1u} u_{1d} \quad (3.6)$$

where  $u_1 = \phi_{1x}$  and  $u_2 = \phi_{2x}$ . A tentative result  $c_{2d} = -2\gamma(\gamma+1) u_{1u}^3 / 3$  can be found by integrating the condition for  $u_{2d}$  across the channel, from  $y = -1$  to  $y = 1$ . It is evident, however, that the solution for  $\phi_2$  can only satisfy the Prandtl relation in such an averaged sense. The difficulty arises because the small shock-wave curvature implies a streamline curvature that is inconsistent with the wall curvature, and so the solution (3.4) is not complete immediately behind the shock wave. To satisfy both the shock relations and the wall boundary condition an "inner" solution satisfying a Prandtl-Glauert equation is needed for  $x - x_{so} = O(\epsilon^{1/2})$ . The correction to be added to the expansion (2.7) is found to be

$$- \epsilon^{5/2} f''(x_{so}) (4/\pi^3) \sum_{n=1}^{\infty} (-1)^n n^{-3} \exp(-n\pi X) \cos n\pi y \quad (3.7)$$

where  $X = \{(\gamma+1)u_{1u} \epsilon\}^{-1/2} (x - x_{so})$ . As the intersection of the shock wave and the wall is approached, the series can be summed to show explicitly the expected logarithmic singularity in the pressure gradient. Also it can now be verified, by an integral condition expressing mass conservation, that  $c_{2d}$  has the value anticipated above. Although needed to provide the flow details near the shock wave, this inner solution is not, therefore, really required for the evaluation of  $c_{2d}$ . The analogous correction for axisymmetric flow was also given in reference 9.

At the channel entrance and exit, an expansion of the form (2.7) in general will not match with solutions in the external flow, and a Prandtl-Glauert equation is again needed for a distance  $\Delta x = O(\epsilon^{1/2})$ ; an example will be shown later. Near the channel throat, within a short distance  $x = O(\epsilon)$ , the terms  $\phi_{yy}$  and  $(\gamma+1) \phi_x \phi_{xx}$  in the potential equation are of the same order of magnitude. For the case of acceleration from subsonic to supersonic speed, if  $f''(0) = -1$ , the first approximation to the solution has the simple polynomial form

$$\phi = \epsilon^3 \frac{1}{2} (\gamma+1)^{1/2} \left\{ \frac{x^2}{(\gamma+1) \epsilon^2} + \frac{x}{(\gamma+1)^{1/2} \epsilon} \left( y^2 - \frac{1}{3} \right) + \frac{y^2}{6} \left( \frac{y^2}{2} - 1 \right) \right\} \quad (3.8)$$

Although this expression should, strictly speaking, be obtained as a solution of the nonlinear equation  $\phi_{yy} = (\gamma+1) \phi_x \phi_{xx}$ , it is actually seen to contain just the largest terms in the Taylor expansion, about  $x = 0$ , of the solution  $\epsilon \phi_1 + \epsilon \phi_2$  given above. In other circumstances, if the flow is not quite choked



or if a shock wave is present very close to the throat, a special formulation for  $x = O(\epsilon)$  and/or for  $x = O(\epsilon^{1/2})$  may be essential, as noted in references 5, 8, 9, 16, and 17.

### Cascade Flows

A limiting case of transonic cascade flow has been studied in reference 11. The ratio of blade spacing to blade chord length is  $O(1)$ ; the stagger angle  $\tan^{-1} \lambda = \tan^{-1} (d/\upsilon) = O(1)$ , where  $\upsilon$  = blade spacing and  $d = \lambda \upsilon$ ; the blade thickness, camber and angle of attack are  $O(\epsilon^2)$ ; and for high subsonic speeds ahead of the cascade the Mach number  $M_\infty$  is expressed by  $M_\infty^2 = 1 - K\epsilon$ . There is then a region analogous to a channel in which a nearly one-dimensional flow is described by an asymptotic expansion of the form (2.7). Ahead of the cascade, however, the largest flow perturbations are two-dimensional. As for an isolated airfoil the length scale in a transverse direction is  $O(\epsilon^{-1/2})$ . On this larger scale the spacing between the blades appears very small, and in the limit the flow is the same as the flow past a scalloped wall, as sketched in figure 1. Since the "outer" solutions do not match directly to the "channel" solutions, additional solutions are needed near the leading edges, and likewise near the trailing edges. Here  $y = O(1)$  and the length scale in the  $x$ -direction is  $O(\epsilon^{1/2})$ , so that an "edge" solution describes the flow in a thin strip transverse to the flow and containing one of the edges; a similar situation arises at trailing edges. These edge regions are indicated in figure 1.

The outer solution has the form

$$\phi = \epsilon^{3/2} \tilde{\phi}_{3/2}(\tilde{x}, \tilde{y}) + \epsilon^2 \tilde{\phi}_2(\tilde{x}, \tilde{y}) + \dots \quad (3.9)$$

where  $\tilde{x} = x$ ,  $\tilde{y} = \epsilon^{1/2} K^{1/2} (y - \lambda x)$ . The upper and lower blade surfaces are  $y = \epsilon^2 f_u(x)$  and  $y = \epsilon^2 f_v(x)$ , respectively. If it is required that there be no mass flow  $O(\epsilon^2)$  around the leading edges, it is found (ref. 11) that the velocity in the leading-edge regions remains  $u = 1 + \epsilon u_{1\infty} + \dots$ , as in the undisturbed flow, and that the first term in the angle of attack has a specific value, such that  $\alpha = \epsilon^2 f_u'(d)/d + \dots$ . The expansion of  $\alpha$  in terms of  $\epsilon$  then has the form

$$\alpha = \epsilon^2 f_u'(d)/d + \epsilon^{5/2} \alpha_{5/2} + \dots \quad (3.10)$$

For parabolic surfaces a complex perturbation velocity is found to be

$$\tilde{\phi}_{3/2\tilde{x}} - i \tilde{\phi}_{3/2\tilde{y}} = -\Delta_u / (K^{1/2} \pi) \ln (1 - e^{2\pi i \tilde{z}/d}) \quad (3.11)$$

where  $\tilde{z} = \tilde{x} + i \tilde{y}$  and  $\Delta_u = f_u'(d) - f_u'(0)$ .

Near the edge  $x = d$  the potential has the form

$$\phi = \epsilon^2 (\upsilon/\pi) \hat{\phi}_2(\hat{x}, \hat{y}; \epsilon) + \dots \quad (3.12)$$

where  $\hat{x} = \pi(x - d)/\{(\epsilon K)^{1/2} \upsilon\}$ ,  $\hat{y} = \pi(y - \upsilon)/\upsilon$  and matching with the outer solution shows that  $\hat{\phi}_2 = O(\ln \epsilon)$  as  $\epsilon \rightarrow 0$ . A conformal transformation  $\hat{x} + i\hat{y} = \zeta - 1 - \ln \zeta$  maps the local flow onto the upper half of the  $\zeta$ -plane. The complex perturbation velocity is

$$\hat{\phi}_{2\tilde{x}} - i \hat{\phi}_{2\tilde{y}} = \frac{\Delta_u}{\pi} \left\{ \frac{\zeta}{\zeta-1} \ln \frac{d/\nu}{2(\epsilon K)^{1/2}} - \ln(\zeta-1) \right\} + \frac{\Delta_d}{\pi} \left\{ \frac{1}{\zeta-1} + \ln \frac{\zeta-1}{\zeta} \right\} + \frac{d\alpha_{5/2}}{\nu K^{1/2} (\zeta-1)} - i f'_u(0) + i \frac{f_u(d)}{d} \quad (3.13)$$

where  $\Delta_d = f_u'(d) - f_u'(0)$ . It can be shown that this result matches properly with the channel and outer solutions. Analogous inner solutions are needed for thin regions containing the trailing edges.

At low supersonic speeds, such that  $M_\infty^2 = 1 + K\epsilon$ , the flow ahead of a cascade in terms of coordinates  $\tilde{x}$  and  $\tilde{y}$  is again equivalent to the flow past a scalloped wall. For  $\tilde{y} = O(1)$  the characteristics and the weak shock waves from the leading edges can still be considered parallel. Here the first approximation is given by the linear wave equation of supersonic small-disturbance theory. At larger distances disturbances from the forward part of a blade will overtake the shock wave from the leading edge of that blade, whereas disturbances further to the rear are overtaken by the shock from the next blade. A limiting characteristic separates these disturbances and extends to infinity. This effect becomes important for  $y = O(\epsilon^{-1})$ , i.e.,  $\tilde{y} = O(\epsilon^{-1/2})$ , where a nonlinear far-field description is required. The solution gives an "N-wave" for the pressure and shows that the shock-wave strength is  $O\{\epsilon y\}^{-1}$  as  $\epsilon y \rightarrow \infty$ . The flow inclination angle approaches a value which remains constant along the limiting characteristic and which is found to equal the average blade slope between  $x = 0$  and  $x = d$ , namely  $\epsilon^2 f_u(d)/d$ . Thus the flow far ahead of the cascade is affected and has a prescribed "unique incidence angle" equal to the value  $\epsilon^2 f_u(d)/d$  at the limiting characteristic; a second approximation to this value can also be derived.

### Three-Dimensional Flows

Three-dimensional flow through a transonic compressor rotor has been studied (refs. 12, 13) as an extension to the cascade flow presented in reference 11. The problem has an additional small parameter  $\delta$  which orders the difference between the undisturbed velocity relative to a moving blade and sonic velocity. If velocities are made dimensionless with respect to the sonic velocity in the undisturbed flow and lengths by the ratio of this sonic velocity to the constant angular velocity, then the dimensionless undisturbed velocity relative to the blade  $U_0$  is

$$U_0^2 = R^2 + M_{0a}^2 \quad (3.14)$$

where, because of the way in which lengths are nondimensionalized,  $R$  is both the dimensionless radius and the tangential component of the velocity relative to the blade. The Mach number of the undisturbed axial flow is  $M_{0a}$ ; i.e., the incoming flow in absolute (engine- or laboratory-fixed coordinates) terms is in the axial direction with no swirl or radial component. Since  $U_0$  is a Mach number, the radius  $R_{so}$  at which the relative Mach number is one is  $R_{so}^2 = 1 - M_{0a}^2$  and  $U_0^2 = 1 + R^2 - R_{so}^2$ . Hence, if  $\delta = O(U - 1) = O(R - R_{so})$  then a stretched radial coordinate  $z$  can be defined and  $U_0$  written in terms of  $z$  and  $\delta$  as follows:

$$z = \frac{R - R_{so}}{\delta} \quad (3.15a)$$

$$U_o^2 = 1 + 2\delta R_{so} z + \delta^2 z^2 \quad (3.15b)$$

As in the cascade-flow problem the thickness of the blades is taken to be  $O(\epsilon^2)$ . Then, in the channel-like part of the flow between the blades, the perturbation to the flow velocity is  $O(\epsilon)$ , again just as in the cascade or two-dimensional channel-flow problems. It is seen, then, that the various physical problems which can be considered are characterized mathematically by the relative orders of  $\delta$  and  $\epsilon$ . For  $\delta \ll \epsilon$ , the flow is dominated by the constriction provided by the channel with very little effect due to the shear in the incoming undisturbed flow  $U_o$ ; the flow is essentially two-dimensional with three-dimensional effects relegated to higher-order terms. For  $\delta \gg \epsilon$ , the inverse is true in that the flow is dominated by the incoming shear flow and effects of the side walls or blades arise only in higher-order terms. For  $\delta = O(\epsilon)$ , however, both shear and flow constriction effects are of equal importance and the interplay between them most pronounced. It is this case which is considered in references 12 and 13.

A model problem consisting of a shear flow in a three-dimensional channel with blade-like flow constrictions on opposing walls was studied first (refs. 14, 15). The flow field considered is similar to that through an axial-flow rotor with zero stagger angle. Solutions are presented both for  $\delta = O(\epsilon)$  and  $\delta \gg \epsilon$ . In the more interesting case,  $\delta = O(\epsilon)$ , it is shown that just as for two-dimensional nozzle flows, there are limits on the average Mach number which can occur in the entrance flow when choking occurs at the minimum area. That is, for isentropic flow through a nozzle with a given area ratio, there are two Mach numbers at the nozzle entrance for which sonic velocity occurs at the throat, one supersonic and one subsonic. In the problem under consideration, this same result is found only for average (across the span) Mach numbers; this then has consequences on the allowable positions for the sonic surface in the incoming flow. In addition to this similarity to one-dimensional flow interpretations, it is demonstrated that when a shock wave occurs downstream of the minimum area, the main effect of a variation in back pressure is to change the shock location. This is true even when, because of the fact that the flow is a shear flow, the shock wave fills only part of the channel. In that event, variations in back pressure do indeed change the shape of the shock wave and because signals can move through the subsonic flow beneath the wave, the flow upstream of the wave is affected. However, the upstream influence of these pressure signals is limited to a distance  $O(\epsilon^{1/2})$  upstream of the shock wave; the essential result of changes in back pressure is a change in location of the wave. Finally, it is shown that for  $\delta \gg \epsilon$ , the analogy with one-dimensional flows breaks down. For example, the Mach number at which bifurcation in solutions occurs is not unity as it is in the case when  $\delta = O(\epsilon)$ .

The formulation of the problem of transonic flow through a compressor rotor follows that of the cascade (two-dimensional) flow quite closely. Thus, at a constant radius, the flow appears to be that through a cascade with the added feature that as the span of the blades is traversed, the stagger angle changes. However, the fact that the flow is three-dimensional causes several fundamental differences as might be expected.

The limit process chosen is important because it sets the physical problem considered. As mentioned previously  $\delta = O(\epsilon)$  is the case considered, but it remains to relate  $\delta$  to a physical quantity. In references 12 and 13, with  $\delta = O(R - R_{so})$  and since  $R - R_{so}$  is of the order of the blade span, then  $\delta$  is chosen to be of the order of the (dimensionless) blade chord and in particular the constant axial

component of the blade chord at the hub  $C_a$ . Since  $(R - R_{so})/\delta = O(1)$ , this assumes that in the limit  $\epsilon \rightarrow 0$ , so  $\delta \rightarrow 0$ , the blade aspect ratio remains unchanged. To ensure that the complete channel geometry remains unchanged in the limit, the dimensionless blade spacing at the tips, scaled with respect to  $C_a$ , is also taken to be  $O(1)$ . Thus, if  $R_t$  is the dimensionless tip radius and  $B$  the number of blades,

$$s \equiv \frac{2\pi R_t}{B C_a} \quad (3.16)$$

Thus  $B^{-1} = O(C_a)$  and in the limit as  $\epsilon \rightarrow 0$ ,  $B \rightarrow \infty$  to retain the proper geometric properties during the limit process. The limit process  $B^{-1} \rightarrow 0$  has been used in other asymptotic analyses of cascade flow.

It is necessary to consider the same regions as in the cascade problem, as pictured in figure 1. Indeed in the far field, the boundary of which is again a scalloped wall as in figure 1a, the flow is two-dimensional to lowest order. Because, as indicated in equation (3.15b), the flow is expanded about sonic conditions, at which  $z = 0$ , the distance between corners (edges) is independent of radius to lowest order. This distance is, of course, dependent upon the radius and so there is an error at any order of approximation when an expansion is employed. It can be shown that this error is not cumulative as one passes from one edge to the next. The same small error is made at each edge.

To the order desired, the perturbations to the incoming velocity may be written in terms of a velocity potential. In the channel, the lowest-order term is  $O(\epsilon)$ , with higher-order terms proceeding in powers of  $\epsilon^{1/2}$ . A coordinate system is chosen such that for a given blade  $x$  is measured along the helical line formed by those streamlines of the undisturbed relative flow which pass through the radius associated with the leading edge of the blade. A coordinate  $y$  is defined, locally perpendicular to  $x$ , which is constant along the surface formed by an infinitesimally thin blade at zero angle of attack; the blade shape is defined relative to this surface. Finally,  $z$  is defined in equation (3.15a) as being measured along a radius. Transformations of the governing equation to these variables results in a problem description quite similar to that for flow through a three-dimensional channel (refs. 14, 15) or a cascade (ref. 11).

In the channel,  $\phi_1 = \phi_1(x)$  and  $\phi_{3/2} = \phi_{3/2}(x)$ , with both  $y$  and  $z$  dependence being given in  $\phi_2(x, y, z)$ ; hence, in general, this follows the results found for the cascade. Also, outer far-field solutions ahead of the rotor have the form shown in equation (3.9) with the exception that  $\tilde{\phi}_2 = \tilde{\phi}_2(\tilde{x}, \tilde{y}, \tilde{z})$ . Indeed, the cascade solutions for  $\tilde{\phi}_{3/2}$  may be used. As  $\tilde{y} \rightarrow 0$ , for  $0 < x < d$

(notation in figure 2), the resulting relations for  $\tilde{\phi}_{3/2}$  and  $\tilde{\phi}_2$  are those found for  $y = O(1)$  and  $0 < x < d$ ;

i.e., they match. In addition, the terms  $\alpha_{5/2}$  and  $\alpha_2$  in the expansion for the angle of attack have similar forms. However, in the leading-edge region, the flow is three-dimensional to lowest order; in

equation (3.12),  $\hat{\phi}_2 = \hat{\phi}_2(\hat{x}, \hat{y}, \hat{z}; \epsilon)$ , so cascade solutions do not suffice. Because the governing

equation for  $\hat{\phi}_2$  is linear, the combination  $\hat{\phi}_2 = \hat{\phi}_{2c}(\hat{x}, \hat{y}; \epsilon) + \phi_2^*(\hat{x}, \hat{y}, \hat{z}; \epsilon)$  is employed, where  $\hat{\phi}_{2c}$  is the cascade solution with velocity components as shown in equation (3.13). This is convenient because the cascade solution matches with both the outer solution and the lowest-order channel solution, so the solution for  $\phi_2^*$ , which must be found numerically, is simpler. The governing equation for  $\phi_2^*$  is

$$\frac{z}{z_a} \phi_{2\hat{x}\hat{x}}^* + \phi_{2\hat{y}\hat{y}}^* + \frac{1}{\pi^2 B_o^2} \phi_2^* = - \left( \frac{z}{z_a} - 1 \right) \phi_{2c\hat{x}\hat{x}} \quad (3.17a)$$

$$B_o = \frac{R_t}{S M_{oa} R_{so}} \quad (3.17b)$$

$$z_a = \frac{z_t + z_h}{2} \quad (3.17c)$$

$$\hat{x} = \frac{\pi d_o}{\epsilon^{1/2} C} \left( \frac{x}{d} - 1 \right) \quad (3.17d)$$

$$C^2 = \frac{-2m z_a}{B_o^2} \quad (3.17e)$$

where the subscripts t and h refer to tip and hub conditions respectively and  $d_o$  is the lowest-order term in the expansion for  $d$ . Equation (3.17a) is a very simple form of equation for mixed flow. It can be shown that for  $z_a < 0$  (sonic conditions at  $z = 0$ ) the average Mach number is subsonic and for  $z_a > 0$  it is supersonic. Thus if  $z_a < 0$ , then for  $z < 0$  the flow is subsonic and equation (3.17a) is elliptic, whereas for  $z > 0$  the flow will be supersonic and equation (3.17a) is hyperbolic. Since  $z_t$  is the largest value of  $z$ , the problem considered depends upon the Mach number at the blade tip. In the numerical solutions mixed Dirichlet and Neumann boundary conditions are used with the normal derivatives all being zero and  $\phi = 0$  being the condition used as  $x \rightarrow -\infty$  for all  $y$ .

In the trailing-edge and downstream outer and far-field regions, expansions and methods of solution similar to those described for the leading edge are employed, with one additional feature. A vortex sheet starts at the trailing edge of each blade and extends downstream to infinity; in keeping with the fact that the solution found is for lightly loaded blades, these vortex sheets remain on planes  $y = \text{constant}$ . The pressure (and hence  $u_1$ ) and  $v_{3/2}$  are continuous across these sheets and so the jump  $\Delta\phi$  across each sheet is constant, independent of  $x$ . However  $\phi_z$  is not continuous across the sheet. It is this fact which differentiates the solution for three-dimensional flow from that for the cascade. In cascade flow  $\phi$  is discontinuous across surfaces extending downstream from the trailing edges, but only two-dimensional velocity components are desired and they are continuous. In the three-dimensional flow, there is a spanwise variation in circulation and hence in  $\Delta\phi$ , and  $\phi_z$  is discontinuous across the sheet. The net result is that a periodic discontinuous solution for  $\phi$  is introduced in the trailing-edge and outer and far-field regions.

Solutions in the various regions are used to form composite solutions. Typical results are shown in figure 3, in which lines of constant Mach number at a given radial position and pressure distributions on the suction side of a blade are shown for a typical case when the tip Mach number is subsonic. Details are found in references 12 and 13.

Solutions for the case where the tip Mach number is supersonic were attempted. The numerical solution of equation (3.17a) in the leading- and trailing-edge regions involves mixed hyperbolic (for  $z > 0$ ) and elliptic (for  $z < 0$ ) flow, with given solutions to which these inner solutions must match for all  $z$ . The problem does not appear to be improperly posed since it is mixed; however, convergence to a solution has not been obtained. When the downstream matching condition is removed in the

hyperbolic region, and additional conditions imposed upstream, little improvement is seen. To date, a solution to this problem has not been found.

An interesting result found from these studies is the aforementioned fact that far from the rotor, the flow is two-dimensional to lowest order, for both subsonic and supersonic tips. Thus, if the average Mach number of the undisturbed flow is supersonic, the two-dimensional wave equation holds, while if it is subsonic, the Laplace equation governs the flow. The flow in the leading-edge region is three-dimensional. Hence, it appears that shock waves, which originate at the leading edge of a blade for  $z > 0$  and reflect off the outer shroud to the sonic surface and back many times, eventually coalesce in such a way as to form a two-dimensional wave at the average Mach number of the undisturbed flow, if it is supersonic, and do not coalesce into any recognizable wave if the average Mach number is subsonic. Further work on this problem is needed.

## 4. UNSTEADY FLOWS

### "Low" Frequencies

For "low" reduced frequencies  $\tau^{-1} = O(\epsilon^2)$ , say  $\tau^{-1} = k\epsilon^2$ , the solution (3.3) for  $\phi_{1x}$  remains unchanged, a function only of  $x$ . If the channel walls oscillate with amplitude  $\alpha \ll \epsilon^3$ , or the fluctuations in exit pressure  $p_b$  are small in comparison with  $\epsilon^2$ , the term  $h_2$  in the solution (3.4) for  $\phi_2$  is still independent of  $t$ , and the first approximation  $x_{so}$  to the shock-wave position (2.9) likewise remains independent of  $t$ . But for  $\alpha = O(\epsilon^3)$ , or for changes  $O(\epsilon^2)$  in  $p_b$ ,  $h_2$  does depend on  $t$ , and equation (3.5) is replaced by (refs. 16,17)

$$h_{2x}(x,t) = (3 - 2\gamma) \phi_{1x}^2 / 6 + \{c_2(t) + G(x,t)\} / \{(\gamma+1) \phi_{1x}\} \quad (4.1)$$

where now

$$c_{2u}(t) = -G(0,t) \quad (4.2)$$

$$c_{2d}(t) = c_{2d}^{(s)} + G_d(t) - G(x_1,t) \quad (4.3)$$

Here  $x = x_1$  is the location of the channel exit;  $c_{2d}^{(s)}$  is the steady-state value of  $c_{2d}$ ; and  $G_d(t)$  is proportional to an unsteady term in the exit pressure, which in some examples is prescribed as a boundary condition. The first approximation  $x_{so}$  to the shock position (2.9) is now a function of time; i.e., the shock-wave displacement is now  $O(1)$ . Again an inner solution is needed just downstream of the shock wave to complete the description of the flow, but not for the calculation of  $c_{2d}$ . This solution is now written for  $x - x_{so}(t) = O(\epsilon^{1/2})$ , so that the coordinate  $X$  in equation (3.7) is measured relative to the instantaneous shock-wave position. The potential near the throat again has the form (3.8), but with  $x$  replaced by  $x + \epsilon G_x$ , again for  $f''(0) = -1$ . The shape of the sonic line is then found by setting  $\phi_{1x} = 0$ .

The Prandtl relation (2.4) leads to a nonlinear ordinary differential equation for  $x_{so}$ :

$$\frac{dx_{so}}{dt} = - \frac{1}{4ku_{1u}} \left\{ \frac{2}{3} \gamma (\gamma+1) u_{1u}^3 + N(t) \right\} \quad (4.4)$$

where  $N(t) = c_{2d}(t) - c_{2u}(t)$ . For a simple example, the channel walls are taken to have the parabolic

form  $f(x) = \{(\gamma+1) u_{1\infty}^2/2\} \{1 - (x/x_1)^2\}$  for  $-x_1 < x < x_1$ , with periodic forcing expressed by  $G(x_1, t) - G(0, t) - G_d(t) = \beta \sin t$ , where  $\beta = \text{constant}$ . Then  $\phi_{1x} = \pm |u_{1\infty} x/x_1|$  and

$$\frac{dx_{so}}{dt} + \frac{\gamma(\gamma+1) u_{1\infty}^2}{6 k x_1^2} \left( x_{so}^2 - \frac{x_{so}^{(s)^3}}{x_{so}} \right) = \frac{\beta x_1}{4 k |u_{1\infty}| x_{so}} \sin t \quad (4.5)$$

The shock-wave motions are identical for a case with stationary walls and oscillating back pressure such that  $G_d(t) = -\beta \sin t$  and for a case in which the back pressure is constant and the walls oscillate in pitch with  $G(x, t) = \beta(x/x_1) \sin t$ . (The notation again is slightly different from that of the original references.)

For this example the singular points of the differential equation (4.4) are saddle points and centers located periodically along the time axis (i.e., along  $x_{so} = 0$ ). The integral curves show two quite different types of behavior (ref. 16) depending on whether or not the integral curve from a saddle point later returns to  $x_{so} = 0$ ; in a dividing case, the integral curve joins successive saddle points. The different cases are sketched in figure 4. In case (a) the shock wave periodically disappears upstream, reappears at the throat, moves a limited distance downstream and then again accelerates upstream through the throat. In case (c) the motion approaches a specific periodic motion unless the shock wave is initially too close to the throat. The pattern changes from c) to b) to a) as the amplitude of oscillation increases, or as the frequency decreases, or as the back pressure increases (such that the steady-state shock position moves upstream).

The shock-wave position in a numerical example corresponding to case (a) of figure 2 is shown in figure 5. It is seen that the shock disappears upstream at a particular time  $t = t_*$ . The details of the motion through the throat and the upstream part of the channel can be studied in terms of suitable shorter time scales. In a time interval  $t - t_* = O(\epsilon)$  the shock-wave speed  $\tau^{-1} dx_s/dt$  has increased from  $O(\epsilon^2)$  to  $O(\epsilon^{3/2})$ , and an implicit solution can be derived for the shock position  $x_s = O(\epsilon^{1/2})$ . The time required for passage through this region is found to be  $O(\epsilon \ln \epsilon)$ . In the upstream part of the duct the shock speed is  $O(\epsilon)$ . Composite representations for  $dx_s/dt$  in terms of  $x_s$  were constructed in references 16 and 17. For the special case of parabolic walls, these results can be combined into a single expression for the shock-wave speed:

$$k \epsilon^2 \frac{dx_s}{dt} = -\frac{1}{6} \epsilon^2 \gamma(\gamma+1) u_{1\infty}^2 \frac{x_s^2}{x_1^2} + \frac{1}{4} \epsilon^{3/2} (\gamma+1) |u_{1\infty}| \left\{ \frac{x_s}{\epsilon^{1/2} x_1} - \left[ \frac{x_s^2}{\epsilon x_1^2} + \frac{2N(t_*)}{(\gamma+1) u_{1\infty}^2} \right]^{1/2} \right\} + \dots \quad (4.6)$$

For  $x_s = O(1)$  and positive, this result is correct to  $O(\epsilon^2)$  and is consistent with equation (4.4). Elsewhere, for small  $|x_s|$  and for  $x_s < 0$ , the first term on the right side is of higher order than the second term. For  $x_s = O(1)$  and negative, the largest part of the second term is proportional to  $x_s$ , and integration gives

$$\frac{x_s}{x_1} = - \frac{1}{|u_{1\infty}|} \left\{ \frac{N(t_*)}{2(\gamma+1)e} \right\}^{1/2} \exp \left\{ \frac{(\gamma+1)|u_{1\infty}|}{2kx_1} \frac{t-t_*}{\epsilon} - \frac{1}{2} \ln(1/\epsilon) \right\} \quad (4.7)$$

for the position of the shock wave as it moves upstream from the throat and then out of the channel at the time when  $x_s = -x_1$ . The integration constant has been chosen for proper matching with an implicit solution which can be obtained (ref. 17) for  $x_s = O(\epsilon^{1/2})$ .

In the periodic flow corresponding to case (c) of figure 4, the largest pressure changes,  $O(\epsilon)$ , occur at points which are sometimes ahead of and sometimes behind the shock wave. The phase of the resulting aerodynamic pitching moment depends strongly on the frequency parameter  $\tau\epsilon^2$ . This is of particular interest in the case of oscillating walls. For small  $\tau\epsilon^2$ , the time lag is small and the moment is nearly in phase with the angular displacement of the walls. For  $\tau\epsilon^2 = O(1)$ , there is another component in phase with the angular velocity of the walls, and for large  $\tau\epsilon^2$  this is the only component. If the amplitude  $\alpha$  of the wall oscillations is somewhat smaller, so that  $\alpha \ll \tau^{-1}\epsilon$ , the shock-wave equation (4.4) becomes linear and these phase changes can be shown analytically. An especially simple periodic solution is obtained when  $\tau\epsilon^2$  is large (i. e.,  $k$  is large) and  $\tau\alpha/\epsilon$  is small, again for parabolic walls and for  $G(x,t) = \beta (x/x_1) \sin t$ :

$$\frac{x_{so}}{x_{so}^{(s)}} = 1 - \frac{\beta x_1}{4k|u_{1\infty}|x_{so}^{(s)2}} \cos t \quad (4.8)$$

where the steady-state position  $x_{so}^{(s)}$  has been chosen as the mean position of the shock wave. The shock wave is furthest upstream, giving the largest high-pressure region behind the shock, at the time when the downstream walls have the largest outward velocity.

If the solution (4.8) were regarded as the response to a periodic wall oscillation which starts at time zero, the most obvious choice for an initial condition would be to set  $x_s = x_{so}^{(s)}$  at  $t = 0$ . This choice, however, would give a nonzero mean value for  $x_{so} - x_{so}^{(s)}$ . Consideration of higher-order terms show more complete differential equation would contain a small term proportional to  $x_s$ , and therefore a transient term in the solution with exponential decay that is slow in comparison with the reference time  $\tau$ . The solution to this initial-value problem thus has zero mean, as in equation (4.8). The same conclusion can be reached in a more systematic way by use of a two-time expansion.

Unsteady transonic flows in asymmetric channels, and in particular in channels with relatively large curvature, have also been studied (ref. 18). In this case, the wall shape is written as  $y_w = \pm 1 + \epsilon f_1(x) \pm \epsilon^2 f_2(x)$ . Thus, the equation for the channel centerline is  $y = \epsilon f_1(x)$  and  $\pm (1 + \epsilon^2 f_2(x))$  are terms which describe walls symmetric about the centerline. Hence  $\epsilon$  is a measure of the radius of curvature of the channel at the throat  $x = 0$ . The large curvature leads to flow structures and shock-wave shapes very different from those found in symmetric channel flows. Indeed, the shape of the shock wave is found as part of the solution for the inner region immediately downstream of the shock. Only oscillations in back pressure have been considered; details are given in reference 18.



## "Moderate" Frequencies

For "moderate" frequencies  $\tau^{-1} = O(\epsilon)$ , say  $\tau^{-1} = k\epsilon$ , the first time-dependent term in the velocity is  $O(\epsilon^2)$  if the fluctuations in exit pressure are  $O(\epsilon^2)$  or if the channel walls oscillate with amplitude  $\alpha = O(\epsilon^3)$ . In this case the function  $h_2(x, t)$  in equation (3.4) satisfies the first-order linear partial differential equation

$$2k h_{2xt} + (\gamma+1) (\phi_{1x} h_{2x})_x = (\gamma+1) (3-2\gamma) \phi_{1x}^3/6 + G_x \quad (4.9)$$

where  $\phi_{1x}$  is once more the known solution (3.3). The characteristics  $dx/dt = (\gamma+1)\phi_{1x}/(2k)$  correspond to disturbances traveling upstream relative to the flow, at speed  $u-a$ . In the subsonic region behind the shock wave the disturbances of course move upstream toward the shock, whereas in the supersonic region ahead of the shock the disturbances are carried downstream by the flow, also toward the shock wave. The differential equation (4.9) then states that  $2k$  times the rate of change of  $h_{2x}$  along the characteristics is equal to the right-hand side, and the solution can then be found by integration along characteristics. Some numerical results are given in reference 19.

For parabolic walls and simple harmonic wall oscillations, expressed for convenience in the exponential form  $G(x, t) = \beta (x/x_1) e^{it}$ , analytical solutions for  $h_{2x}$  are given by (ref. 17)

$$h_{2x} - \frac{1}{6} \left( \frac{u_{1\infty}}{x_1} \right)^2 \left\{ (3-2\gamma) x^2 - (\gamma+1) \right\} = \frac{\beta e^{i(t-\chi)}}{(\gamma+1) |u_{1\infty}| (1+v^2)^{1/2}} \quad x < x_{so} \quad (4.10)$$

$$= - \frac{c_{2d}^{(s)} x_1}{(\gamma+1) |u_{1\infty}| x} - \left\{ 1 - \frac{x_1}{x} \exp \left( i v \ln \frac{x}{x_1} \right) \right\} \frac{\beta e^{i(t+\chi)}}{(\gamma+1) |u_{1\infty}| (1+v^2)^{1/2}} \quad x > x_{so} \quad (4.11)$$

where  $v = \tan \chi = 2k(\gamma+1)^{-1} x_1/|u_{1\infty}|$ , and it has been assumed that  $h_{2x}$  approaches a constant value as  $x \rightarrow x_1$ . The Prandtl relation requires that a term  $4k(\gamma+1)^{-1} dx_{s1}/dt$  be included in the second of equations (3.6). It follows that

$$\frac{dx_{s1}}{dt} = \frac{\beta e^{it}}{4k |u_{1\infty}| (1+v^2)^{1/2}} \left\{ -2i \sin \chi + \frac{x_1}{x_{so}} \exp \left[ i \left( \chi - v \ln \frac{x_1}{x_{so}} \right) \right] \right\} \quad (4.12)$$

This result is used later for comparison with a numerical solution of the Euler equations.

If the amplitude of the wall oscillations is increased to  $\alpha = O(\epsilon^2)$ , or if the back-pressure fluctuations are  $O(\epsilon)$ , the time dependence appears in the first approximation  $\phi_1(x, t)$ . This case was first discussed in reference 8. Now  $u_1 = \phi_{1x}$  satisfies the quasilinear first-order equation

$$2k u_{1t} + (\gamma+1) u_1 u_{1x} = -f' + G_x \quad (4.13)$$

which has characteristics  $dx/dt = (\gamma+1)u_1/(2k)$ . Some progress toward an analytical solution can be made in the special case  $f(x) = \{(\gamma+1) u_{1\infty}^2/2\} \{1 - (x/x_1)^2\}$ ,  $G(x, t) = \beta (x/x_1) e^{it}$ . If  $s$  is measured along characteristics and  $r$  is constant along characteristics, with the choice  $s=t$  made for greatest convenience, the general solution is found to be

$$\frac{1}{x_1} x(r,s) = A(r) e^{(s-r)/v} + B(r) e^{-(s-r)/v} - \frac{\beta e^{is}}{(\gamma+1) u_{1\infty}^2 (1+v^2)} \quad (4.14)$$

$$\frac{1}{|u_{1\infty}|} u(r,s) = A(r) e^{(s-r)/v} - B(r) e^{-(s-r)/v} - \frac{i v \beta e^{is}}{(\gamma+1) u_{1\infty}^2 (1+v^2)} \quad (4.15)$$

Downstream of the shock wave the functions  $A(r)$  and  $B(r)$  can be determined if  $u$  is specified at the exit  $x = x_1$ , where one can define  $r$  by setting  $r = s$  at  $x = x_1$ . If  $u = O(x - x_*)$  as the sonic line  $x = x_*$  is

approached, then  $x \rightarrow -\infty$  as  $x \rightarrow x_*$  and so it is required that  $B(r) = 0$ ;  $A(r)$  can be determined by defining  $r$  to be continuous across the shock wave. The shock-wave position  $r = R(s)$  is then found from the Prandtl relation, which leads to

$$u_{1u} - u_{1d} = \frac{4k}{\gamma+1} \left. \frac{\partial x}{\partial r} \right|_{r=R} \frac{dR}{ds} \quad (4.16)$$

A rather messy first-order equation is thereby obtained for  $R(s)$ . In principle the behavior of the integral curves could be studied and numerical solutions obtained. For this particular limiting case, however, the value of an analytical formulation seems diminished when even an elementary example becomes so complicated.

The advantage of analytical solutions of course is the explicit representation of physical effects and their dependence on parameters for test cases having rather simple geometry. But the asymptotic solutions have to be compared with numerical solutions obtained from a set of equations which are in some sense more complete, and such numerical solutions are needed for parameter ranges which lie beyond the reach of the asymptotic solutions. Unsteady transonic cascade flows have been studied numerically using the linearized unsteady potential equation, the full unsteady potential equation, and the unsteady Euler equations (e.g., refs. 20 - 23, respectively).

The Euler solutions of references 22 and 23 were obtained for an unstaggered cascade, for parameter ranges such that a shock wave is present between successive blades, so that comparisons with the asymptotic solutions are possible. To carry out these calculations a finite-volume scheme was developed utilizing Van Leer's flux-vector splitting (ref. 24) for a moving H-mesh, with a smooth limiter to provide the desired monotonicity property. A periodicity condition was imposed ahead of and behind the cascade; an absorbing boundary condition (ref. 25) was used at the downstream computational boundary. The initial flow is described by a steady-state numerical solution, and periodic wall oscillations are introduced starting at time zero.

A comparison of numerical and analytical predictions of shock-wave motion is shown in figure 6 for parabolic blades having 2% thickness ratio, each oscillating  $180^\circ$  out of phase with the adjacent blades, at a reduced frequency  $\tau^{-1} = 0.1$  and with small amplitude  $0.1^\circ$ . It is reasonable to regard this frequency as  $O(\epsilon)$ , and so the comparison is made with the integral of equation (4.12). The predicted amplitudes of the shock-wave motion are about  $0.05 x_1$  and agree very closely, but there is a small discrepancy in phase. The ripples evident in the numerical solution appear to have been caused by the interpolation of the cell-averaged Mach number. Following a transient of the type discussed following equation (4.8), which in this case lasts for about one period, the mean shock-wave position becomes nearly the same as the initial steady-flow position. The agreement deteriorates with increasing amplitude, and is also found to be poor (ref. 22) for a 5% blade with  $0.25^\circ$  amplitude, which corresponds to a smaller (numerical) shock-wave amplitude of about  $0.03 x_1$ . A partial

analytical solution for higher-order terms shows clearly that this loss of accuracy with increasing thickness should be expected. Euler solutions for a nozzle with fluctuating back pressure were also obtained in reference 26. In one comparison the calculated shock-wave position agreed closely with that predicted for the same case using the asymptotic formulation of reference 16.

For a higher frequency  $\tau^{-1} = 0.5$ , numerical solutions for the centerline pressure and velocity are plotted against  $x$  in figures 7 and 8, for 5% blades with oscillation amplitude  $2.5^\circ$ . Since the wavelength of disturbances carried downstream is no longer large, and since the pressure perturbations obviously are not of the same order as the velocity perturbations, this frequency must be regarded as  $O(1)$ . The pressure distribution near  $x = x_1$  calls into question the assumption that the channel solution for the pressure should approach a constant value at  $x = x_1$ . It may be that the inner solution (as yet unknown) for  $x - x_1 = O(\epsilon^{1/2})$  allows adjustment of the pressure to its constant value further downstream. The importance of using an absorbing condition at the downstream boundary of a relatively small computational domain is shown for the same case in figure 9. As would be expected, the effect of the downstream boundary condition on the shock-wave motion is seen to become important at the time when a reflected disturbance first reaches the shock wave. A transient again is evident, here lasting for about five periods. Analytical considerations show that a first approximation for the duration of this transient does not depend on frequency; for increased frequency, however, a constant time interval of course corresponds to a larger number of periods.

### Supersonic Flow

Solutions for supersonic flow are included here because when applied to flows with Mach numbers in the transonic range, they provide a comparison which allows evaluation of the assumptions typically made in deriving solutions for transonic flow problems. Thus, whereas in transonic channel flow only one family of characteristics may be used because  $u + a \gg u - a$ , in supersonic flow both families are employed. In addition, the jump in velocity across the wave is  $O(1)$  rather than being  $O(\epsilon)$  as in transonic channel flow. Finally, the jump in entropy  $\Delta s$  across a shock wave is not negligible even at lowest order when the flow is supersonic.

The unsteady flow field in a two-dimensional supercritical supersonic diffuser has been studied recently (refs. 27, 28). The formulation of the problem is similar to those channel-flow problems already discussed, but differs in some important respects. For example, if the ratio of the half height of the inlet lip to the length of the diffuser is defined as  $\epsilon^{1/2}$ , then expansions of  $u$  and the thermodynamic variables proceed in integer powers of  $\epsilon$ . The expansion for  $v$  is in odd powers of  $\epsilon^{1/2}$ . For  $\epsilon \ll 1$ , then, the channel is very long compared to its width. This results in a great mathematical simplification; for example, the lowest-order perturbation in  $u$  is independent of  $y$ . However, since the length-to-width ratio is  $O(\epsilon^{-1/2})$ , then for  $\epsilon = 0.1$ , say, this ratio is roughly 3 so that problems of technical interest can be considered in numerical examples. A similar formulation of this problem is considered in reference 29 for steady flow; the one described here appears to be more convenient for unsteady flows.

The relation which replaces equation (2.5) for the wall shape is, for symmetric walls,

$$y_w = \pm [1 + \epsilon (f(x) + g(x,t))] \quad (4.17)$$

Thus, the change in area is  $O(\epsilon)$  rather than  $O(\epsilon^2)$  as in fully transonic flows. The corresponding expansion for the dimensionless (here with respect to the undisturbed velocity) velocity component  $u$  is

$$u = u_r + \varepsilon u_1(x, t) + \varepsilon^2 u_2(x, y, t) + \dots \quad (4.18)$$

with similar expansions for the pressure, density, temperature, etc. The  $v$  velocity component is written as

$$v = \varepsilon^{3/2} v_{3/2}(x, y, t) + \varepsilon^{5/2} v_{5/2}(x, y, t) + \dots \quad (4.19)$$

Equation (4.18) illustrates one of the significant differences between the transonic and supersonic flow formulations in that  $u_r$  is a constant reference velocity with different values  $u_{ru}$  upstream and  $u_{rd}$  downstream of the shock wave. Here  $u_{ru}$  is the velocity of the undisturbed flow entering the diffuser and  $u_{rd}$  is the flow velocity immediately downstream of a shock wave into which the entering velocity is  $u_{ru}$ . Thus, in the limit  $\varepsilon \rightarrow 0$  a uniform stream at  $u_{ru}$  enters a shock wave and emerges at  $u_{rd}$ , so that the jump in velocity across the wave  $(u_{rd} - u_{ru}) = O(1)$ . For nonzero  $\varepsilon$ , then, the flow velocity is expanded about  $u_{ru}$  upstream of the shock wave and about  $u_{rd}$  downstream of the shock wave; these relations are joined by the jump conditions which hold across the shock wave. Two different unsteady flow problems are considered in references 27 and 28, one for  $\tau = O(1)$  and the other for  $\tau = O(\varepsilon^{-1})$ , where  $\tau$  is defined as in earlier sections except that the undisturbed flow velocity is employed rather than  $a^*$ . Solutions are found for unsteady flow resulting from impressed oscillations in the back pressure and from oscillations in the wall shape downstream of the shock wave. The latter case allows consideration of separated flows downstream of the shock wave if the distribution of displacement thickness associated with the separated flow, represented by  $g(x, t)$  in equation (4.17), can be obtained. Asymptotic methods do not suffice for such a computation, but numerical solutions of the Navier-Stokes equations for flows with forced back-pressure oscillations are available (ref. 30), from which distributions of displacement thickness over  $x$  can be found as a function of the relative Mach number of the flow entering the wave; these are used in references 27 and 28.

The expansion for the shock-wave position  $x_s$  is

$$x = x_{s0}(t) + \varepsilon x_{s1}(t) + \varepsilon^2 x_{s2}(y, t) + \dots \quad (4.20)$$

For  $\tau = O(1)$ , the flow is truly unsteady and  $x_{s0} = \text{constant}$  so the first time-dependent term is  $x_{s1}$ ; the term truly unsteady is used to indicate the fact that the lag times associated with the propagation of signals from the walls or exit plane are very important. From equation (4.20), it is seen that for  $x_{s0} = \text{constant}$ , small oscillations in shock-wave position occur for oscillations in back pressure or wall shape (eq. (4.17)) of order  $\varepsilon$ . For the case  $\tau = O(\varepsilon^{-1})$ , the flow is quasi-steady; that is, signals from the exit plane or the walls propagate infinitely fast compared to the period of oscillations of the back pressure or wall; the flow is composed of a series of steady-state flows, each with different boundary conditions. For this case it is found that  $x_{s0} = x_{s0}(t)$  so that shock-wave motion with amplitude  $O(1)$  takes place for oscillations with amplitude  $O(\varepsilon)$  in back pressure and wall shapes.

The equations found for the instantaneous position of the shock wave are, for each case,

$$\frac{dx_{s1}}{dt} = \tau [1 + u_{rd} - 2(\gamma - 1)/(\gamma + 1)]^{-1} \tilde{u}_1(x_{s0}^s, t) \quad \tau = O(1) \quad (4.21a)$$

$$\begin{aligned} \frac{dx_{so}}{dt} = & -\epsilon\tau \frac{\gamma+1}{4} \left\{ \left[ \frac{u_{rd}}{M_{rd}^2 - 1} + \frac{1 - M_{\infty}^2 (1 - u_{rd})}{M_{\infty}^2 - 1} \right] [f(x_{so}) - f(x_{so}^s)] \right. \\ & \left. + g(x_{so}, 0) - g(x_{so}^s, 0) \right\} + \frac{a_{rd}^2}{\gamma u_{rd}} \frac{\tilde{p}_{lb}(t)}{p_{rd}} + \frac{u_{rd}}{(1 - M_{rd}^2)} \tilde{g}(1, t) \} \quad \tau = O(\epsilon^{-1}) \quad (4.21b) \end{aligned}$$

where  $x_{so}^s$  represents the steady-state value of  $x_{so}$ ; i.e., it is assumed that unsteady oscillations are

imposed upon a flow initially at steady-state conditions. Also,  $\tilde{u}_1$ ,  $\tilde{g}$ , and  $\tilde{P}_1$  represent the differences between the quantity and its steady-state value at the same location. The subscript b on  $P_1$  indicates that this is the exit or back pressure imposed upon the flow. It may be noted that equation (4.21a)), for the case  $\tau = O(1)$ , is linear, as expected for the case where oscillations are small. For this same reason,  $u_1$  is evaluated at the lowest-order shock-wave position,  $x_{so}$ . Because the flow is truly unsteady, the equation for  $u_1$  is complicated by the inclusion of several lag times and is not repeated here; details are given in references 27 and 28.

Equation (4.21b), which holds for  $\tau = O(\epsilon^{-1})$ , is a nonlinear equation, reflecting the large-amplitude shock-wave displacement associated with  $\tau \gg 1$ . Since the flow is quasi-steady, there are no time lags in the equation; e.g., a disturbance in back pressure at time  $t_0$  is felt by the shock wave at  $t_0$ , indicating an infinite propagation speed of disturbances based on a time scaled by the period of the impressed back pressure or wall oscillations. Another difference, not apparent in equation (4.21a) and (4.21b) because a detailed expression for  $u_1$  in equation (4.21a) is not provided, is that in equation (4.21b) the shock location depends only upon the local cross-sectional areas at the shock wave and at the exit, whereas in  $u_1$ , and thus for  $x_{s1}$  in equation (4.21a), the detailed distribution of area is important. Finally, the nonlinear terms in equation (4.21b) provide a restoring condition such that shock-wave motion continues after all imposed oscillations are removed, until equilibrium is reached. This means that another lag time is introduced into the problem.

Although it is easy to differentiate asymptotically between solutions for  $\tau = O(1)$  and those for  $\tau = O(\epsilon^{-1})$ , it is not at all a simple matter to decide which should be used for a given set of physical parameters. Hence, a unified equation for shock-wave position is presented in references 27 and 28; it reproduces either equation (4.21a) or (4.21b) in the proper limit process and allows a relatively large range of physically interesting problems to be considered. Comparisons of results with completely numerical solutions (ref. 28) show that integrals of the unified differential equation reproduce numerical solutions with good accuracy.

Typical results for stationary walls but impressed oscillations in back pressure are shown in figure 10. It is seen that for the conditions chosen, the average position of the shock wave moves upstream until the shock wave is actually moving upstream of the throat of the diffuser. Finally, the decrease of the back pressure is no longer strong enough to pull the shock wave back and it is disgorged from the diffuser; i.e., an engine "unstart" occurs. For a given initial position and stable oscillation of the shock wave, it is found that such unstarts can arise if the amplitude of the impressed pressure oscillations is increased or the frequency is decreased.

Finally, using the aforementioned distributions of displacement thickness, it is possible to show self-sustained oscillations using the unified solution. That is, a quarter-cycle of oscillations of the back pressure is used to start the shock wave in motion, after which the back pressure is held constant. Under some conditions, continuing self-sustained oscillations occur. This phenomenon has

been found experimentally (e.g., ref. 31) in flows in which separation occurs downstream of the shock wave. In references 27 and 28, a model is proposed which relates the motion of the shock wave to the change in core-flow area (external to the displacement thickness) as the shock motion causes the size of the separation bubble and thus the displacement thickness to vary in magnitude. Briefly, if the core-flow area at the diffuser exit increases or decreases, with back pressure held constant, the shock wave must move downstream or upstream, respectively. Thus, as found experimentally, flow separation is a necessary prerequisite to self-sustained oscillations. Since a certain minimum shock Mach number ( $M_s \approx 1.3$ ) must occur before the flow is separated by the shock wave, two modes are considered: mode one, in which the shock Mach number exceeds this limiting value at all times, and mode two, in which the limiting value is exceeded during only part of the cycle. In mode two, as soon as the shock Mach number decreases below the limiting value for separation, the separated-flow region is convected downstream and is rejoined with a post-shock separated region only after the shock Mach number again exceeds the minimum value for separation.

A typical result is shown in figure 11. Here, conditions are such that self-sustained oscillations do occur in mode two; both the instantaneous shock position and position of the leading edge of the separated region are shown. It is shown that the self-sustained oscillations choose their own period, independent of the period of the initiating oscillations in back pressure. An obvious conclusion from the studies is that such oscillations can be decreased or removed by removing the boundary layer downstream of the shock wave.

### Shock-Wave Structure

Although the solutions discussed here are for inviscid flow in the main, it is instructive to consider flows at Reynolds numbers such that the longitudinal viscosity is important in some regions of the flow where shock waves form. This occurs at moderate Reynolds numbers such that to the desired order of approximation, the boundary layer is negligibly thin, but the Mach number is close enough to unity that the shock-wave thickness is not. A similar flow picture is seen in numerical simulations of transonic flow fields involving shock-capturing techniques when truncation errors and artificial viscosity cause a smearing of the waves; the structure of the shock-wave closely parallels that found in flows at moderate Reynolds numbers.

When the shock wave is outside the throat region, the formulation of the problem is similar to that employed for inviscid flow, but an extra shock-wave structure region must be considered (ref. 32). Thus, there is an inner shock-adjustment region in which the correction (3.7) is again found. Solutions for  $v$  are the same as those found for inviscid flow, to the desired order as is the first-order solution for  $u$ . It is only in higher-order terms in  $u$ , of order  $\epsilon^2$  and  $\epsilon^3$ , that viscous corrections arise. A composite solution including equation (3.7) and the viscous-flow corrections may then be constructed, to be used as the outer solution to which solutions in the thin ( $O(\epsilon)$ ) inner shock-structure regions must match. As expected, the lowest-order solution in the shock-structure region is Taylor's solution for the structure of a weak shock wave. Relations for the velocity components, consisting of this and higher-order terms, are matched with the outer composite solutions to provide the terms in the equation for the location of the sonic line within the shock wave to first-order accuracy. When this equation is compared with the corresponding equation for the location of an infinitesimally thin shock wave in an inviscid flow under the same conditions, it is found that they are the same. Thus, as the longitudinal Reynolds number becomes very large, the shock wave becomes very thin until it becomes a discontinuity at the sonic line, which has not moved as the Reynolds number is changed; that is, the terms in the equation for its location are independent of Reynolds number. Moreover, as shown in reference 32, the velocity distribution within a shock wave at moderate Reynolds number is very close to that found in numerical computations when artificial viscosity and/or truncation errors cause a thickening or smearing of the wave. Hence, the practice of locating the shock wave at the sonic surface in numerical computations appears to be well justified.

In those cases where a shock wave forms in the thin regions enclosing a sonic throat, the methods employed in reference 32 cannot be used; indeed the nonlinear viscous-transonic equation for unsteady flow holds in this region (ref. 4). Since the flow is irrotational to the order considered, the first-order governing equation for unsteady flow can be written in terms of the velocity perturbation in the flow direction  $u_1$  as follows:

$$k_s u_{1\bar{x}\bar{x}\bar{x}} - (u_{1\bar{x}})^2 - u_1 u_{1\bar{x}\bar{x}} + u_{1yy} - 2k u_{1\bar{x}t} = 0 \quad (4.22a)$$

$$k_s = \frac{1}{\text{Re}(\epsilon(\gamma+1))^{3/2}} \left[ 1 + \frac{\gamma-1}{\text{Pr}} \right] \quad (4.22b)$$

$$u = 1 + \epsilon u_1 + \dots \quad (4.22c)$$

where the Reynolds number  $\text{Re}$  is based upon the longitudinal viscosity (as is the Prandtl number  $\text{Pr}$ ), the critical sonic speed, and the channel half-width at the throat. Equation (4.22a) is written for quasi-steady flow in the thin inner throat region with  $\tau$  and the stretched independent variable  $\bar{x}$  defined as

$$\tau = k^{-1} \{(\gamma+1)\epsilon\}^{-1/2} \quad (4.23a)$$

$$x = ((\gamma+1)\epsilon)^{1/2} \bar{x} \quad (4.23b)$$

A similarity transformation in terms of an arbitrary function of time

$$s = \bar{x} + b y^2 + \beta(t) \quad (4.24a)$$

$$u_1 = z(s) + 4 b^2 y^2 - 2k\beta' \quad (4.24b)$$

allows equation (4.22a) to be written as a second-order differential equation in  $z$

$$k_s z'' - z z' + 2b z + 8 b^2 s = 0 \quad (4.25)$$

Equations (4.24) and (4.25) comprise the aforementioned extension (ref. 5) of the Tomotika and Tamada (ref. 1) transformation for steady flow, and in this case applied to unsteady viscous transonic flows. When  $k_s \equiv 0$ , the flow is inviscid up to and downstream of a shock wave in the flow; solutions to equation (4.25) include the jump conditions across the wave. For  $k_s = O(1)$ , thick shock waves occur and solutions to equation (4.25) must be found numerically. For  $k_s \ll 1$ , the problem is a classical singular-perturbation problem and an inner region enclosing the shock wave is required; again the lowest-order solution is the Taylor weak-shock solution. An example solution is shown in figure 12 for an unsteady decelerating flow for  $\epsilon = 0.1$ ,  $\beta = e^{-2t/4}$  and  $k_s = 0.01$  at  $t = 0.35$  (steady flow at  $t \rightarrow \infty$ ). The isotachs clearly show the location and structure of the shock wave. Details of the calculation and example flow pictures for  $k_s = O(1)$  and  $k_s \equiv 0$  are given in reference 4; the results are also applicable to steady flow, of course.

## CONCLUDING REMARKS

The number of examples considered supports the assertion in the introduction that internal transonic flows are most amenable to solution by means of systematic asymptotic techniques. Both steady and unsteady two-dimensional flows are included and even some three-dimensional flows,

although in one case numerical computations are required for inner regions. The flows considered have been inviscid, in the main. However, as indicated in the one example of supersonic diffuser flow, and as shown in reference 33 in the calculation for a transonic channel flow, the inclusion of a boundary layer is relatively simple, since solutions are written in terms of arbitrary wall shapes. Although the range of parameters is limited to the transonic or near-transonic regime, it is worth noting that it is quite difficult to locate shock waves for Mach numbers near one, using numerical techniques. In this regard, some of the results presented here have proven quite useful as baseline solutions for transonic flow codes. It appears that they would be useful also in formulating numerical codes for internal flows, because the various (inner) regions where important physical effects interact are located and their length scales are given.

## REFERENCES

1. Tomotika, A., and Tamada, K.: Studies on two-dimensional transonic flows of compressible fluid, Part 1. Quarterly of Applied Mathematics, vol. 7, 1950, pp. 381-397.
2. Sichel, M.: The effect of longitudinal viscosity on the flow at a nozzle throat. Journal of Fluid Mechanics, vol. 25, 1966, pp. 769-786.
3. Ryzhov, O.S.: Zh. Vychisl. Mat. Mat. Fiz., vol. 8, 1968, pp. 472-479. English translation: Some properties of transonic flows of a real gas. Journal of Computational Mathematics and Mathematical Physics, vol. 8, 1968, pp. 330-342.
4. Adamson, T. C., Jr., and Richey, G. K.: Unsteady transonic flows with shock waves in two-dimensional channels. Journal of Fluid Mechanics, vol. 60, 1973, pp. 363-382.
5. Adamson, T. C., Jr.: Unsteady transonic flows in two-dimensional channels. Journal of Fluid Mechanics, vol. 52, 1972, pp. 437-449.
6. Szaniawski, A.: Transonic approximations to the flow through a nozzle. Archiwum Mechaniki Stosowanej, vol. 17, 1965, pp. 79-85.
7. Kopystynski, J., and Szaniawski, A.: Structure of flow in a nozzle throat. Archiwum Mechaniki Stosowanej, vol. 17, 1965, pp. 453-466.
8. Adamson, T. C., Jr., Messiter, A. F., and Richey, G. K.: On the matching of solutions for unsteady transonic nozzle flows. Archiwum Mechaniki Stosowanej, vol. 26, 1974, pp. 617-628.
9. Messiter, A. F., and Adamson, T. C., Jr.: On the flow near a weak shock wave downstream of a nozzle throat. Journal of Fluid Mechanics, vol. 69, 1975, pp. 97-108.
10. Messiter, A. F., and Adamson, T. C., Jr.: Asymptotic solutions for nonsteady transonic channel flows. Symposium Transsonicum II, K. Oswatitsch & D. Rues, eds., Springer, 1976, pp. 41-48.
11. Messiter, A.F., and Adamson, T.C., Jr.: Transonic small-disturbance theory for lightly loaded cascades. AIAA Journal, vol. 19, 1981, pp. 1047-1054.
12. Kamath, H.: An analysis of the transonic flow through a lightly loaded compressor rotor. Ph.D. Thesis, The University of Michigan, 1988.



13. Kamath, H., and Adamson, T.C., Jr.: Transonic flow through a lightly loaded compressor rotor. To be submitted, 1988.
14. Adamson, T. C., Jr.: Three-dimensional transonic shear flow in a channel. *Transonic Flow Problems in Turbomachinery*, T. C. Adamson, Jr. and M. F. Platzer, eds., Hemisphere, 1978, pp. 70-78.
15. Adamson, T. C., Jr., and Sichel, M.: Transonic shear flow in a three-dimensional channel. *Journal of Fluid Mechanics*, vol. 123, 1982, pp. 443-457.
16. Adamson, T. C., Jr., Messiter, A. F., and Liou, M.-S.: Large-amplitude shock-wave motion in two-dimensional transonic channel flows. *AIAA Journal*, vol. 16, 1978, pp. 1240-1247.
17. Messiter, A. F., and Adamson, T. C., Jr.: Forced oscillations of transonic channel and inlet flows with shock waves. *AIAA Journal*, Vol. 22, 1984, pp. 1590-1599.
18. Chan, J. S.-K., and Adamson, T. C., Jr.: Unsteady transonic flows with shock waves in an asymmetric channel. *AIAA Journal*, Vol. 16, 1978, pp. 377-384.
19. Richey, G. K., and Adamson, T. C., Jr.: Analysis of unsteady transonic flow with shock waves. *AIAA Journal*, Vol. 14, 1976, pp. 1054-1061.
20. Verdon, J. M., and Caspar, J. R.: A linearized unsteady aerodynamic analysis for transonic cascades. *Journal of Fluid Mechanics*, vol. 149, 1984, pp. 403-429.
21. Shankar, V., Ide, H., and Goebel, T.: Unsteady full potential computations for complex configurations. *AIAA Paper 87-0110*, 1987.
22. Li, C.-C.: Unsteady transonic cascade flows. Ph.D. Thesis, The University of Michigan, 1988.
23. Li, C.-C., Messiter, A. F., and Van Leer, B.: Unsteady transonic cascade flow with in-passage shock wave. Note submitted to *AIAA Journal*, 1988.
24. Van Leer, B.: Flux-vector splitting for the Euler equations. *Lecture Notes in Physics*, vol. 170, 1982, pp. 507-512.
25. Hedstrom, G. W.: Nonreflecting boundary conditions for nonlinear hyperbolic systems, *Journal of Computational Physics*. vol. 30, 1979, pp. 222-237.
26. Bolcs, A., Fransson, T.H., and Platzer, M.F.: Numerical simulation of inviscid transonic flow through nozzles with fluctuating back pressure. *American Society of Mechanical Engineers GT Paper*, 1988.
27. Biedron, R.T.: Unsteady flow in a supercritical supersonic inlet. Ph.D. Thesis, The University of Michigan, 1988.
28. Biedron, R. T., and Adamson, T. C., Jr.: Unsteady flow in a supercritical supersonic diffuser. *AIAA Paper 87-0162*, 1987, to appear in *AIAA Journal*.
29. Lin, C. Q., and Shen, S. F.: Inviscid compressible flow with shock in two-dimensional slender nozzles. *Journal of Fluid Mechanics*, vol. 157, 1985, pp. 265-287.
30. Liou, M.-S.: Private communication, 1987.

31. Sajben, M., Bogar, T.J., and Kroutil, J.C.: Forced Oscillation experiments in supercritical diffuser flows. AIAA Journal, vol. 22, 1984, pp. 465-470.
32. Mace, J., and Adamson, T. C., Jr.: Shock waves in transonic channel flows at moderate Reynolds numbers. AIAA Journal, vol. 24, 1986, pp. 591-598.
33. Liou, M.-S., and Sajben, M.: Analysis of unsteady viscous transonic flow with a shock wave in a two-dimensional channel. AIAA Paper 80-1095, 1980.

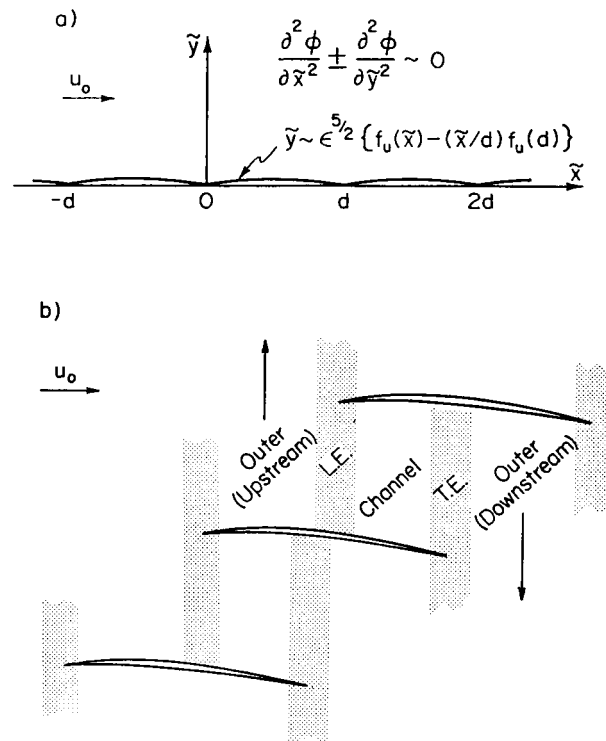


Figure 1. Asymptotic description of cascade flow. a) Approximate flow problem at large distances. b) Outer, edge, and channel flow regions.

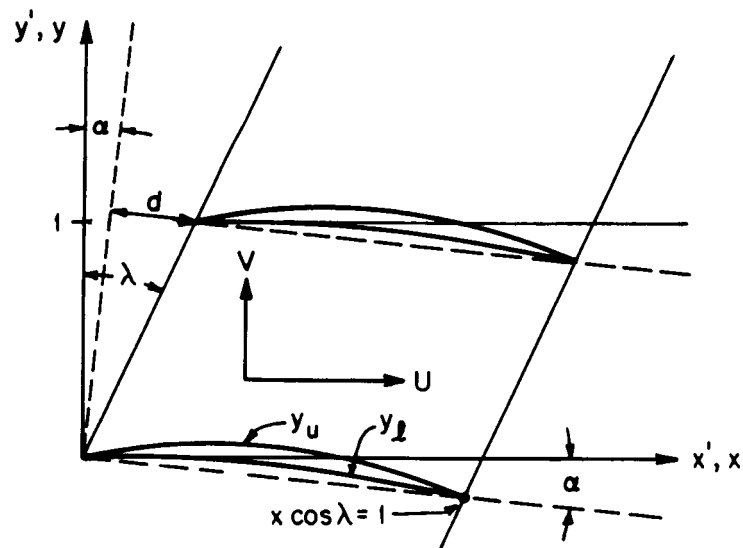


Figure 2. Sketch of two adjoining airfoils at an arbitrary radius, showing the stagger angle  $\lambda$ , the angle of attack  $\alpha$ , and the notation used.

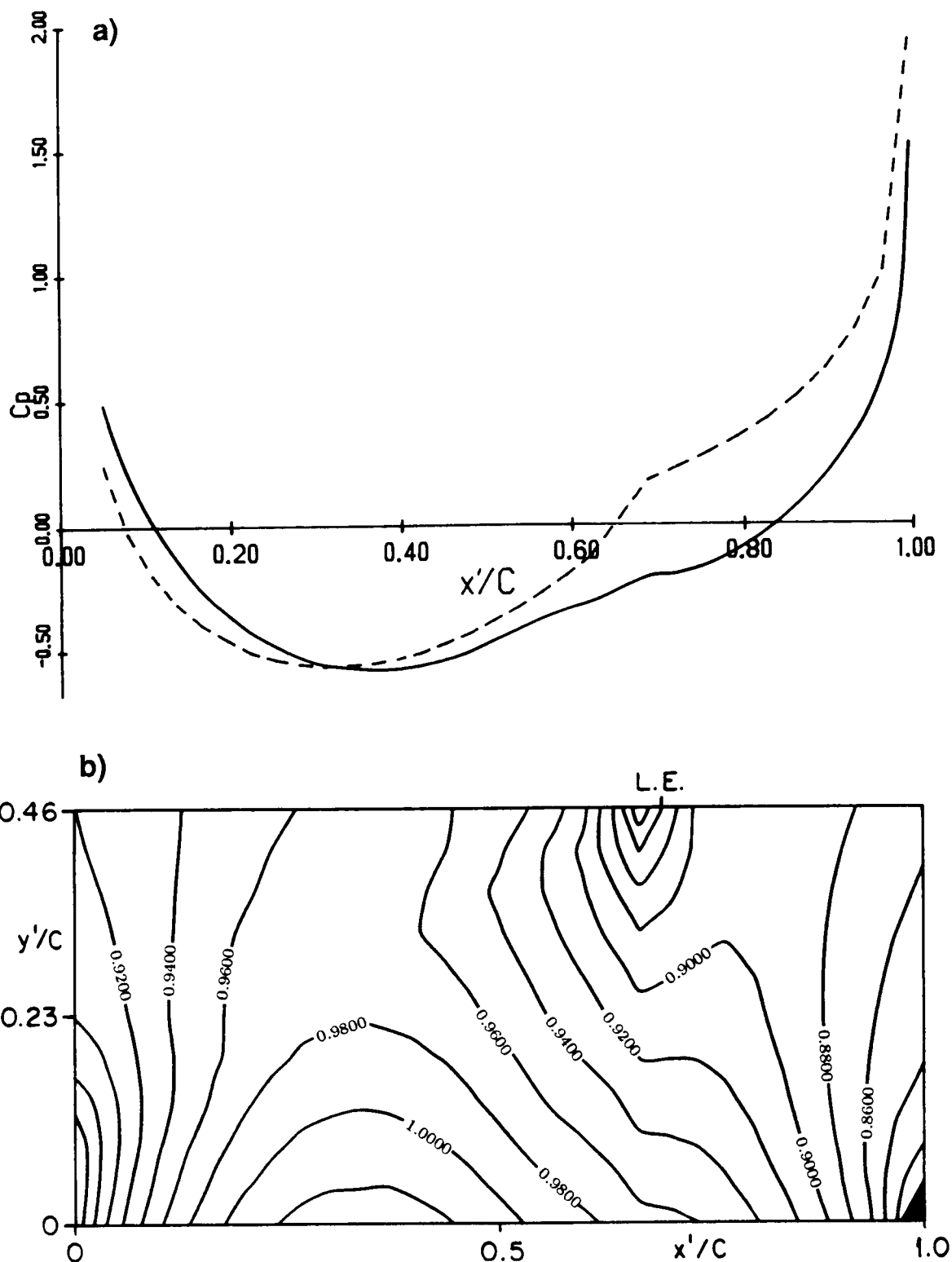


Figure 3. Calculated a) pressure distribution on the suction surface and b) lines of constant Mach number at a radial position near the tip for a compressor rotor with cambered circular-arc airfoils;  $t/c = 0.035$ , max. camber  $= 1/4 (t/c)$ , axial Mach no.  $= 0.52$ , relative tip Mach no.  $= 0.95$ ; 31 blades;  $c_a = \delta = 0.105$ ,  $s = 1.527$ ,  $\alpha = 1.13^\circ$ ,  $\lambda_{tip} = 56.68^\circ$ . Dashed lines in (a) show first-order solutions only.

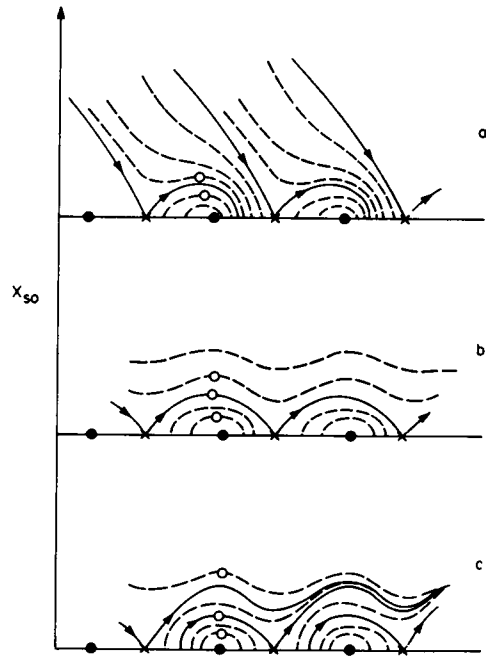


Figure 4. Sketch of possible configurations for integral curves through saddle points (—); other integral curves (----); • center; x saddle point. a) Integral curves leaving x reach time axis before next x; b) Integral curves leaving x reach time axis at next x; c) Integral curves leaving x never return to time axis. Details in reference 17.

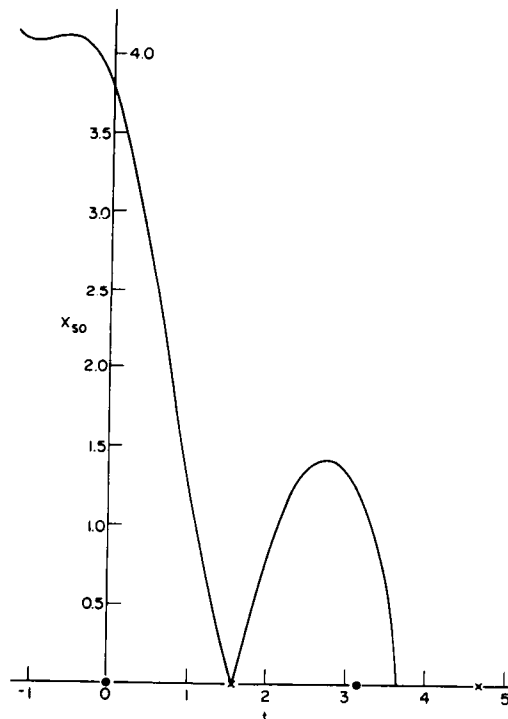


Figure 5. Calculated curve through the saddle point illustrating the case sketched in figure 4a, for  $c_{2d} = 0$ ,  $G = 4 \sin 2t$ ,  $\gamma = 1.4$ ,  $\tau = 100$ ,  $\epsilon = 0.10$ . Solution found by numerical integration of equation for  $x_{so}$ . Details in reference 17.

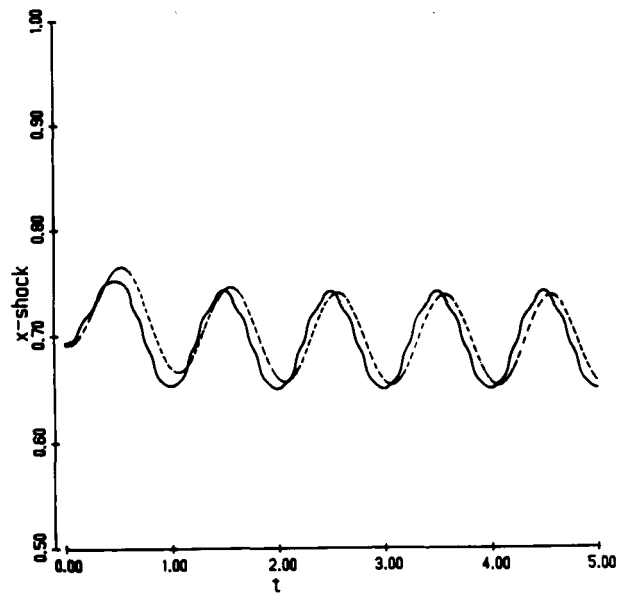


Figure 6. Numerical (—) and asymptotic (----) shock-wave displacement for unstaggered cascade with blade thickness ratio 2%, reduced frequency 0.1, and oscillation amplitude  $0.1^\circ$ .

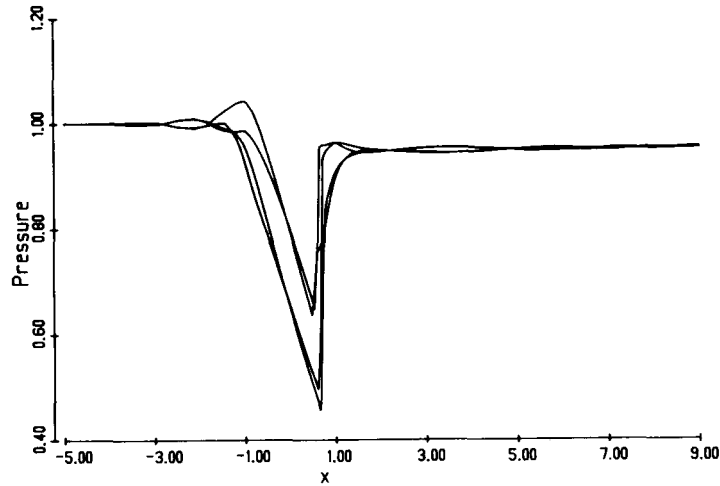


Figure 7. Calculated centerline pressure at times one-quarter period apart, for unstaggered cascade with blade thickness ratio 5%, reduced frequency 0.5, and oscillation amplitude  $0.25^\circ$ .

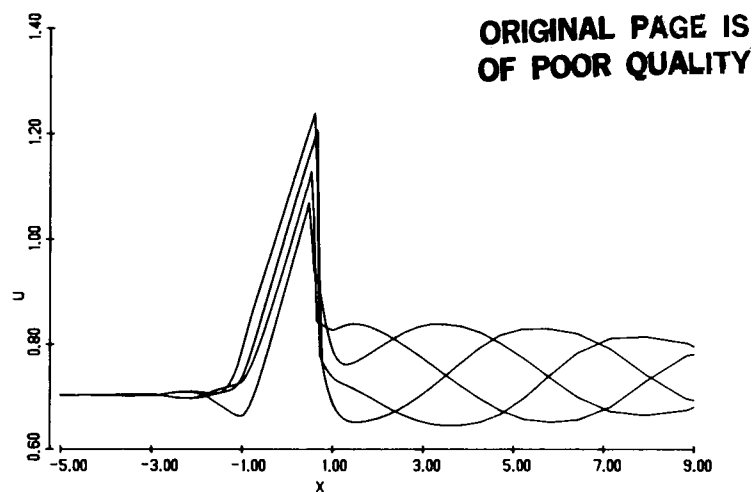


Figure 8. Calculated centerline velocity at times one-quarter period apart, for unstaggered cascade with blade thickness ratio 5%, reduced frequency 0.5, and oscillation amplitude  $0.25^\circ$ .

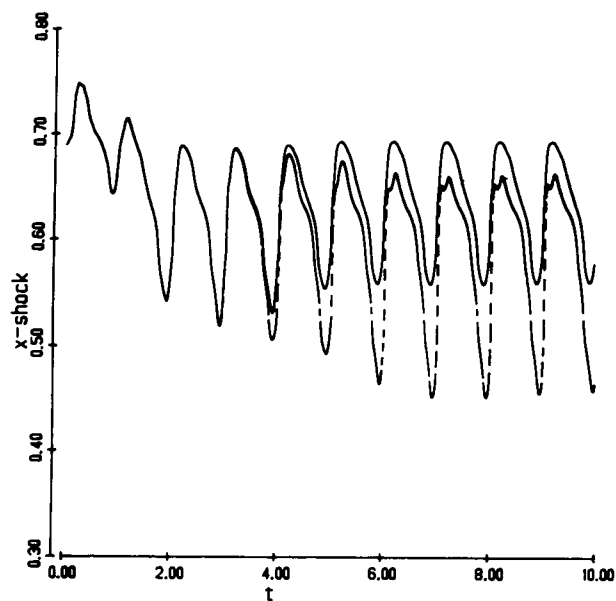


Figure 9. Effect of absorbing (—) and reflecting (---) downstream boundary conditions on shock-wave motion for unstaggered cascade with blade thickness ratio 5%, reduced frequency 0.5, and oscillation amplitude  $0.25^\circ$ .

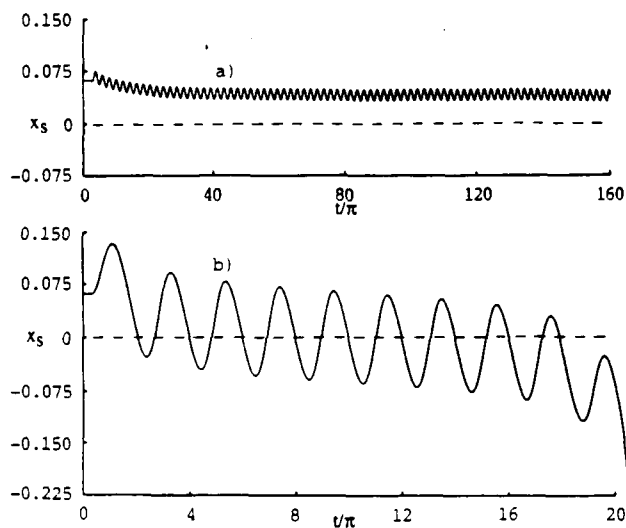


Figure 10. Effect of frequency of back-pressure oscillations on shock-wave response. Dashed line denotes diffuser throat;  $h = 1$  ft.,  $L = 12.65$  ft.,  $x_s^s = 0.062$ ,  $u_\infty = 1400$  ft./sec.,  $M_\infty = 1.50$ ,  $\epsilon = 0.00625$ ,  $\Delta p_b/p_o = -0.03 \sin 2\pi f_t t$ ; a)  $f_t = 80$  Hz,  $\tau = 0.22$ ; b)  $f_t = 10$  Hz,  $\tau = 1.76$ . Details in reference 29.

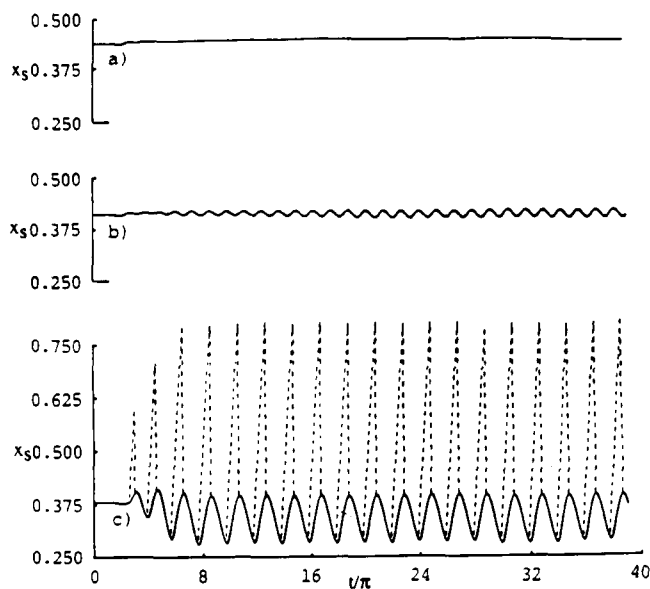


Figure 11. Effect of initial shock-wave position on self-sustained oscillations. a)  $x_s^s = 0.442$ ; b)  $x_s^s = 0.415$ ; c)  $x_s^s = 0.379$ . In curve c) dashed line indicates location of separation point (Mode 2). Throat is at 0.30. Details in reference 29.

ORIGINAL PAGE IS  
OF POOR QUALITY



ORIGINAL PAGE IS  
OF POOR QUALITY

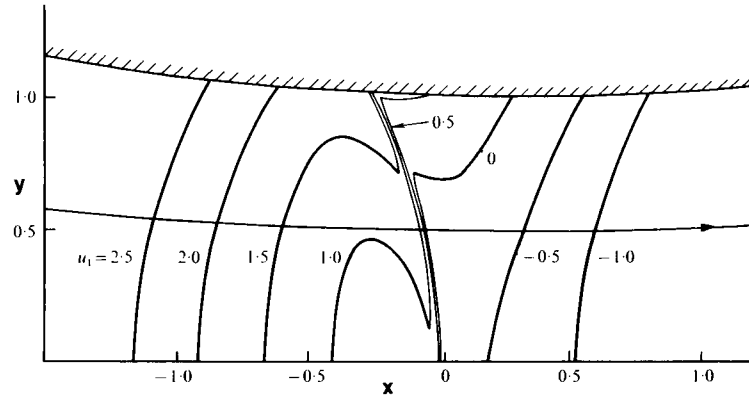


Figure 12. Flow picture for thin shock in unsteady decelerating flow showing isotachs and a streamline at  $t = 0.35$ ;  $k_s = 0.01$ ,  $\beta = (1/4) e^{-2t}$ ,  $\epsilon = 0.1$ ,  $\gamma = 1.4$ . Details in reference 4.

## WAVE DRAG DUE TO LIFT FOR TRANSONIC AIRPLANES\*

Julian D. Cole  
Rensselaer Polytechnic Institute

and

Norman D. Malmuth  
Rockwell International Science Center

### Summary

Lift dominated pointed aircraft configurations are considered in the transonic range. These are treated as lifting wings of zero thickness with aspect ratio of order one. An inner expansion which starts as Jones' theory is matched to a nonlinear outer transonic theory as in Barnwell's earlier work. New expressions for the wave drag due to the equivalent body are derived. Some examples of numerical calculations for different configurations are presented.

### 1. Introduction

In 1946, R. T. Jones (ref. 1) published a paper giving a formula for the lift and induced drag of "low aspect ratio pointed wings below and above the speed of sound". The work presented here, and earlier in the references cited below, represents an extension of Jones' ideas to the transonic range. It is reassuring that, under suitable circumstances, Jones' formula for the lift and induced drag not only continues to hold but is even valid for wings whose aspect ratio is order one. Under these circumstances, also shock waves and wave drag generally appear.

The basic ideas of how this type of flow behaves are set out in the report of Barnwell (ref. 2). The principal result is that the lift produces a flow that looks, in the outer region, like the flow past an equivalent axisymmetric body. This physical effect shows up in the inner and outer expansions used by Barnwell. Cheng and Hafez used similar ideas to define the apparent body and general equivalence rule in a series of papers (ref. 3, 4). Cramer (ref. 5) also studied the problem (with zero thickness as is done here) and essentially verified the results of Cheng and Hafez.

In this paper and ref. 6, we have also considered wing-like configurations with zero thickness and aspect ratio  $O(1)$  as in fig. 1. Thickness effects can be incorporated relatively easily. Inner and outer expansions are defined in essentially the same manner as Barnwell although the asymptotic matching is carried out in a different way using an intermediate limit. Then wave drag associated with the outer expansion is considered. Several computations and an optimization are carried out to show the effect of planform and longitudinal distribution of lift on the transonic wave drag.

---

\* This work was partially supported by the Air Force Office of Scientific Research under grant AFOSR 88-0037, and Rockwell North American Aircraft.

## 2. Basic Equations and Boundary Conditions

The problem is studied in the framework of inviscid aerodynamics. Since entropy increases across the shock waves are of third order in the flow perturbation, the full potential equation can be used as a starting point. The flow is thus, to this approximation, isentropic

$$\frac{p}{p_\infty} = \left( \frac{\rho}{\rho_\infty} \right)^\gamma \quad (2.1)$$

The potential equation is an expression of the continuity equation

$$\nabla \cdot \rho \vec{q} = 0, \quad \rho = \text{density}, \quad \vec{q} = \text{velocity} \quad (2.2)$$

$\Phi$  is the velocity potential such that  $\vec{q} = \nabla \Phi$ ,

$$(a^2 - \Phi_x^2) \Phi_{xx} + a^2 (\Phi_{yy} + \Phi_{zz}) = 2\Phi_x (\Phi_y \Phi_{xy} + \Phi_z \Phi_{xz}) + 2\Phi_y \Phi_z \Phi_{yz} + \Phi_y^2 \Phi_{yy} + \Phi_z^2 \Phi_{zz} \quad (2.3)$$

and  $a$  is the local speed of sound  $\sqrt{\gamma p / \rho}$ . The total enthalpy integral can be written

$$\frac{a^2}{U^2} = \frac{1}{M_\infty^2} + \frac{\gamma - 1}{2} \left( 1 - \frac{q^2}{U^2} \right) \quad (2.4)$$

$U$  = free stream speed,  $M_\infty$  = Mach number at infinity.

The boundary condition of flow tangent to the surface can be written

$$\nabla \Phi \cdot \nabla B = 0 \quad (2.5)$$

on  $B(x, y, z) = 0$ , which defines the surface.

We consider here an untwisted wing of zero thickness specified by an angle of attack  $\alpha$  and a camber function  $m(x)$ . The chord of the wing  $c = 1$  and the span  $2b$  is  $O(1)$ . Thus

$$B(x, y, z) = 0 = y - \alpha f(x) + O(\alpha^3) \begin{pmatrix} 0 < x < 1 \\ -z_{LE} < z < z_{LE} \end{pmatrix} \quad (2.6)$$

where  $f(x) = m(x) - x$  and  $m(1) = 1$ . For a straight trailing edge at  $y = 0$ , the trailing vortex sheet lies in the plane  $y = 0, x > 1$ . The planform is specified by  $(\pm z_{LE}(x)), z_{LE}(1) = b$ .

Another boundary condition that must be satisfied is the "Kutta condition" at a trailing edge where the flow is locally subsonic. This condition implies that the pressure loading at a trailing edge is zero. In approximations, such as the inner expansion which follows, each term satisfies this condition. Another interpretation of this condition is that unphysical pressure jumps are not allowed in the inner solutions.

## 3. Inner Expansion and Far Field ( $r^* \rightarrow \infty$ )

The approximation in general is based on  $\alpha \rightarrow 0, M_\infty \rightarrow 1$  and in the usual transonic way ( $K = \frac{1 - M_\infty^2}{\epsilon_1(\alpha)} = \text{transonic similarity parameter, fixed}$ ).  $\epsilon_1(\alpha)$  = parameter of outer expansion, defined later. In the inner expansion, the observer remains a fixed distance  $O(1)$  from the wing, and distances are measured from the wing surface.

The inner limit process thus has

$$\alpha \rightarrow 0 \quad (x, y^*, z; K \text{ fixed})$$

where

$$\begin{aligned} y^* &= y - \alpha f(x) & 0 < x < 1 \\ &= y & x > 1 \end{aligned} \quad (3.1)$$

The form of the inner expansion for the potential is thus

$$\Phi(x, y, z; \alpha; M_\infty) = U \{ x + \alpha \varphi_1(x, y^*, z) + \alpha^2 \bar{\varphi}_2(x, y^*, z) + \bar{O}(\alpha^3) \} \quad (3.2)$$

The presence of the overbar denotes the possibility of logarithmic switchback terms introduced into the inner expansion for purposes of matching with the outer expansion. Anticipating the result, we note here

$$\bar{\varphi}_2(x, y^*, z) = \log^2 \frac{1}{\sqrt{\epsilon_1}} \varphi_{22}(x) + \log \frac{1}{\sqrt{\epsilon_1}} \varphi_{21}(x) + \varphi_2(x, y^*, z) \quad (3.3)$$

Note also that the velocity components of the inner expansion are

$$\begin{aligned} \frac{q_x}{U} &= 1 + \alpha \varphi_{1x} + \alpha^2 (\bar{\varphi}_{2x} - f' \varphi_{1y^*}) + \bar{O}(\alpha^3) \\ \frac{q_y}{U} &= \alpha \varphi_{1y^*} + \alpha^2 \varphi_{2y^*} + \bar{O}(\alpha^3) \text{ etc.} \end{aligned}$$

Substituting the assumed expansion into the full potential equation we obtain the equations for the first two approximations (in divergence forms, as follows from (2.2)) and the corresponding conditions of tangent flow

$$\nabla^{*2} \varphi_1 = 0, \quad \varphi_{1,y^*}(x, 0, z) = f'(x) \begin{pmatrix} 0 < x < 1 \\ -z_{LE} < z < z_{LE} \end{pmatrix} \quad (3.4)$$

$$\nabla^{*2} \varphi_2 = \frac{\partial}{\partial x} \left\{ \frac{\gamma+1}{2} \varphi_{1x}^2 + (\nabla^* \varphi_1)^2 \right\}, \quad \varphi_{2,y^*}(x, 0\pm, z) = f'(x) \varphi_{1x}(x, 0\pm, z) \quad (3.5)$$

where

$$\nabla^* = \left( \frac{\partial}{\partial y^*}, \frac{\partial}{\partial z} \right) = \text{inner transverse gradient}$$

$$\nabla^* \varphi_1 = \text{inner transverse velocity perturbation}$$

$$\nabla^{*2} = \frac{\partial^2}{\partial y^{*2}} + \frac{\partial^2}{\partial z^2} = \text{inner transverse Laplacian}$$

The first equation (3.4) can be thought of as the Prandtl-Glauert equation of linearized theory but with  $M_\infty$  close to one. The second equation (3.5) shows how, in the inner representation, either compression  $\varphi_{1x} < 0$  or expansion  $\varphi_{1x} > 0$ , provides an effective volume source and can cause stream tube divergence. We note the expression for the x-component of the mass flux vector.

$$\frac{\rho q_x}{\rho_\infty U} = 1 - \alpha^2 \left( \frac{(\gamma + 1)}{2} \varphi_{1x}^2 + \frac{1}{2} (\nabla^* \varphi_1)^2 \right) + \bar{O}(\alpha^3) \quad (3.6)$$

The quadratic form in (3.6) is almost the RHS of (3.5); the additional term comes from  $\nabla^* \cdot (\varphi_{1x} \nabla^* \varphi_1)$ .

The inner expansion is the driver of the entire procedure. But as is now shown it is not valid as  $r^* = \sqrt{y^{*2} + z^2}$  tends to infinity. On physical grounds, we would expect the transonic flow far away, which in general contains shock waves, to be described by an equation of mixed elliptic-hyperbolic type. The Laplace eqn. (3.4) is of course always elliptic.

Further, we show that the second term  $\alpha^2 \varphi_2$  becomes much greater than the first  $\alpha \varphi_1$  as  $r^* \rightarrow \infty$ . The general symmetry of the solution  $\varphi_1, \varphi_2$  is

$$\begin{aligned} \varphi_1(x; y^*, z) &= -\varphi_1(x; -y^*, z) & \text{odd} & \quad \text{Lifting, vortex sheet} \\ \varphi_2(x; y^*, z) &= \varphi_2(x; -y^*, z) & \text{even} & \quad \text{Non-lifting, source} \end{aligned}$$

We study now the behavior of these solutions near infinity in  $r^*$ . The solution for  $\varphi_1$  can be represented by a dipole sheet (or vortices) or, most directly, by the use of the complex variable

$$\xi = z + iy^* = r^* e^{i(\frac{\pi}{2} - \theta^*)} \quad (3.7)$$

The complex potential for the wing, which is flat in a cross-plane  $x = \text{const.}$ , and for the trailing vortex sheet is

$$\begin{aligned} \varphi_1 + i\psi_1 &= -if'(x) \left\{ \xi - \sqrt{\xi^2 - z_{LE}^2(x)} \right\} & 0 < x < 1 \\ &= -if'(1) \left\{ \xi - \sqrt{\xi^2 - b^2} \right\} & x > 1 \end{aligned} \quad (3.8)$$

The transverse components of velocity perturbation  $\nabla^* \varphi_1 = (v_1, w_1)$  are found from

$$\begin{aligned} w_1 - iv_1 &= -if'(x) \left\{ 1 - \frac{\xi}{\sqrt{\xi^2 - z_{LE}^2(x)}} \right\} & 0 < x < 1 \\ &= -if'(1) \left\{ 1 - \frac{\xi}{\sqrt{\xi^2 - b^2}} \right\} & x > 1 \end{aligned} \quad (3.9)$$

The first approximation to the pressure distribution and the lift can be found from

$$\begin{aligned} \frac{p}{p_\infty} &= \left( \frac{a^2}{a_\infty^2} \right)^{\frac{\gamma}{\gamma-1}}, \quad \frac{a^2}{a_\infty^2} = 1 + \frac{\gamma-1}{2} M_\infty^2 \left( 1 - \frac{q^2}{U^2} \right) = 1 - \alpha(\gamma-1)\varphi_{1x} + \dots \\ \frac{p}{p_\infty} &= 1 - \alpha\gamma\varphi_{1x} + \dots \end{aligned} \quad (3.10)$$

The dominant term is a dipole potential where the dipole strength  $D_1(x)$  is equal to the lift  $l_1(x)$  up to the station  $x$ . (cf 3.15)

$$\varphi_1(r^*, \theta^*; x) = \frac{l_1(x)}{2\pi} \frac{\cos \theta^*}{r^*} + O\left(\frac{1}{r^{*3}}\right) \quad (3.20)$$

An unyawed symmetric planform has been assumed. For more general planforms we can use

$$D_1(x) = \int_{-z_{LE}}^{z_{LE}} [\varphi_1]_{y=0} dz.$$

The potential problem for  $\varphi_2$  can be thought of as describing the flow past a thin wing with thickness and a volume distribution of sources. Thus, the far field contains a source term like  $\log r^*$  and a particular solution due to the RHS. From (3.20) the RHS, has a term

$$\frac{\gamma+1}{2} \varphi_{1x}^2 + \varphi_{1r^*}^2 + \frac{1}{r^{*2}} \varphi_{1\theta^*}^2 = \frac{\gamma+1}{2} \left(\frac{l_1''}{2\pi}\right)^2 \frac{\cos^2 \theta^*}{r^{*2}} + O\left(\frac{1}{r^{*4}}\right)$$

Thus

$$\frac{\partial^2 \varphi_2}{\partial r^{*2}} + \frac{1}{r^*} \frac{\partial \varphi_2}{\partial r^*} + \frac{1}{r^{*2}} \frac{\partial^2 \varphi_2}{\partial \theta^{*2}} = \frac{\gamma+1}{4} \frac{\partial}{\partial x} \left\{ \left(\frac{l_1''}{2\pi}\right)^2 \right\} \frac{1 + \cos 2\theta^*}{r^{*2}} + O\left(\frac{1}{r^{*4}}\right) \quad (3.21)$$

Taking account of the particular solution, the far field of  $\varphi_2$  is

$$\begin{aligned} \varphi_2(r^*, \theta^*; x) = & \frac{\gamma+1}{4} \frac{l_1' l_1'''}{(2\pi)^2} \log^2 r^* + S_2(x) \log r^* + g_2(x) \\ & - \frac{\gamma+1}{8} \frac{l_1'' l_1'''}{(2\pi)^2} \cos 2\theta + \bar{O}\left(\frac{1}{r^{*2}}\right) \end{aligned} \quad (3.22)$$

Thus, there is a non-uniformity as  $r^* \rightarrow \infty$  (since  $\alpha \varphi_1 \sim \frac{\alpha}{r^*}$ ,  $\alpha^2 \varphi_2 \sim \alpha^2 \log^2 r^*$ ) roughly when  $r^* \log^2 r^* \sim \frac{1}{\alpha}$ . This shows the need for an outer expansion. An expression for the source strength  $S_2(x)$  can be found from the boundary value problem for  $\varphi_2$ , but  $g_2(x)$  is undetermined from an inner problem.  $g_2(x)$  must be found by matching with the outer nonlinear boundary value problem. The presence of shock waves in the outer flow is reflected in  $g_2$ .

#### 4. Outer Expansion and Near Field ( $\tilde{r} \rightarrow 0$ ).

The first few terms of the outer expansion necessary to match with  $\varphi_1, \bar{\varphi}_2$  are considered. The limit process associated with this expansion is the typical transonic expansion necessary to give the small disturbance equation (ref. 7). The representative point runs to infinity as  $\alpha \rightarrow 0, M_\infty \rightarrow 1$ . The limit process associated with this expansion has  $(x, \tilde{y}, \tilde{z}, K)$  fixed as  $\alpha \rightarrow 0$  where  $(\tilde{y}, \tilde{z}) = \sqrt{\epsilon_1}(y, z)$ .

The general form of the expansion for the potential is

$$\Phi(x, y, z; M_\infty, \alpha) = U \{x + \epsilon_1(\alpha)\phi_1(x, \tilde{y}, \tilde{z}; K) + \epsilon_2(\alpha)\phi_2(x, \tilde{y}, \tilde{z}; K) + \epsilon_3(\alpha)\phi_3(x, \tilde{y}, \tilde{z}; K) \dots\} \quad (4.1)$$

where  $\epsilon_1, \epsilon_2, \epsilon_3$  are found from matching. In order to match, it is necessary to obtain an RHS term similar to that in (3.5),  $\frac{\gamma+1}{2}(\phi_x^2)_x$ .  $\phi_2$  can be made to match with the dominant dipole of inner  $\phi_1$  and this forcing term then appears in the RHS of the equation for  $\phi_3$ .  $\phi_1$  is a switchback type of function necessary for matching and turns out to be the axisymmetric flow produced by an equivalent body of revolution. Some details are now shown.

$$\begin{aligned} \frac{q_x}{U} &= \frac{1}{U} \frac{\partial \Phi}{\partial x} = 1 + \epsilon_1 \phi_{1x} + \epsilon_2 \phi_{2x} + \epsilon_3 \phi_{3x} + \dots \\ \frac{q_y}{U} &= \frac{1}{U} \frac{\partial \Phi}{\partial y} = \epsilon_1^{3/2} \phi_{1\tilde{y}} + \epsilon_2 \epsilon_1^{1/2} \phi_{2\tilde{y}} + \epsilon_3 \epsilon_1^{1/2} \phi_{3\tilde{y}} + \dots \quad \text{etc.} \\ \frac{a^2}{U^2} &= 1 + \epsilon_1(K - (\gamma - 1)\phi_{1x}) - \epsilon_2(\gamma - 1)\phi_{2x} - \epsilon_3(\gamma - 1)\phi_{3x} + O(\epsilon_1^2) \end{aligned}$$

The full potential equation (2.3) takes the form

$$\begin{aligned} &\{1 + \epsilon_1(K - (\gamma - 1)\phi_{1x}) - \epsilon_2(\gamma - 1)\phi_{2x} - \epsilon_3(\gamma - 1)\phi_{3x} \dots - 1 - 2\epsilon_1\phi_{1x} - 2\epsilon_2\phi_{2x} - 2\epsilon_3\phi_{3x} \dots\} \\ &\quad \{\epsilon_1\phi_{1xx} + \epsilon_2\phi_{2xx} + \epsilon_3\phi_{3xx} + \dots\} + \{1 + O(\epsilon_1)\} \{\epsilon_1^2 \tilde{\nabla}^2 \phi_1 + \epsilon_1 \epsilon_2 \tilde{\nabla}^2 \phi_2 + \epsilon_1 \epsilon_3 \tilde{\nabla}^2 \phi_3\} \\ &= 2\{1 + \dots\} \epsilon_1^3 (\phi_{1\tilde{y}} \phi_{1x\tilde{y}} + \phi_{1\tilde{z}} \phi_{1x\tilde{z}}) + \dots \\ &\quad \tilde{\nabla}^2 = \frac{\partial^2}{\partial \tilde{y}^2} + \frac{\partial^2}{\partial \tilde{z}^2} \end{aligned} \quad (4.2)$$

Thus, choosing  $\epsilon_1 \epsilon_3 = \epsilon_2^2$  we have

$$(K - (\gamma + 1)\phi_{1x})\phi_{1xx} + \tilde{\nabla}^2 \phi_1 = 0, \quad (4.3)$$

$$(K - (\gamma + 1)\phi_{1x})\phi_{2xx} - (\gamma + 1)\phi_{2x}\phi_{1xx} + \tilde{\nabla}^2 \phi_2 = 0 \quad (4.4)$$

$$O(\epsilon_1 \epsilon_3) \quad (K - (\gamma + 1)\phi_{1x})\phi_{3xx} - (\gamma + 1)\phi_{3x}\phi_{1xx} + \tilde{\nabla}^2 \phi_3 = (\gamma + 1)\phi_{2x}\phi_{2xx} \quad (4.5)$$

$\phi_1$  satisfies the usual nonlinear transonic small-disturbance (K-G) equation.  $\phi_2$  satisfies its linear variational equation and  $\phi_3$  a forced variational equation. All the equations are of conservation type and can be written

$$(K\phi_{1x} - \frac{(\gamma + 1)}{2}\phi_{1x}^2)_x + \tilde{\nabla} \cdot (\tilde{\nabla} \phi_1) = 0 \quad (4.6)$$

$$(K\phi_{2x} - (\gamma + 1)\phi_{1x}\phi_{2x})_x + \tilde{\nabla} \cdot (\tilde{\nabla} \phi_2) = 0 \quad (4.7)$$

$$(K\phi_{3x} - (\gamma + 1)\phi_{1x}\phi_{3x})x + \tilde{\nabla} \cdot (\tilde{\nabla}\phi_3) = \frac{(\gamma + 1)}{2}(\phi_{2x}^2)_x \quad (4.8)$$

The near field behavior  $\tilde{r} \rightarrow 0$  of these solutions, obtained from  $\tilde{\nabla}^2\phi = RHS$ , is given by

$$\phi_1(x_1\tilde{r}) = \mathbf{S}_1(x) \log \tilde{r} + \mathbf{G}_1(x) + O(\tilde{r}^2 \log^2 \tilde{r}) \quad (4.9)$$

$$\begin{aligned} \phi_2(x_1\tilde{r}, \theta) = & \frac{\mathbf{D}_2(x) \cos \theta}{2\pi} \frac{1}{\tilde{r}} + (\gamma + 1) \frac{(\mathbf{S}'_1 \mathbf{D}'_2)}{2\pi} \cos \theta \left\{ \frac{1}{4} \tilde{r} \log^2 \tilde{r} - \frac{1}{4} \tilde{r} \log \tilde{r} + \frac{\tilde{r}}{4} \right\} \\ & + \left( (\gamma + 1) \frac{(\mathbf{G}'_1 \mathbf{D}'_2)'}{2\pi} - K \frac{\mathbf{D}''_2}{2\pi} \right) \cos \theta \left\{ \frac{\tilde{r}}{2} \log \tilde{r} - \frac{\tilde{r}}{4} \right\} + \bar{O}(\tilde{r}^3) \end{aligned} \quad (4.10)$$

$$\begin{aligned} \phi_3(x_1, \tilde{r}, \theta) + & \frac{(\gamma + 1)}{4} \frac{\mathbf{D}'_2 \mathbf{D}''_2}{(2\pi)^2} \log^2 \tilde{r} + \mathbf{S}_3(x) \log \tilde{r} + \mathbf{G}_3(x) - \frac{(\gamma + 1)}{8} \frac{\mathbf{D}'_2 \mathbf{D}''_2}{(2\pi)^2} \cos 2\theta \\ & + \frac{(\gamma + 1)^2}{16} \frac{(\mathbf{S}'_1 \mathbf{D}'_2 \mathbf{D}''_2)'}{(2\pi)^2} \tilde{r}^2 \log^3 \tilde{r} + O(\tilde{r}^2 \log^2 \tilde{r}) \end{aligned} \quad (4.11)$$

where  $\tilde{r} = \sqrt{\tilde{y}^2 + \tilde{z}^2}$ ,  $\theta = \tan^{-1} \frac{\tilde{z}}{\tilde{y}} = \tan^{-1} \frac{z}{y}$

The source strength  $\mathbf{S}_3$  and doublet strength  $\mathbf{D}_2$  are found by matching with the inner solution. The source strength  $\mathbf{S}_1$  is found in a special way in the matching. The functions  $\mathbf{G}_1(x)$ ,  $\mathbf{G}_3(x)$  are found when the boundary value problems defined by the singular behavior as  $\tilde{r} \rightarrow 0$  in (4.9, 10, 11) are solved (numerically).

## 5. Asymptotic Matching

A matching limit, intermediate to the inner and outer limits, is defined by a class of functions  $\eta(\alpha)$  such that  $\sqrt{\epsilon_1} \ll \eta(\alpha) \ll 1$ . A coordinate

$$r_\eta = \eta(\alpha)r \quad (5.1)$$

is held fixed in this limit. Thus

$$r = \frac{r_\eta}{\eta} \rightarrow \infty, \quad \tilde{r} = \frac{\sqrt{\epsilon_1}}{\eta} r_\eta \rightarrow 0$$

In the intermediate limit the representative physical radius again runs to infinity as  $\alpha \rightarrow 0$ ,  $M_\infty \rightarrow 1$  but not as fast as in the outer limit. For matching, the inner and outer limit expansions must read the same in the intermediate coordinate. Thus

$$\alpha\varphi_1 + \alpha^2\bar{\varphi}_2 + \cdots \leftrightarrow \epsilon_1\phi_1 + \epsilon_2\phi_2 + \epsilon_3\phi_3 + \cdots$$

( $\leftrightarrow$  denotes "matches to")

Note that in the matching



$$\log \tilde{r} = \log \frac{\sqrt{\epsilon_1} r_\eta}{\eta} = \log \frac{r_\eta}{\eta} - \log \frac{1}{\sqrt{\epsilon_1}} \quad (5.2a)$$

and

$$\log^2 \tilde{r} = \log^2 \frac{r_\eta}{\eta} - 2 \log \frac{r_\eta}{\eta} \log \frac{1}{\sqrt{\epsilon_1}} + \log^2 \frac{1}{\sqrt{\epsilon_1}} \quad (5.2b)$$

Note also that

$$\frac{\cos \theta^*}{r^*} = \frac{y - \alpha f(x)}{y^2 + z^2 - 2\alpha y f(x)} = \frac{\cos \theta}{r} + \alpha f(x) \frac{\cos 2\theta}{r^2} + \dots \quad (5.3)$$

Writing these out using the near field expansions of this section and the far field expansion of the previous section we have

$$\begin{aligned} & \alpha \left( \frac{l_1 \cos \theta}{r_\eta/\eta} + \dots \right) + \alpha^2 \log^2 \frac{1}{\sqrt{\epsilon_1}} \varphi_{22}(x) + \alpha^2 \log \frac{1}{\sqrt{\epsilon_1}} \varphi_{21}(x) + \alpha^2 \left\{ \frac{(\gamma+1)}{4} \frac{l_1'' l_1'''}{(2\pi)^2} \log^2 \frac{r_\eta}{\eta} \right. \\ & \quad \left. + S_2(x) \log \frac{r_\eta}{\eta} + g_2(x) - \frac{(\gamma+1)}{8} \frac{l_1'' l_1'''}{(2\pi)^2} \cos 2\theta + \bar{O}(\eta^2) \right\} + \dots \\ & \Leftrightarrow \epsilon_1 \left\{ S_1(x) \left( \log \frac{r_\eta}{\eta} - \log \frac{1}{\sqrt{\epsilon_1}} \right) + G_1(x) + \dots \right\} + \epsilon_2 \left\{ \frac{D_2(x) \cos \theta}{2\pi \sqrt{\epsilon_1} r_\eta/\eta} + \dots \right\} + \dots \\ & \quad + \epsilon_3 \left\{ \frac{(\gamma+1)}{4} \frac{D_2' D_2''}{(2\pi)^2} \left( \log^2 \frac{r_\eta}{\eta} - 2 \log \frac{r_\eta}{\eta} \log \frac{1}{\sqrt{\epsilon_1}} + \log^2 \frac{1}{\sqrt{\epsilon_1}} \right) + \right. \\ & \quad \left. + S_3(x) \left( \log \frac{r_\eta}{\eta} - \log \frac{1}{\sqrt{\epsilon_1}} \right) + G_3(x) - \frac{(\gamma+1)}{8} \frac{D_2' D_2''}{(2\pi)^2} \cos 2\theta + \dots \right\} \quad (5.4) \end{aligned}$$

Comparison of these two expansions shows that they match in an intermediate region with the choices

$$\begin{aligned} \frac{\epsilon_2}{\sqrt{\epsilon_1}} &= \alpha & D_2(x) &= l_1(x) \\ \epsilon_3 &= \alpha^2, & S_1(x) &= \frac{(\gamma+1)}{2} \frac{D_2' D_2''}{(2\pi)^2} = \frac{(\gamma+1)}{2} \frac{l_1'' l_1'''}{(2\pi)^2} \\ \epsilon_3 \log \frac{1}{\sqrt{\epsilon_1}} &= \epsilon_1 & S_3(x) &= S_2(x), G_3(x) = g_2(x) \end{aligned} \quad (5.5)$$

In summary

$$\epsilon_1 = \alpha^2 \log \frac{1}{\sqrt{\epsilon_1}}, \quad \epsilon_2 = \alpha^2 \log^{1/2} \frac{1}{\sqrt{\epsilon_1}}, \quad \epsilon_3 = \alpha^2$$

$\epsilon_1(\alpha)$  is defined implicitly by the relationship above.  $S_1(x)$  is chosen by an internal switch-back in the outer expansion. The switchback functions in the inner expansion are

$$\varphi_{22}(x) = -\frac{1}{2}\mathbf{S}_1(x) = -\frac{(\gamma+1)}{4} \frac{l_1' l_1''}{(2\pi)^2} \quad (5.6)$$

$$\varphi_{21}(x) = \mathbf{G}_1(x) - \mathbf{S}_3(x) = \mathbf{G}_1(x) - S_2(x) \quad (5.7)$$

The principal physical result of the matching is the source distribution for the apparent body that generates the first axisymmetric outer potential  $\phi_1(x, \tilde{r})$

$$\mathbf{S}_1(x) = \frac{(\gamma+1)}{2} \frac{l_1' l_1''}{(2\pi)^2} \quad (5.8)$$

This body depends only on the longitudinal distribution of lift  $l_1(x)$ . A correction axisymmetric flow is provided by the source  $\mathbf{S}_3$

$$\mathbf{S}_3(x) = S_2(x) \quad (5.9)$$

which generates the axisymmetric part of  $\phi_3(x, \tilde{r}, \theta)$ .  $\phi_3(x, \tilde{r}, \theta)$  can be decomposed into

$$\phi_3(x, \tilde{r}, \theta) = \Omega_3(x, \tilde{r}) + \psi_3(x, \tilde{r}) \cos 2\theta \quad (5.10)$$

using the form of  $\phi_2$

$$\phi_2(x, \tilde{r}, \theta) = \psi_2(x, \tilde{r}) \cos \theta \quad (5.11)$$

Then for  $\Omega_3(x, \tilde{r})$

$$(K - \gamma + 1\phi_{1x})\Omega_{3xx} - (\gamma + 1)\Omega_{3x}\phi_{1xx} + \tilde{\nabla}^2\Omega_3 = \frac{(\gamma+1)}{4}(\psi_{2x}^2)_x \quad (5.12)$$

By considering the omitted terms, an overlap domain can be shown to exist for matching to this order. Also consideration of higher order terms in both expansions shows that the matching can be continued. Thus, the outer expansion reads

$$\Phi = U\{x + \alpha^2 \log \frac{1}{\sqrt{\epsilon_1}} \bar{\phi}(x, \tilde{r}, \theta) + \bar{O}(\alpha^4)\} \quad (5.13)$$

where

$$\bar{\phi} = \phi_1(x, \tilde{r}) + \frac{1}{\log^{1/2} \frac{1}{\sqrt{\epsilon_1}}} \phi_2(x, \tilde{r}, \theta) + \frac{1}{\log \frac{1}{\sqrt{\epsilon_1}}} \phi_3(x, \tilde{r}, \theta)$$

It can thus be noted that the collection of terms  $\phi_1, \phi_2, \phi_3$  which can be computed individually satisfy together the small-disturbance (K-G) equation

$$(K - (\gamma + 1)\bar{\phi}_x)\bar{\phi}_{xx} + \tilde{\nabla}^2\bar{\phi} = O\left(\frac{1}{\log^{3/2} \frac{1}{\sqrt{\epsilon_1}}}\right) \quad (5.14)$$

## 6. Wave Drag

There is of course induced drag associated with the trailing vortex system; the drag in dominant order, associated with  $\varphi_1$ , is just that of Jones' theory. From the point of view of induced drag, the wing considered here, which is flat spanwise, is an optimum. The spanwise circulation distribution (cf 3.14) is elliptical. The wave drag is connected to the shock wave system in the outer flow field. It could be calculated from the entropy increase in the wave system.

For small disturbances to a free stream we have the result for the wave drag  $D_w$

$$D_w = \rho_\infty T_\infty c^2 \int \int_{-\infty}^{\infty} [S]_s dy dz + \dots \quad (6.1)$$

where  $[S]_s$  = jump in specific entropy across a shock. The integral is taken over all the shocks in the system. Using the expression for the entropy jump in transonic small disturbance theory (cf. ref. 7, cf. p 165 ff. for a discussion of wave drag)

$$D_w = -\rho_\infty U^2 \frac{(\gamma+1)}{12} \alpha^4 \log^2 \frac{1}{\sqrt{\epsilon_1}} c^2 \int_0^\infty \tilde{r} d\tilde{r} \int_0^{2\pi} [\bar{\phi}_x]_s^3 d\theta + \dots \quad (6.2)$$

Consider the differential conservation form associated with (5.14)

$$\tilde{r} \left( K \frac{\bar{\phi}_x^2}{2} - \frac{(\gamma+1)}{3} \bar{\phi}_x^3 - \frac{1}{2} (\tilde{\nabla}^2 \phi)^2 \right)_x + (\tilde{r} \bar{\phi}_{\tilde{r}} \bar{\phi}_x)_{\tilde{r}} + \frac{1}{\tilde{r}} (\bar{\phi}_x \bar{\phi}_\theta)_\theta = 0 \quad (6.3)$$

Integrating this divergence form over all space outside a small cylinder

$$(-\infty < x < \infty) \quad \tilde{r}_c \rightarrow 0$$

around the  $x$ -axis enables the entropy jump of (6.2) to be related to radial momentum flow. (6.3) is not conserved across shocks so that shock jumps appear such as

$$[K \frac{\bar{\phi}_x^2}{2} - \frac{(\gamma+1)}{3} \bar{\phi}_x^3 - \frac{1}{2} (\tilde{\nabla} \bar{\phi})^2]_s.$$

Let  $\tilde{D}_w = \frac{D_w}{\rho_\infty U^2 c^2 \epsilon_1^2}$ . Then

$$\tilde{D}_w = - \lim_{\tilde{r}_c \rightarrow 0} \tilde{r}_c \int_{-\infty}^{\infty} dx \int_0^{2\pi} d\theta \bar{\phi}_x \bar{\phi}_{\tilde{r}}|_{\tilde{r}_c} - \lim_{\substack{\tilde{r}_c \rightarrow 0, \\ x_2 \rightarrow \infty}} \int_{\tilde{r}_c}^{\infty} r dr \int_0^{2\pi} d\theta \frac{(\tilde{\nabla} \bar{\phi})^2}{2} |_{x_2} \quad (6.4)$$

If we consider the dominant term in (6.4)

$$\tilde{D}_{w_1} = \int_0^1 dx \int_0^{2\pi} d\theta \lim_{\tilde{r}_c \rightarrow 0} (\tilde{r}_c \phi_1 \phi_{1x} \phi_{1\tilde{r}}) \quad (6.5)$$

From (4.9),  $\phi_{1x} = S'_1(x) \log \tilde{r} + G'_1(x)$ ,  $\phi_{1\tilde{r}} = \frac{S_1(x)}{\tilde{r}}$  and using

$$\int_0^1 S_1(x) S'_1(x) dx = \frac{S_1^2(1)}{2} - \frac{S_1^2(0)}{2} = 0$$

in which  $\mathbf{S}_1(1) = \mathbf{S}_1(0) = 0$ , we have

$$\tilde{D}_{w_1} = -2\pi \int_0^1 \mathbf{S}_1(x) \mathbf{G}'_1(x) dx = 2\pi \int_0^1 \mathbf{S}'_1(x) \mathbf{G}_1(x) dx \quad (6.6)$$

This drag formula is exactly that of a slender body in transonic flow (cf ref. 7, p161). Higher order terms in the drag formula can be found.

## 7. Applications and Remarks

Several applications have been made of the theory in its present form. For flat wings  $f' = -1$ .  $l_1(x)$  is given by (3.15). The effective source strength for the equivalent body  $\mathbf{S}_1(x) = \frac{(\gamma+1)}{2} \frac{l'_1 l''_1}{(2\pi)^2}$  (cf eqn. 5.5). Equation (4.3)

$$(K - (\gamma + 1)\bar{\phi}_{1x})\bar{\phi}_{1xx} + \phi_{1\tilde{r}\tilde{r}} + \frac{1}{\tilde{r}}\phi_{1\tilde{r}} = 0 \quad (7.1)$$

is solved numerically with a small-disturbance code using (4.9) as the boundary condition for various  $K$ . The dominant term of the wave drag coefficient  $C_{Dw}$  is calculated from eqn (6.6). The results are plotted as  $C_{Dw}$  vs  $M_\infty$  for two different angles of attack in fig. 2. Substantial drag due to lift is evident. The planform shape and the distribution of  $l_1(x)$  which is typical appears in fig. 3.

Another set of calculations incorporates a parabolic body of revolution (thickness ratio .057) and adds the source strength of this body to  $\mathbf{S}_1(x)$ . A series of planforms with semi-span  $z_{LE}(x)$  given by

$$z_{LE}(x) = \frac{x(\mu - x^{\mu-1})}{\mu - 1} \quad (7.2)$$

and shown in fig. 4 was considered for various  $\mu, M_\infty = .995, \alpha = .2$  rad. The idea is to optimize the  $L/D$  figure of merit  $C_{Dw}/(AR = \text{aspect ratio})$  by a choice of planform. A minimum drag occurs for  $\mu = 2.5$ . The planform shape and curve of  $C_{Dw}$  vs.  $\mu$  appears in fig. 5. Also shown in figs. (6a - 6c) for  $\mu = 1.2, 2, 10$  are isobars which make evident the shock wave which occurs. The wave drag for small  $\mu$  is large because of the small sweep and for large  $\mu$  because of rapid changes of  $l_1$  near the wing tip. These preliminary studies are meant to show the relative effectiveness of various planforms.

It would be very useful to extend this work to give efficient ways of calculating the higher order terms in the wave drag. It is also possible to incorporate the effects of wing thickness  $\delta \sim (\alpha^2 \log \frac{1}{\sqrt{\epsilon_1}})$  into the formulation in a more systematic way. A first step in this direction is given in ref. 6.

## Acknowledgement

The authors are indebted to E. Bonner of North American for valuable discussions and support.

### References

1. Jones, R. T. : Properties of Low-Aspect - Ratio Pointed Wings at Speeds Below and Above the Speed of Sound. NACA Rep. 835, 1946.
2. Barnwell, R. W. : Analysis of Transonic Flow about Lifting Wing-Body Configurations. NASA TR R-440, June 1975.
3. Cheng, H. K. and Hafez, M. M. : Equivalence rule and Transonic Flow Theory Involving Lift. *AIAA J.* v. 11, No. 8, Aug. 1973, pp 1210-1212.
4. Cheng, H. K. and Hafez, M. M. : Equivalence Rule and Transonic Flows Involving Lift. USCAE Report 124, Univ. of Southern California, Apr. 1973. See also Cheng, H. K. and Hafez, M. M.: *J. Fluid Mechanics*, v. 72, 161.
5. Cramer, M. S.: Lifting Three-Dimensional Wings in Transonic Flow. *J. Fluid Mech.* (1979) v. 95, pp223-240. See also: A Note on 'Lifting Three-Dimensional Wings in Transonic Flow', *J. Fluid Mechanics*, (1981), v. 109, pp 257-258.
6. Malmuth, N., Wu, C. C. and Cole, J. D.: "Transonic Wave Drag - Estimation and Optimization using the Nonlinear Area Rule", *J. Aircraft* v. 24, No. 3, Mar. 1987, pp 203-210.
7. Cole, J. D. and Cook, L. P.: *Transonic Aerodynamics*, North-Holland 1986.

## POINTED TRANSONIC WING

---

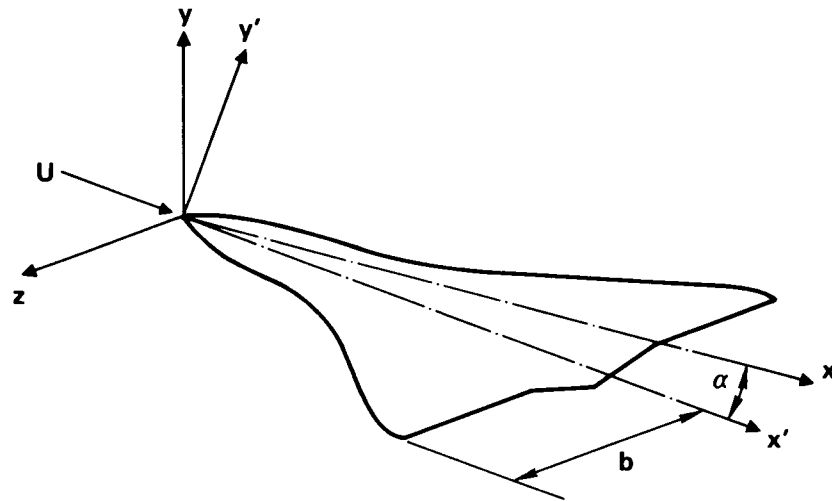


Figure 1 Pointed Transonic Wing

## DRAG RISE DUE TO LIFT CHARACTERISTICS OF MODEL FIGHTER PLANFORM 100 x 50 GRID SINE TIP FAIRING

---

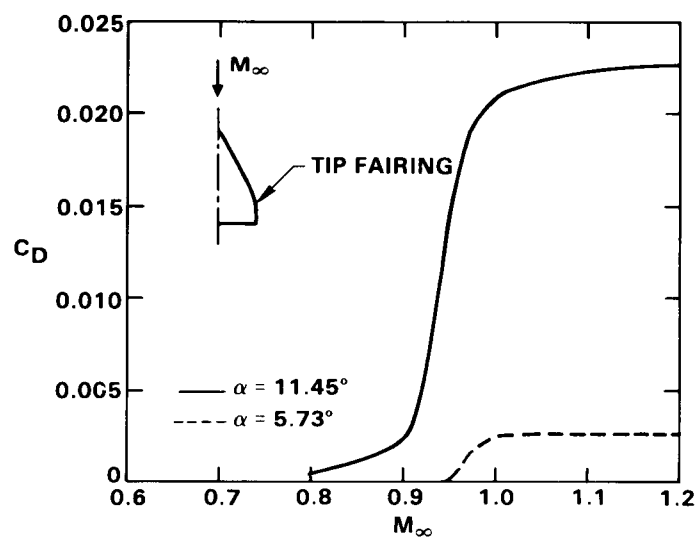


Figure 2 Drag Rise Due to Lift Characteristics of Model Fighter Planform

## LIFT LOADING OF MODEL WING WITH SINE TIP FAIRING

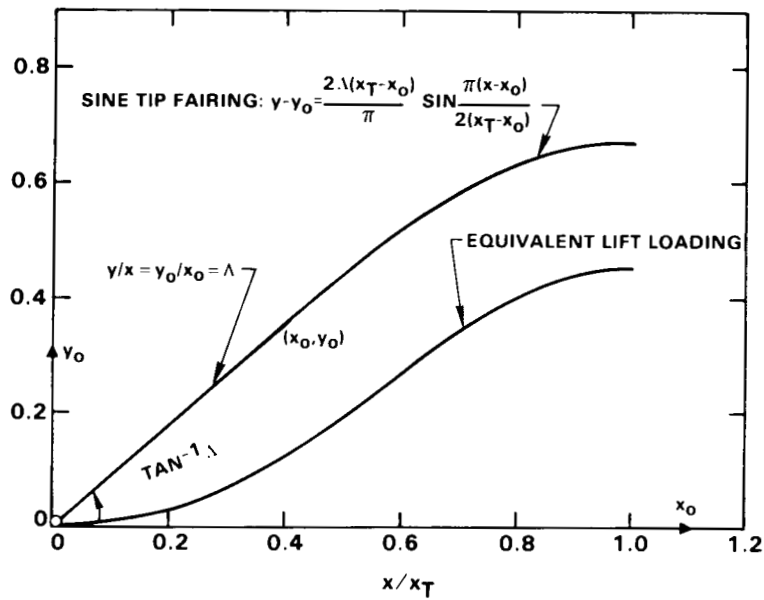


Figure 3 Lift Loading of Model Wing with Sine Tip Fairing

## “ $\mu$ ” FAMILY OF WING BODIES IN WHICH SEMISPAN $$s = \frac{\mu x - x^\mu}{\mu - 1}$$

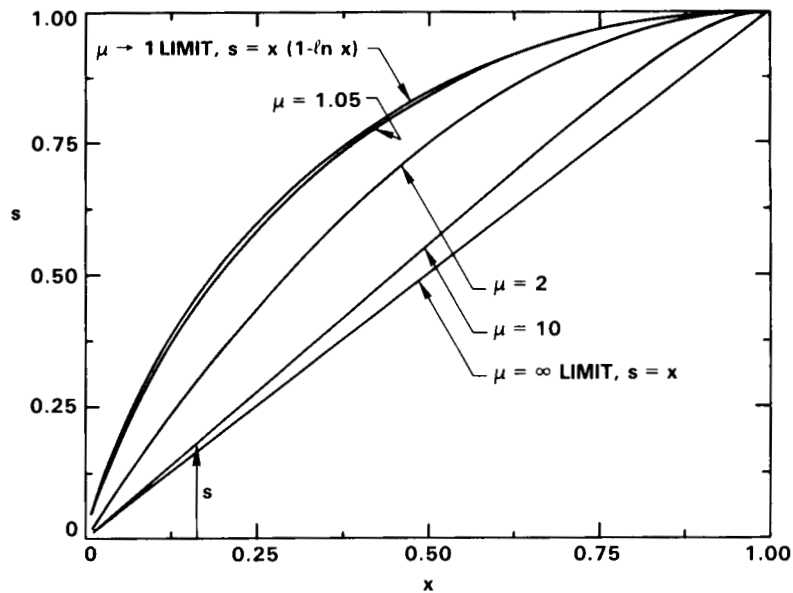


Figure 4 “ $\mu$ ” Family of Wing-Bodies in which Semispan =  $\frac{x(\mu - x^{\mu-1})}{\mu - 1}$

## DRAG/ASPECT RATIO FOR $\mu$ W+B FAMILY

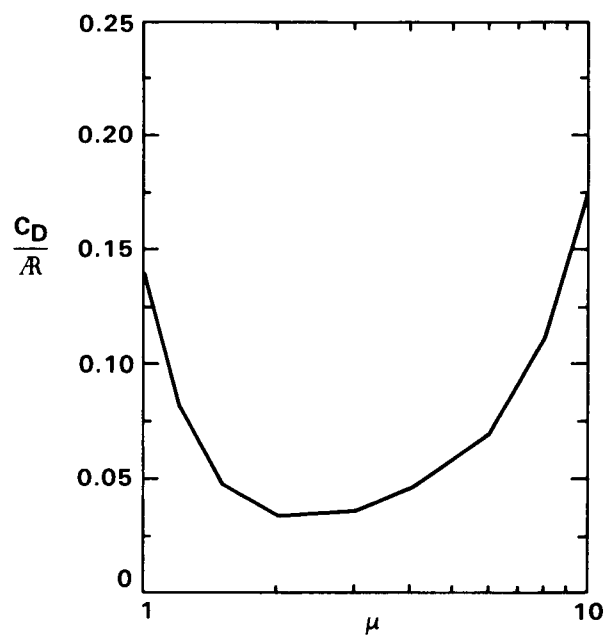


Figure 5 Wave Drag/Aspect Ratio,  $L/D$  Figure of Merit for  $\mu$  Wing-Body Family,  $M_\infty = .995$ ,  $\alpha = .2$  rad.

### ISOMACHS OF $\mu = 1.2$ WING-BODY $M_\infty = 0.995$ , $\alpha = 0.2$ RAD., $\Delta M = 0.1$

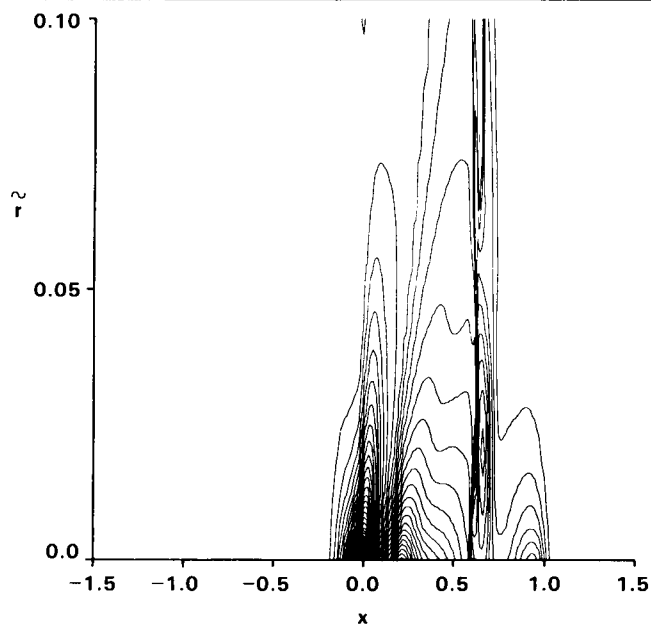


Figure 6a Isomachs of  $\mu = 1.2$  Wing-Body,  $M_\infty = .995$ ,  $\alpha = .2$  rad.



**ISOMACHS OF  $\mu = 2$  WING-BODY**  
 **$M_\infty = 0.995$ ,  $\alpha = 0.2$  RAD.,  $\Delta M = 0.1$**

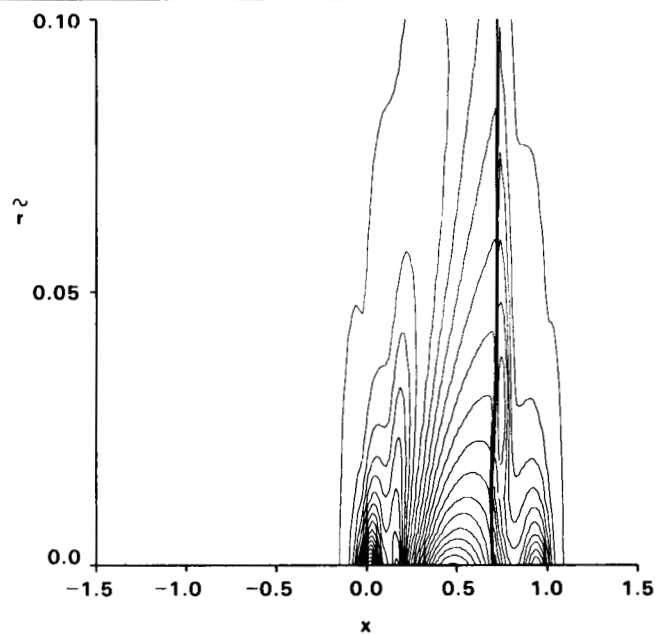


Figure 6b Isomachs of  $\mu = 2.0$  Wing-Body,  $M_\infty = .995$ ,  $\alpha = .2$  rad.

**ISOMACHS OF  $\mu = 10$  WING-BODY**  
 **$M_\infty = 0.995$ ,  $\alpha = 0.2$  RAD.,  $\Delta M = 0.1$**

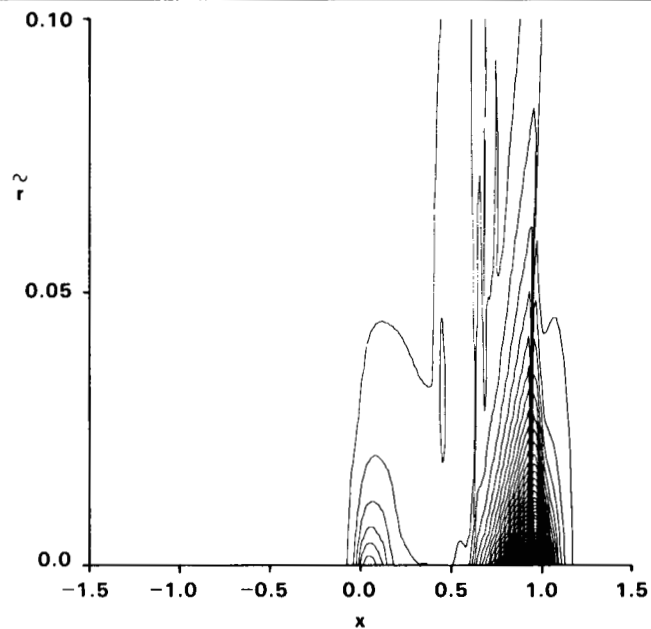


Figure 6c Isomachs of  $\mu = 10.0$  Wing-Body,  $M_\infty = .995$ ,  $\alpha = .2$  rad.

## VECTOR POTENTIAL METHODS

M. Hafez  
University of California  
Davis, CA

## SUMMARY

In this paper vector potential and related methods, for the simulation of both inviscid and viscous flows over aerodynamic configurations, are briefly reviewed. The advantages and the disadvantages of several formulations are discussed and alternate strategies are recommended. The paper consists of the following sections

Introduction

Scalar Potential

Modified Potential

Alternate Formulations of Euler Equations

Least-Squares Formulation

Variational Principles

Remarks on Iterative Techniques and Related Methods

Viscous Flow Simulation

Conclusions

## INTRODUCTION

Most of the recent successful attempts to solve Euler equations are based on the primitive variable formulation where the governing equations are written in a divergence form representing the conservation laws of mass, momentum and energy. The main reason is the capability of correctly capturing flow discontinuities (shocks and wakes) with the help of artificial viscosity terms, explicitly added to the equations or implicitly built in the numerical schemes. Moreover, the conservation laws are basically a hyperbolic system of equations which can be easily integrated in time (using for example explicit schemes like Runge Kutta methods) to obtain the steady state solution. This fact is particularly attractive if unstructured grids are used for simulating flows over complex three-dimensional configurations. Such a calculation can be very efficient on present computers since it is fully vectorizable and indeed very impressive results were obtained using multigrid convergence acceleration techniques.

Artificial viscosity may lead, however, to artificial vorticity, artificial boundary layers and separation. To minimize the contamination of the inviscid solution with such artificial viscous effects, higher order schemes are preferred and to avoid overshoots and undershoots near shocks, flux limiters are applied. Finite-difference schemes, with the total variation diminishing property, are proposed. Because of their diagonal dominance, relaxation methods are applicable and hence they are used as smoothers for multigrid techniques. The limiters, however, are highly nonlinear and some difficulties are expected, such as nonexistence and nonuniqueness of the discrete solution of the conservation laws, as well as slow

convergence and limit cycles. Research efforts will continue to construct high resolution schemes particularly to capture contact discontinuities, and successful applications of multigrid acceleration techniques will follow.

The purpose of the present paper is to examine alternate approaches, particularly for aerodynamic applications. The rationale, here, is very simple; far away from the body, the disturbances are small and the flow can be adequately described by a single equation, with a single unknown (the potential function) and a single parameter (Mach number); the potential formulation is valid, as long as the vorticity in the field is negligible.

One obvious choice is the zonal approach, where the potential formulation is restricted to the irrotational flow zone while the Euler primitive variable formulation is used for the inviscid rotational flow zone. One problem with this approach is the matching of the two local solutions along the interface or in the overlap domain of the two zones. The quality of the solution and the convergence of the overall calculations will depend on the numerical treatment of the interface problem.

Another approach is to augment the potential formulation with the rotational effects. This can be done using the Helmholtz decomposition theorem, where the velocity vector can be represented as the sum of a gradient of a scalar potential function and the curl of a divergence free vector. The correction to the potential formulation automatically vanishes, when the flow is irrotational. The problem with this formulation is the implementation of proper boundary conditions for the corrections particularly for multiply connected domains.

Related to this approach is the use of a variational principle and the Clebsch transformation. The connections to least-squares formulations are also delineated.

Extensions of these methods for viscous flow simulations are discussed and the relation to some viscous/inviscid interaction procedures are depicted.

In the following, recent work on scalar potential methods are reviewed first and then details of the above approaches are studied. Finally, some concluding remarks are drawn.

### SCALAR POTENTIAL

In the recent literature, one can find excellent reviews of methods of solution of the potential equation (See for example Caughey (1), Holst (2) and South (3)). In this section, only the most recent developments will be reviewed.

Steady inviscid flows, with constant entropy and total enthalpy, can be described by a potential function satisfying the continuity equation in conservation form

$$\nabla \cdot (\rho \nabla \phi) = 0 \quad (1)$$

where

$$\rho = (1 - \frac{\gamma-1}{2} M_\infty^2 (|\nabla \phi|^2 - 1))^{-\frac{1}{\gamma-1}} \quad (1')$$

and  $M_\infty$  is the free stream Mach number.

The full potential equation (1) is nonlinear and of mixed type (elliptic in the subsonic region and hyperbolic in the supersonic region). It admits expansion as well as compression shocks. Honest discretization of equation (1) leads to a discrete system of equations with the same properties. One way to exclude expansion shocks is to use artificial viscosity methods. No vorticity can be generated due to the artificial viscosity in such calculations since the velocity field is calculated as a gradient of the potential function. Moreover, for pure subsonic flows, no artificial viscosity is needed and the potential solution should satisfy the Euler equations. On the other hand, to obtain the solution of Euler equations, artificial viscosity is usually needed even for pure subsonic flows.

The artificial viscosity can be introduced in the numerical scheme in many ways. Osher et al. (4) introduced a flux biasing scheme which, unlike the retarded density scheme, does not allow for expansion shocks in the discrete solution of equation (1). This scheme is first-order accurate in the supersonic region, while the artificial viscosity is switched off in the subsonic region. Shankar et al. (5) used it successfully for time-dependent calculations. Volpe and Jameson (6) applied a second-order version of the same scheme in their multigrid code and obtained impressive results.

Recently, Mostrel (7) introduced a second-order accurate scheme, with no subsonic/supersonic switching, and proved global linear stability, total variation diminishing (with flux limiters) and discrete entropy inequality. He also introduced a time splitting algorithm for the 2D low-frequency transonic small disturbance equation. In this area, one should mention the unpublished work of Catherall\* who introduced an approximate factorization scheme, AF2, which consists of two factors only, even for three-dimensional flows.

Various methods are used to accelerate the convergence of potential flow calculations. Besides multigrid, generalized conjugate gradients, generalized minimal residuals (GMRES) and extrapolation procedures can be applied on computers with large memories. For two dimensional (and axisymmetric) problems, direct solvers based on banded Gaussian elimination or nested dissection are nowadays feasible and quadratic convergence can be obtained using Newton's method (8-9). For three dimensional problems, block relaxation and domain decomposition procedures are needed. Some of these algorithms are suitable for parallel processors.

Few years ago, many three-dimensional codes were developed for potential flow calculations. There are two common mistakes in most of these codes. The first is to use a two-dimensional vortex as a far-field boundary condition for each spanwise station. The second is to assume that the flow leaves the airfoil section in a direction bisecting the trailing-edge angle as in two-dimensional problems; this is not true for general three-dimensional lifting flows. In all these codes, the wakes are fixed and are not allowed to adjust with the flow. No effort has been spent to correct these codes and it seems there is no interest to do so! In Europe, a finite-element code based on optimal control formulation was developed at the same time to simulate flow over a complete aircraft. It is not clear, however, how the vortex sheets are treated in such calculations.

Recently, an intensive effort was launched at Boeing to develop a similar code (TRANAIR). Some of its innovative ideas are discussed in ref. (10). (An interesting test case is a wing in an incompressible flow where panel methods can

\*Catherall, D., private communication, July 1985.

predict correctly the induced drag. Moreover, theoretical results are available for certain configurations.)

Finally, no progress has been made to further understand the nonuniqueness problem (11) of the lifting potential flows in the transonic regime. Since no multiple solutions of the Euler equations for the lifting airfoil in the transonic regime have been reported, one tends to assume that the potential model is inadequate. It seems, however, that acceptable results can be obtained if boundary layer interactions are taken into account. After all, the potential flow approximation is only meaningful outside the viscous layers. It seems also that the viscous transonic equation (with uniform viscosity) has a unique solution but no proof is available.

### MODIFIED POTENTIAL

In general, due to the absence of entropy and vorticity effects, shocks in potential solutions are stronger. In this section, approximate methods to account for these effects are discussed.

It is argued that the vorticity effects are higher order. In fact, for straight shocks there is an entropy jump, but there is no entropy gradient downstream of the shock and, therefore, no vorticity is generated (it is well known that vorticity is related to the curvature of the shock). If the vorticity is neglected, the flow downstream of a shock can be also described by a potential function. The flow, however, is no longer isentropic. In this model, the entropy jump is accounted for by modifying the shock point operator. It turns out that the equation downstream of the shock is unaltered (since entropy is constant along streamlines). This approximation is completely equivalent to fit a Rankine-Hugoniot shock in potential flows. Special treatment of wakes may be also required (12), (13).

The next step is to construct a simple approximation for the vorticity effects. This can be achieved by augmenting the velocity due to the potential field by a rotational increment due to the entropy gradient. In two dimensions, an ordinary differential equation is solved for the rotational component,  $\bar{u}$ , namely

$$\frac{\partial \bar{u}}{\partial n} = - \rho \frac{d(\Delta S/R)}{d\psi} \quad (2)$$

For more details see ref. (12).

An approximate solution of equation (2) is simply

$$\bar{u} = - \frac{\rho \frac{\Delta S}{R}}{\rho q} = - \frac{\Delta S/R}{\gamma M_\infty^2} \quad (2')$$

Although the rotational correction is formally higher order than the correction due to the modification of the jump condition across the shock\*, it is not recommended to neglect  $\bar{u}$ , particularly for lifting airfoils.

The reason is clear from examining the work of Klopfer and Nixon (14). Across the wake, the static pressure must be continuous while the total pressure, in general, is not. Therefore, the tangential velocity component must jump. If the flow is presented only by a potential function, the jump of the potential across the wake will grow linearly with the distance from the trailing edge (i.e. in the far field,  $r \rightarrow \infty$ !).

On the other hand, this nonuniformity does not occur if the potential field is augmented by the rotational component. In this case, both the entropy and  $\bar{u}$  jump across the wake while  $\phi_x$  does not. This can be shown by expanding the static pressure formula (assuming the wake is aligned with the x - axis)

$$p = (1 - \frac{\gamma-1}{2} M_\infty^2 ((\phi_x + \bar{u})^2 - 1))^{\frac{\gamma}{\gamma-1}} \cdot e^{-\Delta S/R} / \gamma M_\infty^2 \quad (3)$$

The contribution of the entropy term cancels the contribution of the rotational component and therefore  $\phi_x$  must be continuous to guarantee continuous static pressure across the wake.

For the three-dimensional flows, the calculations of the rotational velocity components are more complicated as will be discussed in the next sections. As a crude approximation, the two-dimensional formula can be used in each spanwise station. Dang and Chen (15) used instead, the following formula

$$\vec{q} = \nabla \phi - \frac{\Delta S/R}{\gamma M_\infty^2 (n_x \cos \alpha + n_y \sin \alpha)} \hat{n} \quad (4)$$

where  $\hat{n} = n_x \hat{e}_x + n_y \hat{e}_y$  is normal to the shock surface. In our opinion, the extra computational effort in the calculation of  $\hat{n}$  is not justifiable and the assumption of a locally normal shock is consistent with the other approximations made in the derivation of the rotational velocity component formulas ((2') as well as (4)).

\* From Prandtl relation,  $(1+u_1) \cdot (1+u_2) = a^*{}^2$ , the correction to the shock jump condition to allow for entropy generation is second order, while  $\bar{u}$  is third order.

## ALTERNATE FORMULATIONS OF EULER EQUATIONS

### Two-Dimensional Flows

In this section, no small disturbance approximations are assumed and the treatment of the exact inviscid equations is discussed. It is instructive to consider first a simple case of two-dimensional inviscid incompressible steady flow. The conservation laws are usually written in terms of the continuity and the momentum equations. On the other hand, the following equations are completely equivalent:

$$\begin{aligned} u_x + v_y &= 0 \\ -u_y + v_x &= \omega (\psi) \end{aligned}$$

$$\frac{P}{\rho} + \frac{1}{2} (u^2 + v^2) = H(\psi) \quad (5)$$

where  $\omega$  and  $H$  are constants along streamlines. Equation (5) represents conservation of mass, vorticity and total enthalpy. The first two equations are linear in  $u$  and  $v$ ; the pressure is decoupled and is obtained from Bernoulli's law. If equation (5) is used, contact discontinuities (wakes) must be fitted and no artificial viscosity is needed in such calculations.

The exact equation for two-dimensional inviscid compressible flows is

$$W_t + F_x + G_y = 0 \quad (6)$$

where  $W = (\rho, \rho u, \rho v, \rho e)^T$  and  $F$  and  $G$  are the corresponding flux vectors. The Jacobian of  $F$  has the eigenvalues  $u \pm a, 0, 0$ , and similarly the Jacobian of  $G$  has the eigenvalues  $v \pm a, 0, 0$ , where  $a$  is the speed of sound. Four modes are identifiable: two acoustic modes, entropy mode and vorticity mode. In fact, for steady flows, the above equations can be rewritten in the following nonconservative form:

$$(a^2 - u^2) u_x - uvv_x - uvu_y + (a^2 - v^2) v_y = 0 \quad (6a)$$

$$-u_y + v_x = \omega \quad (6b)$$

$$\frac{D\Delta S/R}{Dt} = 0 \quad (6c)$$

$$\frac{DH}{Dt} = 0 \quad (6d)$$

where  $\frac{D}{Dt}$  is the substantial derivative.

The vorticity  $\omega$  is calculated from the Crocco's relation

$$\omega = \rho \frac{d\Delta S/R}{d\psi} - \rho \frac{dH}{d\psi} \quad (7)$$

The speed of sound is given by

$$a^2 = (\gamma - 1) \left( H - \frac{q^2}{2} \right) \quad (8)$$

where  $q^2 = u^2 + v^2$ , and the density and the pressure relations are

$$\rho = (M_\infty^2 a^2)^{\frac{1}{\gamma-1}} \cdot e^{-\Delta S/R} \quad (9)$$

$$p = (M_\infty^2 a^2)^{\frac{\gamma}{\gamma-1}} \cdot e^{-\Delta S/R} / \gamma M_\infty^2 \quad (9')$$

$\Delta S/R$  must have the proper jump across the shock to satisfy the Rankine Hugoniot relations.

It is clear from equations (6a) and (6b) that the corresponding characteristics have the same form for rotational and irrotational flows.

A shock fitting procedure must be used with this nonconservative formulation. In refs. (12), (16), the author used the Prandtl relations across the shock

$$q_{1n} q_{2n} = a^*{}^2 - \frac{\gamma-1}{\gamma+1} q_t^2 \quad (10a)$$

$$q_{t_1} = q_{t_2} = q_t \quad (10b)$$

For flows with constant entropy and total enthalpy, the vorticity vanishes and the irrotational motion can be represented by a potential field. The weak solution admitted by the potential equation (1) reflects conservation of mass under the isentropic assumption. On the other hand, in the modified potential formulation, the Prandtl relations are forced across the shock, which implies that the mass, including entropy effects, is conserved. To fully account for the entropy effects, a rotational velocity field due to the vorticity generated by the shock curvature must be added to the potential field; therefore, it is natural to use the decomposition

$$u = \phi_x + \tilde{u} \quad (11a)$$

$$v = \phi_y + \tilde{v} \quad (11b)$$

Obviously, such a decomposition is not unique; the rotational velocity components are not independent. A feasible constraint is

$$\tilde{u}_x + \tilde{v}_y = 0 \quad (12)$$



Such a constraint is automatically satisfied if a perturbative stream function  $\tilde{\psi}$  is introduced, such that

$$\tilde{u} = \tilde{\psi}_y \text{ and } \tilde{v} = -\tilde{\psi}_x \quad (13-14)$$

Thus, the governing equations for  $\phi$  and  $\tilde{\psi}$  are

$$(\rho\phi_x)_x + (\rho\phi_y)_y = -(\rho\tilde{\psi}_y)_x + (\rho\tilde{\psi}_x)_y \quad (15a)$$

$$\tilde{\psi}_{xx} + \tilde{\psi}_{yy} = -\omega \quad (15b)$$

Equations (12) & (13) are solved in ref. (13). Chaderjian and Steger (17) used a similar approach for the lifting airfoil problem, where both  $\phi$  and  $\tilde{\psi}$  are chosen to be continuous across the wake.

Another choice is

$$u = \phi_x + \tilde{\psi}_y/\rho \quad (16a)$$

$$v = \phi_y - \tilde{\psi}_x/\rho \quad (16b)$$

In this case the governing equations are

$$(\rho\phi_x)_x + (\rho\phi_y)_y = 0 \quad (17a)$$

$$(\tilde{\psi}_y/\rho)_y + (\tilde{\psi}_x/\rho)_y = -\omega \quad (17b)$$

With proper boundary conditions for  $\tilde{\psi}$ ,  $\phi$  can vanish identically. The solution of the transonic stream function equation is discussed in refs. (12) and (18). In ref. (19), Papailiou et al. used the decomposition

$$\rho u = \phi_x + \tilde{\psi}_y \quad (18a)$$

$$\rho v = \phi_y - \tilde{\psi}_x \quad (18b)$$

The corresponding equations are

$$\phi_{xx} + \phi_{yy} = 0 \quad (19a)$$

and 
$$(\tilde{\psi}_y/\rho)_y + (\tilde{\psi}_x/\rho)_x = -\omega \quad (19b)$$

In all these cases, a partial differential equation for the correction must be solved. Other decompositions require only the solution of ordinary differential equations. For example, the choice of  $\tilde{v} = 0$  in (11b) leads to

$$(\rho\phi_x)_x + (\rho\phi_y)_y = -(\rho\tilde{u})_x \quad (20a)$$

and 
$$\tilde{u}_y = -\omega \quad (20b)$$

For certain grids, aligned locally with the flow, this decomposition is obviously useful. Another example is based on a multiplicative correction,

$$u = \lambda\phi_x \quad (21a)$$

$$v = \lambda\phi_y \quad (21b)$$

The corresponding equations are

$$(\bar{\rho}\phi_x)_x + (\bar{\rho}\phi_y)_y = 0 \quad (22a)$$

$$\phi_x \lambda_y - \phi_y \lambda_x = -\omega \quad (22b)$$

where  $\bar{\rho} = \lambda\rho \quad (23)$

The general Clebsch representation has both additive and multiplication corrections, as will be discussed later. Based on this discussion, the full stream function formulation is the most recommended one. It is not widely used for transonic flows, however, because of the difficulties associated with the nonunique relationship between the density and the flux. The same remark holds for axisymmetric flows (including swirl).

### Three-Dimensional Flows

The conservation laws are given by

$$w_t + F_x + G_y + H_z = 0 \quad (5')$$

The eigenvalues of the Jacobians of F, G, and H are  $u \pm a, 0, 0, 0$ ,  $v \pm a, 0, 0, 0$  and  $w \pm a, 0, 0, 0$ . Acoustic, entropy and vorticity modes are still identifiable but the problem is more complicated since the vorticity has in general three nonzero components.

For steady flows, the governing equations can be rewritten in the form:

$$\nabla \cdot \rho \vec{q} = 0 \quad (24)$$

$$\nabla \times \vec{q} = \vec{\omega} \quad (25)$$

Assuming  $\rho$  and  $\vec{\omega}$  are given, equations (24) and (25) are four equations in three unknowns. There is, however, a relation between the vorticity components

$$\nabla \cdot \vec{\omega} = 0 \quad (26)$$

The Crocco relation is used to calculate two of the vorticity components

$$\vec{q} \times \vec{\omega} = -T\nabla S + \nabla H \quad (27)$$

The streamwise vorticity component can be calculated using equation (26). Alternatively, taking the cross product of (27) with  $\vec{q}$ , one can obtain the following formula for the vorticity (see refs. (21), (22), (24))

$$\vec{\omega} = \lambda \rho \vec{q} + \frac{\vec{q}}{|\vec{q}|^2} \times (T\nabla S - \nabla H) \quad (28)$$

Equation (26) leads to an equation for  $\lambda$

$$\rho \vec{q} \cdot \nabla \lambda = - \nabla \cdot \left[ \frac{\vec{q}}{|\vec{q}|^2} \times (\nabla S - \nabla H) \right] \quad (29)$$

The entropy and the total enthalpy transport equations are

$$\vec{q} \cdot \nabla S = 0 \quad (30)$$

$$\vec{q} \cdot \nabla H = 0 \quad (31)$$

While  $H$  and  $\lambda$  are continuous across a shock,  $S$  jumps. The speed of sound, the density and the pressure are obtained from equations (8), (9) and (9'), where  $q^2 = |\vec{q}|^2$ .

Using the Helmholtz theorem,  $\vec{q}$  can be decomposed into the gradient of a scalar function plus the curl of another vector

$$\vec{q} = \nabla \phi + \nabla \times \vec{\psi} \quad (32)$$

The first term on the right hand side of equation (27) is curl free, while the second term is divergence free. A feasible constraint on  $\vec{\psi}$  is

$$\nabla \cdot \vec{\psi} = 0 \quad (33)$$

Hence, equations (24) and (25) reduce to

$$\nabla \cdot (\rho \nabla \phi) = - \nabla \cdot (\rho \nabla \times \vec{\psi}) \quad (34)$$

$$\nabla^2 \vec{\psi} = - \vec{\omega} \quad (35)$$

The correction to the potential solution becomes a major effort, it requires the solution of three Poisson's equations in three dimensions.

The boundary condition for the potential problem is

$$\vec{n} \cdot \nabla \phi = - \vec{n} \cdot \nabla \times \vec{\psi} \quad (36)$$

where  $\vec{n}$  is normal to the solid surface. Two linear combinations of the stream functions can be kept constant on the boundary surface, and equations (33) can be used to solve for a third linear combination.

For example, in orthogonal coordinates, two components of  $\vec{\psi}$  can be chosen to be constant in the plane tangent to the body, hence  $\vec{n} \cdot \nabla \times \vec{\psi} = 0$ , while the normal derivative of the third component vanishes. The boundary conditions in generalized curvilinear coordinates are given in refs. (20), (21), for simply connected domains.

In a series of interesting papers (22), (23), (24), Dabaghi and Pironneau studied the vector potential method and obtained two- and three-dimensional finite-element solutions for transonic flow problems. The following variational problems are considered. For a given vector field  $\vec{q}$ , find  $\phi$  and  $\vec{\psi}$  such that:

$$(\nabla\phi, \nabla w) = (\vec{q}, \nabla w) \quad (37)$$

$$\begin{aligned} (\nabla x \vec{\psi}, \nabla x \vec{v}) + (\nabla \cdot \vec{\psi}, \nabla \cdot \vec{v}) \\ = (\vec{q}, \nabla x \vec{v}) \end{aligned} \quad (38)$$

where  $w$  and  $\vec{v}$  are proper weighting functions ( $\vec{v} x \vec{n}|_{\Gamma} = 0$ ,  $\int_{\Gamma} \vec{v} \cdot \vec{n} d\gamma = 0$ ;  $\Gamma$  is the boundary of a simply connected domain). It can be shown rigorously that the Helmholtz decomposition is unique

$$\vec{q} = \nabla\phi + \nabla x \vec{\psi} \text{ and } \nabla \cdot \vec{\psi} = 0 \quad (39)$$

The variational form of the vector identity

$$\nabla x \nabla x \vec{\psi} = -\Delta \vec{\psi} + \nabla \nabla \cdot \vec{\psi} \quad (40)$$

is given by

$$(\nabla \vec{\psi}, \nabla \vec{v}) = (\nabla x \vec{\psi}, \nabla x \vec{v}) + (\nabla \cdot \vec{\psi}, \nabla \cdot \vec{v}) + 2 \int_{\Gamma} \frac{\vec{\psi} \cdot \vec{v}}{R} d\gamma \quad (41)$$

where  $R$  is the mean radius of curvature of  $\Gamma$ . Therefore, equation (38) for  $\vec{\psi}$  is equivalent to

$$\begin{aligned} -\Delta \vec{\psi} &= \vec{\omega} \\ \frac{\partial \vec{\psi}}{\partial n} \cdot \vec{n} - 2 \frac{\vec{\psi} \cdot \vec{n}}{R} &= 0 \text{ on } \Gamma \\ \vec{\psi} \times \vec{n}|_{\Gamma} &= 0 \end{aligned} \quad (42)$$

In general, the three components of  $\vec{\psi}$  are coupled through the boundary conditions. The formulation has been extended to multiply connected domains by Dominguez (25). Across the wakes, the potential function jumps and the circulations (the difference in potential values) remain constant, while the normal component of the gradient of the potential is continuous. If the wake surface is denoted by  $\Sigma_j$  and the circulation by  $\lambda_j$  then

$$\left[ \phi \right]_{\Sigma_j} = \lambda_j, \quad \left[ \frac{\partial \phi}{\partial n} \right]_{\Sigma_j} = 0 \quad (43)$$

The following constraints must be imposed on  $\vec{\psi}$ :

$$\int_{\Gamma_i} \vec{\psi} \cdot \vec{n} d\gamma = \mu_i \quad (44)$$

where  $\mu_i$  are constants. The decomposition is no longer unique. It is unique, however, when  $\mu_i$  are given and  $\lambda_j$  are adjusted so that

$$\nabla\phi + \nabla x \vec{\psi} = \vec{q} \text{ on } \Sigma \quad (45)$$

The extra difficulty for nonsimply connected domains stems from the fact that

$$\nabla \times \vec{q} = 0, \nabla \cdot \vec{q} = 0, \vec{q} \cdot \vec{n}|_{\Gamma} = 0 \quad (46a)$$

does not imply  $\vec{q} = 0$  (see ref. (26)).

Unlike the primitive variable formulation of Euler equations, a special treatment of the Kutta condition (pressure is continuous at trailing edges) is required.

Another choice for the velocity decomposition is

$$\vec{q} = \nabla \phi + (\nabla \times \vec{\Psi})/\rho \quad (46b)$$

With proper nonhomogeneous boundary conditions for  $\vec{\Psi}$ ,  $\phi$  can vanish identically. This case is simply an extension of the stream function formulation to three dimensional flows. The equation for  $\vec{\Psi}$  is

$$\nabla \times (\nabla \times \vec{\Psi})/\rho = \vec{\omega} \quad (47)$$

and the boundary condition is

$$\vec{n} \cdot \nabla \times \vec{\Psi}|_{\Gamma} = \vec{q} \cdot \vec{n} \quad (48)$$

Hirasaki and Hellums (27)-(29) and Richardson and Cornish (29) studied a similar problem. A partial differential equation on the surface of the boundary must be solved. The corresponding variational formulation is given by Dabaghi and Pironneau (24). The problem is to find a function  $g$  such that

$$\vec{\Psi} \times \vec{n}|_{\Gamma} = g \quad (49)$$

implies equation (48).

It is shown that  $g = \nabla f$  where  $f|_{\Gamma}$  is the unique solution of a Laplace-Beltrami equation

$$\int_{\Gamma} \left( \frac{\partial f}{\partial s_1} \frac{\partial w}{\partial s_1} + \frac{\partial f}{\partial s_2} \frac{\partial w}{\partial s_2} \right) d\gamma = - \int_{\Gamma} \vec{q} \cdot \vec{n} w d\gamma \quad (50)$$

where  $w$  is a weighting function and  $(s_1, s_2)$  is a set of an orthogonal local coordinate system on  $\Gamma$ .

In ref. (20), Papailiou et al. used the decomposition

$$\rho \vec{q} = \nabla \phi + \nabla \times \vec{\Psi} \quad (51)$$

and  $\nabla \cdot \vec{\Psi} = 0$ .

Therefore, the equations for  $\phi$  and  $\vec{\Psi}$  are

$$\nabla^2 \phi = 0 \quad (52a)$$

$$-\nabla^2 \vec{\Psi} = \frac{1}{\rho} \nabla \rho \times (\rho \vec{q}) + \rho \vec{\omega} \quad (52b)$$

Lagging the density in the right hand side of equation (52b) may lead to convergence difficulties for transonic flow calculations.

In all these variations, the stream vector  $\vec{\psi}$  has three components. In ref. (30), another method is proposed. One of the components of  $\vec{\psi}$  is chosen to vanish identically, and viscous flows over a three-dimensional trough are calculated. The application to inviscid transonic flow calculations is given in ref. (31).

Giese (32) proposed also a representation of the flux vector in three dimensions using two scalar stream functions ( $\psi$  and  $\theta$ )

$$\rho \vec{q} = \nabla \psi \times \nabla \theta \quad (53)$$

The continuity equation is automatically satisfied since  $\nabla \cdot \rho \vec{q} = \nabla \cdot \nabla \psi \times \nabla \theta = 0$ . In this formulation, the body is a stream surface. The equations for  $\psi$  and  $\theta$  are obtained from

$$\nabla \times (\nabla \psi \times \nabla \theta / \rho) = \vec{\omega} \quad (54)$$

No numerical solutions are reported in the literature for transonic flow problems. In ref. (33) an application to hypersonic flows around a body of revolution at an angle of attack is discussed.

Recently, Rose (34) proposed to solve the Cauchy-Riemann equations using a finite element scheme where a three-dimensional potential solution in the element and only two dimensional stream function solutions on the boundary faces of the element, are required.

#### LEAST-SQUARES FORMULATIONS

In ref. (35), Fasel proposed to solve the incompressible flow equations using a velocity/vorticity formulation, where the pressure is eliminated. The equations  $\nabla \cdot \vec{q} = 0$  and  $\nabla \times \vec{q} = \vec{\omega}$  are replaced by

$$\nabla^2 \vec{q} = - \nabla \times \vec{\omega} \quad (55)$$

For viscous flow calculations,  $\vec{q} = 0$  on the solid surface and three Poisson's equations for three velocity components are solved, while  $\vec{\omega}$  is obtained from the vorticity transport equation. (Recently, Rose et al. (36) and Osswald et al. (37) solved the system of the first order equations directly).

It seems that, unlike the stream function formulations, there is no difficulty with the boundary conditions. This is not true in general, since conservation of mass is not explicitly imposed and careful treatment of boundary conditions is required, particularly for inviscid flows.

In ref. (38), the author proposed a least squares formulation with a systematic treatment of the boundary conditions. For the continuous problem, the following functional is minimized

$$I(\vec{q}) = \int_{\Omega} \alpha (\nabla \cdot \vec{q})^2 + |\nabla \times \vec{q} - \vec{\omega}|^2 d\Omega \quad (56)$$

where  $\alpha$  is a Lagrange multiplier. The functional  $I$  is discretized first on structured (or unstructured) grids. Minimization of the discrete version of  $I$ ,

with respect to the unknowns at each node leads to a conditioned system of algebraic equations.

To demonstrate the relation between the least-squares and the vector potential formulations, we consider first the two-dimensional incompressible flow case. The equations, in general, are

$$u_x + v_y = s \quad (57)$$

$$-u_y + v_x = \omega \quad (58)$$

where the  $s$  term in equations (57) represents sources or sinks in the field. Equations (57) and (58) are written in the form

$$L \begin{pmatrix} u \\ v \end{pmatrix} = \begin{pmatrix} s \\ \omega \end{pmatrix} \quad (59)$$

The least-squares formulation leads to the second order equations

$$L^* L \begin{pmatrix} u \\ v \end{pmatrix} = L^* \begin{pmatrix} s \\ \omega \end{pmatrix} \quad (60)$$

where  $L^*$  is the adjoint operator.

Alternatively, new variable  $\phi$  and  $\psi$  can be defined by the equation

$$L^* \begin{pmatrix} \phi \\ \psi \end{pmatrix} = \begin{pmatrix} u \\ v \end{pmatrix} \quad (61)$$

Hence, equation (59) becomes

$$LL^* \begin{pmatrix} \phi \\ \psi \end{pmatrix} = \begin{pmatrix} s \\ \omega \end{pmatrix} \quad (62)$$

The variables  $\phi$  and  $\psi$  represents a potential and a stream function. Notice the right-hand side in equation (60) is differentiated while in equation (62), it is unaltered.

The extension to compressible three dimensional flows is given in ref. (39). In cartesian coordinates, the equations are

$$\begin{aligned} (\rho u)_x + (\rho v)_y + (\rho w)_z &= s \\ v_x - u_y &= \omega_3 \\ -w_x + u_z &= \omega_2 \\ w_y - v_z &= \omega_1 \end{aligned} \quad (63)$$

Equation (63) is written in the form

$$\begin{bmatrix} -\rho \partial_x & \partial_y \rho & \partial_z \rho \\ -\partial_y & \partial_x & 0 \\ \partial_z & 0 & -\partial_x \\ 0 & -\partial_z & \partial_y \end{bmatrix} \begin{bmatrix} u \\ v \\ w \end{bmatrix} = \begin{bmatrix} s \\ \omega_3 \\ \omega_2 \\ \omega_1 \end{bmatrix} \quad (64)$$

The variables  $\phi$ ,  $\psi_1$ ,  $\psi_2$  and  $\psi_3$  are introduced via the adjoint operator.

$$\begin{bmatrix} -\rho \partial_x & \partial_y & -\partial_z & 0 \\ -\rho \partial_y & -\partial_x & 0 & \partial_z \\ -\rho \partial_z & 0 & \partial_x & -\partial_y \end{bmatrix} \begin{bmatrix} \phi \\ \psi_3 \\ \psi_2 \\ \psi_1 \end{bmatrix} = \begin{bmatrix} \rho u \\ \rho v \\ \rho \omega \end{bmatrix} \quad (65)$$

or, 
$$-\rho \vec{q} = \rho \nabla \phi + \nabla \times \vec{\psi} \quad (66)$$

If  $s = 0$ ,  $\phi$  can identically vanish. Furthermore, if one of the  $\vec{\psi}$  components is chosen to be zero, a two-component stream function formulation can be obtained. Therefore, vector potential formulations are special cases of least squares.

## VARIATIONAL PRINCIPLES

### Unsteady Flows

When Lagrangian coordinates are used, the equations of motion can be derived from Hamilton's principle (that the difference of kinetic energy and potential energy be stationary). In the Eulerian description, Seliger and Whitham (40) considered the functional

$$\begin{aligned} \iint_R \left[ \left( \frac{1}{2} \rho q_i^2 - \rho e \right) + \phi \left( \frac{\partial \rho}{\partial t} + \frac{\partial (\rho q_i)}{\partial x_i} \right) \right. \\ \left. + \eta \left( \frac{\partial (\rho S)}{\partial t} + \frac{\partial (\rho q_i S)}{\partial x_i} \right) \right. \\ \left. + \beta \left( \frac{\partial (\rho \alpha)}{\partial t} + \frac{\partial (q_i \alpha)}{\partial x_i} \right) \right] dx dt \end{aligned} \quad (67)$$

where  $\phi$ ,  $\eta$  and  $\beta$  are Lagrange multipliers.

The variations with respect to  $q_i$ ,  $\rho$ ,  $S$ ,  $\alpha$  lead to

$$\begin{aligned} \delta q_i: q_i &= \frac{\partial \phi}{\partial x_i} + S \frac{\partial \eta}{\partial x_i} + \alpha \frac{\partial \beta}{\partial x_i} \\ \delta \rho: h &= \frac{1}{2} q_i^2 - \frac{D\phi}{Dt} - \alpha \frac{D\beta}{Dt} - S \frac{D\eta}{Dt} \\ \delta S: \frac{D\eta}{Dt} &= -T \end{aligned}$$



$$\delta\alpha: \frac{D\beta}{Dt} = 0 \quad (68)$$

where 
$$h = e + \frac{p}{\rho} = \frac{\gamma}{\gamma-1} \frac{p}{\rho}.$$

The variations of  $\phi, \eta$  and  $\beta$  reproduce the constraints

$$\delta\phi: \frac{\partial \rho}{\partial t} + \frac{\partial(\rho q_i)}{\partial x_i} = 0$$

$$\delta\eta: \frac{DS}{Dt} = 0$$

$$\delta\beta: \frac{D\alpha}{Dt} = 0 \quad (68')$$

The coordinate  $\alpha$  does not change along a particle path and the terms  $\alpha \nabla \beta$  in the velocity allow the representation of an initial vorticity to be separated from those produced by subsequent entropy gradients. In this representation the vorticity is given by

$$\vec{\omega} = \nabla S \times \nabla \eta + \nabla \alpha \times \nabla \beta \quad (69)$$

Seliger and Whitham (40) derived also a simplified form of the variational principle (67). Upon integration by parts the integrand  $L$  in (67) is equivalent to

$$L = \frac{1}{2} \rho q^2 - \rho e - \rho \frac{D\phi}{Dt} - \rho S \frac{D\eta}{Dt} - \rho \alpha \frac{D\beta}{Dt} \quad (70)$$

(all variations are taken to vanish on the boundary  $R$ )

From Equation (68),

$$L = \rho h - \rho e = p \quad (71)$$

Therefore, one can start directly with the functional

$$\iint_R p \, dX \, dt \quad (72)$$

where

$$p = p(h, S)$$

$$p_h = \rho, \quad p_S = -\rho T$$

Introducing a Clebsch representation for the velocity

$$\vec{q} = \nabla \phi + S \nabla \eta + \alpha \nabla \beta \quad (73)$$

where

$$h = -\phi_t - S\eta_t - \alpha\beta_t - \frac{1}{2}q_i^2 \quad (74)$$

the variations of the integral of the pressure with respect to  $\phi$ ,  $S$ ,  $\eta$ ,  $\alpha$  give exactly the corresponding equations of (68) and (68').

While the form in (72) is far from Hamilton's, it can be considered as a generalization of the well known Bateman principle of isentropic flows. It is noticed, however, that  $\alpha$ ,  $\beta$  are not uniquely defined by (73) since any perfect differential may be added to  $\phi$  with consequent changes in  $\alpha$  and  $\beta$ . From the equations of motion, it can be shown that

$$\frac{\partial (\Pi, \alpha, \beta)}{\partial (x, y, z)} = 0$$

where 
$$\Pi = h + \frac{1}{2}q_i^2 + \phi_t + S\eta_t + \alpha\beta_t \quad (75)$$

Therefore,  $\Pi = \Pi(\alpha, \beta, t)$  and  $\alpha$  and  $\beta$  can be obtained from the Hamiltonian form

$$\frac{D\alpha}{Dt} = -\frac{\partial \Pi}{\partial \beta}, \quad \frac{D\beta}{Dt} = \frac{\partial \Pi}{\partial \alpha} \quad (76)$$

It is sometimes advantageous to retain  $\Pi \neq 0$  and to use (75) in place of (74). The variational principle (72) is not modified but the variations with respect to  $\alpha$  and  $\beta$  then give (76) as required.

In fact, some of these ideas are very old. The velocity representation in (68) was first introduced by Clebsch in 1859, for the case of incompressible flow. Lamb (1932) considered a barotropic flow ( $p = p(\rho)$ ), where any velocity can be represented by

$$\vec{q} = \nabla\phi + \alpha\nabla\beta$$

and the momentum equations can be integrated to yield

$$\int \frac{dp}{\rho} + \frac{1}{2}q_i^2 = -\phi_t - \alpha\beta_t$$

where 
$$\frac{D\alpha}{Dt} = 0 \quad \text{and} \quad \frac{D\beta}{Dt} = 0.$$

The alternative Hamiltonian form of  $\alpha$  and  $\beta$  equations was first introduced by Stuart in 1900.

Recently, Buneman (41) showed that the flow equations can be put in a Hamiltonian form, with benefit for numerical schemes. He considered the isentropic flow case with Clebsch variables

$$\rho \vec{q} = -\sigma \nabla \mu - \rho \nabla \phi \quad (77)$$

Thus, the vortical and irrotational parts of the flow are represented in a symmetric manner. Note that there would be a similar third term if entropy changes are taken into account. In terms of  $\rho$ ,  $\phi$ ,  $\sigma$  and  $\mu$ , the following functional derivatives are obtained

$$\begin{aligned} \frac{\partial \Pi}{\partial \phi} &= \nabla \cdot \rho \vec{q} = -\frac{\partial \rho}{\partial t} \\ \frac{\partial \Pi}{\partial \rho} &= c \gamma \rho^{\gamma-1} - \frac{1}{2} \left(\frac{\sigma}{\rho}\right)^2 (\nabla \mu)^2 + \frac{1}{2} (\nabla \phi)^2 = \frac{\partial \phi}{\partial t} \\ \frac{\partial \Pi}{\partial \sigma} &= -\vec{q} \cdot \nabla \mu = \frac{\partial \mu}{\partial t} \\ \frac{\partial \Pi}{\partial \mu} &= -\nabla \cdot \sigma \vec{q} = -\frac{\partial \sigma}{\partial t} \end{aligned}$$

$$\text{where} \quad \Pi = C \rho^\gamma + (\sigma \nabla \mu + \rho \nabla \phi)^2 / 2\rho \quad (78)$$

and  $c$  is a constant.

The first equation is conservation of mass, and the second is a generalized Bernoulli equation. The third and the fourth equations are statements that the vortex parameters  $\mu$  and  $\sigma/\rho$  follow the flow. With this Hamiltonian form, one can stagger data for densities and potentials in space as well as in time. Also, densities can be updated by leap-frogging over potentials and vice-versa. No numerical solutions based on this formulation have been reported.

On the other hand, Ecer and Akay (42) were successful to calculate rotational and transonic flows using a variational principle similar to (67). They considered the functional

$$\begin{aligned} \iint_R \left[ \left( \frac{1}{2} \text{eq}_i^2 - \rho e \right) + \phi \left( \frac{\partial \rho}{\partial t} + \frac{\partial (\rho q_i)}{\partial x_i} \right) \right. \\ \left. + \beta_k \rho \frac{D \alpha_k}{Dt} \right] dx dt \\ + \iint_{\Gamma_1} f_\phi dr dt + \iint_{\Gamma_2} f_{\beta_k} dr dt \end{aligned} \quad (79)$$

where  $\Gamma_1$  and  $\Gamma_2$  are those portions of the boundaries where the following flux type quantities are specified.

$$f_{\phi} = \rho \vec{q} \cdot \vec{n} \quad (80)$$

$$f_{\beta_k} = \rho \alpha_k \vec{q} \cdot \vec{n} \quad (81)$$

The variations of (79) with respect to  $\alpha$  and  $\beta$  give

$$\delta\beta_k: \rho \frac{D\alpha_k}{Dt} = 0$$

$$\delta\alpha_k: \rho \frac{D\beta_k}{Dt} = \rho \frac{dH}{d\alpha_k} - \frac{p}{R} \frac{\partial S}{\partial \alpha_k} \quad (82)$$

Another choice is also suggested in ref. (42). The total enthalpy is employed as a primary variable to replace the material coordinate  $\alpha$  in (67). The proposed variational principle is, however, incorrect, since the energy equation for unsteady flow is

$$\frac{DH}{Dt} = \frac{1}{\rho} \frac{\partial p}{\partial t} \quad (83)$$

and  $H$  does change along a particle path!

#### Steady Flows

Roberts (43) used directly the following decomposition for steady flows

$$\vec{q} = \vec{q}_0 + \nabla\phi + (S-S_0) \nabla\eta + (H-H_0) \nabla\beta \quad (84)$$

where the equations for  $\eta$  and  $\beta$  are given by

$$\frac{D\eta}{Dt} = -1 \quad (85)$$

$$\frac{D\beta}{Dt} = 1$$

For multiple shocks, multiple  $\eta$  fields must be introduced and the contribution to the velocity is given by

$$\sum_{t=1}^k (S_t - S_{t-1}) \nabla\eta_t \quad (86)$$

Similarly, multiple  $\beta$  fields must be introduced for multiple wakes. On the other hand, for isoenergetic flows,  $\beta$  vanishes identically. Grossman (44) calculated

successfully supersonic conical flows, with strong rotationality due to shocks, using such a decomposition.

For a thin body in a uniform flow, using small disturbance approximations, equation (85) becomes

$$u \frac{\partial \eta}{\partial x} = -T \quad (85')$$

substituting equation (85') into (84) yields

$$\begin{aligned} \vec{q} &\approx 1 + \nabla \phi \cdot \Delta S/R \frac{p}{\rho u} \vec{i} \\ &\approx 1 + \nabla \phi \cdot \frac{\Delta S/R}{\gamma M_\infty^2} \vec{i} \end{aligned} \quad (84')$$

The rotational component in equation (84') is identical with equation (2') which is derived based on Helmholtz decomposition.

A modified form of Clebsch representation was introduced by Hirsch et al. (45).

$$\vec{q} = \nabla \phi + \psi_1 \nabla S + \psi_2 \nabla H \quad (87)$$

Substituting equation (87) into the Crocco relation, one obtains for arbitrary and independent entropy and rothalpy gradients, the two equations for  $\psi_1$  and  $\psi_2$

$$\frac{D\psi_1}{Dt} = T$$

$$\frac{D\psi_2}{Dt} = -1 \quad (88)$$

A simplified representation can be obtained if a unique relation between S and H exists in the inlet flow field. In ref. (46), the authors discussed applications to rotational internal subsonic flows in ducts.

It is clear from the above discussion that the computational effort required for the variational principle formulation is less than that needed for the implementation of least squares or vector potentials. Thanks to Clebsch, we have a generalized Bernoulli equation for rotational, nonisentropic steady and unsteady flows.

#### REMARKS ON ITERATIVE TECHNIQUES AND RELATED METHODS

A common problem in all the various formulations discussed so far is the solution of a nonhomogeneous potential equation, where the right-hand side represents the rotational effects. A crucial point in developing an iterative technique to solve this nonlinear problem is to account for the mixed type nature of this equation.

Moreover, the characteristics of this equation should be based on the total velocity and not on the irrotational part only.

Techniques based on lagging the density as well as the rotational components are not reliable for transonic flow calculations. For example, the potential equation for two dimensional flows may be written in the form

$$(\rho^{n-1} \phi_x)_x + (\rho^{n-1} \phi_y)_y = -(\rho^{n-1} \bar{u})_x - (\rho^{n-1} \bar{v})_y \quad (89)$$

where  $n$  is the iteration count. Obviously, one should expect convergence difficulties since an asymmetric operator is replaced by a symmetric one. In practice, a crude solution may be obtained, if excessive artificial viscosity is used. To construct a scheme, independent of the artificial viscosity, equation (89) may be replaced by

$$\frac{\rho}{a^2} ((a^2 - u^2) \delta\phi_{xx} - 2uv \delta\phi_{xy} + (a^2 - v^2) \delta\phi_{yy}) = -(\rho u)_x - (\rho v)_y \quad (90)$$

It is not important to keep the left-hand side of equation (90) in conservative form and there are well-known methods to solve such a mixed type equation. Note, the potential correction will not affect the correction to the vorticity equation and ideally, the rotational components can be constructed such that they conserve mass. In fact, the Helmholtz decomposition can be applied to the correction rather than the original variables. To demonstrate this application of the Helmholtz theorem, consider the simple Cauchy-Riemann problem

$$\begin{aligned} u_x + v_y &= s \\ u_y - v_x &= -\omega \end{aligned} \quad (91)$$

One can construct the following two-step iterative technique

$$\begin{aligned} \text{step 1:} \quad \delta u_x + \delta v_y &= -(u_x + v_y - s) \\ \delta u_y - \delta v_x &= 0 \end{aligned} \quad (92)$$

$$\begin{aligned} \text{step 2:} \quad \delta u_x + \delta v_y &= 0 \\ \delta u_y - \delta v_x &= -(u_y - v_x + \omega) \end{aligned} \quad (93)$$

The correction in the first step is curl free, and according to the Stokes theorem, it can be represented by a potential. On the other hand, the correction in the second step is divergence free and according to the Gauss theorem, it can be represented by a stream function. (For a general three-dimensional problem, the correction in the second step can be represented as a curl of a divergence free vector.)

One can use Helmholtz decomposition directly on the discrete velocity field. A similar idea is behind the distributive relaxation discussed by Brandt in ref. (47). In such a technique, each discrete equation is satisfied in its turn by distributing changes to the several unknowns appearing in the equation in a specific manner; the main property is that in relaxing one equation, all the

residuals of the other equations are kept unchanged. Application to the Cauchy-Riemann problem on a staggered grid is discussed in ref. (47) and it is completely equivalent to a discrete Helmholtz decomposition.

Brandt also considered Stokes problem, where the above strategy is slightly modified. The equations are

$$\nabla \cdot \vec{q} = s \quad (94)$$

$$-\nabla \vec{q} + \nabla p = f \quad (95)$$

First, lagging the pressure, the velocity components can be updated from the momentum equations. In the second step, the velocity must be corrected to conserve mass (equation (94)). This is done such that the residuals of equation (95) remain unchanged. Therefore, the corrections in the second step are governed by the following discrete equations

$$\nabla_h \cdot \delta \vec{q} = -(\nabla_h \cdot \vec{q} - s) \quad (96)$$

$$-\Delta_h \delta \vec{q} + \nabla_h \delta p = 0 \quad (97)$$

where  $\nabla_h$  and  $\Delta_h$  are the discrete gradient and Laplacian operators on the given grid.

To solve equations (96) and (97), one can introduce a discrete potential function.

$$\delta \vec{q} = \nabla_h \phi \quad (98)$$

Therefore,

$$\Delta_h \phi = \delta p = -(\nabla_h \cdot \vec{q} - s) \quad (99)$$

The discrete equation (99) is used to update the pressure and the velocity fields.

In the first step of such calculations, the vorticity field is established. The potential correction in the second step does not alter the vorticity field, but it enforces the conservation of mass.

These ideas are as old as the pressure correction methods for the solution of Navier Stokes equations of incompressible flows, introduced by Harlow and Welsh (48), Chorin (49), Temam (50), Patankar and Spalding (51), and others. Kim and Moin (52) used a similar decomposition for the continuous problem. Obviously, the discrete potential is preferred to avoid the difficulties associated with the boundary conditions for the intermediate variables.

Returning to the transonic flow problem, one may consider the nonlinear Cauchy-Riemann problem

$$(\rho u)_x + (\rho u)_y = 0 \quad (100)$$

$$u_y - v_x = -\omega \quad (101)$$

where  $\rho(u, v)$ .

The correction to the velocity field can be split into two parts, irrotational and rotational. These components can be calculated in terms of potential and stream functions. An important issue in this discussion is the treatment of shocks (and wakes). Fitting procedures are needed to calculate the entropy jump and the entropy gradient behind curved shocks.

On the other hand, if the momentum equations are used to update the velocity field, and conservation of mass is enforced by a potential correction, it is not clear how to correct the pressure. Recently, there are some attempts to use the pressure correction methods for compressible flow calculations. The relation between the pressure correction and the velocity correction is, however, artificial. Still convergent results may be obtained for steady problems.

### VISCOUS FLOW SIMULATION

In the previous sections, the velocity/vorticity formulation and the pressure correction methods for the solution of the Navier Stokes equations of incompressible viscous flows are discussed. Direct applications of vector potential methods are examined next. For example, in ref. (53), the following decomposition is used:

$$u = \phi_x + \tilde{\psi}_y/\rho, \quad v = \phi_y - \tilde{\psi}_x/\rho \quad (102)$$

The continuity equation gives

$$(\rho\phi_x)_x + (\rho\phi_y)_y = 0 \quad (103)$$

with the boundary condition

$$\phi_n = \tilde{\psi}_s/\rho \quad (104)$$

where  $n$  and  $s$  are the normal and the tangential direction to the surface. The equation for  $\tilde{\psi}$  is

$$(\tilde{\psi}_{x/\rho})_x + (\tilde{\psi}_{y/\rho})_y = -\omega \quad (105)$$

with the boundary condition

$$\tilde{\psi}_{n/\rho} = -\phi_s \quad (106)$$

where  $\omega$  is obtained from the vorticity transport equation. It is assumed that the vorticity outside the viscous layer is negligible and hence a potential model is adequate.

The boundary conditions (104) and (106) represent the coupling between a viscous and an inviscid problem. The perturbative stream function behaves like a displacement thickness which derives the potential calculations. On the other hand, the pressure distribution ( $\phi_x$ ) derives the viscous calculations through the no slip boundary condition. No boundary-layer approximations have been made and



the formulation can be completely equivalent to the Navier Stokes equations. Only an inviscid grid is needed for the potential calculations, while the  $\tilde{\psi}$ - $\omega$  system is restricted to the viscous layer. Therefore, this formulation is a special form of domain decomposition techniques.

Further approximations lead to some simplifications. For example, the density in the potential equation (103) can be calculated in terms of formula (1') and therefore the pressure, according to the isentropic relation is

$$p = \rho_i^{\gamma/\gamma M_\infty^2} \quad (107)$$

On the other hand, the density in the  $\tilde{\psi}$ - $\omega$  system can be evaluated from the total enthalpy relation

$$H = \frac{\gamma p}{(\gamma-1)\rho_v} + \frac{1}{2} (u^2 + v^2) \quad (108)$$

In the transonic regime, H can be assumed constant even in the viscous layer, otherwise H can be evaluated from the energy equation. Unlike  $\rho_i$ , the density  $\rho_v$  has a boundary-layer-type profile like the velocity and the temperature. The pressure, however, can be assumed to be the same in the inviscid and viscous calculations.

One way to implement this formulation is to use, in the viscous layer, the full  $\psi$ - $\omega$  system, with the surface boundary conditions,  $\psi=0$  and  $\psi_n=0$ . The outer boundary conditions are  $\omega=0$  and  $\psi_n = \rho \phi_s$ . Equation (108) is used for the density where the pressure is assumed known.

The next step is to construct  $\tilde{\psi}$ . Equation (105) is solved with the surface boundary condition given by (106). The boundary condition at the edge of the viscous layer is  $\tilde{\psi} = 0$  and  $\omega$  is known from the first step. The output of this calculation is  $\tilde{\psi}$  on the surface.

Finally, the potential equation is solved and the process is repeated until convergence. The problem for  $\tilde{\psi}$  in the second step may be solved coupled with the potential equation to avoid convergence difficulties. In this case, the  $\psi$ - $\omega$  system provides  $\omega$  to the  $\tilde{\psi}$ - $\phi$  system, while the latter feeds back the pressure field and  $\phi_s$  at the edge of the viscous layer.

Extension to three-dimensional flows are possible using multiple stream functions. Alternatively, the viscous calculations can be based on the velocity/vorticity formulation. The role of the potential is simply to provide an approximation for the pressure field, which is needed to calculate the density in compressible flow cases. For incompressible flows, the potential can be dropped, since the pressure is eliminated from both the stream function and the velocity/vorticity formulations. The only advantage of keeping the potential is to restrict the domain of the viscous calculations.

Recently, El Dabaghi (54) obtained finite-element solutions of Navier Stokes equations using a rotational correction to the potential field. He used the decomposition

$$\vec{q} = \nabla \phi + \tilde{q}, \text{ where } \nabla \cdot \tilde{q} = 0 \quad (109)$$

He solved the following potential equation

$$\nabla \cdot \rho \nabla \phi = - \nabla \rho \cdot \vec{q} \quad (110)$$

with the surface boundary condition  $\phi_n = 0$ . The equations for  $\vec{q}$  are very similar to incompressible Navier Stokes equations. In this formulation, the grid for  $\phi$  problem must be fine enough to allow for the resolution of the nonhomogeneous term  $\nabla \rho \cdot \vec{q}$ . Similar ideas were introduced earlier by Dodge (55), Briley (56), Dwoyer (57) and others.

Also, Ecer et al.(58) extended their formulation to treat viscous flows. Their approach is applicable for inviscid flow in the limit of high Reynolds numbers. Also, outside the viscous layer, the potential formulation is recovered.

A composite velocity procedure for potential, Euler and Navier Stokes equations was introduced by Rubin et al. (59). The following velocity decomposition was proposed.

$$u = (U + 1)\phi_x \quad (111)$$

$$v = \phi_y \quad (112)$$

The multiplicative composite form of the axial velocity component consists of the potential component modified by the viscous velocity. The continuity and the tangential momentum equation are solved in a coupled manner to update  $\phi$  and  $U$ . The normal momentum equation in nonconservative form, is used to calculate the entropy. Numerical results for nonlifting airfoils indicate the differences between potential, Euler and Navier Stokes solutions.

Helmholtz decomposition, vorticity generation and trailing-edge condition for incompressible inviscid and viscous flows are discussed by Morino(60), (61). He derived also boundary integral equations for unsteady viscous and inviscid flows. In this work, the solution of the Poisson's equations,  $\nabla^2 \vec{\Psi} = -\vec{\omega}$  is given by

$$\vec{\Psi} = \frac{1}{4\pi} \int_V \frac{\vec{\omega}}{r} dV \quad (113)$$

The rotational component of the velocity vector is then

$$\vec{q}_v = \frac{-1}{4\pi} \int_V \frac{\vec{r} \times \vec{\omega}}{r^3} dV \quad (114)$$

The integral equation approach is also adopted by Kandil and Yates (62) to calculate inviscid vortical transonic flows, where both shocks and wakes are fitted.

In this regard, the work of Wu (63), on numerical boundary conditions for viscous flow problems should be mentioned. Applications to multiple-body problems are given in ref. (64).

## CONCLUSIONS

Unfortunately, no satisfactory results, based on vector potential methods, are available, so far, for real aerodynamic problems. For example, the simulation of transonic flow over a wing, with proper treatment of shocks and wakes, is still missing. At the same time, efforts on conservation laws gain momentum from recent mathematical developments in this field. Nevertheless, one can say, there is a great potential in the alternate formulations, particularly if practical methods for shock (and wake) fitting\* are developed.

## REFERENCES

1. Caughey, D., "The Computation of Transonic Potential Flows", Annual Rev. of Fluid Mech., Vol. 14, 1982.
2. Holst, T., "Numerical Computation of Transonic Flow Governed by the Full Potential Equation", VKI Lecture Series, 1983.
3. South, J., "A Historical Perspective and Overview of Computational Transonics", Habashi, W., (Ed.) Pineridge Press, U.K., 1985.
4. Osher, S., Hafez, M., and Whitlow, W., "Entropy Satisfying Approximations for the Full Potential Equation of Transonic Flow", Mathematics of Computation, Vol. 44, Jan. 1985, pp. 1-30.
5. Shankar, V., IDE, H., Garski, J., and Osher, S., "A Fast, Time-Accurate Unsteady Full Potential Scheme", AIAA 7th CFD Conference, Cincinnati, Ohio, July, 1985.
6. Volpe, G., and Jameson, A., "Transonic Potential Flow Calculations by Two Artificial Density Methods", AIAA Paper, 86-1084, 1986.
7. Mostrel, M. M., "On Some Numerical Schemes for Transonic Flow Problems", Ph.D. Thesis, Univ. of Calif., L.A., 1987.
8. Hafez, M. and Palaniswamy, S., "Calculations of Transonic Flows with Shocks Using Newton's Method and Direct Solver, Part I. Potential Flows", Advances in Computer Methods for Partial Differential Equations, VI, Vichnevetsky, R. and Stepleman, R., (Eds.), IMACS, 1987.
9. Hafez, M., Palaniswamy, S., and Mariani, P., "Calculations of Transonic Flows with Shocks Using Newton's Method and Direct Solver, Part II. Solution of Euler Equations", AIAA Paper, 88-0226, 1988.
10. Johnson, F.T., Bussoletti, J.E., Woo, A.C. and Young, D.P., "A Transonic Rectangular Grid Embedded Panel Method", Advances in Computational Transonics, Habashi, W. (Ed.), Pineridge Press, U.K., 1985.

\*Private communication. G. Moretti, "A General-Purpose Technique for Two-Dimensional Transonic Flows," NASA Lewis Research Center, 1988.

11. Salas, M.D., Jameson, A., and Melnik, R., "A Comparative Study of the Nonuniqueness Problem of the Potential Equation", AIAA Paper, 83-1888, 1983.
12. Hafez, M. and Lovell, D., "Transonic Small Disturbance Calculations Including Entropy Corrections", Symposium on Numerical and Physical Aspects of Aerodynamic Flows, Cebeci, T., (Ed.), Calif. State Univ., Long Beach, 1981.
13. Hafez, M. and Lovell, D., "Entropy and Vorticity Corrections for Transonic Flows", AIAA Paper, 83-1926, 1983.
14. Klopfer, G. and Nixon, D., "Non-isentropic Potential Formulation for Transonic Flows", AIAA Paper, 83-0375, 1983.
15. Dang, T.Q., and Chen, L.T., "An Euler Correction Method for Two-and-Three-Dimensional Transonic Flows", AIAA Paper, 87-522, 1987.
16. Hafez, M., "Numerical Algorithms for Transonic Inviscid Flow Calculations", Advances in Computational Transonics, Habashi, W. (Ed.), Pineridge Press, U.K., 1985.
17. Chaderjian, N. and Steger, J. "The Numerical Simulation of Steady Transonic Rotational Flow Using a Dual Potential Formulation", AIAA Paper 85-0368, 1985.
18. Hafez, M. and Ahmad, J., "Numerical Simulation of Compressible Rotational Flows", Symposium Transsonicum III, Gottingen, Germany, May, 1988.
19. Giannakoglou, K., Chaviaropoulos, P., and Papailiou, K.D., "Numerical Computation of Two Dimensional Rotational Inviscid Transonic Flows, Using the Decomposition of the Flow Field Into a Potential and a Rotational Part", to appear in AIAA J., 1988.
20. Chaviaropoulos, P., Giannakoglou, K., and Papailiou, K., "Numerical Computation of Three-Dimensional Rotational Inviscid Subsonic Flows, Using the Decomposition of the Flow Field into a Potential and a Rotational Part", ASME Paper, 86-GT-169, 1986.
21. Rao, K., Steger, J. and Pletcher, R., "A Three Dimensional Dual Potential Procedure for Inlets and Indraft Wind Tunnels", AIAA Paper, 87-0598, 1987.
22. El Dabaghi, F. and Pironneau, O., "Stream Vectors in Three Dimensional Aerodynamics", Numer. Math. Vol. 48, pp. 561-589, 1986.

23. El Dabaghi, F. and Pironneau, O., "2-D/3-D Finite-Element Solutions of the Steady Euler Equations for Transonic Lifting Flow by Stream Vector Correction",  
Int. J. for Num. Meth. in Fluids, Vol. 7, pp. 1191-1209, 1987.
24. El Dabaghi, F., Periaux, J., Pironneau, O., and Poirier, G., "3-D Finite Elements Solution of Steady Euler Transonic Flow by Stream Vector Correction",  
AIAA Paper, 85-1532, 1985.
25. Dominguez, J., "Etude des equations de la Magneto-hydrodynamique stationnaires et leur approximation par elements finis",  
These de Docteur Ingenier,  
Universite Paris VI, 1982.
26. Foias, C., and Temam, R., "Remarques sur les equations de Navier-Stokes et phenomenes successifs de bifurcation",  
Ann. Sc. Norm. Super. Pisa, IV. Ser. V, pp. 29-63, 1978.
27. Hirasaki, G., and Hellums, J., "A General Formulation of the Boundary Conditions on the Vector Potential in Three-Dimensional Hydrodynamics",  
Quart. Appl. Math., Vol. 26, pp. 331-342, 1968.
28. Hirasaki, G. and Hellums, J., "Boundary Conditions on the Vector and Scalar Potentials in Viscous Three Dimensional Hydrodynamics",  
Quart. Appl. Math., Vol. 28, pp. 293-296, 1970.
29. Richardson, S.H. and Cornish, A.R.H., "Solution of Three Dimensional Incompressible Flow Problems",  
J. of Fluid Mechanics, Vol. 82, pp. 309-319, 1977.
30. Davis, R.L., Carter, J.C., and Hafez, M., "Three Dimensional Viscous Flow Solutions with a Vorticity-Stream Function Formulation",  
AIAA Paper 87-0601, 1987.
31. Sherif, A., and Hafez, M., "Computation of Three Dimensional Flows Using Two-Stream Functions",  
AIAA Paper 83-1948, 1983.
32. Giese, J.H., "Stream Functions for Three Dimensional Flows",  
J. of Math. Physics, Vol. 30, pp. 31-35, 1951.
33. Hayes, W. and Probstein, R., "Hypersonic Flow Theory, Volume 1, Inviscid Flows",  
Academic Press, 1966.
34. Rose, M., "The Numerical Solution of Cauchy - Riemann Type Equations by Compact Schemes",  
ICASE Report, 1988.
35. Fasel, M., "Investigation of the Stability of Boundary Layers by Finite Difference Model of Navier Stokes Equations",  
J. Fluid Mechanics, Vol. 78, pp. 355-383, 1976.

36. Gatski, T., Grosch, C. and Rose, M., "A Numerical Study of the Two-Dimensional Navier-Stokes Equations in Vorticity-Velocity Variables", J. Comput. Phys., Vol. 48, No. 1, pp. 1-22, 1982.
37. Osswald, G., Ghia, K. and Ghia, V., "A Direct Algorithm for Solution of Incompressible Three-Dimensional Unsteady Navier-Stokes Equations", AIAA Paper, 87-1139, 1987.
38. Hafez, M. and Dacles, J., "A Velocity/Vorticity Method for Viscous Incompressible Flow Calculations", 11th International Conference on Num. Methods in Fluid Dynamics, Williamsburg, June, 1988.
39. Hafez, M., "Progress in Finite Elements Techniques for Transonic Flows", AIAA Paper, 83-1919, 1983.
40. Seliger, R. and Whitham, G., "Variational Principles in Continuum Mechanics", Proc. Royal Soc., A. Vol. 305, pp. 1-25, 1968.
41. Buneman, O., "Ideal Gasdynamics in Hamiltonian Form with Benefit for Numerical Schemes", Phys. Fluids, Vol. 23, No. 8, pp. 1716-1717, 1980.
42. Ecer, A. and Akay, H.V., "Applications of Variational Principles in Computing Rotational Flows", Advances in Computational Transonics, Habashi, W. (Ed.), Pineridge Press, U.K., 1985.
43. Roberts, A., "The Treatment of Shocks in Fast Solving Methods", Numerical Methods in Applied Fluid Mechanics, Hunt, B. (Ed.), Academic Press, 1980.
44. Grossman, B., "The Computation of Inviscid Rotational Gasdynamics Flows Using an Alternate Velocity Decomposition", AIAA Paper, 83-1900, 1983.
45. Deconinck, H., and Hirsch, C., "Inviscid Flow Computations: From Potential Models to Euler Equations", Advances in Computational Transonics, Habashi, W. (Ed.), Pineridge Press, U.K., 1985.
46. Lacor, C. and Hirsch, Ch., "Rotational Flows in Three Dimensional Blade Passages", ASME paper , 82-GT-316, 1982.
47. Brandt, A., "Multi-level Adaptive Computations in Fluid Dynamics, AIAA Paper 79-1455, 1979.
48. Harlow, F. and Welch, J., "Numerical Calculations of Time-Dependent Viscous Incompressible Flow of Fluid with Free Surface", Phys. Fluids, Vol. 8, pp. 2182-2189, 1965.

49. Chorin, A., "On the Convergence of Discrete Approximations to the Navier-Stokes Equations",  
Math. of Comp., Vol. 23, No. 106, pp. 341-353, 1969.
50. Temam, R., "On Approximate Solution of the Navier-Stokes Equations by the Method of Fractional Steps: Part I, Archive for Rational Mech. and Analysis, Vol. 32, No. 2, pp. 135-153, 1969.
51. Patankar, S. and Spalding, D., "A Calculation Procedure for Heat, Mass, and Momentum Transfer in Three Dimensional Parabolic Flows",  
Int. J. Heat Mass Transfer, Vol. 15, pp. 1787-1806, 1972.
52. Kim, J. and Moin, P., "Application of a Fractional-Step Method to Incompressible Navier-Stokes Equations"  
J. of Comp. Phys. Vol. 59, No. 2, pp. 308-323, 1985.
53. Hafez, M., Habashi, W., Przybytkowski, S. and Peeters, M., "Compressible Viscous Internal Flow Calculations by a Finite Element Method",  
AIAA Paper, 87-0644, 1987.
54. El Dabaghi, F., "Finite Element Solution by Rotational Correction of Steady Incompressible and Compressible Navier Stokes Equations"  
ICFD Conference on Numerical Methods for Fluid Dynamics, Oxford, March, 1988.
55. Dodge, P., "Numerical Method for 2D and 3D Viscous Flows",  
AIAA J., Vol. 16, No. 4, pp. 393-402, April, 1978.
56. Briley, W., "Numerical Method for Predicting Three-Dimensional Steady Viscous Flow in Ducts",  
J. Comp. Phys., Vol. 14, pp. 8-28, Jan., 1974.
57. Dwoyer, D., "Application of a Velocity-Split Navier-Stokes Solution Technique to External Flow Problems",  
AIAA Paper 79-1449, 1979.
58. Ward, P., Desai, R., Kebede, W., and Ecer, A., "A Variational Finite Element Formulation for Three Dimensional Incompressible Flows",  
ICFD Conference on Numerical Methods for Fluid Dynamics, Oxford, March, 1988.
59. Gordnier, R. and Rubin, S., "Transonic Flow Solutions Using a Composite Velocity Procedure For Potential, Euler, and RNS Equations",  
Computers and Fluids, 1988.
60. Morino, L., "Scalar/Vector Potential Formulation for Compressible Viscous Unsteady Flows",  
NASA Contractor Report, 3921, 1985.
61. Morino, L., "Helmholtz Decomposition Revisited: Vorticity Generation and Trailing Edge Condition",  
Comp. Mech., Vol. 1, pp. 65-90, 1986.

62. Kandil, O. and Yates, C., "Transonic Vortex Flows Past Delta Wings: Integral Equation Approach",  
AIAA J., Vol. 24, No. 11, pp. 1729-1737, 1986.
63. Wu, J.C., "Numerical Boundary Conditions for Viscous Flow Problems",  
AIAA J., Vol. 14, No. 8, pp. 1042-1049, 1976.
64. Kinney, R., Taslim M., and Hung, S., "A Hybrid Computational Approach to Multiple-Body Viscous-Flow Problems: Application to Large-Eddy Breakup in A Boundary Layer"  
J. Comp. Phys., 1988.



## DEVELOPMENTS AND TRENDS IN THREE-DIMENSIONAL MESH GENERATION

Timothy J. Baker

Princeton University  
Princeton, New JerseyAbstract

An intense research effort over the last few years has produced several competing and apparently diverse methods for generating meshes. This paper reviews recent progress and emphasizes the central themes that we can expect to form a solid foundation for future developments in mesh generation.

Introduction<sup>†</sup>

Although long recognized as a major pacing item [24,49], mesh generation has only recently achieved the long sought aim of making possible the calculation of complete aircraft flow fields. Even now mesh generation for complex configurations is not a routine task and a period of maturation is still required before meshes can be quickly and efficiently created for any type of aircraft shape. We are, however, at an important juncture where techniques for tackling the problem are well understood, if not yet fully developed. It is therefore a suitable time to take stock and consider which approaches are likely to stay the course and provide the basis for reliable and efficient flow calculation methods.

Early methods for calculating transonic flow over airfoils and other simple two dimensional shapes were based on conformal mapping techniques [2,3,20,43,70] and simple shearings [5,77]. At that time mesh generation was regarded as a subsidiary part of the flow algorithm. Indeed the problem was essentially that of finding a suitable coordinate transformation, expressing the flow equations in the curvilinear coordinate system and then devising a solution algorithm for the transformed flow equations. The paper of Thompson et al. [88] was a significant break from this tradition. It advocated the idea of using elliptic equation methods to generate meshes around arbitrary shapes. Although this approach had been tried before [104], Thompson et al. were the first to realize its full potential and to exploit the idea as a general technique. The paper had two other important effects. First, it focused attention on mesh generation as a problem in its own right, largely independent of the flow solver. Second, their work also recognized the need to move from a global description in terms of an overall mapping to a local viewpoint based on a mesh defined by a set of points and an ordering of the points corresponding to the coordinate directions. There is, of course, no need to use global mappings, and finite difference formulae can easily be constructed for numerically generated meshes. What is interesting, however, is that the apparently more elegant approach, of using coordinate transformations to achieve a global mapping of the flow equations, did not have sufficient generality to survive as a method for handling complex shapes. At the other extreme, the use of a non-aligned Cartesian mesh [19,65,103] once held the prospect of treating arbitrary geometries at the cost of finding adequate interpolation procedures for applying the solid wall boundary conditions. Unfortunately this cost has proved a formidable obstacle and the non-aligned mesh approach has won few adherents. The lesson,

<sup>†</sup> This paper refers to research described in references 1-106.

which is often repeated, is that mesh generation eschews the most elegant solution without abandoning elegance altogether. In this case the preferred approach is a surface conforming mesh and a flow solver that uses only information about the mesh point positions. It is a compromise between the beauty of global coordinate mappings which prove too rigid and the excessive generality of a non-aligned mesh which is too difficult to couple with the flow solver. In this context it is important to note another early development, the introduction of the finite volume approach [45,66] that treats each mesh cell as a control volume to approximate the integral form of the flow equations. This is an inherently more accurate approach for discretizing the flow equations, a natural way of ensuring conservation and is particularly well suited to the general surface conforming mesh. These concepts are now so widely accepted that it is easy to forget that there was a time when the choice was not so obvious.

The paper of Thompson et al. [88] stimulated a great deal of work using elliptic equations to generate meshes in both two and three dimensions. The possibility of basing numerical mesh generation on hyperbolic and parabolic equation sets has also been explored. One unfortunate aspect of this emphasis on numerical mesh generation is that relatively little attention has been paid to alternative procedures. Algebraic methods [6,28,32,74], in particular, offer many attractive features. The work of Eiseman [28] is perhaps the best known example of this approach. He constructs a set of coordinate surfaces between two boundary surfaces and then defines an interpolatory function to provide a smooth variation in the third coordinate direction. The greater the number of intermediate surfaces used, the greater the degree of mesh smoothness that can be obtained.

A particularly powerful algebraic method is based on transfinite interpolation. This approach to mesh generation was first introduced by Eriksson [31,32], who has developed the idea into an extremely effective technique. In common with all algebraic methods, this approach is very fast compared with numerical mesh generation. The most significant feature of transfinite interpolation, however, is the ability to exercise a high degree of control over the mesh point distribution, particularly, over the slope of the mesh lines which meet the boundary surfaces.

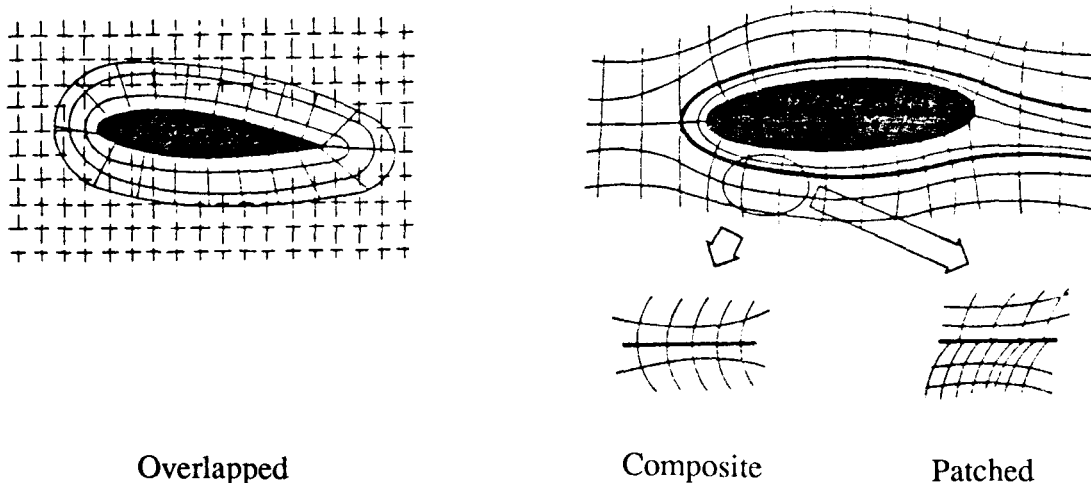


Fig. 1 Multiblock Variants (taken from Kutler, Ref. 49)

The conflicting requirements, of control over mesh quality on the one hand and flexibility to handle arbitrary shapes on the other, have pervaded mesh generation throughout its development. Indeed the essence of mesh generation is the need to maintain as much of both features without seriously degrading either. An important step towards securing a harmonious balance between these two constraints is the use of a multiblock strategy. This concept is to break the flow field into several smaller blocks (essentially an ultra-coarse mesh) and then generate separate meshes in each individual block. This concept was first formulated by Lee et al. [50] and has rapidly gained wide acceptance. There are several variants of this approach (see figure 1), depending on whether there is continuity of mesh lines at the block interfaces (composite), whether the individual blocks are entirely independent and merely overlap one another (overlapped), or block interfaces but no continuity of mesh lines (patched).

At first sight it would seem that a blocked mesh structure is further step away from simplicity and elegance towards messy complexity. However the experience of many researchers who have embraced multiblock in spite of this drawback, provides convincing testimony to its role as an indispensable component of mesh generation for complicated configurations. Again one has been forced to relinquish a global viewpoint (the use of a single mesh) in favor of a local perspective (several blocks each able to accommodate part of the flow field and boundary surface).

The discussion has so far centered on structured meshes composed of quadrilaterals in two dimensions or hexahedra in three dimensions. The mesh is structured in the sense that there is an implied set of coordinate directions within each block. In order to treat complete aircraft, this structure can still prove an impediment unless a large number of blocks are used. One is then faced with the problem of defining the blocks and their interfaces, which becomes increasingly difficult as the number of blocks increases. A radical alternative to a structured mesh is the use of triangles in two dimensions and tetrahedra in three dimensions. There is no longer any inherent regularity in the mesh and one has made a complete transition from the global to a local description. This characteristic gives unstructured meshes maximum flexibility in treating complex geometries while retaining a high degree of control over mesh point distribution. Unfortunately the extreme generality makes the generation of unstructured meshes a singularly difficult task. In two dimensions several triangle mesh generation schemes are available, but in three dimensions tetrahedral mesh generation schemes are scarce. The first report of a tetrahedral mesh around a complete aircraft is given by Bristeau et al. [18] This was a remarkable achievement, which has perhaps not received the recognition it deserves. No details of the mesh generation are given in the publications by this group, an unfortunate omission that has no doubt contributed to the lack of adequate recognition.

There appear to be two main approaches to unstructured mesh generation which have proved successful in three dimensions. The first is based on the Delaunay triangulation and its dual geometric construct, the Voronoi diagram. This idea has been successfully exploited in two dimensions for a variety of applications. For aerodynamic calculations, use of the Delaunay triangulation was initiated by Weatherill [99,100] and developed in three dimensions by Baker [7,8,47,48]. The alternative approach is the moving front technique, successfully applied in two dimensions by Lo [51] and recently developed in three dimensions by Peraire et al. [63] and Löhner [52].

The distinguishing feature of unstructured meshes is their ability to handle three dimensional objects of arbitrary shape and complexity. This is accomplished without the need for introducing blocks, mesh controlling functions and other artifacts, which plague structured mesh generation and prevent its evolution to a fully automated procedure. The criticism that has been leveled at unstructured meshes is the difficulty of constructing efficient flow solvers. It is interesting to observe that the finite element method, which has exploited unstructured

meshes from its inception, has seen little development of the algorithms used to invert the mass matrix and solve the problem. Developments in Computational Fluid Dynamics began with simple structured meshes and this proved to be a stimulus for innovative ideas, which have led to highly efficient flow algorithms. Although it appears unlikely that implicit schemes can be adapted in any simple way to unstructured meshes, advances in explicit schemes (e.g. multi-stage Runge Kutta methods, local time stepping etc.) carry over equally well to triangular meshes. Indeed Jameson's unstructured flow solver [47,48] rivals the best of the structured flow algorithms for computational speed. Recent work by Mavriplis [55] indicates that multigrid will also work very effectively on unstructured meshes.

It is likely that future developments will use combinations of both structured and unstructured meshes. In fact Nakahashi and Obayashi [59] have used such a combination, exploiting a structured mesh near solid boundaries to solve the Navier Stokes equations and a triangular or tetrahedral mesh in the remainder of the flow field. Actually the reverse procedure would be more appropriate for general geometries. It is the near field of closely coupled components such as wing/strut/nacelle and wing/store combinations that prove difficult when one tries to fit hexahedral cells. The likely outcome is that a tetrahedral mesh will be employed in such regions with an structured mesh covering the surrounding space.

In the remainder of this paper we describe some of these ideas in more detail. Several excellent reviews and conference proceedings [30,73,85,86,89] have recently appeared and an AGARDograph containing contributions from several researchers will soon be published. From these publications the reader can get a comprehensive view of the current status of mesh generation. The text of Thompson et al. [90] is an excellent reference for much of the underlying theory. The aim of this paper is to provide a personal view by summarizing the most important developments and by attempting to interpret the many diverse ideas and techniques that have appeared. Also included is a brief discussion of two areas that can be expected to become increasingly important in the future. First, there is the question of mesh quality and, in particular, how changes in cell shape, aspect ratio and mesh stretchings can affect solution accuracy and algorithm performance [36,37,40,64,67,90,92,94,95,98]. These are difficult questions and our present knowledge is rudimentary. But it is likely that this area will receive much more attention, now that the major goal of complete aircraft meshes has been achieved.

The second area is the use of solution adaptive meshes. This is also a field of growing interest and several papers on this subject have already appeared [1,14,17,25,39,41,42,54,57,58,60,61,63,83]. It is evident that the flow field around a complicated object such as a complete aircraft has a complicated structure and widely varying length scales. In order to resolve such features as shed vortices, shock wave patterns and ultimately separated flow, solution adaptive meshes will be needed no matter how many gigawords of computer memory become available. It is against this yardstick that further developments in mesh generation should be measured. How easily can the method cope automatically with an arbitrary shape, first generating an initial mesh and then adapting the mesh to the evolving solution so that all the salient flow features are crisply captured?

## 2. Mesh Generation Methods

In this section we provide thumbnail sketches of those mesh generation techniques that can be applied to complicated three dimensional shapes. For the purpose of illustration, formulae for the two dimensional implementation will be presented, and we therefore consider a transformation from physical coordinates  $x,y$  to another coordinate system defined by  $\xi,\eta$ . A point in the flow field can then be associated with the position vector

$$\mathbf{r}(\xi,\eta) = (x(\xi,\eta), y(\xi,\eta))$$

The reader should consult the references for a detailed derivation of these methods and their generalization to three dimensions.

## 2.1 Numerical Techniques

### 2.1.1 Elliptic Systems

In two dimensions the Laplace system

$$\begin{aligned}\xi_{xx} + \xi_{yy} &= 0 \\ \eta_{xx} + \eta_{yy} &= 0\end{aligned}\tag{1}$$

may be solved to determine the coordinate transformation  $x(\xi, \eta)$ ,  $y(\xi, \eta)$ . In practice the problem is inverted to solve for  $x$  and  $y$  as dependent variables [88,90]. Equations (1) then assume the form,

$$\begin{aligned}\alpha x_{\xi\xi} - \beta x_{\xi\eta} + \gamma x_{\eta\eta} &= 0 \\ \alpha y_{\xi\xi} - \beta y_{\xi\eta} + \gamma y_{\eta\eta} &= 0\end{aligned}\tag{2}$$

where

$$\begin{aligned}\alpha &= x_{\xi}^2 + y_{\xi}^2 \\ \beta &= x_{\xi}x_{\eta} + y_{\xi}y_{\eta} \\ \gamma &= x_{\eta}^2 + y_{\eta}^2\end{aligned}$$

For a boundary conforming mesh, the boundaries are the lines  $\xi = \xi_1, \xi_2$  and  $\eta = \eta_1, \eta_2$  say, and the solution of equations (2) thus defines a mapping from a rectangle in  $(\xi, \eta)$  space to the required region in physical space. The lines  $\xi = \text{const.}$  and  $\eta = \text{const.}$  correspond to mesh lines in physical space and the extremum principle for harmonic functions ensures that mesh lines do not overlap.

### 2.1.2 Control Functions

Unfortunately the Laplace system has a strong smoothing effect and often produces an undesirable mesh point distribution. This is particularly evident in regions of high curvature on the boundaries. Control of mesh point distribution can be accomplished by the introduction of controlling functions to generate a system of Poisson equations

$$\begin{aligned}\xi_{xx} + \xi_{yy} &= P(\xi, \eta) \\ \eta_{xx} + \eta_{yy} &= Q(\xi, \eta)\end{aligned}\tag{3}$$

The source terms  $P$  and  $Q$  are constructed to either attract or repel points about a certain position or line. For example

$$P(\xi, \eta) = -a \operatorname{sgn}(\xi - \xi_0) e^{-c|\xi - \xi_0|}, \quad a > 0, \quad c > 0\tag{4a}$$

attracts  $\xi$ -lines towards the line  $\xi = \xi_0$  while

$$P(\xi, \eta) = -a \operatorname{sgn}(\xi - \xi_0) e^{-c[(\xi - \xi_0)^2 + (\eta - \eta_0)^2]^{1/2}} \quad (4b)$$

attracts  $\xi$ -lines to the point  $(\xi_0, \eta_0)$ . Ways of automating the choice of the amplitude  $a$  and decay factor  $c$  have been suggested, and more general forms of the source terms are available [56,79,90]. However, non-overlapping of mesh lines can no longer be guaranteed and the specification of control functions requires some care.

### 2.1.3 Hyperbolic Systems

Other sets of partial differential equations might be expected to produce satisfactory meshes. An interesting development of Steger and Sorenson [80] along these lines is the solution of the following equations

$$\begin{aligned} x_\xi x_\eta + y_\xi y_\eta &= 0 \\ x_\xi y_\eta - x_\eta y_\xi &= V(\xi, \eta) \end{aligned} \quad (5)$$

which can be shown to define a hyperbolic system. The first equation of this pair is the orthogonality condition; the second determines the local cell area according to a specified area distribution  $V(\xi, \eta)$ . If the  $x$  and  $y$  coordinates of one boundary surface are defined on  $\eta = \eta_1$  say, then the system can be marched out in the direction of increasing  $\eta$ . The outer boundary surface cannot, of course, be specified for a hyperbolic system. This is often quite acceptable for external flow problems, but makes a hyperbolic system unsuitable for generating meshes for some geometries, typically those used in internal flow problems.

## 2.2 Algebraic Methods

### 2.2.1 Multi-Surface Fitting

An interesting approach that was introduced by Eiseman [28] is based on the idea of interpolating curves along specified directions rather than through specific points. Consider two boundary surfaces  $r_1(\xi)$  and  $r_N(\xi)$  corresponding to the lines  $\eta = \eta_1$  and  $\eta = \eta_N$ . Let

$\underline{r}(\xi, \eta) = (x(\xi, \eta), y(\xi, \eta))$  be the position vector of the point  $(x, y)$  and introduce intermediate surfaces  $r_i(\xi)$ ,  $i=2, \dots, N-1$  which are constructed to direct the  $\eta$ -lines from the boundary surface  $\eta = \eta_1$  to the opposite boundary surface  $\eta = \eta_2$ . We now construct a curve that is tangent to the direction  $r_{i+1}(\xi) - r_i(\xi)$  at the position  $\eta = \eta_i$ . Thus we require

$$\frac{\partial \underline{r}}{\partial \eta} = \sum_{i=1}^{N-1} A_i \psi_i(\eta) (r_{i+1}(\xi) - r_i(\xi)) \quad (6)$$

where  $A_i$  are suitable normalizing constants and the  $\psi_i(\eta)$  are univariate interpolating functions subject to the constraints

$$\psi_i(\eta_j) = \delta_{ij} \quad i, j = 1, 2, \dots, N-1$$

On integrating eqn (6) we obtain

$$\underline{r}(\xi, \eta) = r_1(\xi) + \sum_{i=1}^{N-1} A_i G_i(\eta) (r_{i+1}(\xi) - r_i(\xi))$$

where

$$G_i(\eta) = \int_{\eta_1}^{\eta} \psi_i(s) ds .$$

The choice  $r_1(\xi)$  for the integration constant ensures that  $r(\xi, \eta)$  coincides with  $r_1(\xi)$  when  $\eta = \eta_1$ . We can now choose  $A_i = 1/G_i(\eta_N)$  to ensure that  $r(\xi, \eta)$  coincides with the outer boundary surface  $r_N(\xi)$  at  $\eta = \eta_N$ .

This approach offers great generality and a high degree of control over mesh point distribution. From a practical viewpoint it must be difficult to specify the intermediate controlling surfaces for regions contained by highly complicated boundaries (e.g. the space around a nacelle/strut/wing). On the other hand, once one has accepted the need for a blocked mesh, a more specific interpolation procedure such as transfinite interpolation is probably adequate.

### 2.2.2 Transfinite Interpolation

The theory of multivariate interpolation, developed in general terms by Gordon [38], has been successfully exploited by Eriksson [31,32] as a means of generating meshes exhibiting a high degree of control over the mesh point distribution. Unlike Eiseman's multisurface approach, only information about the distribution of boundary points and the slope of mesh lines meeting the boundaries is needed. However, a careful choice of the interpolating functions is required to obtain a smooth mesh when one or more of the boundary surfaces contains a slope discontinuity. This aspect is discussed further in reference 31 which provides a clear description of Eriksson's work. A particularly attractive aspect of this approach is the way in which an interpolating function in two or three dimensions can easily be constructed from univariate interpolants. To illustrate this in two dimensions we again consider a mapping of the rectangular region in  $\xi, \eta$  space defined by the boundaries  $\xi = \xi_1$ ,  $\xi = \xi_2$ ,  $\eta = \eta_1$  and  $\eta = \eta_2$ . We require the vector function  $\mathbf{r}(\xi, \eta) = (x(\xi, \eta), y(\xi, \eta))$  given a prescribed functional variation  $r(\xi_1, \eta)$ ,  $r(\xi_2, \eta)$ ,  $\eta_1 \leq \eta \leq \eta_2$  and  $r(\xi, \eta_1)$ ,  $r(\xi, \eta_2)$ ,  $\xi_1 \leq \xi \leq \xi_2$  on the boundaries. First, we define two projections that correspond to a pair of univariate interpolation schemes,

$$\begin{aligned} \pi_{\xi} \mathbf{r} &= \mathbf{r}(\xi_1, \eta) \phi_1(\xi) + \mathbf{r}(\xi_2, \eta) \phi_2(\xi) \\ \pi_{\eta} \mathbf{r} &= \mathbf{r}(\xi, \eta_1) \psi_1(\eta) + \mathbf{r}(\xi, \eta_2) \psi_2(\eta) \end{aligned} \quad (7)$$

where

$$\begin{aligned} \phi_1(\xi_1) &= 1, & \phi_1(\xi_2) &= 0 \\ \phi_2(\xi_1) &= 0, & \phi_2(\xi_2) &= 1 \\ \psi_1(\eta_1) &= 1, & \psi_1(\eta_2) &= 0 \\ \psi_2(\eta_1) &= 0, & \psi_2(\eta_2) &= 1 \end{aligned} \quad (8)$$

We now define the transfinite interpolating function as the Boolean sum of these projections

$$\begin{aligned}\pi_{\xi} \oplus \pi_{\eta} \mathbf{r} &= (\pi_{\xi} + \pi_{\eta} - \pi_{\xi} \pi_{\eta}) \mathbf{r} \\ &= \mathbf{r}(\xi_1, \eta) \phi_1(\xi) + \mathbf{r}(\xi_2, \eta) \phi_2(\xi) + \mathbf{r}(\xi, \eta_1) \psi_1(\eta) + \mathbf{r}(\xi, \eta_2) \psi_2(\eta) \\ &\quad - \mathbf{r}(\xi_1, \eta_1) \phi_1(\xi) \psi_1(\eta) - \mathbf{r}(\xi_2, \eta_1) \phi_2(\xi) \psi_1(\eta) \\ &\quad - \mathbf{r}(\xi_1, \eta_2) \phi_1(\xi) \psi_2(\eta) - \mathbf{r}(\xi_2, \eta_2) \phi_2(\xi) \psi_2(\eta)\end{aligned}\tag{9}$$

Along the boundaries the interpolating function reduces to the prescribed form. The functions  $\phi_1$ ,  $\phi_2$ ,  $\psi_1$  and  $\psi_2$  can be chosen arbitrarily provided they satisfy the conditions (8). The simplest possible choice corresponding to linear interpolation in  $\xi$  and  $\eta$  is given by,

$$\begin{aligned}\phi_1(\xi) &= \frac{\xi_2 - \xi}{\xi_2 - \xi_1}, & \phi_2(\xi) &= \frac{\xi - \xi_1}{\xi_2 - \xi_1} \\ \psi_1(\eta) &= \frac{\eta_2 - \eta}{\eta_2 - \eta_1}, & \psi_2(\eta) &= \frac{\eta - \eta_1}{\eta_2 - \eta_1}\end{aligned}$$

The projections (7) can be generalized to allow for a specification of the derivative of  $\mathbf{r}$  normal to the boundaries. The univariate interpolants  $\phi$  and  $\psi$  must then be osculatory functions that satisfy conditions (8) together with a further set of constraints on their derivatives at the end points.

### 2.2.3 Sequential Mapping

Another algebraic method that retains something of the spirit of the original coordinate transformation methods based on conformal mappings and shearings is the use of a sequence of mappings [6,44]. This approach has the virtue of retaining a high degree of control over mesh point distribution. By applying several simple mappings it is possible to reduce a relatively complicated configuration to a simple generic shape.

For example, a wing/fuselage/tail combination can be mapped into a pair of surfaces plus part of the symmetry plane. A Joukowski mapping followed by a shearing will take the fuselage into the symmetry plane. Further combinations of conformal mappings and shearings can be constructed to reduce the tail to a single sheet and unwrap the wing. It is then fairly straightforward to interpolate a set of coordinate surfaces which conform with the mapped wing surface and contain the tail sheet. In addition the coordinate surfaces are required to coincide with the mapped fuselage crown line on the symmetry plane. The set of mesh points in mapped space is now passed through the inverse of the original mapping sequence. This restores the aircraft geometry and produces a mesh that conforms with all boundary surfaces. A very similar approach was pursued independently by Shmilovich and Caughey [72].

The technique is fairly powerful, and the surface mesh for two examples of meshes generated by Baker's method are presented in figure 2. This mesh generator was linked to Jameson's finite volume scheme to produce the first published Euler flow solutions over wing/fuselage/tail combinations [44,46]. Although this concept could, in principle, be extended to include engine nacelles, it becomes increasingly difficult to fit the coordinate surfaces in mapped space, and some degree of user intervention would then be required to treat different geometries. As we mentioned earlier, the use of global coordinate transformations is not sufficiently flexible to deal with complete aircraft configurations, leading one to accept that a multiblock approach is unavoidable.



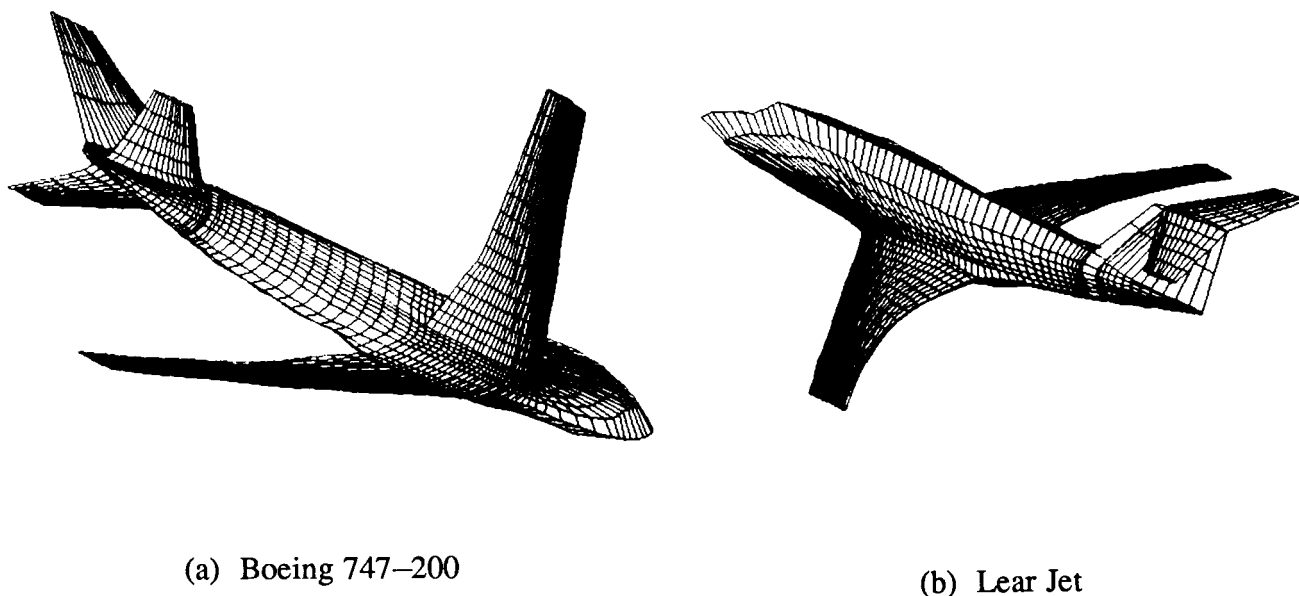


Fig. 2. Surface Mesh from Baker, Ref. 6 and 44

#### 2.2.4 Grid Blending

Recently Steinhoff [82] introduced the idea of blending a collection of meshes, each one of which is generated for a separate region, to form a smooth global mesh. In some respects this idea has some of the features of a multiblock method in so far as it is based on defining several relatively simple, separate meshes rather than a global transformation. Suppose, for example, that there are  $N$  meshes and that the vector

$$\mathbf{r}_{ijk}(m) = (x_{ijk}(m), y_{ijk}(m), z_{ijk}(m))$$

represents the point with indices  $(i,j,k)$  generated by the  $m$ th mesh where  $m=1,2,\dots,N$ . The set of points represented by  $\mathbf{r}_{ijk}(1)$  might be the mesh around the wing,  $\mathbf{r}_{ijk}(2)$  the mesh around the fuselage,  $\mathbf{r}_{ijk}(3)$  the mesh around the tail and so on. The actual point  $\bar{\mathbf{r}}_{ijk}$  corresponding to the indices  $(i,j,k)$  is then formed by the weighted combination

$$\bar{\mathbf{r}}_{ijk} = \frac{\sum_{m=1}^N P_{ijk}(m) \mathbf{r}_{ijk}(m)}{\sum_{m=1}^N P_{ijk}(m)} \quad (10)$$

where the  $P_{ijk}(m)$ ,  $m=1,\dots,N$  are weighting functions constructed so that the  $m$ th mesh dominates in the region where it is needed. The weights for the other meshes should be small in this region, and decay to zero near the boundary surface where the mesh is determined entirely by the component mesh  $r_{ijk}(m)$ .

Although this approach is attractive, the choice of the weighting functions is by no means easy and will presumably have to be done on a trial and error basis for each new configuration. How difficult or easy this task is compared with the construction of a blocked mesh will determine whether the blending mesh approach is a viable technique for treating arbitrary complex configurations.

### 3. Multiblock

The need to handle complicated geometries while maintaining adequate control over mesh point distribution and cell shape can perhaps be best achieved by introducing a multiblock structure. The flow field is broken up into a number of blocks by defining a set of surfaces which will represent the block boundaries. The individual blocks can then be meshed and the flow algorithm constructed to exploit the blocked structure. In fact the flow solution can proceed in each block independently, with information between contiguous blocks being passed at the common interface of two block boundaries. This makes multiblock particularly suitable for computer architectures with a parallel processing capability. Various possibilities arise depending on what degree of continuity is required at the block interfaces (see figure 1).

#### 3.1 Overlapped

If we do not define a precise interface but introduce separate meshes for each component, we obtain a system of overlapped meshes. This approach was originally considered by Atta [4] and has been extensively developed by Benek et al [10–12]. The lack of any constraint at the block boundaries makes mesh generation for the individual blocks much easier. However the penalty for this facility is the problem of transferring information from each component mesh to its neighbor. This difficulty has some similarity with the problem of applying solid wall boundary conditions on a non-aligned mesh. Similar reservations about accuracy of the interpolation procedures and the ease of maintaining conservation apply to overlapped meshes. Recent work by Berger [13] shows that conservation can usually be achieved though with some difficulty, particularly in three dimensions, and it is by no means clear whether stability could be assured in the general case.

#### 3.2 Patched

If we define a block structure and require the separate meshes to conform with the surfaces of their respective block boundaries, we obtain a patched mesh. There will, in general, be no continuity of mesh lines from neighboring blocks at the block interfaces. However, interpolation at the interfaces is now less demanding than that required by an overlapped system, and this approach retains the advantage of allowing a highly refined mesh in specific regions without imposing unnecessary refinement elsewhere. A patched mesh was used by Baker et al. [9] to obtain a refined mesh in the vicinity of the tail for a wing/fuselage/tail combination. This technique has also been successfully applied to solve the Navier–Stokes equations around an F–16 [34,75,76] (see figure 3).

ORIGINAL PAGE IS  
OF POOR QUALITY

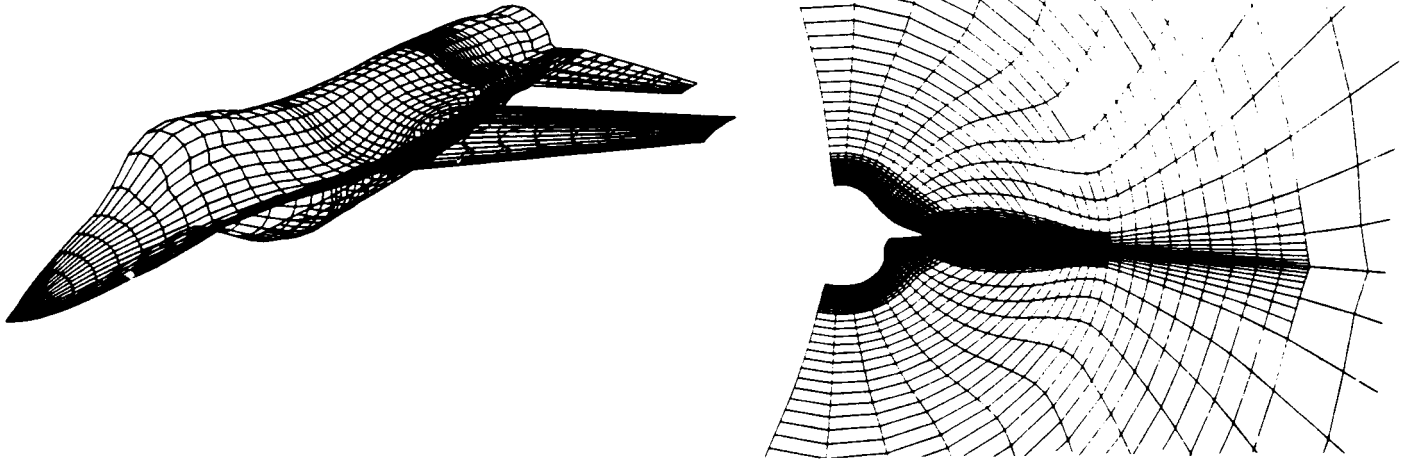


Fig. 3. Mesh from Sorenson, Ref. 75

### 3.3 Composite

The composite method can be regarded as a special case of the patched approach in which mesh lines are required to be continuous across block interfaces. This has the drawback that mesh refinement in one block, involving an increase in the number of mesh points on block boundaries will induce a corresponding refinement in neighboring blocks and so on throughout the entire mesh. However, it is probable that the advantage of mesh line continuity at the block interfaces outweighs the disadvantage of requiring an unduly fine mesh in certain regions. Mesh smoothness is further enhanced by requiring slope continuity as well, and the extra burden this places on the mesh generation within each block is amply justified by improved accuracy that results.

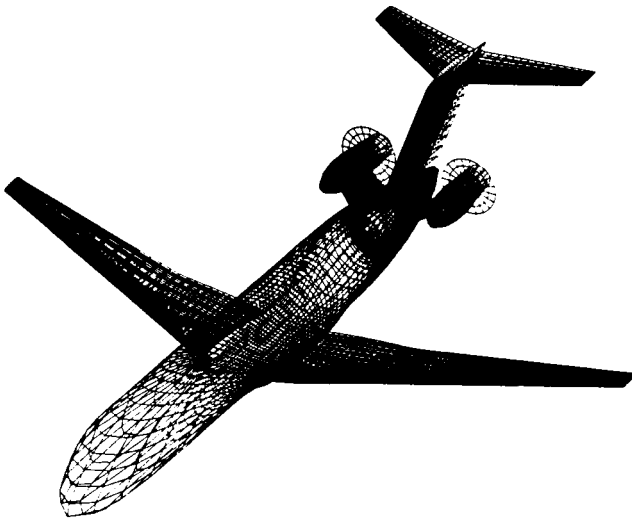


Fig. 4. Surface Mesh  
from Yu et al., Ref. 106

### 3.4 Miscellaneous Results

Over the last two years several examples have appeared in the literature showing flow calculations on structured meshes for aircraft geometries. Yu et al. [105,106] have used a two block Poisson solver to obtain a C-H mesh around a high tail/aft mounted propfan configuration (figure 4). Eberle and Schwarz [27] have generated a single block H-H mesh around a wing/canard/fuselage/tail combination (figure 5). They used an elliptic mesh generator that solves the biharmonic equation, thus gaining a higher degree of smoothness than would be obtained from the Laplace system. A similar configuration, but without a vertical tail, has been treated by Eriksson et al. [33], who used transfinite interpolation to produce a two block H-O mesh (figure 6).

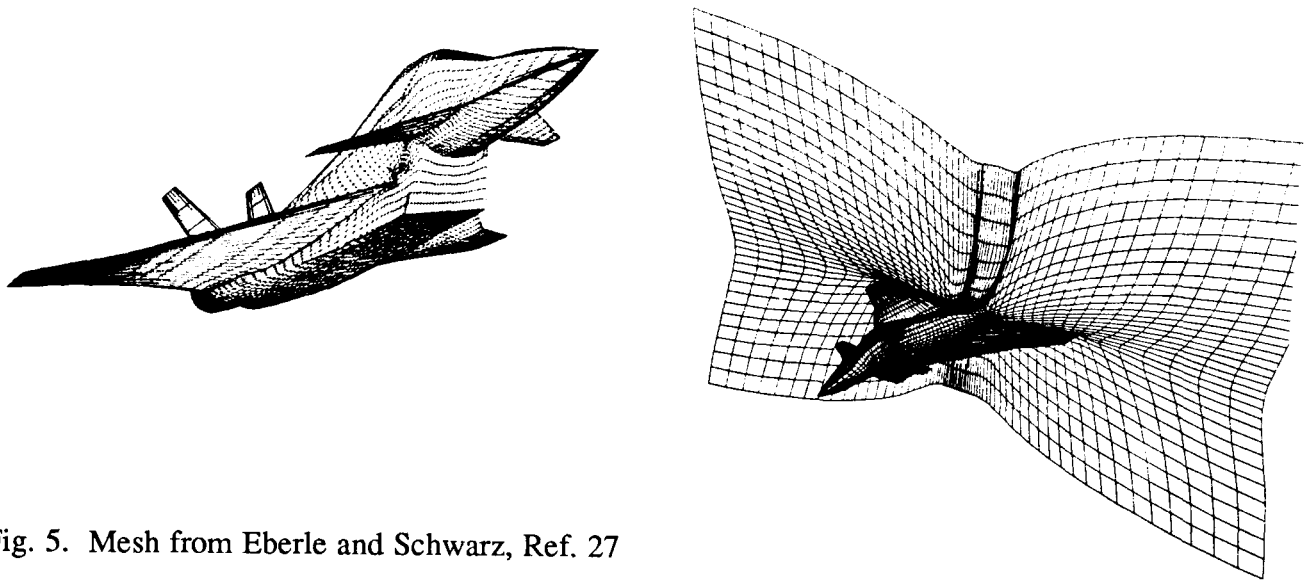


Fig. 5. Mesh from Eberle and Schwarz, Ref. 27

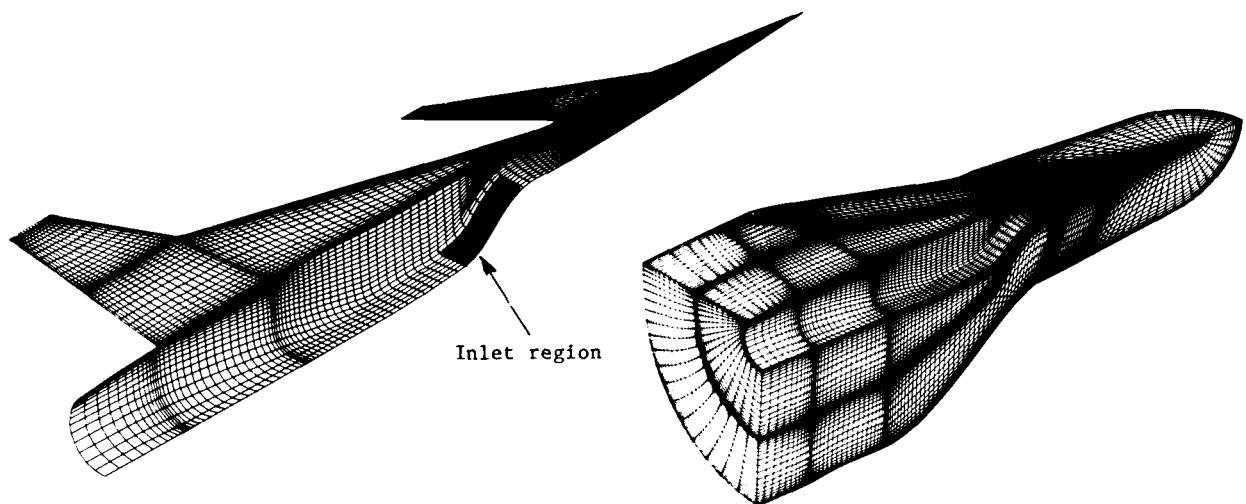


Fig. 6. Mesh from Eriksson et al., Ref. 33

A mesh generator that is based on only one or two blocks must necessarily be restricted to configurations of one generic type. Other types of configuration could be handled only after extensive recoding of the mesh generation software. More general methods based on several blocks have been developed by Weatherill and Forsey [101] and Shaw et al. [71], who use a Poisson solver in each block (figure 7), and also by Fritz et al. [35] and Seibert [69] (figure 8), who generate an initial mesh algebraically and then iterate with a Poisson solver to obtain a smooth point distribution.

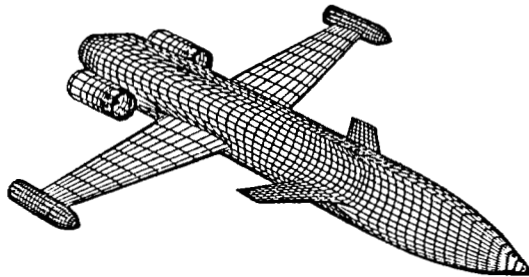


Fig. 7. Mesh from Weatherill and Forsey, Ref. 101

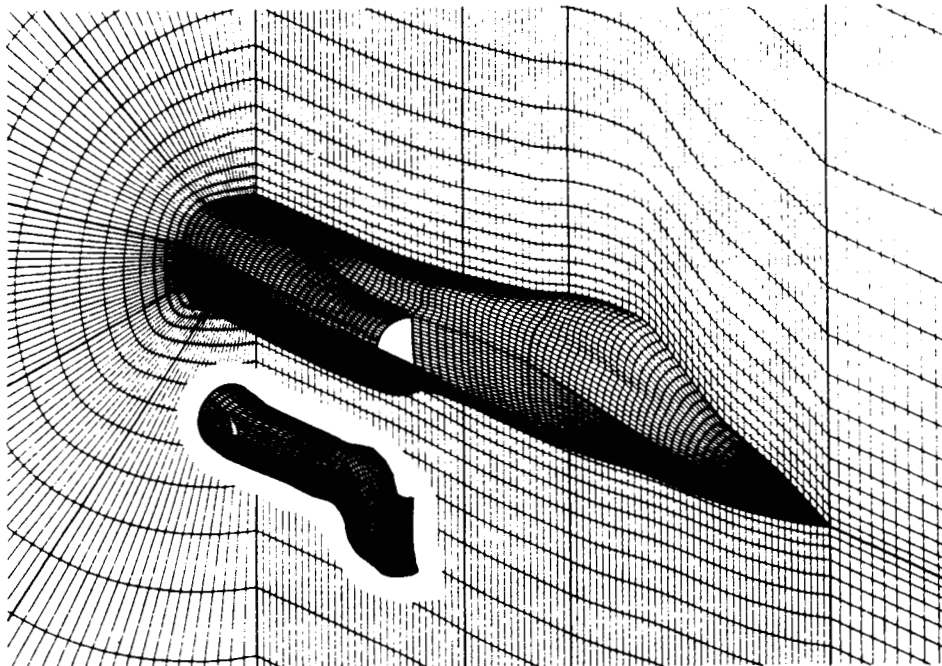


Fig. 8. Mesh from Seibert, Ref. 69

**ORIGINAL PAGE IS  
OF POOR QUALITY**

The inclusion of nacelles, struts and stores introduces an added degree of difficulty. The work of Vigneron et al. [96,97] (figure 9), who used algebraic generation followed by a Poisson type smoothing is therefore particularly impressive. Another outstanding contribution is the paper by Sawada and Takanashi [68]. They used transfinite interpolation to produce a mesh around a complete aircraft with over-wing nacelles (figure 10).

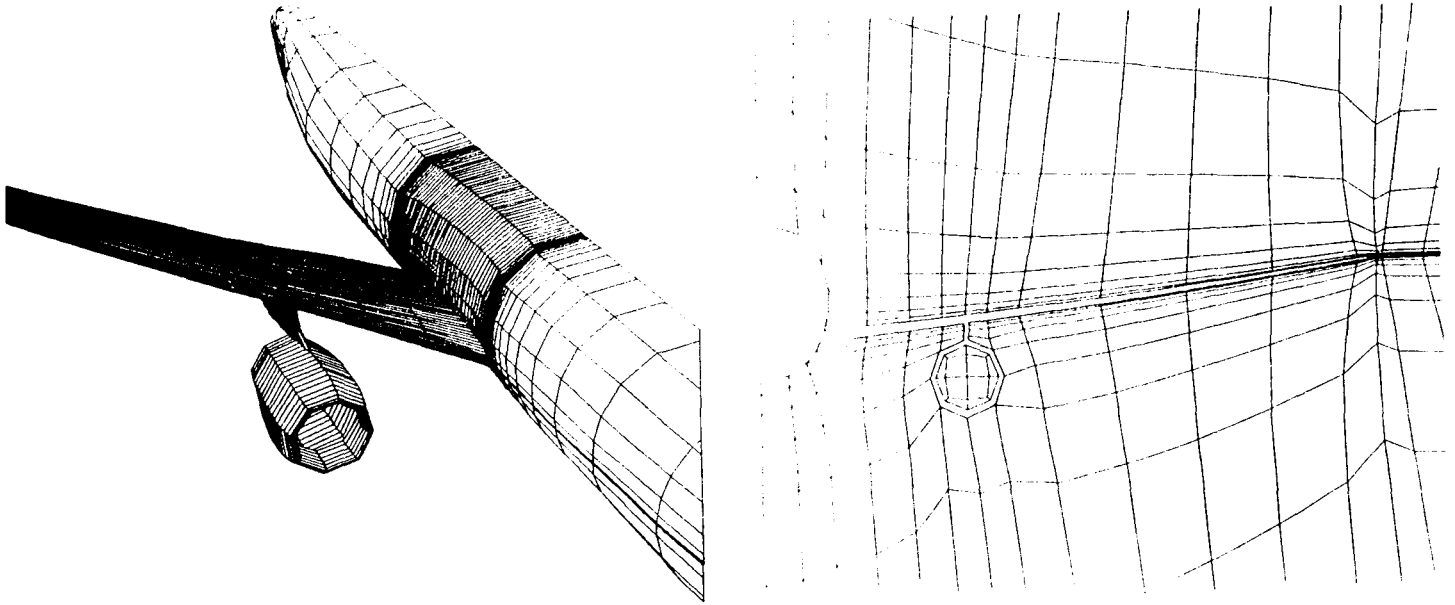


Fig. 9. Mesh from Vigneron et al., Ref. 97

### 3.5 Further Developments

Once one has accepted the need for a multiblock scheme and the extra data structure that this entails, it makes sense to keep the individual blocks fairly simple (i.e. as close to rectangular as possible) in order to simplify the mesh generation process within each block. To treat a complete aircraft configuration may require around 100 blocks, but this can certainly be accommodated if the data structure is sufficiently general and contains complete information about the block face and edge contiguities and the relative orientation of neighboring blocks [15,16,81,87,101,102]. Transfinite interpolation, with prescribed mesh line slopes at the block boundaries would appear to be a perfectly adequate method of mesh generation within each block. This could be followed by a few iterations of a Laplace solver if further smoothness were needed. The remaining problem is the decomposition of the flowfield to give the block structure. Ideally this should be completely automated, but this may be difficult to achieve for arbitrary aircraft shapes. The consequent need for good interactive graphics has been mentioned by several authors and it appears that structured mesh generation for highly complex geometries will continue to rely on the intervention of a skilled user.

ORIGINAL PAGE IS  
OF POOR QUALITY

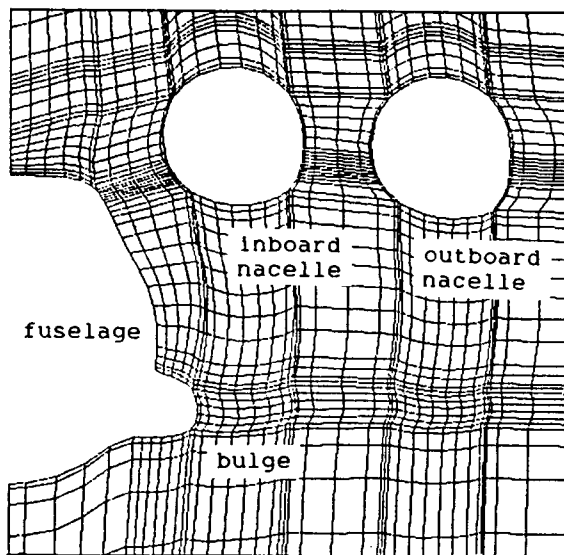
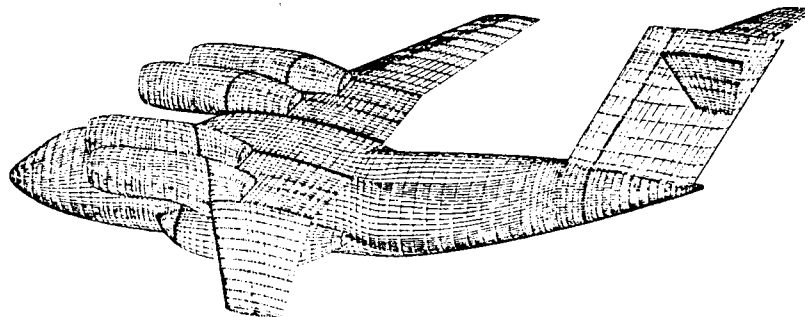


Fig. 10. Mesh from Sawada  
and Takanashi, Ref. 68

#### 4. Triangulations

A review of unstructured mesh generators prior to 1980 has been given by Thacker [84]. Significant developments, however, have taken place since then and efficient triangulation methods are now available for two and three dimensional problems. It is worth noting that any planar triangulation possesses a degree of structure that is not present in three dimensions. First we observe that given a set of  $V$  points in a plane such that  $B$  lie on the convex hull, the number of edges  $E$  and the number of triangles (or faces)  $F$  are specified by the formulae

$$\begin{aligned} E &= 3(V - 1) - B \\ F &= 2(V - 1) - B \end{aligned}$$

In particular, since  $B = O(V^{1/2})$  we see that for a large number of points,

$$E \sim 3V \quad \text{and} \quad F \sim 2V$$

Moreover, if  $k$  denotes the average number of edges meeting at a point then, since each edge is associated with exactly two points, the number of edges is also given by

$$E = \frac{kV}{2}$$

Combining this with the above expression for the number of edges leads to the following expression for  $k$ ,

$$k = 6 - \frac{6}{V} - \frac{2B}{V}$$

and so for large  $V$  we have

$$k \sim 6.$$

The average number of edges meeting at a point is therefore six, and since at least three edges must meet at any point, this places a fairly rigid constraint on the expected variation in the number of edges meeting at any point. In other words, we do not expect too much variation between triangulations for a given set of points in two dimensions. In particular, a high degree of regularity, in terms of the number of edges meeting at any point, is to be expected no matter how we triangulate the points.

There is no such invariance in the number of tetrahedra, triangular faces and edges in three dimensions. It is well known, for example, that a cube can be cut into either five or six tetrahedra. In fact, it is possible to find triangulations of  $N$  points in three space which contain  $O(N)$  points and also triangulations which contain  $O(N^2)$ . Intuitively one would expect that an  $O(N)$  triangulation would be likely to contain better shaped tetrahedra and lead to a greater degree of mesh regularity. The important requirement is, therefore, to find a triangulation scheme and mesh point distribution that will achieve this aim.

#### 4.1 Delaunay Triangulation

The Delaunay triangulation of a set of points and the dual geometric construct, the Voronoi diagram, are extremely fertile concepts that have been the subject of considerable theoretical investigation and have found numerous practical applications. The Voronoi diagram marks off the region of space that lies closer to each point than the other points. This is illustrated for the planar case in figure 11. The solid lines make up the Voronoi diagram which form a tessellation of the space surrounding the points. Each Voronoi tile (e.g. the hatched area around point  $P$ ) consists of the region of the plane that is closer to that point than any other. The edges of the Voronoi diagram are formed from the perpendicular bisectors of the lines connecting neighboring points. In general three edges will meet at a vertex which must be equidistant from three forming points (e.g. points  $P$ ,  $Q_3$ ,  $Q_4$  in figure 11) and hence each vertex is the circumcenter of the triangle formed by three points. This determines a unique triangulation known as the Delaunay triangulation and is such that the circumcircle through each triangle contains no points other than its forming points.

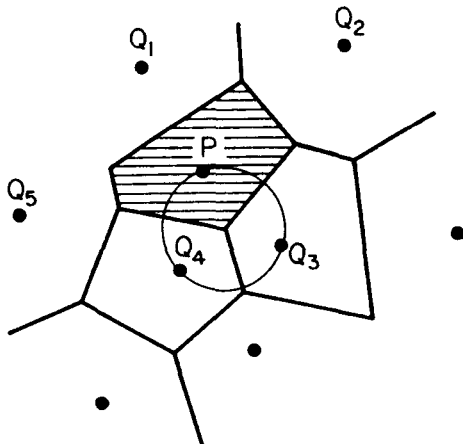


Fig. 11. Voronoi Diagram



The complete mesh is generated by the triangulation of a cloud of points surrounding the aircraft. The point distribution can be defined in any way whatsoever, and it is this generality which makes the Delaunay approach so powerful. The surface geometry for the F-15 was based on a network of points originally generated for use by a panel method. Flow field points were introduced in three sets corresponding to a farfield, midfield and nearfield distribution. The farfield points were generated by defining a Cartesian box with a relatively coarse distribution covering the entire field. A finer distribution of points, again in a regular array, was added in a region extending a few wing chords around the aircraft. Finally, the nearfield points were generated by placing points along normals directed outward from the surface points. Any points which fall inside the aircraft structure are detected and removed. The remaining points are triangulated to create a mesh which varies from a fine distribution of cells near the aircraft to a coarser distribution in the farfield.

The two photographic plates show the surface mesh and a flow solution for the F-15. The mesh was generated for one half of the aircraft; the mesh shown in plate 1 and the surface contours shown in plate 2 have been reflected about the aircraft plane of symmetry. The mesh surrounds one half of the full configuration, including the interior of the duct which extends from the fuselage inlet to the nozzle at the rear. Of the 77,000 points in the mesh, approximately 5,000 are on the aircraft surface, and the complete set of points has been connected to form a collection of 460,000 cells. The surface triangulation shown in plate 1 provides a good indication of the mesh resolution, and plate 2 shows the pressure distribution for a case run at a freestream Mach number of 0.81 and an angle of attack of 4.84 degrees. In the color coded picture (plate 2), red represents low pressure and blue represents high pressure with the fringe bar indicating the graduations in between these extremes.

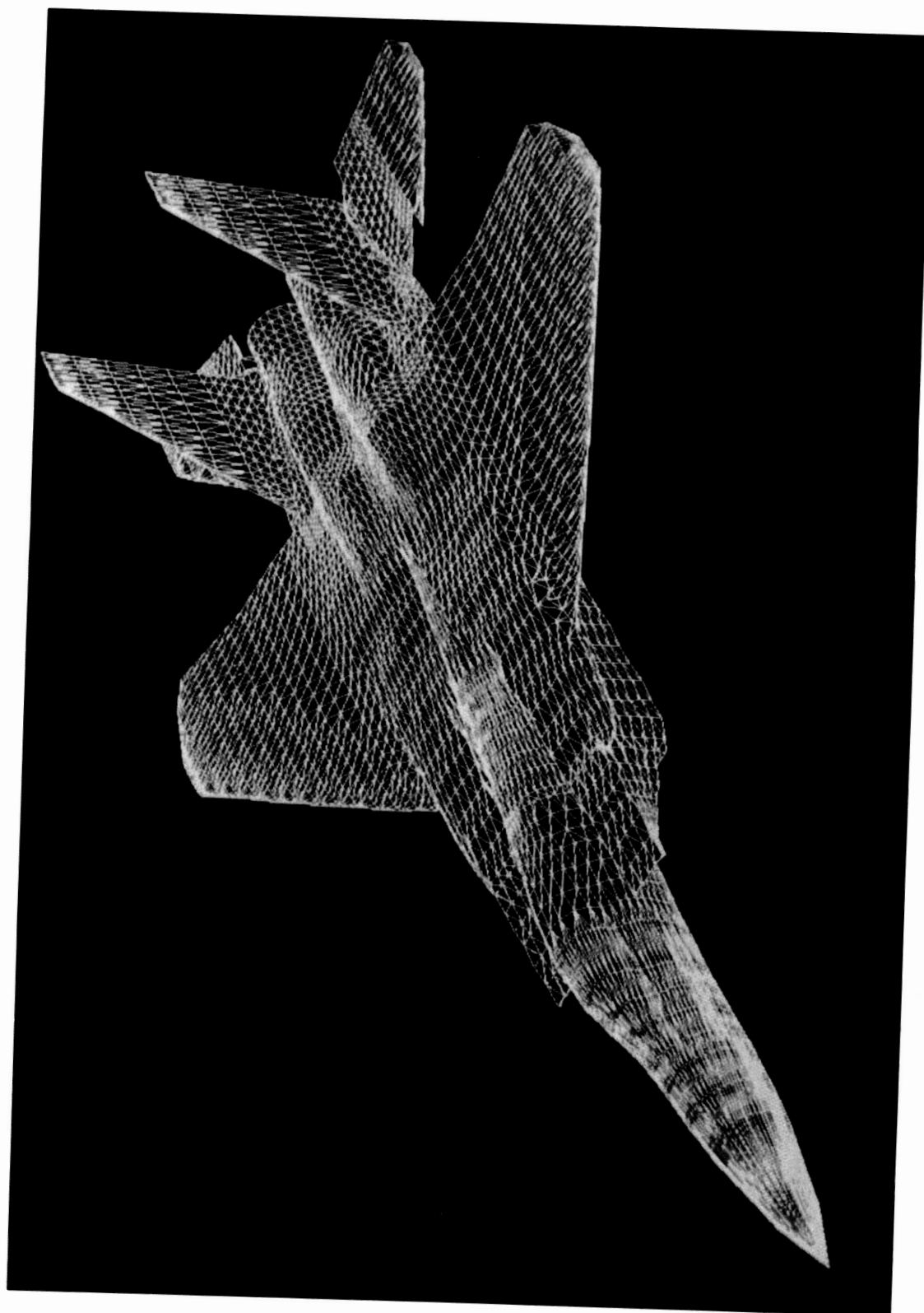


Plate 1

ORIGINAL PAGE  
COLOR PHOTOGRAPH

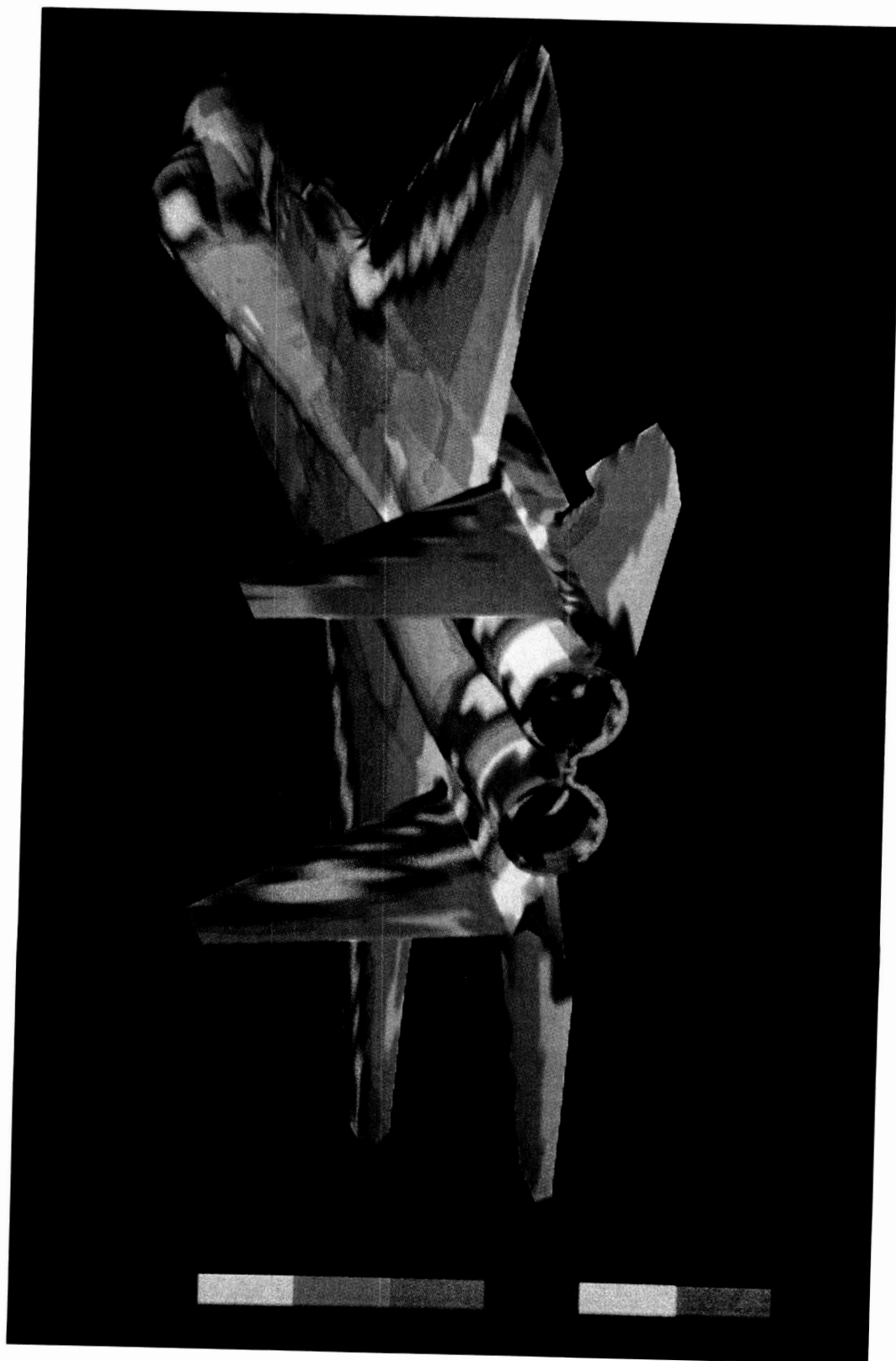
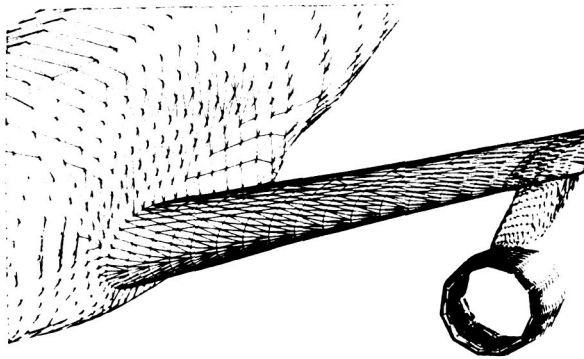


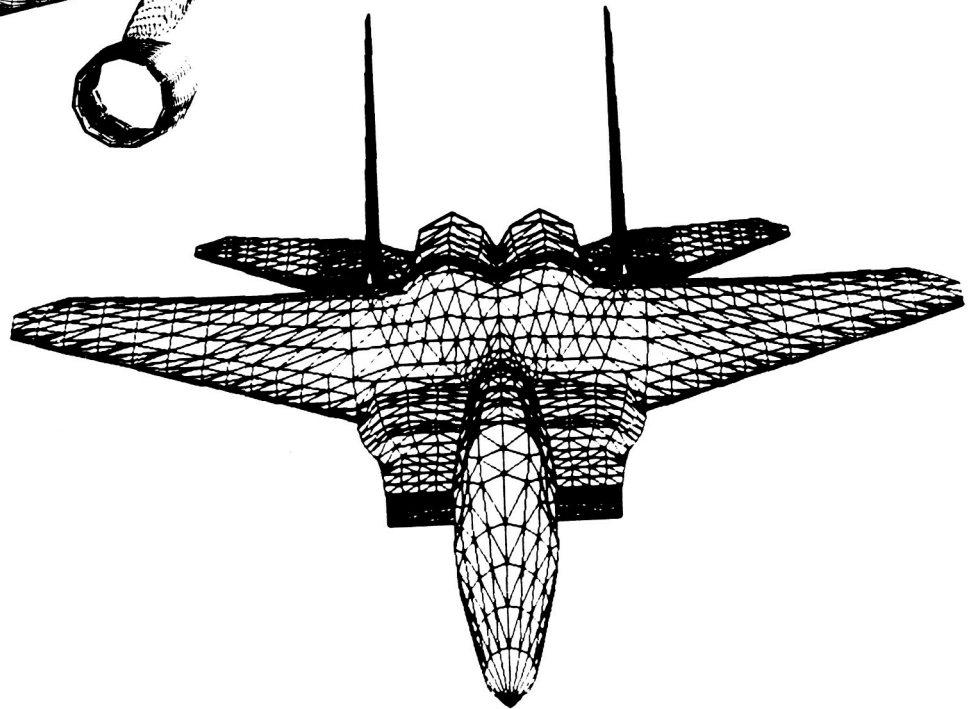
Plate 2

These concepts generalize to higher dimensions. In particular, the Delaunay triangulation of three space is the unique triangulation such that the circumsphere through each tetrahedron contains no points other than its forming points. In two dimensions this circle criterion can be shown to be equivalent to the equiangular property that selects the triangulation which maximizes the minimum of the six angles in any pair of two triangles which make up a convex quadrilateral. No equivalent characterization is known in three dimensions but the circle criterion can still be regarded as selecting a good triangulation for the given set of points.

The Delaunay triangulation has been applied to mesh generation for structural problems by Cavendish et al. [21] and for semi-conductor device simulation by Cendes [22,23] et al. A three dimensional, Delaunay based, mesh generator developed by Baker [7] has been linked to the finite element flow solver of Jameson and reference 47 contains the first published example of an Euler flow calculation over a complete aircraft. Detail of the surface mesh around the inner nacelle/strut/wing area of the Boeing 747-200 is presented in figure 12(a) and figure 12(b) shows the surface triangulation associated with a tetrahedral mesh that was generated for the F-15. The generality and flexibility of this method is clearly evident and the technique is capable of generating tetrahedral meshes around any three dimensional object.



(a) Boeing 747-200



(b) McDonnell Douglas F-15

Fig. 12. Surface Triangulation from Baker, Ref. 7 and 47

#### 4.2 Moving Front

An alternative approach to the triangulation problem is the moving front technique first suggested by Lo [51]. This idea is illustrated in figure 13, where a layer of triangles has already been placed around an internal boundary surface. The outer edges of this layer forms the front and a new triangle is constructed on each edge by connecting the edge to the nearest point in such a way that the shape of the new triangle is acceptable. When triangles have been formed on all front edges, a second layer of triangles will be in place. The procedure is repeated with the new front until the whole set of points has been triangulated.

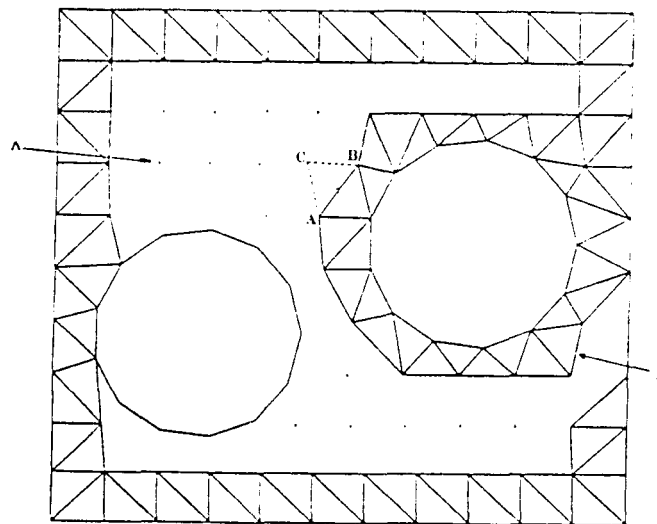


Fig. 13. Moving Front Method (taken from Lo, Ref. 51)

The extension of this idea to three dimensions is not an easy task since the front, formed by a layer of tetrahedra, is now made up of a surface of triangular faces. It is presumably necessary to take care when determining the intersections of planar faces, and to ensure that no overlapping of tetrahedra occurs or that holes are left when the front folds over on itself. Significant progress has been made in this area, however, by Peraire et al. [62,63] and also by Löhner [52]. Figure 14 shows detail of the surface triangulation associated with a tetrahedral mesh that Peraire generated around a wing/canard/fuselage/tail combination.

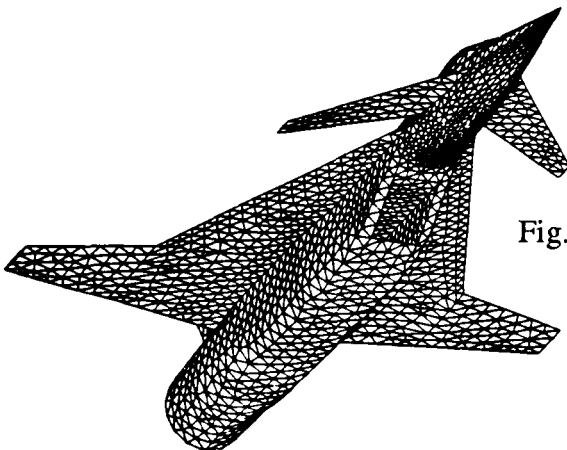


Fig. 14. Surface Triangulation for Wing/Canard/Fuselage/Tail Configuration (taken from Peraire et al., Ref. 63)

## 5. Mesh Type and Solution Accuracy

An inevitable consequence of creating a surface conforming mesh is the introduction of mesh stretching. Some degree of mesh stretching is clearly desirable in order to achieve an efficient distribution of mesh points throughout the flow field. However, the stretching should be smooth to prevent spurious, numerically generated effects from contaminating the flow solution. Investigation of this subject is still in its infancy and an improved understanding of this important area is clearly necessary. Two aspects of mesh distortion are considered below.

### 5.1 Truncation Error

To illustrate ideas we consider a one dimensional stretching from the interval  $0 \leq \xi \leq 1$  to physical space defined by the interval  $x_0 \leq x \leq x_N$ . In most cases there will not be an explicit mapping from  $\xi$  to  $x$ . The variation in mesh width can, however, be regarded as the result of an implied transformation  $x(\xi)$ . We assume that the mapped interval is divided into  $N$  equally spaced increments  $\Delta\xi = 1/N$  and write  $x_j = x(j\Delta\xi)$  with the further requirement

$$x_0 < x_1 < x_2 < \dots < x_j < \dots < x_N$$

We also write  $h_j = x_j - x_{j-1}$   
and let  $h = \max_j h_j$

As Thompson et al. [90] point out, it is necessary to distinguish between two senses of order. First there is the behavior of the error as the number of points in the field is increased while maintaining the same relative point distribution over the field. Consider the approximation to the first derivative  $f_x$  given by

$$\frac{f_{j+1} - f_{j-1}}{x_{j+1} - x_{j-1}} = \frac{f_\xi}{x_\xi} + \frac{\Delta\xi^2}{6x_\xi} (f_{\xi\xi\xi} - \frac{x_{\xi\xi\xi}}{x_\xi} f_\xi) + O(\Delta\xi^4) \quad (11)$$

The first term is, of course, the required derivative  $f_x$ ; the second term is the principal part of the truncation error, which is formally second order. An alternative definition of order is based on the behavior of the error as the relative point distribution is changed so as to reduce the spacing locally with a fixed number of points in the field. Expanding  $f_{j+1}$  and  $f_{j-1}$  as functions of  $x$  about the position  $x_j$  we obtain

$$\frac{f_{j+1} - f_{j-1}}{x_{j+1} - x_{j-1}} = f_x + \frac{1}{2} (h_{j+1} - h_j) f_{xx} + \frac{1}{6} [h_{j+1}^2 - h_{j+1}h_j + h_j^2] f_{xxx} + \text{HOT} \quad (12)$$

But

$$h_{j+1} - h_j = x_{\xi\xi} \Delta\xi^2 + O(\Delta\xi^4)$$

$$h_{j+1}^2 - h_{j+1}h_j + h_j^2 = x_\xi^2 \Delta\xi^2 + O(\Delta\xi^4)$$

Hence

$$\frac{f_{j+1} - f_{j-1}}{x_{j+1} - x_{j-1}} = f_x + \frac{\Delta\xi^2}{2} (x_{\xi\xi} f_{xx} + \frac{x_{\xi}^2}{3} f_{xxx}) + \text{HOT} \quad (13)$$

Now

$$h_j = x_{\xi} \Delta\xi + O(\Delta\xi^2)$$

so we have

$$\frac{f_{j+1} - f_{j-1}}{x_{j+1} - x_{j-1}} = f_x + \frac{h_j^2}{2} \left( \frac{x_{\xi\xi}}{x_{\xi}} f_{xx} + \frac{1}{3} f_{xxx} \right) + \text{HOT} \quad (14)$$

It is apparent that a necessary condition for the approximation to be second order in the second sense is that the term

$$\frac{x_{\xi\xi\xi}}{x_{\xi}^2} = O(1) \quad (15)$$

This is discussed by Thompson et al. [90], who point out that a similar condition is required to maintain local order in two dimensions. A further condition must also be imposed to limit the rate at which the Jacobian approaches zero. This extra condition is essentially a limit on the degree of nonorthogonality that can be tolerated.

It should be noted in passing that expression (13) or (14) is exact for linear  $f$ . This is not the case if we use the exact mapping derivative  $x_{\xi}$  in place of  $x_{j+1} - x_{j-1}$ . For then, we have

$$\frac{f_{j+1} - f_{j-1}}{2\Delta\xi x_{\xi}} = f_x + \frac{\Delta\xi^2}{2} \left( \frac{x_{\xi\xi\xi}}{3x_{\xi}} f_x + x_{\xi\xi} f_{xx} + \frac{x_{\xi}^2}{3} f_{xxx} \right) + \text{HOT}$$

It is therefore preferable to evaluate the metric coefficients numerically by the same difference representation as is used for the dependent variable. This conclusion was probably first stated by Steger [78].

The issue of local accuracy and stability on nonuniform meshes has been examined in some detail by Turkel [92]. He first defines a local stretching factor  $r_j = \frac{h_{j+1}}{h_j}$  and then classifies three groups of stretchings:

(a) Quasi-uniform (or algebraic) if

$$r_j = 1 + O(h^p), \quad p > 0$$

(b) Exponential if (a) is not valid but

$$\frac{r_{j+1}}{r_j} = 1 + O(h) \quad \text{and}$$

(c) faster than exponential if neither (a) nor (b) is true.

Now  $h_{j+1} - h_j = h_j(r_j - 1)$  and it follows that if the stretching is quasi-uniform then from expression (12), the approximation remains locally second order (i.e. second order in the second sense described above). A quasi-uniform stretching must therefore satisfy condition (15). Further we can write

$$\begin{aligned} r_j = \frac{h_{j+1}}{h_j} &= \frac{x_\xi \Delta \xi + \frac{\Delta \xi^2}{2} x_{\xi\xi}}{x_\xi \Delta \xi - \frac{\Delta \xi^2}{2} x_{\xi\xi}} + \text{HOT} \\ &= 1 + \Delta \xi \frac{x_{\xi\xi}}{x_\xi} + \text{HOT} \end{aligned}$$

or

$$r_j = 1 + h_j \frac{x_{\xi\xi}}{x_\xi} + \text{HOT}$$

Thus condition (15) implies that the stretching is quasi-uniform.

Turkel considers several finite difference and quadrilateral based finite volume formulations and his main conclusions are that with quasi-uniform stretchings all second order techniques retain their accuracy locally. If the stretchings are exponential or faster, central difference approximations will usually deteriorate to first order accuracy, and in the case of a cell centered approximation, the finite volume approach can yield an inconsistent scheme.

Another illuminating investigation of truncation error has been provided by Roe [67]. He considers vertex based finite volume schemes and examines the error that arises from using a trapezoidal integration rule to evaluate the flux integral around different cell types. He concludes that only a few specific cell types retain second order accuracy locally. In particular, among quadrilaterals only a parallelogram can admit a locally second order accurate approximation. Furthermore he shows that a triangular mesh can only have first order accuracy.

This rather alarming conclusion would appear to put unstructured meshes at a serious disadvantage. However, recent work by Giles [36] suggests that although the truncation error on an unstructured mesh is first order, the solution error remains second order. Further investigation is required to shed more light on this difficult area. It is clear, however, that future investigations of accuracy must attempt to follow Giles' lead in estimating the solution error and not basing conclusions on the order of the truncation error alone.

## 5.2 Wave Propagation

Consider the scalar wave equation

$$u_t + cu_x = 0, \quad c > 0 \quad (16)$$

which represents the propagation of disturbance traveling to the right with constant velocity  $c$ . We now discretize the spatial terms to obtain the semi-discrete form



$$\frac{du_j}{dt} = -c \frac{(u_{j+1} - u_{j-1}))}{x_{j+1} - x_{j-1}} \quad (17)$$

On a uniform mesh  $x_{j+1} - x_j = h = \text{const.}$  and this equation reduces to

$$\frac{du_j}{dt} = -c \frac{(u_{j+1} - u_{j-1}))}{2h} \quad (18)$$

Equation (16) admits traveling wave solutions of the form

$$e^{i(kx - \omega t)} \quad \text{where} \quad k = \frac{\omega}{c}$$

If we look for similar solutions of the finite difference approximation (18) we obtain a dispersion relation

$$\omega = \frac{c}{h} \sin(kh), \quad -\pi \leq kh \leq \pi$$

In other words, the mesh acts like a dispersive medium so that a component with wave number  $k$  will travel with a phase velocity

$$c^* = c \frac{\sin(kh)}{kh}$$

and a group velocity

$$\frac{d\omega}{dk} = c \cos(kh)$$

We observe that for small values of the wave number  $k$ , the group velocity is close to the continuum solution velocity  $c$ . For higher wave numbers this is no longer the case. In fact, when  $kh = \pi/2$  corresponding to a wave length

$$\lambda \equiv \frac{2\pi}{k} = 4h$$

the component has zero group velocity, and at the highest wave number  $kh = \pi$ , which corresponds to the shortest wavelength

$$\lambda = 2h$$

the component travels upstream at speed  $c$ .

An investigation of the wave propagation characteristics for different time integration schemes has been pursued by Giles and Thompkins [37], Trefethen [91] and Vichnevetsky [93–95]. Of particular interest is recent work by Vichnevetsky [95] who considers a non-uniform mesh and looks for solutions of the form

$$u = A_{\omega}(x,t) e^{i(\phi(x) - \omega t)}$$

The wave number  $k$  and amplitude  $A_\omega$  are now slowly varying functions of  $x$ . As the wave number changes on an expanding mesh, it is possible for the group velocity to decrease, reach zero and become negative (see figure 15). A solution component can therefore undergo a reflection and, if the mesh expands in all directions, it is possible for the wave to become trapped.

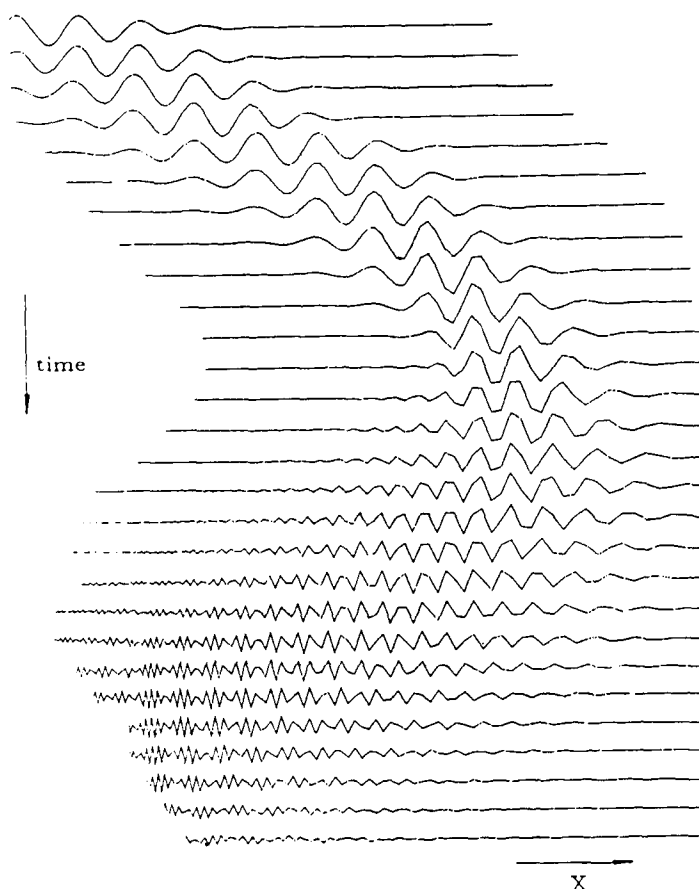


Fig. 15. Wave Reflection on an Expanding Mesh  
(taken from Vichnevetsky, Ref. 95)

Vichnevetsky's analysis and indeed the results of all the investigators in this area is restricted to non-dissipative approximations. When artificial dissipation is present, these waves are damped and no undesired transients are left trapped in the mesh. However, the wave propagation analysis could have important implications for unsteady flow problems where the artificial dissipation should be kept small and not interfere with the true time accurate behavior.

## 6. Adaptive Meshing

It has long been recognized that a mesh determined independently of the flow solution is unlikely to resolve all the flow features. Specific regions of the flow field will be subject to rapid variations in flow variables. Solutions of the Euler equations require the accurate capture of shockwaves and the resolution of vortices that can emanate from sharp edges in three dimensional computations. With the advent of Navier Stokes calculations it becomes necessary to ensure a fine mesh in wake regions and areas of separated flow. It is clearly not possible to achieve the necessary mesh resolution a priori without introducing an unacceptably large number of points throughout the flow field. The use of an adaptive mesh that evolves with the flow solution is therefore an unavoidable requirement. In fact, it is anticipated that an adaptive meshing capability will be an integral part of all three dimensional flow codes within a few years.

### 6.1 Mesh Redistribution

An option that received early attention is use of mesh redistribution to achieve the required density of mesh points. One dimensional mesh stretchings that bunch the mesh lines have been considered, and stretchings in more than one direction have also received attention [29,39,58,90]. Within the framework of numerical generation methods, it is possible to link the source and repulsion terms to some measure of the truncation error or variation in flow variables. Other numerical procedures based on a variational approach have been tried [17,90]. Here some flow property is included in the functional to be minimized. The Euler-Lagrange equation that one obtains can then be solved numerically to generate the new mesh. A common difficulty of all the methods based on mesh redistribution is the need to ensure that the mesh cells do not become too distorted and, in particular, do not cross over each other. It is therefore necessary to monitor very closely changes in cell size and shape, and to halt the mesh adaptation if tolerances on these constraints are exceeded.

### 6.2 Mesh Enrichment

An alternative approach which does not suffer from these difficulties is mesh enrichment. Here the mesh is successively refined whenever the truncation error, or some convenient measure of the flow variables, becomes too large. Notable work in this area is that of Berger and Jameson [14] and Dannenhoffer and Baron [25,26]. The main difficulty of this approach is the need to keep track of the interfaces where refinement occurs. This requirement adds an overhead to the data handling and complicates the flow solver. It is also necessary to ensure conservation and stability at the interfaces where refinement occurs. These problems are difficult to treat in two dimensions; in three dimensions the complexity of this task is increased considerably.

It is in the context of mesh adaption that unstructured meshes enjoy a distinct advantage over structured meshes. A triangular mesh can easily be refined without the need to introduce interfaces [1,23,41,42,53,54,57,60,61,63,83]. In other words the mesh remains entirely transparent to the flow solver. The addition of mesh points can be carried out either by explicitly refining triangles, or alternatively by retriangulating the mesh to include the extra mesh points. This latter approach is particularly well suited to the Delaunay triangulation technique and has been demonstrated very effectively by Holmes et al. [42]. Figure 16 shows the mesh in a channel with a bump for a supersonic onset flow. A Delaunay triangulator was used with adaptive mesh enrichment, and the concentration of triangles which formed around the shockwaves is clearly evident. An example of the former approach has been provided very recently for a three dimensional triangulation by Periaire [63].

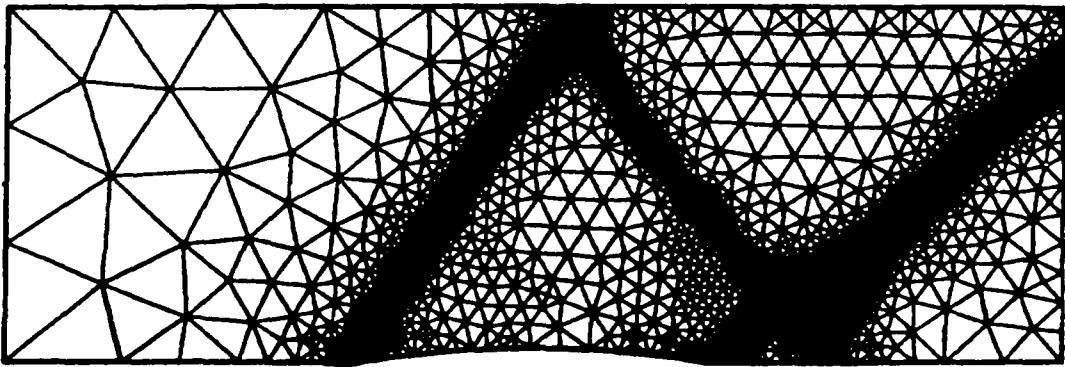


Fig. 16. Mesh Enrichment on a Triangular Mesh  
(taken from Holmes et al., Ref. 42)

### 7. Whither Mesh Generation ?

It is a reckless though irresistible prospect to speculate on the future development of mesh generation methods. This is particularly apposite since we are now at a stage where the primary goal of treating complete aircraft configurations has been achieved. What remains is to bring these 'primitive' methods to a stage where it is possible to handle shapes of arbitrary generality with ease, without the need for special treatment, or undue interaction from the user whenever a different configuration arises. Of particular importance will be the need to achieve the most accurate solution possible for a given number of points and, if feasible, provide an estimate of the accuracy obtained. The development of efficient and robust adaptive meshing techniques is therefore a mandatory requirement. Not only should extra points be added to refine the mesh where needed, but it is also necessary to ensure that the shape and, in particular, aspect ratio of the cells remains acceptable. This may require the addition of points in some areas and the deletion of points in other regions. A deeper understanding of the dependence of the solution on mesh stretching and distortion is therefore required. Techniques that will either enrich or prune the mesh in selected regions must also be implemented as part of an adaptive mesh generation package. It is the author's opinion that it will be the unstructured meshes that best meet these stringent requirements for generality and adaptability. However, much effort has been devoted to the development of structured mesh generation schemes and it is unlikely that they will be abandoned in the near future. Indeed, the future vigor of research into mesh generation can best be served by the competitive pursuit of both approaches.

## References

1. F. Angrand, V. Billey, J. Periaux, C. Pouletty and J.P. Rosenblum, "2-D and 3-D Euler Computations around Lifting Bodies on Self Adapted Finite Element Meshes", Sixth International Symposium on Finite Element Methods in Flow Problems, Antibes, France, June 1986
2. B.G. Arlinger, "Calculation of Transonic Flow around Axisymmetric Inlets", AIAA 13th Aerospace Sciences Meetings, Pasadena, CA, AIAA Paper 75-80, January 1975.
3. B.G. Arlinger and W. Schmidt, "Design and Analysis of Slat Systems in Transonic Flow", 11th ICAS Congress, Lisbon, Portugal, September 1978.
4. E. Atta, "Component-Adaptive Grid Interfacing", AIAA 19th Aerospace Sciences Meeting, AIAA Paper 81-0382, January 1981.
5. T.J. Baker, "A Numerical Method to Compute Inviscid Flow around Axisymmetric Ducted Bodies", IUTAM Symposium Transsonicum II, Grottingen, September 1975, Proc. pub Springer Verlag, 1976.
6. T.J. Baker, "Mesh Generation by a Sequence of Transformations", Appl. Num. Math., Vol. 2, No. 1, December 1986.
7. T.J. Baker, "Three Dimensional Mesh Generation by Triangulation of Arbitrary Point Sets", AIAA 8th Computational Fluid Dynamics Conference, Honolulu, Hawaii, AIAA Paper 87-1124, June 1987.
8. T.J. Baker and A. Jameson, "A Novel Finite Element Method for the Calculation of Inviscid Flow over a Complete Aircraft", Sixth International Symposium on Finite Element Methods in Flow Problems, Antibes, France, June 1986.
9. T.J. Baker, A. Jameson and R.E. Vermeland, "Three-Dimensional Euler Solutions with Grid Embedding", AIAA 23rd Aerospace Sciences Meeting, Reno, AIAA Paper 85-0121, January 1985.
10. J.A. Benek, J.L. Steger and F.C. Dougherty, "A Flexible Grid Embedding Technique with Application to the Euler Equations", AIAA 6th Computational Fluid Dynamics Conference, Danvers, MA, AIAA Paper 83-1944, July 1983.
11. J.A. Benek, P.G. Buning and J.L. Steger, "A 3-D Chimera Grid Embedding Technique", AIAA 7th Computational Fluid Dynamics Conference, Cincinnati, Ohio, AIAA Paper 85-1523, June 1985.
12. J.A. Benek, T.L. Donegan and N.E. Suhs, "Extended Chimera Grid Embedding Scheme with Application to Viscous Flows", AIAA 8th Computational Fluid Dynamics Conference, Honolulu, Hawaii, AIAA Paper 87-1126, June 1987.
13. M.J. Berger, "On Conservation at Grid Interfaces", SIAM J. Num. Anal., Vol. 24, No. 5, pp. 967-984, October 1987.
14. M.J. Berger and A. Jameson, "Automatic Adaptive Grid Refinement for the Euler Equations", AIAA J., Vol. 23, No. 4, pp. 561-568, April, 1985.
15. J.W. Boerstael, "Problem and Solution Formulations for the Generation of 3D

Block-Structured Grids", International Conference on Numerical Grid Generation in Computational Fluid Dynamics, Landshut, FRG, July 1986 (Proc. ed. J. Hauser and C. Taylor, pub. Pineridge Press).

16. J. W. Boerstoeel, "Preliminary Design and Analysis of Procedures for the Numerical Generation of 3D Block-Structured Grids", NLR Tech. Report No. 86102L.
17. J.U. Brackbill and J.S. Saltzman, "Adaptive Zoning for Singular Problems in Two Dimensions", JCP, Vol. 46, pp 342-368, 1982.
18. M.O. Bristeau, O. Pironneau, R. Glowinski, J. Periaux, P. Perrier and G. Poirier, "On the Numerical Solution of Nonlinear Problems in Fluid Dynamics by Least Squares and Finite Element Methods (II). Application to Transonic Flow Simulations", Proc. 3rd International Conference on Finite Elements in Nonlinear Mechanics, FENOMECH 84, Stuttgart, 1984, edited by J. St. Dottsini, North Holland 1985, pp. 363-394.
19. L.A. Carlson, "Transonic Airfoil Analysis and Design Using Cartesian Coordinates", AIAA 2nd Computational Fluid Dynamics Conference, Hartford, June 1975.
20. D.A. Caughey, "A Systematic Procedure for Generating useful Conformal Mappings", Int. J. Num. Meth. Eng., Vol. 12, pp. 1651-1657.
21. J.C. Cavendish, D.A. Field and W.H. Frey, "An Approach to Automatic Three-Dimensional Finite Element Mesh Generation", Int. J. Num. Meth. Eng., Vol. 21, pp. 329-347, 1985.
22. Z.J. Cendes, D. Shenton and H. Shahnasser, "Magnetic Field Computations using Delaunay Triangulations and Complementary Finite Element Methods", IEEE Trans. Magnetics, Vol. MAG-19, No. 6, pp. 2551-2554, Nov. 1983.
23. Z.J. Cendes and D.N. Shenton, "Adaptive Mesh Refinement in the Finite Element Computation of Magnetic Fields", IEEE Trans. Magnetics, Vol. MAG-21, No. 5, pp. 1811-1816, Sept. 1985.
24. D.R. Chapman, "Trends and Pacing Items in Computational Aerodynamics", Lecture Notes in Physics, Vol. 141, (ed. Reynolds and MacCormack), Springer-Verlag, pp. 1-12, 1980.
25. J.F. Dannenhoffer III and J.R. Baron, "Grid Adaptation for the 2-D Euler Equations", AIAA Paper 85-0484, January 1985.
26. J.F. Dannenhoffer III and J.R. Baron, "Adaptive Procedure for Steady State Solution of Hyperbolic Equations", AIAA 22nd Aerospace Sciences Meeting, Reno, AIAA Paper 84-0005, January 1984.
27. A. Eberle and W. Schwarz, "Grid Generation for an Advanced Fighter Aircraft", in Three Dimensional Grid Generation for Complex Configurations - Recent Progress (compiled by Steger and Thompson) AGARDograph No. 309.
28. P.R. Eiseman, "A Multi-Surface Method of Coordinate Generation", JCP, Vol. 33, pp. 118-150, 1979.
29. P.R. Eiseman, "Alternating Direction Adaptive Grid Generation", AIAA J., Vol. 23, No. 4, pp. 551-560, April 1985.

30. P.R. Eiseman and G. Erlebacher, "Grid Generation for the Solution of Partial Differential Equations", ICASE Report No. 87-57.
31. L.E. Eriksson, "Practical Three-Dimensional Mesh Generation Using Transfinite Interpolation", Lecture Series Notes 1983-04, von Karman Institute for Fluid Dynamics, Brussels, Belgium, 1983.
32. L.E. Eriksson, "Generation of Boundary-Conforming Grids Around Wing-Body Configurations using Transfinite Interpolation", AIAA J., Vol. 20, No. 10, pp. 1313-1320, 1982.
33. L.E. Eriksson, R.E. Smith, M.R. Wiese and N. Farr, "Grid Generation and Inviscid Flow Computation about Cranked-Winged Airplane Geometries", AIAA 8th Computational Fluid Dynamics Conference, Honolulu, Hawaii, AIAA Paper 87-1125, June 1987.
34. J. Flores, S.G. Reznick, T.L. Holst and K. Gundy, "Transonic Navier-Stokes Solutions for a Fighter-Like Configuration", AIAA 25th Aerospace Sciences Meeting, Reno, NV, AIAA Paper 87-0032, January 1987.
35. W. Fritz, W. Haase and W. Seibert, "Mesh Generation for Industrial Application of Euler and Navier Stokes Solvers", in Three Dimensional Grid Generation for Complex Configurations - Recent Progress (compiled by Steger and Thompson) AGARDograph No. 309, to appear 1988.
36. M.B. Giles, "Accuracy of Node-Based Solutions on Irregular Meshes", submitted to the 11th International Conference on Numerical Methods in Fluid Dynamics, Williamsburg, VA, June 1988.
37. M.B. Giles and W.T. Thompkins, Jr., "Propagation and Stability of Wavelike Solutions of Finite Difference Equations with Variable Coefficients", JCP, Vol. 58, pp. 349-360, 1985.
38. W.J. Gordon, "Blending-Function Methods of Bivariate and Multivariable Interpolation and Approximation", SIAM J. Num. Anal., Vol. 8, No. 1, pp 158-177, 1971.
39. P.A. Gnoffo, "A Finite-Volume, Adaptive Grid Algorithm Applied to Planetary Entry Flowfields", AIAA J., Vol. 21, No. 9, pp. 1249-1254, Sept. 1983.
40. J.D. Hoffman, "Relationship between the Truncation Errors of Centered Finite-Difference Approximations on Uniform and Nonuniform Meshes", JCP, Vol. 46, pp 469-474, 1982.
41. D.G. Holmes and S.H. Lamson, "Adaptive Triangular Meshes for Compressible Flow Solutions", International Conference on Numerical Grid Generation in Computational Fluid Dynamics, Landshut, FRG, July 1986 (Proc. ed. J. Hauser and C. Taylor, pub. Pineridge Press).
42. D.G. Holmes, S.H. Lamson and S.D. Connell, "Quasi-3D Solutions for Transonic, Inviscid Flows by Adaptive Triangulation", to be presented at ASME Gas Turbine Meeting, June 1988.
43. D.C. Ives, "A Modern Look at Conformal Mapping including Doubly Connected Regions", AIAA 8th Fluid and Plasma Dynamics Conference, Hartford, AIAA Paper

75-842, June 1975.

44. A. Jameson and T.J. Baker, "Solution of the Euler Equations for Complex Configurations", AIAA 6th Computational Fluid Dynamics Conference, Danvers, MA, AIAA Paper 83-1929, July 1983.
45. A. Jameson and D.A. Caughey, "A Finite Volume Method for Transonic Potential Flow Calculations", AIAA 3rd Computational Fluid Dynamics Conference, Albuquerque, NM, June 1977.
46. A. Jameson and T.J. Baker, "Multigrid Solution of the Euler Equations for Aircraft Configurations", AIAA 22nd Aerospace Sciences Meeting, Reno, AIAA Paper 84-0093, January 1984.
47. A. Jameson, T.J. Baker and N.P. Weatherill, "Calculation of Inviscid Transonic Flow over a Complete Aircraft", AIAA 24th Aerospace Sciences Meeting, Reno, NV, AIAA Paper 86-0103, January 1986.
48. A. Jameson and T.J. Baker, "Improvements to the Aircraft Euler Method", AIAA 25th Aerospace Sciences Meeting, Reno, AIAA Paper 87-0452, January 1987.
49. P. Kutler, "A Perspective of Theoretical and Applied Computational Fluid Dynamics", AIAA J., Vol. 23, No. 3, pp. 328-341, 1985.
50. K.D. Lee, M. Huang, N.J. Yu and P.E. Rubbert, "Grid Generation for General Three-Dimensional Configurations", Proc. NASA Langley Workshop on Numerical Grid Generation Techniques, (ed. Smith) Oct. 1980.
51. S.H. Lo, "A New Mesh Generation Scheme for Arbitrary Planar Domains", Int. J. Num. Meth. Eng., Vol. 21, pp. 1403-1426, 1985.
52. R. Lohner, "Generation of Three-Dimensional Unstructured Grids by the Advancing-Front Method", AIAA 26th Aerospace Sciences Meeting, Reno, AIAA Paper 88-0515, January 1988.
53. R. Lohner, K. Morgan, J. Peraire and O.C. Zienkiewicz, "Finite Element Methods for High Speed Flows", AIAA 7th Computational Fluid Dynamics Conference, Cincinnati, Ohio, AIAA Paper 85-1531, July 1985.
54. R. Lohner and K. Morgan, "Improved Adaptive Refinement Strategies for Finite Element Aerodynamic Computations", AIAA 24th Aerospace Sciences Meeting, Reno, AIAA Paper 86-0499, January 1986.
55. D. Mavriplis and A. Jameson, "Multigrid Solution of the Two-Dimensional Euler Equations on Unstructured Triangular Meshes", AIAA 25th Aerospace Sciences Meeting, Reno, AIAA Paper 87-0353, January 1987.
56. J.F. Middlecoff and P.D. Thomas, "Direct Control of the Grid Point Distribution in Meshes Generated by Elliptic Equations", AIAA 4th Computational Fluid Dynamics Conference, Williamsburg, VA, AIAA Paper 79-1462, July 1979.
57. K. Morgan, J. Peraire, R.R. Thareja and J.R. Stewart, "An Adaptive Finite Element Scheme for the Euler and Navier-Stokes Equations", AIAA 8th Computational Fluid Dynamics Conference, Honolulu, Hawaii, June 1987.



58. K. Nakahashi and G.S. Deiwert, "Self-Adaptive-Grid Method with Application to Airfoil Flow", AIAA J., Vol. 25, No. 4, pp. 513-520, April 1987.
59. K. Nakahashi and S. Obayashi, "Viscous Flow Computations Using a Composite Grid", AIAA 8th Computational Fluid Dynamics Conference, Honolulu, Hawaii, AIAA Paper 87-1128, June 1987.
60. B. Palmerio and A. Dervieux, "Application of a FEM Moving Node Adaptive Method to Accurate Shock Capturing", International Conference on Numerical Grid Generation in Computational Fluid Dynamics, Landshut, FRG, July 1986 (Proc. ed. J. Hauser and C. Taylor, pub. Pineridge Press).
61. J. Peraire, M. Vahdati, K. Morgan and O.C. Zienkiewicz, "Adaptive Remeshing for Compressible Flow Computations", JCP, Vol. 72, No. 2, pp. 449-466, 1987.
62. J. Peraire and K. Morgan, "A General Triangular Mesh Generator", to appear in Int. J. Num. Meth. Eng., 1988.
63. J. Peraire, J. Peiro, L. Formaggia, K. Morgan and O.C. Zienkiewicz, "Finite Element Euler Computations in Three Dimensions", AIAA 26th Aerospace Sciences Meeting, Reno, AIAA Paper 88-0032, January 1988.
64. J. Pike, "Grid Adaptive Algorithms for the Solution of the Euler Equations on Irregular Grids", JCP, Vol. 71, pp. 194-223, 1987.
65. T.A. Reyhner, "Transonic Potential Flow Computation about Three-Dimensional Inlets, Ducts and Bodies", AIAA 13th Fluid and Plasma Dynamics Conference, Snowmass, AIAA Paper 80-1364, July 1980.
66. A.W. Rizzi and M. Inouye, "Time Split Finite-Volume Method for Three-Dimensional Blunt Body Flow", AIAA J., Vol. 11, pp. 1478-1485, 1973.
67. P.L. Roe, "Error Estimates for Cell-Vertex Solutions of the Compressible Euler Equations", ICASE Report No. 87-6.
68. K. Sawada and S. Takanashi, "A Numerical Investigation on Wing/Nacelle Interferences of USB Configuration", AIAA 25th Aerospace Sciences Meeting, Reno, NV, AIAA Paper 87-0455, January 1987.
69. W. Seibert, "An Approach to the Interactive Generation of Block-Structured Volume Grids Using Computer Graphics Devices", International Conference on Numerical Grid Generation in Computational Fluid Dynamics, Landshut, FRG, July 1986 (Proc. ed. J. Hauser and C. Taylor, pub. Pineridge Press).
70. C.C.L. Sells, "Plane Subcritical Flow Past a Lifting Aerofoil", Proc. Roy. Soc., London, Vol. 308A, pp. 377-401, 1968.
71. J. Shaw, C.R. Forsey, N.P. Weatherill and K.E. Rose, "A Block Structured Mesh Generation Technique for Aerodynamic Geometries", International Conference on Numerical Grid Generation in Computational Fluid Dynamics, Landshut, FRG, July 1986 (Proc. ed. J. Hauser and C. Taylor, pub. Pineridge Press).
72. A. Shmilovich and D.A. Caughey, "Grid Generation for Wing-Tail-Fuselage Combinations", ASME Mini-Symposium on Advances in Grid Generation, Houston,

Texas, June 1983.

73. R.E. Smith (Editor), Numerical Grid Generation Techniques, Proc. Conference held at NASA Langley, October 1980.
74. R.E. Smith, "Three-Dimensional Algebraic Grid Generation", AIAA 6th Computational Fluid Dynamics Conference, Danvers, MA, AIAA Paper 83-1904, July 1983.
75. R.L. Sorenson, "Elliptic Generation of Compressible Three-Dimensional Grids about Realistic Aircraft", International Conference on Numerical Grid Generation in Computational Fluid Dynamics, Landshut, FRG, July 1986 (Proc. ed. J. Hauser and C. Taylor, pub. Pineridge Press).
76. R.L. Sorenson, "Three-Dimensional Elliptic Grid Generation for an F-16", in Three Dimensional Grid Generation for Complex Configurations – Recent Progress (compiled by Steger and Thompson) AGARDograph No. 309.
77. J.C. South and A. Jameson, "Relaxation Solutions for Inviscid Axisymmetric Transonic Flow over Blunt or Pointed Bodies", AIAA 1st Computational Fluid Dynamics Conference, Palm Springs, CA, pp. 8-17, 1973.
78. J.L. Steger, "Implicit Finite-Difference Simulation of Flow about Arbitrary Two-Dimensional Geometries", AIAA J., Vol. 16, No. 7, pp. 679-686, July 1978.
79. J.L. Steger and R.L. Sorenson, "Automatic Mesh-Point Clustering near a Boundary in Grid Generation with Elliptic Partial Differential Equations", JCP, Vol. 33, No. 3, pp. 405-410, 1979.
80. J.L. Steger and R.L. Sorenson, "Use of Hyperbolic Partial Differential Equations to Generate Body Fitted Coordinates", Proc. NASA Langley Workshop on Numerical Grid Generation Techniques (ed. Smith), October 1980.
81. J.P. Steinbrenner, S.L. Karmen and J.R. Chawner, "Generation of Multiple Block Grids for Arbitrary 3D Geometries", in Three Dimensional Grid Generation for Complex Configurations – Recent Progress (compiled by Steger and Thompson) AGARDograph No. 309.
82. J. Steinhoff, "Blending Methods for Grid Generation", JCP, Vol. 65, pp. 370-385, 1986.
83. B. Stoufflet, J. Periaux, F. Fezoui and A. Dervieux, "Numerical Simulation of 3-D Hypersonic Euler Flows Around Space Vehicles using Adapted Finite Elements", AIAA Paper 87-0560.
84. W.C. Thacker, "A Brief Review of Techniques for Generating Irregular Computational Grids", Int. J. Num. Meth. Eng., Vol. 15, pp. 1335-1341, 1980.
85. J.F. Thompson, ed., Numerical Grid Generation, Nashville, Tennessee, April 1982, Proc. pub. in Appl. Math. Comp., Vol. 10&11, 1982.
86. J.F. Thompson, "Grid Generation Techniques in Computational Fluid Dynamics", AIAA J., Vol. 22, No. 11, pp. 1505-1523, Nov. 1984.
87. J.F. Thompson, "A Composite Grid Generation Code for General 3-D Regions", AIAA

- 25th Aerospace Sciences Meeting, Reno, AIAA Paper 87-0275, January 1987.
88. J.F. Thompson, F.C. Thomas and C.W. Mastin, "Automatic Numerical Generation of Body Fitted Curvilinear Coordinate System for Field Containing any Number of Arbitrary Two-Dimensional Bodies", JCP, Vol. 15, pp. 299-319, 1974.
  89. J.F. Thompson, Z.U.A. Warsi and C.W. Martin, "Boundary-Fitted Coordinate Systems for Numerical Solution of Partial Differential Equations - A Review", JCP, Vol. 47, pp 1-108, 1982.
  90. J.F. Thompson, Z.U.A. Warsi and C.W. Mastin, Numerical Grid Generation-Foundations and Applications, pub. North-Holland, 1985.
  91. L.N. Trefethen, "Group Velocity Interpretation of the Stability Theory of Gustafsson, Kreiss and Sundstrom", JCP, Vol. 49, pp 199-217, 1983.
  92. E. Turkel, "Accuracy of Schemes with Nonuniform Meshes for Compressible Fluid Flows", Appl. Num. Math., Vol. 2, pp 529-550, 1986.
  93. R. Vichnevetsky, "Invariance Theorems Concerning Reflection at Numerical Boundaries", JCP, Vol. 63, No. 2, pp 268-282, 1986.
  94. R. Vichnevetsky, "Wave Propagation Analysis of Difference Schemes for Hyperbolic Equations: A Review", Int. J. Num. Math. Fluids, Vol. 7, pp 409-452, 1987.
  95. R. Vichnevetsky, "Wave Propagation and Reflection in Irregular Grids for Hyperbolic Equations", Appl. Num. Math., Vol. 3, pp. 133-166, 1987.
  96. Y. Vigneron and T. Lejal, "Calculation of Transonic Flow around an Aircraft Configuration with Motorized Nacelle", ICAS Paper 84-2.10.2.
  97. Y. Vigneron, T. Lejal and R. Collercandy, "Computation of Transonic Flows with Nacelle Simulation", Sixth International Symposium on Finite Element Methods in Flow Problems, Antibes, France, June 1986.
  98. M. Vinokur, "On One-Dimensional Stretching Functions for Finite-Difference Calculations", JCP, Vol. 50, pp. 215-234, 1983.
  99. N.P. Weatherill, "The Generation of Unstructured Grids Using Dirichlet Tessellations", Princeton Univ. MAE Report, No. 1715, July 1985.
  100. N.P. Weatherill, "A Method for Generating Irregular Computational Grids in Multiply Connected Planar Domains", to appear in Int. J. Num. Meth. in Fluids, Vol. 8, 1988.
  101. N.P. Weatherill and C.R. Forsey, "Grid Generation and Flow Calculations for Aircraft Geometries", J. Aircraft, Vol. 22, pp. 855-860, 1985.
  102. N.P. Weatherill and J.A. Shaw, "Component Adaptive Grid Generation for Aircraft Configurations", in Three Dimensional Grid Generation for Complex Configurations - Recent Progress (Compiled by Steger and Thompson) AGARDograph No. 309,
  103. B. Wedan and J.C. South, Jr., "A Method for Solving the Transonic Full-Potential Equation for General Configurations", AIAA 6th Computational Fluid Dynamics

Conference, Danvers, MA, AIAA Paper 83-1889, July 1983.

104. A.M. Winslow, "Numerical Solution of the Quasilinear Poisson Equation in a Non-uniform Triangle Mesh", JCP, Vol. 1, No. 2, pp 149-172, 1967.
105. N.J. Yu, "Grid Generation and Transonic Flow Calculations for Three-Dimensional Configurations", AIAA 13th Fluid and Plasma Dynamics Conference, Snowmass, Colorado, AIAA Paper 80-1391, July 1980.
106. N.J. Yu, K. Kusurose, H.C. Chen and D.M. Sommerfield, "Flow Simulations for a Complex Airplane Configuration using Euler Equations", AIAA 25th Aerospace Sciences Meeting, Reno, NV, AIAA Paper 87-0454, January 1987.

# GENERATION OF UNSTRUCTURED GRIDS AND EULER SOLUTIONS FOR COMPLEX GEOMETRIES

Rainald Löhner

Berkeley Research Associates, Springfield, VA

and

Laboratory for Computational Physics and Fluid Dynamics

Naval Research Laboratory, Washington, D.C.

Paresh Parikh

Vigyan Research Associates, Hampton, VA

Manuel D. Salas

Theoretical Aerodynamics Branch

NASA Langley Research Center, Hampton, VA

## ABSTRACT

We describe algorithms for the generation and adaptation of unstructured grids in two and three dimensions, as well as Euler solvers for unstructured grids. The main purpose of the paper is to demonstrate how unstructured grids may be employed advantageously for the economic simulation of both geometrically as well as physically complex flowfields.

## 1. INTRODUCTION

Over the past years the development of flow solvers for unstructured grids has progressed rapidly. While the main emphasis at the beginning was on Euler solvers [1-5], the current emphasis has shifted onto those fields which may be considered 'peripheral', yet very important for a complete simulation capability. These are: efficient implementation on vector and parallel machines [6], adaptive refinement [4,7-14], mesh generation [5,11,15-21] and flow visualization. In what follows, we describe briefly the capabilities we developed in this area. The main emphasis of the present paper is on applications. Therefore, rather than dwelling in depth on each subject, we will show examples to illustrate the relevant points.

## 2. THE GRID GENERATOR: GENERALIZED ADVANCING FRONT

Several algorithms for the generation of unstructured grids have been proposed in the literature. We may group them into two classes: a) those that introduce gridpoints before constructing the triangulation, and b) those that introduce gridpoints while constructing the triangulation. Members of the first family of schemes include the Voronoi/Delauney triangulation schemes [5,7,15,22-24], as well as the advancing-front algorithms [16,20]. The generalized advancing-front scheme [11,12,17-19] belongs to the second family. It is advocated here because it does not require a separate library of modules to introduce points

before triangulating, and also allows to regenerate adaptively the domain in a very simple manner [11]. The main steps involved when generating a grid using the advancing-front technique [11,12,17-19] are as follows:

- F.1 Define the boundaries (surfaces) of the domain to be gridded.
- F.2 Set up a background grid to define the spatial variation of the size, the stretching, and the stretching direction of the elements to be generated. The background grid consists of tetrahedrons. At the nodes we define the desired element size, stretching and stretching direction. This background grid must completely cover the domain to be gridded.
- F.3 Using the information stored on the background grid, set up faces on all these boundaries. This yields the initial front. At the same time, find the generation parameters (element size, stretching and stretching direction) for the new faces from the background grid.
- F.4 Select the next face to be deleted from the front; in order to avoid large elements crossing over regions of small elements, the face forming the smallest new element is selected as the next face to be deleted from the list of faces.
- F.5 For the face to be deleted:
  - F.5.1 Select a 'best point' position for the introduction of a new point **IPNEW**.
  - F.5.2 Determine whether a point exists in the already generated grid that should be used in lieu of the new point. If there is such a point, set this point to **IPNEW** and continue searching (go to F.5.2).
  - F.5.3 Determine whether the element formed with the selected point **IPNEW** does not cross any given faces. If it does, select a new point as **IPNEW** and try again (go to F.5.3).
- F.6 Add the new element, point, and faces to their respective lists.
- F.7 Find the generation parameters for the new faces from the background grid.
- F.8 Delete the known faces from the list of faces.
- F.9 If there are any faces left in the front, go to F.4.

There are several interesting algorithmic aspects which should be mentioned:

- a) Extensive use is made of optimal data structures to perform the search operations involved. In particular, we use heap-lists to find the next face to be deleted (step F.4), quad-trees to find the closest given points to a new point (step F.5.2), and linked lists to find the faces adjacent to a given point (step F.5.3). We combine quad-trees and linked lists to find for any given location the values of generation parameters from the background grid (steps F.3 and F.7). The algorithmic complexity of the overall algorithm should be of  $O(N \log N)$ . In practice, we find it to be closer to  $O(N)$ , as we continuously delete domain points from the lists, and the subroutine-calls require some overhead.
- b) The checking of face-intersection is a non-trivial problem in 3-D. It also requires a large amount of CPU-time due to the algorithmic complexity involved. In order to

make this process faster, a layered face-checking approach was implemented [18]. This resulted in a significant reduction of CPU time.

More details about the implementation and the data structures used can be found in [17,18].

Examples include

a) Multi-Element Airfoil Configuration (2-D)

Figure 1 shows a multi-element airfoil case. Figure 1a gives the boundary information, Figure 1b the background grid used and Figure 1c the final generated grid.

b) Missile Launcher (3-D)

Figure 2 shows a generic missile launcher model. Only half the model is required for computational purposes. The surface definition was given by 39 points, 44 lines and 19 surface segments. The background grid had 48 points and 132 elements. Figure 2a shows the complete surface triangulation. The generated grid contains 14,508 points and 75,894 tetrahedrons. Figure 2b shows the grid along the axis of symmetry, and one can observe finer grid zonings close to the missile and the launcher.

### 3. THE FLOW SOLVER: FINITE-ELEMENT FLUX-CORRECTED TRANSPORT (FEM-FCT)

The design of flow solvers for compressible flows has reached a high degree of sophistication, as witnessed by the many publications dealing with this subject [25-27]. At present, the central question no longer is: 'will it work?', but rather: 'how well will it work for the class of problems to be simulated?'. Therefore, we define the design criteria we applied when constructing our Euler solver:

- a) The solver should be able to operate on unstructured grids.
- b) The solver should be able to operate on moving grids, so that body or interface movement can be simulated.
- c) The solver should be able to simulate transient compressible flow problems with strong shocks.
- d) The phase-accuracy of the solver should be better than second order, so that vortex propagation and linear discontinuities are not spread too fast in time.
- e) The solver should be fast, as transient simulations tend to require longer run-times than steady-state simulations.

Item a) implies that we can only discretize operators, and not stencils. Item b) implies that we must formulate the equations of motion for the fluid in an Arbitrary Lagrangian-Eulerian (ALE) [28] frame of reference. Item c) implies that the solver must have Total Variation Diminishing (TVD) [27,29] properties, and be of first-order accuracy near discontinuities. Item d) implies that for smooth flow regions, the flow solver must reverse to a third- or fourth-order accurate scheme in phase. Finally, item e) implies that if possible we ought not to use Riemann-solvers, as these require more CPU-time per update than ordinary schemes.

We start by writing the governing equations of compressible flow in the following ALE-form

$$\frac{\partial U}{\partial t} + \frac{\partial F_j^a}{\partial x_j} = S, \quad (1)$$

where the summation convention has been employed and

$$U = \begin{Bmatrix} \rho \\ \rho u_i \\ \rho e \end{Bmatrix}, \quad F_j^a = \begin{Bmatrix} \rho(u_j - w_j) \\ \rho u_i(u_j - w_j) + p\delta_{ij} \\ \rho(u_j - w_j)e + u_j p \end{Bmatrix}, \quad S = -\frac{\partial w_j}{\partial x_j} \begin{Bmatrix} \rho \\ \rho u_i \\ \rho e \end{Bmatrix}. \quad (2)$$

Here  $\rho$ ,  $p$ , and  $e$  denote the density, pressure and specific total energy of the fluid respectively, and  $u_i$ ,  $w_i$  are the components of the fluid and grid velocities in the direction  $x_i$  of a Cartesian coordinate system. The equation set is completed by the addition of the state equation

$$p = (\gamma - 1)\rho[e - \frac{1}{2}u_j u_j], \quad (3)$$

which is valid for a perfect gas, where  $\gamma$  is the ratio of the specific heats. We now focus on the TVD aspects of the flow solver. As is well known, for the compressible flows described by Eqn.(1), discontinuities in the variables may arise (e.g. shocks or contact discontinuities). Any numerical scheme of order higher than one will produce overshoots or ripples at such discontinuities (the so-called 'Godunov theorem'). The idea behind Flux-Corrected Transport (FCT), and more generally all TVD schemes, is to combine a high-order scheme with a low-order scheme in such a way that in regions where the variables under consideration vary smoothly (so that a Taylor expansion makes sense) the high-order scheme is employed, whereas in those regions where the variables vary abruptly the schemes are combined, in a conservative manner, in an attempt to ensure a monotonic solution. Note that even if the original partial differential equation is linear, the resulting scheme will be nonlinear. The temporal discretization of Eqn.(1) yields

$$U^{n+1} = U^n + \Delta U, \quad (4)$$

where  $\Delta U$  is the increment of the unknowns obtained for a given scheme at time  $t = t^n$ . Our aim is to obtain a  $\Delta U$  of as high an order as possible without introducing overshoots. To this end, we re-write Eqn.(4) as:

$$U^{n+1} = U^n + \Delta U^l + (\Delta U^h - \Delta U^l), \quad (5)$$

or

$$U^{n+1} = U^l + (\Delta U^h - \Delta U^l). \quad (6)$$



Here  $\Delta U^h$  and  $\Delta U^l$  denote the increments obtained by some high- and low-order scheme respectively, whereas  $U^l$  is the monotone, ripple-free solution at time  $t = t^{n+1}$  of the low-order scheme. The idea behind FCT is to limit the second term on the right-hand side of Eqn.(6):

$$U^{n+1} = U^l + \lim(\Delta U^h - \Delta U^l) , \quad (7)$$

in such a way that no new over/undershoots are created. More details on how the limiting is performed may be found in [30,31]. As the high-order scheme, we employ a two-step form [4,32] of the one-step Taylor-Galerkin schemes described in [1,3]. These schemes belong to the Lax-Wendroff class, and could be substituted by any other high-order scheme which appears more convenient, including implicit schemes. They have been chosen here, because they appear to offer the best accuracy per cost performance of all the schemes tried. Given the system of equations (1), we advance the solution from  $t^n$  to  $t^{n+1} = t^n + \Delta t$  as follows:

a) First step:

$$U^{n+\frac{1}{2}} = U^n + \frac{\Delta t}{2} \cdot \left[ S|^n - \frac{\partial F_j^a}{\partial x_j} \Big|^n \right] \quad (8)$$

b) Second step :

$$\Delta U^n = U^{n+1} - U^n = \Delta t \left[ S|^{n+\frac{1}{2}} - \frac{\partial F_j^a}{\partial x_j} \Big|^{n+\frac{1}{2}} \right] \quad (9)$$

The spatial discretization of Eqns.(8,9) is performed via the classic Galerkin weighted residual method [4,32], using linear elements, i.e. 3-noded triangles in 2-D and 4-noded tetrahedra in 3-D. For Eqn.(9) the following system of equations is obtained:

$$M_C \cdot \Delta U^n = R^n , \quad (10)$$

where  $M_C$  denotes the consistent mass matrix [1,3],  $\Delta U$  the vector of nodal increments and  $R$  the vector of added element contributions to the nodes. As  $M_C$  possesses an excellent condition number, Eqn.(10) is never solved directly, but iteratively, requiring typically three passes [1]. We can then recast the converged solution of Eqn.(10) into the following form:

$$M_L \cdot \Delta U^h = R + (M_L - M_C) \cdot \Delta U^h. \quad (11)$$

Here  $M_L$  denotes the diagonal, lumped mass-matrix (see [1]). We remark that this high-order scheme is better than second-order in phase-space, as the consistent mass adds additional information beyond nearest neighbors when iterating. Numerical experiments (see below) show that this scheme, when applied on a structured mesh, is comparable to a fourth-order accurate scheme. As the low-order scheme, we use the same discretization for

the fluxes and source-terms, but revert to a lumped mass and an added numerical diffusion term on the right:

$$M_L \cdot \Delta U^l = R + DIFF . \quad (12)$$

## NUMERICAL EXAMPLES

### a) Passive Advection of a Square Wave

This is the same example as was used by Boris and Book [33] to demonstrate the accuracy and monotonicity of their FCT-schemes. As the equation being solved (the transport equation) is linear, both amplification- and phase-errors can be identified easily. The wave extends over 20 gridpoints, and is convected with a Courant-number of  $C=0.2$  for 800 steps. In Figure 3 we compare the solutions obtained when using, in the high-order scheme, a lumped mass-matrix and a consistent mass-matrix. Observe that the consistent mass-matrix gives better phase-accuracy. After 800 steps the initial discontinuity is spread over only 5 gridpoints.

### b) Passive Advection in 2-D

This is the same example that Zalesak [34] used to test his FCT-algorithms. Again, as the equation solved is linear, both amplification and phase-errors can be identified easily. The problem statement may be found in [34]. The mesh used for this case, as well as the results obtained are depicted in Figure 4.

### c) Sod-Problem (1-D)

This classic example, taken from [35], solves the Riemann-problem for the compressible Euler equations in 1-D. The same grid as in [35] is employed, and the solutions are shown at times  $t=7.36$  and  $t=14.75$ . Figure 5 shows the results obtained for the described FEM-FCT Euler solver.

### d) Shock-Reflection at a Wall

This problem has also been used extensively to assess the accuracy of schemes used for the solution of steady state problems [29]. As in all the following steady-state examples, local timestepping was used. The problem statement, as well as the pressure distributions obtained for the original Taylor-Galerkin scheme and FEM-FCT are shown in Figure 6. Observe that the shocks are captured so sharply that the underlying grid structure becomes visible in the contour-plots. The steady state solution for this problem took 300 iterations, the residuals dropping 4 orders of magnitude. Figure 6d depicts the variation of the density along the line  $y=0.5$ , and, as one can see, no over/undershoots are present.

### e) Flow Past an Airfoil in Transonic Flow

This example shows that acceptable solutions can be achieved with the present algorithm for the transonic flow regime. The case at hand is a NACA-0012 airfoil, and the Mach number at infinity and angle of attack were set to  $M_\infty = 0.85$  and  $\alpha = 0.0$ . The grid-point distribution was taken from Jameson's FLO52-code [36], and corresponds to a 96 by 16 mesh. The  $c_p$ -distributions on the airfoil-surface obtained for FEM-FCT and

the original two-step Taylor-Galerkin scheme presented in [4,32] are given in Figure 7. Although the solution achieved by FEM-FCT is better than that of the ordinary Taylor-Galerkin scheme, for steady-state aerodynamic applications, where shocks are only locally important, the additional cost of the high-resolution schemes does not make them attractive for production runs. Adaptive refinement [4,7,11,32] is a much more effective way of obtaining sharp shocks for steady flows.

f) Supersonic Flow Past an Object in a Cavity (3-D)

This example shows a 3-D solution for a fairly complex geometry. The problem statement, as well as the grid employed and the solution obtained, may be seen in Figure 8. The grid consisted of 5,426 points and 27,462 tetrahedra. The free-stream Mach-number was set to  $M_\infty = 1.5$ . The flow impinges on the back wall of the cavity, creating a recirculation zone in the cavity. This is visible in the particle paths plotted in Figure 8c.

h) Transonic Flow Past Pathfinder in a Wind-Tunnel (3-D)

This example shows a 3-D solution for the Pathfinder wing-body-tail configuration in a windtunnel. The problem statement, as well as the grid employed and the solution obtained may be found in Figures 9a-c. The grid consisted of 10,280 points and 55,865 tetrahedra. The free-stream Mach-number was set to  $M_\infty = 0.82$ , and convergence was achieved in 2000 steps.

#### 4. ADAPTIVE REFINEMENT

A very attractive feature of unstructured grids is the ease with which adaptive refinement can be incorporated into them. The addition of further degrees of freedom does not destroy any previous structure. Thus, the flow solver requires no further modification when operating on an adapted grid. For many practical problems, the regions that need to be refined are extremely small as compared to the overall domain. Therefore, the savings in storage and CPU requirements typically range between 10-100 as compared to an overall fine mesh. We find that for the majority of the daily production-type runs, adaptive refinement makes the difference between being or not being able to run the problems to an acceptable accuracy in a reasonable time. Without it, we would be forced to use much coarser grids, with lower accuracy, for the same expense.

Any adaptive refinement scheme is composed of three main ingredients. These are

- 1) an optimal-mesh criterion,
- 2) an error indicator, and
- 3) a method to refine and derefine the mesh.

They give answers to the questions

- 1) how should the optimal mesh be ?,
- 2) where is refinement (derefinement) required ?, and
- 3) how should the refinement (derefinement) be accomplished ?

Many variants of each of these subtopics have been explored and shown to be useful for a certain class of problems [4,7,8,9-14,37]. Therefore, as was the case with the flow solvers, we need to define our design criteria before proceeding further. Again, we seek a method

that is efficient and reliable for transient compressible flow problems. This leads us to the following design criteria for the error indicator:

- a) The error indicator should be fast.
- b) The error indicator should be dimensionless, so that several 'key variables' can be monitored at the same time.
- c) The error indicator should be bounded, so that no further user intervention becomes necessary as the solution evolves.
- d) The error indicator should not only mark the regions with strong shocks to be refined, but also weak shocks, contact discontinuities and other 'weak features' in the flow.

For the refinement method, the design criteria are as follows:

- e) The method should be conservative, i.e. a mesh change should not result in the production or loss of mass, momentum or energy.
- f) The method should not produce elements that are too small, as this would reduce too severely the allowable timestep of the explicit flow solvers employed.
- g) The method should be fast. In particular, it should lend itself to some degree of parallelism.
- h) The method should not involve major storage overhead.

An error indicator that meets the design criteria a)-d) was proposed in [37]. In general terms, it is of the form

$$error = \frac{h^2 |second\ derivatives|}{h |first\ derivatives| + \epsilon |mean\ value|}$$

By dividing the second derivatives by the absolute value of the first derivatives the error indicator becomes bounded, dimensionless, and the 'eating up' effect of strong shocks is avoided. The terms following  $\epsilon$  are added as a 'noise' filter in order not to refine 'wiggles' or 'ripples' which may appear due to loss of monotonicity. The value for  $\epsilon$  thus depends on the algorithm chosen to solve the PDEs describing the physical process at hand. The multidimensional form of this error indicator is given by

$$E^I = \sqrt{\frac{\sum_{k,l} (\int_{\Omega} N_{,k}^I N_{,l}^J d\Omega \cdot U_J)^2}{\sum_{k,l} (\int_{\Omega} |N_{,k}^I| \left[ |N_{,l}^J U_J| + \epsilon (|N_{,l}^J| |U_J|) \right] d\Omega)^2}}, \quad (13)$$

where  $N^I$  denotes the shape-function of node I.

Two different methods for grid refinement have been explored. These are 1) local h-refinement, and 2) adaptive remeshing. Table 1 compares the relative merits of both approaches. We may summarize our experience with both approaches as follows:

- For steady-state or mildly unsteady problems, adaptive remeshing represents the best adaptive refinement method currently available. Particularly if large stretching ratios can be realized, it easily outperforms all other methods.

- For strongly unsteady problems, where a new grid is required every 5-10 timesteps, local h-refinement seems to be preferable. Several reasons can be given for this choice. Firstly, h-refinement is more robust than remeshing. The amount of things that can go wrong seems to be much less than when remeshing. Secondly, h-refinement is very well suited to vector- and parallel processors. Thirdly, conservation presents no problem for h-refinement.
- Table 1 also quotes CPU times measured on the CRAY-XMP-24 at NRL. While these times are approximate and could be improved, they indicate a trend. The described grid generator is a scalar procedure. Moreover, the introduction of a new point or element requires substantially more operations than the equivalent operation done with h-refinement. A partial solution to this problem is to generate first a coarser, yet stretched grid, and then to apply global h-refinement [8]. As vectorization of the global h-refinement is straightforward, the savings as compared to just remeshing are substantial (a factor of 4 in 2-D, a factor of 8 in 3-D).
- In our experiments adaptive remeshing maintained the conservation sums very well. The change during one mesh change was less than 0.01%. We attribute this very good performance to the fact that the elements close to shocks were uniform in size.
- The combination of both approaches should be pursued further. In this way, the advantages of each approach can be employed to its fullest extent.

	<u>H-Refinement</u>	<u>Remeshing</u>
- Interpolation/Conservation	easy	not easy
- Minimum h-size	easy	not easy
- Directional Refinement	not easy	easy
- Body/Interface Movement	not easy	easy
- Parallelizable	easy	not easy
- Timings ( $\mu\text{sec}/\text{pt.}/\text{grid}$ )	120	1800

Table 1: H-Refinement vs. Remeshing

## NUMERICAL EXAMPLES

### a) Shock Impinging on Two Obstacles

We consider a strong shock ( $M_s = 10.0$ ) coming from the left that collides with the two bodies shown in Figure 10a. Four levels of refinement were activated. Had the grid been refined uniformly, this would correspond to 152,320 points. For the run shown the highest number of gridpoints required was about 17,000, and during most of the computation

considerably less gridpoints were used. As the physics become more complicated, more grid points are required, and correspondingly larger portions of the domain are refined. The solutions obtained at different times are depicted in Figures 10b-c. We show the grid, the density contours, and a blow-up of the velocities at times  $T=4.0$ ,  $T=6.0$  and  $T=8.0$ . For the density contours about 100 levels were chosen, so that any 'wobble' in the plot corresponds to approximately 1% deviation from a smooth solution. The adaptive refinement procedure is capable of producing very accurate calculations with sharp, detailed resolution of flow structures.

#### b) Shock-Box Interaction

In this case we consider a weak shock ( $M_s = 1.4$ ) that interacts with a box some distance from the ground. A maximum of four layers was activated, but we also imposed a minimum h-size limit for the refinement. Thus, in the finest regions of the base mesh only three levels of refinement were used. The solutions obtained at different times are depicted in Figures 11a-c. Again, we typically show 60-80 contour levels for the relevant quantities. Besides the obvious shock reflections, one can also see the vortex shedding process that begins at the sharp corner of the box. More details and further studies of this class of problems may be found in [38].

#### c) Object Falling into Supersonic Free Stream

The problem statement is as follows: an object is placed in a cavity surrounded by a free stream at  $M_\infty = 1.5$ . After the steady-state solution is reached (time  $T=0.0$ ), a body motion is prescribed, and the resulting flowfield disturbance is computed. Adaptive remeshing was performed every 100 timesteps initially, while at later times the grid was modified every 50 timesteps. No subsequent h-refinement was used in this case, as the mesh adaptation process is not done very often. The maximum stretching ratio specified was  $S = 5.0$ . Figures 12a,b show two different stages during the computation at times  $T=20$  and  $T=175$ . Initially, the velocity flows counterclockwise around the object. At later times, this motion is reversed in the cavity. One can also see how the location and strength of the shocks changes due to the motion of the object. Notice how the directionality of the flow features is reflected in the mesh.

## 5. CONCLUSIONS

We have described several algorithms for the generation and adaptation of unstructured grids in two and three dimensions, as well as Euler solvers that operate on these grids. The main purpose of the paper was to demonstrate how unstructured grids may be employed advantageously for the economic simulation of both geometrically as well as physically complex flowfields. Numerous examples taken from daily production runs were shown, demonstrating the capabilities developed. Future developments will center on the following areas:

- extension of Euler-solvers to the Navier-Stokes equations,
- incorporation of chemistry in the current non-reacting flow models,
- extension of local adaptive h-refinement and adaptive remeshing to 3-D, and
- adaptive gridding for time-dependent, viscous flows.

## 6. ACKNOWLEDGEMENTS

This work was partially funded by the Office of Naval Research through the Naval Research Laboratory, the Applied and Computational Mathematics Program of DARPA, the NASA Johnson Space Center and SBIR-Grant-No. NAS1-18419.

We would also like to acknowledge the support of C. Gumbert (TAB, NASA LRC), who provided a number of very useful graphics interfaces for the IRIS.

## 7. REFERENCES

- [1] J. Donea - A Taylor Galerkin Method for Convective Transport Problems; *Int. J. Num. Meth. Eng.* 20, 101-119 (1984).
- [2] T.J.R. Hughes, M. Mallet and A. Mizukami - A New Finite Element Formulation for Computational Fluid Dynamics: II. Beyond SUPG; *Comp. Meth. Appl. Mech. Eng.* 54, 3, 341-355 (1986).
- [3] R. Löhner, K. Morgan and O.C. Zienkiewicz - The Solution of Nonlinear Systems of Hyperbolic Equations by the Finite Element Method; *Int. J. Num. Meth. Fluids* 4, 1043-1063 (1984).
- [4] R. Löhner, K. Morgan and O.C. Zienkiewicz - An Adaptive Finite Element Procedure for High Speed Flows; *Comp. Meth. Appl. Mech. Eng.* 51, 441-465 (1985).
- [5] M. Tanemura, T. Ogawa and N. Ogita - A New Algorithm for Three-Dimensional Voronoi Tessellation; *J. Comp. Phys.* 51, 191-207 (1983).
- [6] R. Löhner, K. Morgan and O.C. Zienkiewicz - Effective Programming of Finite Element Methods for CFD on Supercomputers; pp.117-125 in *The Efficient Use of Vector Computers with Emphasis on CFD* (W. Schönauer and W. Gentzsch eds.), Vieweg Notes on Numerical Fluid Mechanics, Vol 9, Vieweg Verlag (1985).
- [7] D.G. Holmes, S.H. Lamson and S.D. Connell - Quasi-3D Solutions for Transonic, Inviscid Flows by Adaptive Triangulation; Proc. ASME Gas Turbine Conf., Amsterdam, June 1988.
- [8] R. Löhner - Adaptive Remeshing for Transient Problems; accepted for publication in *Comp. Meth. Appl. Mech. Eng.* (1988).
- [9] K. Morgan, J. Peraire, R.R. Thareja and J.R. Steward - An Adaptive Finite Element Method for the Euler and Navier-Stokes Equations; AIAA-87-1172-CP (1987).
- [10] J.T. Oden, P. Devloo and T. Strouboulis - Adaptive Finite Element Methods for the Analysis of Inviscid Compressible Flow: I. Fast Refinement/Unrefinement and Moving Mesh Methods for Unstructured Meshes; *Comp. Meth. Appl. Mech. Eng.* 59, 327-362 (1986).
- [11] J. Peraire, M. Vahdati, K. Morgan and O.C. Zienkiewicz - Adaptive Remeshing for Compressible Flow Computations; *J. Comp. Phys.* 72, 449-466 (1987).
- [12] J. Peraire, K. Morgan, J. Peiro and O.C. Zienkiewicz - An Adaptive Finite Element Method for High Speed Flows; AIAA-87-0558 (1987).

- [13] M.M. Pervaiz and J.R. Baron - Spatio-Temporal Adaptation Algorithm for Two-Dimensional Reacting Flows; AIAA-88-0510 (1988).
- [14] R.A. Shapiro and E.M. Murman - Adaptive Finite Element Methods for the Euler Equations; AIAA-88-0034 (1988).
- [15] T.J. Baker - Three Dimensional Mesh Generation by Triangulation of Arbitrary Point Sets; AIAA-87-1124-CP (1987).
- [16] S.H. Lo - A New Mesh Generation Scheme for Arbitrary Planar Domains; *Int. J. Num. Meth. Eng.* 21, 1403-1426 (1985).
- [17] R. Löhner - Some Useful Data Structures for the Generation of Unstructured Grids; *Comm. Appl. Num. Meth.* 4, 123-135 (1988).
- [18] R. Löhner and P. Parikh - Generation of Three-Dimensional Unstructured Grids by the Advancing-Front Method; AIAA-88-0515 (1988).
- [19] J. Peraire, J. Peiro, L. Formaggia, K. Morgan and O.C. Zienkiewicz - Finite Element Euler Computations in Three Dimensions; AIAA-88-0032 (1988).
- [20] N. van Phai - Automatic Mesh Generation with Tetrahedron Elements; *Int. J. Num. Meth. Eng.* 18, 237-289 (1982).
- [21] M.A. Yerry and M.S. Shepard - Automatic Three-Dimensional Mesh Generation by the Modified-Octree Technique; *Int. J. Num. Meth. Eng.* 20, 1965-1990 (1984).
- [22] A. Bowyer - Computing Dirichlet Tessellations; *The Computer Journal* 24, 2, 162-167 (1981).
- [23] S.W. Sloan and G.T. Houlsby - An Implementation of Watson's Algorithm for Computing 2-Dimensional Delaunay Triangulations; *Adv. Eng. Software* 6, 4, 192-197 (1984).
- [24] D.F. Watson - Computing the N- Dimensional Delaunay Tessellation with Application to Voronoi Polytopes; *The Computer Journal* 24, 2, 167-172 (1981).
- [25] A. Jameson - The Evolution of Computational Methods in Aerodynamics; *ASME J. Appl. Mech.* 50, 1052-1069 (1983).
- [26] R. Löhner - Finite Elements in CFD: What Lies Ahead; *Int. J. Num. Meth. Eng.* 24, 1741-1756 (1987).
- [27] P. Woodward and P. Colella - The Numerical Simulation of Two-Dimensional Fluid Flow with Strong Shocks; *J. Comp. Phys.* 54, 115-173 (1984).
- [28] J. Donea - An Arbitrary Lagrangian-Eulerian Finite Element Method for Transient Dynamic Fluid-Structure Interactions; *Comp. Meth. Appl. Mech. Eng.* 33, 689-723 (1982).
- [29] H.C. Yee, R.F. Warming and A. Harten - Implicit Total Variation Diminishing (TVD) Schemes for Steady-State Calculations, *J. Comp. Phys.* 57, 327-360 (1985).



- [30] R. Löhner, K. Morgan, M. Vahdati, J.P. Boris and D.L. Book - FEM-FCT: Combining Unstructured Grids with High Resolution; accepted for publication in *Comm. Appl. Num. Meth.* (1988).
- [31] R. Löhner, K. Morgan, J. Peraire and M. Vahdati - Finite Element Flux-Corrected Transport (FEM-FCT) for the Euler and Navier-Stokes Equations; ICASE Rep. 87-4, *Int. J. Num. Meth. Fluids* 7, 1093-1109 (1987).
- [32] R. Löhner, K. Morgan, J. Peraire and O.C. Zienkiewicz - Finite Element Methods for High Speed Flows; AIAA-85-1531-CP (1985).
- [33] J.P. Boris and D.L. Book - Flux-corrected Transport. I. SHASTA, a Transport Algorithm That Works; *J. Comp. Phys.* 11, 38 (1973).
- [34] S.T. Zalesak - Fully Multidimensional Flux-Corrected Transport Algorithm for Fluids; *J. Comp. Phys.* 31, 335-362 (1979).
- [35] G. Sod - A Survey of Several Finite Difference Methods for Systems of Nonlinear Hyperbolic Conservation Laws; *J. Comp. Phys.* 27, 1-31 (1978).
- [36] A. Jameson, W. Schmidt and E. Turkel - Numerical Solution of the Euler Equations by Finite Volume Methods Using Runge-Kutta Time Stepping Schemes; AIAA-81-1259 (1981).
- [37] R. Löhner - An Adaptive Finite Element Scheme for Transient Problems in CFD; *Comp. Meth. Appl. Mech. Eng.* 61, 323-338 (1987).
- [38] J.D. Baum and R. Löhner - Numerical Simulation of Shock-Elevated Box Using an Adaptive Finite Element Shock Capturing Scheme, AIAA-89-0653.

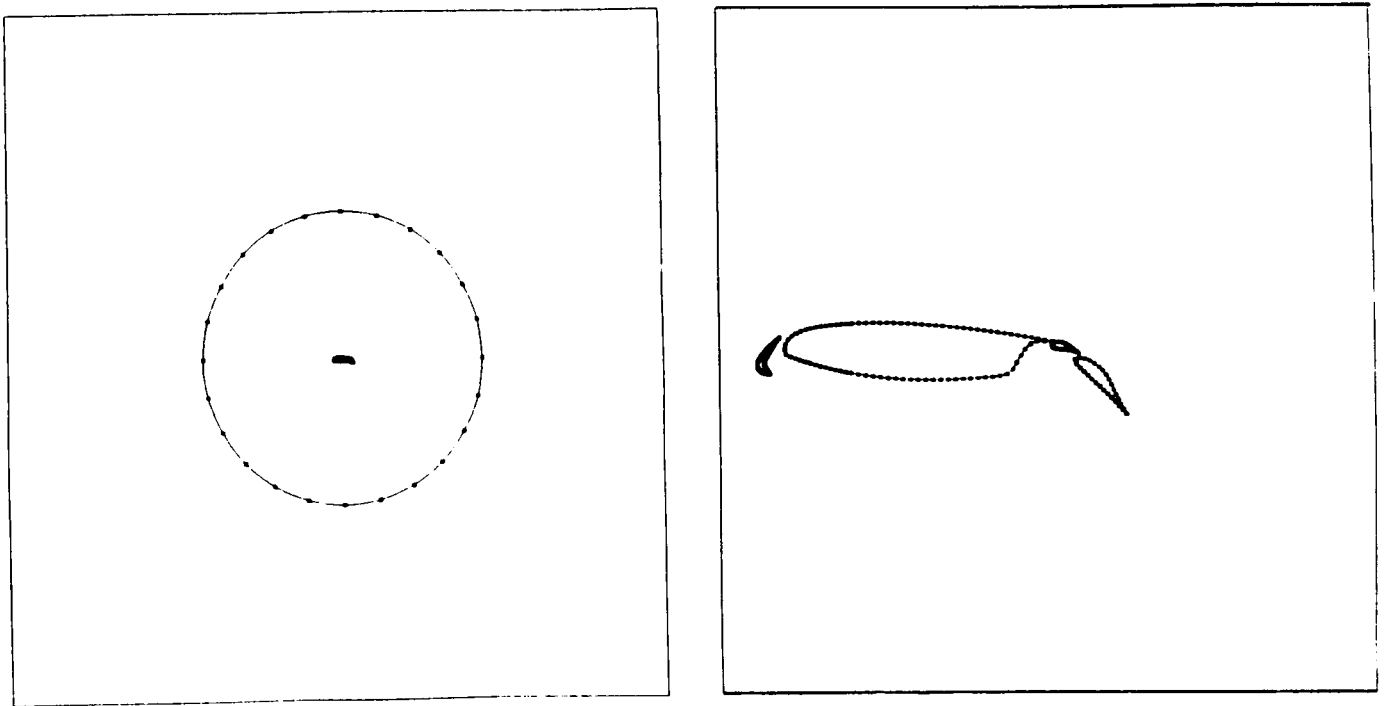


Figure 1(a). Multielement airfoil configuration: boundary information.

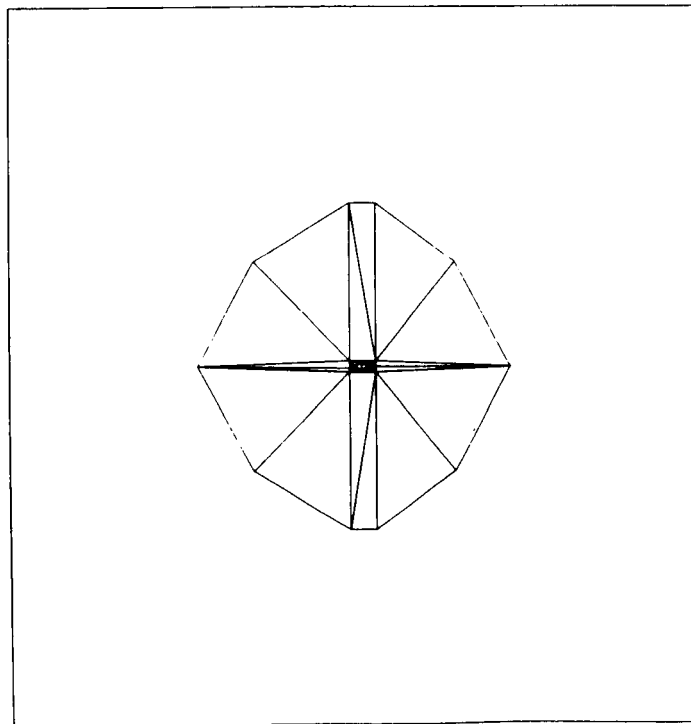


Figure 1(b). Multielement airfoil configuration: background grid.

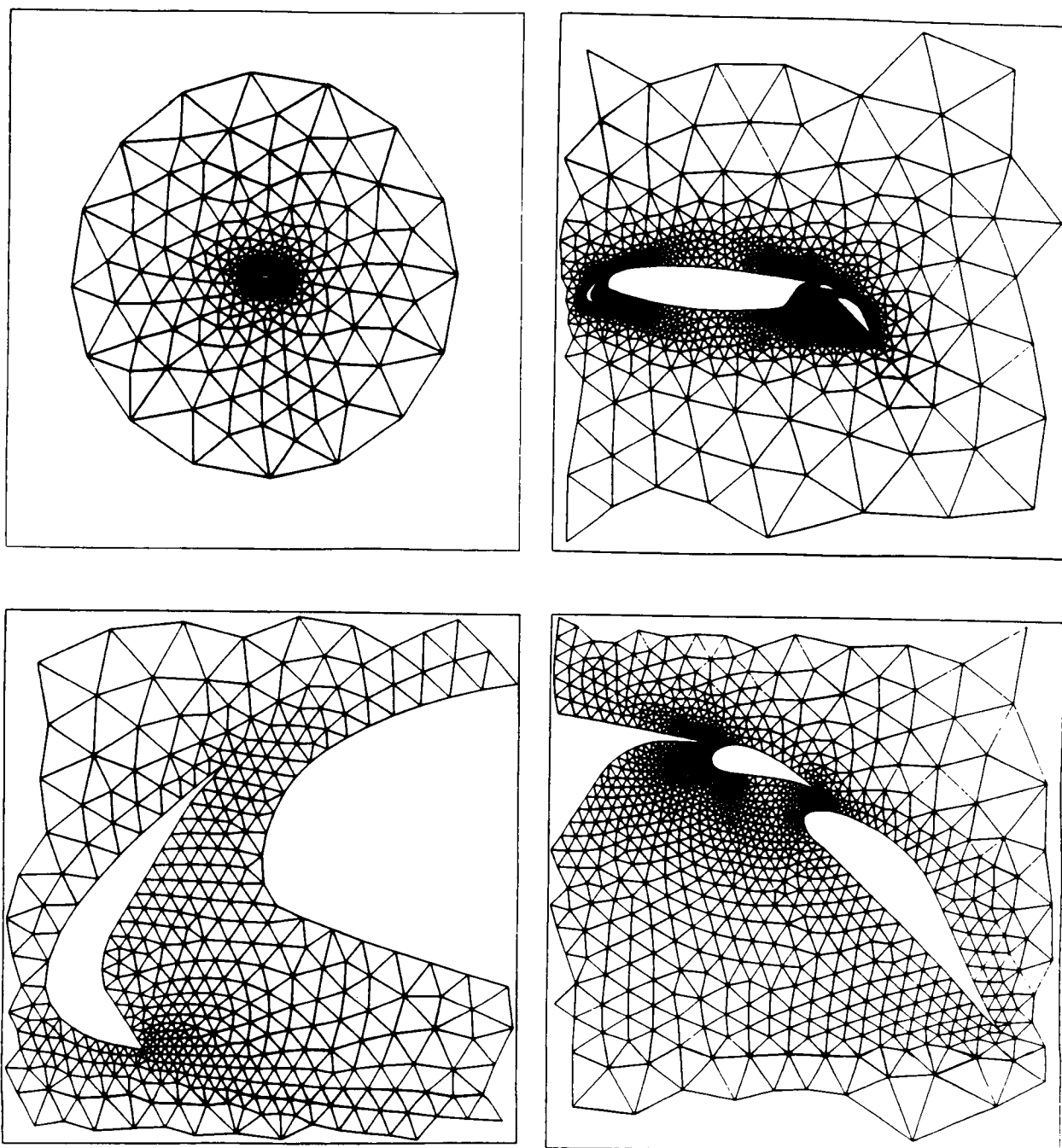


Figure 1(c). Multielement airfoil configuration: generated grid.

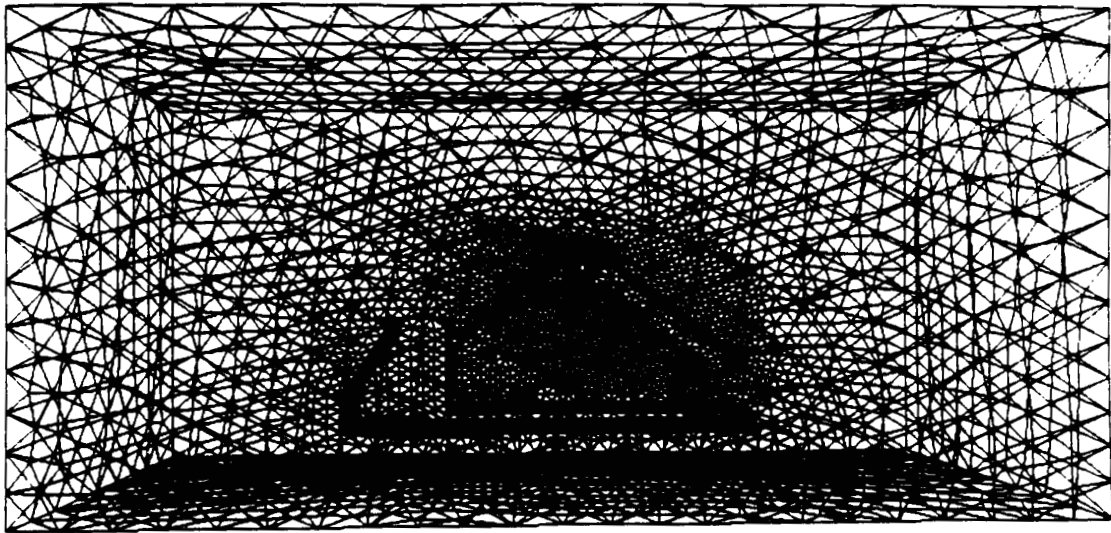


Figure 2(a). Missile launcher: surface triangulation.

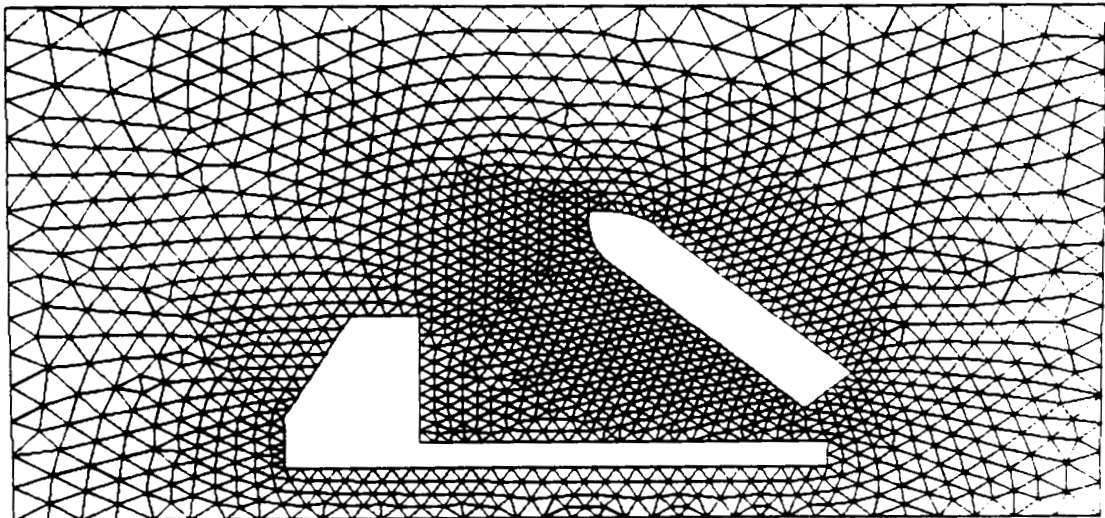
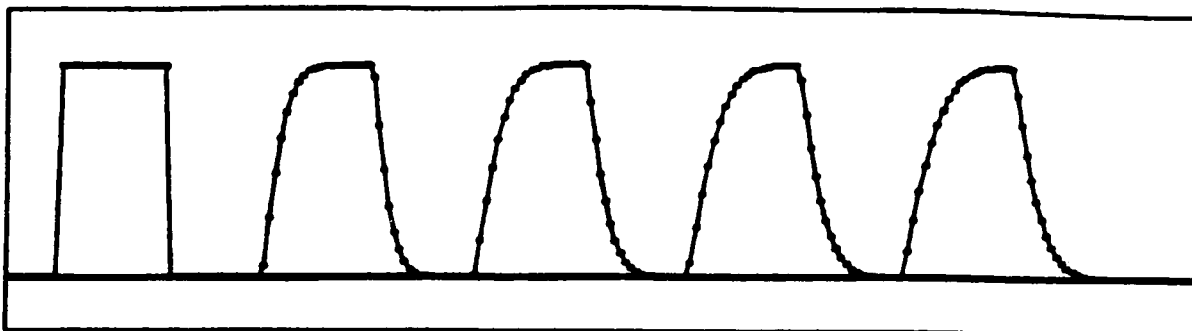
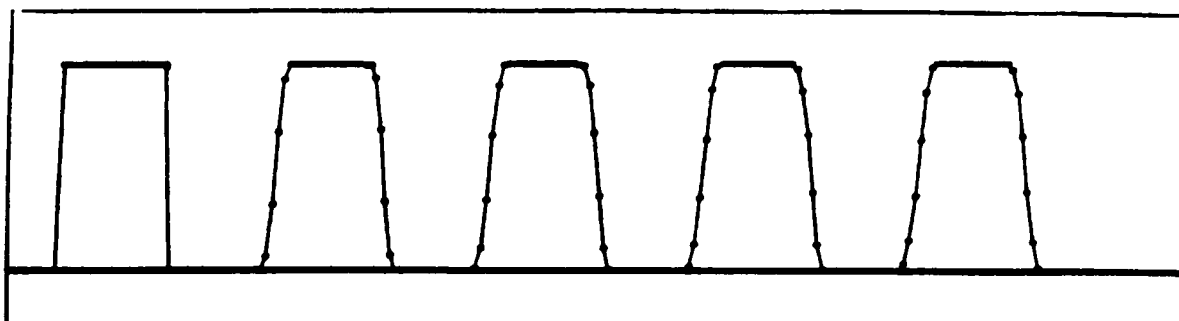


Figure 2(b). Missile launcher: grid in plane of symmetry.

ORIGINAL PAGE IS  
OF POOR QUALITY

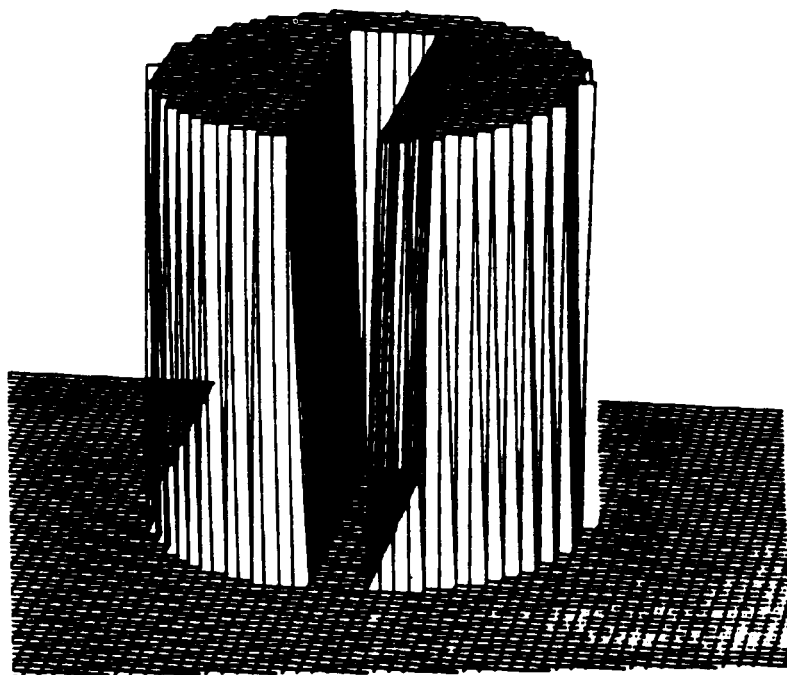


(a) High-order scheme: lumped-mass Taylor-Galerkin ( $niter=1$ ).

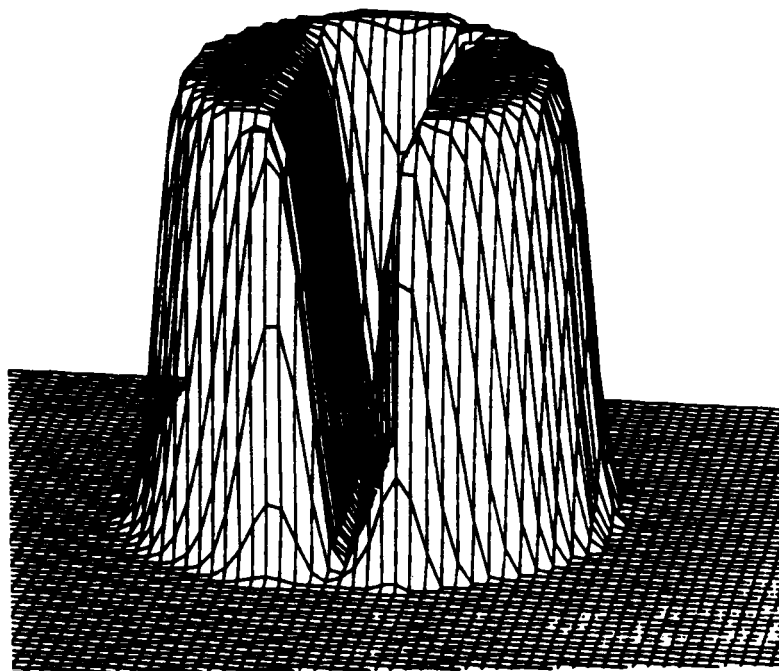


(b) High-order scheme: consistent-mass Taylor-Galerkin ( $niter=3$ ).

Figure 3. Passive advection of a square wave (1-D);  $C=0.2$ , plot every 200 steps.



(a) Solution at time  $t=0.0$



(b) Solution after 628 iterations ( $\frac{1}{4}$  revolution). The perspective view has been rotated with the cylinder.

Figure 4. Passive advection in 2-D: Zalesak's example.

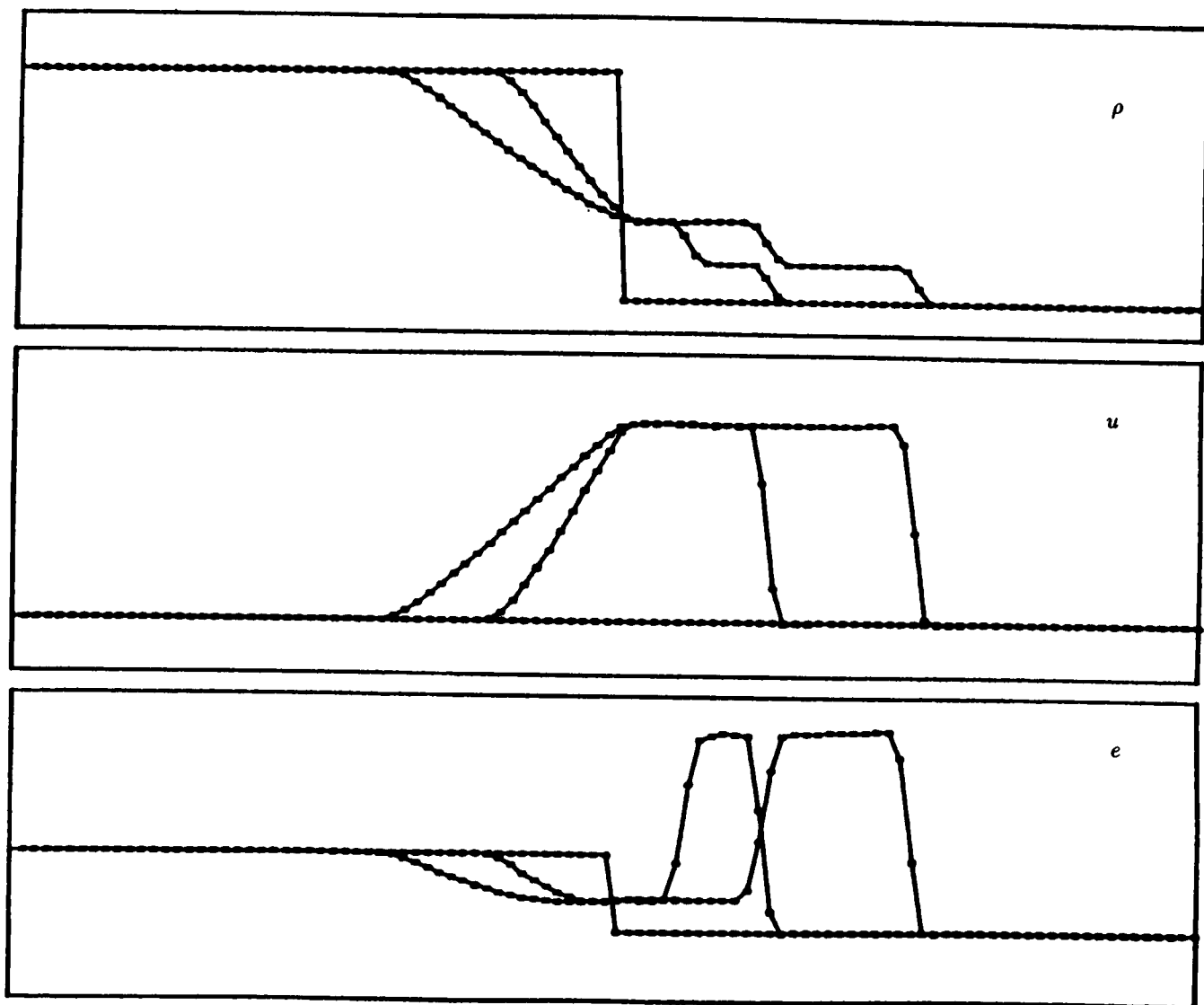
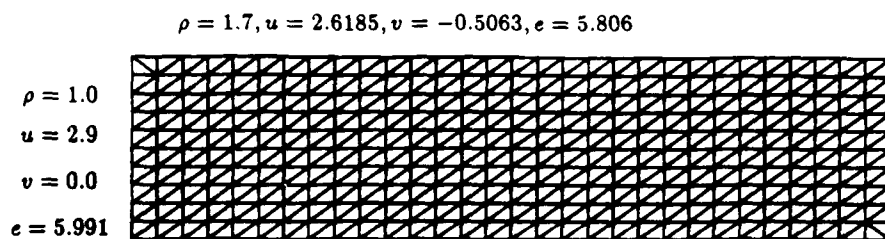


Figure 5. Sod-problem (1-D). Solutions at times  $t=7.37$  and  $t=14.75$ .



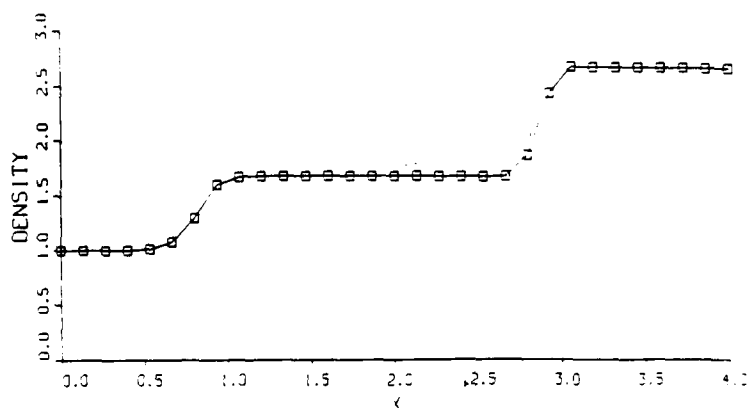
(a) Grid.



(b) Pressure distribution obtained for Taylor-Galerkin scheme [10,12] (C.I.=0.1).



(c) Pressure distribution obtained for FEM-FCT (C.I.=0.1).



(d) Density distribution along line  $y=0.5$ .

Figure 6. Shock reflexion at a wall (steady state).



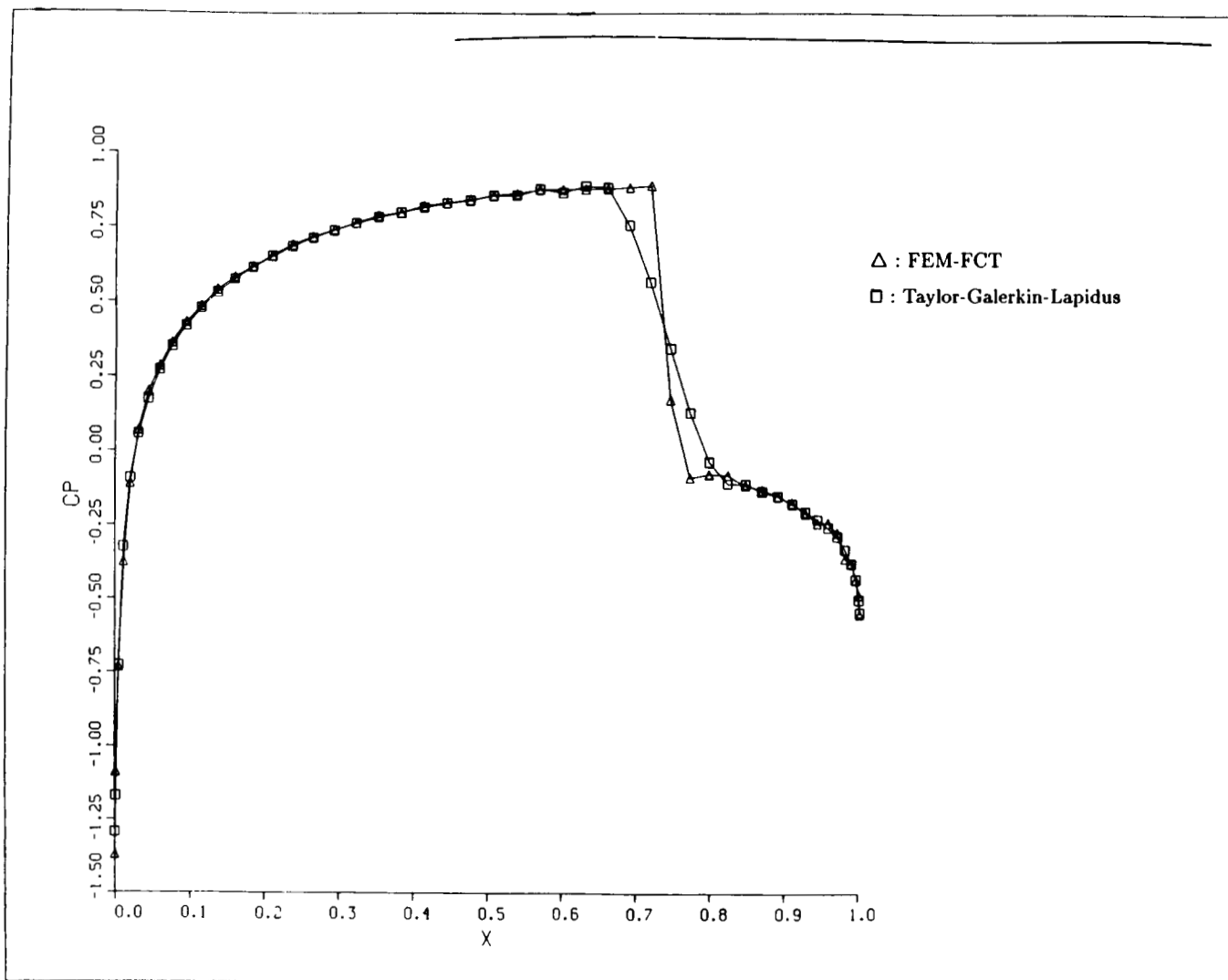
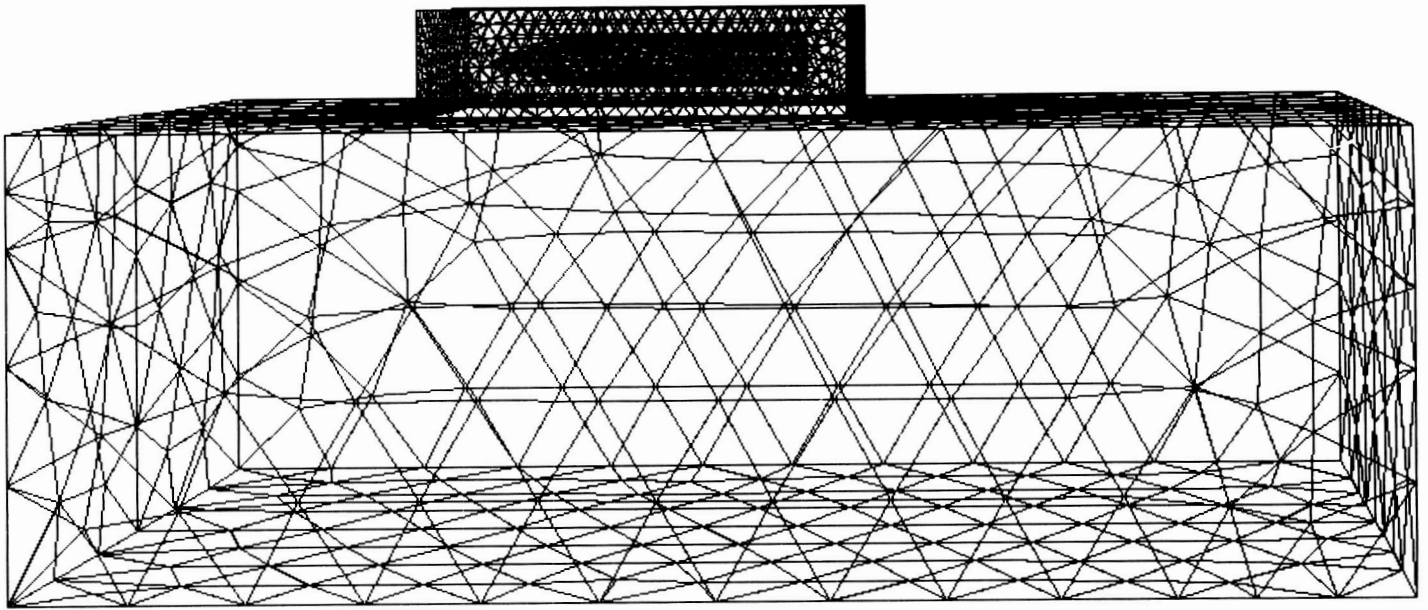
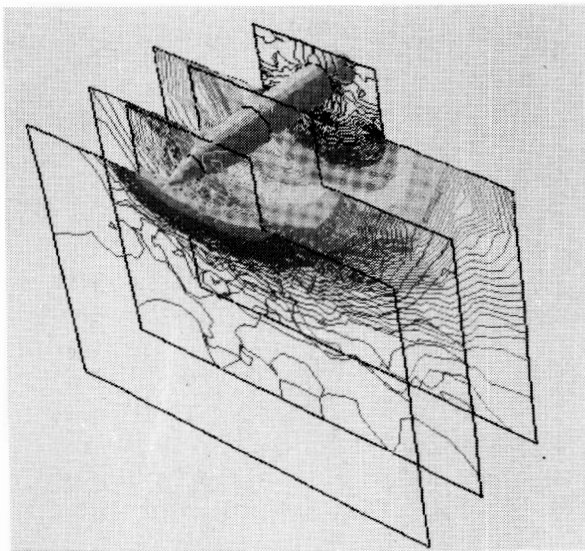


Figure 7. Comparison of Taylor-Galerkin-Lapudus and FEM-FCT for NACA-0012.

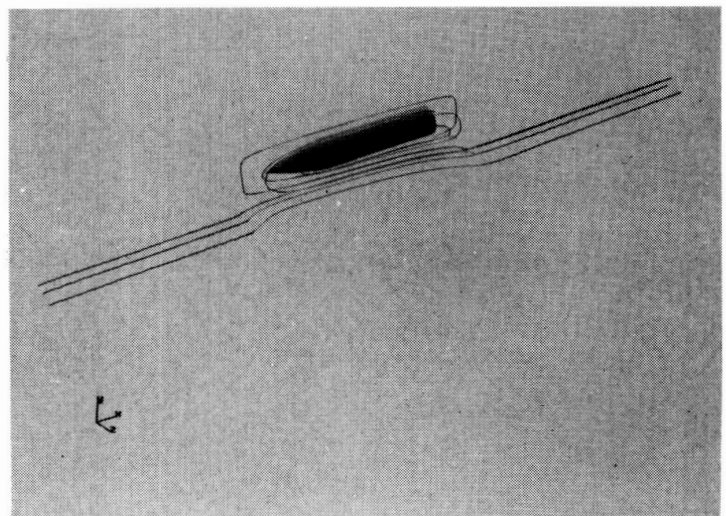
ORIGINAL PAGE IS  
OF POOR QUALITY



(a) Surface triangulation.

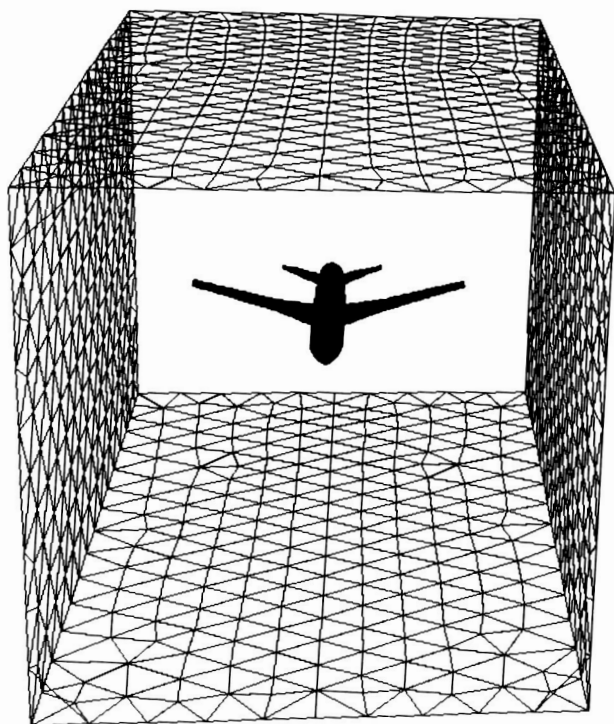


(b) Pressure contours in selected planes.

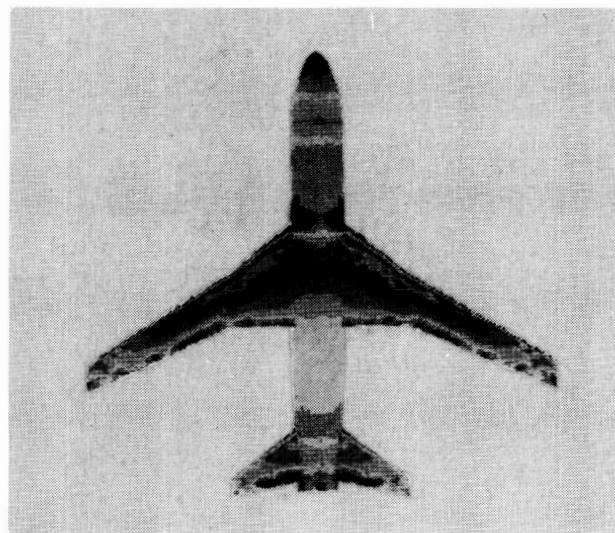


(c) Particle paths.

Figure 8. Supersonic flow past an object in cavity.



(a) Surface triangulation.



(b) Pressure contours.

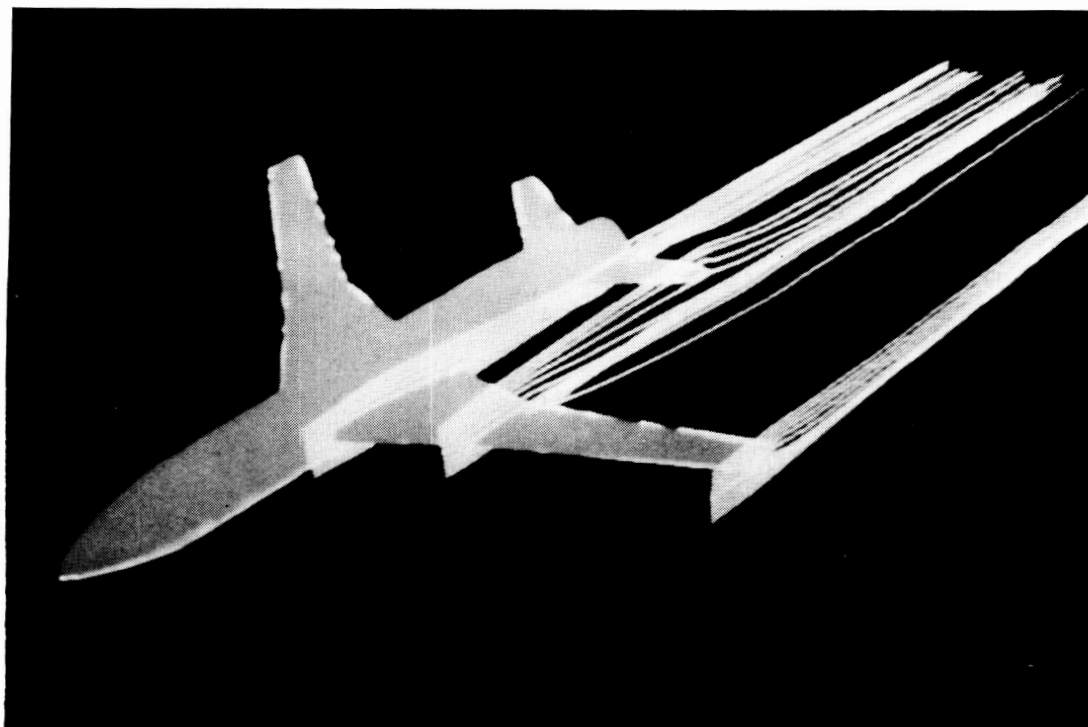


Figure 9. Transonic flow past Pathfinder in tunnel.

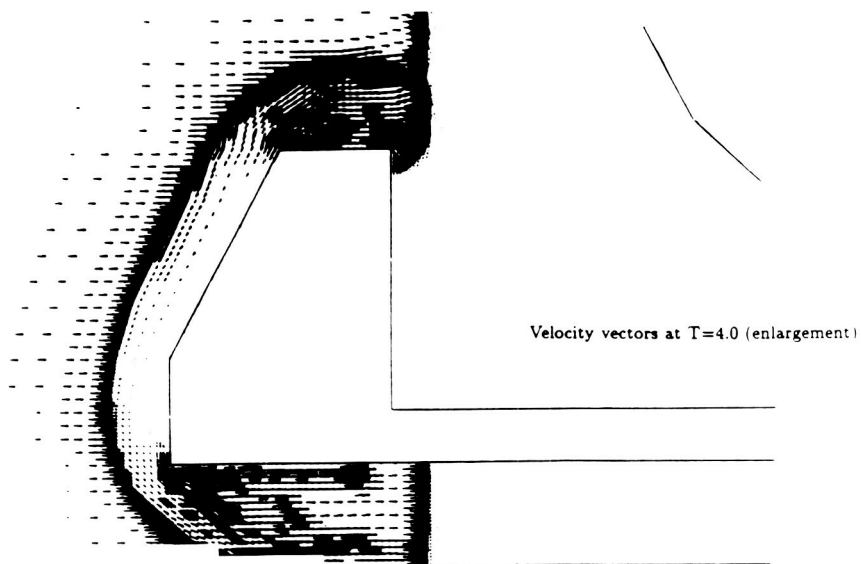
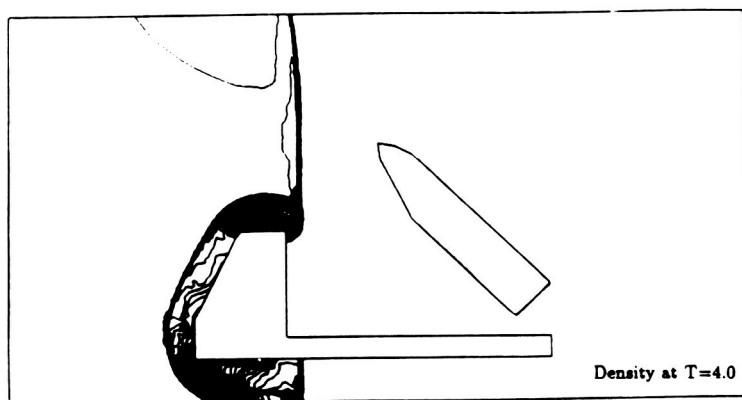
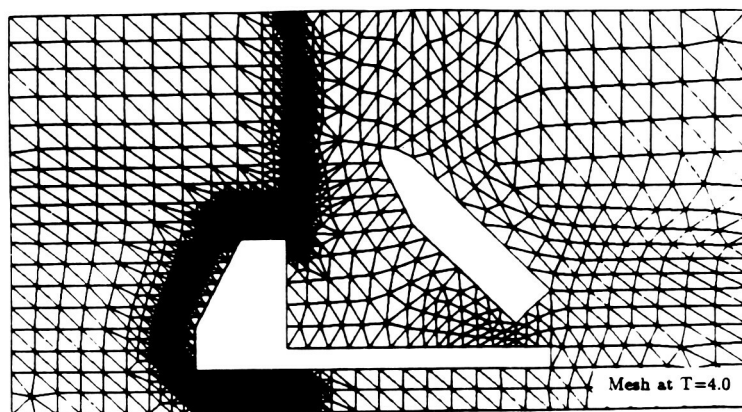


Figure 10(a). Shock impinging on two obstacles.

ORIGINAL PAGE IS  
OF POOR QUALITY

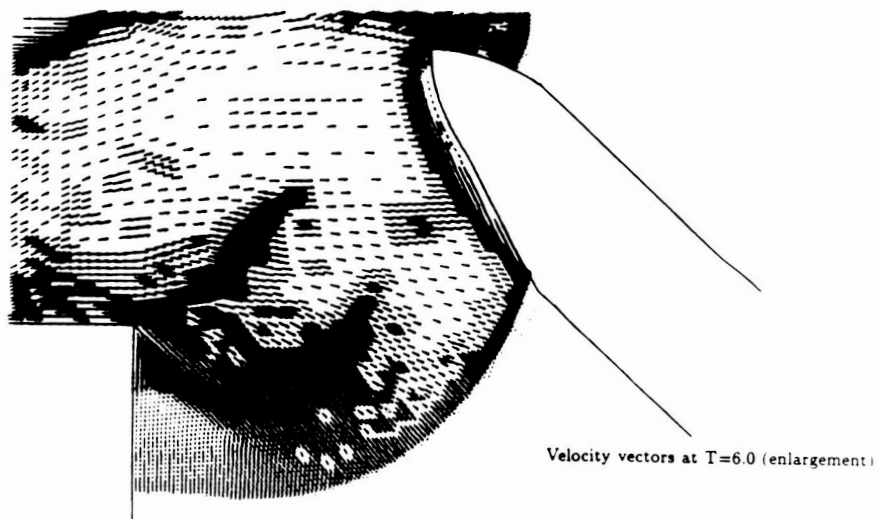
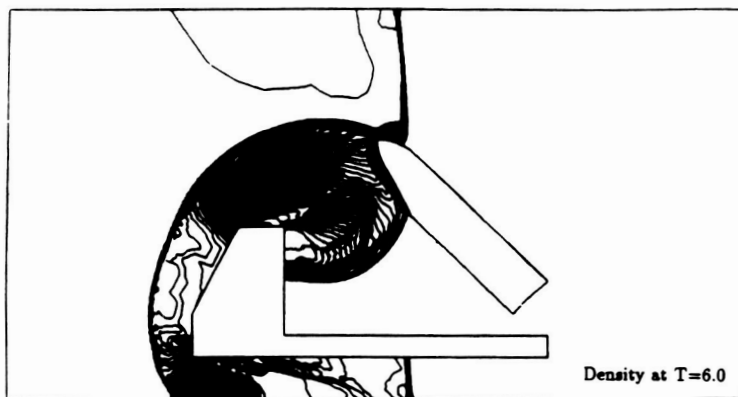
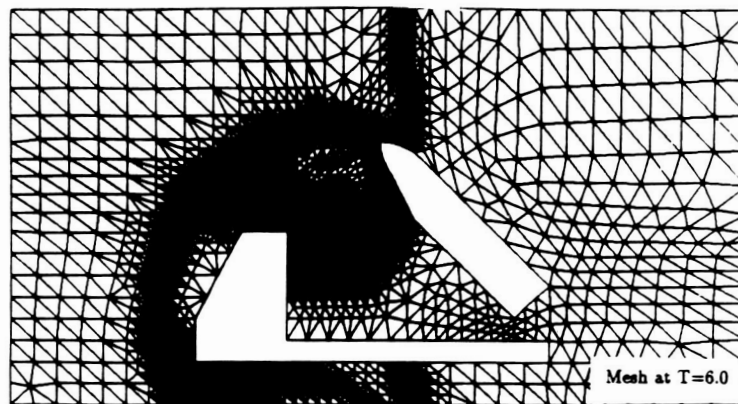


Figure 10(b). Shock impinging on two obstacles.

ORIGINAL PAGE IS  
OF POOR QUALITY

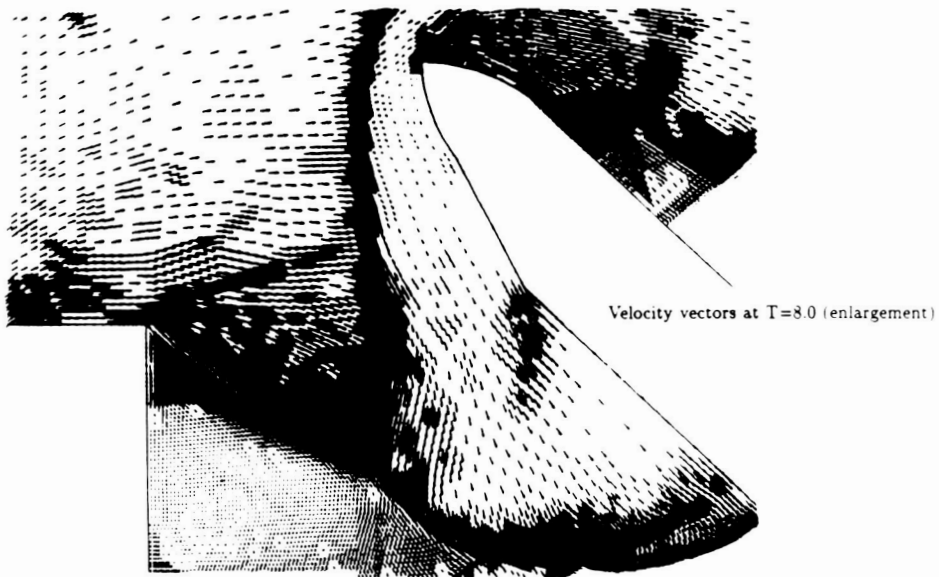
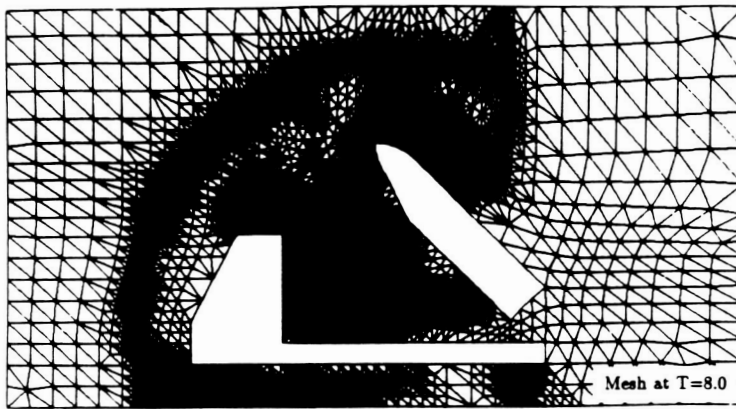
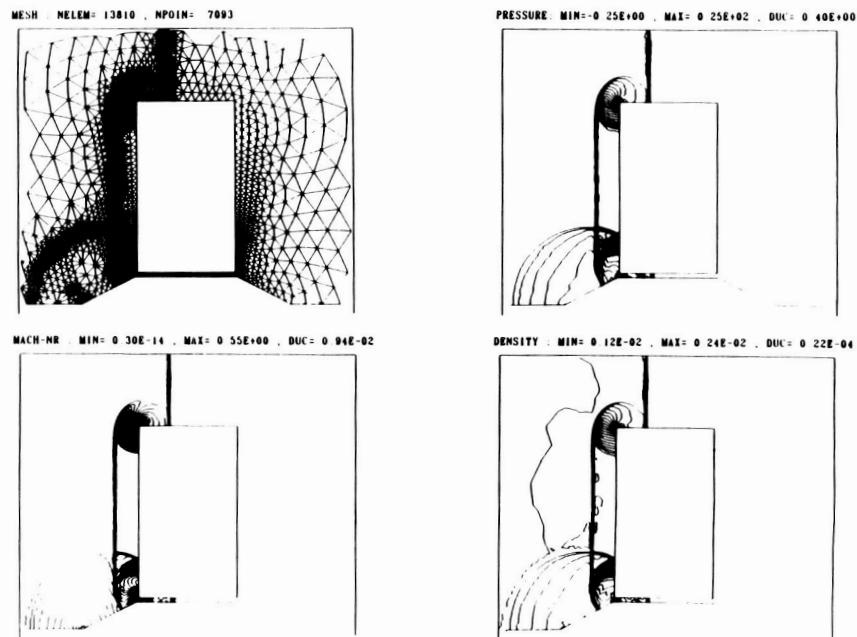


Figure 10(c). Shock impinging on two obstacles.

# SHOCK INTERACTION WITH AN ELEVATED RAIL CAR

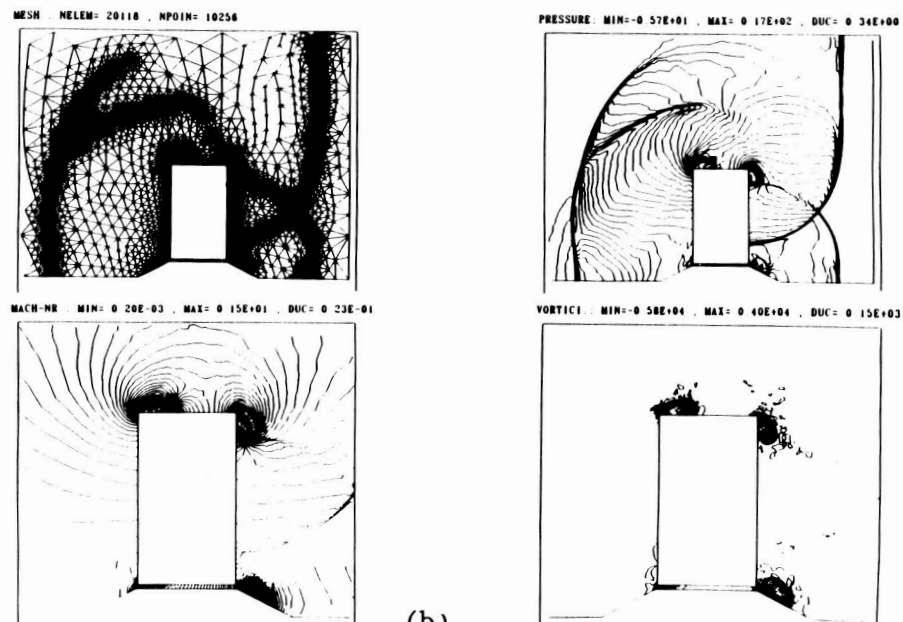
$t=6.0$  ms



(a)

# SHOCK INTERACTION WITH AN ELEVATED RAIL CAR

$t=22.0$  ms



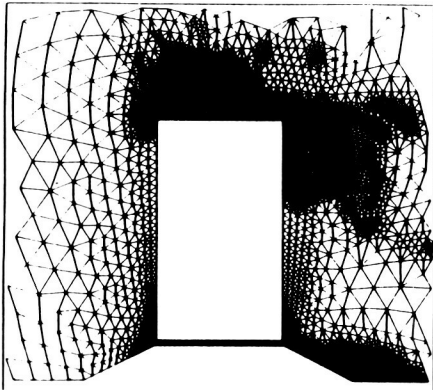
(b)

Figure 11. Shock-box interaction.

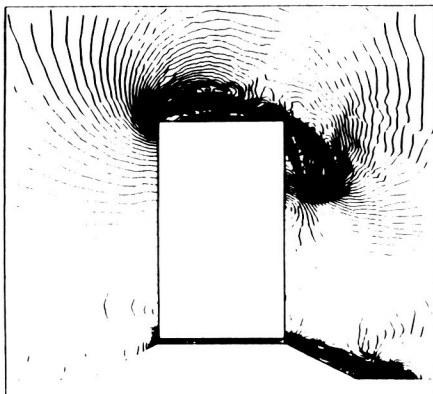
# SHOCK INTERACTION WITH AN ELEVATED RAIL CAR

$t=38.0$  ms

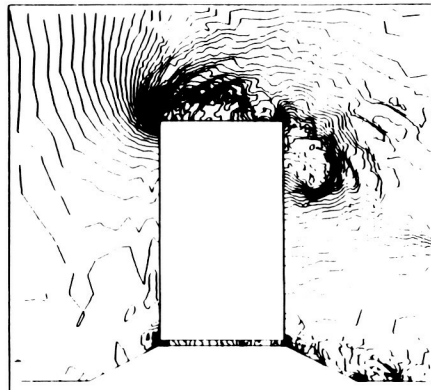
MESH : NELEM= 16522 , NPOIN= 8477



MACH-NR : MIN= 0.57E-03 , MAX= 0.10E+01 , DUC= 0.17E-01



PRESSURE: MIN=-0.32E+01 , MAX= 0.10E+02 , DUC= 0.22E+00



VORTICI : MIN=-0.65E+04 , MAX= 0.30E+04 , DUC= 0.16E+03

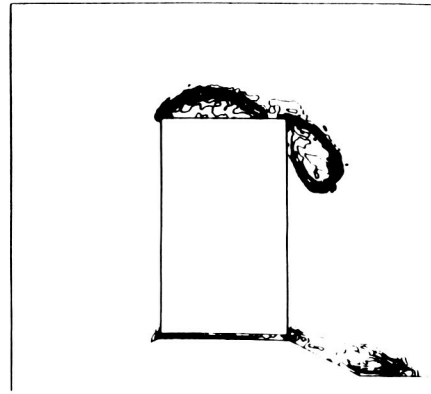
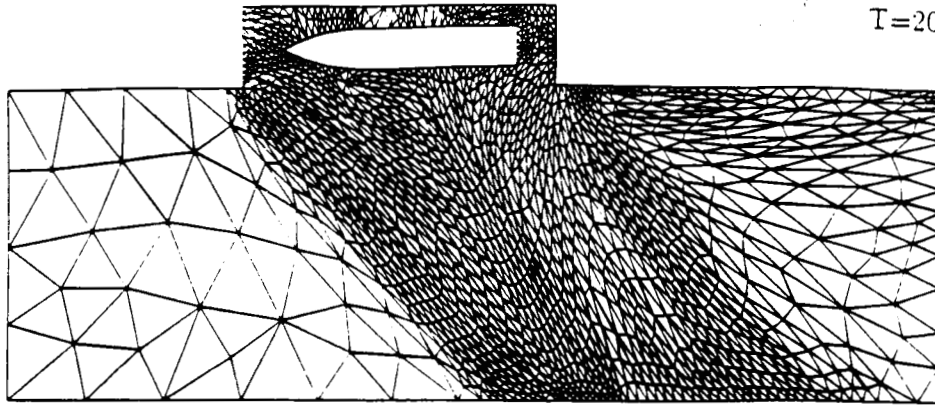


Figure 11(c) Shock-box interaction (concluded).

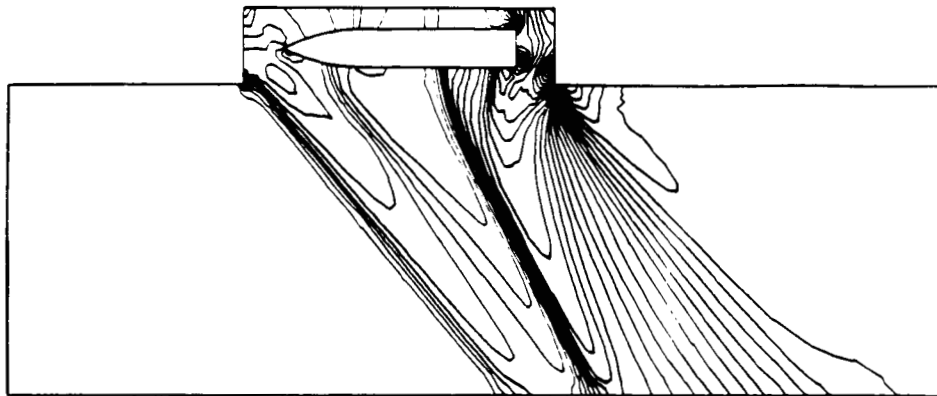
ORIGINAL PAGE IS  
OF POOR QUALITY



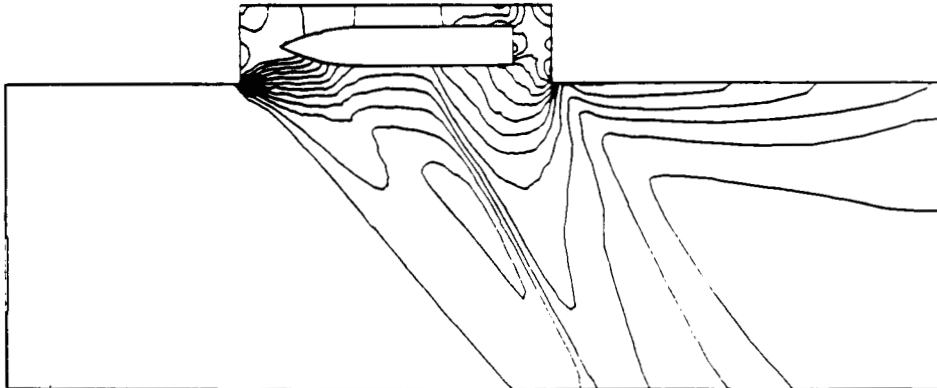
$T=20$



Mesh: NELEM=2264. NPOIN=1251

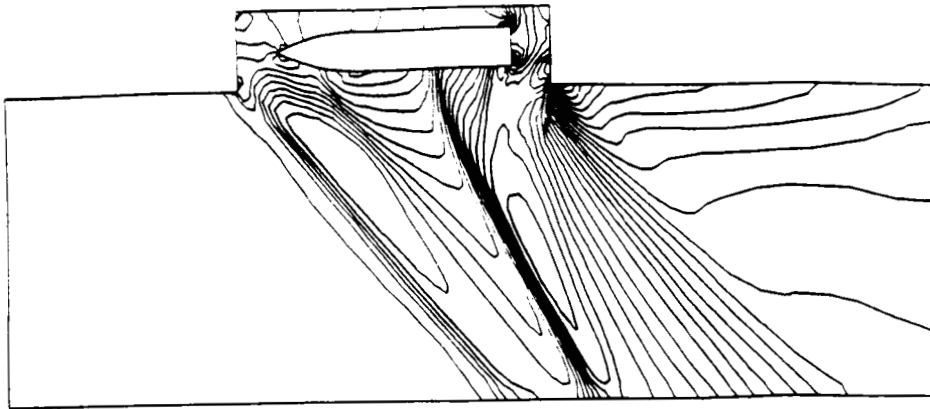


Pressure: Min=0.60, Max=2.30, Duc=0.05

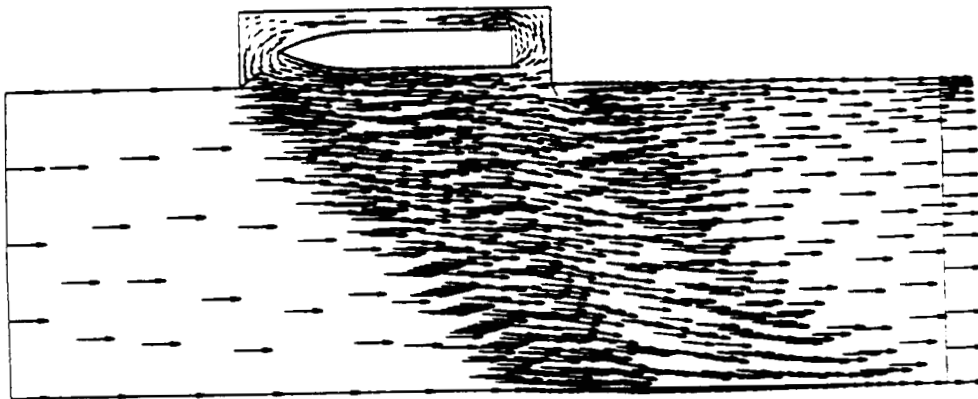


Mach-Nr.: Min=0.00, Max=1.60, Duc=0.10

Figure 12(a). Object falling into  $Ma = 1.5$  free stream,  $T = 20$ .



Density: Min=0.81, Max=2.20, Duc=0.05

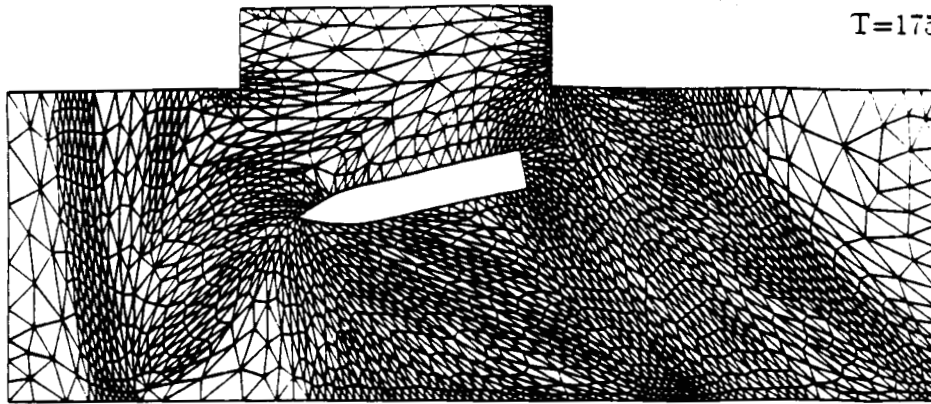


Velocity Vectors

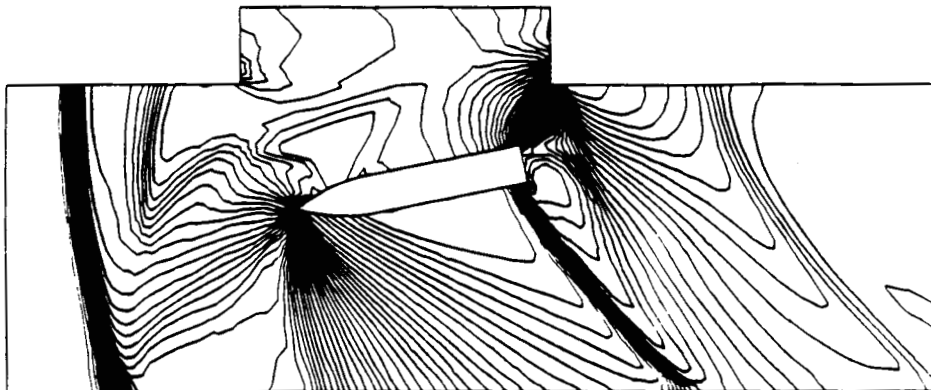
Figure 12(a). Concluded.

**ORIGINAL PAGE IS  
OF POOR QUALITY**

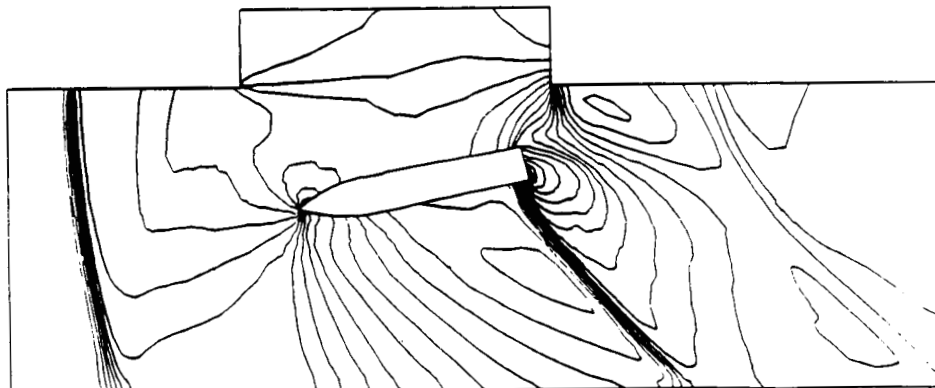
$T=175$



Mesh: NELEM=3047, NPOIN=1648

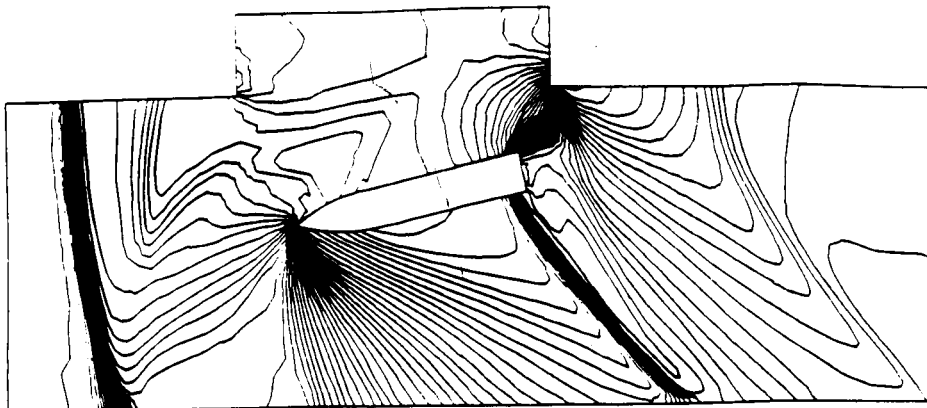


Pressure: Min=0.40, Max=3.30, Duc=0.05

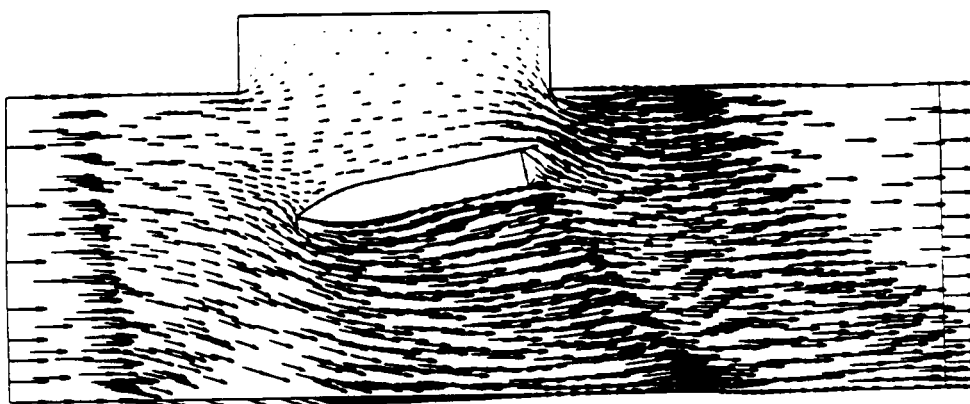


Mach-Nr.: Min=0.00, Max=1.90, Duc=0.10

Figure 12(b). Object falling into  $Ma = 1.5$  free stream,  $t = 175$ .



Density: Min=0.56, Max=3.10, Duc=0.05



Velocity Vectors

Figure 12(b). Concluded.

ORIGINAL PAGE IS  
OF POOR QUALITY



## Report Documentation Page

1. Report No. NASA CP-3020, Vol. I, Part 1		2. Government Accession No.		3. Recipient's Catalog No.	
4. Title and Subtitle  Transonic Symposium: Theory, Application, and Experiment				5. Report Date March 1989	
				6. Performing Organization Code	
7. Author(s)  Jerome T. Foughner, Jr., Compiler				8. Performing Organization Report No. L-16501	
				10. Work Unit No. 505-60-11-01	
9. Performing Organization Name and Address NASA Langley Research Center Hampton, VA 23665-5225				11. Contract or Grant No.	
				13. Type of Report and Period Covered Conference Publication	
12. Sponsoring Agency Name and Address National Aeronautics and Space Administration Washington, DC 20546-0001				14. Sponsoring Agency Code	
15. Supplementary Notes					
16. Abstract  In order to assess the state of the art in transonic flow disciplines and to glimpse at future directions, the NASA Langley Research Center held a Transonic Symposium on April 19-21, 1988. Emphasis was placed on steady, three-dimensional external, transonic flow and its simulation, both numerically and experimentally.  Papers were presented by researchers from NASA, industry, and universities. The symposium included technical sessions on wind tunnel and flight experiments; computational fluid dynamics applications (industry overviews and configuration analysis design); inviscid methods and grid generation; viscous methods and boundary-layer stability; and wind tunnel techniques and wall interference.  The proceedings are published in two volumes as follows because of the range of classifications: Volume I, Unclassified (Parts 1 and 2); and Volume II, Unclassified, FEDD Restricted.					
17. Key Words (Suggested by Author(s)) Aerodynamics External transonic flow Numerical simulation Experimental simulation				18. Distribution Statement  Unclassified - Unlimited  Subject Category 02	
19. Security Classif. (of this report) Unclassified		20. Security Classif. (of this page) Unclassified		21. No. of pages 424	
				22. Price A18	